Physics of Atomic Nuclei, Vol. 65, No. 1, 2002, pp. 1–10. Translated from Yadernaya Fizika, Vol. 65, No. 1, 2002, pp. 3–12.
Original Russian Text Copyright © 2002 by Ishkhanov, Kapitonov, Tutyn', Shirokov.

NUCLEI
Experiment

New Data on the Mechanism of Decay of the Giant Dipole Resonance in the ^{58}Ni Nucleus

B. S. Ishkhanov, I. M. Kapitonov, I. A. Tutyn', and E. V. Shirokov

Institute of Nuclear Physics, Moscow State University, Vorob'evy gory, Moscow, 119899 Russia
Received November 27, 2000; in final form, April 25, 2001

Abstract—New data on the mechanism of decay of the giant dipole resonance in the ^{58}Ni nucleus are obtained from an analysis of the experimental cross sections for the photonucleon reactions $^{58}\mathrm{Ni}(\gamma, p_i)^{57}\mathrm{Co}$ and $^{58}\mathrm{Ni}(\gamma, n_i)^{57}\mathrm{Ni}$. The method used in this analysis takes into account both the energy spread of the dipole strength concentrated in various isospin components of the giant dipole resonance and the spread of the spectroscopic strength of the populated nucleon-hole states over the levels of the final nuclei. The entire body of experimental spectroscopic information about the levels of the final nuclei ^{57}Co and ^{57}Ni is employed. It is found that the probability of the semidirect mechanism of decay of the giant dipole resonance in the ^{57}Ni nucleus lies in the range 0.16–0.3. The probability of semidirect processes is much higher in the (γ, n) channel (0.28–0.62) than in the (γ, p) channel (0.07–0.17).
© 2002 MAIK "Nauka/Interperiodica".

1. INTRODUCTION

Modern investigations of a giant dipole resonance (GDR) in nuclei are expected to furnish information about its shell structure and decay mechanism. As a matter of fact, the only type of experiments that presently makes it possible to obtain such data is that which admits a separation of partial photonuclear channels—that is, channels of GDR decay that lead to the population of individual levels of the final nucleus. Since a GDR decays predominantly via nucleon emission, it is important above all to have information about (γ, p_i) and (γ, n_i) reactions, where the index i numbers levels of the final nucleus $A-1$ from the ground-state level for which $i = 0$. The energies of levels of the final nucleus that are populated in GDR decays are much lower than the energies of decaying GDR states. Much is known about the structure of these low-lying states populated in GDR decays. This information comes from independent data of other experiments—in particular, from precision experiments that studied one-nucleon-transfer reactions. In many cases, knowledge of the nature of the populated states enables one to obtain, without resort to involved theoretical calculations, reliable information about the shell structure of high-lying GDR states and about the mechanism of their decay.

Strategies adopted in such investigations were described in detail elsewhere (for an overview, see [1–3]). For the first time, the concepts underlying the interpretation of partial photonuclear experiments were formulated in [4]. Later on, they were refined, and the most comprehensive account of these can be found in [3, 5].

In order to study partial photonucleon channels, symbolized by convention as (γ, p_i) and (γ, n_i), one has to employ the spectrometry of photonucleons or the spectrometry of γ' rays removing the excitation of final nuclei $A-1$. In the latter case, use is made of the term "deexcitation" and of the notation $(\gamma, x\gamma')$, where x is an undetected particle emitted from the nucleus (most often, this is a nucleon). Experiments that explore deexcitation processes are especially important, since they make it possible to fix reliably individual levels populated in the final nucleus.

The majority of present-day (γ, p_i) and (γ, n_i) experiments have been performed for $1d2s$-shell nuclei ($A = 16$–40). A breakthrough in qualitatively understanding the origin of the GDR in light nuclei was made owing to these experiments—in particular, the decisive role of the configuration-splitting phenomenon in the formation of the GDR was revealed [1, 6].

Among heavier nuclei, only two $1f2p$-shell nuclei, ^{45}Sc and ^{58}Ni, were investigated by the methods of partial photodisintegration (see [6, 10] and [7, 10], respectively). Especially rich information is available for the ^{58}Ni nucleus, which was studied both in experiments relying on the spectrometry of protons [8] and neutrons [9] and in deexcitation experiments [7, 10]. An interpretation of data from these experiments was already given in [7]. Since then, however, a more efficient method for data analysis has been developed and

data on the structure of the populated states of final nuclei $A-1$ have become significantly vaster; owing to this, much more comprehensive and more detailed information about the GDR in the ^{58}Ni nucleus can be extracted from available data on the (γ, p_i) and (γ, n_i) reactions on this nucleus. Here, we aim at obtaining precisely this information.

2. INPUT DATA

The analysis described in the present article has been performed on the basis of data on 26 partial photonucleon reactions $^{58}\mathrm{Ni}(\gamma, p_i)^{57}\mathrm{Co}$ and $^{58}\mathrm{Ni}(\gamma, n_i)^{57}\mathrm{Ni}$ in the GDR region. These data were obtained in a single $(\gamma, x\gamma')$ experiment [7, 10] and were supplemented with information about the (γ, p_0) and (γ, n_0) channels from photonucleon-spectrometry experiments [9, 11].

The integrals of these cross sections over the GDR region in the ^{58}Ni nucleus,

$$\sigma^{\mathrm{int}}(i) = \sigma^{\mathrm{int}}(\gamma, x_i) = \int_0^{E_m} \sigma(\gamma, x_i) dE,$$

where $x = p$ or n and $E_m = 32$ MeV, are given in Tables 1 and 2, along with the spectroscopic features of the populated levels of the final nuclei ^{57}Co and ^{57}Ni (these features were extracted from data on one-nucleon-pickup reactions and are contained in the ENSDF international nuclear-data file [12]). For each populated level, we indicate the excitation energy E_i, the spin–parity J^π, the hole configuration nl_j with respect to the ground state of the target nucleus ^{58}Ni (here, n is the principal quantum number; l is the orbital angular momentum of the nucleon in the shell being considered; and j is its total angular momentum, $j = l + 1/2$ or $l - 1/2$), and the quantity $C_i^2 S_i$ [where S_i is the relevant spectroscopic factor and $C^2 = 2T/(2T+1)$, with T being the isospin of the populated level]. In addition, we have used data on the total (inclusive) photoproton cross section $\sigma(\gamma, p)$ and the total (inclusive) photoneutron cross section $\sigma(\gamma, n)$ as functions of the excitation energies of the target nucleus from the experiments reported in [13–15] and on their sum $\sigma(\gamma, p) + \sigma(\gamma, n)$, which is an accurate approximation to the photoabsorption cross section. These photonucleon cross sections are related to the partial (exclusive) cross sections $\sigma(\gamma, p_i)$ and $\sigma(\gamma, n_i)$, which were discussed above, by the equations

$$\sigma(\gamma, p) = \sum_{i=0} \sigma(\gamma, p_i), \quad \sigma(\gamma, n) = \sum_{i=0} \sigma(\gamma, n_i).$$

More detailed information about all experiments that studied the photodisintegration of ^{58}Ni and which are of importance for us can be found in [7, 10].

An essentially new element in the present study is that the analysis performed here is based on the entire body of information about the spectroscopic features of states of the final nuclei ^{57}Co and ^{57}Ni that was obtained in one-nucleon-pickup reactions on ^{58}Ni target nuclei (see Table 3). In all, data on approximately 150 levels of the ^{57}Co and ^{57}Ni nuclei were obtained in experiments of this type. The way in which we have used these data in our analysis of the GDR in the ^{58}Ni nucleus will be described below.

3. BASIC PRINCIPLES OF DATA ANALYSIS

In general, the formation and decay of GDRs proceeds as follows. Upon the absorption of an $E1$ photon by a nucleus, there arises a collective doorway state of the dipole type. This state is a superposition of $1p1h$ particle–hole configurations, and it decays via nucleon emission into a continuous spectrum with the formation of a nucleus in a $1h$ hole state (semidirect mechanism characterized by a width $\Gamma^\uparrow$) or via consecutive transitions into more complicated states—$2p2h$, $3p3h$, etc.—(preequilibrium stage) up to thermal equilibration (compound-nucleus stage). At each of these stages, nucleon emission into a continuous spectrum can occur, which leads to the emergence of statistical decay products. The probability of statistical decay is characterized by a width $\Gamma^\downarrow$. The total decay width of the collective dipole state in question is $\Gamma = \Gamma^\uparrow + \Gamma^\downarrow$.

Knowledge of the nature of final-nucleus states that are populated in the nucleonic decays of GDR states makes it possible to reveal the role of various mechanisms of this decay. For example, the semidirect decay of the doorway ($1p1h$) state leads to the population of that level of the final nucleus $A-1$ which is a nucleonic hole ($1h$) with respect to the ground state of the primary nucleus A. The decay of a GDR at the equilibrium stage or at the equilibration stage leads to the population of states of the final nucleus $A-1$ that are not nucleonic holes. In this case, the populated states have a more complicated structure ($1p2h$, $2p3h$, etc.). Knowledge of the cross sections for partial photonuclear reactions (γ, p_i) and (γ, n_i) and of the hole structure of populated states from independent data on one-nucleon-transfer reactions makes it possible to isolate reliably the semidirect branch of GDR decay. Concurrently, these data enable one to establish the shell structure of the dipole resonance being considered.

In the ^{58}Ni nucleus, the external $1f2p$ shell is unfilled. In nuclei belonging to this type, the GDR

Table 1. Integrated cross sections $\sigma^{\mathrm{int}}(i)$ for the reactions $^{58}\mathrm{Ni}(\gamma, p_i)^{57}\mathrm{Co}$, their semidirect components $\sigma^{\mathrm{int}}_{\mathrm{ph}}(i)$, and features of the populated levels of the ^{57}Co nucleus

^{57}Co					$\sigma^{\mathrm{int}}(i)$, MeV mb	$\sigma^{\mathrm{int}}_{\mathrm{ph}}(i)$, MeV mb
i	E_i, MeV	$J^\pi, T = 3/2$	nl_j	C^2S		
0	0	$7/2^-$	$1f_{7/2}$	3.8–5.53	31	10.1–31*
2	1.377	$3/2^-$	$2p_{3/2}$	0.06	29.7	0.9–1.9
5	1.757	$3/2^-$	$2p_{3/2}$	0.11–0.19	10.0	2.7–3.3
6	1.897	$7/2^-$	$1f_{7/2}$	0.92–1.37	7.7	1.9–5.8
7	1.919	$5/2^-$	$1f_{5/2}$		10.8	
8	2.133	$3/2^+; 5/2^+$	$1d_{3/2,5/2}$	0.04–0.10; 0.03	12.5	0.1; 0.1
8	2.133	$5/2^-$	$1f_{5/2}$			
9	2.311	$7/2^-$	$1f_{7/2}$	0.14–0.20	6.1	0.3–0.8
20	2.730	$7/2^-; 5/2^-$	$1f_{7/2,5/2}$	0.03–0.04; 0.05	3.1	0.1–0.2; 0.8–2.1
21	2.743	(9/2; 11/2)			5.3	
22	2.804	5/2			11.1	
23	2.879	$3/2^-$	$2p_{3/2}$		12.1	
24	2.980	$1/2^+$	$2s_{1/2}$	1.05–1.31	9.9	9.9*
26	3.108	$(3/2)^-$	$2p_{3/2}$		5.8	
29	3.176	$7/2^-; 5/2^-$	$1f_{7/2,5/2}$		2.5	
30	3.184	$3/2^+; 5/2^+$	$1d_{3/2,5/2}$	0.09; 0.14	2.4	
32	3.262					
33	3.273	$7/2^-; 5/2^-$	$1f_{7/2,5/2}$	0.07; 0.11		0.2–0.5; 1.7–4.3
44	3.553	$3/2^+; 5/2^+$	$1d_{3/2,5/2}$	1.5–2.33; 1.0	2.3	2.3*

* Cross-section values associated with levels featuring the greatest admixture of a hole excitation.

consists of two branches formed by $E1$ nucleonic transitions from the partly filled external shell to the nearest free shell (that is, by $1f2p \to 1g2d3s$ transitions) and from the least deep filled shell to the external shell (that is, by $1d2s \to 1f2p$ transitions). In the case of semidirect GDR decay, the emitted nucleon escapes from the shell in which it appeared, leaving the nucleus in the corresponding hole state—$(1f2p)^{-1}$ if it is the $(1f2p)^{-1}(1g2d3s)^1$ particle–hole configuration that decays or $(1d2s)^{-1}$ if it is the $(1d2s)^{-1}(1f2p)^1$ particle–hole configuration that decays. Thus, the type of the populated hole state makes it possible to reconstruct the shell structure of the $E1$ nucleonic transition and to associate a given partial cross section with one shell branch of the GDR or the other.

Let us briefly describe the method for extracting the semidirect components of the integrated partial photonucleon cross sections $\sigma^{\mathrm{int}}_{\mathrm{ph}}(\gamma, x_i)$ ($x = n$ or p) that was used in the present study (a more detailed account of the method is given in [5, 10]). The method was developed for non-self-conjugate nuclei, where the GDR consists of excitations featuring two isospins, $T_< = T_0$ and $T_> = T_0 + 1$, T_0 being the isospin of the ground state. If the GDR is represented in the form of one doorway collective state that is a mixture of excitations characterized by $T_<$ and $T_>$, the expression for $\sigma^{\mathrm{int}}_{\mathrm{ph}}(\gamma, x_i)$ can be written as

$$\sigma^{\mathrm{int}}_{\mathrm{ph}}(\gamma, x_i) = \sigma^{\mathrm{int}}_{<}\frac{\Gamma^{\uparrow}_{<}(i)}{\Gamma_<} + \sigma^{\mathrm{int}}_{>}\frac{\Gamma^{\uparrow}_{>}(i)}{\Gamma_>}, \qquad (1)$$

where $\sigma^{\mathrm{int}}_{<}$ and $\sigma^{\mathrm{int}}_{>}$ are the integrated cross sections for the excitation of the $T_<$ and the $T_>$ GDR component, respectively; $\Gamma_<$ and $\Gamma_>$ are the total decay widths of the corresponding components, the width associated with the spread of the doorway states over complex states of the $2p2h$ type being included in them; and $\Gamma^{\uparrow}_{<}(i)$ and $\Gamma^{\uparrow}_{>}(i)$ are the corresponding widths with respect to nucleon emission at the semidirect decay stage. Considering that $\Gamma_< \approx \Gamma_>$,

Table 2. Integrated cross sections $\sigma^{\rm int}(i)$ for the reactions ^{58}Ni$(\gamma, n_i)^{57}$Ni, their semidirect components $\sigma^{\rm int}_{\rm ph}(i)$, and features of the populated levels of the ^{57}Ni nucleus

^{57}Ni					$\sigma^{\rm int}(i)$, MeV mb	$\sigma^{\rm int}_{\rm ph}(i)$, MeV mb
i	E_i, MeV	$J^\pi, T = 1/2$	nl_j	C^2S		
0	0	$3/2^-$	$2p_{3/2}$	0.72–1.25	35	35*
1	0.780	$5/2^-$	$1f_{5/2}$	0.44–1.14	40	40*
2	1.110	$1/2^-$	$2p_{1/2}$	0.15–0.22	0.43	0.43*
3	2.445	$5/2^-$	$1f_{5/2}$		22	
4	2.580	$7/2^-$	$1f_{7/2}$	2.13–3.30	6.3	3.6*–19.2
5	3.007	$3/2^-$	$2p_{3/2}$	0.007	6.4	0.1–0.2
7	3.230	$7/2^-$	$1f_{7/2}$	0.30–0.61	2.2	0.8–3.1
13	3.850	$3/2^-$	$2p_{3/2}$	0.08	5.4	1.2–2.5
19	4.230	$7/2^-$	$1f_{7/2}$	0.18–0.34	2.0	0.4–1.4
42	5.580	$1/2^+$	$2s_{1/2}$	0.62–1.08	5.4	4.4–6.1

* Cross-section values associated with levels featuring the greatest admixture of a hole excitation.

we find that the ratio of the semidirect components of the integrated cross sections for the (γ, x_a) and (γ, x_b) reactions corresponding to the population of the $i = a$ and b levels can be represented in the form

$$\frac{\sigma^{\rm int}_{\rm ph}(\gamma, x_a)}{\sigma^{\rm int}_{\rm ph}(\gamma, x_b)} \approx \frac{\sigma^{\rm int}_{<}\Gamma^{\uparrow}_{<}(a) + \sigma^{\rm int}_{>}\Gamma^{\uparrow}_{>}(a)}{\sigma^{\rm int}_{<}\Gamma^{\uparrow}_{<}(b) + \sigma^{\rm int}_{>}\Gamma^{\uparrow}_{>}(b)}. \quad (2)$$

If one of the semidirect integrated partial cross sections appearing in the expression on the left-hand side of Eq. (2) is known (it is then called a reference cross section), the other one can determined from this equation, provided that its right-hand side can be computed.

In [5], it is shown that, under the condition that the population of the hole state occurs owing predominantly to the emission nucleons having the same orbital angular momentum l, allowance for the energy spread of the dipole strength concentrated in the $T_<$ and $T_>$ components on the basis of relation (2) yields

$$\frac{\sigma^{\rm int}_{\rm ph}(\gamma, x_a)}{\sigma^{\rm int}_{\rm ph}(\gamma, x_b)} \approx \frac{C^2_a S_a \int\limits_0^{E_m} A^x_a(E)\sqrt{\varepsilon_a}P_l(\varepsilon_a)dE}{C^2_b S_b \int\limits_0^{E_m} A^x_b(E)\sqrt{\varepsilon_b}P_l(\varepsilon_b)dE}, \quad (3)$$

where E is the excitation energy of the target nucleus; ε is the kinetic energy of the emitted nucleon; $P_l(\varepsilon)$ is the penetrability of the Coulomb and the centrifugal barrier; and the factors $A^{x=n,p}_{i=a,b}(E)$ can be represented as

$$A^x_i(E) = C^x(T_<, T_i)\sigma_<(E) + C^x(T_>, T_i)\sigma_>(E),$$

with $C^x(T_<, T_i)$ and $C^x(T_>, T_i)$ being the isospin factors (squares of the isospin Clebsch–Gordan coefficients) that determine the probabilities of the decay of the $T_<$ and $T_>$ GDR components via nucleon emission ($x = p, n$) with the formation of the final nucleus $A - 1$ in a state that is characterized by the isospin T_i. All quantities appearing on the right-hand side of Eq. (3) either are known or can easily be calculated. For various partial isospin transitions in the ^{58}Ni nucleus, the values of C^x are shown near the arrows in Fig. 1. The spectroscopic factors S_i of the populated levels are extracted from data of nucleon-pickup experiments. The penetrability factors $P_l(\varepsilon)$ are calculable. The cross sections $\sigma_<(E)$ and $\sigma_>(E)$ for the isospin GDR components are obtained from an analysis of the energy dependences of the experimental photoproton and photoneutron cross sections, the formulas given by the concept of the isospin splitting of the GDR [16, 17] being taken into account in this analysis.

As the result of an analysis of the experimental photoabsorption cross section σ_γ for the ^{58}Ni nucleus [7, 10] (for σ_γ, we used the sum of the inclusive photoproton and the inclusive photoneutron cross section), this cross section was broken down into the $T_<$ and the $T_>$ component [$\sigma_<(E)$ and $\sigma_>(E)$, respectively]. These components as functions of energy are displayed in Fig. 2, along with the smoothed experimental energy dependence of σ_γ. It is precisely these cross sections that were used in extracting the semidirect components of the partial cross sections.

Table 3. Integrated cross sections $\sigma_{\rm ph}^{\rm int}(i)$ computed for all final levels that manifest themselves in one-nucleon-pickup reactions [the data are grouped according to the final-nucleus species (^{57}Co or ^{57}Ni) and the hole configuration nl_j of the populated level; reference cross sections labeled with an asterisk were borrowed from experimental data]

E_i, MeV	C^2S	$\sigma_{\rm ph}^{\rm int}(i)$, MeV mb	E_i, MeV	C^2S	$\sigma_{\rm ph}^{\rm int}(i)$, MeV mb
$nl_j = 2s_{1/2}$			$nl_j = 1d_{3/2}$		
^{57}Co			^{57}Ni		
2.980	1.05–1.31	9.9*	7.200	0.05	0.03–0.05
^{57}Ni			7.275	0.07	0.04–0.06
5.580	0.62–1.08	4.4–6.1	7.320	0.07	0.04–0.06
8.280[a)]	0.28–0.50	2.0–2.9	7.462	0.07	0.04–0.06
8.515	0.12–0.13	0.5–0.4	7.522	0.35–0.37	0.19–0.13
8.723	0.04	0.1–0.2	7.700	0.06	0.03–0.05
$nl_j = 1f_{5/2}$			7.802	0.25–0.26	0.12–0.20
^{57}Co			7.870	0.10	0.05–0.08
2.728	0.05	0.83–2.15	8.015	0.07	0.03–0.05
3.273	0.11	1.66–4.29	8.100	0.14–0.15	0.07–0.11
3.921	0.12	1.60-4.16	8.130	0.09	0.04–0.07
4.882	0.07	0.78–2.02	8.230	0.13–0.14	0.06–0.10
5.459	0.08	0.79–2.05	8.325	0.06	0.02–0.04
^{57}Ni			8.840[a)]	0.77–1.18	0.88–0.91
0.780	0.44–1.14	40*	$nl_j = 1d_{5/2}$		
$nl_j = 1d_{3/2}$			^{57}Co		
^{57}Co			2.133	0.03	0.08–0.09
2.133	0.04–0.10	0.08–0.13	3.184	0.09	0.21–0.22
3.184	0.14	0.15–0.23	3.553	1.00	2.3*
3.553	1.5–2.33	2.3*	4.318	0.128	0.25–0.26
3.906	0.20	0.18–0.29	4.619	0.05	0.09
4.318	0.19	0.16–0.26	4.772	0.10	0.18
4.619	0.07	0.05–0.09	5.103	0.08	0.13–0.14
4.772	0.16	0.12–0.20	5.222	0.03	0.05
5.103	0.12	0.08–0.14	5.877	0.17	0.23–0.26
5.222	0.04	0.03–0.05	5.987	0.22	0.29–0.33
5.877	0.23–0.26	0.15–0.24	6.398	0.14	0.17–0.20
5.987	0.34	0.19–0.35	6.671	0.06	0.07–0.08
6.013	0.29	0.16–0.30	6.817	0.03	0.03–0.04
6.398	0.21	0.11–0.19	^{57}Ni		
6.671	0.09	0.04–0.08	8.445	0.21–0.22	0.19–0.23
6.817	0.04	0.02–0.03	8.662	0.27–0.28	0.23–0.29
^{57}Ni			8.745	0.10	0.08–0.10
4.372	0.01	0.01–0.02	8.945	0.12–0.13	0.09–0.13
5.980	0.17–0.18	0.13–0.21	9.185	0.08	0.06–0.07
6.027	0.54–1.00	0.63–0.77	9.280	0.12–0.13	0.08–0.12
6.315	0.05	0.04–0.05	9.400	0.15–0.16	0.10–0.14
6.655	0.06	0.04–0.06	9.430	0.09	0.06–0.08
6.730	0.10	0.06–0.10	9.585	0.19–0.20	0.12–0.17

Table 3. (Contd.)

E_i, MeV	C^2S	$\sigma_{ph}^{int}(i)$, MeV mb	E_i, MeV	C^2S	$\sigma_{ph}^{int}(i)$, MeV mb
$nl_j = 1d_{5/2}$			$nl_j = 2p_{3/2}$		
^{57}Ni			^{57}Co		
10.210	0.14–0.15	0.07–0.11	3.365	0.035	0.37–0.85
10.240	0.14–0.15	0.07–0.11	3.469	0.013	0.14–0.31
10.515	0.12–0.13	0.05–0.09	4.530	0.028	0.24–0.57
10.790	0.27–0.28	0.11–0.17	5.057	0.007	0.05–0.13
11.120[a)]	0.07–0.10	0.02–0.06	5.157	0.019	0.14–0.35
11.155[a)]	0.07–0.10	0.02–0.06	5.384	0.006	0.04–0.11
11.195[a)]	0.12–0.17	0.04–0.09	5.524	0.02	0.14–0.34
$nl_j = 2p_{1/2}$			5.638	0.024	0.16–0.41
^{57}Co			5.715	0.007	0.05–0.12
1.505	0.007	0.008–0.014	6.148	0.013	0.08–0.20
3.469	0.016	0.013–0.025	6.306	0.011	0.07–0.16
4.530	0.034	0.024–0.045	6.901	0.014	0.07–0.19
5.057	0.008	0.004–0.010	^{57}Ni		
5.157	0.023	0.014–0.027	0.00	0.72–1.25	35*
5.384	0.007	0.004–0.008	3.850	0.08	1.17–2.52
5.520	0.025	0.014–0.028	4.458	0.03	0.39–0.86
5.638	0.030	0.017–0.033	4.932	0.03	0.35–0.78
5.715	0.009	0.005–0.010	5.089	0.03	0.34–0.77
6.148	0.016	0.008–0.016	5.190	0.02	0.22–0.50
6.306	0.014	0.007–0.014	5.668	0.03	0.30–0.68
6.901	0.017	0.007–0.015	6.230	0.01	0.09–0.20
^{57}Ni			6.550[a)]	0.02–0.03	0.44–0.60
1.110	0.15–0.22	0.43*	6.592[a)]	0.02–0.03	0.56–0.78
$nl_j = 2p_{3/2}$			6.695	0.01	0.08–0.18
^{57}Co			6.955[a)]	0.11–0.13	1.77–3.09
1.377	0.06	0.89–1.89	7.042	0.02	0.15–0.33
1.757	0.11–0.19	2.65–3.31			

E_i, MeV	C^2S	$\sigma_{ph,ref}^{int}$, MeV mb		E_i, MeV	C^2S	$\sigma_{ph,ref}^{int}$, MeV mb	
		31	6.3			31	6.3
$nl_j = 1f_{7/2}$				$nl_j = 1f_{7/2}$			
^{57}Co				^{57}Co			
0.00	3.8–5.53	31*	10.12–10.92	3.921	0.07	0.21–0.30	0.07–0.11
1.897	0.92–1.37	5.66–5.80	1.89–1.99	4.882	0.04	0.10–0.14	0.03–0.05
2.311	0.14–0.20	0.80	0.26–0.28	5.459	0.04	0.09–0.13	0.03–0.05
2.611	0.06–0.07	0.26–0.33	0.09–0.12	^{57}Ni			
2.730	0.03–0.04	0.16	0.05–0.06	2.580	2.13–3.30	18.02–19.18	6.3*
3.273	0.07–0.14	0.34–0.47	0.12–0.15	3.230	0.30–0.61	2.24–3.14	0.79–1.02
3.356	0.11	0.36–0.53	0.12–0.19	3.300	0.02	0.10–0.15	0.03–0.05
3.681	0.10–0.13	0.40–0.45	0.13–0.16	3.362	0.08–0.17	0.55–0.85	0.19–0.27

Table 3. (Contd.)

E_i, MeV	C^2S	$\sigma^{\text{int}}_{\text{ph}(i)}$, MeV mb		E_i, MeV	C^2S	$\sigma^{\text{int}}_{\text{ph, ref}}$, MeV mb	
		31	6.3			31	6.3
$nl_j = 1f_{7/2}$				$nl_j = 1f_{7/2}$			
^{57}Ni				^{57}Ni			
3.700	0.09–0.16	0.63–0.75	0.22–0.25	6.115	0.05	0.14–0.21	0.05–0.07
4.050	0.01	0.04–0.06	0.01–0.02	6.280	0.02	0.06–0.08	0.02–0.03
4.220	0.18–0.34	1.11–1.44	0.39–0.47	6.427	0.02	0.05–0.08	0.02–0.03
4.572	0.13–0.25	0.75–0.99	0.26–0.32	6.520	0.04	0.10–0.15	0.03–0.05
4.892	0.02	0.07–0.11	0.02–0.04	6.845	0.07	0.17–0.25	0.06–0.09
5.132[a)]	0.12–0.13	0.76–1.02	0.25–0.36	6.880	0.04	0.10–0.14	0.03–0.05
5.235[a)]	1.21–2.40	10.09–13.75	3.55–4.49	7.130[a)]	0.72–0.76	3.98–5.48	1.30–1.93
5.367	0.24–0.25	1.40–1.96	0.46–0.69	7.580[a)]	0.06	0.22–0.33	0.08–0.12
5.710	0.05	0.16–0.23	0.05–0.07	7.985	0.04	0.07–0.11	0.02–0.04
5.765	0.06	0.18–0.27	0.06–0.09	8.530[a)]	0.05	0.08–0.12	0.03–0.04
5.795	0.06	0.18–0.27	0.06–0.09	9.110	0.14–0.15	0.21–0.29	0.07–0.10
5.850	0.09	0.27–0.40	0.09–0.14				

[a)] $T = 3/2$ level.

Thus, the procedure that we used to extract the semidirect branch of the GDR employed the following important pieces of information that were taken directly from experimental data:

(i) the energy spread of the dipole strength concentrated in the $T_<$ and the $T_>$ GDR component;

(ii) the spread of the spectroscopic strength of nucleon-hole states of the primary nucleus A over the levels of the final nucleus $A-1$.

For the ^{58}Ni nucleus, this procedure must be applied only to $E1$ nucleon transitions of the following three types:

$$1f_{5/2,\,7/2} \to 1g2d,$$
$$1d_{3/2,\,5/2} \to 1f2p,$$
$$2s_{1/2} \to 2p.$$

For either of the first two types, the orbital angular momentum l of the semidirect nucleon can take two values: 4 and 2 for the first type and 3 and 1 for the second type. Only the emission of an $l = 1$ nucleon is possible for transitions from the $2s_{1/2}$ shell. For all of the l values listed above, the semidirect components of the partial cross sections were computed here on the basis of relation (3). The variations that, in doing this, arose in the values of $\sigma^{\text{int}}_{\text{ph}}(\gamma, x_i)$ were included in the total uncertainty of the result. Yet another important source of uncertainty was associated with that in the experimental spectroscopic factor S_i of the populated level.

4. RESULTS OF THE ANALYSIS

The integrated cross section summed over all protonic channels indicated in Table 1 is equal to 162 ± 40 MeV mb. The analogous result for all neutronic channels from Table 2 is 125 ± 30 MeV mb. These are, respectively, 30 and 40% of the integrated total (inclusive) photoproton and photoneutron cross sections [13–15]. In the experimental γ' spectra, we were unable to single out transitions that would indicate that the photodisintegration of ^{58}Ni nuclei leads to the population of states in ^{57}Cu and ^{57}Ni nuclei above 3.6 and 5.6 MeV, respectively. On one hand, this is because attempts at detecting γ' transitions from such high levels run into considerable methodological difficulties. On the other hand, excited states of ^{57}Co and ^{57}Ni above the nucleon-separation energy decay by emitting one more nucleon, so that they do not manifest themselves in the relevant γ' spectra. It should be emphasized from the outset, however, that this apparently significant incompleteness of the experimental pattern of the partial photodisintegration of ^{58}Ni has virtually no effect on the eventual conclusion of our analysis, since partial cross sections

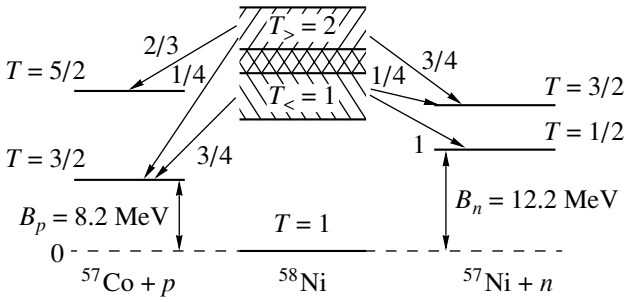

Fig. 1. Isospin diagram of the nucleonic decay of the giant dipole resonance in the ^{58}Ni nucleus.

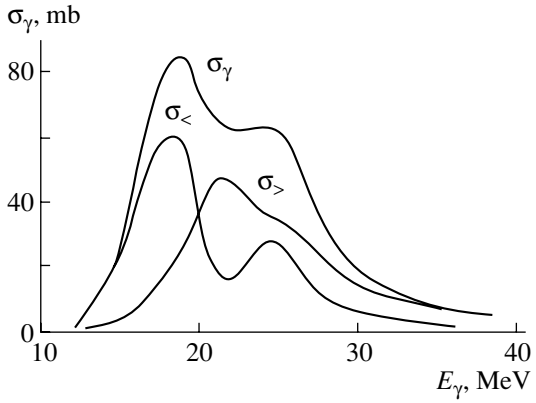

Fig. 2. Isospin components of the giant dipole resonance in the ^{58}Ni nucleus.

known to date are sufficient for reconstructing all quantities that are of interest to us.

From the data presented in Tables 1 and 2, it follows that, of all the observed partial channels, only four are associated with the decay of $E1$ nucleon transitions from the internal shell of the ^{58}Ni nucleus. These are cross sections for the population of the $i =$ 8, 24, and 44 levels of the ^{57}Co nucleus and the $i = 42$ level of the ^{57}Ni nucleus. All these levels are of a positive parity (the parity of the $i = 8$ level in ^{57}Co has not yet been established definitively). Two of these have the $(2s_{1/2})^{-1}$ hole structure and are populated upon the decay of the $1p1h$ configuration $(2s_{1/2})^{-1}(2p)^1$, while the other two have the $(1d_{3/2,5/2})^{-1}$ hole structure and are populated upon the decay of the $1p1h$ configuration $(1d_{3/2,5/2})^{-1}(1f2p)^1$.

The remaining populated levels are of a negative parity, which corresponds to the hole structure of the $1f2p$ shell. They are populated upon the decay of the $1p1h$ configuration $(1f2p)^{-1}(1g2d3s)^1$.

Summing the partial cross sections for the population of negative-parity states with allowance for the data from Table 3 on the semidirect component of high-lying levels, we obtain a lower bound on the contribution of the $1f2p \to 1g2d3s$ branch to the GDR in the ^{58}Ni nucleus. The resulting values are 0.25 and 0.32 for the protonic and the neutronic channel, respectively, and 0.28 for photoabsorption. The eventual results are presented in Table 4.

Knowing partial photonucleon cross sections and the spectroscopic factors of the populated states from data on one-nucleon-pickup reactions and using the procedure described in the preceding section, we can obtain the probability of the semidirect mechanism of the decay of the GDR in the ^{58}Ni nucleus.

From Tables 1 and 2, one can see that it is necessary to take into account hole excitations in seven subshells ($1f_{7/2}$, $1f_{5/2}$, $2p_{3/2}$, $2p_{1/2}$, $1d_{5/2}$, $1d_{3/2}$, and $2s_{1/2}$); that is, it is necessary to have seven reference partial cross sections. We adopt the following hypothesis: the partial cross sections for the population of levels involving the greatest admixture of a hole excitation of each type are fully saturated by the semidirect decay (this is definitively so for purely hole states). In Tables 1 and 2, asterisks label cross sections associated with levels featuring the greatest admixture of a hole of each of the types indicated above. According to the ENSDF data, three of these levels can be believed to be purely hole ones ($i = 24$ level of the ^{57}Co nucleus and the $i = 1$ and 2 levels of the ^{57}Ni nucleus). They absorb the entire spectroscopic strength of the corresponding hole states that was observed in pickup reactions. The $i = 0$ level of the ^{57}Ni nucleus is very close to a purely hole one. According to the ENSDF data, it contributes 0.84 to 1.0 of the entire spectroscopic strength of the $2p_{3/2}$ neutron hole. The $i = 0$ level of the ^{57}Co nucleus saturates 0.73 of the spectroscopic strength of the $1f_{7/2}$ proton hole. Since the semidirect cross section calculated for the $i = 4$ level of the ^{57}Ni nucleus on the basis of this reference cross section proved to be in excess of the experimental value, the version was considered where the cross section for the ^{57}Ni $i = 4$ level, which also has a significant spectroscopic factor, was in turn a reference cross section. Since the $i = 44$ level of the ^{57}Co nucleus absorbs a major part of the spectroscopic strength of the $1d$ proton hole, the cross section for the population of this level was chosen to be a reference cross section for the $1d_{3/2,5/2}$ configurations. It was assumed that the partial cross sections labeled with asterisks are saturated entirely (or almost entirely) by the contribution from the semidirect decay of the GDR in the ^{58}Ni nucleus. It is precisely these cross sections that were chosen for reference ones. The semidirect components of the remaining partial cross sections were computed

Table 4. Integrated cross sections and their semidirect components (in MeV mb) for $E1$ nucleon transitions forming the GDR in the ^{58}Ni nucleus (fractions of the corresponding transitions in the cross sections are indicated parenthetically)

	(γ, p)	(γ, n)	$(\gamma, p) + (\gamma, n)$
All transitions	570	250–380	830–950
Transitions	>140	>120	>260
$1f2p \to 1g2d3s$	(>0.25)	(>0.32)	(>0.28)
Semidirect branch of transitions $1f2p \to 1g2d3s$	16–49 (0.07–0.35)	84–102 (0.20–0.85)	100–151 (0.11–0.58)
Semidirect branch of all transitions	41–97 (0.07–0.17)	108–156 (0.28–0.62)	149–253 (0.16–0.30)

according to the procedure described in the preceding section.

The calculated values of $\sigma_{\rm ph}^{\rm int}(i)$ are also quoted in Table 3, where they are combined in groups corresponding to the same values of nl_j. In contrast to Tables 1 and 2, Table 3 includes all levels that were detected experimentally and which are known to involve an admixture of the spectroscopic strength of the hole states being discussed. The scatter of the values of $\sigma_{\rm ph}^{\rm int}(i)$ takes into account the uncertainty in the spectroscopic factor of a given level and the possible range of the orbital angular momenta of the emitted nucleon. As was indicated above, two versions of the reference cross section were used for the $1f_{7/2}$ hole configuration.

By and large, the results of the calculations for $\sigma_{\rm ph}^{\rm int}(i)$ lend support to the assumption that the reference cross sections that we chose receive an overwhelming contribution from the semidirect decay of the GDR. In all cases, with the exception of one (that of the $i = 4$ level of the ^{57}Ni nucleus), the cross section for semidirect decay did not exceed the experimental value. This indicates that the fraction of the semidirect mechanism in the reference cross section was not exaggerated. It is also worth noting that the spectroscopic factors are very small for all levels that are not displayed in Tables 1 and 2 because the corresponding partial cross sections were not observed. For such levels, the cross sections for semidirect decay must be close to zero, which is a good illustration of the correlation between the partial cross section and the spectroscopic factor in the case where photonucleon reactions are governed by the semidirect mechanism.

Summing the semidirect partial cross sections for protons and for neutrons separately, we obtain the values of 41–83 and 108–150 MeV mb for, respectively, the integrated semidirect proton and the integrated semidirect neutron cross section. Taking into account the unobservable part of the spectroscopic strength of hole levels—it admits an increase of 14 MeV mb in the semidirect cross section for protons and an increase of 6 MeV mb in the semidirect cross section for neutrons—we obtain the following ranges for the probabilities of the semidirect decay of the GDR in the ^{58}Ni nucleus:

0.07–0.17 for the photoproton channel,
0.28–0.62 for the photoneutron channel,
0.16–0.30 for photoabsorption.

Available data make it possible to estimate the probability of the semidirect mechanism for the $1f2p \to 1g2d3s$ branch of the GDR in the ^{58}Ni nucleus. In order to do this, it is necessary to calculate $\sum_i \sigma_{\rm ph}^{\rm int}(i)$ for the observed partial transitions in the above branch and to determine the fraction of these transitions in it. The results of this calculation are quoted in Table 4.

5. CONCLUSION

All the results obtained in the present study are compiled in Table 4, where they are contrasted against the integrated values of the experimental inclusive photonucleon cross sections [denoted by (γ, p) and (γ, n)] and against their sum [denoted by $(\gamma, p) + (\gamma, n)$], which nearly exhausts the integrated photoabsorption cross section. In relation to the data in [7], these results refine significantly the shell structure of the GDR in the ^{58}Ni nucleus and the mechanism of its decay.

An analysis of the data presented in Table 4 leads to the following conclusions:

(i) The probability of the semidirect mechanism of the decay of the GDR in ^{58}Ni, which belongs to the class of $1f2p$-shell nuclei, lies predominantly in the range 16–30%; this is approximately one-half as great as the corresponding probabilities typical of the majority of $1d2s$-shell nuclei ($A = 16$–40).

(ii) The probability of semidirect processes in the (γ, n) channel (28–62%) is much higher than that in the (γ, p) channel (7–17%).

A reduction of the probability of semidirect GDR decay with increasing mass number (and, accordingly, a growth of the probability of statistical decay) is a natural trend that was reliably established and which was discussed in [10, 18].

As to the higher probability of semidirect decay in the neutronic channel in relation to the protonic channel, this is explained by a considerable excess of the neutron threshold in ^{58}Ni (12.2 MeV) over the proton threshold (8.2 MeV). This distinction is due to the Coulomb interaction between the protons, which results in that the nuclear potential well for protons in the majority of stable nuclei, including ^{58}Ni, is shallower than that for neutrons (accordingly, the threshold is lower). Because of a high neutron threshold, the photoneutron cross sections for the population of high-lying final levels, which are of a nonhole origin in the majority of cases, are strongly suppressed; as a result, the total photoneutron cross section is associated, to a greater extent in relation to the photoproton one, with low-lying levels, which are predominantly of a hole origin—that is, it involves a greater fraction of the semidirect component.

REFERENCES

1. R. A. Eramzhyan, B. S. Ishkhanov, I. M. Kapitonov, and V. G. Neudatchin, Phys. Rep. **136**, 229 (1986).
2. B. S. Ishkhanov, I. M. Kapitonov, and R. A. Éramzhyan, Fiz. Élem. Chastits At. Yadra **23**, 1770 (1992) [Sov. J. Part. Nucl. **23**, 774 (1992)].
3. B. S. Ishkhanov, I. M. Kapitonov, and R. A. Éramzhyan, Fiz. Élem. Chastits At. Yadra **26**, 873 (1995) [Phys. Part. Nucl. **26**, 367 (1995)].
4. I. M. Kapitonov, Yad. Fiz. **37**, 569 (1983) [Sov. J. Nucl. Phys. **37**, 338 (1983)].
5. B. S. Ishkhanov, I. M. Kapitonov, and I. A. Tutyn', Yad. Fiz. **58**, 1180 (1995) [Phys. At. Nucl. **58**, 1103 (1995)].
6. B. S. Ishkhanov, I. M. Kapitonov, V. G. Neudachin, *et al.*, Usp. Fiz. Nauk **160** (3), 57 (1990) [Sov. Phys. Usp. **33**, 204 (1990)].
7. B. S. Ishkhanov, I. M. Kapitonov, and I. A. Tutyn', Yad. Fiz. **56** (8), 1 (1993) [Phys. At. Nucl. **56**, 991 (1993)].
8. B. S. Dolbilkin, in *Proceedings of the VII Workshop on Electromagnetic Interactions of Nuclei at Low and Intermediate Energies* (Inst. Yad. Issled. Akad. Nauk SSSR, Moscow, 1990), p. 289.
9. I. M. Glatky, A. M. Lapik, B. S. Ratner, *et al.,* Nucl. Phys. A **512**, 167 (1990).
10. I. A. Tutyn', Candidate's Dissertation in Physics and Mathematics (Nauchn. Issled. Inst. Yad. Fiz. Mosk. Gos. Univ., Moscow, 1995).
11. H. Miyase, S. Oikawa, A. Suzuki, *et al.*, *PINCS* (Asilomar, 1973), Vol. 1, p. 533.
12. I. N. Boboshin and V. V. Varlamov, Nucl. Instrum. Methods Phys. Res. A **369**, 113 (1996).
13. B. S. Ishkhanov, I. M. Kapitonov, I. M. Piskarev, *et al.*, Yad. Fiz. **11**, 485 (1970) [Sov. J. Nucl. Phys. **11**, 272 (1970)].
14. B. I. Goryachev, B. S. Ishkhanov, I. M. Kapitonov, *et al.*, Pis'ma Zh. Éksp. Teor. Fiz. **8**, 76 (1968) [JETP Lett. **8**, 46 (1968)].
15. S. C. Fultz, R. A. Alvarez, B. L. Berman, and P. Meyer, Phys. Rev. C **10**, 608 (1974).
16. R. Ö. Akyüz and S. Fallieros, Phys. Rev. Lett. **27**, 1016 (1971).
17. S. Fallieros and B. Goulard, Nucl. Phys. A **147**, 593 (1970).
18. B. S. Ishkhanov, I. M. Kapitonov, and I. A. Tutyn', Izv. Akad. Nauk, Ser. Fiz. **62**, 2295 (1998).

Translated by A. Isaakyan

Physics of Atomic Nuclei, Vol. 65, No. 1, 2002, pp. 102–108. Translated from Yadernaya Fizika, Vol. 65, No. 1, 2002, pp. 107–113.
Original Russian Text Copyright © 2002 by Gershtein, Luchinsky.

ELEMENTARY PARTICLES AND FIELDS
Theory

Ortho–Para Conversion in the Muonic Molecule $pp\mu$

S. S. Gershtein* **and A. V. Luchinsky****

Institute for High Energy Physics, Protvino, Moscow oblast, 142284 Russia

Received January 22, 2001; in final form, May 10, 2001

Abstract—The ortho–para conversion due to the interaction between the nuclear magnetic moments and the atomic electron is considered in the muonic molecule $(pp\mu)e$ produced in the ortho state. It is shown that the rate of this transition is $w \approx 0.466\,\mathrm{s}^{-1}$, which is much less than the rate of the transition induced by the mixing of states having opposite parities with respect to the inversion of the muon coordinates.
© 2002 MAIK "Nauka/Interperiodica".

1. INTRODUCTION

Previously, measurement of muon capture by a proton was the most important check on the validity of universal weak $V-A$ interaction. Presently, it can be (and is planned to be) employed for a precision investigation of the induced pseudoscalar, whose value is predicted within chiral theories [1]. In this connection, it seems reasonable to deduce additional estimates for muon–atom and muon–molecule processes, which control the probability of weak muon capture in hydrogen.

As was shown in [2], the mechanism of muon exchange in collisions of muonic atoms with protons of the medium leads to a rather fast transition of $p\mu$ atoms from the upper level of the hyperfine structure ($F = 1$) to the lower one ($F = 0$), F being the absolute value of the total spin of the muonic atom involved. According to the estimates presented in [2, 3], the rate of this transition is $w_{F=1\to F=0} \approx 10^{10}\varphi\ \mathrm{s}^{-1}$, where φ is the ratio of the density of the hydrogen target employed to the density of liquid hydrogen at 20 K (more recent calculations yield $w_{F=1\to F=0} \approx 5.6 \times 10^{10}\varphi\,\mathrm{s}^{-1}$ [3]). Since the rates of muon capture from the different states of the hyperfine structure of the muonic atom $p\mu$ differ considerably ($w_{F=1} \approx 659\ \mathrm{s}^{-1}$, $w_{F=0} \approx 14.6\ \mathrm{s}^{-1}$), the transition under consideration changes strongly the probability of muon capture in hydrogen—this probability becomes approximately four times as great as that in the case of a statistical distribution in the levels of the hyperfine structure ($g_{F=1} = 3/4$, $g_{F=0} = 1/4$), $w_{\mathrm{st}} \approx 160\ \mathrm{s}^{-1}$ [4]. This result agrees well with data from experiments in gaseous hydrogen at pressures of about 10–20 atm, where the $F = 1 \to F = 0$ transition to the lower state of the hyperfine structure occurs almost completely and where the production of muonic molecules $pp\mu$ can be disregarded at the currently available experiment accuracy. According to data from [5], the capture rate in gaseous hydrogen is $1/\tau_{p\mu} \approx 4w_{\mathrm{st}}$ [5, 6]. At large densities (similar to those of liquid hydrogen), the process proceeds in a different way. In that case, the rate of production of muonic molecules $pp\mu$ is about $2.7 \times 10^6\ \mathrm{s}^{-1}$, and muon capture by a proton occurs predominantly in muonic molecules $pp\mu$ rather than in muonic atoms $p\mu$. In collisions of muonic atoms $p\mu$ with the nuclei of hydrogen molecules H_2, muonic molecules $pp\mu$ are produced mainly via the $E1$ dipole transition accompanied by the conversion of the molecule electron [7, 8]. Therefore, the muonic molecule appears to be in the rotational state having the orbital angular momentum of $K = 1$—that is, in the ortho state—with the total spin of the protons being $I = 1$. Since a fast transition of muonic atoms $p\mu$ to the lower $F = 0$ state of the hyperfine structure precedes the formation of a muonic molecule and since the spin flip in the formation of a muonic molecule can be disregarded, the total spin of the muonic molecule $pp\mu$ is $S = 1/2$. With respect to each proton, the muon then appears to be in the state where the weights of the spin-singlet and the spin-triplet state are 3/4 and 1/4, respectively. This means that the muon-capture rate in liquid hydrogen must be $1/\tau_{pp\mu} \approx 3w_{\mathrm{st}} \approx 480\,\mathrm{s}^{-1}$; within rather large experimental errors (about 10–15%), this agrees with the data from [9, 10].

In what is concerned with the proposal to measure precisely the probability of muon capture in hydrogen, it is necessary to take into account some additional factors in the case of capture occurring in a muonic molecule. The ratio $\gamma = |\Psi_{pp\mu}(0)|^2/|\Psi_{p\mu}(0)|^2$ (here, $|\Psi_{p\mu}(0)|^2$ and $|\Psi_{pp\mu}(0)|^2$ are the squared moduli of the muon wave functions at the proton-location point

*e-mail: gershtein@mx.ihep.su
**e-mail: mpti9502@mx.ihep.su

in the muonic atom $p\mu$ and the muonic molecule $pp\mu$, respectively), which is one of these factors, was reliably calculated in [11]. There are two more factors: the probability that, because of hyperfine interaction between the spin and the rotation of the muonic molecule, its spin is 3/2 (that is, the muon appears to be in the triplet state with respect to the protons) and the probability of the transition of the muonic molecule from the ortho to the para state, where, with respect to each proton, the weights of the spin-triplet and the spin-singlet state in the state of the muon are 3/4 and 1/4, respectively. The probability of the first of these two factors can be obtained from the calculations of the hyperfine structure of the muonic molecule $pp\mu$ that were performed in [12], where it was shown that its effect is rather small. If a muonic molecule $pp\mu$ was initially produced in the ortho state having the total spin of $S = 1/2$ (that is, in a state featuring 3/4 of singlet state between the muon and the protons), then, owing to the interaction with the rotation of the muonic molecule, the probability of the singlet state is $Q^{(3)} = 0.7499$ at the total angular momentum of $J = 3/2$ and $Q^{(1)} = 0.7494$ at $J = 1/2$. Thus, the admixture of the triplet state does not exceed 0.1%.

As to the transition of a muonic molecule from the ortho to the para state, two mechanisms are possible here, each changing both the orbital angular momentum and the total spin of the nuclei involved [13]. One of these mechanisms is associated with the hyperfine interaction of the muon spin with the spins of the nuclei. Without this interaction, the muon wave function would be even, in the adiabatic approximation (Σ_g), with respect to the interchange of the nuclei, but, upon its inclusion, the odd function (Σ_u) corresponding to a different total nuclear spin (that which is equal to zero in the $K = 1$ rotational state of the muonic molecule) is admixed to the even component. Since the electric-dipole moment for the muon transition between the states Σ_g and Σ_u ($\mathbf{d}_{ug} = \langle\Sigma_u|e\mathbf{r}_\mu|\Sigma_g\rangle$) differs from zero—it is proportional to the radius vector between the nuclei—this can induce the $K = 1 \to K = 0$ $E1$ transition between the rotational states of the muonic molecule. This transition must be accompanied by the conversion of the electron occurring in the orbit of the hydrogen-like atom having a muonic molecule $pp\mu$ as a nucleus.[1)] The probability of the ortho–para conversion in the muonic molecule $pp\mu$ via this mechanism was calculated in [12] with allowance for nonadiabatic effects.

[1)]With a high probability, the muonic molecule $pp\mu$ produced upon a collision of a muonic atom $p\mu$ with one of the nuclei of a H_2 molecule either becomes the nucleus of an excited muonic molecular system $[(pp\mu), p]e$ (like a H_2^+ ion) or escapes from it, capturing the electron.

The ortho–para conversion in the muonic molecule $pp\mu$ can also be due to the mechanism of direct interaction between the magnetic moments of its nuclei and the magnetic moment of the orbital electron. The objective of the present study is to calculate the probability of this mechanism, which causes electron conversion. From a dimensional analysis, it can easily be deduced that its efficiency is considerably lower than the efficiency of the first mechanism; this is because the admixture of Σ_u to Σ_g is determined by the interaction between the magnetic moments of the protons and the muon in the muonic molecule, while electron conversion in the second mechanism is controlled by the interaction of the electron with the magnetic moments of the protons in the hydrogen-like atom having $pp\mu$ for the nucleus. Nevertheless, the calculation of its probability is of interest not only from the physical but also from the methodological point of view. To illustrate the last statement, we recall that, in baryons containing two heavy quarks, there exist excited states such that transitions from them to the ground state must be accompanied by simultaneous changes in the spin and in the angular momentum of the heavy-quark pair [14], in just the same way as this occurs in a muonic molecule $pp\mu$ undergoing ortho–para conversion.

2. INTERACTION

In the muonic molecule $pp\mu$, the ortho–para conversion accompanied by changes in the total nuclear spin and the angular momentum ($K = 1 \to K = 0$) can be induced by a nonuniform magnetic field generated by the magnetic moment of the electron occurring in the K orbit of the hydrogen-like atom $pp\mu$. In order to calculate this process, it is convenient, however, to employ the method developed by Fermi for calculating the hyperfine structure of atoms [15] and to consider the nuclear magnetic field acting on the orbital electron.

Since the size of the $pp\mu$ system is far less than the Bohr radius for an electron, we can assume, for a first approximation, that the electron moves in the Coulomb field of a pointlike charge.

The operator for electron interaction with the magnetic field induced by the magnetic moments of the nuclei is then given by

$$V = -\frac{e}{mc}\frac{\mathbf{A}\cdot\mathbf{p} + \mathbf{p}\cdot\mathbf{A}}{2} - \frac{e\hbar}{mc}\mathbf{H}\cdot\mathbf{s} \qquad (1)$$
$$= \frac{ie\hbar}{mc}\left(\mathbf{A}\cdot\boldsymbol{\nabla} + \frac{\boldsymbol{\nabla}\cdot\mathbf{A}}{2}\right) - \frac{e\hbar}{mc}\mathbf{H}\cdot\mathbf{s},$$

where $\mathbf{A}$ and $\mathbf{H}$ are, respectively, the vector potential and the magnetic field induced by the nuclei of the muonic molecule $pp\mu$ and $(-e)$, m, and $\mathbf{s}$ are the electron charge, mass, and spin, respectively.

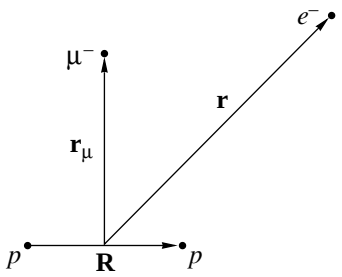

Figure.

The vector potential of a magnetic dipole occurring at the coordinate origin and having the magnetic moment $\boldsymbol{\mu}$ is given by

$$\mathbf{A}_0(\mathbf{r};\boldsymbol{\mu}) = \left[\boldsymbol{\nabla}\frac{1}{r}\times\boldsymbol{\mu}\right].$$

The magnetic field induced by this dipole is

$$\mathbf{H}_0(\mathbf{r};\boldsymbol{\mu}) = [\boldsymbol{\nabla}\times\mathbf{A}_0(\mathbf{r};\boldsymbol{\mu})] = \left[\boldsymbol{\nabla}\times\left[\boldsymbol{\nabla}\frac{1}{r}\times\boldsymbol{\mu}\right]\right] \quad (2)$$

$$= \frac{3(\mathbf{n}\cdot\boldsymbol{\mu})\mathbf{n}-\boldsymbol{\mu}}{r^3} + \frac{8\pi}{3}\boldsymbol{\mu}\delta(\mathbf{r}),$$

where $\mathbf{n} = \mathbf{r}/r$. In deriving this expression, we have used the formula

$$\frac{\partial^2}{\partial x_i \partial x_j}\frac{1}{r} = 3\frac{n_i n_j}{r^3} - \frac{\delta_{ij}}{r^3} - \frac{4\pi}{3}\delta_{ij}\delta(\mathbf{r}),$$

which can easily be proven by means of a simple integration. As a rule, formula (2) is used for $r \neq 0$ and the last term is discarded. In calculating relevant matrix elements, however, integration with respect to the electron coordinates is performed over the entire space, including the coordinate origin; therefore, it is necessary to take into account the term involving the delta function.

The vector potential of two magnetic dipoles $\boldsymbol{\mu}_1$ and $\boldsymbol{\mu}_2$ located at the points $-\mathbf{R}/2$ and $\mathbf{R}/2$, respectively, is

$$\mathbf{A}(\mathbf{r}) = \mathbf{A}_0(\mathbf{r}+\mathbf{R}/2;\boldsymbol{\mu}_1) + \mathbf{A}_0(\mathbf{r}-\mathbf{R}/2;\boldsymbol{\mu}_2).$$

Expanding it in powers of the small ratio R/r (r is the distance between the electron and the center), we arrive at

$$\mathbf{A}(\mathbf{r}) \approx \mathbf{A}_0(\mathbf{r};\boldsymbol{\mu}_1) + \left(\frac{\mathbf{R}}{2}\cdot\boldsymbol{\nabla}\right)\mathbf{A}_0(\mathbf{r};\boldsymbol{\mu}_1) \quad (3)$$

$$+ \mathbf{A}_0(\mathbf{r};\boldsymbol{\mu}_2) - \left(\frac{\mathbf{R}}{2}\cdot\boldsymbol{\nabla}\right)\mathbf{A}_0(\mathbf{r};\boldsymbol{\mu}_2)$$

$$= \mathbf{A}_0(\mathbf{r};\boldsymbol{\mu}_1+\boldsymbol{\mu}_2)$$

$$+ \frac{3}{2}\frac{(\mathbf{R}\cdot\mathbf{n})}{r^3}[\mathbf{n}\times\boldsymbol{\mu}] + \frac{[\boldsymbol{\mu}\times\mathbf{R}]}{2r^3} + \frac{2\pi}{3}[\boldsymbol{\mu}\times\mathbf{R}]\delta(\mathbf{r}),$$

where $\boldsymbol{\mu} = \boldsymbol{\mu}_1 - \boldsymbol{\mu}_2$.

Similarly, the magnetic field is

$$\mathbf{H}(\mathbf{r}) = \mathbf{H}_0(\mathbf{r}+\mathbf{R}/2;\boldsymbol{\mu}_1) + \mathbf{H}_0(\mathbf{r}-\mathbf{R}/2;\boldsymbol{\mu}_2) \quad (4)$$

$$\approx \mathbf{H}_0(\mathbf{r};\boldsymbol{\mu}_1) + \left(\frac{\mathbf{R}}{2}\cdot\boldsymbol{\nabla}\right)\mathbf{H}_0(\mathbf{r};\boldsymbol{\mu}_1) + \mathbf{H}_0(\mathbf{r};\boldsymbol{\mu}_2)$$

$$- \left(\frac{\mathbf{R}}{2}\cdot\boldsymbol{\nabla}\right)\mathbf{H}_0(\mathbf{r};\boldsymbol{\mu}_2)$$

$$= \mathbf{H}_0(\mathbf{r},\boldsymbol{\mu}_1+\boldsymbol{\mu}_2) + \frac{3}{2r^4}\{(\mathbf{R}\cdot\boldsymbol{\mu})\mathbf{n}$$

$$+ (\mathbf{n}\cdot\boldsymbol{\mu})\mathbf{R} + (\mathbf{n}\cdot\mathbf{R})\boldsymbol{\mu}$$

$$- 5(\mathbf{n}\cdot\mathbf{R})\,(\mathbf{n}\cdot\boldsymbol{\mu})\mathbf{n}\} + \frac{4\pi}{3}\boldsymbol{\mu}(\mathbf{R}\cdot\boldsymbol{\nabla})\delta(\mathbf{r}).$$

The matrix element of $(\boldsymbol{\mu}_1+\boldsymbol{\mu}_2)$ between the ortho and para states (having different values of the total nuclear spin) is zero; therefore, the first terms in (3) and (4) can be discarded. Similarly, the interaction between the muon magnetic moment and the electron can be neglected. Other interaction terms in (3) and (4) involve the products of the operators $\boldsymbol{\mu} = \boldsymbol{\mu}_1 - \boldsymbol{\mu}_2$ and $\mathbf{R}$; these products change simultaneously the total spin of the nuclei and the angular momentum of the muonic molecule—that is, they lead to ortho–para conversion. The components of the vector $\mathbf{n}$ appearing in these terms change the orbital angular momentum of the electron by unity. According to the structure of the interaction, the conversion electron can therefore have the orbital-angular-momentum values of $l = 1$ and 3 in the final state.

3. INITIAL AND FINAL STATES

The initial-state wave function has the form

$$\Psi^{(i)} = F_{1,m_K}(\mathbf{R},\mathbf{r}_\mu)\psi_{(0,0)}(\mathbf{r})\chi_{m_s}S_{1,m_S},$$

where $F_{K,m_K}(\mathbf{R},\mathbf{r}_\mu)$ is the wave function for the muonic molecule $pp\mu$ in a rotational state characterized by the orbital angular momentum K and its projection m_K (the notation for vectors is illustrated in the figure); $\psi_{(0,0)}(\mathbf{r}) = e^{-r/a}/\sqrt{\pi a^3}$ is the wave function for the electron in the effective field of the $pp\mu$ system; $a = \hbar^2/(me^2) \approx 0.529\times10^{-8}$ cm is Bohr radius for the electron; χ_{m_s} is the spin wave function for the electron; m_s is the spin projection onto a fixed axis; and S_{I,m_S} is the spin wave function of the $pp\mu$ system in the state where the nuclear spin is I, the total spin is $S = 1/2$, and its projection onto a fixed axis is m_S. The energy of this state is $E_1 = -109$ eV.

The energy of the para state, $E_0 = -250$ eV, is lower than the energy of the ortho state by 141 eV. The energy difference is transferred to the electron ejected into the continuous spectrum. The final-state wave function is

$$\Psi^{(f)} = F_{0,0}(\mathbf{R},\mathbf{r}_\mu)\psi^{(-)}(\mathbf{r})S_{0,m'_S}\chi_{m'_s},$$

where the electron wave function in the continuous spectrum has the form

$$\psi^{(-)} = \frac{1}{2ka}\sum_{l=0}^{\infty} i^l(2l+1)e^{-i\delta_l}R_{kl}(r)P_l\left(\frac{\mathbf{k}\cdot\mathbf{r}}{kr}\right),$$

$$R_{kl}(r) = \frac{C_{kl}}{(2l+1)!}(2kr)^l e^{-ikr} \times F(i/ka+l+1, 2l+2, 2ikr),$$

$$k = \frac{\sqrt{2m\Delta E}}{\hbar}.$$

Here, $\Delta E \approx 129.4$ eV is the conversion-electron energy and we have used the same notation as in [15] and conventional units (not atomic units adopted for this case in [15]).

The wave functions (in the atomic units for the muonic atom) for the system $pp\mu$ can be conveniently expressed in terms of hyperspherical coordinates ρ and χ [16], which are related to the Jacobi coordinates R and r_μ by the equations

$$\begin{cases} \rho^2 &= 2MR^2 + 2\mu r_\mu^2, \\ \tan\dfrac{\chi}{2} &= \sqrt{\dfrac{\mu}{M}}\dfrac{r_\mu}{R}, \end{cases} \quad \begin{cases} R &= \dfrac{\cos(\chi/2)}{\sqrt{2M}}\rho, \\ r_\mu &= \dfrac{\sin(\chi/2)}{\sqrt{2\mu}}\rho, \end{cases}$$

$$M = \frac{M_p}{2m_\mu}, \quad \mu^{-1} = 1 + \frac{m_\mu}{2M_p},$$

where m_μ and M_p are the muon and the proton mass, respectively. The wave functions for the muonic molecule then take the form

$$F_{K,m_K}(\mathbf{R},\mathbf{r}_\mu) = f_K(\rho)\phi_g(\rho|\chi,\vartheta)\frac{Y_{K,m_K}(\Phi,\Theta)}{\sqrt{2\pi}},$$

where Θ and Φ are angles that specify the direction of the axis of the muonic molecule, ϑ is the angle between the vectors $\mathbf{R}$ and $\mathbf{r}_\mu$, $Y_{K,m_K}(\Phi,\Theta)$ are ordinary spherical harmonics, $\phi_g(\rho|\chi,\vartheta)$ are hyperspherical harmonics used in [16], and the index g indicates that we considered here states that are even (gerade) with respect to the inversion of the muon coordinates.

This enables us to use, in calculating the matrix elements for the variable R, their tabular values that were obtained by means of the algorithm developed in [16] and which were placed at our disposal by V.V. Gusev.

The wave functions (5) satisfy the normalization condition

$$\int_0^\infty \rho^5 d\rho \int_0^\pi \sin^2\chi d\chi \int_0^\pi \sin\vartheta d\vartheta \times \int_0^\pi \sin\Theta d\Theta \int_0^{2\pi} d\Phi F^2_{K,m_K}(\rho,\chi,\vartheta,\Theta,\Phi) = \frac{1}{2\pi}.$$

4. MATRIX ELEMENTS IN THE ORBITAL VARIABLES OF THE ELECTRON

The orbital angular momentum of the conversion electron can take the values of $l = 1$ and 3, the interference between the states characterized by the different values of l being absent because the corresponding Legendre polynomials are orthogonal. We now consider these states individually.

1. At $l = 1$, we have

$$\psi_f = i\frac{C_{k1}e^{-i\delta_1}}{2}\frac{r}{a}e^{-ikr}F\left(\frac{i}{ka}+2,4,2ikr\right)\frac{\mathbf{k}\cdot\mathbf{r}}{kr}.$$

Only the last term in (4) makes a nonzero contribution to the matrix element $\langle l=1|\mathbf{H}\cdot\mathbf{s}|l=0\rangle_e$,

$$\langle l=1|\mathbf{H}\cdot\mathbf{s}|l=0\rangle_e = \frac{4\pi}{3}(\boldsymbol{\mu}\cdot\mathbf{s})\langle l=1|\mathbf{R}\cdot\boldsymbol{\nabla}\delta(\mathbf{r})|l=0\rangle_e$$

$$= -i\frac{C_{k1}e^{i\delta_1}}{2}\frac{4\pi}{3}\frac{\boldsymbol{\mu}\cdot\mathbf{s}}{\sqrt{\pi a^3}} \times \int \frac{r}{a}e^{-(1/a+ik)r}F\left(\frac{i}{ka}+2,4,2ikr\right) \times \frac{\mathbf{k}\cdot\mathbf{r}}{kr}(\mathbf{R}\cdot\boldsymbol{\nabla})\delta(\mathbf{r})d^3r = i\frac{C_{k1}e^{i\delta_1}}{2}\frac{4\sqrt{\pi}}{3a^{5/2}}(\boldsymbol{\mu}\cdot\mathbf{s}) \times (\mathbf{R}\cdot\boldsymbol{\nabla})\left[e^{-(1/a+ik)r}F\left(\frac{i}{ka}+2,4,2ikr\right)\frac{\mathbf{k}\cdot\mathbf{r}}{k}\right]_{r=0}$$

$$= i\frac{2\sqrt{\pi}}{3}\frac{C_{k1}e^{i\delta_1}}{a^{5/2}}(\boldsymbol{\mu}\cdot\mathbf{s})\left(\mathbf{R}\cdot\frac{\mathbf{k}}{k}\right).$$

The matrix element $\langle l=1|\mathbf{A}\cdot\boldsymbol{\nabla}|l=0\rangle_e$ is controlled by the third term in (3),

$$\langle l=1|\mathbf{A}\cdot\boldsymbol{\nabla}|l=0\rangle_e = \left\langle l=1\left|\frac{[\boldsymbol{\mu}\times\mathbf{R}]}{2r^3}\cdot\boldsymbol{\nabla}\right|l=0\right\rangle_e$$

$$= i\frac{C_{k1}e^{i\delta_1}}{2}\frac{[\boldsymbol{\mu}\times\mathbf{R}]}{2\sqrt{\pi a^3}}\int_0^\infty \frac{1}{a}e^{-(1/a+ik)r} \times F\left(\frac{i}{ka}+2,4,2ikr\right)dr \times \int\frac{(\mathbf{k}\cdot\mathbf{n})\mathbf{n}}{k}d\Omega = i\frac{\sqrt{\pi}}{4}\frac{C_{k1}e^{i\delta_1}}{a^{5/2}} \times \left(1-e^{-2\delta/ka}\right)\frac{[\boldsymbol{\mu}\times\mathbf{R}]\cdot\mathbf{k}}{k},$$

where $\delta = \arctan ka$. The last term in (3) contributes to $\left\langle l=1\left|\dfrac{\boldsymbol{\nabla}\cdot\mathbf{A}}{2}\right|l=0\right\rangle_e$,

$$\left\langle l=1\left|\frac{\boldsymbol{\nabla}\cdot\mathbf{A}}{2}\right|l=0\right\rangle_e = \left\langle l=1\left|\frac{1}{2}\frac{2\pi}{3}[\boldsymbol{\mu}\times\mathbf{R}]\cdot\boldsymbol{\nabla}\delta(\mathbf{r})\right|l=0\right\rangle_e$$

$$= -i\frac{C_{k1}e^{i\delta_1}}{2}\frac{\sqrt{\pi}}{3a^{3/2}}[\boldsymbol{\mu}\times\mathbf{R}]\int\frac{1}{a}e^{-(1/a+ik)r}$$
$$\times F\left(\frac{i}{ka}+2,4,2ikr\right)\frac{(\mathbf{k}\cdot\mathbf{r})}{k}\boldsymbol{\nabla}\delta(\mathbf{r})d^3r$$
$$= i\frac{\sqrt{\pi}}{3a^{5/2}}\frac{C_{k1}e^{i\delta_1}}{2}[\boldsymbol{\mu}\times\mathbf{R}]\cdot\mathbf{k}.$$

Thus, we arrive at

$$\langle l=1|V|l=0\rangle_e = \frac{\sqrt{\pi}}{2}\frac{C_{k1}e^{i\delta_1}}{a^{5/2}}\frac{|e|\hbar}{mc}$$
$$\times\left[\frac{[\boldsymbol{\mu}\times\mathbf{R}]\cdot\mathbf{k}}{k}\left(\frac{1}{3}+\frac{1-e^{-2\delta/ka}}{2}\right)\right.$$
$$\left.+\,i\frac{4}{3}\frac{(\boldsymbol{\mu}\cdot\mathbf{s})(\mathbf{R}\cdot\mathbf{k})}{k}\right].$$

2. At $l=3$, we have

$$\psi_f = -i\frac{C_{k3}e^{-i\delta_3}k^2}{360}\frac{r^3}{a}e^{-ikr}$$
$$\times F\left(\frac{i}{ka}+4,8,2ikr\right)\frac{\mathbf{k}\cdot\mathbf{r}}{kr}\left[5\left(\frac{\mathbf{k}\cdot\mathbf{r}}{kr}\right)^2-3\right].$$

For the first term of the interaction (1),

$$\left\langle l=3\left|\mathbf{A}\cdot\boldsymbol{\nabla}+\frac{\boldsymbol{\nabla}\cdot\mathbf{A}}{2}\right|l=0\right\rangle_e = 0.$$

The penultimate term in (4) contributes to $(\mathbf{H}\cdot\mathbf{s})$. Using the formulas from the mathematical appendices in [15] to calculate integrals involving confluent hypergeometric functions and performing the required transformations, we obtain

$$\langle l=3|V|l=0\rangle_e$$
$$= \frac{15}{2}\frac{|e|\hbar}{mc}\left\langle l=3\left|\frac{1}{r^4}(\mathbf{n}\cdot\boldsymbol{\mu})(\mathbf{n}\cdot\mathbf{R})(\mathbf{n}\cdot\mathbf{s})\right|l=0\right\rangle_e$$
$$= i\frac{15}{2}\frac{|e|\hbar}{mc}\frac{C_{k3}e^{i\delta_3}k^2}{360}\frac{1}{a}\int r^3e^{-ikr}$$
$$\times F\left(\frac{i}{ka}+4,8,2ikr\right)\frac{\mathbf{k}\cdot\mathbf{r}}{kr}\left[5\left(\frac{\mathbf{k}\cdot\mathbf{r}}{kr}\right)^2-3\right]$$
$$\times\frac{1}{r^4}(\mathbf{n}\cdot\boldsymbol{\mu})(\mathbf{n}\cdot\mathbf{R})(\mathbf{n}\cdot\mathbf{s})\frac{1}{\sqrt{\pi a^3}}e^{-r/a}d^3r$$
$$= i\frac{|e|\hbar}{mc}\frac{\sqrt{\pi}}{2}\frac{C_{k3}e^{i\delta_3}}{\sqrt{a}}k^2$$
$$\times\frac{-2+15e^{-2\delta/ka}+(ka)^2(-3+15e^{-2\delta/ka})}{1+13(ka)^2+36(ka)^4}$$
$$\times\left[\left(\boldsymbol{\mu}\cdot\frac{\mathbf{k}}{k}\right)\left(\mathbf{R}\cdot\frac{\mathbf{k}}{k}\right)\left(\mathbf{s}\cdot\frac{\mathbf{k}}{k}\right)\right.$$
$$-\frac{1}{5}\left((\boldsymbol{\mu}\cdot\mathbf{R})\left(\frac{\mathbf{k}}{k}\cdot\mathbf{s}\right)\right.$$
$$\left.\left.+\,(\boldsymbol{\mu}\cdot\mathbf{s})\left(\frac{\mathbf{k}}{k}\cdot\mathbf{R}\right)+(\mathbf{s}\cdot\mathbf{R})\left(\frac{\mathbf{k}}{k}\cdot\boldsymbol{\mu}\right)\right)\right].$$

5. RATE OF THE ORTHO–PARA CONVERSION CAUSED BY THE MECHANISM UNDER CONSIDERATION

The total probability of ortho–para conversion from the two states of the hyperfine structure of the muonic molecule ($J=3/2$ and $J=1/2$) can be obtained by means of averaging over the initial states of the partial transitions [that is, the transitions from the states characterized by the different projections of the total spin of the muonic molecule ($m_S=\pm1/2$) and different projections of the angular momentum ($m_K=0,\pm1$)] and summation over the spin of the conversion electron. Performing integration with respect to the angular variables of the muonic molecule and denoting by U the matrix element of the distance R between the nuclei of the muonic molecule,

$$U = \langle K=0|R|K=1\rangle/a_\mu,$$

where $a_\mu=\hbar^2/m_\mu e^2$ is the Bohr radius for the muon, we can obtain expressions for the partial-transition probabilities. The results are presented in the table. The symbols α and β stand for the projection values of $1/2$ and $-1/2$, respectively.

The symbols D_1, D_2, and D_3 appearing in the table are spelled out as

$$D_1 = \frac{\pi}{12}\frac{1}{1-e^{-2\pi/ka}}\alpha^4\frac{\Delta E}{\hbar}$$
$$\times\left(\frac{m^2}{m_\mu M_p}\right)^2 g^2U^2\left(1+\frac{1}{(ka)^2}\right)$$
$$\times\left(\frac{1}{3}+\frac{1-e^{-2\delta/ka}}{2}\right)^2,$$
$$D_2 = \frac{4\pi}{27}\frac{1}{1-e^{-2\pi/ka}}\alpha^4\frac{\Delta E}{\hbar}$$
$$\times\left(\frac{m^2}{m_\mu M_p}\right)^2 g^2U^2\left(1+\frac{1}{(ka)^2}\right),$$
$$D_3 = \frac{\pi}{12}\frac{\Delta E}{\hbar}\alpha^4\left(\frac{m^2}{m_\mu M_p}\right)^2 g^2U^2\left(1+\frac{1}{(ka)^2}\right)$$
$$\times\frac{(4(ka)^2+1)(9(ka)^2+1)}{1-e^{-2\pi/ka}}$$
$$\times\left(\frac{-2+15e^{-2\delta/ka}+(ka)^2(-3+15e^{-2\delta/ka})}{1+13(ka)^2+36(ka)^4}\right)^2,$$

where $\alpha=e^2/(\hbar c)\approx1/137$ is the fine-structure constant and $g\approx2.79$ is the proton magnetic moment.

Table

m_K	$m_S \to m'_S$	$m_s \to m'_s$	Partial probabilities
1	$\alpha \to \alpha$	$\alpha \to \alpha$	$\frac{1}{27}(2\sqrt{D_1} - \sqrt{D_2})^2 + \frac{8D_3}{4725}$
		$\alpha \to \beta$	$4D_3/945$
	$\beta \to \beta$	$\beta \to \alpha$	$2D_3/1575$
		$\beta \to \beta$	$\frac{1}{27}(2\sqrt{D_1} + \sqrt{D_2})^2 + \frac{8D_3}{4725}$
	$\alpha \to \beta$	$\alpha \to \alpha$	$4D_3/945$
		$\alpha \to \beta$	$8D_3/315$
		$\beta \to \alpha$	$4D_2/27 + 8D_3/4725$
		$\beta \to \beta$	$4D_3/945$
	$\beta \to \alpha$	$\alpha \to \alpha$	$8D_1/27 + 2D_3/1575$
		$\alpha \to \beta$	$4D_2/27 + 8D_3/4725$
		$\beta \to \alpha$	$8D_3/4725$
		$\beta \to \beta$	$8D_1/27 + 2D_3/1575$
0	$\alpha \to \alpha$	$\alpha \to \alpha$	$D_2/27 + 4D_3/1575$
		$\alpha \to \beta$	$16D_3/4725$
		$\beta \to \alpha$	$16D_3/4725$
		$\beta \to \beta$	$D_2/27 + 4D_3/1575$
	$\alpha \to \beta$	$\alpha \to \alpha$	$8D_1/27 + 16D_3/4725$
		$\alpha \to \beta$	$8D_3/945$
		$\beta \to \alpha$	$4D_2/27 + 4D_3/1575$
		$\beta \to \beta$	$8D_1/27 + 16D_3/4725$

The total rate is given by

$$w = \frac{32D_1}{9} + \frac{4D_2}{3} + \frac{8D_3}{45}.$$

The quantity U is equal to an integral with respect to the hyperspherical coordinates,

$$U = \int_0^\infty \rho^5 d\rho \int_0^\pi \sin^2\chi d\chi \int_0^\pi \sin\vartheta d\vartheta$$
$$\times f_1(\rho) f_0(\rho) \phi_g^2(\rho|\chi,\vartheta) \frac{\rho\cos(\chi/2)}{\sqrt{2M}}.$$

6. CONCLUSION

Using the tabular values of the functions for the muonic molecule, we arrive at

$$U = 3.5019,$$
$$D_1 = 0.0462\ \mathrm{s}^{-1},$$
$$D_2 = 0.219\ \mathrm{s}^{-1},$$
$$D_3 = 0.0561\ \mathrm{s}^{-1},$$
$$w = 0.466\ \mathrm{s}^{-1}.$$

Thus, the conclusions drawn from estimates based on a dimensional analysis have been confirmed: in the muonic molecule $pp\mu$, the probability of the ortho–para transition due to atomic-electron conversion caused by the interaction between the magnetic moment of the electron and the magnetic moments of the nuclei is much less than that for the mechanism of the electric-dipole transition that can occur owing to the admixture of the odd state Σ_u [12]. Since, however, the calculated rate of the ortho–para transition [12] exceeds considerably the experimental estimate [10], it seems reasonable to perform, as was proposed in [17], precise measurements of the probability of muon capture by a proton not in liquid but in gaseous hydrogen, where the production of muonic molecules can be disregarded with the needed accuracy.

ACKNOWLEDGMENTS

We are grateful to V.V. Gusev and L.I. Ponomarev for stimulating discussions and placing the tabulated

wave functions for the muonic molecule at our disposal and to A.A. Vorobyov, who stimulated us to perform this research.

This work was supported in part by the Russian Foundation for Basic Research (project nos. 99-02-16558 and 00-15-96645).

REFERENCES

1. V. Bernard *et al.,* Phys. Rev. D **50**, 6899 (1994); H. W. Fearing *et al.,* Phys. Rev. D **56**, 1783 (1997).
2. S. S. Gershteĭn, Zh. Éksp. Teor. Fiz. **34**, 463, 993 (1958) [Sov. Phys. JETP **7**, 685, 318 (1958)].
3. L. Bracci *et al., The Atlas of the Cross Sections of Mesic Atomic Processes,* IFUP-TH 21/90 (Pisa, 1990).
4. Ya. B. Zel'dovich and S. S. Gershteĭn, Zh. Éksp. Teor. Fiz. **35**, 821 (1958) [Sov. Phys. JETP **8**, 570 (1958)].
5. A. Alberigi Quaranta *et al.,* Phys. Rev. **177**, 2118 (1969).
6. V. M. Bystritskiĭ *et al.,* Zh. Éksp. Teor. Fiz. **67**, 1631 (1974) [Sov. Phys. JETP **40**, 811 (1975)].
7. Ya. B. Zel'dovich and S. S. Gershteĭn, Zh. Éksp. Teor. Fiz. **35**, 970 (1958) [Sov. Phys. JETP **8**, 676 (1958)].
8. S. Cohen, D. L. Judd, and R. J. Riddel, Phys. Rev. **110**, 1471 (1958); **119**, 384 (1960).
9. R. H. Hildebrand, Phys. Rev. Lett. **8**, 34 (1962); E. J. Bleser *et al.,* Phys. Rev. Lett. **8**, 288 (1962); J. E. Rothberg *et al.,* Phys. Rev. **132**, 2664 (1963); E. Bertolini *et al.,* in *Proceedings of the International Conference on High Energy Physics, Geneva, 1962,* p. 421.
10. G. Bardin *et al.,* Nucl. Phys. A **352**, 365 (1981); Phys. Lett. B **104B**, 320 (1981).
11. D. I. Abramov, L. N. Bogdanova, V. V. Gusev, and L. I. Ponomarev, Yad. Fiz. **61**, 520 (1998) [Phys. At. Nucl. **61**, 457 (1998)].
12. D. D. Bakalov *et al.,* Nucl. Phys. A **384**, 302 (1982).
13. S. Weinberg, Phys. Rev. Lett. **4**, 575 (1960).
14. S. S. Gershteĭn, V. V. Kiselev, A. K. Likhoded, and A. I. Onishchenko, Yad. Fiz. **63**, 334 (2000) [Phys. At. Nucl. **63**, 274 (2000)]; S. S. Gershtein *et al.,* Phys. Rev. D **62**, 054021 (2000).
15. L. D. Landau and E. M. Lifshitz, *Course of Theoretical Physics,* Vol. 3: *Quantum Mechanics: Non-Relativistic Theory* (Nauka, Moscow, 1989, 4th ed.; Pergamon, New York, 1977, 3rd ed.).
16. V. V. Gusev *et al.,* Few-Body Syst. **9**, 137 (1990).
17. A. A. Vorobyov *et al.,* Hyperfine Interact. **118**, 130 (1999).

Translated by O. Chernavskaya

Physics of Atomic Nuclei, Vol. 65, No. 1, 2002, pp. 109–120. From Yadernaya Fizika, Vol. 65, No. 1, 2002, pp. 114–125.
Original English Text Copyright © 2002 by Pirogov.

ELEMENTARY PARTICLES AND FIELDS
Theory

Parametrizing and Rephasing Neutrino Mixing*

Yu. F. Pirogov

Institute for High Energy Physics, Protvino, Moscow oblast, 142284 Russia
Received July 7, 2000; in final form, December 4, 2000

Abstract—Neutrino mixing in Standard Model extensions, both renormalizable and effective, with arbitrary numbers of singlet and left-handed doublet neutrinos is investigated in a systematic fashion. The charged and neutral (Z-boson- and Higgs-boson-mediated) lepton currents are written under a general Majorana condition, and the independence of observables from the choice of condition, rephasing invariance, is studied. A parametrization of the neutrino mixing matrices in the doublet–singlet factorized form is developed. Its relationship with the seesaw mechanism is shown in the limit of small doublet–singlet mixing. The structure of the mixing matrices relevant to neutrino-oscillation experiments is explicated.
© *2002 MAIK "Nauka/Interperiodica".*

1. INTRODUCTION

The lepton sector of the minimal Standard Model (SM) of electroweak interactions is amazingly simple and symmetric. Owing to the supposed absence of right-handed neutrinos and neutrino masses, the SM predicts no flavor and CP violation for leptons. Nevertheless, there is no known rule that would prohibit neutrinos from acquiring masses. More than this, there are numerous indications of the contrary. If so, lepton mixing has to occur with all subsequent phenomena such as flavor and CP violation and neutrino oscillations (for a recent review, see, e.g., [1]).

Lepton mixing should generally be much more complicated than quark mixing. There are two main reasons for this. First, the number of (iso)singlet neutrinos is a priori arbitrary relative to that of (iso)doublet ones. Second, the Majorana masses for neutrinos are possible in addition to the Dirac ones. As a result, three types of associated problems arise. First, what is the total number of physical parameters, and how many of them are masses, mixing angles, and CP-violating phases? Second, what do the lepton currents, both the vector and scalar ones, look like in terms of the mixing matrices? And third, how to parametrize the matrices explicitly? In the previous paper [2] (see also references therein), we systematically studied the parameter-counting problem for SM extensions, both renormalizable and effective, with arbitrary numbers of singlet and left-handed doublet neutrinos. Here, we address the second and third problems.

The gauge interactions of Majorana neutrinos for SM extensions with arbitrary numbers of singlet and left-handed doublet neutrinos were studied in [3], where a parametrization of the neutrino mixing matrices was also proposed. The Yukawa neutrino interactions within renormalizable SM extensions with an equal number of singlet and doublet neutrinos were considered in [4]. The studies reported in [3, 4] were carried out traditionally under the canonical Majorana condition. In the present paper, these results are generalized under an arbitrary Majorana condition for any SM extensions, both renormalizable and effective, with arbitrary numbers of singlet and left-handed doublet neutrinos. The freedom in choosing the Majorana condition, rephasing invariance, is put as a cornerstone of the whole study.

In Section 2, the structure of neutrino interactions, both gauge and Yukawa interactions, is studied under an arbitrary Majorana condition. In Section 3, the properties of the interactions under Majorana neutrino rephasing, including the requirements of CP invariance, are considered. A parametrization of the mixing matrices in the doublet–singlet factorized form is proposed in Section 4. Its relationship, under small doublet–singlet mixing, with the seesaw mechanism [5] is shown. And finally, the patterns of neutrino-mixing matrices, relevant to neutrino-oscillation experiments, are discussed in Section 5.

2. LAGRANGIANS AND MIXING MATRICES

Weak basis. The most general renormalizable $SU(2)_W \times U(1)_Y$-invariant lepton Lagrangian of the SM supplemented with right-handed neutrinos reads

$$\mathcal{L} = \overline{l_L^0} i\not{D} l_L^0 + \overline{e_R^0} i\not{D} e_R^0 + \overline{\nu_R^0} i\not{\partial} \nu_R^0 \qquad (1)$$
$$- \left(\overline{l_L^0} Y^e e_R^0 \phi + \overline{l_L^0} Y^\nu \nu_R^0 \phi^C + \frac{1}{2} \overline{\nu_L^{0C}} M^\dagger \nu_R^0 + \text{h.c.} \right).$$

*This article was submitted by the author in English.

In (1), the lepton doublet l_L^0 and singlet e_R^0 and ν_R^0 fields with a zero superscript mean those in a weak basis where, by definition, the symmetry properties are well stated. It is supposed that the ordinary chiral families of the SM with the doublet left-handed Weyl neutrinos in number $d \geq 3$ are supplemented with the singlet (sterile) Weyl neutrinos in number $s \geq 0$. Let us denote such a renormalizable SM extension as $(d, s)_r$. A priori, one should retain s and d as arbitrary integers, both $s \leq d$ and $s > d$ being allowed. We omit, in the present analysis, the possible vectorlike lepton doublets. Hence, with allowance for the most probable exclusion of the fourth heavy chiral family [6], one should set, in fact, $d = 3$. Nevertheless, we retain d as a free parameter to clarify better the parameter-space structure of the extended SM. Further, $\not{D} \equiv \gamma^\alpha D_\alpha$ is the generic covariant derivative that reduces to the ordinary one, $\not{\partial} = \gamma^\alpha \partial_\alpha$, for the hypercharge-zero singlet neutrinos. Here and in what follows, the notation $\nu_L^{0C} \equiv (\nu_R^0)^C = C\overline{\nu_R^0}^T$, etc., is used for the particle–antiparticle conjugates of chiral fermions in the weak basis. Y^e and Y^ν are arbitrary complex $d \times d$ and $d \times s$ Yukawa matrices, respectively, and M is a complex symmetric $s \times s$ matrix of the Majorana masses for the singlet neutrinos. Finally, ϕ is the Higgs isodoublet and $\phi^C \equiv i\tau_2\phi^*$ is its charge conjugate.

One can generalize the preceding considerations to the most exhaustive Dirac–Majorana case with left-handed Majorana masses. The direct Majorana mass term for the doublet neutrinos is excluded in the minimal SM by the symmetry and renormalizability requirements. But in the extended SM as a low-energy effective theory, it could stem from the SM-invariant operator of the fifth dimension:

$$-\mathcal{L}' = \frac{1}{2\Lambda}\left(\phi^{C\dagger}\tau_i\phi\right)\left(\overline{l_R^{0C}} h\, i\tau_2\tau_i l_L^0\right) + \text{h.c.} \quad (2)$$

Here, τ_i, $i = 1, 2, 3$, are the Pauli matrices; h is a $d \times d$ symmetric constant matrix; $\Lambda \gg v$ is a lepton-number-violating mass scale (supposedly of order of the singlet Majorana masses); and v is the Higgs vacuum expectation value. The above operator with the effective isotriplet field $\Delta_i = (1/\Lambda)\left(\phi^{C\dagger}\tau_i\phi\right)$ reflects the oblique radiative corrections in the low-energy Lagrangian produced by the physics beyond the SM. With the Higgs doublet as

$$\phi = \begin{pmatrix} iw^+ \\ \dfrac{1}{\sqrt{2}}(v + H + iz) \end{pmatrix}, \quad (3)$$

H being the physical Higgs boson and z and w^+ being the would-be Goldstone bosons, formula (2) yields (in the unitary gauge) the following mass and Yukawa term for the neutrinos:

$$-\mathcal{L}' = \frac{1}{2}\left(1 + \frac{H}{v}\right)^2 \overline{\nu_R^{0C}}\mu\,\nu_L^0 + \text{h.c.}, \quad (4)$$

where $\mu = hv^2/\Lambda$. Such an effective SM extension will be denoted in what follows as (d, s). Note that, if the isotriplet Δ_i were considered to be elementary in the renormalizable framework, it would change only the emerging Yukawa interactions, not affecting the mass and mixing matrices.

Let us now introduce the complete one-handed neutrino collection (which can always be chosen, say, as left-handed)

$$n_L^0 = (\nu_L^0, \nu_L^{0C}), \quad (5)$$

so that $(n_L^0)^C \equiv n_R^{0C} = (\nu_R^{0C}, \nu_R^0)$. In this notation, the total neutrino mass matrix $\mathcal{M}_0^n$ defined by the mass Lagrangian

$$-\mathcal{L}_{\text{mass}}^n = \frac{1}{2}\,\overline{n_R^{0C}}\mathcal{M}_0^n n_L^0 + \text{h.c.} \quad (6)$$
$$\equiv -\frac{1}{2}\, n_L^{0T} C^{-1}\mathcal{M}_0^n n_L^0 + \text{h.c.}$$

is clearly symmetric with allowance for $C^T = -C$. More particularly, it has the form

$$\mathcal{M}_0^n = \begin{pmatrix} \mu & m \\ m^T & M \end{pmatrix}, \quad (7)$$

where $m \equiv Y^* v/\sqrt{2}$ is an arbitrary $d \times s$ matrix of the Dirac masses; m^T is obtained by transposing it; and M and μ are, respectively, the $s \times s$ and $d \times d$ symmetric Majorana mass matrices from (1) and (4).

Mass basis. Let us now consider the mass basis n_L, where, by definition, the neutrino mass matrix is diagonal. It is understood that the true neutrino mass eigenfields are $d + s$ four-component fields $\mathcal{N}(n_L)$ bringing the neutrino kinetic Lagrangian to the diagonal positive form and simultaneously satisfying some subsidiary Majorana condition to halve the number of degrees of freedom. The most general condition of this type has the form [7–9]

$$\mathcal{N}_\varphi^C \equiv \varphi\,\mathcal{N}_\varphi, \quad (8)$$

where $\mathcal{N}_\varphi^C \equiv C\overline{\mathcal{N}}_\varphi^T$ and $\varphi = \text{diag}\,(\varphi_1, \ldots, \varphi_{d+s})$ is a diagonal phase matrix. Here and in what follows, we use the notation with the subscript φ to stress that the quantity at hand generally depends on φ. Note that the maximum number of independent Majorana specific phases in φ might be $d + s - 1$ because an overall neutrino phase is unobservable. Expressing $\mathcal{N}_\varphi$ in terms of Weyl spinors as $\mathcal{N}_\varphi = \varphi_L n_L \oplus \varphi_R n_R^C$ with some diagonal phase matrices φ_L and φ_R, one finds that the Majorana condition is satisfied if $\varphi_L\varphi_R = \varphi^*$.

Without loss of generality, one can set, e.g., $\varphi_L = I$ and $\varphi_R = \varphi^*$, so that

$$\mathcal{N}_\varphi = n_L \oplus \varphi^* n_R^C. \tag{9}$$

This choice is advantageous because it results in the simplest form for the charged current, which is left-handed (see below). Note that Eqs. (8) and (9) do not impose any constraint on the original Weyl fields n_L.

In these terms, we demand the kinetic part of the neutrino Lagrangian to be

$$\mathcal{L}^n_{\text{kin}} = \frac{1}{2}\overline{\mathcal{N}}_\varphi\, i\partial\!\!\!/ \mathcal{N}_\varphi - \frac{1}{2}\overline{\mathcal{N}}_\varphi \mathcal{M}^n_{\text{diag}} \mathcal{N}_\varphi, \tag{10}$$

with a nonnegative diagonal mass matrix $\mathcal{M}^n_{\text{diag}}$ independent of φ. To this end, we choose the $(d+s)\times(d+s)$ unitary transformation $\mathcal{U}^n_\varphi$,

$$n^0_L = \mathcal{U}^n_\varphi n_L, \tag{11}$$

so that

$$\mathcal{U}^{nT}_\varphi \mathcal{M}^n_0 \mathcal{U}^n_\varphi = \varphi \mathcal{M}^n_{\text{diag}}, \tag{12}$$

with[1)]

$$\mathcal{M}^n_{\text{diag}} = \text{diag}\,(m^\nu_1, \ldots, m^\nu_d; M^N_1, \ldots, M^N_s). \tag{13}$$

With allowance for $\overline{\mathcal{N}}_\varphi = \overline{\mathcal{N}^C_\varphi}\varphi \equiv -\mathcal{N}^T_\varphi C^{-1}\varphi$, the neutrino kinetic Lagrangian takes the required form (10). At $s \le d$ for the $(d,s)_r$ extension, $d-s$ elements m^ν are zero. This reflects the fact that, in this case, the rank of the $(d+s)\times(d+s)$ matrix given by (7) with $\mu = 0$ is $2s$. At $s > d$, the rank of the matrix is generally $d+s$; hence, there is no massless neutrinos.

Similarly, the charged lepton fields e_χ ($\chi = L, R$) in the mass basis are defined as

$$e^0_\chi = \mathcal{U}^e_\chi e_\chi \tag{14}$$

with the unitary $d\times d$ matrices $\mathcal{U}^e_\chi$, and the bidiagonalization of the relevant mass matrix has the form

$$\mathcal{U}^{e\dagger}_L \mathcal{M}^e_0 \mathcal{U}^e_R = \mathcal{M}^e_{\text{diag}} = \text{diag}\,(m^e_1, \ldots, m^e_d). \tag{15}$$

By means of the global symmetries of the kinetic part of Lagrangian (1), one can arrange, without loss of generality, the charged-lepton weak basis to coincide with the mass one. This means that $\mathcal{M}^e_0$ can be chosen to be diagonal ab initio, so that $\mathcal{U}^e_L = \mathcal{U}^e_R = I$. The associated neutrinos are usually referred to as the flavor ones.[2)] Traditionally, the corresponding basis is used in discussing the neutrino-oscillation phenomenon. When there is an admixture of the heavy Majorana neutrinos, it is only the coherent part of the light neutrinos that has the meaning of the flavor state. Note that flavor states modified in this way are nonorthogonal and process-dependent. But in fact, there is no need for such a particular choice. Moreover, the mass basis suffices to describe neutrino oscillations without resort to weak eigenstates [10].

Now, the charged-current Lagrangian in the mass basis reads

$$-\mathcal{L}_W = \frac{g}{\sqrt{2}} W^-_\alpha \overline{e_L}\gamma^\alpha V_\varphi \mathcal{N}_{\varphi L} + \text{h.c.}, \tag{16}$$

W^- being a charged gauge boson and the rectangular $d\times(d+s)$ mixing matrix for the charged currents being

$$V_\varphi = \mathcal{U}^{e\dagger}_L P^{en} \mathcal{U}^n_\varphi. \tag{17}$$

Here, P^{en} is the charged-current matrix in the weak basis,

$$P^{en} = \begin{pmatrix} I_d & O_{d\times s} \end{pmatrix}, \tag{18}$$

I_d being the d-dimensional identity matrix and $O_{d\times s}$ being the $d\times s$ zero matrix. The lepton mixing matrix V_φ is the counterpart of the quark CKM matrix. It follows from (17) and (18) that

$$V_\varphi V^\dagger_\varphi = I_d, \tag{19}$$

though $V^\dagger_\varphi V_\varphi \ne I_{d+s}$. Equation (19) can be regarded as the one-sided unitarity condition at $s \ne 0$. Note that, because of the supposed absence of vectorlike lepton doublets, the right-handed charged currents do not emerge.

The neutral-current Lagrangian with the SM neutral-current operator $T_3 - s^2_{\text{W}} Q$ in the mass basis is

$$-\mathcal{L}_Z = \frac{g}{c_{\text{W}}} Z_\alpha \Big(-\frac{1}{2}\overline{e_L}\gamma^\alpha e_L + s^2_W \overline{e}\gamma^\alpha e + \frac{1}{2}\overline{\mathcal{N}}_{\varphi L}\,\gamma^\alpha X_\varphi \mathcal{N}_{\varphi L} \Big), \tag{20}$$

Z being a massive neutral gauge boson. Here, the $(d+s)\times(d+s)$ neutrino mixing matrix for the neutral currents is

$$X_\varphi = \mathcal{U}^{n\dagger}_\varphi P^n \mathcal{U}^n_\varphi \tag{21}$$

with the onto-doublet neutrino projection operator $P^n = (P^n)^2$,

$$P^n = \text{diag}\,(\underbrace{1, \ldots, 1}_{d}; \underbrace{0, \ldots, 0}_{s}). \tag{22}$$

In (20), one sets $c_{\text{W}} \equiv \cos\theta_{\text{W}}$ and $s_W \equiv \sin\theta_{\text{W}}$, with θ_{W} being the Weinberg angle. Clearly, X_φ is a Hermitian projection-operator matrix: $X_\varphi = X^\dagger_\varphi$ and $X_\varphi = X^2_\varphi \ne I$. Due to (17) and (18), the relation

$$X_\varphi = V^\dagger_\varphi V_\varphi \tag{23}$$

[1)] The notation corresponds to the partition $\mathcal{N}_\varphi \equiv (\nu, N)_\varphi$ and tacitly implies the seesaw hierarchy $m^\nu \ll M^N$ for all the elements, with ν being (quasi)doublet neutrinos and N being (quasi)singlet ones. Nevertheless, there might be experimental indications of the existence of at least one light singlet neutrino [1].

[2)] Unfortunately, this is unlike the quark sector where flavor is synonymous with the mass eigenstate.

between the neutral- and charged-current mixing matrices is obeyed. For the $(d,0)$ extension, one has $P^n = I_d$, so that $X_\varphi \equiv I_d$; thus, the $d \times d$ matrix V_φ is unitary. Moreover, for the renormalizable $(d,0)_r$ extension, one can always set $\mathcal{U}_\varphi^n = I$, whence it follows that $V_\varphi = I_d$. Hence, the lepton-flavor conservation of the minimal SM is readily recovered.

The Yukawa Lagrangian for the renormalizable extension $(d,s)_r$ has the form

$$-\mathcal{L}_{\rm Y} = \frac{H}{v}\,\overline{e}\,\mathcal{M}^e_{\rm diag} e + \frac{z}{v}\,\overline{e}\,\mathcal{M}^e_{\rm diag} i\gamma_5\, e \qquad (24)$$
$$+\left(\frac{1}{2}\frac{H+iz}{v}\,\overline{\mathcal{N}}_{\varphi R}\Big(\varphi^* X_\varphi^T \varphi \mathcal{M}^n_{\rm diag} + \mathcal{M}^n_{\rm diag} X_\varphi\Big)\mathcal{N}_{\varphi L} + \sqrt{2}i\frac{w^-}{v}\Big(\overline{e_L}\, V_\varphi \mathcal{M}^n_{\rm diag}\mathcal{N}_{\varphi R} - \overline{e_R}\mathcal{M}^e_{\rm diag} V_\varphi \mathcal{N}_{\varphi L}\Big) + {\rm h.c.}\right).$$

Here, one makes use of the constraint

$$X_\varphi^T \varphi \mathcal{M}^n_{\rm diag} X_\varphi = 0, \qquad (25)$$

which follows from the more particular constraint

$$P^n \mathcal{U}_\varphi^{n*} \varphi \mathcal{M}^n_{\rm diag} \mathcal{U}_\varphi^{n\dagger} P^n = 0, \qquad (26)$$

the latter reflecting the absence of the $d \times d$ symmetric left-handed Majorana mass term μ in (7).

For the general extension (d,s), the constraint in (25) should be discarded. This results in addition of a number of interaction terms to the Yukawa Lagrangian. For example, according to (4), one should add, in the unitary gauge, the term

$$-\mathcal{L}'_{\rm Y} = \frac{1}{2}\Big(\frac{H}{v}\Big)^2 \overline{\mathcal{N}}_{\varphi R}\,\varphi^* X_\varphi^T \varphi \times \mathcal{M}^n_{\rm diag} X_\varphi \mathcal{N}_{\varphi L} + {\rm h.c.} \qquad (27)$$

In (4), the term linear in H is canceled by a similar term that should now be present in $\mathcal{L}_{\rm Y}$.

3. REPHASING INVARIANCE

Let us consider the group of transformations consisting of the Majorana field rephasing $\mathcal{N}_\varphi \to \Phi^{1/2}\mathcal{N}_\varphi$ followed by the transformations

$$\begin{aligned} \varphi &\to \varphi\Phi^*, \\ V_\varphi &\to V_\varphi \Phi^{*1/2} \end{aligned} \qquad (28)$$

with a diagonal phase matrix $\Phi = {\rm diag}\,(\Phi_1, \ldots, \Phi_{d+s})$. As a result, one also gets $X_\varphi \to \Phi^{1/2} X_\varphi \Phi^{*1/2}$. All the Lagrangians are clearly rephasing-invariant. It follows from (28) that independent rephasing-invariant quantities containing φ may be chosen as $V_\varphi\varphi^{*1/2}(\varphi^{1/2} X_\varphi \varphi^{*1/2})$ and $\varphi^{1/2}\mathcal{N}_\varphi$. Thus, rephasing allows one to extract a number of neutrino phases from V_φ and to reabsorb them in φ, or vice versa. Observables depend only on the sum of the complementary phases of V_φ and $\varphi^{*1/2}$, as well as of $\mathcal{N}_\varphi$ and $\varphi^{1/2}$, but not separately on each of them (in addition to phases in the rephasing-invariant combinations of the matrix V_φ itself). Clearly, it is not a particular choice of the Majorana condition but invariance with respect to this choice that is physically meaningful.[3)]

Rephasing invariance permits one to choose φ that is the most appropriate for the problem at hand. The reason is that only the Higgs vertices and the neutrino wave functions (and, thus, the $\langle \mathcal{N}_\varphi \overline{\mathcal{N}_\varphi^C}\rangle$ propagators) depend explicitly on φ, whereas the gauge vertices and the $\langle \mathcal{N}_\varphi \overline{\mathcal{N}_\varphi}\rangle$ propagators do not depend on it. As a result, if the matrix element for a particular process does not contain φ explicitly, then one can extract, by means of rephasing, as many Majorana specific phases from V_φ as is possible. Rephasing invariance then ensures that, for other φ, these phases, though being superficially present in V_φ, would not enter into the final results nevertheless.

To illustrate, the amplitude for (chirality conserving) $\mathcal{N}\mathcal{N}$ oscillations

$$\mathcal{A}_0(t) = V_\varphi e^{-iEt} V_\varphi^\dagger \qquad (29)$$

clearly does not depend on the Majorana specific phases capable of being stored in φ, whereas the amplitude for the (chirality-flip) $\mathcal{N}\mathcal{N}^C$ oscillations

$$\mathcal{A}_1(t) = V_\varphi e^{-iEt} \varphi^* \mathcal{M}^n_{\rm diag} E^{-1} V_\varphi^T \qquad (30)$$

does depend on the phases. In the above, E is the diagonal energy matrix for the light neutrinos. The same is true for the neutrino-mass elements $\nu\nu^C$ in the weak basis

$$\mathcal{M}^{n\,*}_{\nu_e\nu_{e'}} = \big(V_\varphi \varphi^* \mathcal{M}^n_{\rm diag} V_\varphi^T\big)_{\nu_e\nu_{e'}}, \qquad (31)$$

which determine the rates of neutrinoless double β decay (at $e' = e$) or $e\bar{\mu}$ conversion (at $e' = \mu$). Note that, according to (24) and (27), the (chirality-flip) Yukawa interactions might also serve as a probe for the Majorana specific phases.

[3)] Let us stress that, owing to rephasing invariance, fixing a choice for φ has nothing to do with the real physical properties of the Majorana neutrinos—in particular, with those concerning C conjugation. The latter properties are described additionally by the fact that, if the neutrino mass eigenstates do possess definite C parity $\eta_C = {\rm diag}\,(\pm 1)$, then C conjugation for the Majorana eigenfields should be consistently redefined [8] as $\mathcal{N}_\varphi \stackrel{C}{\to} \mathcal{N}_\varphi^{C_\varphi} \equiv \eta_C \varphi^* \mathcal{N}_\varphi^C$, where traditionally $\mathcal{N}_\varphi^C \equiv C\overline{\mathcal{N}}_\varphi^T$. It follows hereof that the modified (anti-)self-charge conjugacy condition $\mathcal{N}_\varphi^{C_\varphi} = \eta_C \mathcal{N}_\varphi$ is indeed satisfied independently of φ. Hence, an attempt at ascribing physics content to the Majorana condition being chosen superficially in the self- or anti-self-charge conjugate form would be misleading.

Canonical Majorana condition. Sometimes, it might be tempting to go over to a basis where the Majorana neutrino wave functions have a canonical form. Namely, the rephasing by $\Phi = \varphi$ yields $\varphi \to I$, with I being the identity matrix, and the transformed fields $\mathcal{N}_I$ satisfy the canonical Majorana condition $\mathcal{N}_I^C = \mathcal{N}_I$. Under this condition, all physical mixing parameters reside only in mixing matrices. With allowance for the X_φ Hermiticity property $X_\varphi = X_\varphi^\dagger$, or $\mathrm{Re}\, X_\varphi^T = \mathrm{Re}\, X_\varphi$ and $\mathrm{Im}\, X_\varphi^T = -\mathrm{Im}\, X_\varphi$, the neutrino neutral-current parts of Lagrangians (20) and (24) can now be reexpressed as

$$-\mathcal{L}_Z^n = \frac{g}{4c_\mathrm{W}} Z_\alpha \overline{\mathcal{N}}_I \gamma^\alpha \Big(i\,\mathrm{Im}\, X_I - \gamma_5\,\mathrm{Re}\, X_I \Big)\mathcal{N}_I \tag{32}$$

and[4)]

$$-\mathcal{L}_\mathrm{Y}^n = \frac{1}{2}\frac{H}{v}\overline{\mathcal{N}}_I \Big(\mathrm{Re}\, X_I + i\gamma_5\,\mathrm{Im}\, X_I\Big)\mathcal{M}^n_\mathrm{diag}\mathcal{N}_I \tag{33}$$
$$+\frac{1}{2}\frac{z}{v}\overline{\mathcal{N}}_I \Big(\mathrm{Im}\, X_I - i\gamma_5\,\mathrm{Re}\, X_I\Big)\mathcal{M}^n_\mathrm{diag}\mathcal{N}_I + \mathrm{h.c.}$$

***CP* invariance.** It is well known that, for a field theory not to explicitly violate CP, there should be allowed a weak basis where all the parameters in the Lagrangian are real. Under this condition, the neutrino mass matrix $\mathcal{M}^n$, being symmetric, can always be reduced to the (real) diagonal form (generally, not positive definite) by means of an orthogonal transformation $\mathcal{U}^n = \mathcal{O}^n$ with the effect

$$\mathcal{O}^{nT}\mathcal{M}^n\mathcal{O}^n = \eta_M \mathcal{M}^n_\mathrm{diag}. \tag{34}$$

Here, $\eta_M \equiv \mathrm{diag}\,(\pm 1)$ is the mass-signature matrix, which is completely determined by the original $\mathcal{M}^n$. Clearly, the mixing matrix $V_{\eta_M} \equiv \mathcal{R} = P^{en}\mathcal{O}^n$ is real. Here and in what follows, the basis where $\mathcal{U}_L^e = \mathcal{U}_R^e = I$ is generally chosen for the sake of simplicity. In the rephasing-invariant form, one gets $V_\varphi = \mathcal{R}\,(\varphi\eta_M)^{1/2}$; hence, the condition for CP invariance has the form

$$V_\varphi = V_\varphi^* \varphi \eta_M, \tag{35}$$

as well as

$$X_\varphi = \eta_M \varphi^* X_\varphi^* \varphi \eta_M. \tag{36}$$

Let us stress that CP conservation does not mean that V_φ and X_φ must be real in general.

In the mass basis, one can define CP conjugation (in the unitary gauge) as

$$e(x) \to \gamma_0 e^C(x^P), \tag{37}$$
$$\mathcal{N}_\varphi(x) \to \eta_{CP}\varphi^*\gamma_0\mathcal{N}_\varphi^C(x^P),$$
$$W^\pm(x) \to -W^{\mp\,P}(x^P),$$
$$Z(x) \to -Z^P(x^P),$$
$$H(x) \to H(x^P)$$

(with $x^P \equiv (x_0, -\mathbf{x})$, etc.). The definition is clearly rephasing-invariant. Here, $i\eta_{CP}$, with $\eta_{CP} \equiv \mathrm{diag}\,(\pm 1)$, is the matrix of the (relative) CP parities for the neutrino mass eigenstates [8, 9]. In the above, η_{CP} is not arbitrary, but it is to be properly defined for consistency. Namely, under (37) the whole Lagrangian can be shown to transform into itself, where the substitution

$$V_\varphi \to V_\varphi^* \varphi \eta_{CP} \tag{38}$$

is made. Imposing the requirement of CP invariance, one arrives with allowance for (35) at the identity

$$\eta_{CP} \equiv \eta_M. \tag{39}$$

This identity ensures the consistency of the description of CP invariance directly in terms of rephasing-invariant quantities, which, being built of V_φ and φ, depend on η_M, with the description in terms of the explicit CP transformations (37), which depends on η_{CP}.

In particular, in the case of CP conservation, one finds for the amplitudes in (29)–(31) that

$$\mathcal{A}_0(t) = V_\varphi e^{-iEt}\eta_{CP}\,\varphi^* V_\varphi^T, \tag{40}$$
$$\mathcal{A}_1(t) = V_\varphi e^{-iEt}\eta_{CP}\mathcal{M}^n_\mathrm{diag}E^{-1}V_\varphi^\dagger,$$
$$\mathcal{M}^{n\,*}_{\nu_e\nu_{e'}} = \big(V_\varphi\,\eta_{CP}\mathcal{M}^n_\mathrm{diag}V_\varphi^\dagger\big)_{\nu_e\nu_{e'}}.$$

At $\nu_e = \nu_{e'}$, the last line explicitly demonstrates the possibility for the (partial) compensation of various contributions to the lepton-number-violating $e\bar{e}$ transition under CP conservation. At $\varphi = \eta_{CP}$, the matrix V_φ (as well as X_φ) becomes pure real, $V_{\eta_{CP}} \equiv \mathcal{R}$, so that

$$\mathcal{A}_0(t) = \mathcal{R}\,e^{-iEt}\,\mathcal{R}^T, \tag{41}$$
$$\mathcal{A}_1(t) = \mathcal{R}\,e^{-iEt}\eta_{CP}\mathcal{M}^n_\mathrm{diag}E^{-1}\mathcal{R}^T,$$
$$\mathcal{M}^n_{\nu_e\nu_{e'}} = \big(\mathcal{R}\,\eta_{CP}\mathcal{M}^n_\mathrm{diag}\mathcal{R}^T\big)_{\nu_e\nu_{e'}}.$$

The basis $\mathcal{N}_{\eta_{CP}}$ may be referred to as a CP-associated one. In a sense, it might present the most natural choice for a CP-conserving theory, all other bases being equivalent, though probably less convenient. To compare, under the canonical Majorana condition $\varphi = I$, the elements of V_I (and X_I) in the CP-conserving theory should be, according to (35), either pure real or imaginary [8, 9, 11], and this has nothing to do with maximal CP violation, as might superficially seem.

[4)] Under the condition $\varphi = I$, the Yukawa term for the renormalizable extension $(n, n)_r$ was found in [4].

4. DOUBLET–SINGLET PARAMETRIZATION

General case. A mathematical parametrization of the neutrino mixing matrix $\mathcal{U}^n$ is given in [3]. An alternative physical prescription, heavily relying on the doublet–singlet neutrino content and thus being useful for practical purposes, is proposed in the present study. For the sake of simplicity, the subscript φ will be omitted in what follows. First of all, we note that, by means of the global symmetries of the Lagrangian, one can always ensure, without loss of generality, that $\mathcal{U}^e_L = \mathcal{U}^e_R = I$.[5] Now, before applying any restrictions on the neutrino mass matrix $\mathcal{M}^n$, the $(d+s)\times(d+s)$ unitary mixing matrix $\mathcal{U}^n$ is arbitrary and can be decomposed in a unique way (at least in a neighborhood of unity) as

$$\mathcal{U}^n = \mathcal{U}^n_d\,\mathcal{U}^n_s\,\mathcal{U}^n_m. \tag{42}$$

Here, $\mathcal{U}^n_d$ is a unitary $d\times d$ matrix in the doublet neutrino subspace. This matrix is spanned by d^2 generators and depends on $d(d-1)/2$ mixing angles and $d(d+1)/2$ phases. More particularly, one can set

$$\mathcal{U}^n_d = \begin{pmatrix} U^\nu_d & 0 \\ 0 & I_s \end{pmatrix} \tag{43}$$

with a $d\times d$ unitary matrix U^ν_d. There is still a freedom of redefining d charged lepton phases which is left after the mass matrix in (15) is diagonalized. According to (17) and (42), this freedom can be used to eliminate d phases from $\mathcal{U}^n_d$. It clearly leaves only $d(d-1)/2$ independent phases in this matrix (and an equal number of mixing angles).

Now, one can write the following explicit parametrization for U^ν_d $(d>1)$ in terms of the modified Pontryagin coordinates of the second kind [3]:

$$U^\nu_d = u_{\rm diag}(\alpha)\prod_{\substack{f,g=1,\ldots,d\\ f<g}}\otimes\, u_{fg}(\theta_{fg},\delta_{fg}). \tag{44}$$

The product above should be understood in some particular (but a priori unspecified) order. Here, $u_{\rm diag}$ is a diagonal $d\times d$ phase matrix $u_{\rm diag}(\alpha) = {\rm diag}\,(e^{i\alpha_1},\ldots\ldots,e^{i\alpha_d})$, which distinguishes equivalent parametrizations and is at our disposal. (At $d=1$, one has $U^\nu_1 = e^{i\alpha_1}$.) The basic matrix u_{fg} ("complex rotation"), one of a set of $d(d-1)/2$ unitary $SU(2)$ submatrices, acts in the f–g plane, $f\neq g$, and depends only on one mixing angle θ_{fg} and one phase δ_{fg}:

$$u_{fg} = \exp\begin{pmatrix} 0 & \theta_{fg}e^{i\delta_{fg}} \\ -\theta_{fg}e^{-i\delta_{fg}} & 0 \end{pmatrix} = \begin{pmatrix} \cos\theta_{fg} & \sin\theta_{fg}e^{i\delta_{fg}} \\ -\sin\theta_{fg}e^{-i\delta_{fg}} & \cos\theta_{fg} \end{pmatrix}. \tag{45}$$

By means of the identity

$$u_{\rm diag}(\alpha)\,u_{fg}(\theta_{fg},\delta_{fg})\,u^\dagger_{\rm diag}(\alpha) = u_{fg}(\theta_{fg},\alpha_f+\delta_{fg}-\alpha_g), \tag{46}$$

one can eliminate $d-1$ δ's from U^ν_d and transform these phases into the same number of Majorana specific ones, the dth of the latter phases being unphysical.[6] It clearly leaves $(d-1)(d-2)/2$ CKM-like phases and $d-1$ Majorana specific ones. Thus, under proper phase redefinitions, the matrix U^ν_d may be chosen in experimentally viable cases of $d=2$ and 3, respectively, as

$$U^\nu_2 = \begin{pmatrix} c & s \\ -s & c \end{pmatrix}\begin{pmatrix} e^{i\alpha} & 0 \\ 0 & 1 \end{pmatrix} \tag{47}$$

and

$$U^\nu_3 = \begin{pmatrix} c_3 & s_3 & 0 \\ -s_3 & c_3 & 0 \\ 0 & 0 & 1 \end{pmatrix}\begin{pmatrix} c_2 & 0 & s_2 \\ 0 & 1 & 0 \\ -s_2 & 0 & c_2 \end{pmatrix} \times \begin{pmatrix} 1 & 0 & 0 \\ 0 & c_1 & s_1e^{i\delta} \\ 0 & -s_1e^{-i\delta} & c_1 \end{pmatrix}\begin{pmatrix} e^{i\alpha_1} & 0 & 0 \\ 0 & e^{i\alpha_2} & 0 \\ 0 & 0 & 1 \end{pmatrix}, \tag{48}$$

where $c\equiv\cos\theta$ and $s\equiv\sin\theta$ for respective θ's. Clearly, one can shift the ordinary phase δ to any of the s_i, $i=1,2,3$.

Further, $\mathcal{U}^n_s$ is the counterpart of $\mathcal{U}^n_d$ in the singlet neutrino subspace with indices $f=d+1,\ldots,d+s$ being spanned by s^2 generators and dependent on $s(s-1)/2$ mixing angles and $s(s+1)/2$ phases. One has

$$\mathcal{U}^n_s = \begin{pmatrix} I_d & 0 \\ 0 & U^N_s \end{pmatrix} \tag{49}$$

with an $s\times s$ unitary matrix U^N_s. Clearly, $\mathcal{U}^n_d$ and $\mathcal{U}^n_s$ commute with each other. According to (17), the matrix $\mathcal{U}^n_s$ is irrelevant to observables. Hence, by means of global symmetries, one can always ensure, without loss of generality, that $U^N_s = {\rm diag}\,(e^{i\alpha_{d+1}},\ldots,e^{i\alpha_{d+s}})$, with α's being at our disposal. This choice is advantageous to subsequently expose the Majorana specific phases in $\mathcal{U}^n$.

[5] For this reason, lepton mixing is synonymous with the neutrino one.

[6] Strictly speaking, this is true only for the $(d,0)$ case. For the (d,s) extension, the Majorana specific phases could be exposed only after taking into account the matrix $\mathcal{U}^n_m$.

Finally, $\mathcal{U}_m^n$ is a unitary $(d+s)\times(d+s)$ matrix spanned by $2sd$ generators that mix the two subspaces. The last property follows from inversion of (11) for the transformation between the weak and mass neutrino bases. This matrix depends generally on the sd mixing angles and on the same number of phases. It follows from (21) and (42) that the neutral-current mixing matrix takes the form

$$X = \mathcal{U}_m^{n\dagger} P^n \mathcal{U}_m^n. \tag{50}$$

In other words, it depends exclusively on the parameters of $\mathcal{U}_m^n$, the rest of the parameters present in $\mathcal{U}_d^n$ manifesting themselves only through charged currents (and thus through neutrino oscillations). To achieve this goal, the chosen order of matrices $\mathcal{U}_d^n$ and $\mathcal{U}_s^n$ relative to $\mathcal{U}_m^n$ in (42) is crucial. The factorization property of the charged and neutral currents makes the parametrization in (42) very convenient in practice. Altogether, the total neutrino mixing matrix $\mathcal{U}^n$ for the general (d,s) extension contains $d(d-1)/2+sd$ physical mixing angles and the same number of phases, in agreement with [2, 3]. Similarly to (44) and (45), one can propose, for $\mathcal{U}_m^n$, the explicit representation

$$\mathcal{U}_m^n = \prod_{\substack{f=1,\ldots,d\\ g=1,\ldots,s}} \otimes\, u_{f,d+g}(\omega_{f,d+g}) \tag{51}$$

with a fixed but a priori unspecified order of submatrices and with $\omega_{f,d+g}$ being ds arbitrary complex numbers. When restricted to a 2×2 complex plane, the matrices $u_{f,d+g}$ are quite similar to those given by (45). By means of the identity in (46) with diagonal phases from U_s^ν, one can eliminate s phases from ds ones in $\mathcal{U}_m^n$ and get, in the end, $d+s-1$ Majorana specific phases in $\mathcal{U}^n$.

As for the renormalizable $(d,s)_r$ extension, the $d\times d$ symmetric matrix constraint (26) reduces $d(d+1)/2$ phases and the same number of moduli, d of the latter ones corresponding to masses and $d(d-1)/2$ to mixing angles. As a result, $\mathcal{U}^n$ contains sd-independent physical mixing angles and $d(s-1)$ phases, precisely as it should according to the general counting of [2]. Superficially, the above constraint restricts only the parameters in $\mathcal{U}_m^n$ and does not touch those in U_d^ν. But it can be shown that, at $d\geq s>0$, due to the presence of $d-s$ massless neutrinos, it is additionally possible to eliminate, from U_d^ν, the parameters corresponding to $U(d-s)$ symmetry. It leaves, in U_d^ν, $ds-s(s+1)/2$ independent θ's and $d(s-1)-s(s-1)/2$ δ's. Note that the constraint does not invalidate the charged-neutral-current factorization property.

This gives a complete solution to the problem. There are two important cases with neutral currents remaining diagonal.

Only Dirac masses. For the particular case of the $(d,s)_r$ extension with only Dirac masses, a further reduction of parameters is possible. For the $d\times s$ Dirac mass term, diagonalization of the neutrino mass matrix by $\mathcal{U}_d^n\,\mathcal{U}_s^n$ yields

$$m_{\text{diag}} = U_d^{\nu T} m\, U_s^N, \tag{52}$$

with the nonnegative elements on the quasidiagonal, the rest being zero. Let us recall that U_s^N is unobservable. At $0<s\leq d$, one has s nonzero entries in m_{diag}. Hence, there is the $U(d-s)\times U(1)^{s-1}$ left-out symmetry in the doublet neutrino subspace, which reduces the number of parameters in U_d^ν to $sd-s(s+1)/2$ mixing angles and $sd-s(s+1)/2-d+1$ phases. At $0<d<s$, there are d nonzero entries, the left-out symmetry in the doublet neutrino subspace is only $U(1)^{d-1}$, and one recovers the CKM-like scheme for d Dirac neutrinos with $d(d-1)/2$ mixing angles and $(d-1)(d-2)/2$ phases. This explicit counting is completely in accordance with the general one in [2].

Finally, there still remains, in $\mathcal{U}_m^n$, the maximal (with $\pi/4$ angles) mixing between the pairs of the mass-degenerate eigenfields. For a proper choice of φ, the ensuing orthogonal transformation $\mathcal{O}^n$ reduces the neutrino mass matrix to the real diagonal form $\mathcal{M}_{\text{diag}}^n = \big(m_1(1,-1),\ldots,m_p(1,-1),0,\ldots,0\big)$, with $p=\min(d,s)$. It corresponds to p pairs of the mass-degenerate Majorana neutrinos with the opposite CP parities plus $|s-d|$ massless neutrinos. The emerging mixing matrix X in (50) is superficially nondiagonal. Via the reversed transition to the Dirac basis, the neutral currents may nevertheless be represented in an explicitly flavor-conserving form independent of φ. As for massless neutrinos, there is no difference whether they are considered as Weyl or Majorana ones. The neutral-current Lagrangian $\mathcal{L}_Z^n$ for the doublet massless neutrinos is flavor-conserving, singlet massless neutrinos being sterile.

Only Majorana masses. In the case of (d,s) extension with only Majorana masses, one has $\mathcal{U}_m^n\equiv I$; hence, $X\equiv P^n$. The neutrino part of interactions now becomes

$$\mathcal{L}_Z^n = \frac{g}{4c_{\text{W}}} Z_\alpha\, \overline{\mathcal{N}}\gamma^\alpha\gamma_5 P^n \mathcal{N} \tag{53}$$

and (in the unitary gauge)

$$-\mathcal{L}_{\text{Y}}^n = \left(\frac{H}{v}+\frac{1}{2}\Big(\frac{H}{v}\Big)^2\right)\overline{\mathcal{N}}\mathcal{M}_{\text{diag}}^n P^n\mathcal{N}, \tag{54}$$

both Lagrangians being explicitly independent of φ. Owing to presence of the onto-doublet neutrino projection operator P^n, the singlet neutrinos are ensured to be sterile.

Small doublet–singlet mixing. It is instructive to discuss the mixing matrices under the condition

of a small doublet–singlet mixing, the case of importance for phenomenology. In particular, this is so in the framework of the seesaw approximation (see below). Making use of the equivalent representation for (51) as

$$\mathcal{U}_m^n = \exp\begin{pmatrix} 0 & \omega \\ -\omega^\dagger & 0 \end{pmatrix}, \qquad (55)$$

where ω is an arbitrary complex $d \times s$ matrix, one finds at small ω that

$$\mathcal{U}_m^n \qquad (56)$$
$$= \begin{pmatrix} 1 - \frac{1}{2}\omega\omega^\dagger & \omega\big(1 - \frac{1}{6}\omega^\dagger\omega\big) \\ -\omega^\dagger\big(1 - \frac{1}{6}\omega\omega^\dagger\big) & 1 - \frac{1}{2}\omega^\dagger\omega \end{pmatrix} + \mathcal{O}(\omega^4)$$

and

$$\mathcal{U}^n \qquad (57)$$
$$= \begin{pmatrix} U_d^\nu\big(1 - \frac{1}{2}\omega\omega^\dagger\big) & U_d^\nu\omega\big(1 - \frac{1}{6}\omega^\dagger\omega\big) \\ -\omega^\dagger\big(1 - \frac{1}{6}\omega\omega^\dagger\big) & 1 - \frac{1}{2}\omega^\dagger\omega \end{pmatrix} + \mathcal{O}(\omega^4).$$

Hence, one has

$$V = \Big(U_d^\nu \big(1 - \tfrac{1}{2}\omega\omega^\dagger\big) U_d^\nu\, \omega \Big) + \mathcal{O}(\omega^3), \qquad (58)$$

as well as

$$X = \begin{pmatrix} 1 - \omega\omega^\dagger & \omega \\ \omega^\dagger & \omega^\dagger\omega \end{pmatrix} + \mathcal{O}(\omega^3). \qquad (59)$$

These expressions can readily be generalized with any finite accuracy in ω.[7)]

Finally, the constraint for the $(d,s)_r$ extension given by (25) yields

$$\varphi^{\nu *} m^\nu_{\rm diag} = -\omega\varphi^{N*} M^N_{\rm diag}\omega^T + \mathcal{O}(\omega^4). \qquad (60)$$

This determines $m^\nu_{\rm diag}$ and a part of the ω's in terms of M^N and the rest of the ω's. For example, in the simplest case of $s = 1$, the solution to the equation can be shown to be given by the d-dimensional vector ω with one nonzero component $\omega_d = (-\varphi^\nu_d/\varphi^N)^{1/2}|\omega|$, so that $m_d = |\omega|^2 M$. Reversing, one gets generically $\omega = \mathcal{O}(|\, m^\nu_{\rm diag}/M^N_{\rm diag}|^{1/2})$. The general solution to Eq. (60) is given by an $s \times s$ nonzero matrix with the proper constraints following from the equation. As a result, the parameters in $\mathcal{U}^n$ are shared between the independent ones in $\mathcal{U}^n_d$ and $\mathcal{U}^n_m$ as is shown in the table. The relations above have their close counterparts in the framework of the seesaw approximation (see below).

The part $\mathcal{U}^n|_{d\times d}$ of the total mixing matrix $\mathcal{U}^n$ that spans the $d \times d$ subspace of the doublet neutrinos reads

$$\mathcal{U}^n|_{d\times d} = U_d^\nu\Big(1 - \frac{1}{2}\omega\omega^\dagger\Big) + \mathcal{O}(\omega^4). \qquad (61)$$

It includes the $d \times d$ Hermitian combination $\omega\omega^\dagger$ for the $d \times s$ matrix ω. This brings in additional mixing angles and phases. But even if these terms are disregarded, when $\mathcal{U}^n|_{d\times d} = U_d^\nu$ is unitary, the number of physical phases in it being relevant for the Majorana neutrinos, $d(d-1)/2$, would exceed $(d-1)(d-2)/2$ given by the CKM-like unitary matrix for the Dirac neutrinos. In essence, this difference is due to the freedom of fixing, in U_d^ν, out of the initial $d(d+1)/2$ phases, only d phases in the Majorana case, instead of $2d-1$ ones in the Dirac case.

Seesaw approximation. In order to evaluate the mixing magnitudes and to study the decoupling limit, it is useful to compare the general results for small mixing with those obtained within the seesaw mechanism by the explicit diagonalization of the neutrino mass matrix. By the unitary global transformation $U(s)$ of the singlet neutrinos, the mass matrix M in (7) can be reduced to the diagonal form

$$M = \varphi^N M^N_{\rm diag}. \qquad (62)$$

Moreover, d phases of the Dirac mass matrix m can be eliminated owing to the freedom of redefining the charged-lepton phase. This freedom is still left after the simultaneous diagonalization of the charged-lepton mass matrix by the biunitary $d \times d$ transformation. Thus, the total neutrino mass matrix $\mathcal{M}^n$ clearly contains $s(d+1)$ independent moduli, s of them corresponding to physical masses and sd ones to mixing angles, as well as $d(s-1)$ phases. This explicit counting for the $(d,s)_r$ extension is in accordance with the general one presented in [2].

The results of [12] for the neutrino-mass diagonalization in the $(n,n)_r$ extension can readily be generalized to the $(d,s)_r$ one. Under the condition $M^N_{\rm diag} \gg |m|$ for all the elements, the seesaw neutrino mixing matrix can be found to be

$$\mathcal{U}^{n'}_m = \begin{pmatrix} 1 - \frac{1}{2}\xi^\dagger\xi & \xi^\dagger\big(1 - \frac{1}{2}\xi\xi^\dagger\big) \\ -\xi\big(1 - \frac{1}{2}\xi^\dagger\xi\big) & 1 - \frac{1}{2}\xi\xi^\dagger \end{pmatrix} + \mathcal{O}(\xi^4), \qquad (63)$$

where the $s \times d$ matrix ξ is $\xi \equiv M^{-1}m^T$, $|\xi| \ll 1$. Clearly, ξ results in sd mixing angles and $d(s-1)$

[7)] Clearly, the above results are not applicable in the case of pseudo-Dirac neutrinos where ω's are generally not small. Here, (55) could be properly modified by decomposing the mixing matrix $\mathcal{U}^n_m$ into the product of two parts, $\mathcal{U}^n_m \equiv \mathcal{U}^n_{m2}\mathcal{U}^n_{m1}$. The part $\mathcal{U}^n_{m1}$ should produce a transition to the pseudo-Dirac basis by a set of (mutually commuting) pairwise transformations at (nearly) $\pi/4$ angles. The part $\mathcal{U}^n_{m2}$ due to the rest of the ω's could result in the remaining flavor-violating corrections.

Independent mixing parameters for the renormalizable $(d,s)_r$ extension

Case	Parameters	$\mathcal{U}^n$	$\mathcal{U}_d^n$	$\mathcal{U}_m^n$
$d \geq s > 0$	Angles	ds	$d(d-1)/2$	$s(s+1)/2$
			$-(d-s)(d-s-1)/2$	
	Phases	$d(s-1)$	$d(d-1)/2$	$s(s-1)/2$
			$-(d-s)(d-s+1)/2$	
$s > d > 0$	Angles	ds	$d(d-1)/2$	$sd-d(d-1)/2$
	Phases	$d(s-1)$	$d(d-1)/2$	$sd-d(d+1)/2$
$d=s=n$	Angles	n^2	$n(n-1)/2$	$n(n+1)/2$
	Phases	$n(n-1)$	$n(n-1)/2$	$n(n-1)/2$

phases in the neutrino mixing matrix. Up to next-to-leading order in ξ, the matrix $\mathcal{U}_m^{n'}$ brings $\mathcal{M}_0^n$ from the texture form

$$\mathcal{M}_0^n = \begin{pmatrix} 0 & \xi^T M \\ M\xi & M \end{pmatrix} \tag{64}$$

to the block-diagonal form $\mathcal{M}^{n'} = \mathcal{U}_m^{n'T}\mathcal{M}_0^n\mathcal{U}_m^{n'}$ with

$$\mathcal{M}^{n'} \tag{65}$$
$$= \begin{pmatrix} -\xi^T M\xi & 0 \\ 0 & M + \frac{1}{2}\left(M\xi\xi^\dagger + \xi^* \xi^T M\right) \end{pmatrix} + \mathcal{O}(\xi^3).$$

Now, by means of the unitary $d\times d$ transformation $U_d^{\nu'}$, one can diagonalize the mass matrix for light neutrinos,

$$\varphi^\nu m_{\mathrm{diag}}^\nu = -U_d^{\nu' T}\xi^T\varphi^N M_{\mathrm{diag}}^N \xi\, U_d^{\nu'} + \mathcal{O}(\xi^4), \tag{66}$$

so that $\xi = \mathcal{O}((m^\nu/M^N)^{1/2})$. Similarly, by the unitary $s\times s$ transformation $U_s^{N'} = I_s + \mathcal{O}(\xi^2)$, one can diagonalize the mass matrix for the heavy neutrinos. Under the condition that the left-handed Majorana mass term μ is $\mathcal{O}(1/M)$, Eq. (66) is straightforwardly generalized to

$$\varphi^\nu m_{\mathrm{diag}}^\nu \tag{67}$$
$$= U_d^{\nu' T}\left(\mu - \xi^T\varphi^N M_{\mathrm{diag}}^N \xi\right) U_d^{\nu'} + \mathcal{O}(1/M^3).$$

The full neutrino mixing matrix in the seesaw framework has the form $\mathcal{U}^n = \mathcal{U}_m^{n'}\mathcal{U}_d^{n'}\mathcal{U}_s^{n'}$. Comparing it with that in the doublet–singlet parametrization (42), one finds that the parametrizations differ by the order of the matrices. As a result, this leads to somewhat different representations for V (and X). In the absence of the direct masses for the doublet neutrinos, the model-independent matrix ω is related to the seesaw matrix ξ as

$$\xi = (U_d^\nu \omega)^\dagger + \mathcal{O}(\omega^3), \tag{68}$$

where $U_d^{\nu'} = U_d^\nu + \mathcal{O}(\omega^2)$. In this, all the quantities ω, U_d^ν, and ξ generally depend on φ. The parameters of ξ are clearly shared between the independent ones in U_d^ν and ω in accordance with the table.

In the limit $\xi = \mathcal{O}(m/M) \to 0$ and, hence, $m^\nu \to 0$, one has to substitute effectively $U_d^\nu \to I_d$ because of neutrino mass degeneracy. Thus, all light-neutrino-mixing effects in the seesaw framework disappear at $v/M \ll 1$, signaling the onset of decoupling. In particular, it follows from (24) and (27) that the Higgs boson decouples from the νN current in the seesaw framework in the leading order $\mathcal{O}(M)$, only Yukawa couplings $\mathcal{O}(v)$ generally being left. As for NNH vertices, they are $\mathcal{O}(v^2/M)$ in the limit $M \gg v$.[8)] The seesaw matrix ξ (and, more generally, ω) results in the nonuniversality and nonunitarity of the lepton charged and neutral currents, and it can be estimated experimentally to be small, typically $|\xi| \leq \mathcal{O}(10^{-1}$–$10^{-2})$ [13].

[8)] This contradicts the statement of [4] made within the seesaw framework on a significant enhancement of the νNH and NNH vertices. The enhancement could clearly take place at large M only if the suppression ($\sim 1/M$ or $1/M^2$) of the mixing elements is disregarded. Otherwise, it could be just a numerical effect at not overly large M.

Some comments are finally in order. It is clear from the above that the seesaw form of $\mathcal{U}^{n'}_m$, given by (63), closely resembles the most general one given by (56). In fact, this seesawlike structure does not depend on the particular expression (7) for the neutrino mass matrix, the latter restricting only the number of independent parameters through constraint (60). Whereas the seesaw results, under condition $m^\nu \neq 0$, can strictly be applicable only at $\xi \neq 0$, the advantage of the model-independent parametrization is that it can straightforwardly be generalized to a case of arbitrary ω. The mixings and masses become completely disentangled. In particular, one can have, e.g., $\omega = 0$ at $m^\nu \neq 0$, or $m^\nu = 0$ at $\omega \neq 0$. In addition, it is possible to have finite ω at $M \gg v$ and thus produce enhancement in vertices involving heavy neutrinos. Clearly, the violation of decoupling can originate in the given framework only owing to the nonrenormalizable Lagrangian (2). This general parametrization completely exhausts all the possibilities for the neutrino masses, including these of the pure Dirac and Majorana origins.

5. NEUTRINO OSCILLATIONS

The structure of $\mathcal{U}^n$ for the SM general extension (d, s) (in practice, $d = 3$) could be used in discussing the pattern of light-neutrino oscillations. Both Dirac and Majorana light neutrinos are permitted a priori. Because the Dirac neutrino can be regarded as a pair of mass-degenerate Majorana ones (with opposite CP parities), SM extensions featuring at least a few additional light degrees of freedom are of interest. The primordial abundances of light nuclei in standard big-bang nucleosynthesis restrict the number of relativistic two-component neutrinos in equilibrium to be less than 3.2 (95% C.L.) [14]. Hence, depending on the model, the number of the light sterile neutrinos could still be accommodated. Sticking to as simple a neutrino content as is possible, one can encounter two different scenarios: with and without one sterile light Majorana neutrino.

No light singlet neutrino. At any s, that part of the neutrino mixing matrix $\mathcal{U}^n$ which is relevant to oscillations reduces, in this case, to $\mathcal{U}^n|_{d\times d}$. In the leading $\mathcal{O}(\omega)$ approximation, it is the $d \times d$ unitary matrix U^ν_d. This effectively simplifies the (d, s) extension to $(d, 0)$ in the light-lepton sector [in practice, it is the $(3, 0)$ one and the corresponding mixing matrix is given by (48)]. As is stated before, U^ν_d depends generally on $d(d-1)/2$ physical mixing angles and on the same number of phases. But, according to (29), neutrino oscillations with chirality conservation (coinciding here with the total-lepton-number conservation, $\Delta L = 0$) are insensitive to $d-1$ phases capable of residing in the Majorana condition matrix φ. This reduces the number of observable phases to $(d-1)(d-2)/2$, precisely as in the Dirac case. Hence, there is no difference here for $\Delta L = 0$ neutrino oscillations between the Majorana and Dirac cases [15]. This effective suppression could be evaded though for chirality-flip (here also, lepton-number-violating, $|\Delta L| = 2$) oscillations. But, according to (30), these ones are in turn chirally suppressed; i.e., their intensity is $\mathcal{O}((m^\nu/E)^2)$ at neutrino energies $E > m^\nu$ [15, 16]. It follows that, in this case, it would be hard to observe, in oscillations, specific Majorana CP violation, if any.

Finally, in the absence of light singlet neutrinos, chirality-conserving light-neutrino oscillations are described within the given assumptions just by the $d \times d$ unitary matrix U^ν_d of the CKM-like type with $d(d-1)/2$ mixing angles and $(d-1)(d-2)/2$ phases. Allowance for $\mathcal{O}(\omega^2)$ terms due to the doublet–singlet mixing would reveal additional CP-violating phases in U^ν_d (plus those in ω itself). In addition, it is clear that, in this case, neutrino oscillations are mainly sensitive to a different set of mixing parameters than the neutral-current mixing matrix, the latter one being determined entirely by the doublet–singlet mixing matrix $\mathcal{U}^n_m(\omega)$. Hence, the two phenomena essentially disentangle in this case.

Light singlet neutrino. As for the case with a light singlet neutrino, the doublet–singlet mixing can no longer be ignored and should be taken into account, producing the observable effect. Among singlet neutrinos, only the light one is relevant in the leading $\mathcal{O}(\omega)$ order to light-neutrino mixing. In the approximation used, one can effectively set $s = 1$, thus reducing the problem to the $(d, 1)$ case. The matrix $\mathcal{U}^n_m$ in (56) is given by its part not higher than $\mathcal{O}(\omega)$, where $\omega = (\omega_1, \ldots, \omega_d)$. Thus, $\mathcal{U}^n$ effectively depends on $d(d+1)/2$ physical mixing angles and an equal number of phases, in accordance with [2]; $d(d-1)/2$ of each of them reside in the doublet–doublet mixing U^ν_d, and d in the doublet–singlet mixing $\mathcal{U}^n_m(\omega)$. Such an approximate $(d+1) \times (d+1)$ matrix $\mathcal{U}^n$ is unitary to the given accuracy and presents the most general mixing matrix in this approximation. Owing to explicit φ independence of the helicity-conserving (now not coinciding any longer with lepton-number-conserving) oscillations, the number of phases relevant to these oscillations, reduces to $d(d-1)/2$, as if there were $d+1$ Dirac neutrinos.

Actually, one has $d = 3$, and experiments might suggest a pairwise neutrino mixing [1]. It consists only of the mixing of a pair of doublet neutrinos (chosen here as ν_1 and ν_2) between themselves and the mixing of the light singlet neutrino ($N_1 \equiv \nu_4$)

only with the remaining doublet neutrino ν_3, i.e., $\omega = (0, 0, \omega_3)$. Hence, in the case at hand, the neutrino mixing $(3, 1)$ reduces to the product of two cases, $(2, 0)$ and $(1, 1)$, each of them corresponding to one mixing angle and one Majorana specific phase (the latter being unobservable in the helicity-conserving oscillations). For proper redefinitions, the mixing matrix $\mathcal{U}^n$ thus becomes

$$\mathcal{U}^n = \begin{pmatrix} \begin{pmatrix} c_1 & s_1 \\ -s_1 & c_1 \end{pmatrix} \begin{pmatrix} e^{i\alpha_1} & 0 \\ 0 & 1 \end{pmatrix} & 0 \\ 0 & \begin{pmatrix} c_2 & s_2 \\ -s_2 & c_2 \end{pmatrix} \begin{pmatrix} e^{i\alpha_2} & 0 \\ 0 & 1 \end{pmatrix} \end{pmatrix}. \quad (69)$$

Under the given assumptions, Eq. (69) describes the general mixing for four light neutrinos [one of them being (quasi)sterile], which is consistent with experimental data. For the charged-current mixing matrix $V = P^{en}\mathcal{U}^n$, one accordingly has

$$V = \begin{pmatrix} c_1 & s_1 & 0 & 0 \\ -s_1 & c_1 & 0 & 0 \\ 0 & 0 & c_2 & s_2 \end{pmatrix} \begin{pmatrix} e^{i\alpha_1} & 0 & 0 & 0 \\ 0 & 1 & 0 & 0 \\ 0 & 0 & e^{i\alpha_2} & 0 \\ 0 & 0 & 0 & 1 \end{pmatrix}. \quad (70)$$

For the neutral-current mixing matrix $X = \mathcal{U}^n P^n \mathcal{U}^{n\dagger} = V^\dagger V$, the result is

$$X = \begin{pmatrix} \begin{pmatrix} 1 & 0 \\ 0 & 1 \end{pmatrix} & 0 \\ 0 & \begin{pmatrix} c_2^2 & c_2 s_2 e^{-i\alpha_2} \\ c_2 s_2 e^{i\alpha_2} & s_2^2 \end{pmatrix} \end{pmatrix}. \quad (71)$$

Clearly, $c_2, s_2 \neq 0$ results in flavor violation in neutral currents. Let us recall that, to describe completely lepton interactions, one should also specify the matrix η_{CP} of neutrino CP signatures, as well as the matrix φ of the Majorana condition to which the mixing matrices above correspond. In particular, only then can one decide whether there is CP violation or not in general. But in chirality-conserving oscillations, CP will always be conserved because all the phases here are the specific Majorana ones.

6. SUMMARY

The neutrino gauge and Yukawa interactions for the SM extensions, both renormalizable and effective, have been systematically investigated under an arbitrary Majorana condition. Independence from the particular choice of this condition has been demonstrated by means of explicit rephasing invariance. This invariance has been used to exhibit manifestations of the specific Majorana phases. The parametrization of the neutrino mixing matrices in the doublet–singlet factorized form has been proposed. Its relation to the seesaw approximation has been shown. The patterns of neutrino mixing relevant to neutrino oscillation experiments are exposed.

ACKNOWLEDGMENTS

I am grateful to V.V. Kabachenko for stimulating discussions.

REFERENCES

1. S. M. Bilenky *et al.*, *Summary of the NOW'98 Phenomenology Working Group*; hep-ph/9906251.
2. Yu. F. Pirogov, Eur. Phys. J. C **17**, 407 (2000); hep-ph/0002299.
3. J. Schechter and J. W. F. Valle, Phys. Rev. D **22**, 2227 (1980).
4. A. Pilaftsis, Z. Phys. C **55**, 275 (1992); hep-ph/9901206.
5. T. Yanagida, Prog. Theor. Phys. B **135**, 66 (1978); in *Proceedings of the Workshop on Unified Theory and Baryon Number of the Universe,* Ed. by O. Swada and A. Sugamoto (KEK, 1979), p. 95; M. Gell-Mann, P. Ramond, and R. Slansky, in *Supergravity*, Ed. by P. van Nieuwenhuisen and D. Freedman (North-Holland, Amsterdam, 1979), p. 315.
6. Yu. F. Pirogov and O. V. Zenin, Eur. Phys. J. C **10**, 629 (1999); hep-ph/9808396.
7. J. Bernabeu and P. Pascual, Nucl. Phys. B **228**, 21 (1983); A. Barroso and J. Maalampi, Phys. Lett. B **132B**, 355 (1983); P. J. O'Donnell and U. Sarkar, Phys. Rev. D **52**, 1720 (1995); hep-ph/9305338.
8. B. Kaiser, Phys. Rev. D **30**, 1023 (1984).
9. S. M. Bilenky, N. P. Nedelcheva, and S. T. Petcov, Nucl. Phys. B **247**, 61 (1984).
10. C. Giunti, C. W. Kim, and U. W. Lee, Phys. Rev. D **44**, 3635 (1991); **45**, 2414 (1992); Phys. Lett. B **421**, 237 (1998); hep-ph/9709494; C. Giunti, C. W. Kim, J. A. Lee, and U. W. Lee, Phys. Rev. D **48**, 4310 (1993); hep-ph/9305276.

11. L. Wolfenstein, Phys. Lett. B **107B**, 77 (1981); J. Schechter and J. W. F. Valle, Phys. Rev. D **24**, 1883 (1981); Erratum: **25**, 283 (1982).
12. W. Buchmüller and D. Wyler, Phys. Lett. B **249**, 458 (1990); W. Buchmüller and C. Greub, Phys. Lett. B **256**, 465 (1991); Nucl. Phys. B **363**, 365 (1991).
13. M. Gronau, C. N. Leung, and J. L. Rosner, Phys. Rev. D **29**, 2539 (1984); P. Langacker and D. London, Phys. Rev. D **38**, 886, 907 (1988); S. M. Bilenky, W. Grimus, and H. Neufeld, Phys. Lett. B **252**, 119 (1990).
14. D. Tytler, J. M. O'Meara, N. Suzuki, and D. Lubin, astro-ph/0001318.
15. J. Schechter and J. W. F. Valle, Phys. Rev. D **23**, 1666 (1981); M. Doi, T. Kotani, H. Nishiura, *et al.*, Phys. Lett. B **102B**, 323 (1981).
16. J. Bahcall and H. Primakoff, Phys. Rev. D **18**, 3463 (1978).

Physics of Atomic Nuclei, Vol. 65, No. 1, 2002, pp. 11–17. Translated from Yadernaya Fizika, Vol. 65, No. 1, 2002, pp. 13–19.
Original Russian Text Copyright © 2002 by Bondarenko, Geltenbort, Korobkina, Morozov, Panin.

NUCLEI
Experiment

Cooling and Heating of Ultracold Neutrons during Storage

L. N. Bondarenko, P. Geltenbort[1)], E. I. Korobkina, V. I. Morozov, and Yu. N. Panin

Russian Research Centre Kurchatov Institute, pl. Kurchatova 1, Moscow, 123182 Russia

Received July 28, 2000; in final form, February 12, 2001

Abstract—The rare processes of weak heating and cooling of ultracold neutrons reflected from the surface of fluorosubstituted oil are studied. The probability of these processes is estimated at 10^{-6} per single reflection at energy transfer commensurate with the primary neutron energy. Weak heating and cooling are shown to be a manifestation of a more general phenomenon—quasielastic neutron reflection whose probability is dependent on temperature. © *2002 MAIK "Nauka/Interperiodica".*

1. INTRODUCTION

In the preliminary article [1], we reported on the observation of the rare process of weak cooling of ultracold neutrons (UCN) stored in a vessel whose walls were covered with Fomblin fluorosubstituted oil. In [2, 3], this rare process was revealed for UCN reflected from the surface of various materials. The results of those studies were at odds with the prevalent concept of absolutely elastic UCN reflection from material surfaces and stimulated theoretical studies to explain the observed phenomenon [4, 5].

In this article, we present the results of a more detailed study of the rare processes of weak heating and cooling of neutrons reflected from the surface of Fomblin oil, which is widely used in UCN storage experiments—in particular, in those that are aimed at measuring the neutron lifetime.

2. WEAK UCN COOLING IN THE CASE OF SUBBARRIER REFLECTION

Weak UCN cooling has been studied with the aid of a gravitation spectrometer employing a plunging absorber (Fig. 1) intended for generating a narrow energy spectrum of UCN and for subsequently analyzing its variations with time. A cylindrical vessel of diameter 64 cm used to store UCN and inserted into a vacuum casing was the hub of our facility. Ultracold neutrons produced by a source were fed into the vacuum casing, whereupon they penetrated into the storage vessel through a narrow ring-shaped slit formed by the top edge of the vessel ledge of height $a = 12.3$ cm and the bottom edge of the movable cylinder. Neutrons that ascended at altitudes in excess of a (these were neutrons whose kinetic energy near the vessel bottom was above $E_b = mga$, where m is the neutron mass and g is the acceleration due gravity) could be accumulated in the vessel. While the vessel was filled, the movable cylinder was held at the highest position, opening the slit for UCN to enter the vessel. On filling, the cylinder was lowered to close the slit. To increase the frequency of UCN reflections, a few layers of lead shot 3.5 mm in diameter were strewed on special horizontal grids in the vessel and at its bottom. The entire inner surface of the vessel and the shot surface were covered with Fomblin oil. The presence of the shot ensured a virtually isotropic distribution of the UCN flux in the volume. A polyethylene disk 58 cm in diameter arranged at an altitude h_d with respect to the bottom was used to form the upper boundary of the UCN spectrum. The disk efficiently absorbed UCN that could reach altitudes of $h > h_d$, with the result that a narrow spectrum of neutrons was formed in the vessel. The maximum altitude at which UCN belonging to the main part of the spectrum could ascend was within the range $a < h < h_d$. The relative fraction of UCN that could reach altitudes of $h > h_d$ was determined by the time parameters of the accumulation procedure and the so-called spectrum purification from above. Upon the formation of the primary spectrum of UCN and their storage, the disk was used to measure the spectrum by consecutively moving it down to a preset altitude h and by determining the number of UCN that remained in the vessel.

The measuring run included the procedures of (1) filling the vessel over a period of $t_f = 175$–300 s with a disk positioned at the altitude h_d; (2) bounding the spectrum from above (purification) over a period of $t_c = 100$ s with the disk fixed at the altitude h_d; (3) lifting the disk to the altitude of $h_{\max} = 15.5$ cm and storing UCN in the vessel (evolution) for $t_{\rm ev} = 20$, 620, and 1200 s at this disk position; (4) moving the disk down to an altitude h and removing UCN

[1)] Laue–Langevin Institute, 38042 Grenoble, France.

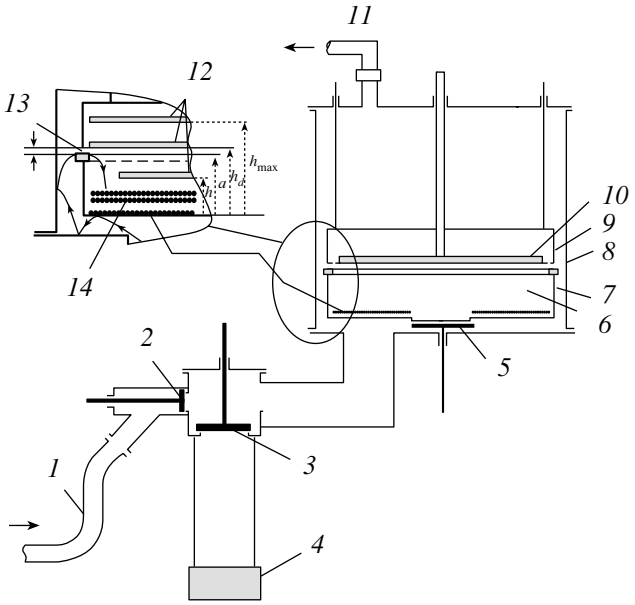

Fig. 1. Layout of the spectrometer and its position in the UCN beam: (*1*) inlet UCN guide, (*2*) inlet valve, (*3*) detector valve, (*4*) UCN detector, (*5*) outlet valve, (*6*) storage vessel, (*7*) bottom cylinder of the storage vessel, (*8*) outer vacuum casing of the spectrometer, (*9*) movable top cylinder, (*10*) polyethylene disk used to absorb UCN, (*11*) evacuation, (*12*) absorber position at various altitudes h of the disk, (*13*) inlet slit, and (*14*) additional sample in the form of lead-shot layers.

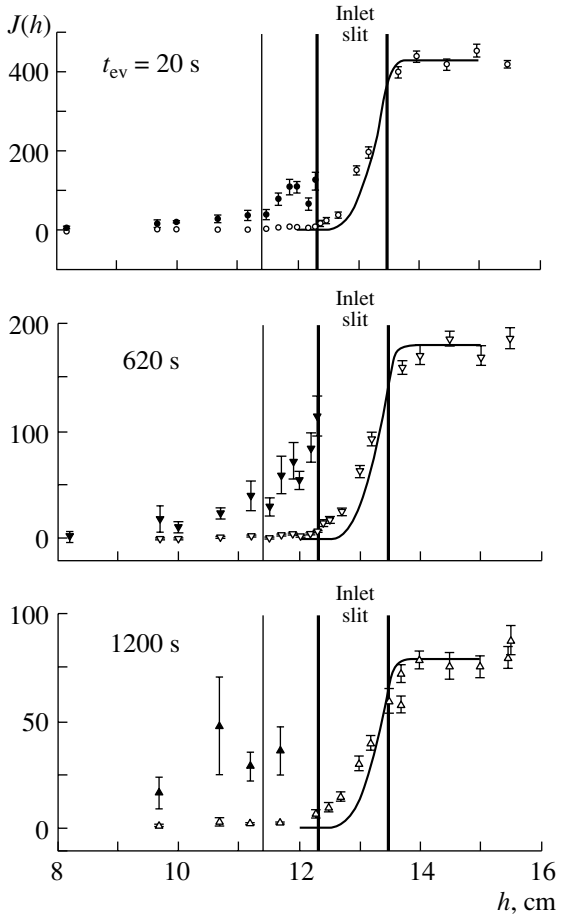

Fig. 2. Calculated and experimental dependences $J(h)$ for various times of spectrum evolution. The experimental results are presented for $h < 12.3$ cm both (open circles) on a full scale and (closed circles) with a 15-fold magnification. The solid curve represents the calculated dependences normalized to the experimental data for $h >$ 14 cm.

with a maximum altitude above a preset value of h by means of their absorption in the disk over a period of $t_m = 200$ s; (5) recording UCN that remained in the vessel after the completion of procedure (4) over a period of $t_r = 200$ s [during this procedure, the disk was held at the altitude h, the shutter of the bottom vessel was opened, and UCN flowed onto the detector that recorded their number $J(h)$]; and (6) measuring the detector background over a period of 50 s.

A consecutive fulfillment of these procedures made it possible to measure the dependence $J(h) = \text{const} \times \int_0^h F(x)dx$, where $F(x)$ is the spectrum of UCN in the vessel in terms of the maximum altitude at which they ascend. Numerically, the UCN energy measured in neV was nearly coincident with their maximum altitude in centimeters.

In the first run, the measurements were performed at $h_d = 13.475$ cm and the inlet-slit width of $d =$ 1.175 cm (the mean value along the perimeter). The calculated frequency of UCN reflections in the vessel was $f = 19$ Hz, the mean UCN speed near the bottom was 160 cm/s, and the measured time of neutron storage was $\tau = 680.0(9.5)$ s. Figure 2 shows the dependences $J(h)$ for the evolution times of 20, 620, and 1200 s. The solid curve in the figure represents the dependences $J(h)$ calculated under the assumption [6] that the reflection of UCN from the surface is absolutely elastic. These dependences are normalized in such a way that the experimental and the calculated dependences $J(h)$ are consistent on average in the region of h values much higher than the upper boundary of the spectrum ($h > 14$ cm). It can be seen that the experimental and the calculated distributions deviate, the degree of this deviation growing with evolution time. The tail of the distributions on the left, which extends as far as 3 to 4 cm below the ledge, is the most important feature of the deviation. This tail can be associated with a spurious experimental effect caused by the deficient time t_m over which UCN having the maximum altitude of ascent above that of the disk are removed from the vessel. In this case, UCN whose maximum altitude of ascent is greater than h can remain in the vessel even when the disk is below the

vessel ledge, mimicking the effect of the presence of UCN whose energy is below the inlet barrier.

However, two circumstances show that the observed distributions at $h < a$ do not stem from this spurious effect. First, it follows from the calculations performed in [6] that, at $t_m = 200$ s, the eventual value of J for altitudes $h < a$ that is due to this effect cannot be greater than 1.4×10^{-8} of the total number of UCN in the vessel. Thus, the spurious effect can yield only $J(h = 12.3\ \text{cm}) = 420 \times 1.4 \times 10^{-8} = 6 \times 10^{-6}$ for $t_{\text{ev}} = 20$ s, the experimental value being $J \approx 8$ at this altitude. Second, the spurious effect would manifest itself in the same way for all evolution times as a constant instrumental effect causing a distortion of the true dependences $J(h)$, but the figure demonstrates that the number of experimental counts for $h \leq a$ remains virtually unchanged with increasing evolution time, while the total number of UCN decreases because of decay and losses at the walls. It follows that UCN whose maximum altitude of ascent is less than a do indeed arise in the vessel, their relative fraction in the spectrum growing with evolution time.

The appearance of such UCN could be associated with the trivial effect of gradual cooling (and also heating) in the interactions of stored UCN with acoustic vibrations. An experimental investigation of 5- to 800-Hz vessel-wall vibrations that was performed with a B&K 4370 accelerometer has revealed that the maximum speed of the walls does not exceed $v_w = 100\ \mu$m/s. The change in the UCN energy due to multiple scattering on the vibrating wall is described in terms of a diffusion along the axis of energy E. For the random motion of neutrons that is accompanied by discontinuous energy jumps of $\overline{\Delta E}$, the diffusion coefficient is $D = \overline{\Delta E}^2/(2\Delta t)$, where $\Delta t = 1/f$ is the time between subsequent reflections. The probability that, after a lapse of time t, a neutron that had the energy E_0 at the initial instant has energy E in a unit interval is

$$\rho(E,t) = \frac{1}{2\sqrt{\pi D t}} e^{\frac{-(E\ -\ E_0)^2}{4Dt}}. \qquad (1)$$

In the experiment, the vibrations in question would manifest themselves in the broadening of the original UCN spectrum. In this case, the quantity obtained by averaging the variation of the maximum altitude over the UCN flux is $\Delta h = \dfrac{16 v_w}{3\pi}\sqrt{\dfrac{h}{2g}}$, while the diffusion coefficient is $D = (\Delta h)^2 f/2$. Figure 3 shows the calculated maximum-altitude distributions of monoenergetic UCN whose initial altitudes of ascent were 12.3 and 13.475 cm, which corresponds to the boundaries of the spectrum formed in the experiment. The calculations based on Eq. (1) were performed for the wall speed of 100 μm/s and for the evolution times of 20 and 1020 s. The figure shows that the root-mean-square deviation from the initial altitude of ascent is 0.2 to 0.3 cm for $t_{\text{ev}} = 1020$ s. Therefore, acoustic vibrations of the walls can in principle lead to a deviation of the experimental distributions $J(h)$ from the calculated distributions in the region $a < h < h_d$ (see Fig. 2). They can account for appearance of UCN whose altitude of ascent is below the height a of the ledge, but not more than by 0.2 to 0.3 cm. It follows from (1) that, for example, the probability of observing UCN whose altitude of ascent is 11.3 cm (1 cm below the ledge height) after 1200 s of storage does not exceed 5×10^{-8} even for neutrons of the lower spectrum boundary. This means that the appearance of UCN in the vessel such that their maximum altitude of ascent is below 11.3 cm cannot be explained by acoustic cooling. Such neutrons can be generated only by the rare processes of quasielastic reflection, in which case the energy of a neutron undergoes a discontinuous drop that is quite sizable in magnitude, but which is not greater than 3 neV. The relative fraction of cooled UCN must then grow linearly with increasing evolution time (the number of reflections). Let us show this explicitly. We denote by N_u the number of UCN that have not suffered cooling, by N_c the number of cooled UCN, by λ_c the probability of cooling per unit time, by $\lambda_l = \tau^{-1}$ the total probability of UCN losses in the vessel, and by λ_l^* the analogous probability for cooled UCN. The variation of the number of cooled and uncooled UCN with time is determined by the set of equations

$$\frac{dN_u}{dt} = -(\lambda_l + \lambda_c)N_u, \qquad (2)$$

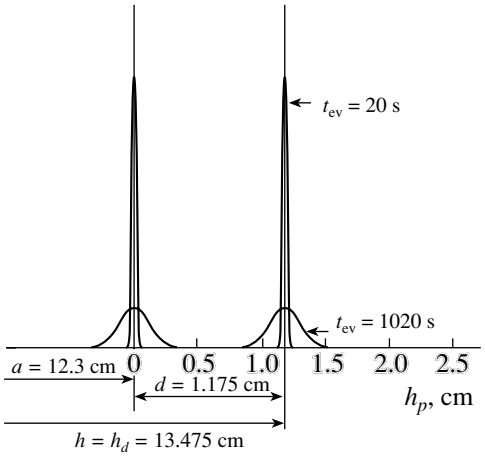

Fig. 3. Calculated distributions of UCN with respect to the altitude ($h = a + h_p$) from the bottom after $t_{\text{ev}} = 20$ and 1020 s of evolution that arise under the effect of acoustic vibrations of the vessel walls. The initial altitudes (12.3 and 13.475 cm) correspond to the boundaries of the distribution being formed.

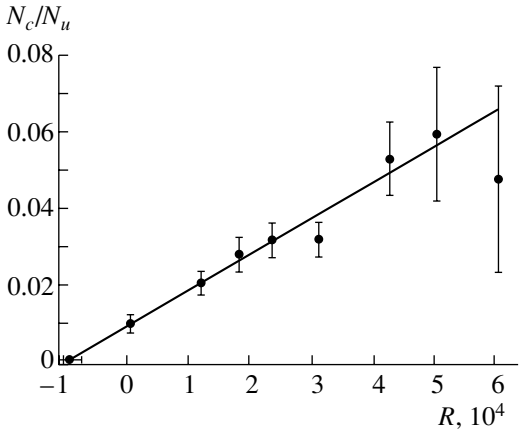

Fig. 4. Ratio of the counting rate for cooled UCN (N_c) to the counting rate for uncooled UCN (N_u) as a function of the number of reflections (R).

$$\frac{dN_c}{dt} = \lambda_c N_u - \lambda_l^* N_c.$$

Since $N_u(t) = N_u(0)e^{-(\lambda_l+\lambda_c)t}$, then $dN_c/dt = \lambda_c N_u(0)e^{-(\lambda_l+\lambda_c)t} - \lambda_l^* N_c$ and

$$N_c(t) = N_c(0)e^{-\lambda_l^* t} + \frac{\lambda_c N_u(0)}{\lambda_l - \lambda_l^* + \lambda_c}\left[e^{-\lambda_l^* t} - e^{-(\lambda_l+\lambda_c)t}\right],$$

where $N_c(0)$ is the initial number of cooled UCN generated in the vessel by the commencement of evolution at the stage of filling and spectrum purification. Setting $\lambda_l^* = \lambda_l$, which is valid for this experiment with a high degree of precision, we obtain $N_c(t) = N_c(0)e^{-\lambda_l t} + N_u(0)e^{-\lambda_l t}[1 - e^{-\lambda_c t}]$. For $t \ll \lambda_c^{-1}$, the total number of UCN in the vessel is $N \approx N_u$; therefore, we have

$$\frac{N_c(t)}{N(t)} \approx \frac{N_c(0)}{N_u(0)} + \lambda_c t \approx \frac{N_c(0)}{N(0)} + f\mu_c t, \quad (3)$$

where μ_c is the probability of UCN cooling upon a single reflection.

Figure 4 shows the results of the measurements performed at $h_d = 13.9$ cm, $d = 16$ mm, $t_f = 220$ s, $t_c = 100$ s, $t_m = 200$ s, and $f = 38$ Hz. The frequency of UCN reflections was increased by inserting additional shot. The number of UCN cooled 1.2 cm below the ledge height (N_c) and the total number of UCN (N) that survived in the vessel at the end of the evolution time were measured in the experiment. The number of reflections is $R = ft_{\rm ev}$. The figure shows that the experimental points fit in a straight line quite well, thus supporting the occurrence of the rare process of UCN cooling. The ratio $N_c(0)/N(0)$ is about 0.8%, and extrapolation of the linear dependence $N_c(R)/N(R)$ to 0 cuts the number $R_0 = -8500$ of reflections on the abscissa. This is an approximate number of reflections suffered by UCN in the course of filling ($t_f/2 \cong 110$ s) and purification ($t_c = 100$ s): $220 \cdot 38 \approx 8400$. In accordance with (3), the probability of cooling 1.2 cm below the ledge is $\mu_c = 8.5(9) \times 10^{-7}$.

3. WEAK HEATING OF UCN IN THE CASE OF SUBBARRIER REFLECTION

Since the gravitation spectrometer is not efficient in searches for weak heating and its investigation, further studies were performed with the setup shown in Fig. 5. Ultracold neutrons from a source were fed in an aluminum storage vessel of diameter 20 cm and length 70 cm; its inner surface was covered with Fomblin oil. In order to increase the frequency of reflections, an additional surface of aluminum sheet was arranged in the vessel, and this surface was also covered with Fomblin oil. The vessel temperature could be varied in the range between −15 and +70°C. A filter for bounding the UCN spectrum from above was installed in the vertical neutron guide connecting the UCN source with the setup, the position of the filter being 45 cm below the vessel bottom. The filter was implemented as an aluminum chamber 7 cm in diameter and 5 cm high. It had an enlarged inner surface covered with Fomblin oil and small inlet and outlet holes. Having penetrated through the filter, UCN had energies in the range 0–106 neV, the admixture of neutrons of higher energies being negligible. In ascending along the neutron guide, UCN slowed down, so that their energies in the vessel were in the range 0–52 neV at a mean speed of $v_u = 2.2$ m/s, the frequency of reflections being $f = 40$ Hz. Two proportional gas detectors were connected to the vessel by means of vertical neutron guides. The detector D_1, with an inlet diaphragm of diameter 6 mm, measured the density of the total UCN flux. The detector D_2, with an aluminum foil (13 μm) at the inlet, measured the flux density of UCN that could overcome an energy barrier of 52 neV ($E_{\rm lim}^{\rm Al} = 52$ neV). This flux was generated by (a) neutrons that initially had energies above 52 neV and which penetrated into the vessel through the filter (in the following, they are referred to as background neutrons) and (b) neutrons that had initial energies below 52 neV, but which were weakly heated upon reflections, with the result that their energies became higher than 52 neV.

If there is weak heating and if there are no background neutrons, the state of the neutron gas in the vessel is described by the set of two equations

$$\frac{dN_u}{dt} = -(\lambda_l + \lambda_0)N_u - \lambda_{\rm up}N_u + \phi S_0, \quad (4)$$

$$\frac{dN_{\rm up}}{dt} = \lambda_{\rm up}N_u - (\lambda_l^* + \lambda_0^*)N_{\rm up},$$

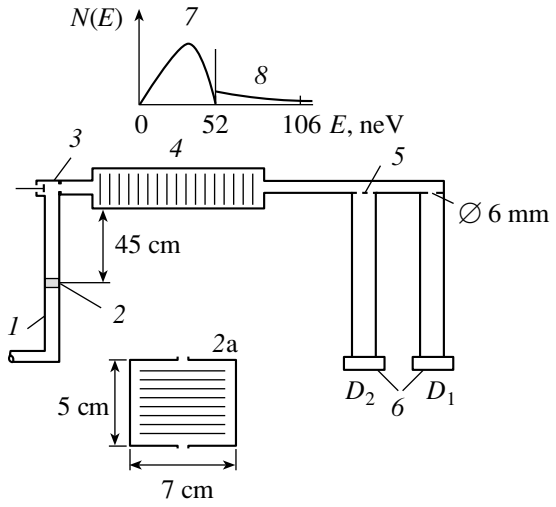

Fig. 5. Layout of the setup for studying the weak heating of the UCN: (*1*) inlet neutron guide, (*2*) special filter, (*2*a) same filter on an enlarged scale, (*3*) UCN inlet valve, (*4*) storage vessel, (*5*) aluminum foil, (*6*) UCN detectors, (*7*) the main UCN spectrum at the bottom of the storage vessel, and (*8*) background admixture of UCN with energies between 52 and 106 neV on an enlarged scale.

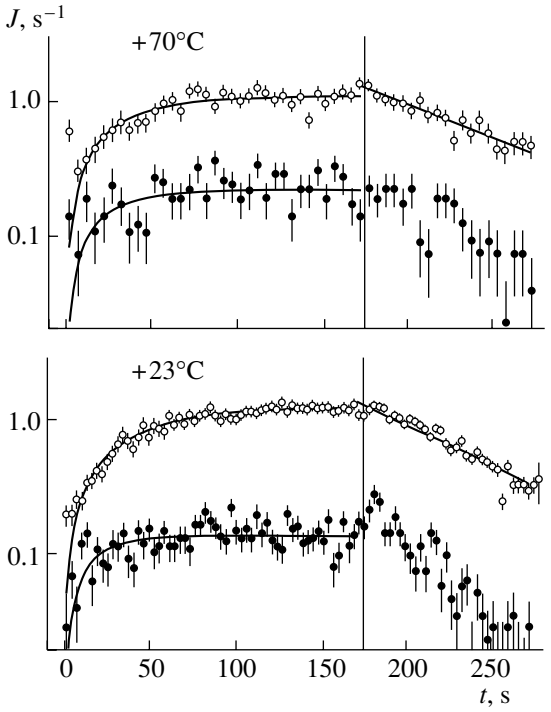

Fig. 6. Counting rate in the detectors (○) D_1 and (●) D_2 as a function of time for the temperatures of $T = +70°\mathrm{C}$ and $T = +23°\mathrm{C}$.

where N_u is the number of UCN that did not undergo weak heating; N_{up} is the number of UCN that underwent weak heating; λ_l and λ_0 are, respectively, the probability of losses in the vessel and the probability of leakage from it through the inlet hole of area S_0 for UCN that did not undergo weak heating; λ_l^* and λ_0^* are the analogous probabilities for UCN that underwent weak heating; ϕ is the flux density of UCN from the main spectrum of the source; and $\lambda_{\mathrm{up}} = \mu_{\mathrm{up}} f$ is the quantity obtained by averaging, over the density spectrum, the probability of weak heating (per unit time) that caused the growth of the UCN energy above 52 neV, with μ_{up} being the analogous probability per single reflection. If the vessel was filled for a long time, in which case we can set $dN_u/dt = 0$ and $dN_{\mathrm{up}}/dt = 0$, the numbers of UCN are

$$N_u = \frac{\phi S_0}{\lambda_l + \lambda_0 + \lambda_{\mathrm{up}}},$$

$$N_{\mathrm{up}} = \frac{\phi S_0 \lambda_{\mathrm{up}}}{(\lambda_l + \lambda_0 + \lambda_{\mathrm{up}})(\lambda_l^* + \lambda_0^*)},$$

and the corresponding flux densities are $\phi_u = N_u v_u/(4\Omega)$ and $\phi_{\mathrm{up}} = N_{\mathrm{up}} v_{\mathrm{up}}/(4\Omega)$, where v_u and v_{up} are the mean speeds of neutrons that did not suffer and that suffered weak heating, respectively, and Ω is the vessel volume.

If there were no background UCN, the counting rates J_{tot} and J_{up} in the detectors D_1 and D_2 would determine the quantities $\phi_u = J_{\mathrm{tot}}/(S_1\epsilon)$ and $\phi_{\mathrm{up}} = J_{\mathrm{up}}/(S_2\epsilon\mu_p)$, where S_1 and S_2 are the areas of the inlet detector diaphragms, ϵ is the detection efficiency, and μ_p is the coefficient characterizing the penetration of UCN of energy above $E_{\mathrm{lim}}^{\mathrm{Al}}$ through the aluminum foil. In this case, the weak-heating probability could be determined as $\lambda_{\mathrm{up}} = J_{\mathrm{up}}(\lambda_l^* + \lambda_0^*)S_1/(J_{\mathrm{tot}}\mu_p S_2)$. In the presence of a background, we have

$$\lambda_{\mathrm{up}} = \left(\frac{J_{\mathrm{up}} S_1}{J_{\mathrm{tot}} S_2} - \frac{\phi_b S_1}{J_{\mathrm{tot}}}\right) \frac{\lambda_l^* + \lambda_0^*}{\mu_p};$$

that is, additional measurements are necessary for determining the quantity ϕ_b corresponding to the flux density of background neutrons recorded by the detector.

Figure 6 presents the detector counting rates measured in the course of filling the vessel with neutrons over 175 s and their subsequent storage at two values of the vessel temperature. In either case, the detector D_2 records neutrons penetrating through the 52-neV barrier created by the foil. However, its counting rate increases noticeably with increasing temperature of the vessel, while the number of accumulated UCN remains virtually unchanged. The basic gas-kinetic properties of the storage vessel undergo virtually no changes at the higher temperature: the characteristic filling time is $\tau_f = 1/(\lambda_l + \lambda_0) \approx 40$ s and the time of neutron storage in the vessel is $\tau_{\mathrm{st}} = 1/\lambda_l \approx 80$ s. This is because λ_l is given by

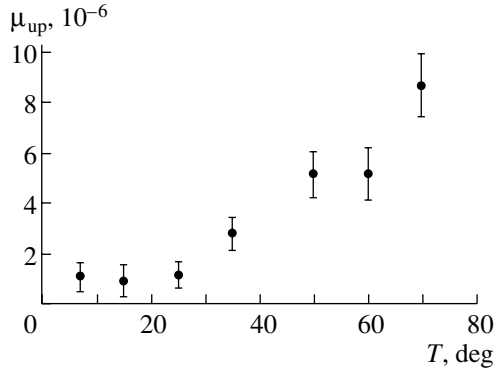

Fig. 7. The probability $\mu_{\rm up}(T)$ of the weak heating of UCN versus temperature.

$\lambda_l = \lambda_\beta + \lambda_F + \lambda_h$, where $\lambda_\beta = 1.13 \times 10^{-3}$ s^{-1} is the beta-decay probability, $\lambda_F \approx 4 \times 10^{-4}$ s^{-1} is the probability of the capture and inelastic scattering of UCN undergoing reflection from the vessel surface and the additional surface, and $\lambda_h \approx 1.1 \times 10^{-2}$ s^{-1} is the probability of UCN leakage from the vessel through the operating holes for evacuation and the diaphragm of the detector D_1. Among these probabilities, only λ_F depends on temperature, but it is small, only 2.5% of $\lambda_l + \lambda_0$. Therefore, the counting rate for background UCN must undergo virtually no changes, just as the counting rate in detector D_1 and the basic gas-kinetic properties of the vessel. Thus, a noticeable increase in the counting rate in the detector D_2 with increasing temperature indicates that, in the vessel, there are some UCN whose energy increased above 52 neV upon weak heating caused by reflections from the walls.

In order to estimate the spectral composition of UCN, recorded by the detector D_2, the aluminum foil was covered with a thin Fomblin oil layer (30 μm), whereupon the inlet detector barrier increased up to 106 neV. As a result, the counting rate in the detector D_2 reduced to the level of the intrinsic background, whence we concluded that the main spectrum of both weakly heated and background UCN was localized in the range 52–106 neV.

In order to determine the contribution of background neutrons to the counting rate in the detector D_2, the measurements were repeated without the additional surface in the vessel. The frequency of UCN reflections then decreased to 15 Hz. Accordingly, $\lambda_{\rm up}$ would have to decrease by a factor of 2.8, while $\phi_b S_1/J_{\rm tot}$ would have to remain virtually unchanged. Therefore, two experiments featuring different frequencies of reflections would make it possible to determine, from two measured values of the ratio $J_p/J_{\rm tot}$, both the quantity $\phi_b S_1/J_{\rm tot}$ and the probability $\lambda_{\rm up}$. By measuring the mean value of the ratios $J_p/J_{\rm tot}$ over the time interval of 125–175 s in the temperature range between +5 and +70°C, we showed that the relative fraction of background UCN in the counting rate in detector D_2 is rather high (90–95% of the total counting rate in the temperature region below 25°C). Therefore, the weak heating of UCN could be reliably identified only in the region of elevated temperatures, where the contribution of the background is less pronounced because of an increase in the probability of this process. Figure 7 presents the experimental temperature dependence of the probability $\mu_{\rm up}$. In order to estimate the absolute value of $\mu_{\rm up}$, the speed of heated UCN, $v_{\rm up}$, was set to the mean speed of 52- to 106-neV neutrons (3.9 m/s). Thus, $\lambda_l^* + \lambda_0^* = (v_{\rm up}/v_u)(\lambda_l + \lambda_0)$ is equal to 4.4×10^{-2} s^{-1}. The coefficient μ_p was taken to be equal to 0.3, which corresponded to the quantity obtained by averaging, over the isotropic flux distribution, the penetration coefficient for 3.9-m/s UCN passing through the foil. Figure 7 shows that $\mu_{\rm up}$ is about 1×10^{-6} for $T \leq 25$°C, but that it grows noticeably with increasing temperature. Because of the approximations used, the estimate obtained for the absolute value of the weak-heating probability can differ from the true value by a factor of 2 to 3. Therefore, the data presented in the figure rather illustrate the magnitude of the effect and its temperature dependence.

4. CONCLUSION

The observation of the rare processes of weak heating and cooling of UCN due to their reflection from the surface of the same material gives reasons to assume that these processes are two branches of a single phenomenon, the quasielastic reflection of UCN. For the Fomblin oil surface, the probability of quasielastic reflection is about 10^{-6} per reflection event at room temperature. The resulting change in the UCN energy is commensurate with the initial neutron energy. The observed temperature dependence indicates that quasielastic reflection is caused by interaction with the collective motion of nuclei whose speed is commensurate with the speed of UCN. The occurrence of such processes is theoretically predicted in [4, 5]. However, model calculations of the probabilities of neutron heating and cooling with allowance for the macroscopic properties of the reflecting medium (thermal conductivity, self-diffusion coefficient, ratio of heat capacities, etc.) are necessary for verifying these theoretical predictions. On the other hand, more detailed experimental investigations into the energy distribution of UCN after their quasielastic reflection are required.

From the practical point of view, the observation of weak heating of UCN is important for measuring the neutron lifetime by the storage method. Since the upper boundary of the spectrum is close to 106 neV, the weak heating of UCN can open an additional channel of neutron leakage from vessels covered with Fomblin oil. In the most precise measurements of the neutron lifetime by the storage method [7–10], this channel was disregarded since it had not been known by that time. Therefore, it is necessary to reanalyze the measurements in those studies with allowance for the effect of the weak heating of UCN on the accuracy of the results obtained there. We analyzed here the experiment reported in [10], and this analysis, together with additional experiments, allowed us to conclude that this channel of UCN leakage has virtually no effect on either the final result or its accuracy owing to the special features of the procedure used in that study.

ACKNOWLEDGMENTS

We are grateful to S.T. Belyaev, A.L. Barabanov, V.V. Nesvizhevsky, and A.V. Strelkov for numerous discussions on the analysis and the interpretation of the experimental data obtained here.

This work was supported by the Russian Foundation for Basic Research (project no. 98-02-16810) and by INTAS (grant no. 99-508).

REFERENCES

1. L. N. Bondarenko, E. I. Korobkina, V. I. Morozov, *et al.,* Pis'ma Zh. Éksp. Teor. Fiz. **68**, 663 (1998) [JETP Lett. **68**, 691 (1998)].
2. V. I. Morozov *et al.,* in *Proceedings of the Second UCN Workshop, Pushkin, Russia, 1999,* p. 509.
3. P. Geltenbort, V. V. Nesvizhevsky, D. G. Kartashov, *et al.,* Pis'ma Zh. Éksp. Teor. Fiz. **70**, 175 (1999) [JETP Lett. **70**, 170 (1999)].
4. S. T. Belyaev and A. L. Barabanov, Nucl. Instrum. Methods Phys. Res. A **440**, 703 (2000).
5. A. L. Barabanov and S. T. Belyaev, in *Proceedings of the Second UCN Workshop, Pushkin, 1999, Russia,* p. 520.
6. S. S. Arzumanov *et al.*, Preprint No. IAÉ-6182/2, RNTs KI (Russian Research Centre Kurchatov Institute, Moscow, 2000).
7. W. Mampe, P. Ageron, *et al.,* Nucl. Instrum. Methods Phys. Res. A **284**, 111 (1989); Phys. Rev. Lett. **63**, 593 (1989).
8. W. Mampe, L. N. Bondarenko, V. I. Morozov, *et al.,* Pis'ma Zh. Éksp. Teor. Fiz. **57**, 77 (1993) [JETP Lett. **57**, 82 (1993)].
9. A. Pichlmaier, J. Butterworth, P. Geltenbort, *et al.,* Nucl. Instrum. Methods Phys. Res. A **440**, 517 (2000).
10. S. Arzumanov, L. Bondarenko, S. Chernyavsky, *et al.,* Nucl. Instrum. Methods Phys. Res. A **440**, 511 (2000).

Translated by E. Kozlovskiĭ

Physics of Atomic Nuclei, Vol. 65, No. 1, 2002, pp. 121–126. From Yadernaya Fizika, Vol. 65, No. 1, 2002, pp. 126–131.
Original English Text Copyright © 2002 by Beilin, Kuksa.

ELEMENTARY PARTICLES AND FIELDS
Theory

Flavor-Changing Neutral Currents and Top-Quark Properties in Standard Model Extensions*

V. A. Beilin and V. I. Kuksa

Institute of Physics, Rostov State University, pr. Stachki 194, Rostov-on-Don, 344090 Russia

Received March 31, 2000; in final form, November 22, 2000

Abstract—The structure and the generation of flavor-changing neutral currents are considered in a Standard Model extension involving a singlet quark of the up type. Anomalous top-quark properties caused by singlet–ordinary mixing is described in a phenomenological way. It is shown that, for single top production and for asymmetry in electron–positron annihilation, there is an enhancement in relation to predictions of the Standard Model. © *2002 MAIK "Nauka/Interperiodica".*

1. INTRODUCTION

The Standard Model (SM) is being tested intensively now over a wide energy region with a high precision. In particular, rare processes caused by flavor-changing neutral currents (FCNC) represent a relevant range for testing the SM and for seeking new-physics signals due to their extreme sensitivity to the type of SM extension. This is because standard FCNC occur only at the loop level, so that the rates of corresponding processes are very low. Therefore, we have a low standard background with a fixed signature and, as a consequence, a good opportunity to pick out signals beyond the SM.

The most popular extensions of the SM with FCNC that arise in the quark sector at the tree level are the following:

(i) supersymmetry (with a singlet quark and an extra Z boson),

(ii) multiple-Higgs-doublet models (without discrete symmetry),

(iii) models involving new dynamical interactions of heavy quarks (top quark),

(iv) composite or soliton structure of a heavy quark,

(v) extension involving horizontal symmetry.

Investigation of top-quark properties should play an important role in testing the SM. Because of its very large mass, the top quark is expected to hold clues to many problems in high-energy physics. For example, single top production due to FCNC in the process $e^+ e^- \to Z \to t\bar{c}$, $\bar{t}c$ at energies near the threshold, $\sqrt{s} \geq m_t$, leads to a good discerned kinematical structure [1]. This fact implies that the invariant mass of the jet with a charm quark must be close to zero and should be helpful for identifying such events, which were attainable at LEP2 when this experimental installation was in operation.

The large top mass affects the FCNC coupling in almost all of the aforementioned types of SM extensions. We will consider here only the first two types: supersymmetry and the multiple-Higgs-doublet model. A wide class of supersymmetry extensions contains a so-called singlet quark in the fermion sector [2]. Singlet-quark mixing with ordinary (standard) quarks leads to the emergence of FCNC at the tree level. In realistic models of mixing, the FCNC quark coupling is proportional to the quark mass. Therefore, the rate of processes that are caused by FCNC and which involve a top quark can be drastically enhanced in relation to the SM predictions. In the two-Higgs-doublet model without discrete symmetry, a flavor-changing scalar interaction also arises at the tree level [1, 3]. In this case, Yukawa coupling for the interaction is related to the masses of fermions inherent in relevant vertices. Naturally, this fact leads to an enhancement of some effects that involve a top quark. We should also assume that the mass-generation mechanism is significantly complicated in relation to the standard Higgs mechanism; from this point of view, the Higgs sector of the SM is only some approximation to the true high-energy theory. Thus, new-physics phenomena can be manifested through effective interactions of the top quark—in particular, through FCNC interactions. This observation stimulated some discussion on the so-called anomalous top-quark FCNC coupling [4, 5], which generates specific rare processes. A short classification list of the rare processes in the quark sector is given below:

(i) rare leptonic, semileptonic, and nonleptonic decays of hadrons, $M \to l^+l^-$, $M'l^+l^-$, M_1M_2;

(ii) rare radiative decays $M \to M'\gamma$;

*This article was submitted by the authors in English.

(iii) $M^0 - \overline{M}^0$ mixing in neutral meson systems (mass splitting Δm, oscillation);

(iv) CP-violating effects;

(v) nondiagonal boson decay $Z \to q_\alpha \bar{q}_\beta, \bar{q}_\alpha q_\beta$;

(vi) nondiagonal quark-pair production in e^+e^-, ep, and $p\bar{p}$ interactions.

The set of experimental data on rare processes is not complete yet. Most of the data are only some experimental limits on the branching ratios and give us a wide region for putting new physics into consideration. Research programs of collider experiments lean toward top-quark and Higgs-meson properties. It should be noted that investigations of top rare decays are included in CDF, D0, DELPHI, and Fermilab programs [6, 7]. Measurements of the mass splitting Δm_s for the B_s^0 mesons are in progress now in the OPAL, ALEPH, and DELPHI collaborations [8–10]. The high-energy production of top and Higgs particles is planned to be investigated at LHC.

2. PHENOMENOLOGY OF ANOMALOUS FCNC TOP-QUARK COUPLING

The top-quark FCNC coupling is usually considered in a phenomenological way as the additional part to the SM Lagrangian of lowest dimension [4, 11]:

$$\Delta L^{\text{eff}} = \frac{1}{\Lambda}\left[k_\gamma e \bar{t}\sigma_{\mu\nu} c F^{\mu\nu} + k_g g_s \bar{t}\sigma_{\mu\nu}\frac{\lambda^a}{2} c G_a^{\mu\nu}\right] \quad (1)$$
$$- \frac{g}{2\cos\theta_{\text{W}}}\left[k_L \bar{t}\gamma_\mu L c + k_R \bar{t}\gamma_\mu R c\right] Z^\mu + \text{h.c.}$$

Here, $F^{\mu\nu}$ and $G^{\mu\nu}$ are, respectively, the $U_{\text{em}}(1)$ and the $SU_c(3)$ field strength tensor; e, g, and g_s are, respectively, the $U_{\text{em}}(1)$, the $SU_w(2)$, and the $SU_c(3)$ coupling constant; k_γ, k_g, k_L, and k_R are the strengths of the corresponding anomalous interactions; Θ_{W} is the known Weinberg angle; and Λ is the cutoff parameter for the effective theory (~ 1 TeV).

From LEP2 experimental data on the tcZ and $tc\gamma$ couplings, we get the experimental limits $k_L^2 < 0.533$ and $k_\gamma^2 < 0.176$ (95% C.L.) [12].

In a model with a singlet quark, the structure of FCNC quark–boson coupling at the tree level is determined by the simple expression [2]

$$\Delta L_Z = g_{ik}\bar{q}_i\gamma^\mu L q_k Z_\mu. \quad (2)$$

Here, $g_{ik} = \frac{g}{2\cos\Theta_{\text{W}}} U_{Di}^* U_{Dk}$, U_{Dk} being the mixing-matrix element that characterizes the value of singlet-ordinary mixing of d_k and D (down singlet quark); for the case of up singlet quark $g_{ik} = -\frac{g}{2\cos\Theta_{\text{W}}} U_{Ui}^* U_{Uk}$, U_{Uk} characterizing u_k–U mixing, where U stand for an up singlet quark.

In the model involving two Higgs doublets, FCNC quark-scalar coupling arises from the Lagrangian [1]

$$L_\Phi = \lambda_{ij}^u \bar{Q}_i \tilde{\Phi}_1 u_j + \lambda_{ij}^d \bar{Q}_i \Phi_1 d_j \quad (3)$$
$$+ \xi_{ij}^u \bar{Q}_i \tilde{\Phi}_2 u_j + \xi_{ij}^d \bar{Q}_i \Phi_2 d_j,$$

where λ_{ij}^q and ξ_{ij}^q are "bare" coupling constants. In (3), the FCNC coupling arises at the tree level as the result of a vacuum shift in the doublet Φ_1 only (model without a discrete symmetry).

The anomalous FCNC couplings in (2) and (3) have some similar special features:

(a) $g_{ik} \sim \sqrt{m_i m_k}/m_U$, where m_i, m_k, and m_U are the masses of, respectively, q_i, q_k, and U quarks (seesaw mechanism of mixing);

(b) $\xi_{ik} \sim \sqrt{m_i m_k}/v$, where v is a vacuum shift (Cheng–Sher ansatz);

(c) $\xi_{ik} \sim (m_i + m_k)/(2v)$ (sum-rule ansatz).

From expressions (a)–(c), it can be seen that the quark mass plays an important role in the formation of FCNC coupling. Therefore, we should expect that the anomalous FCNC top coupling emerges in the most interesting SM extensions—in supersymmetry and in the two-Higgs-doublet model.

Further, we will consider a phenomenology of the anomalous FCNC top-quark coupling in the model involving the up singlet quark U. In this model, an extra Yukawa term that describes $qU\Phi$ interaction [13] is

$$\Delta L_{\text{Y}} = \lambda_a \bar{Q}'_{La}\Phi U'_R + \text{h.c.}, \qquad a = 1, 2, 3. \quad (4)$$

After a vacuum shift, it leads to the mixing of the singlet U quark with ordinary up-type quarks. This fact in turn leads to the reconstruction of charged- and neutral-current structures. The charged currents are described now by a 4×3 mixing matrix; that is,

$$J_\mu^+ = \frac{1}{\sqrt{2}} g(u, c, t, U)\gamma_\mu V(4\times 3)\begin{pmatrix} d \\ s \\ b \end{pmatrix}, \quad (5)$$

where $V(4 \times 3)$ is not unitary and differs from the Kobayashi–Maskawa matrix. More important changes occur in the structure of neutral currents. In addition to standard diagonal terms, we also have nondiagonal terms, which describe FCNC at the tree level:

$$\Delta J_\mu^0 = -\frac{g}{2\cos\Theta_{\text{W}}}(U_L)_{4i}^*(U_L)_{4k}\bar{u}_{Li}\gamma_\mu u_{Lk}, \quad (6)$$
$$i, k = 1, 2, 3, 4 \quad (u, c, t, U).$$

In (6), U_L is the unitary matrix that diagonalizes the mass matrix in the up-quark sector. The element

$(U_L)_{4k}$ corresponds to u_k–U mixing. As a rule, it is described by the seesaw mechanism,

$$|U_{4k}|^2 \simeq (m_k/m_U)^p, \tag{7}$$

where $p = 1$ corresponds to the linear seesaw and $p = 2$ corresponds to the quadratic seesaw [see the above expression for the FCNC coupling g_{ik} in (a)]. It follows that, for $m_U < 1$ TeV, we should expect a noticeable t–U mixing that can be observed in rare processes.

3. PHENOMENOLOGICAL CONSEQUENCES OF SINGLET–ORDINARY QUARK MIXING

We now consider some main consequences of singlet-quark mixing with the standard quarks—in particular, t–U mixing. At the same time, we can interpret results obtained for the model with a singlet quark as those suitable for the two-Higgs-doublet model. To carry out this interpretation, we should substitute m_U for v in the Cheng–Sher ansatz (b) and the Z boson for the Higgs particle. A special feature of the model with a singlet quark consists of two possibilities. On one hand, the large top mass can be explained by its mixing with a superheavy singlet quark. On the other hand, the initial large top mass leads to a large mixing with the singlet quark.

To calculate the rate of FCNC processes involving the top quark, we need some information on the matrix element U_{4i} in (6). We can obtain an upper limit on the mixing value from experimental data on the rare decay $D^0 \to \mu^+\mu^-$ and the mass splitting Δm_D in the D^0–$\bar{D}^0$ system. In the last case, the constraint becomes more strict [14]:

$$\Delta m_D < 4.6 \times 10^{-14}\text{GeV} \tag{8}$$
$$\longrightarrow |U^*_{Uu}U_{Uc}| < 3.3 \times 10^{-4}\text{GeV}.$$

We can evaluate a lower bound on the singlet quark mass: $m_U > 220$ GeV for the linear seesaw $p = 1$ from (8) with the seesaw mechanism (7). In the case of a quadratic seesaw, the bound is less stringent. From (8) and (7) for $p = 1$, we also obtain some limits on the mixing angles:

$$|U_{Uu}| < 3.7 \times 10^{-3}, \quad |U_{Uc}| < 0.8 \times 10^{-1}, \tag{9}$$
$$|U_{Ut}| < U_{\max} = 1/\sqrt{2}.$$

Thus, known data on rare processes in the up-quark sector give us a lenient bound on the mass m_U and on singlet-quark mixing. The value of t–U mixing can be near its maximum, and c–U mixing is about 0.1. From this value and from (6), it follows that the FCNC tcZ coupling may be anomalously large in relation to the SM prediction at the loop level. The unitarity condition gives an additional constraint on mixing angles. In the model with singlet quarks, the Kobayashi–Maskawa matrix is generalized to a 4×4 unitary matrix that is constructed from the $V(3 \times 4)$ matrix (5) and $(U_L)_{4i}$ elements [13]. The structure of the $U(4 \times 4)$ mixing matrix is

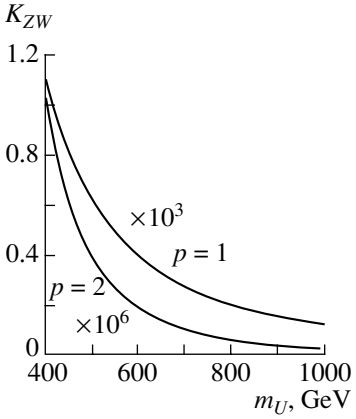

Fig. 1. Normalized $t \to cZ$ branching ratio as a function of m_U.

$$U(4 \times 4) = \begin{pmatrix} & & - & U_{uU} \\ & U_{\alpha\beta} & - & U_{cU} \\ - & - & U_{tb} & U_{tU} \\ U_{Ud} & U_{Us} & U_{Ub} & U_{UU} \end{pmatrix}, \quad \alpha, \beta = 1, 2, \tag{10}$$

where that part of the matrix which contains u_k–U mixings is indicated in detail. If t–U mixing is large, we can write the unitary condition for $U(4 \times 4)$ in the form

$$(|U_{tb}|^2 + |U_{tU}|^2)^{1/2} \approx 1, \tag{11}$$
$$(|U_{tU}|^2 + |U_{UU}|^2)^{1/2} \approx 1.$$

In the SM, $|U_{tb}| \approx 1$, but, for SM extensions involving more than three generations ($n > 3$), we have $0 < |U_{tb}| < 0.9993$ (90% C.L.) [14]; that is, there are virtually no restrictions about U_{tb}. An additional piece of information on the value should be given by a measurement of $\text{Br}(t \to bW)$. The existing data on $t \to cZ, uZ, bW$ decays [15, 16],

$$\text{Br}(t \to bW) = 0.87^{\pm 0.13 \pm 0.13}_{\pm 0.30 \pm 0.11},$$
$$\text{Br}(t \to cZ) + \text{Br}(t \to uZ) < 33\%, \quad (95\%\,\text{C.L.}),$$

set no new limits in relation to the estimates in (8), so that we need more precise measurements.

It is important that the large singlet–ordinary mixing leads to the enhancement of the "rare" $t \to cZ$ decay channel. The expression for the branching ratio normalized to the unsuppressed channel $t \to bW$ is

$$K_{ZW} \equiv \frac{\text{Br}(t \to cZ)}{\text{Br}t \to bW)} \tag{12}$$

$$\approx \frac{1}{2}\frac{1-3x_Z^2+2x_Z^3}{1-3x_W^2+2x_W^3}\frac{|U_{tU}^*U_{cU}|^2}{|U_{tb}|^2},$$

where $x_Z=(m_Z/m_t)^2$ and $x_W=(m_W/m_t)^2$. Figure 1 displays K_{ZW} versus the U-quark mass for the linear ($p=1$) and the quadratic ($p=2$) seesaw mechanism. At the SM loop level, the decay $t\to cZ$ has the branching ratio $\mathrm{Br}(t\to cZ)\sim 10^{-13}$ [17, 18]; in the two-Higgs-doublet model without a discrete symmetry, this decay becomes possible at the tree level, and we have $\mathrm{Br}(t\to cZ)\geq 10^{-7}$ for this case [1, 3]. As can be seen from Fig. 1, the corresponding values in the singlet-quark model are an order of magnitude greater in amplitude. The known experimental limit on the anomalous tcZ coupling is $k_Z^2<0.533$ [12], where, in accordance with (6), $k_Z=(g/2\cos\Theta_\mathrm{W})|U_{tU}^*U_{cU}|$, and it does not furnish any extra information.

The large t–U mixing leads to a reconstruction of the C_V–C_A structure for the $t\bar{t}Z$ and $U\bar{U}Z$ couplings. In the SM, the structure of the diagonal $q\bar{q}Z$ ($q=u,c,t$) vertices is specified by the standard values,

$$(C_V)_\mathrm{st}=\frac{1}{4}\left(1-\frac{8}{3}\sin^2\Theta_\mathrm{W}\right), \qquad (13)$$
$$(C_A)_\mathrm{st}=-\frac{1}{4}.$$

For the model where the singlet quark is not mixed with the ordinary quark, we have [2, 13]

$$C_V^0=-\frac{2}{3}\sin^2 2\Theta_\mathrm{W}, \quad C_A^0=0. \qquad (14)$$

If the value of the t–U mixing U_{tU} is not zero, then, for the t and U quarks, we obtain

$$C_V^t=(C_V)_\mathrm{st}-\frac{1}{4}|U_{tU}|^2, \qquad (15)$$
$$C_A^t=(C_A)_\mathrm{st}+\frac{1}{4}|U_{tU}|^2,$$
$$C_V^U=(C_V)_\mathrm{st}-\frac{1}{4}|U_{UU}|^2,$$
$$C_A^U=(C_A)_\mathrm{st}+\frac{1}{4}|U_{UU}|^2.$$

This deviation from the standard values can be directly checked by measuring the forward–backward asymmetry A_FB in reactions leading to $t\bar{t}$ and $U\bar{U}$ production. In the case of pure Z exchange, A_FB is expressed in terms of C_V and C_A in a simple way (this is the Born approximation for the process $e^+e^-\to Z\to f\bar{f}$):

$$A_\mathrm{FB}^f=\frac{3}{4}\frac{2C_V^eC_A^e}{(C_V^e)^2+(C_A^e)^2}\frac{2C_V^fC_A^f}{(C_V^f)^2+(C_A^f)^2}. \qquad (16)$$

For a real process, the γ–Z interference and QCD corrections must be taken into account. Nevertheless, it is known [19] that QCD corrections to the forward–backward asymmetry to the second order are less than 10%.

To illustrate the effect of t–U mixing [see Eq. (15)], we consider the relation

$$a^f=\frac{A_\mathrm{FB}^f}{(A_\mathrm{FB}^f)_\mathrm{st}} \qquad (17)$$
$$=\frac{C_V^fC_A^f}{(C_V^f)_\mathrm{st}(C_A^f)_\mathrm{st}}\frac{(C_V^f)_\mathrm{st}^2+(C_A^f)_\mathrm{st}^2}{(C_V^f)^2+(C_A^f)^2}.$$

Illustrations of the effects specified by Eqs. (15) and (17) can be found in Fig. 2, where C_V, C_A, and a^f are plotted versus the U-quark mass m_U. From the figure, it can be seen that the effect of t–U mixing is appreciable in the mass region $m_U\leq 1$ TeV. At $m_U\sim m_t$, we will have a drastic discrepancy between these results and the SM predictions.

We will now calculate the cross section of single top production in e^+e^-, ep, and $p\bar{p}$ collisions. For e^+e^- interaction, single top production due to pair $t\bar{c}+\bar{t}c$ formation is of greatest interest. The expression for the cross section coincides with that from [5], where k_γ and k_Z are set to $k_\gamma\approx 0$ (loop-level contribution of the singlet quark) and $k_Z=U_{tU}^*U_{cU}$ {tree-level contribution of the singlet quark [see (6)]}.

As a result, the expression for the cross section $\sigma(e^+e^-\to Z\to t\bar{c})$ takes the form

$$\sigma(s)\approx\frac{g^4(1+a_e^2)}{2^{10}\pi s\cos^4\Theta_\mathrm{W}}\left(1-\frac{m_t^2}{s}\right)^2 \qquad (18)$$
$$\times\frac{(2+m_t^2/s)}{(1-m_Z^2/s)^2}|U_{tU}^*U_{cU}|^2,$$

where $a_e=1-4\sin^2\Theta_\mathrm{W}$ and $\sqrt{s}$ is the total energy. Figure 3 shows $\sigma(e^+e^-\to Z\to t\bar{c})$ versus $\sqrt{s}$ at various values of m_U. As can be seen, the maximum values of σ are in the region $\sqrt{s_\mathrm{max}}\approx 200$–$400$ GeV, where $\sigma(s)_\mathrm{max}\approx 0.4$–$0.7$ fb for $m_U=400$ GeV. If $m_U=600$ or 1000 GeV, $\sigma(s)_\mathrm{max}\approx 0.2$–$0.3$ fb and 0.05–0.1 fb, respectively. In spite of the very low value of the cross section, we have some energy gain and, as was noted in the Introduction, a good distinctive kinematical signature of single top production. An estimation of the cross sections for single top production in ep and $p\bar{p}$ interactions yields values less up to an order of magnitude in relation to e^+e^- interaction.

The cross section $\sigma(e^+e^-\to Z\to Uc)$ can be found with the aid of (18) by making the substitutions $m_t\to m_U$ and $U_{tU}\to U_{UU}$. It is obvious that, at $m_U\sim m_t$, we have $\sigma_U\sim\sigma_t$. The cross section for the subprocess $uq\to Z\to Uq$ occurring in single U

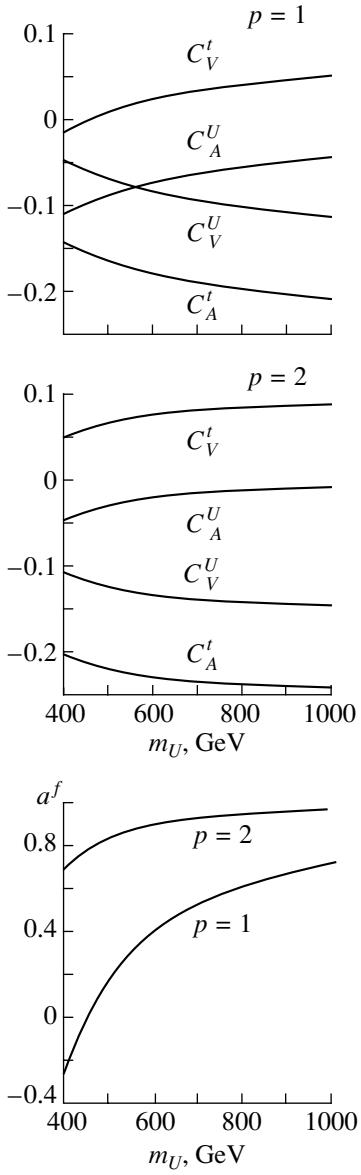

Fig. 2. C_V, C_A, and a^f for $p = 1$ and $p = 2$ as functions of m_U.

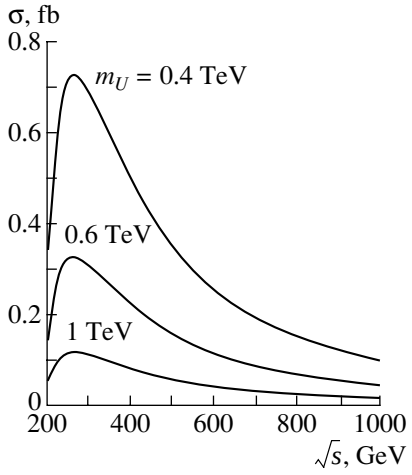

Fig. 3. Cross section $\sigma(e^+e^- \to t\bar{c})$ as a function of $\sqrt{s}$ for various values of m_U.

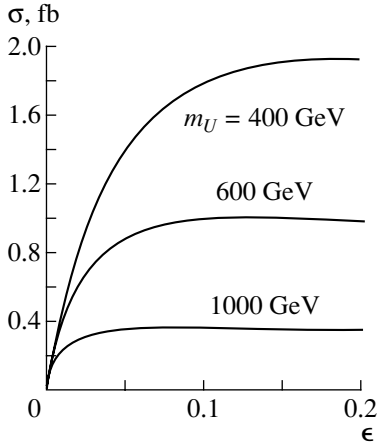

Fig. 4. Cross section $\sigma(eu \to eU)$ as a function of $\epsilon = 1 - m_U/\sqrt{s}$ at various values of m_U.

production $p\bar{p} \to U\bar{H}, \bar{U}H$ can be found with the aid of (18) upon the substitution $a_e \to a_q$, where $a_u = 1 - 8\sin^2\Theta_W/3$, $a_d = 1 - 4\sin^2\Theta_W/3$, $m_t \to m_U$, $U_{cU} \to U_{uU}$, and $U_{tU} \to U_{UU}$. Thus, we have some additional suppression up to order m_u/m_c ($p = 1$) or m_u^2/m_c^2 ($p = 2$) in relation to $\sigma(e^+e^- \to t\bar{c})$.

The rate of single U production in ep collisions can be found by calculating the subprocess cross section $\sigma(eu \to Z \to eU)$ in the t channel. We have calculated an approximate value of σ near the threshold of U production, i.e., for $\sqrt{s} - m_U \ll \sqrt{s}$ [20]:

$$\sigma(s) \approx \frac{g^4(3 + 2a_e + 3a_e^2)}{2^9\pi\cos^4\Theta_W}\frac{1}{\sqrt{s}m_U} \qquad (19)$$

$$\times \left[1 + \frac{m_Z^2}{m_U(\sqrt{s} - m_U)}\right]^{-1} |U_{UU}^* U_{uU}|^2.$$

The results for $\sigma(s)$ are presented in Fig. 4 at various values of m_U as the curve $\sigma(s)$ versus $\epsilon = 1 - m_U/\sqrt{s}$. The value of $\sigma(s)$ in ep collisions is on the same order of magnitude as the value of σ for U production in e^+e^- collisions.

4. CONCLUSION

Recently, precision tests of the SM at the loop level have received much attention of experimentalists because rare processes are a convenient tool for studying of SM in different aspects. Superstrings and the two-Higgs-doublet model are of particular interest because of appearance of FCNC at the tree

level. This fact in turn can strongly enhance the rate of rare processes in these models. In the present paper, we have shown that the enhancement occurs in the model involving a singlet up-type quark as well. A large top-quark mass causes large top–singlet mixing and results in anomalous properties of the top quark. These features are manifested in rare-decay branching ratios, in the asymmetry A_{FB}, and in the cross sections for single top production. It has been shown that these effects can in principle be detected in the singlet-quark mass region $m_U \leq 1$ TeV. It should be noted that singlet–ordinary mixing effects are accessible at energies of about m_t; i.e., indirect signals, as might have been expected, should be checked at the Tevatron in the near future (unfortunately, LEP2 is closing down now).

We have no definitive information about the mass of a singlet up-type quark. A low limit on the mass follows from rare processes in the up-quark sector—namely, from mixing in the D^0–$\bar{D}^0$ system and from rare D-meson decays. Unfortunately, it is not possible, as far as we know, to deduce more stringent upper limits from known experimental data on these processes. Furthermore, an accurate determination of singlet-quark properties depends on some progress in the experimental investigation of D mesons and top physics.

REFERENCES

1. D. Atwood, L. Reina, and A. Soni, Phys. Rev. D **53**, 1199 (1996).
2. V. Barger, M. S. Berger, and R. S. N. Phillips, Phys. Rev. D **52**, 1663 (1995).
3. M. Luke and M. S. Savage, Phys. Lett. B **307**, 387 (1993).
4. T. Han, K. Whisnant, *et al.*, Phys. Rev. D **55**, 7241 (1997).
5. V. F. Obraztsov, S. R. Slabospitsky, and O. P. Yushchenko, Yad. Fiz. **62**, 113 (1999) [Phys. At. Nucl. **62**, 108 (1999)].
6. T. Han, K. Whisnant, *et al.*, Phys. Lett. B **385**, 311 (1996).
7. S. Parke, Preprint No. FERMILAB-PUB-94/322-T (1994).
8. L. Ackerstaff *et al.*, Preprint No. CERN-PPE/97-064 (1997).
9. P. Abreu *et al.*, Preprint No. CERN-PPE/97-51 (1997).
10. R. Barate *et al.*, Preprint No. CERN-EP/98-117 (1998).
11. T. Han, R. D. Peccei, and X. Zhang, Nucl. Phys. B **454**, 527 (1995).
12. P. Abreu *et al.*, Preprint No. CERN-EP/98-177 (1998).
13. V. Beilin, G. Vereshkov, and V. Kuksa, Yad. Fiz. **56** (8), 186 (1993) [Phys. At. Nucl. **56**, 1099 (1993)].
14. Particle Data Group (D. E. Groom *et al.*), Eur. Phys. J. C **15**, 1 (2000).
15. J. Incandela *et al.*, Nuovo Cimento A **109**, 741 (1996).
16. F. Abe *et al.*, Preprint No. FERMILAB-PUB-97/270-E (1997).
17. B. Grzgadkowski, J. F. Gunion, and P. Krawczyk, Phys. Lett. B **268**, 106 (1991).
18. G. Eilam, J. L. Hewett, and A. Soni, Phys. Rev. D **44**, 1473 (1991).
19. V. Ravindran and W. L. van Neerven, Phys. Lett. B **445**, 214 (1998).
20. V. Beilin, G. Vereshkov, and V. Kuksa, Yad. Fiz. **58**, 931 (1995) [Phys. At. Nucl. **58**, 862 (1995)].

Physics of Atomic Nuclei, Vol. 65, No. 1, 2002, pp. 127–134. From Yadernaya Fizika, Vol. 65, No. 1, 2002, pp. 132–139.
Original English Text Copyright © 2002 by Likhoded, Slabospitsky.

ELEMENTARY PARTICLES AND FIELDS
Theory

Asymmetry in Charmed-Particle Production in a Σ^- Beam*

A. K. Likhoded** **and** **S. R. Slabospitsky**

Institute for High Energy Physics, Protvino, Moscow oblast, 142284 Russia

Received August 24, 2000; in final form, February 13, 2001

Abstract—We present a calculation of the inclusive x_F distributions of charmed hadrons produced in a high-energy Σ^- beam. The calculation is based on the modified mechanism of charmed-quark fragmentation, as well as on the mechanism of c-quark recombination with the valence quarks from initial hadrons. We predict additional asymmetry in the production of charmed hadrons due to different distributions of the valence s and d quarks in a Σ^- beam. © *2002 MAIK "Nauka/Interperiodica".*

1. INTRODUCTION

In the hadronic production of particles with open charm, an interesting situation connected with the interaction of charmed quarks with the hadronic remnant takes place (see [1–3] and references therein).

Let us recall that this problem does not arise in the case of e^+e^- annihilation, where a heavy quark is hadronized owing to its own radiation and where the description is entirely reduced to the fragmentation function,

$$\frac{1}{\sigma_{c\bar{c}}}\frac{d\sigma}{dz} = D(z, Q^2), \qquad (1)$$

where the fraction z of the c-quark momentum is taken by charmed hadron; Q^2 is the square of the total energy in e^+e^- annihilation; and σ and $\sigma_{c\bar{c}}$ are the cross sections for charmed-hadron and $c\bar{c}$-pair production, respectively.

It is well known that a simple application of the factorization approach (1) to the charmed-particle production in hadronic interaction leads to a considerable deviation from experimental data. Indeed, there is a substantial difference in the yields of different charmed hadrons in the fragmentation region of initial hadrons, i.e., when $|x| \to 1$ (here, $x \equiv 2p_H/\sqrt{s}$, p_H is the momentum of charmed hadron, and s is the total energy squared).

The asymmetry A of the charmed-particle yield (or the leading-particle effect) is defined as

$$A = \frac{\dfrac{d\sigma}{dx}(\text{leading}) - \dfrac{d\sigma}{dx}(\text{nonleading})}{\dfrac{d\sigma}{dx}(\text{leading}) + \dfrac{d\sigma}{dx}(\text{nonleading})}. \qquad (2)$$

Here, the labels "leading" and "nonleading" refer to charmed hadrons, respectively, with and without light quarks identical to valence quarks from the initial hadrons. For example, in a $\pi^-(\bar{u}d)$ beam, $D^0(c\bar{u})$ and $D^-(\bar{c}d)$ mesons are leading particles, while $\bar{D}^0(\bar{c}u)$ and $D^+(c\bar{d})$ should be considered as nonleading ones.

There are many theoretical articles devoted to describing this phenomenon [4]. In [5, 6], the interaction of c quarks with the quarks of the initial hadrons was taken into account and good agreement with data was obtained in describing the spectrum at large x and the x-asymmetry dependence in π^-N and Σ^-N interactions.

Recent data on charm production in Σ^- beams [2, 3] are of special interest because the beam hadron (here Σ) has an s quark, with the result that the distributions of valence quarks in the Σ^- baryon differ from those in the proton [7]. This should lead to a set of observable effects; in particular, the asymmetry in the yield of charmed hadrons should differ from that in proton–proton collisions.

Preliminary data presented by the SELEX collaboration [3] on the charm yield in Σ^-p and π^-p collisions show, however, some disagreement with other experiments [2] and general theoretical assumptions—in particular, in the expected yields of charmed particles and antiparticles in the central region.

In this article, we consider this problem very briefly from the general theoretical point of view (Section 2). In Section 3, we give a short description of the fragmentation mechanism. Our approach to calculating x distributions of charmed particles produced via the recombination mechanism is given in Section 4. We present the predictions for the differential distributions of charmed hadrons produced in Σ^-N interactions in Section 5. A short summary of the results is given in the Conclusion.

*This article was submitted by the authors in English.

**e-mail: likhoded@mx.ihep.su

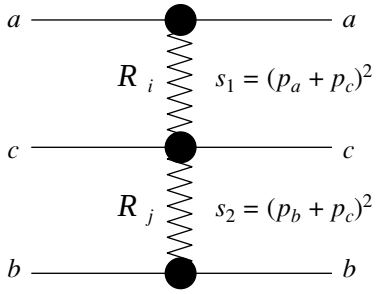

Fig. 1. Six-particle amplitude $M_{3\to3}$.

2. ASYMPTOTIC BEHAVIOR IN THE CENTRAL REGION

Prior to presenting a detailed discussion of the behavior of the spectrum and of the charge asymmetry in the hadron yield, we consider the general behavior of charmed-particle spectra.

According to the generalized optical theorem [8], the inclusive spectrum is related to the discontinuity of the six-particle amplitude as (see Fig. 1)

$$E\frac{d^3\sigma}{d^3p} = \frac{1}{s}\mathrm{disc}M_{3\to3}, \tag{3}$$

where s is the total energy squared.

Let us introduce the invariants (see Fig. 1)

$$s_1 = (p_a + p_c)^2, \quad s_2 = (p_b + p_c)^2.$$

At high energies, the asymptotic behavior of the amplitude $M_{3\to3}$ as a function of these invariants $s_{1,2}$ is determined by leading Regge trajectories—the Pomeron ($\mathcal{P}$) and secondary trajectories ($\mathcal{R}_i$)—related to ρ, ω, f, and A_2 mesons. In this approach, the $\mathcal{PP}$, $\mathcal{RP}$, and $\mathcal{RR}$ contributions become important.

In the central region ($x \sim 0$), where the kinematical invariants s_1 and s_2 are large, one has

$$s_1 \approx \sqrt{s}m_\perp e^{-y}, \quad s_2 \approx \sqrt{s}m_\perp e^{y}, \tag{4}$$

where y is the rapidity, $m_\perp = \sqrt{m^2 + p_T^2}$, and p_T is the transverse momentum.

The double Regge representation is a good approximation for the amplitude $M_{3\to3}$ (see Fig. 1) in this kinematical region. Therefore, one has

$$E\frac{d^3\sigma}{d^3p} \approx \frac{1}{s}\sum_{i,j}\tilde{f}_{ij}s_1^{\alpha_i}s_2^{\alpha_j}, \tag{5}$$

where α_i and α_j are the intercepts of the leading Regge trajectories [8, 9]. For the Pomeron trajectory, one has $\alpha_P \approx 1$; the f, ρ, ω, and A_2 trajectories have the intercept of $\alpha_R \approx 1/2$.

The unknown functions $\tilde{f}_{ij}(m_\perp)$ of $m_\perp$ seem to be universal and do not depend on the type of product particles [8, 10]. These functions can be determined from a fit to experimental data. The dependence on the quantum numbers of initial and final particles is entirely determined by the coupling constants of the secondary Reggeons $\mathcal{R}$ included in the definition of the functions $\tilde{f}_{ij}(m_\perp)$.

Substituting (4) into (5), we obtain

$$E\frac{d^3\sigma}{d^3p} = \tilde{f}_{\mathcal{PP}}(m_\perp) - \sum_{i,j}\frac{\tilde{f}_{ij}(m_\perp)}{s^{1-(\alpha_i+\alpha_j)/2}}e^{(\alpha_j-\alpha_i)y}. \tag{6}$$

This equation provides a good description of the transition to the asymptotic regime in the central region for all yields of π and K mesons [10].

For the D and B mesons, Eq. (6) is simplified owing to the fact that the contribution of the trajectories associated with the charmed c quark in the D meson (J/ψ, χ_c trajectories) or the beauty b quark in the B meson (Υ, χ_b trajectories) is strongly suppressed by the Zweig rule for coupling to the initial mesons or nucleons. Therefore, the sum appearing in Eq. (6) does not include contributions with two secondary Reggeons ($\mathcal{RR}$ contributions) in the upper and lower "shoulder" of the diagram in Fig. 1. Thus, one gets the simpler expression

$$E\frac{d^3\sigma(D)}{d^3p} \approx \tilde{f}_{\mathcal{PP}}(m_\perp) \tag{7}$$
$$-\frac{1}{\sqrt[4]{s}}\{\tilde{f}_{\mathcal{RP}}(m_\perp)e^{y/2} + \tilde{f}_{\mathcal{PR}}(m_\perp)e^{-y/2}\}.$$

Note that the contribution of the first $\mathcal{PP}$ term in Eq. (7) is the same for the particle and for the antiparticle and is proportional to the total cross section for the interaction of initial hadrons. Thus, the normalized cross section

$$\frac{1}{\sigma_{\mathrm{tot}}^{hh}}E\frac{d^3\sigma(hh\to DX)}{d^3p}$$

in the high-energy limit has one universal limiting value independent of the type of colliding hadrons.

For the case of D_s-meson production in Σ or K beams, the leading intercept is related to the ϕ meson, $\alpha_j = \alpha_\phi \approx 0$, and there is no contribution from the third $\mathcal{PR}$ term in Eq. (7). The ϕ trajectory can be associated with the Σ particle only because there are no valence strange quarks in the proton. As a result, one has only two terms:

$$\frac{1}{\sigma_{\mathrm{tot}}}E\frac{d^3\sigma(D_s)}{d^3p} \approx \tilde{f}_{\mathcal{PP}}(m_\perp) - \frac{1}{\sqrt{s}}\tilde{f}_{\mathcal{RP}}(m_\perp)e^{y}. \tag{8}$$

The contribution of secondary trajectories determines the difference between the yields of the particle and the antiparticle in the central region. For instance, for pp and $p\bar{p}$ collisions, one has

$$\Delta_{pp} \sim \frac{a}{s^{1/4}}\cosh\frac{y}{2}, \quad \Delta_{p\bar{p}} \sim \frac{b}{\sqrt{s}}\sinh\frac{y}{2},$$

where the coefficients a and b depend on both combinations of secondary Reggeon couplings and on the particle type (D or B meson).

In most experiments with a fixed target, the point $y = 0$ ($x = 0$) is not usually reached because of experimental conditions, and the measured spectrum starts from $x \sim 0.1$. Upon the simple substitution $y \simeq \ln(x\sqrt{s}/m_\perp)$, Eq. (7) for D mesons takes the form

$$\frac{1}{\sigma_{\rm tot}} E\frac{d^3\sigma(D)}{d^3p} \simeq \tilde{f}_{\mathcal{PP}}(m_\perp) - \left\{\tilde{f}_{\mathcal{RP}}(m_\perp)\sqrt{m_\perp}\sqrt{x} + \tilde{f}_{\mathcal{PR}}(m_\perp)\frac{\sqrt{m_\perp}}{\sqrt{sx}}\right\}. \quad (9)$$

For D_s-meson production in Σ or K beams, one has

$$\frac{1}{\sigma_{\rm tot}} E\frac{d^3\sigma(D_s)}{d^3p} \simeq \tilde{f}_{\mathcal{PP}}(m_\perp) - \tilde{f}_{\mathcal{RP}}(m_\perp)m_\perp x. \quad (10)$$

The asymmetry in the particle yield depends on the quantum numbers of initial hadrons and observed charmed particles and is determined by the second term in these expressions, which is different for the D and the D_s case. One can see that the transition to the asymptotic behavior at fixed x occurs much faster than in the fixed-rapidity regime. It is also seen that the behavior in the vicinity of $x = 0$ is determined by the value of the intercept of the secondary trajectory associated with the valence quark common to the beam hadron and the observed particle.

It is evident that the applicability region of the above expressions is severely restricted by the need for satisfying the condition of large values of the invariants s_1 and s_2 in the case of the Regge approximation. However, the general conclusions on the character of the asymptotic behavior of charmed-particle spectra are quite definite, on one hand, and agree well with the parton-model predictions, on the other hand.

We wish to emphasize once again that, from general theoretical considerations, one should expect equal yields of charmed particles and antiparticles in the central region ($x \approx 0$) when $s \to \infty$:

$$E\frac{d^2\sigma(D)}{d^3p}\bigg|_{x\approx 0} \approx E\frac{d^2\sigma(\bar{D})}{d^3p}\bigg|_{x\approx 0}. \quad (11)$$

We will show that this behavior agrees with parton-model predictions as well.

3. FRAGMENTATION MECHANISM

In [5, 6], a phenomenological model was developed where the hadronization of a charmed c quark is described by the sum of two mechanisms, namely,

$$\frac{d\sigma_H}{dx} = \frac{d\sigma_H^F}{dx} + \frac{d\sigma_H^R}{dx}, \quad (12)$$

where the first term corresponds to charmed-quark fragmentation, while the second term takes into account the interaction of a charmed c quark with valence quarks from initial hadrons (recombination).

In the fragmentation mechanism, the inclusive cross section for charmed-hadron (D-meson) production has the form

$$E_H\frac{d^3\sigma^F}{d^3p_H} = \int E_c\frac{d^3\sigma(h_1h_2 \to cX)}{d^3p_c}D(z)\delta(\mathbf{p}_H - z\mathbf{p}_c)d^3p_c, \quad (13)$$

where the fraction $z = |\mathbf{p}_H|/|\mathbf{p}_c|$ of the c-quark momentum is carried away by the charmed hadron H.

The parametrization of the fragmentation function $D(z)$ (for example, in the form proposed in [11] or [12]) can be found from a fit to data on the reaction $e^+e^- \to D(c\bar{q})X$. However, the situation is more complicated in hadronic collisions. Indeed, the use of the fragmentation function is justified at asymptotically large values of the invariant mass of the $c\bar{c}$ pair or high p_T. However, in the hadronic production of charmed particles, the main contribution to the inclusive charm-production cross section comes from c quarks with low values of the invariant mass of the $c\bar{c}$ pair ($M_{c\bar{c}} \geq 2m_c$) [13]. These quarks dominate in the small-x region. At the same time, there are a large number of partons from initial hadrons in the same (central) region of x. Therefore, the c quark, in combination with one of these partons, can easily produce a charmed hadron. Such a process occurs almost without any loss of the c-quark momentum (i.e., $\mathbf{p}_H \approx \mathbf{p}_c$). Therefore, in the small-x region, one should expect the coincidence of the spectra of charmed hadrons and c quarks. At the same time, one may use the conventional fragmentation mechanism at high x.

Following these arguments, we have proposed a modified form of the fragmentation function [6],

$$D^{\rm MF}(z, M_{c\bar{c}}) \sim z^{-\alpha(M_{c\bar{c}})}(1-z), \quad (14)$$

with two additional conditions imposed on $\alpha(M_{c\bar{c}})$:

$$\alpha(M_{c\bar{c}}) \to -\infty, \quad D(z) \to \delta(1-z) \quad \text{for } M_{c\bar{c}} \to 2m_c; \quad \alpha(M_{c\bar{c}}) \to \alpha_c \approx -2.2, \quad D(z) \to z^{-\alpha_c}(1-z) \quad \text{for } M_{c\bar{c}} \approx M_0. \quad (15)$$

The explicit form of $\alpha(M_{c\bar{c}})$ is

$$\alpha(M_{c\bar{c}}) = \frac{1 - 3\mu(M_{c\bar{c}})}{1 - \mu(M_{c\bar{c}})},$$

where

$$\mu(M_{c\bar{c}}) = \left(\frac{\ln(\frac{M_{c\bar{c}}}{2m_c}q_0)}{\ln q_0}\right)^{0.464}, \quad q_0 \approx 0.12.$$

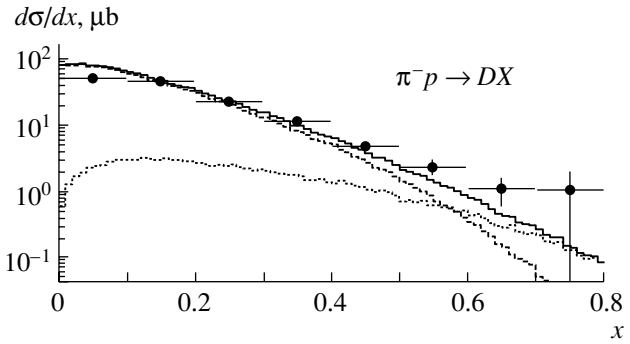

Fig. 2. Differential distributions $d\sigma/dx$ at $E_\pi = 250$ GeV [1]. The dotted (dashed) histogram corresponds to the recombination (fragmentation) contribution, while the solid histogram represents their sum (see [6] for details).

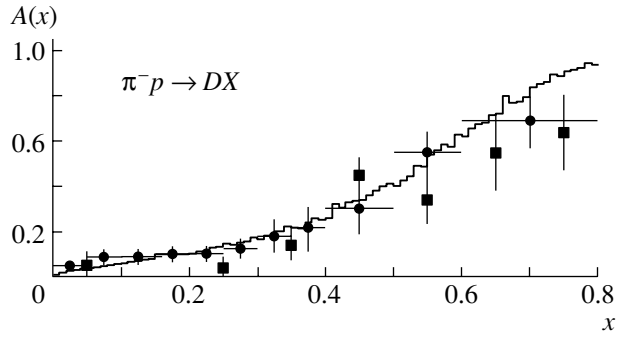

Fig. 3. Description of the asymmetry $A(x)$ in $\pi^- p$ collisions (see [6] for details).

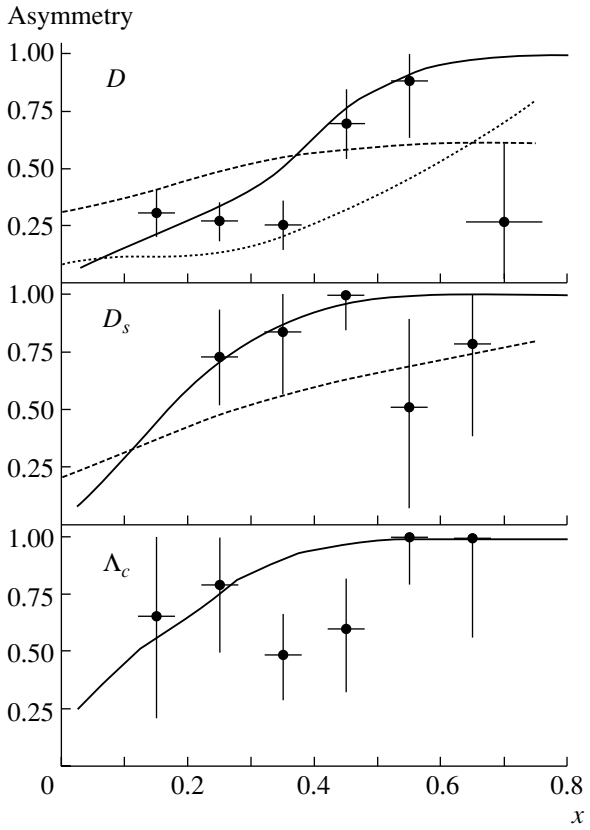

Fig. 4. Asymmetry in charmed-hadron production in $\Sigma^- p$ interactions at $P_{\rm lab} = 340$ GeV [2]. The solid curves represent our predictions, the dotted curve corresponds to PYTHIA results, and the dashed curves are the predictions of Piskounova [4].

Note that the use of the fragmentation function assumes the absence of the interaction of the product heavy c quark with the remaining initial hadrons. Therefore, there should be no difference between the spectra of charmed and anticharmed hadrons. Moreover, any modification of the fragmentation mechanism cannot reproduce the production asymmetry (leading-particle effect).

4. RECOMBINATION MECHANISM

The fragmentation mechanism can be applied to the production of a $c\bar{c}$ pair in the color-singlet state or to the high-p_T production of open charm. On the other hand, for the hadronic production of a color $c\bar{c}$ pair with small p_T, one should take into account the possibility of interaction of charmed c and $\bar{c}$ quarks with the initial-hadron remnants. It follows that, because of the different valence quarks in the initial hadrons, one may expect different inclusive spectra of final charmed hadrons.

In the parton model, a heavy c quark should interact, with a high probability, with its nearest neighbor in the rapidity space to form a color-singlet state with this neighbor. In some cases, the heavy antiquark (quark) may approach closely (in the rapidity space) a valence light quark (diquark) from the initial hadron. This would result in the formation of a fast heavy meson (baryon) in the fragmentation region of the initial hadron.

The model developed in [5, 6] is used here to describe the production asymmetry for charmed hadrons. In this model, the interaction of charmed quarks with valence quarks from the initial hadrons is described in terms of the recombination function [5, 6]. The recombination of the valence q_V and $\bar{c}$ quarks into a D meson is described by the function

$$R_M(x_q, z; x) = \frac{\Gamma(2-\alpha_q-\alpha_c)}{\Gamma(1-\alpha_c)\Gamma(1-\alpha_q)} \times \xi_q^{(1-\alpha_q)}\xi_c^{(1-\alpha_c)}\delta(1-\xi_q-\xi_c), \qquad (16)$$

where $\xi_q = x_q/x$; $\xi_c = z/x$; and the fractions x_q, z, and x of the initial-hadron c.m. momentum are carried away by the valence q quark, the charmed c quark, and the $D(\bar{c}q)$ meson, respectively. The corresponding recombination of three quarks into a

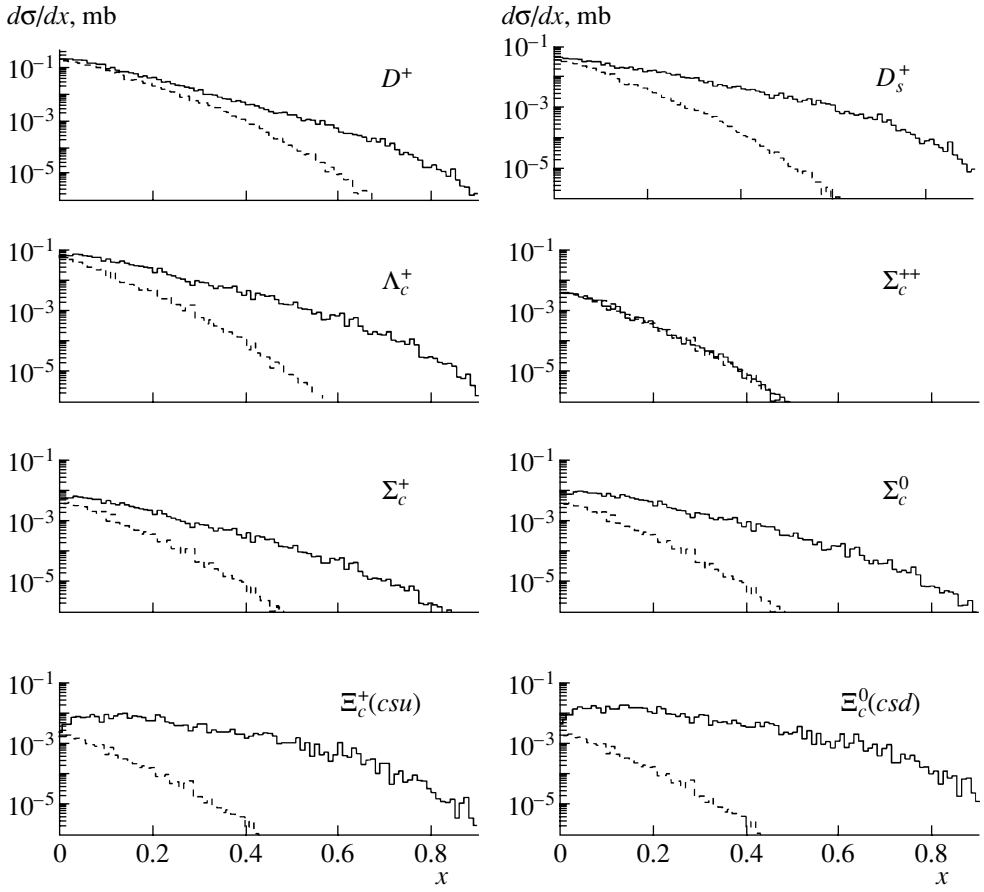

Fig. 5. x distributions of charmed mesons ($D^{*\pm}$ and $D_s^{*\pm}$) and baryons produced in $\Sigma^- p$ interactions at $P_{\rm lab} = 600$ GeV. The solid (dashed) histograms correspond to leading (nonleading) charmed-hadron production.

baryon can be described by means of the similar recombination function

$$R_B(x_1, x_2, z; x) = \frac{\Gamma(3-\alpha_1-\alpha_2-\alpha_c)}{\Gamma(1-\alpha_1)\Gamma(1-\alpha_2)\Gamma(1-\alpha_c)} \times \xi_1^{(1-\alpha_1)}\xi_2^{(1-\alpha_2)}\xi_c^{(1-\alpha_c)}\delta(1-\xi_1-\xi_2-\xi_c). \quad (17)$$

These functions take into account momentum conservation and the proximity of partons in the rapidity space. Indeed, the recombination function is the square of the modulus of the heavy-meson (baryon) wave function in momentum space taken in the infinite-momentum frame in the valence-quark approximation.

In terms of the function $R(x_V, z; x)$ describing the recombination of the quarks q_V and $\bar{c}$ into a meson, we represent the corresponding contribution to the inclusive spectrum of D meson as [5, 6]

$$x^* \frac{d\sigma^R}{dx} = R_0 \int x_V z^* \frac{d^2\sigma}{dx_V dz} R(x_V, z; x) \frac{dx_V}{x_V} \frac{dz}{z}. \quad (18)$$

Here, $x^* = 2E/\sqrt{s}$ and $x = 2p_L/\sqrt{s}$, where E and p_L are the energy and the longitudinal momentum of the D meson in the c.m. frame of the initial hadrons; x_V and z are the momentum fractions carried away by the valence quark and the heavy antiquark, respectively; and $x_V z^* d^2\sigma/(dx_V dz)$ is the double-differential cross section for the simultaneous production of the quarks q_V and $\bar{c}$ in a hadronic collision. The equation describing the production of a charmed baryon has a similar form.

The constant term R_0 of the model determines the relative contribution of recombination. We fitted data on charmed-hadron production in $\pi^- N$ collisions and found that $R_0 \approx 0.8$ [6].

Note that the use of arecombination with valence quarks provides a good description of the leading-particle effect. At the same time, its contribution to the total inclusive cross section for the production of charmed particles is rather small (about 10%). This mechanism dominates in the high-x region.

Note that the description provided by this model for the production of a charmed D meson in $\pi^- N$

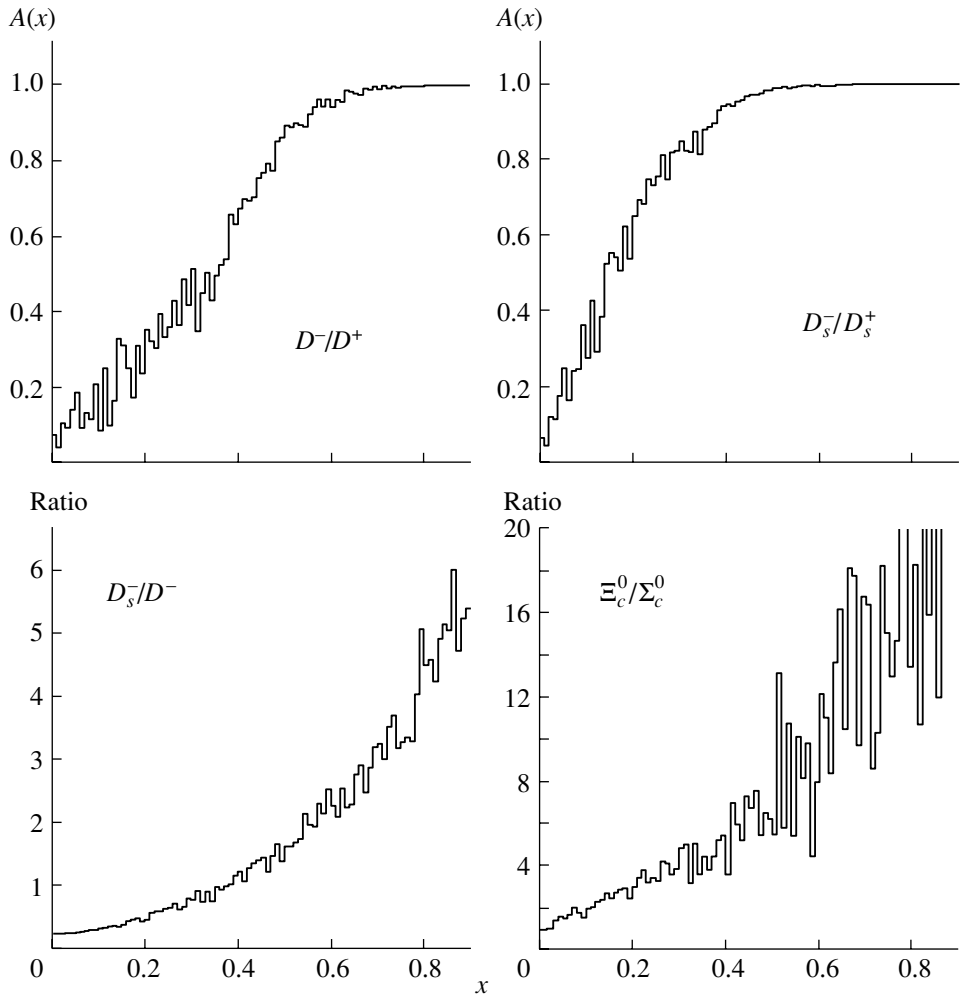

Fig. 6. Production asymmetry $A(x)$ from (2) for $D^{*\pm}$ and $D_s^{*\pm}$ mesons (two upper histograms) produced in $\Sigma^- p$ interactions at $P_{\rm lab} = 600$ GeV. The two lower plots present the ratio of the spectra of charmed hadrons with and without strange quarks (i.e., the D_s^{*-}/D^{*-} and $\Xi_c^0(cds)/\Sigma_c^0(cdd)$ ratios).

interactions is successful to a greater or lesser extent (see Figs. 2, 3 and [6] for details).

5. CHARM PRODUCTION IN A Σ^- BEAM

In this section, we consider charmed-hadron production in a high-energy beam of Σ^- hyperons. First of all, we expect that the distributions of the valence d and s quarks will behave differently. Indeed, as a first approximation, the distribution of the valence quark in the baryon $B(q_1q_2q_3)$ can be represented as [5, 6]

$$V_{q_1}^B(x) \propto x^{-\alpha_1}(1-x)^{\gamma_b-\alpha_2-\alpha_3}, \qquad (19)$$

where α_i is the intercept of the leading Regge trajectory for the q_i quark and $\gamma_B \simeq 4$. Note that, because of violation of flavor $SU(N)$ symmetry, we have different intercepts for $d(u)$ and s quarks [9, 11]:

$$\alpha_u = \alpha_d = \frac{1}{2}, \quad \alpha_s \approx 0, \quad \alpha_c \approx -2.2. \qquad (20)$$

As a result, the x dependence of the valence d and s quarks in the $\Sigma^-(sdd)$ hyperon has the form [7]

$$V_d^\Sigma \sim \frac{1}{\sqrt{x}}(1-x)^{3.5}, \quad V_s^\Sigma \sim (1-x)^3. \qquad (21)$$

It is seen from Eq. (21) that the valence s quark in the Σ^- hyperon has a harder x distribution than that for the d quark. A comparative analysis of the gluon distributions for the π and K mesons showed [14] that the total gluon distributions for these mesons are almost indistinguishable, irrespective of the form of initial distributions of valence quarks. Therefore, we arrive at the conclusion that the gluon distributions for the Σ hyperon and the nucleon are nearly identical. As a result, we expect a harder x dependence of the s-quark distribution in the Σ hyperon than that of the u-quark distribution in the nucleon. Thus, one may expect that the spectrum of D_s mesons produced in a Σ beam is slightly harder than the spectrum of D^0

mesons produced in a nucleon beam. On the other hand, the d quark in the Σ hyperon should be slightly softer than that in the nucleon. As a result, we should observe the different $x_{\rm F}$ dependences of the spectra of charmed hadrons with d or s quarks, namely, $D^-(\bar{c}d)$ and $D_s^-(\bar{c}s)$, $\Xi_c^0(cds)$ and $\Sigma_c^-(cdd)$, etc.

We use the leading-order formulas to calculate the cross sections for quark–antiquark and gluon–gluon annihilation into a $c\bar{c}$ pair. We set m_c to 1.25 GeV and the strong coupling constant to 0.3. For the cross section for $\Sigma^- p$ interaction at $P_{\rm lab} = 600$ GeV, one then has

$$\sigma(\Sigma^- p \to c\bar{c}X) \simeq 8\ \mu{\rm b}. \qquad (22)$$

In our calculations, we do not aim at reproducing the absolute value of this cross section (see [13], for a detailed consideration of this problem), but we concentrate on describing the $x_{\rm F}$ distribution of charmed mesons and baryons.

Recently, we calculated the asymmetry of the x spectra for D, D_s, and Λ_c hadrons produced in a Σ^- beam of energy 340 GeV. The WA89 collaboration compared these predictions with their experimental data [2]. This comparison is presented in Fig. 4. It can be seen that the asymmetry in D-meson production in a Σ^- beam differs from that in a π^- beam and that there is more pronounced asymmetry for D_s-meson production.

Below, we present the predictions for charmed-hadron production in a 600-GeV Σ^- beam. The corresponding distributions (integrated with respect to p_T) are presented in Fig. 5. We can see from these graphs that, indeed, the final-state charmed-quark interaction being considered (recombination) leads to noticeable distinctions between the $x_{\rm F}$ spectra. These distinctions can be explicitly seen in Fig. 6, where we present the corresponding asymmetry A [see Eq. (2) for definition]. The most nontrivial prediction of the proposed model is presented in the two lower plots in Fig. 6, where we display the ratio of the inclusive spectra of $D_s^{*-}(\bar{c}s)$ and $D^{*-}(\bar{c}d)$ mesons, as well as of Ξ_c^0 and Σ_c^0 baryons. Indeed, because of the difference of the valence d and s quarks in the Σ^- beam [see Eq. (21)], we expect additional asymmetry in leading-charmed-particle production.

6. CONCLUSION

In this article, we have emphasized once again that the interaction of product charmed quarks with valence quarks from initial hadrons is the source of the observed asymmetry in charmed-hadron production. Note that the model under consideration also provides an additional method for measuring the valence-quark distributions in the Σ baryons.

Upon the completion of this study, we received the article of the E791 collaboration [15] with its latest results on the inclusive x and p_T distributions of charmed hadrons produced in a π^- beam. In particular, this collaboration observed a noticeable asymmetry in the production of Λ_c^+ and Λ_c^- baryons in the forward region (about 13%). Note that our model cannot explain this result. Because of the equal numbers of valence $\bar{u}$ and d quarks in a π^- beam, we expect the equal yields of $\Lambda_c^+(cud)$ and $\Lambda_c^-(cud)$ baryons in a π^- beam. Moreover, the majority of theoretical models [4] also predict zero asymmetry for the production of these particles.

ACKNOWLEDGMENTS

We are grateful to E. Chudakov, A. Kushnirenko, O. Piskounova, and J.S. Russ for stimulating discussions.

This work was supported in part by the Russian Foundation for Basic Research (project no. 99-02-16558) and by the Federal Ministry for Higher Education (grant no. RF E00-33-062).

REFERENCES

1. E791 Collab. (J. C. Anjos), hep-ex/9912039; E791 Collab. (E. M. Aitala *et al.*), Phys. Lett. B **411**, 230 (1997); hep-ex/9708040; E791 Collab. (E. M. Aitala *et al.*), Phys. Lett. B **371**, 157 (1996); WA82 Collab. (M. I. Adamovich *et al.*), Phys. Lett. B **305**, 402 (1993); E769 Collab. (G. A. Alves *et al.*), Phys. Rev. Lett. **77**, 2388 (1996); E769 Collab. (G. A. Alves *et al.*), Phys. Rev. Lett. **72**, 812 (1994).
2. WA89 Collab. (M. I. Adamovich *et al.*), Eur. Phys. J. C **8**, 593 (1999); hep-ex/9803021.
3. SELEX Collab. (M. Lori *et al.*), hep-ex/9910039; SELEX Collab. (M. Lori), Nucl. Phys. B (Proc. Suppl.) **75**, 16 (1999); SELEX Collab. (F. G. Garcia and S. Y. Jun), hep-ex/9905003.
4. R. Vogt and S. J. Brodsky, Nucl. Phys. B **478**, 311 (1996); hep-ph/9512300; T. Gutierrez and R. Vogt, Nucl. Phys. B **539**, 189 (1999); hep-ph/9808213; J. C. Anjos, J. Magnin, F. R. Simao, and J. Solano, hep-ph/9806396; E. Cuautle, G. Herrera, and J. Magnin, Eur. Phys. J. C **2**, 473 (1998); hep-ph/9711354; G. Herrera and J. Magnin, Eur. Phys. J. C **2**, 477 (1998); hep-ph/9703385; J. C. Anjos, G. Herrera, J. Magnin, and F. R. A. Simao, Phys. Rev. D **56**, 394 (1997); hep-ph/9702256; O. I. Piskounova, hep-ph/9904208; T. Tashiro, H. Noda, K. Kinoshita, and S. Nakariki, hep-ph/9810284; G. H. Arakelyan and S. S. Yeremyan, hep-ph/9808325; G. H. Arakelyan, Yad. Fiz. **61**, 1682 (1998) [Phys. At. Nucl. **61**, 1570 (1998)]; hep-ph/9711276; E. Norrbin and T. Sjöstrand, hep-ph/0005110; Phys. Lett. B **442**, 407 (1998); hep-ph/9809266.

5. V. G. Kartvelishvili, A. K. Likhoded, and S. R. Slabospitsky, Yad. Fiz. **32**, 236 (1980) [Sov. J. Nucl. Phys. **32**, 122 (1980)]; **33**, 832 (1981) [**33**, 434 (1981)]; A. K. Likhoded, S. R. Slabospitsky, and M. V. Suslov, Yad. Fiz. **38**, 727 (1983) [Sov. J. Nucl. Phys. **38**, 433 (1983)].
6. A. K. Likhoded and S. R. Slabospitsky, Yad. Fiz. **60**, 1097 (1997) [Phys. At. Nucl. **60**, 981 (1997)]; A. K. Likhoded and A. I. Onishchenko, Yad. Fiz. **62**, 742 (1999) [Phys. At. Nucl. **62**, 693 (1999)]; hep-ph/0002202.
7. V. V. Kiselev, A. K. Likhoded, and S. R. Slabospitsky, Preprint No. 86-45, IFVÉ (Inst. for High Energy Physics, Protvino, 1986).
8. A. H. Mueller, Phys. Rev. D **2**, 2963 (1970); O. V. Kancheli, Pis'ma Zh. Éksp. Teor. Fiz. **11**, 397 (1970) [JETP Lett. **11**, 267 (1970)].
9. P. D. B. Collins, *An Introduction to Regge Theory and High Energy Physics* (Cambridge Univ. Press, Cambridge, 1977; Atomizdat, Moscow, 1980).
10. M. N. Kobrinsky, A. K. Likhoded, and A. N. Tolstenkov, Yad. Fiz. **20**, 775 (1974) [Sov. J. Nucl. Phys. **20**, 414 (1975)]; P. V. Shlyapnikov, A. K. Likhoded, and A. N. Tolstenkov, Yad. Fiz. **26**, 294 (1977) [Sov. J. Nucl. Phys. **26**, 79 (1977)].
11. V. G. Kartvelishvili, A. K. Likhoded, and V. A. Petrov, Phys. Lett. B **78B**, 615 (1978).
12. C. Peterson, D. Schlatter, I. Schmitt, and P. Zerwas, Phys. Rev. D **27**, 105 (1983).
13. M. Mangano, P. Nason, and G. Ridolfi, Nucl. Phys. B **405**, 507 (1993).
14. A. B. Batunin, V. V. Kiselev, and A. K. Likhoded, Yad. Fiz. **49**, 554 (1989) [Sov. J. Nucl. Phys. **49**, 346 (1989)].
15. E791 Collab. (E. M. Aitala *et al.*), Phys. Lett. B **495**, 42 (2000); hep-ex/0008029.

Physics of Atomic Nuclei, Vol. 65, No. 1, 2002, pp. 135–152. From Yadernaya Fizika, Vol. 65, No. 1, 2002, pp. 140–157.
Original English Text Copyright © 2002 by Simonov.

ELEMENTARY PARTICLES AND FIELDS
Theory

Perturbative Expansions in QCD and Analytic Properties of α_s*

Yu. A. Simonov**

Institute of Theoretical and Experimental Physics, Bol'shaya Cheremushkinskaya ul. 25, Moscow, 117259 Russia

Received June 21, 2001

Abstract—It is shown that analytic properties of standard QCD perturbation theory contradict known spectral properties and contain, in particular, infrared-generated Landau ghost poles and cuts. As an outcome, a rigorous background perturbation theory is developed and its analytic properties are shown to be in agreement with general requirements. In the limiting case of large N_c, where QCD amplitudes contain only pole singularities, the strong coupling constant $\alpha_s(Q^2)$ is shown to be a meromorphic function of external momenta as well. Some simple models and examples are given where nonperturbative β function and $\alpha_s(Q^2)$ can be written explicitly. The general form of amplitudes at large N_c is given in the framework of background perturbation theory, and its correspondence with standard perturbation theory at high momenta is demonstrated in the example of e^+e^- annihilation. For timelike momenta, the background coupling constant differs drastically from the standard one, but the background series averaged over energy intervals has the same (AF) behavior at high momenta in the Euclidean and in the Minkowskian region.
© 2002 MAIK "Nauka/Interperiodica".

1. INTRODUCTION

The standard perturbation theory (SPT) in QCD is well developed both on the theoretical and on the phenomenological level [1, 2] and constitutes the major and best understood part of QCD. Successful applications of perturbative expansions to processes featuring high momenta are numerous and impressive.

However, there are a few basic difficulties in SPT [it is assumed that renormalization-group (RG) improvements, such as partial summation of large logarithms, are automatically included in SPT], namely:

(i) The analytic properties of SPT amplitudes do not correspond to the expected spectral behavior. In particular, there appear ghost poles and cuts even in the Euclidean region of momenta, where one expects amplitudes to be holomorphic.

These ghost singularities are due to the analytic properties of RG-improved $\alpha_s(Q^2)$ and are associated with the infrared (IR) divergence of $\alpha_s(Q^2)$. Also in the Minkowskian region of momenta, $\alpha_s(Q^2)$ have logarithmic cuts that must not appear in a physical amplitude and which are therefore an artifact of SPT.

In short, the analytic behavior of amplitudes that are computed in SPT has nothing to do with physical thresholds and cuts due to creation of hadrons. Therefore, one may only speak about some duality relations between SPT amplitudes and physical amplitudes integrated over a sufficiently large energy interval.

(ii) Another basic defect of SPT is the lack of convergence of standard perturbative series. There are arguments that the latter is an asymptotic series [3], and it is not clear, in all cases, where the series should be cut off. (Some hints that the three-loop contribution impairs the physical results in the 1- to 1.5-GeV region are contained in [3, 4].) Moreover, Landau ghost poles give rise to the appearance of the so-called IR renormalons [5], which make the sum of perturbative series undefined even in the Borel sense.

Attempts at associating IR renormalons with nonperturbative contributions may have only a qualitative character at best. Strictly speaking, the notion of the sum of an SPT series therefore has no definite meaning, and one may only hope that, at high Euclidean momenta, the first few terms of the RG-improved perturbative series describe the asymptotic behavior of physical amplitudes with reasonable accuracy.

A few approaches have been developed to improve the situation. First of all, it was understood long ago that, in addition to SPT, nonperturbative contributions should also be taken into account. Technically, the latter were introduced as local terms (condensates) in the operator-product expansion (OPE), and QCD sum rules were proposed on this basis [6]. In this way, one can approach the low-energy region around 1 to 2 GeV, and a lot of useful physical information has been obtained by this method over the last 20 years [7].

*This article was submitted by the author in English.

**e-mail: simonov@heron.itep.ru

However, in this method, one does not solve the two problems of SPT described above, but instead postulates that, in addition to the first few SPT terms, one can add a few power-law terms to imitate the behavior of physical amplitudes not only in the asymptotic region but also in the region of a few GeV. At lower energies, the OPE series have at least double divergence: due to the explosion of α_s near the Landau ghost pole and due to the explosion of the power-law terms C_n/Q^{2n}.

It is important to note that the original OPE and QCD sum rules [6] were properly defined only in the Euclidean region, and the transition to the timelike region is assumed to be done a posteriori, upon performing all calculations in the Euclidean region.

Defining $\alpha_s(Q^2)$ in the Minkowskian region of Q^2, $Q^2 < 0$, is a problem in itself within SPT, since a formal analytic continuation of expressions for $\alpha_s(Q^2)$ that involve two or more loops yields complex expressions violating explicit unitarity conditions in the nonasymptotic region.

Moreover, as was stressed in [8], the invariant coupling $\bar{g}(Q)$ can be defined only in the spacelike domain, and "inside the RG formalism there is no simple means for defining $\bar{g}(Q)$ in the timelike region."

A new formalism for defining $\alpha_s(Q^2)$ both in the space- and in the timelike region was developed in [9] (see [8] for a review and further references), where $\alpha_s(Q^2)$ is forced to be analytic for $Q^2 > 0$ and where a special procedure is envisaged to continue α_s analytically into the timelike region.

It is clear, however, that this is not a unique way of analytic definition in the entire complex plane of z, and, in particular, $\alpha_s(z)$ has nevertheless a divergent first derivative at $z = 0$, which is not justified from the physical point of view.

In what follows, we shall choose a completely different strategy. To simplify the matter, we shall consider below the limiting case of large N_c. In this case, one can be sure that all physical amplitudes contain only poles as functions of external momenta [10], and we shall require that perturbative expansions reproduce the meromorphic properties of physical amplitudes—i.e., that $\alpha_s(Q^2)$ have singularities only in the timelike region and that those be poles.

To achieve this goal, one needs to use background perturbation theory (BPT) instead of the standard one, and we shall derive rigorous formalism based on BPT developed in the 1970s and 1980s [11] and generalized in [12–14] to include a nonclassical background and averaging over background fields.

In this way, one obtains a systematic formalism that makes it possible to express all terms of BPT in terms of irreducible correlation functions for background fields (integrals thereof) and the renormalized coupling constant α_B, which we shall denote $\alpha_B(s)$ to distinguish it from $\alpha_s(s)$ in SPT.

It was argued in [14] that $\alpha_B(s)$ and physical amplitudes satisfy the same RG equations—in particular, the Ovsyannikov–Callan–Simanzyk (OCS) equations—and the important distinction between $\alpha_B(Q^2)$ and $\alpha_s(Q^2)$ lies in the character of the Q^2 dependence of the former. It was demonstrated in [12–14] that $\alpha_B(Q^2)$ has the property of freezing or saturation at small Q^2; i.e., it tends to a finite limit $\alpha_B(0)$ when $Q^2 \to 0$ and has no singularities in the entire Euclidean region $Q^2 \geq 0$.

This behavior of $\alpha_B(Q^2)$ was tested repeatedly in e^+e^- annihilation [13, 14], in the fine structure of charmonium [15] and bottomonium levels [16], and recently [4] in a comparison with accurate lattice data on the small-distance behavior of $\alpha_L(R)$. In all cases, the same form of solution for α_B was used without free parameters, which produced results in good agreement with experimental and lattice data. In this way, the phenomenon of freezing (saturation) was demonstrated both theoretically as a result of confinement in background fields [12] and phenomenologically in comparison with lattice and experimental data.

With all that, some important theoretical questions were not answered: First of all, what happens to $\alpha_B(s)$ in the Minkowskian (timelike) region and what are the analytic properties of $\alpha_B(s)$ in the entire s-plane? Second, what is the connection between $\alpha_B(s)$ and other nonperturbative definitions of $\alpha(s)$, e.g., lattice definitions of α–$\alpha_L(s)$?

In the present paper, our objective is to study the problem of BPT in the large-N_c limit in order to elucidate several aspects.

First, we formulate the foundations of BPT and rules for calculating perturbative series, starting from the purely nonperturbative term.

Second, we derive RG equations, taking into account the fact that nonperturbative background is in general not a classical solution and is subject to vacuum averaging, which, owing to the 't Hooft identity, can be performed independently of perturbative-field averaging.

Third, we find the most general solution to RG equations and, in particular, the nonperturbative β function, which has a known lowest term expansion; at the same time, $\alpha_B(Q^2)$ is represented as the sum of pole terms.

To understand which kind of singularities $\alpha_B(Q^2)$ may have without ceasing to be compatible with analytic properties of physical amplitudes, we consider

a simplified model and demonstrate that any finite-order perturbative expansion has additional singularities that are eliminated when a partial summation of the perturbative series is performed.

As a next step, we formulate a generic perturbative expansion for a physical amplitude, choosing the example of e^+e^- annihilation into hadrons and write it as a sum over poles in the timelike region with calculable coefficients.

At this point, one may wonder how this meromorphic expansion is related to the SPT expansion, where the perturbative series is in powers of $\alpha_s(Q^2)$, which contains logarithmic functions of Q^2 and which is not meromorphic. The answer to this question was given in the analysis of the lowest term of e^+e^- annihilation—the hadronic part of the photon self-energy. The latter is the sum over meson poles at large N_c and has a proper logarithmic behavior $\ln Q^2$ at large Q^2. We demonstrate that a similar correspondence takes place also for higher terms of BPT and formulate conditions on the coefficients of the meromorphic expansion that are necessary to reproduce the known SPT expansion at large Q^2.

A discussion on practical applications and on a comparison with other approaches concludes the paper.

The exact structure of the paper is as follows. In Section 2, general rules of BPT are given and Green's functions for valence quarks, gluons, and hadrons are written explicitly. In Section 3, RG equations are written for the case of the most general background, the point of the RG scheme is discussed, and a particular solution to the RG equations for the β function and $\alpha_B(Q^2)$ is presented. In Section 4, a simple model is discussed where some BPT subseries can be summed up explicitly. In Section 5, nonasymptotic terms in the spectral sums are calculated. In Section 6, the behavior of perturbative series in the region of timelike Q^2 is studied in detail. The discussion and outlook are contained in the concluding section.

2. BACKGROUND PERTURBATION THEORY FOR AN ARBITRARY BACKGROUND

The gluon field plays two different roles in QCD:

(i) Gluons propagate, and, at small distances, this process can be described perturbatively, leading, in particular, to color Coulomb interaction between quarks (antiquarks).

(ii) Gluons form a kind of condensate, which serves as a background for propagating perturbative gluons and quarks. This background is Euclidean and ensures the phenomena of confinement and chiral-symmetry breaking (CSB).

Correspondingly, we shall break down the total gluon field A_μ into a perturbative part a_μ and a nonperturbative (NP) background B_μ:

$$A_\mu = B_\mu + a_\mu. \tag{1}$$

There are many questions about this partition, which may be answered now only partially. For example, what exactly is the criterion of partition? The possible answer is that perturbative fields a_μ get their dimension from distance (momentum); therefore, all correlation functions for the fields a_μ (in the absence of B_μ) are singular and made of inverse powers of $(x-y)$ and logarithms, where the only dimensional parameter of perturbative QCD ($\Lambda_{\rm QCD}$) appears. Obviously, any dimensional constant, like hadronic masses or string tension, cannot therefore be obtained as a perturbation series. In contrast to that, the NP fields B_μ have dimensions of mass owing to the violation of scale invariance, which is intrinsically present in the gluodynamics Lagrangian. The origin of partition in (1) is clearly seen in the solutions to nonlinear equations for field correlation functions [17]: a perturbative solution to those leads to a singular powerlike field correlation function, whereas, at large distances, there is a self-consistent solution to the equations, decaying exponentially with distance with an arbitrary mass scale, since the equations in [17] are scale-invariant. A full solution including intermediate distances produces mixed perturbative–nonperturbative terms containing both inverse powers of distance and exponentials. For these terms, the criterion of partition fails.

One can avoid formally the question of the partition principle (and of double counting) using the 't Hooft identity [13], which allows one to integrate in (1) independently over B_μ and a_μ:

$$Z = \frac{1}{N'}\int DB_\mu \eta(B) D\psi D\bar\psi Da_\mu e^{L_{\rm tot}}. \tag{2}$$

Here, the weight $\eta(B)$ is arbitrary and may be taken to be a constant.

To define perturbation theory series in ga_μ, one starts from (1) and rewrites the Lagrangian as

$$\begin{aligned} L_{\rm tot} &= L_{\rm gf} + L_{\rm gh} + L(B+a) \\ &= L_0 + L_1 + L_2 + L_{\rm int} + L_{\rm gf} + L_{\rm gh}, \end{aligned} \tag{3}$$

where L_i have the form

$$L_0 = -\frac{1}{4}(F^a_{\mu\nu}(B))^2; \quad L_1 = a^c_\nu D^{ca}_\mu(B) F^a_{\mu\nu}; \tag{4}$$

$$L_2(a) = \frac{1}{2} a_\nu (\hat D^2_\lambda \delta_{\mu\nu} - \hat D_\mu \hat D_\nu + ig\hat F_{\mu\nu}) a_\mu$$

$$= \frac{1}{2} a^c_\nu [D^{ca}_\lambda D^{ad}_\lambda \delta_{\mu\nu} - D^{ca}_\mu D^{ad}_\nu - g\, f^{cad} F^a_{\mu\nu}] a^d_\mu;$$

$$D^{ca}_\lambda = \partial_\lambda \cdot \delta_{ca} + g f^{cba} B^b_\lambda \equiv \hat D_\lambda,$$

$$F^a_{\mu\nu} = \partial_\mu B^a_\nu - \partial_\nu B^a_\mu + g f^{abc} B^b_\mu B^c_\nu;$$

$$L_{\rm int} = -\frac{1}{2}(D_\mu(B)a_\nu \qquad (5)$$

$$- D_\nu(B)a_\mu)^a g f^{abc} a^b_\mu a^c_\nu - \frac{1}{4} g^2 f^{abc} a^b_\mu a^c_\nu f^{aef} a^e_\mu a^f_\nu;$$

$$L_{\rm gh} = -\theta^+_a (D_\mu(B) D_\mu(B+a))_{ab} \theta_b. \qquad (6)$$

It is convenient to prescribe, to a_μ and B_μ, the gauge transformations

$$a_\mu \to U^+ a_\mu U, \qquad (7)$$

$$B_\mu \to U \left(B_\mu + \frac{i}{g}\partial_\mu \right) U \qquad (8)$$

and to impose on a_μ the background gauge condition

$$G^a \equiv (D_\mu a_\mu)^a = \partial_\mu a^a_\mu + g f^{abc} B^b_\mu a^c_\mu = 0. \qquad (9)$$

In this case, the ghost field has to be introduced as in (6) and the gauge-fixing term is

$$L_{\rm gf} = -\frac{1}{2\xi}(G^a)^2.$$

One can write the resulting partition function as

$$Z = \frac{1}{N'} \int DB \eta(B) Z(J,B), \qquad (10)$$

where

$$Z(J,B) = \int D\psi D\bar\psi D a_\mu D\theta D\theta^+ \qquad (11)$$

$$\times \exp\left(L_{\rm tot} + \int J_\mu a_\mu dx \right).$$

We now can identify the propagator of a_μ from the quadratic terms in Lagrangian $L_2(a)$, $\frac{1}{2\xi}(G^a)^2$:

$$G^{ab}_{\nu\mu} = \left[\hat D^2_\lambda \delta_{\mu\nu} - \hat D_\mu \hat D_\nu \right. \qquad (12)$$

$$\left. + ig\hat F_{\mu\nu} + \frac{1}{\xi}\hat D_\nu \hat D_\mu \right]^{-1}_{ab}.$$

It will sometimes be convenient to choose $\xi = 1$ and end up with the well-known form of propagator in—what one would call—the background Feynman gauge:

$$G^{ab}_{\nu\mu} = (\hat D^2_\lambda \delta_{\mu\nu} - 2ig\hat F_{\mu\nu})^{-1}. \qquad (13)$$

Integration over ghost and gluon degrees of freedom in (11) yields

$$Z(J,B) = {\rm const} \cdot ({\rm det} W(B))^{-1/2}_{\rm reg} \qquad (14)$$

$$\times [{\rm det}(-D_\mu(B) D_\mu(B+a))]_{a=\delta/\delta J}$$

$$\times \left\{ 1 + \sum_{l=1}^{\infty} \frac{S_{\rm int}}{l!}\left(a = \frac{\delta}{\delta J} \right) \right\}$$

$$\times \exp\left(-\frac{1}{2} J W^{-1} J \right)\Big|_{J_\nu = D_\mu(B) F_{\mu\nu}(B)},$$

where $W = G^{-1}$ and G is defined in (12) and (13).

Let us mention the important property of the background Lagrangian (3): under gauge transformations, the fields a_μ and B_μ transform as in (7) and (8) and all terms of (3), including the gauge-fixing one, $\frac{1}{2}(G^a)^2$, are gauge-invariant. That was actually one of the aims put forward by 't Hooft in [11], and it has important consequences too:

(i) Any amplitude in perturbative expansion in ga_μ of (11) and (14) corresponding to a generalized Feynman diagram is separately gauge-invariant (for color-singlet initial and final states, of course).

(ii) Due to gauge invariance of all terms, the renormalization is especially simple in the background-field formalism [11], since the counterterms appear only in a gauge-invariant combination, e.g., $F^2_{\mu\nu}$; hence, the Z factors Z_g and Z_A are connected. We shall exploit this fact in Sections 6 and 7.

Let us now address the term L_1 in (3), $L_1 = 2{\rm tr}(a_\nu D_\mu F_{\mu\nu})$, which is usually missing in the standard background-field formalism [11], since one tacitly assumes there that the background B_μ is a classical solution,

$$D_\mu(B) F_{\mu\nu}(B) = 0. \qquad (15)$$

Here, we do not impose condition (15) and consider any background, classical or purely quantum fluctuations. Let us estimate the influence of the vertex L_1. In general, it leads to the shift of the current J_μ in the expression for the perturbative series (14). Physically, this means that, at each point, the background B_μ can generate a perturbative gluon via the vertex $(a_\mu D_\nu F_{\nu\mu})$, and this vertex is proportional to the degree of "nonclassicality" of B_μ. For the semiclassical vacuum, like the instanton model, the expectation value $\langle (D_\mu F_{\mu\nu})^2 \rangle$ over the instanton ensemble is less than $O(\rho^4/R^4)$ and is small (at most, of the order of a few percent), while the expectation value $\langle D_\mu F_{\mu\nu} \rangle$ vanishes in the symmetric vacuum. All this is true, provided that the instanton gas stabilizes at small density.

Let us estimate the effect of L_1 in the general quantum case. To this end, we calculate, as in [12], the contribution of L_1 to the gluon propagator.

If one denotes by $\langle\ \rangle_a$ the integral Da_μ with the weight $L_{\rm tot}$ as in (11), we obtain

$$\langle a_{\mu_1}(x_1) a_{\mu_2}(x_2) \rangle_a = G_{\mu_1\mu_2}(x_1,x_2) + \Delta^B_{\mu_1\mu_2}, \quad (16)$$

$$\Delta^B_{\mu_1\mu_2} \equiv \int d^4y_1 d^4y_2 G_{\mu_1\nu_1}(x_1,y_1)$$

$$\times D_\rho F_{\rho\nu_1}(y_1) D_\lambda F_{\lambda\nu_2}(y_2) G_{\nu_2\mu_2}(y_2,x_2).$$

The gluon Green's function $G_{\mu\nu}$ is given in (13) and depends on the background field B_μ, as well as D_μ and $F_{\rho\lambda}$. To get a simple estimate of Δ, we replace $G_{\mu\nu}$ by the free Green's function $G^{(0)}_{\mu\nu}$ and take into account the fact that

$$\langle D_\rho F_{\rho\nu_1}(y_1) D_\lambda F_{\lambda\nu_2}(y_2)\rangle_B \to \frac{\partial}{\partial y_{1\rho}} \frac{\partial}{\partial y_{2\lambda}} \langle F_{\rho\nu_1}(y_1) F_{\lambda\nu_2}(y_2)\rangle, \quad (17)$$

and, for the latter, we use the representation [18] in terms of two independent Lorentz structures, $D(y_1 - y_2)$ and $D_1(y_1 - y_2)$. The contribution of D (that of D_1 is of a similar character) in the momentum space is

$$\Delta^B_{\mu_1\mu_2}(k) \sim \frac{k^2\delta_{\mu_1\mu_2} - k_{\mu_1}k_{\mu_2}}{k^4} D(k), \quad (18)$$

where

$$D(k) = \int d^4y e^{iky} D(y). \quad (19)$$

Inserting, in (19), the exponential falloff for $D(y)$ found in lattice calculations [19], we obtain

$$D(k) = \frac{\langle F^2(0)\rangle}{(N_c^2 - 1)} \frac{\pi^2\mu}{(\mu^2 + k^2)^{5/2}}. \quad (20)$$

At $\mu \simeq 1$ GeV, $D(k) \simeq 0.12$. Thus, $\Delta^B(k)$ is a soft correction to the perturbative gluon propagator fast decreasing with k (in proportion to k^{-5}).

3. RENORMALIZATION-GROUP IMPROVEMENT OF PERTURBATIVE SERIES AND ANALYTIC PROPERTIES OF $\alpha_s(Q^2)$

The most important property of the background method discussed in the preceding section is the gauge invariance of the total Lagrangian including the gauge-fixing term L_{gf}.

As a consequence of this, the counterterms in the renormalization procedure have to be gauge-invariant too, and this fact establishes a connection between the Z factors of the charge and of the background field [11]; namely, if

$$g_0 = Z_g g, \quad B^{(0)}_\mu = Z_B^{1/2} B_\mu, \quad (21)$$

then we have

$$Z_g Z_B^{1/2} = 1. \quad (22)$$

This property is very important for the BPT and for the method of field correlation functions in general. Indeed, the combinations entering into the latter have the form

$$\Delta_n \equiv \text{tr}\langle g F^{(B)}_{\mu_1\nu_1}(1)\Phi(1,2) g F^{(B)}_{\mu_2\nu_2}(2)\Phi(2,3) \ldots g F^{(B)}_{\mu_n\nu_n}(n)\Phi(n,1)\rangle_B, \quad (23)$$

where $F^{(B)}_{\mu_i\nu_i}$ is made of the background field B_μ only and the parallel transporters $\Phi(i,k)$ making Eq. (23) gauge-invariant also depend on gB_μ. Hence, expression in (23) contains only the combinations gB_μ, which, according to (22), are invariant under RG transformations.

Therefore, in all RG relations—in particular, in OCS equations—the background fields (averaged as in Δ_n or nonaveraged) appear on the same ground as the external momenta; hence, all relations can be kept intact. For example, OCS equations for some physical amplitude Γ now have the form [14]

$$\left\{-\frac{\partial}{\partial \ln\lambda} + \beta\frac{\partial}{\partial g^2} + m(\gamma_m - 1)\frac{\partial}{\partial m} - \gamma_\Gamma\right\} \times \Gamma(\lambda p_1, \ldots, \lambda p_N, \lambda^{2k}\Delta_k, g, \nu) = 0, \quad (24)$$

where we have defined as usual

$$\frac{d\alpha_s(\lambda)}{d\ln\lambda} = \beta(\alpha_s) \quad (25)$$

and similarly for γ_m, with boundary conditions

$$\alpha_s(\lambda = 1) = \alpha_s(\nu). \quad (26)$$

In writing the right-hand side of (26), we tacitly assume that α_s also depends on all external parameters $\{p_i\}$ and $\{\Delta_k\}$, in addition to the dimensional regularization parameter ν (or its equivalent in other schemes, μ). The reason why external parameters are not usually written lies in the fact that RG equations [like (24) and (25)] define only the dependence on one scale parameter, e.g., λ, and, through it, on ν (μ), while the dependence on external parameters is not fixed, and they may in principle enter into α_s in arbitrary dimensionless combinations, unless additional information is obtained from perturbation expansion (BPT or SPT).

A few words should be said about the choice of renormalization scheme for BPT.

It is convenient to use the $\overline{MS}$ scheme, since, in the presence of a background as well, the modified Feynman amplitudes of BPT are divergent at small distances (large momenta), and, when these momenta are much larger than the average magnitude of the background fields, one can neglect the latter; e.g., using OPE, one expects corrections of the form $g^2\langle F^2_{\mu\nu}\rangle/p^4$, which do not alter Z factors. In particular, the difference $\Gamma - \Gamma_{\text{pert}} \equiv \Delta\Gamma$, where Γ_{pert} is the usual sum of Feynman amplitudes without a background, is convergent in the ultraviolet (UV) region, so that all UV divergences of Γ are the same as in Γ_{pert}.

Now, we address the possible solutions to Eq. (25). The SPT expansion for $\beta(\alpha_s)$ has the form

$$\beta_{\text{pert}}(\alpha_s) = -\frac{b_0}{2\pi}\alpha_s^2 - \frac{b_1}{4\pi^2}\alpha_s^3 \quad (27)$$

$$-\frac{b_2}{64\pi^3}\alpha_s^4-\frac{b_3}{(4\pi)^4}\alpha_s^5-\ldots,$$

where the first coefficients are[1)]

$$SU(3):\quad n_f=0,\ b_0=11,\ b_1=51, \tag{28}$$
$$b_2(\overline{MS})=2857,\ b_3(\overline{MS})=58486;$$

$$SU(N_c):\quad n_f=0,\ b_0=\frac{11}{3}N_c,\ b_1=\frac{17}{3}N_c^2. \tag{29}$$

Following (27), we will seek $\beta(\alpha_s)$ in the form

$$\beta(\alpha_s)=-\frac{b_0}{2\pi}\frac{\alpha_s^2}{\left[1-\frac{b_1}{2\pi b_0}\varphi'\left(\frac{1}{\alpha_s}\right)\right]}, \tag{30}$$

where $\varphi(x)$ is an unknown function and $\varphi'(x)$ is the derivative with respect to the argument x. Solving (30) for α_s, one obtains

$$\alpha_s=\frac{4\pi}{b_0}\left[\ln\mu^2C^2+\frac{2b_1}{b_0^2}\varphi\left(\frac{1}{\alpha_s}\right)\right]^{-1}, \tag{31}$$

where we have made the substitution $\lambda\to\mu$ and C^2 is an arbitrary function of external parameters having dimensions of $(\text{mass})^{-2}$.

From (27), one concludes that the only condition on φ is the expansion in powers of α_s:

$$\left[1-\frac{b_1}{2\pi b_0}\varphi'\left(\frac{1}{\alpha_s}\right)\right]^{-1}=1+\frac{b_1}{2\pi b_0}\alpha_s \tag{32}$$
$$+\frac{b_2}{32\pi^2b_0}\alpha_s^2+\frac{b_3}{128\pi^3b_0}\alpha_s^3.$$

One can rewrite (31) in the form

$$\chi(Q^2)=z-\frac{b_1}{2\pi b_0}\varphi(z), \tag{33}$$

where $z\equiv1/\alpha_s$ and

$$\chi(Q^2)\equiv\frac{b_0}{4\pi}\ln\mu^2C^2,$$

Q^2 being the representative of the external parameters.

As a simple example, one can consider the photon self-energy function $\Pi(Q^2)$ entering into the e^+e^- annihilation process, in which case Q^2 is the only external momentum, while background fields create masses of the bound-state spectrum. In this case, one can take the form appearing in the lowest approximation of BPT [14], which leads to the substitution

$$\ln\mu^2C^2=\ln\frac{m^2}{\Lambda^2}+\psi\left(\frac{Q^2+M_0^2}{m^2}\right), \tag{34}$$
$$\Lambda^2=\nu^2\exp\left[-\frac{4\pi}{b_0}\alpha_s(\nu^2)\right].$$

[1)]Note that the definition of our coefficients b_i differ from that in [1].

Here, $\psi(x)\equiv\Gamma'(x)/\Gamma(x)$ is the Euler function, which has only simple poles at $x=-n$, $n=0,1,2,\ldots$.

This example clearly shows that $\chi(Q^2)$ is a meromorphic function of Q^2, and we must require that α_s also be a meromorphic function of Q^2, analytic in the Euclidean region $\mathrm{Re}Q^2\geq0$, since the BPT would otherwise violate the analytic properties of amplitudes in the limit $N_c\to\infty$.

In this way, we are lead to the conclusion that $\varphi(z)$ should be a meromorphic function of $z=1/\alpha_s$, since in this case the right-hand side of Eq. (33) is a meromorphic function of Q^2 (meromorphic function of a meromorphic function of some argument is again meromorphic). Thus, one can equalize functions on the two sides of Eq. (33) since they have the same analytic properties.

We do not specify, at this point, the character of possible singularities; the resulting physical amplitude should have only simple poles at bound-state energies, while any finite series of BPT may have poles of higher order and additional poles, as will be seen in the examples given below.

To illustrate the possible forms of $\varphi(z)$, we consider one example of a meromorphic function, namely,

$$\varphi\left(\frac{1}{\alpha_s}\right)=\psi\left(\frac{1}{\alpha_s}+\Delta\right),\quad \Delta=\text{const}. \tag{35}$$

A perturbative expansion of ψ has the form

$$\psi'(z)=\frac{1}{z}+\frac{1}{2z^2}+\frac{1}{6z^3}+\ldots,\quad z\to\infty, \tag{36}$$

or, applying it to (35), one has

$$\psi'\left(\frac{1}{\alpha_s}+\Delta\right)=\frac{\alpha_s}{1+\alpha_s\Delta} \tag{37}$$
$$+\frac{\alpha_s^2}{2(1+\alpha_s\Delta)^2}+\frac{\alpha_s^3}{6(1+\alpha_s\Delta)^3}+\ldots.$$

Therefore, one obtains

$$\left[1-\frac{b_1}{2\pi b_0}\psi'\left(\frac{1}{\alpha_s}+\Delta\right)\right]^{-1} \tag{38}$$
$$=1+\frac{b_1}{2\pi b_0}\alpha_s+\frac{b_1}{2\pi b_0}\alpha_s^2\left[-\Delta+\frac{1}{2}+\frac{b_1}{2\pi b_0}\right]$$
$$+\frac{b_1}{2\pi b_0}\alpha_s^3\Bigg[\Delta^2-\Delta+\frac{1}{6}$$
$$+\left(\frac{b_1}{2\pi b_0}\right)(1-2\Delta)+\left(\frac{b_1}{2\pi b_0}\right)^2\Bigg].$$

From (38), one can find the "theoretical" value of b_2 and b_3, namely,

$$b_2^{(\text{th})}=16\pi b_1\left(\frac{1}{2}-\Delta+\frac{b_1}{2\pi b_0}\right) \tag{39}$$
$$=3173.4-16\pi b_1\Delta,$$

$$b_3^{(\mathrm{th})} = 64\pi^2 b_1[\Delta^2 - \Delta + \frac{1}{3} + \gamma\left(\frac{1}{2} - \Delta\right) + \gamma^2], \quad \gamma = \frac{b_1}{2\pi b_0}.$$

Now, since $\psi(z)$ has poles at $z = 0, -1, -2, \ldots$, $\psi\left(1/\alpha_s + \Delta\right)$ has poles at the following values of α_s

$$\alpha_s = -\frac{1}{\Delta}, -\frac{1}{1+\Delta}, -\frac{1}{2+\Delta}, \ldots. \qquad (40)$$

Correspondingly, $\psi'(z)$ has double poles, and, as a consequence of (30), $\beta(\alpha_s)$ has zeros at the values of α_s given in (40). These zeros condense at $\alpha_s = 0$ from the negative side.

The poles of $\beta(\alpha_s)$ are defined by the zeros of the denominator in (30); i.e., they are given by

$$1 = \frac{b_1}{2\pi b_0}\psi'\left(\frac{1}{\alpha_s} + \Delta\right). \qquad (41)$$

For $\Delta > 0$ and $\alpha_s > 0$, there is one root of (41) at $\alpha_s = \alpha_s^{(\Delta)}$ if $\Delta \le \Delta_0$, where Δ_0 is defined by

$$\psi'(\Delta_0) = \frac{2\pi b_0}{b_1} = 1.355, \quad \Delta_0 = 1.145. \qquad (42)$$

For $\Delta \le \Delta_0$, one obtains one pole of $\beta(\alpha_s)$ given by (41), while, for $\Delta > \Delta_0$, there are no poles of $\beta(\alpha_s)$ for $\alpha_s \ge 0$, and $\beta(\alpha_s)$ is a monotonically decreasing function.

For $\alpha_s < 0$, one has an infinite number of poles of $\beta(\alpha_s)$, which lie between the zeros of $\beta(\alpha_s)$ described by Eq. (40).

We now come to the analytic properties of $\alpha_s(Q^2)$, having in mind parametrization (34) for $\Pi(Q^2)$ in e^+e^- annihilation.

The poles of α_s are to be found from the equation

$$\ln\frac{m^2}{\Lambda^2} + \psi\left(\frac{Q^2 + M_0^2}{m^2}\right) + \frac{2b_1}{b_0^2}\psi\left(\frac{1}{\alpha_s} + \Delta\right) = 0, \qquad (43)$$

and we require that, for $\mathrm{Re}Q^2 \ge 0$, $\alpha_s(Q^2)$ have no poles, which gives the condition

$$\ln\frac{m^2}{\Lambda^2} + \psi\left(\frac{M_0^2}{m^2}\right) + \frac{2b_1}{b_0^2}\min\psi\left(\frac{1}{\alpha_s} + \Delta\right) \ge 0. \qquad (44)$$

Now, $\psi(z) > 0$ for $z > 1.46$, and $m^2 = 4\pi\sigma = 2.5\ \mathrm{GeV}^2$; since M_0^2, as will be seen, corresponds to the difference of double-hybrid mass and hybrid mass, it can lie in the interval $1 \le M_0 \le 1.5$ GeV, and the accurate calculations in [4, 15, 16] strongly prefer $M_0 = 1$ GeV. Hence, one obtains, for the sum of two first terms in (44), the minimum value

$$\ln\frac{m^2}{\Lambda^2} + \psi\left(\frac{M_0^2}{m^2}\right) = 3.32 - \begin{pmatrix} 0.755 \\ 2.5 \end{pmatrix}, \qquad (45)$$

where the upper (lower) figure in parenthesis refers to $M_0 = 1.5$ GeV (1 GeV).

Finally, one can see that, for $\Delta > \Delta_0$, one has $\psi(\Delta) > -0.5$ and the left-hand side of (44) is positive; hence, for all $Q^2 > 0$ as well, the left-hand side of Eq. (43) is always positive. In this way, we have proven that $\alpha_s(Q^2)$ has no poles for all $Q^2 > 0$ if $\Delta > \Delta_0$.

The resulting form of $\alpha_B(Q^2)$ valid in the entire Q^2 plane is now

$$\alpha_B = \frac{4\pi}{b_0}\left[\ln\frac{m^2}{\Lambda^2} + \psi\left(\frac{Q^2 + M_0^2}{m^2}\right) + \frac{2b_1}{b_0^2}\psi\left(\frac{1}{\alpha_B} + \Delta\right)\right]^{-1}, \qquad (46)$$

where $\Delta > \Delta_0 = 1.145$. For $Q^2 < 0$, the function $\alpha_B(Q^2)$ in (46) has zeros and poles that do not necessarily coincide with the poles of $\psi\left(\frac{Q^2 + M_0^2}{m^2}\right)$, i.e., with the unperturbed spectrum $-Q^2 = M_0^2 + nm^2$ computed with $\alpha_s = 0$, i.e., without the influence of valence-gluon excitations.

But this is as it should be, since the amplitude $\Pi(Q^2)$ must have poles at the final positions

$$-Q^2 = (M^{(n)})^2, \quad n = 0, 1, 2, \ldots, \qquad (47)$$

which take into account valence (and Coulomb) gluon effects.

4. SIMPLE MODEL FOR CONSTRUCTING PERTURBATION SERIES

In this section, we shall consider a simple model that is to illustrate the analytic properties of individual terms of BPT and of its infinite sum. Our discussion in this section will be formally similar to the lectures [20] where old-fashioned perturbation theory was used for SPT, except that we use confined states instead of free quarks and gluons. To this end, we define a quantum-mechanical Hamiltonian H_0 that produces bound states (equivalent to an infinite number of mesonic states) and two second-quantized operators $V_1(t)$ and $V_2(t)$ that create additional valence gluons, to be bound together with a quark and an antiquark into a sequence of hybrid states. We define the total Hamiltonian

$$H = H_0 + V_1(t) + V_2(t) \qquad (48)$$

and

$$V_1(t) = e^{i\omega_1 t}v_1 a^+ + \mathrm{h.c.}, \qquad (49)$$

$$V_2(t) = e^{i\omega_2 t}v_2 b^+ a^+ a + \mathrm{h.c.}, \qquad (50)$$

where a, a^+ and b, b^+ are annihilation (creation) operators. We do not specify the d-space dependence of

$v_1(x)$ and $v_2(x)$; t is the common time of the instant form of dynamics. It is clear that V_1 and V_2 are prototypes of the terms $\bar{\psi}\hat{a}\psi$ and $a^2\partial a$ in the QCD Lagrangian; here, to simplify matters, we disregard, in $a_\mu(\mathbf{x})$ or $A_\mu(\mathbf{k})$, the dependence on the polarization μ and the momentum $\mathbf{k}$, but we introduce b and a to distinguish between gluon emission from quarks (in V_1) and from gluons (in V_2).

We assume that H_0 has only a discrete spectrum of mesons (confinement); for the Green's function, we therefore have

$$i\frac{\partial}{\partial t}G_0(t) = H_0(t)G_0(t), \tag{51}$$
$$G_0(t) = \sum_n \varphi_n^{(0)}\varphi_n^{(0)+}e^{-iE_n^{(0)}t},$$

while, for the Fourier transform, one has

$$G_0(E) = \int_0^\infty e^{-iEt}G_0(t)dt = i\sum_n \frac{\varphi_n^{(0)}\varphi_n^{(0)+}}{E - E_n^{(0)}}. \tag{52}$$

For the full Green's function, one can write

$$i\frac{\partial}{\partial t}G(t) = (H_0 + V(t))G(t), \tag{53}$$

$$V(t) = V_1(t) + V_2(t),$$

with the solution

$$G(q_1, q_2; t) \tag{54}$$
$$= \langle q_1|\exp\left[-i\int_0^t (H_0 + V(t'))dt'\right]|q_2\rangle.$$

The perturbative series has the form

$$G(t) = G_0(t) + \int G_0(t - t_1)(-i)V(t_1)G_0(t_1)dt_1$$
$$+ \int\int G_0(t - t_1)(-i)V(t_1)dt_1 \tag{55}$$
$$\times G_0(t_1 - t_2)(-i)V(t_2)G_0(t_2)dt_2 + \ldots.$$

For the energy-dependent Green's function $G(E)$, the perturbative series can be written by taking into account the vacuum state for the operators a and b,

$$a|\mathrm{vac}\rangle = b|\mathrm{vac}\rangle = 0, \tag{56}$$

which yields

$$G(E) = G_0(E) + G_0(E)(-i\tilde{V}_1)G_0(E - \omega_1)(-i\tilde{V}_1)G_0(E) \tag{57}$$
$$+ G_0(E)(-i\tilde{V}_1)G_0(E - \omega_1)(-i\tilde{V}_2)G_0(E - \omega_1 - \omega_2)(-i\tilde{V}_2)G_0(E - \omega_1)(-i\tilde{V}_1)G_0(E)$$
$$+ G_0(E)(-i\tilde{V}_1)G_0(E - \omega_1)(-i\tilde{V}_1)G_0(E)(-i\tilde{V}_1)G_0(E - \omega_1)(-i\tilde{V}_1)G_0(E)$$
$$+ G_0(E)(-i\tilde{V}_1)G_0(E - \omega_1)(-i\tilde{V}_1)G_0(E - 2\omega_1)(-i\tilde{V}_1)G_0(E - \omega_1)(-i\tilde{V}_1)G_0(E) + \ldots.$$

If one introduces the "gluon propagator"

$$K_1(E) = (-i\tilde{V}_1)G_0(E - \omega_1)(-i\tilde{V}_1), \tag{58}$$

then the partial summation of diagrams with gluons emitted by quarks only yields

$$G^{(K_1)}(E) = G_0(E) + G_0(E)K_1(E)G_0(E) + \ldots \tag{59}$$
$$= G_0(E)\frac{1}{1 - K_1G_0}.$$

For the "gluon-b" propagator, we similarly have

$$k_2(E) = (-i\tilde{V}_2)G_0(E - \omega_1 - \omega_2)(-i\tilde{V}_2) \tag{60}$$

and the "full gluon propagator" is given by

$$K_2(E) = K_1(E) + (-i\tilde{V}_1)G_0(E - \omega_1) \tag{61}$$
$$\times [1 + k_2G_0(E - \omega_1) + (k_2G_0(E - \omega_1))^2 + \ldots]$$
$$\times (-i\tilde{V}_1) = (-i\tilde{V}_1)G_0(E - \omega_1)$$
$$\times \frac{1}{1 - k_2G_0(E - \omega_1)}(-i\tilde{V}_1).$$

One should note that $\tilde{V}_i$ are operators and that the denominators in (59) and (61) are formal operator expressions. Now, to analyze the perturbative expansion (57) or its partial sums (59) and (61), one should specify the unperturbed spectrum (52) and define matrix elements of $\tilde{V}_i$ between the unperturbed eigenfunctions $\varphi_n^{(0)}$. For the sake of simplicity, we assume that the spectrum is linear in n,

$$E_n^{(0)} = M_0 + mn, \quad n = 0, 1, \ldots, \tag{62}$$

and, for $V_{nk}^{(i)} \equiv (\varphi_n^{(0)+}\tilde{V}_i\varphi_k^{(0)})$, one can assume that, at large n and k, this matrix element factorizes, $V_{nk}^{(i)} = c_n^{(i)+}c_k^{(i)}$.

As a consequence, one has

$$G^{(K_1)}(E) = \sum_n \frac{\varphi_n c_n^{(1)+}}{E - E_n}\Omega_1(E - \omega_1) \tag{63}$$
$$\times \frac{1}{1 - g(E)\Omega_1(E - \omega_1)}\sum_n{}' \frac{c_{n'}^{(1)}\varphi_{n'}^+}{E - E_{n'}},$$

where we have defined

$$\Omega_1(E-\omega_1) \equiv -\sum_k \frac{|c_k^{(1)}|^2}{E-E_k-\omega_1}, \qquad (64)$$

$$g(E) \equiv \sum_n \frac{|c_n^{(1)}|^2}{E-E_n}. \qquad (65)$$

It is clear that $\Omega_1(E-\omega_1)$ has poles at the "gluon-excited," i.e., "hybrid-state," masses $E = E_k + \omega_1$; however, the partial sum $G^{(K_1)}(E)$ has shifted poles owing to the vanishing of the denominator in (63), in addition to unperturbed poles at E_n.

A similar situation occurs for $K_2(E)$. If one defines

$$\Omega_2(E-\omega_1) = \sum_k \frac{|c_k^{(2)}|^2}{E-E_k-\omega_1}, \qquad (66)$$

$$\Pi_2(E-\omega_1-\omega_2) = -\sum_k \frac{|c_k^{(2)}|^2}{E-E_k-\omega_1-\omega_2}, \qquad (67)$$

then one can rewrite (61) as

$$K_2(E) = \frac{(-i\tilde{V}_1)|\varphi_n\rangle}{E-E_n-\omega_1} \qquad (68)$$
$$\times\left\{\delta_{mn} + c_n^{(2)+}\frac{\Pi_2(E-\omega_1-\omega_2)c_m^{(2)}}{1-\Omega_2(E-\omega_1)\Pi_2(E-\omega_1-\omega_2)}\right\}$$
$$\times \frac{\langle\varphi_m|(-i\tilde{V}_1)}{E-E_m-\omega_1}.$$

This exercise was undertaken to illustrate that the "full gluon propagator" $K_2(E)$ has, in addition to unperturbed "one-gluon poles" $1/(E-E_n-\omega_1)$, also shifted "two-gluon poles" due to the vanishing of the denominator in (68), but not "two-gluon poles" themselves.

To make our model more realistic and finally to incorporate in it QCD features, one should make several steps. First, one must take into account negative-energy states corresponding to the background in time motion; i.e., as in the Feynman propagator, we replace (cf. [20])

$$\frac{1}{E-E_n} \to \frac{1}{E^2-E_n^2} \to \frac{1}{s-(M_n^{(0)})^2}. \qquad (69)$$

Correspondingly, the hybrid propagators take the form

$$\frac{1}{E-\omega_1-E_n} \to \frac{1}{s-(M_n^{(1)})^2}, \qquad (70)$$
$$\frac{1}{E-\omega_1-\omega_2-E_n} \to \frac{1}{s-(M_n^{(2)})^2},$$

where $M_n^{(1)}$ and $M_n^{(2)}$ are hybrid masses with one and two gluons, respectively.

Now, one must take into account the structure of the operators $\tilde{V}_1$ and $\tilde{V}_2$ in QCD. Both describe the emission of one gluon from the quark and the gluon line, respectively, and both are local field operators, whereas the wave functions refer to the nonlocal instantaneous bound-state objects, namely, mesons ($q\bar{q}$), one-gluon hybrids ($q\bar{q}g$), and two-gluon hybrids ($q\bar{q}gg$). We denote by $\varphi_n^{(0)}(\mathbf{x})$, $\varphi_{n,\nu_1}^{(1)}(\mathbf{x},\mathbf{y})$, and $\varphi_{n,\nu_1\nu_2}^{(2)}(\mathbf{x},\mathbf{y},\mathbf{z})$ the full set of the corresponding eigenfunctions. Note that the string pieces between quarks and gluons formed by background field are straight lines given by vectors $\mathbf{x}$ and $\mathbf{y}$ in $\varphi_n^{(1)}$ and by $\mathbf{x},\mathbf{y}$, and $\mathbf{z}$ in $\varphi_n^{(2)}$, and they contribute to the rotational and vibrational eigenenergies. We also note that the string vibration in this background picture is described by the full set of one-gluon, two-gluon, and multigluon hybrid states.

Here, we have introduced, in hybrid eigenfunctions, additional lower indices ν_1 and ν_1,ν_2 to describe the quantum numbers of additional bound gluons. Note that ν_i are multidimensional vectors with integer components. Correspondingly, the hybrid masses depend on the same quantum numbers:

$$M_n^{(0)} = M^{(0)}(n_r, L; J^{PC}), \qquad (71)$$

$$M_n^{(1)} = M^{(1)}(n_r, L; n_r', L'; J^{PC}), \qquad (72)$$

$$M_n^{(2)} = M^{(2)}(n_r, L; n_r', L'; n_r'', L''; J^{PC}). \qquad (73)$$

Here, n_r and L refer to the radial quantum number and angular momentum of quark with respect to antiquark, and each additional gluon has its own n_r and L with respect to the neighboring quark or gluon. We have not yet taken into account spin degrees of freedom of q, $\bar{q}$, and gluons, which create the fine and the hyperfine structure of levels, and we shall neglect those, since we are interested in the dominant contributions to the masses at large excitations, and our final goal is to obtain the result of summation over all excitations in $G(E)$ and to establish some relation between SPT and BPT, which requires analyzing highly excited states in the sums.

Now, the local character of the operators $\tilde{V}_1$ and $\hat{V}_2$ mentioned above leads to the following properties of matrix elements (since $\tilde{V}_i$ acts only on one of the end points of vectors $\mathbf{x}$ and $\mathbf{y}$, it does not affect the quantum wave function, unless $\tilde{V}_i$ contains derivative with respect to the coordinates as in $\tilde{V}_2$, and, in this case, it changes quantum numbers by a discrete number):

$$\langle n_r, L|\tilde{V}^{(1)}|\bar{n}_r, \bar{L}; n_r', L'\rangle \sim \delta_{n_r\bar{n}_r}\delta_{L\bar{L}},$$

$$\langle n_r, L; n_r', L'|\tilde{V}^{(2)}|\bar{n}_r, \bar{L}; \bar{n}_r', \bar{L}'; n_r'', L''\rangle \sim \delta_{n_r\bar{n}_r}\delta_{L\bar{L}}\delta_{\bar{n}_r'n_r'}\delta_{\bar{L}'L'}. \quad (74)$$

Moreover, we assume that $(M_n^{(i)})^2$ depends on all quantum numbers linearly,

$$(M_n^{(i)})^2 = m^2\left(a\sum_i n_r^{(i)} + b\sum L^{(i)}\right). \quad (75)$$

Let us now apply these rules to the computation of the "full gluon propagator" $K_2(E)$ and try to find a correspondence with the standard perturbative calculations.

To this end, we assume that the sum entering into $K_1(E)$ is convergent; i.e.,

$$\langle n|K_1(E)|m\rangle = \sum_{\bar{n},\nu}\frac{\langle n|-i\tilde{V}_1|\bar{n},\nu\rangle\langle\bar{n},\nu|-i\tilde{V}_1|m\rangle}{Q^2+M^2(\bar{n},\nu)} \sim \frac{1}{Q^2}, \quad (76)$$

where we have denoted $\bar{n}(\nu) = n_r, L(n_r', L')$ and have made the substitution $s \to -Q^2$.

The same type of expression for $k_2(E)$ yields

$$\langle n,\nu|k_2(E)|\tilde{n},\tilde{\nu}\rangle = \sum_{\bar{n},\bar{\nu},\nu'}\frac{\langle n,\nu|-i\tilde{V}_2|\bar{n},\bar{\nu},\nu'\rangle\langle\bar{n},\bar{\nu},\nu'|-i\tilde{V}_2|\tilde{n},\tilde{\nu}\rangle}{Q^2+M^2(\bar{n},\bar{\nu},\nu')}. \quad (77)$$

Due to the properties in (75), the sum in (77) is actually a double sum in, say, L' and n_r', while M^2 depends on them linearly, and we assume, at this point, that the coefficients in (77) do not depend on ν'. Therefore, one must regularize this expression, making one subtraction at $s = 0$, and renormalize the retaining logarithmic divergence. This is in full correspondence with the standard perturbative calculation of a one-gluon loop correction to gluon propagator. As a result, $k_2(E)$ takes the form

$$\langle n,\nu|k_2(E)|\tilde{n},\tilde{\nu}\rangle \sim Q^2\ln\left(\frac{Q^2-M^2(n,\nu)-\delta M^2}{\mu^2}\right)\delta_{n\tilde{n}}\delta_{\nu\tilde{\nu}}, \quad (78)$$

where

$$\delta M^2 = M^2_{\min}(n,\nu,\nu') - M^2(n,\nu) \quad (79)$$

and minimization is performed with respect to ν'.

Now, one can consider $K_2(E)$; extracting coupling constant g_0 from $\tilde{V}_1$ and $\tilde{V}_2$, one has the series (at large s)

$$K_2(s) \sim \frac{g_0^2}{Q^2} - C\frac{g_0^4}{Q^2}\ln\frac{Q^2+\bar{M}^2}{\mu^2} + \ldots \sim \frac{g_0^2}{Q^2}\left(1+g_0^2C\ln\frac{Q^2+\bar{M}^2}{\mu^2}\right)^{-1}. \quad (80)$$

Expression (80) is similar for the running coupling constant, but with the mass $\bar{M}^2$ corresponding to the freezing coupling constant derived in [12] and studied later in [13, 14]. We note that the logarithms in (80) appear as the result of summation over the stringlike spectrum (75) with the coefficients asymptotically constant, which is the property of the matrix elements of eigenfunctions of linear interaction [14]. Therefore, this property and the correspondence found above can be valid only in the asymptotic region, while, at finite s, there are corrections that should be taken into account. In the next section, we inspect this problem more carefully.

5. NONASYMPTOTIC TERMS IN THE SPECTRAL SUMS

We start with the definition of the photon vacuum polarization function $\Pi(q^2)$ and, after a short review of asymptotic correspondence between the spectral sum and perturbative expansion, inspect more carefully correction terms and a comparison between OPE and spectral sum.

We define the photon vacuum polarization function $\Pi(q^2)$ as a correlation function for electromagnetic currents for the process $e^+e^- \to$ hadrons in a usual way:

$$-i\int d^4x e^{iqx}\langle 0|T(j_\mu(x)j_\nu(0))|0\rangle = (q_\mu q_\nu - g_{\mu\nu}q^2)\Pi(q^2). \quad (81)$$

Here, the imaginary part of Π is related to the total hadronic ratio R as

$$R(q^2) = \frac{\sigma(e^+e^- \to \text{hadrons})}{\sigma(e^+e^- \to \mu^+\mu^-)} = 12\pi\,\mathrm{Im}\Pi\left(\frac{q^2}{\mu^2}, \alpha_s(\mu)\right). \quad (82)$$

There are two standard approaches to calculating $\Pi(q^2)$. The first one employs a purely perturbative expansion, which is now known to $O(\alpha_s^3)$ [21]. The second one is the OPE approach [6], which includes the NP contributions in the form of local condensates. For two light quarks of equal masses ($m_u = m_d = m$), it yields

$$\Pi(Q^2) = -\frac{1}{4\pi^2}\left(1+\frac{\alpha_s}{\pi}\right)\ln\frac{Q^2}{\mu^2} + \frac{6m^2}{Q^2} + \frac{2m\langle q\bar{q}\rangle}{Q^4} + \frac{\alpha_s\langle FF\rangle}{12\pi Q^4} + \ldots. \quad (83)$$

To make explicit this renormalization of α_B, one can write the perturbative expansion of the function $\Pi(Q^2)$ (83) as

$$\Pi(Q^2) = \Pi^{(0)}(Q^2) \quad (84)$$

$$+\alpha_B\Pi^{(1)}(Q^2)+\alpha_B^2\Pi^{(2)}(Q^2)+\ldots.$$

We now again use the large-N_c approximation, in which case $\Pi^{(0)}$ contains only simple poles in Q^2 [5, 14],

$$\Pi^{(0)}(Q^2)=\frac{1}{12\pi^2}\sum_{n=0}^{\infty}\frac{C_n}{Q^2+M_n^2}, \qquad (85)$$

and the mass M_n is an eigenvalue of the Hamiltonian $H^{(0)}$, which contains only quarks and background field B_μ,

$$H^{(0)}\Psi_n=M_n\Psi_n. \qquad (86)$$

In what follows, we are mostly interested in the long-distance effective Hamiltonian which is obtained from $G_{q\bar{q}}$ for large distances, $r\gg T_g$, where T_g is the gluonic correlation length of the vacuum, $T_g\approx 0.2$ fm [19],

$$G_{q\bar{q}}(x,0)=\int DB\eta(B) \qquad (87)$$

$$\times\,\mathrm{tr}(\gamma_\mu G_q(x,0)\gamma_\mu G_q(0,x))=\langle x|e^{-H^{(0)}|x|}|0\rangle.$$

At these distances, one can neglect in G_q the quark spin insertions $\sigma_{\mu\nu}F_{\mu\nu}$ and use the area law

$$\langle W_C\rangle\to\exp(-\sigma S_{\min}), \qquad (88)$$

where $S_{\min}$ is the minimal area inside the loop C.

The Hamiltonian in (87) is then readily obtained by the method of [22]. In the c.m. frame, at the orbital angular momentum of $l=0$, it has the familiar form

$$H^{(0)}=2\sqrt{\mathbf{p}^2+m^2}+\sigma r+\mathrm{const}, \qquad (89)$$

where the constant appears owing to the self-energy parts of quarks [23], while, for $l=2$, a small correction from the rotating string appears [22], which is neglected here for a first approximation.

We can now use the results of the semiclassical analysis of $H^{(0)}$ [24], where the values of M_n and C_n have been already found.

These results can be represented as ($n=n_r+l/2$, $n_r=0,1,2,\ldots$, and $l=0,2$)

$$M_n^2=2\pi\sigma(2n_r+l)+M_0^2, \qquad (90)$$

where M_0^2 is a weak function of the quantum numbers n_r and l comprising the constant term of (89); in what follows, we shall set it to the ρ-meson mass: $M_0^2\simeq m_\rho^2$ (see [23] for more discussion).

For C_n, one semiclassically obtains [24]

$$C_n(l=0)=\frac{2}{3}e_q^2N_cm^2,\quad m^2\equiv 4\pi\sigma, \qquad (91)$$

$$C_n(l=2)=\frac{1}{3}e_q^2N_cm^2.$$

Using the asymptotic expressions (90) and (91) for M_n and C_n and starting with $n=n_0$, one can write

$$\Pi^{(0)}(Q^2)=+\frac{1}{12\pi^2}\sum_{n=0}^{n_0-1}\frac{C_n}{Q^2+M_n^2} \qquad (92)$$

$$-\frac{e_q^2N_c}{12\pi^2}\psi\left(\frac{Q^2+M_0^2+n_0m^2}{m^2}\right)$$

$$+\,\text{divergent constant},$$

where we have used the equality

$$\sum_{n=n_0}^{\infty}\frac{1}{Q^2+M_n^2} \qquad (93)$$

$$=-\frac{1}{m^2}\psi\left(\frac{Q^2+M_0^2+n_0m^2}{m^2}\right)$$

$$+\,\text{divergent constant}$$

and $\psi(z)=\Gamma'(z)/\Gamma(z)$.

In (92), we have separated the first n_0 terms to treat them nonsemiclassically, while keeping, for other states with $n\geq n_0$, the semiclassical expressions (90) and (91). In what follows, however, we shall set $n_0=1$ for the sake of simplicity. It was shown in [14] that, even in this case, our results reproduce e^+e^- experimental data to a high precision.

Let us now consider the asymptotic behavior of $\Pi^{(0)}(Q^2)$ at large Q^2. Using the asymptotic expression for $\psi(z)$,

$$\psi(z)_{z\to\infty}=\ln z-\frac{1}{2z}-\sum_{k=1}^{\infty}\frac{B_{2k}}{2kz^{2k}}, \qquad (94)$$

where B_n are Bernoulli numbers, one finds from (92) that

$$\Pi^{(0)}(Q^2)=-\frac{e_q^2N_c}{12\pi^2}\ln\frac{Q^2+m^2}{\mu^2}+O\left(\frac{m^2}{Q^2}\right). \qquad (95)$$

One can easily see that, at $Q^2\gg M_0^2$, this term coincides with the first term in the OPE (83), the logarithmic one. Taking the imaginary part of (95) for $Q^2\to -s$, one obtains

$$R(q^2)=12\pi\mathrm{Im}\,\Pi^{(0)}(-s)=N_ce_q^2; \qquad (96)$$

i.e., this means that we have got from $\Pi^{(0)}$ the same result as for free quarks. This fact is an explicit manifestation of quark–hadron duality.

We can now identify $\Pi^{(0)}(Q^2)$ as

$$\Pi^{(0)}(Q^2)=-\frac{e_q^2N_c}{12\pi^2}\psi\left(\frac{Q^2+M_0^2}{m^2}\right) \qquad (97)$$

and compare this expression with the OPE series (83).

To this end, one can use the asymptotic expansion for $\psi(z)$,

$$\psi(z)_{z\to\infty} = \ln z - \frac{1}{2z} - \sum_{k=1}^{\infty} \frac{B_{2k}}{2kz^{2k}} \qquad (98)$$
$$= \ln z - \frac{1}{2z} - \frac{1}{12z^2} + \frac{1}{120z^4} - \frac{1}{252z^6} + \ldots,$$

and the expansion

$$\psi(z) = -C - \sum_{k=0}^{\infty} \left(\frac{1}{z+k} - \frac{1}{k+1} \right), \qquad (99)$$
$$C = 0.577.$$

Two features are immediately seen when comparing expansion (98) with the OPE (83) (see also discussion in [13, 14]):

(i) At $m = 0$, the term $O(1/Q^2)$ is absent, since one cannot construct a local gauge-invariant operator having dimensions of mass squared. One should stress that this type of operator may appear from the interference of perturbative and nonperturbative contributions [25] and is welcome on phenomenological grounds [26]. However, in the framework of BPT accepted in this paper, the term $\Pi^{(0)}(Q^2)$ is solely due to NP contributions and cannot have OPE terms $O(1/Q^2)$.

(ii) The generic terms in $\Pi^{(0)}(Q^2)$ from expansion (97) have the magnitude m^{2n}/Q^{2n}, while the corresponding OPE terms are much smaller; e.g., one should compare $-(\pi/3)\left(\alpha_s\langle FF\rangle/Q^4\right) \approx -0.04\,\mathrm{GeV}^4/Q^4$ (OPE) with $-m^4/12Q^4 \approx -0.5\,\mathrm{GeV}^4/Q^4$ [spectral decomposition (97)].

In the remaining part of this section, we shall discuss the possible solutions to problems (i) and (ii).

Concerning item (i), one should say that (97) is an approximate expression for $\Pi^{(0)}$ valid for large Q^2, i.e., reproducing correctly the logarithmic term in (95). However, if one is interested in the next asymptotic terms, one should take into account corrections to C_n and M_n in (92).

The first major correction comes from the fact that we have considered in (93) that levels with $n_r + 1, l = 0$ and $n_r, l = 2$ are degenerate (in the lowest approximation where one neglects the spin-dependent force) and have therefore used the sum of the coefficients in (91) for C_n in (92). However, this is not true for the ρ meson, where the coefficient with $l = 0$ yields 2/3 of C_n. Therefore, one should use, instead of $\psi(z)$ in (93) and (97), the corrected expression

$$\psi(z) \to \tilde{\psi}(z) \equiv \psi(z) + \frac{1-\gamma}{z}, \qquad (100)$$

where $(1-\gamma)/z$ cancels the corresponding pole (with $k = 0$) in (99) and replaces it with the correct coefficient $\gamma = \gamma_0 = 2/3$.

Moreover, in the analysis performed in [14], it was realized that the value of $\gamma_0 = 2/3$ (which does not take into account the radiative correction to the ρ width) yields some 10% discrepancy in the leptonic width of ρ meson. Now, the destiny of the $1/q^2$ term in the asymptotic expansion (98) depends on the exact value of γ. Indeed, using (98), one obtains the expansion

$$\tilde{\psi}(z) = \ln z + \frac{1}{z}\left(1 - \gamma - \frac{1}{2}\right) + O\left(\frac{1}{z^2}\right), \quad (101)$$

where $z = (Q^2 + M_0^2)/m^2 \to Q^2/m^2$.

One can see that the requirement that $O(1/Q^2)$ terms be absent implies the following condition for γ:

$$\gamma = \frac{2}{3}\kappa_{\mathrm{rad}} = \frac{1}{2}. \qquad (102)$$

Here, $\kappa_{\mathrm{rad}} = 1 - \Delta\kappa$, with $\Delta\kappa$ being the radiative correction due to gluon exchanges in the leptonic width of ρ meson. It is clear that the condition is in the correct ballpark, and one should take into account other possible corrections, to be discussed below.

Until now, we have considered the lowest approximation for M_n^2 and C_n, Eqs. (90) and (91), where M_n^2 is linear in n and C_n is n-independent. However, there are corrections to this semiclassical behavior [27], yielding

$$M_n^2 = 4\pi\sigma n + M_0^2 + b/n, \qquad (103)$$
$$C_n = C_n^{(0)}\,(1 + a/n)\,,$$

where $C_n^{(0)}$ is given in (91). To see the effect of these corrections, we first set $b = 0$ and consider the sum [cf. Eq. (93)], which can be expressed in terms of $\psi(z)$ again:

$$\sum_{n=n_0=1}^{\infty} \frac{1 + a/n}{Q^2 + M_0^2 + m^2} \qquad (104)$$
$$= -\left\{ \frac{1}{m^2}\left(1 - \frac{am^2}{Q^2 + M_0^2}\right) \right.$$
$$\left. \times\ \psi\left(\frac{Q^2 + M_0^2 + m^2}{m^2}\right) - C\frac{a}{Q^2 + M_0^2} \right\},$$
$$C = 0.577.$$

Thus, we see that the correction a/n yields a power-law correction $am^2/(Q^2 + M_0^2)$, which modifies the asymptotic expansion of $\psi(z)$ (98) and can occasionally diminish some terms to bring them closer in agreement with those in the OPE (83). The same is true for the mass correction b/n in (103) as well, which yields the power-law correction $bm^2/(Q^2 + M_0^2)^2$ as a factor in an expression like

(104). However, since the coefficients in (98) decrease fast, the overall cancellation in all terms seems to be improbable; therefore, problem (ii) remains unsolved.

6. ANALYTIC PROPERTIES OF $\alpha_B(s)$

In this section, we shall discuss the analytic structure of BPT in the limit $N_c \to \infty$ in the entire complex plane of $-s = Q^2$ and establish connection between our results and SPT. In what follows, the basic role will be played by the function $\Pi(Q^2)$, and we shall use this example as a typical one, generalizing it to other amplitudes at the end of this section.

Our starting point is the BPT for $\Pi(Q^2)$, Eq. (84). The analytic properties of $\Pi^{(0)}(Q^2)$ are given in Eq. (85), which shows a sequence of purely nonperturbative poles,

$$s = -Q^2 = (M_n^{(0)})^2, \quad n = 0, 1, 2, \ldots. \tag{105}$$

The inclusion of α_B to all orders leads to the following changes in the unperturbed spectrum (105). Gluon exchanges play two different roles: (a) instantaneous Coulomb interaction shifts NP poles, and (b) gluons a_μ propagating in the confining film form hybrid states. Correspondingly, the NP poles, are mixed and shifted by the hybrid states. Therefore, one has the following hierarchy of the shifts of the original NP-meson masses:

$$M_n^{(0)} \to M_n^{(0)}(O(\alpha_B^k)) \equiv M_n^{(0)}(k). \tag{106}$$

The one-gluon hybrid state (apart from the Coulomb shift, which we disregard for the sake of simplicity at this moment) with mass $M_n^{(1)}$ is also shifted because of mixing with a meson and higher hybrid states, the mixing being characterized by the power of α_B; therefore, one has

$$M_n^{(1)}(O(\alpha_B^k)) \equiv M_n^{(1)}(k). \tag{107}$$

In a similar way, one has shifted states $M_n^{(m)}(k)$ for m-hybrid configurations (with m gluons).

As is clear from the schematic example of Section 4, the $O(g_0^2)$ terms [the second term on the right-hand side of (57)] refer to one-gluon hybrid states and do not contain any analytic structure of $\alpha_B(Q^2)$, since they are not yet renormalized (and of course not yet RG-improved, i.e., resummed).

This renormalization process, leading to the nontrivial dependence of $\alpha_B(Q^2)$, starts with the $O(g_0^4)$ diagrams in SPT [and the $O(\tilde{V}_1^2\tilde{V}_2^2)$ ones in the example of Section 4—see the third term on the right-hand side of (57)].

This term and its QCD analog have singularities of the double hybrid [the term $G_0(E-\omega_1-\omega_2)$ in (57)] corresponding to the gluon-loop diagram and accompanying the $O(g_0^4)$ diagrams in SPT.

Next, one can do a RG improvement of this $O(g_0^4)$ result, which leads to the resummation presented in $K_2(E)$, Eq. (68). In this approximation, one can write

$$\alpha_B = \frac{4\pi}{b_0}\left[\ln\frac{m^2}{\Lambda^2} + \tilde{\psi}(Q^2)\right]^{-1}, \tag{108}$$

where $\tilde{\psi}(Q^2)$ is a meromorphic function with poles at the double-hybrid position, i.e., at

$$s = M_n^2(k=0). \tag{109}$$

In the particular case where $\tilde{\psi}(Q^2) = \psi\left(\dfrac{Q^2+M_0^2}{m^2}\right)$ and $M_0 \equiv M_0^{(2)}(k=0)$, the form (108) coincides with that suggested in [14].

In the large-Q^2 limit, one has

$$\tilde{\psi}(Q^2) \to \ln\frac{Q^2+M_0^2}{m^2}, \tag{110}$$

and α_B has the same freezing form, which was extensively used before in [12–16]:

$$\bar{\alpha}_B = \frac{4\pi}{b_0}\left(\ln\frac{Q^2+M_0^2}{\Lambda^2}\right)^{-1}. \tag{111}$$

We now can compare the form (108) with our model solution (46). Indeed, when $(Q^2+M_0^2)/m^2$ is large, one can retain, in the denominator of (46), the first two terms, and one has the form coinciding with (108). In the next approximation, one can retain, in (108), the term

$$\frac{2b_1}{b_0^2}\psi\left(\frac{1}{\alpha_B}+\Delta\right),$$

which yields the next-order approximation, where $M_n^{(2)}(0)$ is shifted to the higher order position $M_n^{(2)}(2)$ and so on.

Thus, one can see that, while the $O(g_0^4)$ term contains double hybrid poles, the RG improvement leads to shifted poles, which do not correspond to the final physical poles, the latter being the result of infinite resummation to all orders.

Let us now discuss the imaginary part of $\Pi(Q^2)$. It is clear that $\Pi^{(0)}(Q^2)$ contains NP poles. The term $O(g_0^2)$ [equivalent to the second term on the right-hand side of (57)] contains double NP poles from $(G_0(E))^2$ and one-gluon hybrid poles from $G_0(E-\omega_1)$. The $O(g_0^4)$ term contains double NP poles, double one-gluon hybrid poles, and two-gluon hybrid poles—the latter are associated with α_B in the lowest order. The same type of classification goes on for higher terms. The outcome for the expansion in (84) is that, in the term $\alpha_B^k\Pi^{(k)}(Q^2)$, part of the

singularities are associated with α_B^k and another part with $\Pi^{(k)}(Q^2)$.

Thus, we see that the requirements of (i) logarithmic behavior of $\tilde{\psi}(Q^2)$ at large Q^2 and (ii) meromorphic analytic properties in the entire Q^2 plane lead to one possible representation of $\tilde{\psi}(Q^2)$,

$$\tilde{\psi}(Q^2) = \psi\left(\frac{Q^2+M_0^2}{m^2}\right) + \sum_{k=0}^{N} \frac{a_k}{Q^2+m_k^2}, \quad (112)$$

where N is finite, so that the logarithmic asymptotic expression for $\psi(z)$ is not modified.

Let us now compare our Eq. (31) with the SPT, more explicitly with Gell-Mann–Low equation written in the form adopted by Radyushkin [9]:

$$L = \ln\frac{Q^2}{\Lambda^2} = \frac{4\pi}{b_0\alpha_s} + \frac{2b_1}{b_0^2}\ln\frac{\alpha_s}{4\pi} \quad (113)$$
$$+ \tilde{\Delta} + \frac{b_2 b_0 - 8b_1^2}{2b_0^3}\frac{\alpha_s}{4\pi} + O\left(\left(\frac{\alpha_s}{4\pi}\right)^2\right).$$

Here, $\tilde{\Delta}$ is a parameter of integration that fixed the definition of Λ. This should be compared with our Eq. (31) which we can write in a similar form

$$\ln\frac{m^2}{\Lambda^2} + \psi\left(\frac{Q^2+M_0^2}{m^2}\right) = \frac{4\pi}{b_0\alpha_s} - \frac{2b_1}{b_0^2}\varphi\left(\frac{1}{\alpha_s}\right). \quad (114)$$

It is clear that our analysis with expansion (32) is equivalent to the analysis of (113) for large Q^2 and small α_s. As we have found in (39), the predicted values of $b_2^{(\mathrm{th})}$ and $b_3^{(\mathrm{th})}$ depend on Δ; keeping the choice

$$\varphi\left(\frac{1}{\alpha_s}\right) = \psi\left(\frac{1}{\alpha_s}+\Delta\right),$$

one finds from (39) for $\Delta \geq \Delta_0 = 1.145$ that

$$b_2^{(\mathrm{th})} < 238.15, \quad b_3^{(\mathrm{th})} \geq 18266. \quad (115)$$

To repair the values obtained and to get agreement with $\overline{MS}$-calculated values [21], one can use the modified $\psi(z)$ function like that in (112), namely,

$$\varphi\left(\frac{1}{\alpha_s}\right) = \psi\left(\frac{1}{\alpha_s}+\Delta\right) \quad (116)$$
$$+ \sum_{k=0}^{N} \tilde{A}_k \frac{\alpha_s}{1+\alpha_s(\Delta+k)}.$$

It is important that the positions of poles of $\psi(k)$ do not change—the only change is in the coefficients of those pole terms that can modify expansion (37), yielding agreement with the $\overline{MS}$ coefficients in expansion (27).

We now consider the problem of an analytic continuation of $\alpha_s(Q^2)$ and $\alpha_B(Q^2)$ from the Euclidean region $Q^2 \geq 0$ to the timelike region $Q^2 < 0$.

One can see that the freezing form $\overline{\alpha}_B$ (110) is well defined for $Q^2 \geq -M_0^2$ and has a logarithmic branch point at $Q^2 = -M_0^2$.

However, this is an artifact of representation (112), which is valid in the asymptotic region where $(Q^2 + M_0^2)/\Lambda^2 \gg 1$; otherwise, one should use the original form (108).

Choosing it in the form

$$\alpha_B = \frac{4\pi}{b_0}\left[\ln\frac{m^2}{\Lambda^2} + \psi\left(\frac{Q^2+M_0^2}{m^2}\right)\right]^{-1}, \quad (117)$$

one can see that $\alpha_B(Q^2)$ is defined in the entire complex plane Q^2 and has only isolated poles there at the zeros of the denominator in (117). These poles result from the partial resummation of two-gluon hybrid poles that are present in $\psi\left(\frac{Q^2+M_0^2}{m^2}\right)$ and which occur at $s \equiv -Q^2 = M_0^2 + nm^2$, $n = 0, 1, 2, \ldots$. We note that this resummation is the standard RG improvement of perturbative series, where large logarithms are summed up in a geometric series (or are a result of solving RG equations). The crucial point is that the most important physical thresholds are contained in $\Pi^{(0)}(Q^2)$ and have nothing to do with singularities of $\alpha_B(Q^2)$ [or of $\alpha_s(Q^2)$].

In a similar way, the singularities that appear from the asymptotic solution of (46) for small α_B, namely, term $\ln\alpha_B(Q^2)$, do not produce additional logarithmic cuts and result from the asymptotic expansion of Eq. (46), where only the meromorphic function $\alpha_B(s)$ is obtained in the exact solution.

Thus, as we discussed above, Eq. (46) or its generalized form

$$\alpha_B = \frac{4\pi}{b_0}\left[\ln\frac{m^2}{\Lambda^2} + \tilde{\psi}(Q^2) + \varphi\left(\frac{1}{\alpha_B}\right)\right]^{-1}, \quad (118)$$

where $\tilde{\psi}(Q^2)$ is given in (112) and $\varphi(1/\alpha_B)$ is given in (116), produces $\alpha_B(Q^2)$, which is a meromorphic function of Q^2 in the entire complex plane of Q^2.

Let us now examine more carefully the creation of the imaginary part of $\Pi(Q^2)$, which leads to the positive hadronic ratio $R(s)$. We start with $\Pi^{(0)}(Q^2)$ [(85) and (83)]; $\Pi^{(0)}$ in SPT and BPT coincide asymptotically, namely,

$$\Pi^{(0)}(\mathrm{SPT}) = -\frac{e_q^2 N_c}{12\pi^2}\ln\frac{Q^2}{\mu^2}, \quad (119)$$
$$\Pi^{(0)}(\mathrm{BPT}) = -\frac{e_q^2 N_c}{12\pi^2}\ln\frac{Q^2+M_0^2}{\mu^2}.$$

Defining $s = -Q^2$ and $\arg(M_0^2 - s) = 0$ for $s < M_0^2$, one has [if one disregards the fact that (119) is true only for $Q^2 \to +\infty$]

$$\operatorname{Im}\Pi^{(0)}((\mathrm{BPT}) \tag{120}$$
$$= \frac{\Pi^{(0)}(s+i\varepsilon) - \Pi^{(0)}(s-i\varepsilon)}{2i} = \frac{e_q^2 N_c}{12\pi}\Theta(s - M_0^2),$$

and, for SPT, one has, on the right-hand side, $\Theta(s)$ instead of $\Theta(s - M_0^2)$.

Note, however, that expression (119) for $\Pi^{(0)}(\mathrm{BPT})$ is the asymptotic form at large positive Q^2 and, in getting the result in (120), the analytic continuation of the logarithmic asymptotic expression was performed unlawfully, strictly speaking.

To perform calculations in BPT more rigorously, one should use (85) in the region $s > M_0^2$, and one gets

$$\operatorname{Im}\Pi^{(0)}(s+i\varepsilon) = -\frac{e_q^2 N_c}{12\pi^2}\operatorname{Im}\psi\left(\frac{-s+M_0^2}{m^2}\right) \tag{121}$$
$$= +\frac{e_q^2 N_c}{12\pi^2}\operatorname{Im}\sum_{k=0}^{\infty}\frac{m^2}{M_0^2 - s + km^2}$$
$$= \frac{e_q^2 N_c}{12\pi} m^2 \sum_{k=0}^{\infty}\delta(M_0^2 - s + km^2).$$

One can introduce the average of $\operatorname{Im}\Pi^{(0)} = (s+i\varepsilon)$ over some energy interval (this is the "duality interval" discussed, e.g., in [7]) comprising N poles:

$$\langle \operatorname{Im}\Pi^{(0)}(s_0+i\varepsilon)\rangle_N \tag{122}$$
$$= \int_{s_0}^{s_0+Nm^2}\frac{ds\,\operatorname{Im}\Pi^{(0)}(s+i\varepsilon)}{Nm^2} = \frac{e_q^2 N_c}{12\pi}.$$

One can see that (122) coincides with (120), thus justifying the procedure of direct analytic continuation of the logarithms in (119), where the averaging over the duality interval is performed.

One can also see that the standard SPT expression (119) yields the correct answer for the same reason: the imaginary part of the asymptotic expression (both of SPT and BPT) coincides with the correct averaged imaginary part. We note that, for SPT, this check is impossible, since the correct procedure is not available.

We now address the more delicate point of the analytic continuation of $\alpha(s)$. In BPT, as was discussed above, $\alpha_B(s)$ is given by (118) or, in the "one-loop approximation," by (117) and is a meromorphic function; hence, its analytic continuation is a direct and unique procedure. For example, separating one pole in $\psi\left(\dfrac{Q^2+M_0^2}{m^2}\right)$, $M_n^2 = M_0^2 + nm^2$, one finds, for α_B (117), in its vicinity that

$$\alpha_B(s \simeq M_n^2 + i\varepsilon) = \frac{4\pi}{b_0\psi'(z_0)(z - z_0)}, \tag{123}$$

where z_0 is to be found from the equation $\ln(m^2/\Lambda^2) + \psi(z_0) = 0$, and $z = (M_0^2 - s)/m^2$. Using the relations from the Appendix, one gets

$$\operatorname{Im}\alpha_B(s \simeq M_n^2 + i\varepsilon) \tag{124}$$
$$= \frac{4\pi^2}{b_0}\frac{m^2\delta(M_n^2 - s - \delta_0 m^2)}{\left[\delta_0^{-2}(n) + S_2(n) + \zeta(2)\right]},$$

where δ_0 and $S_k(n)$ are defined in the Appendix,

$$\delta_0^{-1}(n) = \ln\frac{m^2}{\Lambda^2} - C + S_1(n).$$

We now compare this exact procedure with the suggested one using the asymptotic form of (117), Eq. (111). As before, we have

$$\operatorname{Im}\bar{\alpha}_B \equiv \frac{\bar{\alpha}_B(s+i\varepsilon) - \bar{\alpha}_B(s-i\varepsilon)}{2i} \tag{125}$$
$$= \frac{4\pi^2\Theta(s - M_0^2)}{b_0\left\{\ln^2\left|\dfrac{M_0^2 - s}{\Lambda^2}\right| + \pi^2\right\}}.$$

One can notice, however, that averaging over some duality interval in (124) yields

$$\langle \operatorname{Im}\alpha_B\rangle_{Nm^2} \simeq \frac{4\pi^2}{b_0}\frac{1}{N}\sum_{k=0}^{N}\frac{1}{\delta_0^{-2}(n+k) + \pi^2/3}, \tag{126}$$

and this result, as is shown in the Appendix, asymptotically agrees with (125), specifically at large s, in which case the denominator in (125) grows. To make contact with SPT calculations, we consider, instead of $\Pi(Q^2)$, the so-called Adler function $D(Q^2) = Q^2 d\Pi(Q^2)/dQ^2$ expanded as

$$D(Q^2) = \sum_q e_q^2\left\{1 + \frac{\alpha_s(Q^2)}{\pi}\right. \tag{127}$$
$$\left. + d_2\left(\frac{\alpha_s(Q^2)}{\pi}\right)^2 + d_3\left(\frac{\alpha_s(Q^2)}{\pi}\right)^3 + \ldots\right\},$$

where the coefficients d_3 and d_2 were found in [21] and [28], respectively:

$$d_2(\overline{MS}) = 1.986 - 0.115 n_f, \tag{128}$$
$$\bar{d}_3(\overline{MS}) = 18.244 - 4.216 n_f + 0.086 n_f^2.$$

The procedure suggested in [9] to go over from $D(Q^2)$ to $R(s)$ is straightforward, provided that one knows the discontinuity of $\Pi(Q^2)$ (see the relevant

discussion in [8, 9] and the recent publication of Shirkov [29]); that is,

$$R(s) = \frac{1}{2\pi i}\int\limits_{-s-i\varepsilon}^{-s+i\varepsilon} D(\sigma)\frac{d\sigma}{\sigma}, \qquad (129)$$

where the integration contour goes on the two sides of the cut on the real axis starting at $s = 0$.

To proceed further, one inserts the one- or the two-loop expression for $\alpha_s(Q^2)$ into (129), whereupon one obtains an expansion for $R(s)$ [9],

$$R(s) = \sum_q e_q^2\left\{1 + \sum_{k=1} d_k \Phi\left\{\left(\frac{\alpha_s}{\pi}\right)^k\right\}\right\}, \quad (130)$$

where Φ is the transformation defined by (129). In this procedure, $\ln Q^2$ in the denominator of $\alpha_s(Q^2)$ transforms into $\ln s$ with coefficients less than unity and asymptotically tending to it.

Let us now consider what happens with our expression (117) for $\alpha_B(Q^2)$, which is valid not only for large Q^2 but in the entire Q^2 plane. We assume that, in BPT, the function $D(Q^2)$ is given by the same expansion (127), where only α_s should be replaced by $\alpha_B(Q^2)$, and we use (117) for $\alpha_B(Q^2)$ to insert into (129). In this way, one obtains

$$\Phi\left\{\left(\frac{\alpha_B}{\pi}\right)^k\right\} = \frac{1}{2\pi i}\left(\frac{4}{b_0}\right)^k \qquad (131)$$
$$\times \sum_{n=0}\int\limits_{s+i\varepsilon}^{s-i\varepsilon}\frac{ds'}{[\psi'(z_0)(z-z_0)]^k s'},$$

where use is made of the notation from [9].

As is shown in the Appendix,

$$\psi'(z_0) \simeq \left(\ln\frac{M_0^2 + nm^2}{\Lambda^2}\right)^2.$$

Here, the pole of the kth order is at $s' = M_0^2 + nm^2 - \delta_0(n)m^2$, and n satisfies the condition $M_0^2 + nm^2 \le s$. For arbitrary k, one obtains

$$\Phi\left\{\left(\frac{\alpha_B}{\pi}\right)\right\} = 0. \qquad (132)$$

This is a property of the integral in (131) with the weight ds/s that any function representable as a finite sum of poles yields zero since

$$\int\limits_{s-i\varepsilon}^{s+i\varepsilon}\frac{dz}{z(z-s_n)^k} = 0.$$

However, in the asymptotic region of $s, s \gg m^2$, in which case the number of poles is large, one can use the asymptotic form of α_B (112), and the result is

$$\Phi\left\{\left(\frac{\alpha_B}{\pi}\right)\right\} \simeq \frac{4}{b_0}\left(\frac{1}{\pi}\arctan\left(\frac{\pi}{\ln\dfrac{s}{\Lambda^2}}\right)\right. \qquad (133)$$
$$\left. + \frac{2(M_0)^2}{s\left(\ln\dfrac{s}{\Lambda^2}\right)^3} + \ldots\right).$$

This result can be most easily obtained from (129), where the contour of integration C_R is modified to be a circle of radius $R = s$ with the center at $\sigma = 0$, namely,

$$R(s) = \frac{1}{2i\pi}\int\limits_{C_R} D(\sigma)\frac{d\sigma}{\sigma}, \qquad (134)$$

$$\Phi\left\{\left(\frac{\alpha_B}{\pi}\right)^k\right\} = \frac{1}{2i\pi}\int\limits_{C_R}\frac{d\sigma}{\sigma}\left(\frac{\alpha_B(\sigma)}{\pi}\right)^k.$$

The result in (132) is obtained from (134) trivially by introducing the angular variable $\sigma = s\exp(i\phi)$. For large $s, s \gg m^2, (M_0)^2$, one can use, in (134), the asymptotic form of $\alpha_B(\sigma)$ from (112).

Thus, one obtains

$$R(s) = N_c\sum_q e_q^2\left[1 + \bar{\Phi}\left\{\frac{\alpha_B}{\pi}\right\}\right. \qquad (135)$$
$$\left. + d_2\bar{\Phi}\left\{\left(\frac{\alpha_B}{\pi}\right)^2\right\} + d_3\bar{\Phi}\left\{\left(\frac{\alpha_B}{\pi}\right)^3\right\} + \ldots\right].$$

Comparing with $\Phi\left\{\left(\dfrac{\alpha_s}{\pi}\right)^k\right\}$ from the study of Radyushkin [9], one can see very close correspondence with our $\bar{\Phi}\left\{\left(\dfrac{\alpha_B}{\pi}\right)^k\right\}$.

7. DISCUSSION AND CONCLUSIONS

In this study, we have developed background perturbation theory (BPT) in the large-N_c limit, where all physical amplitudes and their perturbative expansions have only isolated singularities (poles).

Using this fact, we have proposed a nonperturbative solution for $\beta(\alpha)$ and $\alpha(Q^2)$ containing all terms of the loop expansion.

By choosing a specific meromorphic function, we have simulated both $\beta(\alpha_B)$ and $\alpha_B(Q^2)$ satisfying the necessary criteria of analyticity of α_B in the Euclidean region of Q^2 and analyticity of $\beta(\alpha)$ for positive values of α_B.

We have constructed time-dependent old-fashioned perturbation theory to investigate the analytic properties of different terms of the perturbation series and have shown that those reduce to isolated poles (simple poles and those of higher degree) shifted with respect to unperturbed bound-state positions.

This has enabled us to modify the original ansatz for $\beta(\alpha)$ and $\alpha_B(Q^2)$ to achieve a full correspondence with the standard perturbative expansion of $\beta(\alpha)$.

Finally, we have studied the problem of analyticity of $\alpha_B(Q^2)$ and of its analytic continuation into the region of timelike Q^2, where $\alpha_B(Q^2)$ has singularities, and have compared this procedure with analytic continuation in SPT.

We have found a striking similarity of the perturbative series for $R(s)$ in the case of SPT and BPT at large s. However, our BPT series have correct physical singularities, in contrast to SPT.

More detailed calculations and a comparison with experimental data may solve the problem of applicability of both methods and are planned for the subsequent publication.

ACKNOWLEDGMENTS

This work was supported by the Russian Foundation for Basic Research (project no. 00-02-17836) and by INTAS (grant no. 110).

APPENDIX

To find the poles of

$$\alpha_B(s) = \frac{4\pi}{b_0}\left[\ln\frac{m^2}{\Lambda^2} + \psi\left(\frac{M_0^2 - s}{m^2}\right)\right]^{-1},$$

one must find the roots $z_0(n)$ of the equation

$$\ln\frac{m^2}{\Lambda^2} + \psi(z_0) = 0, \qquad (A.1)$$

which can be represented as

$$z_0(n) = -n + \delta, \quad \delta \ll 1, \quad n = 0, 1, 2.$$

The following relations will be useful:

$$\psi(-n+\delta) = \sum_{k=0}^{n}\frac{1}{k-\delta} + \psi(1+\delta), \quad n \geq 0,$$

$$\psi(1+\delta) = -C + \delta\{\zeta(2) - \delta\zeta(3) + \ldots\},$$

where $\zeta(2) = \pi^2/6$, $\zeta(3) = 1.202$.

Hence, one can write an expansion in powers of δ:

$$\psi(-n+\delta) = -\frac{1}{\delta} - C + S_1(n) + \delta(1 + S_2(n) + \zeta(2)) + O(\delta^2),$$

where $S_k(n) = \sum_{k=1}^{n}\frac{1}{k}, C = 0.577$, and Eq. (A.1) takes the form

$$-\frac{1}{\delta} - C + S_1(n) + \delta(1 + S_2(n) + \zeta(2)) = -\ln\frac{m^2}{\Lambda^2}.$$

To the lowest order, one has

$$\delta \simeq \delta_0 = \left[\ln\frac{m^2}{\Lambda^2} - C + S_1(n)\right]^{-1} + O(\delta_0^3). \quad (A.2)$$

In a similar way, one obtains $\psi'(z_0)$,

$$\psi'(z_0) = \frac{1}{\delta^2} + S_2(n) + \zeta(2) + O(\delta).$$

For $n \gg 1$, we have $S_2(n) \approx \zeta(2) = \pi^2/6$.

In this way, α_B in the vicinity of the pole is

$$\alpha_B(s \simeq M_n^2 + i\varepsilon) = \frac{4\pi}{b_0}\left\{\left[\delta_0^{-2}(n) + S_2(n) + \zeta(2)\right] \times (M_n^2 - s - \delta_0 m^2)\right\}^{-1},$$

where $M_n^2 = M_0^2 + nm^2$.

Now, the following asymptotic expression is valid for $S_1(n)$

$$S_1(n) = C + \ln n + \frac{1}{2n} + O\left(\frac{1}{n^2}\right).$$

Therefore, δ_0 (A.2) can be rewritten as

$$\delta_0 \simeq \left[\ln\frac{m^2}{\Lambda^2} + \ln\left(n + \frac{1}{2}\right)\right]^{-1} = \left[\ln\frac{m^2(n+1/2)}{\Lambda^2}\right]^{-1} \simeq \left[\ln\frac{M_n^2}{\Lambda^2}\right]^{-1},$$

and the averaged imaginary part of α_B in (126) has the form

$$\langle \mathrm{Im}\,\alpha_B\rangle_{Nm^2} = \frac{4\pi^2}{b_0 N}\sum_{k=0}^{N}\frac{1}{\left(\ln\frac{M_{n+k}^2}{\Lambda^2}\right)^2 + \frac{\pi^2}{3}} \simeq \frac{4\pi^2}{b_0\left(\ln\frac{\overline{M}^2}{\Lambda^2}\right)^2},$$

where $\overline{M}^2 \sim s$ is in the middle of the averaging interval, which is asymptotically close to the expression in Eq. (125).

REFERENCES

1. F. J. Ynduráin, *The Theory of Quark and Gluon Interactions*, 3rd ed. (Springer-Verlag, Berlin, 1999).
2. L. D. Faddeev and A. A. Slavnov, *Gauge Fields* (Benjamin, New York, 1980).
3. See, e.g., discussion in Chap. 10 of [1].
4. A. M. Badalian and D. S. Kuzmenko, hep-ph/0104097.
5. G. 't Hooft, in *Proceedings of the International School "The Whys of Subnuclear Physics," Erice, 1977*, Ed. by A. Zichichi (Plenum, New York, 1977).
6. M. A. Shifman, A. I. Vainshtein, and V. I. Zakharov, Nucl. Phys. B **147**, 385 (1979).
7. *Vacuum Structure and QCD Sum Rules,* Ed. by M. A. Shifman (North-Holland, Amsterdam, 1992); S. Narison, *QCD Spectral Sum Rules* (World Sci., Singapore, 1989).
8. D. V. Shirkov, hep-ph/0012283.
9. A. Radyushkin, Preprint No. E-2-82-159, OIYaF (Joint Inst. for Nuclear Research, Dubna, 1982); hep-ph/9907228; N. V. Krasnikov and A. A. Pivovarov, Phys. Lett. B **116B**, 168 (1982).
10. G. 't Hooft, Nucl. Phys. B **72**, 461 (1974).
11. B. S. De Witt, Phys. Rev. **162**, 1195, 1239 (1967); J. Honerkamp, Nucl. Phys. B **48**, 269 (1972); G. 't Hooft, Nucl. Phys. B **62**, 44 (1973); Acta Univ. Wratislaviensis **368**, 345 (1976) (Lectures at Karpacz); L. F. Abbot, Nucl. Phys. B **185**, 189 (1981).
12. Yu. A. Simonov, Yad. Fiz. **58**, 113 (1995) [Phys. At. Nucl. **58**, 107 (1995)]; hep-ph/9311247; Pis'ma Zh. Éksp. Teor. Fiz. **57**, 513 (1993) [JETP Lett. **57**, 525 (1993)].
13. Yu. A. Simonov, in *Lecture Notes in Physics* (Springer-Verlag, Berlin, 1996), Vol. 479, p. 139.
14. A. M. Badalian and Yu. A. Simonov, Yad. Fiz. **60**, 714 (1997) [Phys. At. Nucl. **60**, 630 (1997)].
15. A. M. Badalian and V. L. Morgunov, Phys. Rev. D **60**, 116008 (1999); hep-ph/9901430.
16. A. M. Badalian and B. L. G. Bakker, Phys. Rev. D **62**, 094031 (2000); hep-ph/0004021.
17. Yu. A. Simonov, hep-ph/9712250.
18. H. G. Dosch and Yu. A. Simonov, Phys. Lett. B **205**, 339 (1988).
19. M. Campostrini, A. Di Giacomo, and G. Mussardo, Z. Phys. C **25**, 173 (1984); A. Di Giacomo and H. Panagopoulos, Phys. Lett. B **285**, 133 (1992); A. Di Giacomo, E. Meggiolaro, and H. Panagopoulos, Nucl. Phys. B **483**, 371 (1997); hep-lat/9603017.
20. G. Sterman, in *Lecture Notes in Physics* (Springer-Verlag, Berlin; Heidelberg, 1996), Vol. 479, p. 209.
21. S. G. Gorishny, A. L. Kataev, and S. A. Larin, Phys. Lett. B **259**, 144 (1991); M. A. Samuel and L. R. Surguladze, Phys. Rev. Lett. **66**, 560 (1991).
22. A. Yu. Dubin, A. B. Kaidalov, and Yu. A. Simonov, Yad. Fiz. **56** (12), 213 (1993) [Phys. At. Nucl. **56**, 1745 (1993)]; Phys. Lett. B **323**, 41 (1994).
23. Yu. A. Simonov, hep-ph/0105141.
24. P. Cea, G. Nardulli, and G. Preparata, Z. Phys. C **16**, 135 (1982); Phys. Lett. B **115B**, 310 (1982).
25. Yu. A. Simonov, Pis'ma Zh. Éksp. Teor. Fiz. **69**, 471 (1999) [JETP Lett. **69**, 505 (1999)]; Phys. Rep. **320**, 265 (1999).
26. K. G. Chetyrkin, S. Narrison, and V. I. Zakharov, hep-ph/9811275.
27. V. S. Popov, V. M. Vainberg, and V. D. Mur, Pis'ma Zh. Éksp. Teor. Fiz. **41**, 439 (1985) [JETP Lett. **41**, 539 (1985)]; Yad. Fiz. **44**, 1103 (1986) [Sov. J. Nucl. Phys. **44**, 714 (1986)]; B. M. Karnakov, V. D. Mur, and V. S. Popov, Zh. Éksp. Teor. Fiz. **107**, 976 (1995) [JETP **80**, 360 (1995)].
28. K. G. Chetyrkin, A. L. Kataev, and F. V. Tkachov, Nucl. Phys. B **174**, 345 (1980); M. Dine and J. Sapirstein, Phys. Rev. Lett. **43**, 668 (1979); W. Celmaster and R. Gonsalvez, Phys. Rev. D **21**, 3112 (1980).
29. D. V. Shirkov, hep-ph/0105317.

Physics of Atomic Nuclei, Vol. 65, No. 1, 2002, pp. 153–160. Translated from Yadernaya Fizika, Vol. 65, No. 1, 2002, pp. 158–166.
Original Russian Text Copyright © 2002 by Achasov, Kozhevnikov.

ELEMENTARY PARTICLES AND FIELDS
Theory

Spectroscopy of the Heavy Resonances ρ', ρ'', ω', and ω''

N. N. Achasov* **and A. A. Kozhevnikov****

Institute of Mathematics, Siberian Division, Russian Academy of Sciences, Universitetskii pr. 4, Novosibirsk, 630090 Russia

Received September 22, 2000

Abstract—The spectroscopy of the isovector resonances ρ' and ρ'' and the isoscalar resonances ω' and ω'' is considered on the basis of their masses and coupling constants extracted from data on e^+e^- annihilation, τ-lepton decays, and the reaction $K^-p \to \pi^+\pi^-\Lambda$. The total widths of these resonances and the branching fractions for their decay modes are calculated. It is argued that the shift of the apparent position of the peak in the energy dependence of the cross section with respect to the bare mass is significant for broad resonances. The results are compared with the predictions of available models for the ρ', ρ'', ω', and ω'' resonances. © *2002 MAIK "Nauka/Interperiodica".*

1. INTRODUCTION

The situation around the $\rho' \equiv \rho'_1 \equiv \rho(1450)$, $\rho'' \equiv \rho'_2 \equiv \rho(1700)$ and $\omega' \equiv \omega'_1 \equiv \omega(1420)$, $\omega'' \equiv \omega'_2 \equiv \omega(1600)$ resonances (the respective isospin values are $I = 1$ and 0) is still intricate. Although typical peaks associated with these structures were observed in some channels of single-photon e^+e^- annihilation, τ-lepton decays, $N\bar{N}$ annihilation, photoproduction, etc., specific values of the masses and partial widths of these resonances have not yet been reliably determined; therefore, they are not presented in the main body of the particle tables [1]. The contributions of these resonances have been seen in the reaction $K^-p \to \pi^+\pi^-\Lambda$, e^+e^- annihilation, and the four-pion decays of the τ lepton. A few years ago, we made an attempt to treat available data on these processes within a unified approach based on a model that takes into account the energy dependence of the partial widths, the mixing of heavy resonances with one another, and their mixing with the $\rho(770)$ and $\omega(782)$ mesons from the ground-state vector nonet in the isovector [2] and the isoscalar [3] channel, respectively. In doing this, we considered the resonance masses and coupling constants as free parameters to be determined from a fit to data. This choice of free parameters is particularly convenient because it is precisely these parameters that play a key role in investigating the nature of $J^{CP} = 1^{--}$ heavy resonances and because the function χ^2 used in determining the allowed intervals of the parameters being extracted can be represented, in this case, as the sum of independent contributions, so that the covariance matrix (see the section "Statistics" in [1]) has a diagonal form. However, experimental results on the resonance parameters are usually presented in terms of masses and branching ratios. The partial and total widths computed on the basis of values found for the coupling constants were not quoted in our previous publications [2, 3] for the reasons of space limitations. Here, we fill this gap by presenting the results of our calculations for the partial and total decay widths of the $\rho'_{1,2}$ and $\omega'_{1,2}$ resonances. In these calculations, we used experimental data on the cross sections for the reactions $e^+e^- \to \pi^+\pi^-\pi^0$ [4, 5] and $e^+e^- \to \omega\pi^0$ [6] and the data on the spectral function v_1 that were obtained in studying the decay processes $\tau^- \to \omega\pi^-\nu_\tau$ and $\tau^- \to \pi^+\pi^-\pi^-\pi^0\nu_\tau$ [7]. We also discuss the question of why a resonance of mass in excess of 1400 MeV must be broad within the generally accepted $q\bar{q}$ quark model and the question of why the bare mass of such a resonance is shifted toward greater values in relation to the position of the respective peak observed in the energy dependence of the cross section. As is shown below, the latter has a direct bearing on the spectroscopy of the $\rho(1300)$ resonance observed with the LASS detector [8] and the $\omega(1200)$ resonance observed with the SND detector [5].

The mass shift of a resonance whose width is large and grows fast with increasing energy is discussed in Section 2. A qualitative discussion of the couplings of the $V'_{1,2}$ mesons ($V = \rho, \omega$) to the states composed of the pseudoscalar and the vector meson is also given in that section. The results of the calculation of the total widths of the $V'_{1,2}$ mesons and of the branching fractions for their decays are presented in Section 3.

*e-mail: achasov@math.nsc.ru
**e-mail: kozhev@math.nsc.ru

Section 4 contains our considerations on the $\rho(1300)$ and $\omega(1200)$ resonance states, which were observed in recent experiments. The conclusions drawn from the present analysis are summarized in Section 5.

2. QUALITATIVE CONSIDERATIONS ON THE MASS SHIFTS OF HEAVY RESONANCES AND THEIR COUPLING CONSTANTS

First, we will try to understand why the situation around resonances of mass exceeding 1400 MeV remains intricate despite a great many experiments devoted to a determination of their masses and partial widths. It is well known [1] that some pieces of evidence for the existence of the $\rho'_{1,2}$ and $\omega'_{1,2}$ resonances were obtained in studying reactions producing VP final states, where V and P are a vector and a pseudoscalar meson, respectively. It is also known that a typical value of the VVP coupling constant is $g_{\omega\rho\pi} \simeq 14$ GeV^{-1}. All other coupling constants of this type can be expressed in terms of $g_{\omega\rho\pi}$ by using the Clebsch–Gordan coefficients of the $SU(3)$ group. Theoretical models do not provide specific values of the $V'_{1,2}VP$ coupling constants. For example, QCD sum rules [9], which are used to estimate the coupling constant $g_{\omega\rho\pi}$ [10], yield no predictions here because the contributions of higher resonances are suppressed upon the Borel transformation. The predictions of quark models are uncertain to a considerable extent because different approaches give different values of the coupling constants. By way of example, we indicate that Gerasimov and Govorkov [11] present the values of $|g_{\rho'_1\omega\pi}| = 4$–$24$ GeV^{-1} and $|g_{\rho'_2\omega\pi}| = 3$–$5$ GeV^{-1} and that Godfrey and Isgur [12] obtained $|g_{\rho'_1\omega\pi}| \approx 6$ GeV^{-1} and $|g_{\rho'_2\omega\pi}| \approx 2$ GeV^{-1}; at the same time, the value quoted in [13] is $|g_{\rho'_1\omega\pi}| \approx 5$ GeV^{-1}. For this reason, we do not rely on theoretical predictions and determine the required values of the $V'_{1,2}VP$ coupling constants from available data, following [2, 3], where it was found that the values of the coupling constants under consideration lie in the ranges $|g_{\rho'_1\omega\pi}| = 10$–$18$ GeV^{-1} and $|g_{\rho'_2\omega\pi}| = 2$–$13$ GeV^{-1} and that the couplings of the isovector and isoscalar resonances to VP states are on the same order of magnitude: $|g_{\rho'_{1,2}\omega\pi}| \sim |g_{\omega'_{1,2}\rho\pi}|$. The above implies that there are no theoretical or phenomenological grounds for $V'_{1,2}VP$ coupling constants to be substantially suppressed in relation to VVP coupling constants. Assuming that $g_{\rho'_{1,2}\omega\pi} \sim g_{\omega'_{1,2}\rho\pi} \simeq 10$ GeV^{-1} and that $m_{\rho'_1} \approx m_{\omega'_1} = 1400$ MeV, we obtain

$$\Gamma_{\rho'_1\to\omega\pi} = g^2_{\rho'_1\omega\pi} q^3_{\omega\pi}(m_{\rho'_1})/12\pi \sim 280 \text{ MeV}, \quad (2.1)$$

$$\Gamma_{\omega'_1\to\rho\pi} = g^2_{\omega'_1\rho\pi} q^3_{\rho\pi}(m_{\omega'_1})/4\pi \sim 820 \text{ MeV}.$$

Hereafter,

$$q_{bc}(m_a) = \left\{\left[m_a^2 - (m_b + m_c)^2\right]\right. \quad (2.2)$$
$$\left.\times\ \left[m_a^2 - (m_b - m_c)^2\right]\right\}^{1/2}/2m_a$$

is the momentum of the outgoing particle b or c in the reference frame comoving with the initial particle a in the decay $a \to b + c$. Three isotopic modes of the decay $\omega'_1 \to \rho\pi$ are taken into account. In order to give a feeling of a fast growth of the partial widths with respect to $V'_{1,2} \to VP$ decays as the energy is increased, we present the relevant values at a mass of 1200 MeV: 92 and 295 MeV. Proceeding as before and assuming that $m_{\rho'_2} \approx m_{\omega'_2} = 1750$ MeV, we obtain

$$\Gamma_{\rho'_2\to\omega\pi} \sim 880 \text{ MeV}, \quad (2.3)$$
$$\Gamma_{\omega'_2\to\rho\pi} \sim 2600 \text{ MeV}.$$

Needless to say, the qualitative conclusions on the partial widths with respect to $V'_{1,2} \to VP$ decays will not change even upon halving the above coupling constants. Since heavy vector resonances can decay not only via VP modes [1], we conclude that the $\rho'_{1,2}$ and $\omega'_{1,2}$ resonances are in fact rather broad, which hampers the identification of these resonances manifesting themselves as rather smooth structures in the energy dependence of the reaction cross section.

The shift of the resonance peak in relation to the bare mass toward smaller values [2, 3] is yet another feature that hinders the identification of the resonances. We will demonstrate this by considering the energy dependence of the cross section for the production of an individual resonance R of bare mass m_R in some channel f of e^+e^- annihilation: $e^+e^- \to R \to f$. The cross section for this process has the form

$$\sigma(s) = 12\pi m_R^3 \Gamma_{Re^+e^-}(m_R) g^2_{Rf} \frac{s^{-3/2} W_{Rf}(s)}{(s - m_R^2)^2 + s\Gamma_R^2(s)}, \quad (2.4)$$

where s is the square of the total energy in the c.m. frame and $\Gamma_{Re^+e^-}(m_R)$ is the leptonic width of the resonance at $\sqrt{s} = m_R$. The partial width with respect to the hadronic decay $R \to f$ has the form

$$\Gamma_{Rf}(s) = g^2_{Rf} W_{Rf}(s),$$

where g_{Rf} is the coupling of the resonance R to the final state f and $W_{Rf}(s)$ is the dynamical phase space for the decay $R \to f$ with allowance for the possible intermediate states (for example, those in the decay $\omega \to \rho\pi \to 3\pi$). The total width can be represented in the form

$$\Gamma_R(s) = \sum_f \Gamma_{Rf}(s).$$

The position of the peak can be found by equating the derivative of $\sigma(s)$ with respect to s to zero. This yields

$$s - m_R^2 = \frac{1}{G(s)} \left\{ 1 \pm \left[1 + s\Gamma_R^2 F(s) G(s) \right]^{1/2} \right\}, \tag{2.5}$$

where the functions $G(s)$ and $F(s)$ are given by

$$G(s) = \left[\ln \left(s^{-3/2} W_{Rf} \right) \right]', \tag{2.6}$$

$$F(s) = \left[\ln \left(s^{5/2} \Gamma_R^2 / W_{Rf} \right) \right]'.$$

Here and below, $\Gamma_R \equiv \Gamma_R(s)$, $W_{Rf} \equiv W_{Rf}(s)$, and the prime denotes differentiation with respect to s. In the limit of a slowly varying or a small width, Eq. (2.5) must take the form $s - m_R^2 = 0$. Therefore, we must choose the lower (minus) sign in (2.5), which is still a rather complicated equation for determining the peak position and which can be solved only numerically. However, the required qualitative conclusions can be drawn by taking its right-hand side at $s = m_R^2$. It can be proven that, for the resonances being considered, the phase spaces of their main decay modes increase with energy faster than the respective leptonic width decreases. The energy dependence of the leptonic width is described by the formula

$$\Gamma_{Rl^+l^-}(s) = \Gamma_{Rl^+l^-}(m_R^2) \left(\frac{m_R}{s^{1/2}} \right)^3.$$

It follows that the function $G(s)$ and, the more so, the function $F(s)$ are positive. Hence, the factor appearing in Eq. (2.5) immediately to the right of $G^{-1}(s)$ is negative. From this, we conclude that the position of the peak is indeed shifted to the left from the bare resonance mass. To the first order in $G(s)F(s)$, the function $G(s)$ drops out from the resulting expression, so that the position of the resonance peak is determined by the approximate formula

$$s_R \approx m_R^2 - \frac{1}{2} s\Gamma_R^2 F(s)|_{s=m_R^2}. \tag{2.7}$$

It can be seen that, in the case of a sufficiently narrow resonance such that its width satisfies the relation $\Gamma_R \leq 150$ MeV [$\rho(770)$, $\omega(782)$, or $\phi(1020)$], the position of the peak is determined by the bare mass m_R to a high precision.

A completely different type of situation occurs when the resonance width is large and grows fast with energy. This case is realized for the $\rho'_{1,2}$ and $\omega'_{1,2}$ resonances [see (2.1) and (2.3)]. The position of the peak is shifted from the bare mass m_R toward smaller mass values. This was revealed in the treatment of experimental data in [2, 3]. For the above resonances, all phase spaces corresponding to their main decay modes grow fast with energy, whereas their coupling constants are not suppressed in relation to the $\rho(770)$ and $\omega(782)$ resonances. From this, it follows that, although the bare masses of the ρ'_2 and ω'_2 resonances are approximately equal to 1900 MeV, they appear, in the energy dependence of the cross sections, as peaks in the range 1500–1600 MeV.

3. TOTAL WIDTHS OF THE $\rho'_{1,2}$ AND $\omega'_{1,2}$ RESONANCES AND THEIR BRANCHING RATIOS

We now proceed to present the results obtained by calculating the total widths of the resonances indicated in the title of this section and the branching fractions for their decay modes. The expressions for these widths were obtained in [2, 3]. As in [2, 3], the parameters of a resonance are given here for each individual channel being considered because experimental data obtained in different experiments and associated with different channels can disagree. According to the procedure adopted in this section, the calculation of the partial widths, the masses, and the coupling constants, along with the respective errors, precedes the calculation of the total widths and the errors in them. The leptonic widths of the $\rho'_{1,2}$ resonances were taken from [2], whereas the leptonic widths of the $\omega'_{1,2}$ resonances and their errors were computed by the formula

$$\Gamma_{\omega'_{1,2}} = \frac{4\pi\alpha^2 m_{\omega'_{1,2}}}{3 f^2_{\omega'_{1,2}}} \tag{3.1}$$

with the values of the mass and the leptonic coupling constants $f_{\omega'_{1,2}}$ from [3]. Moreover, we take into consideration new data on the reactions $e^+e^- \to \pi^+\pi^-\pi^0$ [4, 5] and $e^+e^- \to \omega\pi^0$ [6] and on the decay of the τ lepton [7] (these data appeared after the publication of [2, 3]).

The results of the computation for the branching fractions and the total widths are presented in Tables 1–3. Considering that VP do not exhaust the possible decay modes, we conclude that the simple qualitative estimates in (2.1) and (2.3) are compatible with experimental data.

4. COMMENTS ON THE SPECTROSCOPY OF HEAVY VECTOR RESONANCES

First, the observation of the resonance state $\rho(1300)$ with the LASS detector [8] in the mass spectrum of the $\pi^+\pi^-$ pair produced in the reaction $K^-p \to \pi^+\pi^-\Lambda$ rekindled the discussion on the possible existence of the $\rho(1250)$ meson in addition to the $\rho(1450)$ state, which is required for describing the behavior of the cross sections for some reactions—in particular, the cross section for e^+e^- annihilation.

Table 1. Masses and total widths (in MeV) and leptonic widths (in keV) of the ρ_1' resonance and its branching fractions (%) according to calculations with the coupling constants from [2] and from the present study

Parameter	Channel					
	$\pi^+\pi^-$	$\rho\eta$	$2\pi^+2\pi^-$	$\pi^+\pi^-2\pi^0$	$J/\psi \to 3\pi$	$K^-p \to \pi^+\pi^-\Lambda$
$m_{\rho_1'}$	1370^{+90}_{-70}	1460 ± 400	1350 ± 50	1400^{+220}_{-140}	1570^{+250}_{-190}	1360^{+180}_{-160}
$B_{\rho_1' \to \pi^+\pi^-}$	1.1 ± 1.1	~ 3.7	~ 1.4	~ 8.0	~ 0	~ 0.7
$B_{\rho_1' \to \omega\pi^0}$	86.5 ± 41.5	~ 56.9	93.6 ± 60.0	77.8 ± 62.2	66.5 ± 65.5	93.3 ± 82.7
$B_{\rho_1' \to \rho\eta}$	~ 5.6	~ 3.6	~ 5.0	~ 6.6	~ 13.2	~ 5.5
$B_{\rho_1' \to K^*\bar{K}+\text{c.c.}}$	0	~ 4.3	0	~ 0.4	~ 15.0	0
$B_{\rho_1' \to 4\pi}$	~ 6.8	~ 31.5	~ 0.2	~ 7.2	~ 4.4	~ 0.7
$\Gamma_{\rho_1' \to l^+l^-}$	$6.4^{+1.2}_{-1.4}$	~ 13	$5.4^{+2.6}_{-1.8}$	$6.3^{+3.3}_{-2.5}$	–	–
$\Gamma_{\rho_1'}$	763 ± 500	~ 2222	~ 518	~ 970	~ 3444	~ 460

Note: The symbol $\sim$ denotes that the central parameter value is given and that the error exceeds this central value. The ρ_1' resonance is not seen either in the reaction $e^+e^- \to \omega\pi^0$ or in the decay of the τ^- lepton. The parameters in columns 2–5 refer to the e^+e^--annihilation channels indicated there. The branching fractions for the decays of the ρ_1' resonance into $\rho\eta$ and $K^*\bar{K}$ + c.c. were computed according to the relations of $SU(3)$ symmetry for $V'VP$ coupling constants.

Table 2. Masses and total widths (in MeV) and leptonic widths (in keV) of the ρ_2' resonance and its branching fractions (%) according to calculations with the coupling constants from [2] and from the present study

Parameter	Channel						
	$\pi^+\pi^-$	$\omega\pi^0$	$\rho\eta$	$2\pi^+2\pi^-$	$\pi^+\pi^-2\pi^0$	$J/\psi \to 3\pi$	$\tau^- \to (4\pi)^-\nu_\tau$
$m_{\rho_2'}$	1900^{+170}_{-130}	1710 ± 90	1910^{+1000}_{-370}	1851^{+270}_{-240}	1790^{+110}_{-70}	2080^{+160}_{-900}	1860^{+260}_{-160}
$B_{\rho_2' \to \pi^+\pi^-}$	~ 0	~ 0	~ 0.4	~ 1.2	~ 0.4	~ 0	1.5 ± 1.4
$B_{\rho_2' \to \omega\pi^0}$	~ 16.7	22.3 ± 8.0	~ 1.6	13.4 ± 3.9	31.0 ± 18.6	~ 28.4	18.9 ± 2.8
$B_{\rho_2' \to \rho\eta}$	~ 5.9	6.3 ± 2.0	~ 0.3	4.6 ± 1.4	9.6 ± 8.6	~ 11.5	10.3 ± 2.2
$B_{\rho_2' \to K^*\bar{K}+\text{c.c.}}$	~ 8.9	8.7 ± 2.8	~ 0.9	6.7 ± 2.0	14.0 ± 11.2	~ 17.8	6.8 ± 1.5
$B_{\rho_2' \to 4\pi}$	~ 68.5	61.2 ± 7.8	~ 96.9	74.0 ± 32.1	45.0 ± 18.0	~ 42.2	62.6 ± 5.0
$\Gamma_{\rho_2' \to l^+l^-}$	1.8 ± 1.5	5.2 ± 1.5	~ 1.1	$4.02^{+0.28}_{-0.27}$	4.5 ± 1.3	–	9.3 ± 0.6
$\Gamma_{\rho_2'}$	~ 303.9	1886 ± 613	~ 3284	3123 ± 296	3151 ± 1281	~ 9386	3255 ± 388

Note: The ρ_2' resonance is not seen in the reaction $K^-p \to \pi^+\pi^-\Lambda$. The value of the leptonic width was extracted from the analysis of τ-lepton decay under the assumption of vector-current conservation (this makes it possible to express the spectral function of the vector current in terms of the cross sections for the scattering $e^+e^- \to 4\pi$ to various isospin states of the final pions [14]).

However, the results presented in Table 1 suggest that the resonance peak observed with the LASS facility is rather due to the $\rho(1450)$ resonance included in the "Review of Particle Physics" [1].

Second, the situation around the $\omega(1200)$ resonance observed in the reaction $e^+e^- \to \pi^+\pi^-\pi^0$ with the SND detector [5] is similar. This state is considered here on the basis of the approach proposed in [2, 3]. However, the present study differs from [3] in that, here, we use new data on the above reaction [4, 5] to determine the $\omega(1200)$ mass and coupling constants and neglect the contribution of the $\phi_{1,2}'$ resonances because the intervals allowed for their coupling constants include zero, as was indicated in [3]. It should be noted, however, that these coupling constants are known to a poor precision . Our analysis reveals that the new data from [4, 5] can be interpreted without taking into account the above excitations of the $\phi(1020)$ meson. It has been found that, within the errors of the analysis, the resulting values of the $\omega_{1,2}'$ masses and coupling constants agree with those obtained in [3]. These new values of the resonance

Table 3. Masses and total widths (in MeV) and leptonic widths (in eV) of the $\omega'_{1,2}$ resonances and their branching fractions (in %) according to calculations with the coupling constants derived in [3] and in the present study

Parameter	Channel				
	$\pi^+\pi^-\pi^0$	$\omega\pi^+\pi^-$	K^+K^-	$K^0_SK^\pm\pi^\mp$	$K^{*0}K^\mp\pi^\pm$
$m_{\omega'_1}$	1430^{+110}_{-70}	~ 1400	~ 1460	~ 1500	~ 1380
$B_{\omega'_1\to 3\pi}$	~ 21.6	~ 8	~ 67	~ 96	~ 34
$B_{\omega'_1\to K^*\bar{K}+\text{c.c.}}$	~ 0.2	~ 0	~ 1	~ 4	0
$B_{\omega'_1\to K^*\bar{K}\pi}$	~ 0	0	0	0	0
$B_{\omega'_1\to\omega\pi^+\pi^-}$	~ 78.2	~ 92	~ 31.2	~ 0	~ 65.8
$\Gamma_{\omega'_1\to l^+l^-}$	144^{+94}_{-58}	~ 0.2	~ 8	~ 8	~ 48
$\Gamma_{\omega'_1}$	~ 903	~ 129	~ 173	~ 1252	~ 112
$m_{\omega'_2}$	1940^{+170}_{-130}	2000 ± 180	1780^{+170}_{-300}	~ 2120	1880^{+600}_{-1000}
$B_{\omega'_2\to 3\pi}$	~ 22.1	~ 34.2	~ 88.8	~ 91.2	~ 60.1
$B_{\omega'_2\to K^*\bar{K}+\text{c.c.}}$	~ 3.5	~ 5.8	~ 11.2	~ 15.8	~ 8.9
$B_{\omega'_2\to K^*\bar{K}\pi}$	~ 68.2	~ 53.4	0	0	~ 30.9
$B_{\omega'_2\to\omega\pi^+\pi^-}$	~ 6.2	~ 6.6	0	0	~ 0
$\Gamma_{\omega'_2 l^+l^-}$	109^{+58}_{-46}	531 ± 225	0	~ 189	1162 ± 922
$\Gamma_{\omega'_2}$	~ 14000	~ 5757	~ 2420	~ 9854	~ 13820

Note: The symbol $\sim$ denotes that the central parameter value is given and that the error exceeds this central value. The branching fractions for the decays $\omega'_{1,2}\to K^*\bar{K}+\text{c.c.}$ were computed according to the relations of $SU(3)$ symmetry for $V'VP$ coupling constants.

parameters are used to fill the respective entries in Table 3. The relevant energy dependences of the cross sections that were calculated by the formulas from [3] are presented in Figs. 1 and 2. Eventually, we conclude that the $\omega(1200)$ state observed with the SND detector [5] is nothing but the $\omega(1420)\equiv\omega'_1$ resonance presented in [1]. As was indicated in Section 2, the shift of the observed peak with respect to the position associated with the bare mass can be explained by a large total width of the resonance and its fast growth with energy. According to (2.7), the huge width of the ω'_2 resonance (see Table 2) causes the shift of the apparent peak from the bare-mass value of about 1900–2000 MeV to a value of about 1600 MeV. The large partial widths agree qualitatively with the simple estimates in (2.1) and (2.3).

The new SND data [5] make it possible to draw some conclusions on the quark structure of the $\omega'_{1,2}$ resonances by using the numerical values of the radial wave function $R_S(0)$ for a bound $q\bar{q}$ state at the origin. Taking into account the results presented in [18] and the fact that the ω'_1 resonance is usually interpreted in spectroscopy as the 2^3S_1 state [1, 12], we obtain

$$|R_S(0)|^2 = 6\pi m^3_{\omega'_1}/f^2_{\omega'_1} = (25\pm 10)\times 10^{-3}\ \text{GeV}^3. \quad (4.1)$$

Within the errors, this value agrees with the value of $(38\pm 4)\times 10^{-3}\ \text{GeV}^3$ obtained for the $\omega(782)$ meson. On the other hand, the ω'_2 resonance is associated with the 1^3D_1 state [1, 12]; hence, we must consider the second derivative of the radial wave function at the origin [18]:

$$|R''_D(0)|^2 = \frac{3\pi m^7_{\omega'_2}}{25 f^2_{\omega'_2}} = (10\pm 8)\times 10^{-3}\ \text{GeV}^7. \quad (4.2)$$

It should be noted that the S-wave characteristic [defined by analogy with (4.1)] of the ω'_2 resonance is equal to $|R_S(0)|^2 = (35\pm 23)\times 10^{-3}\ \text{GeV}^3$. We give this value because, strictly speaking, the spectroscopic identification $\omega'_2\equiv 1^3D_1$ [1, 12] is hypothetical at present.

The results obtained by processing recent data from [6] on the reaction $e^+e^-\to\omega\pi^0$ are quoted in the present article. Within the errors, the values obtained for the parameters of the $\rho'_{1,2}$ resonances agree with those reported in [2]. In particular, the ρ'_1 resonance is not needed for adequately describing these data; more precisely, its parameters extracted from the data are compatible with zero within the large error. For this

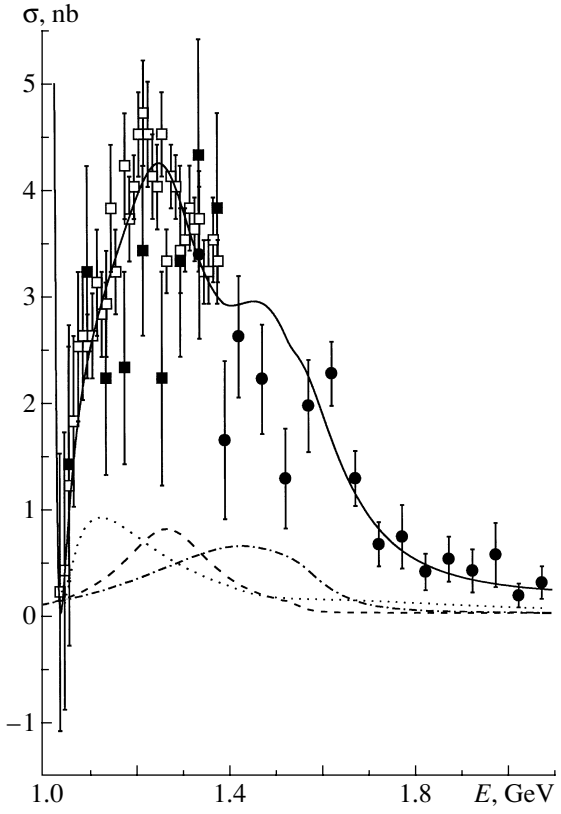

Fig. 1. Cross section for the reaction $e^+e^- \to \pi^+\pi^-\pi^0$ at energies above 1 GeV. Shown in the figure are the contributions of the (solid curve) $\omega + \phi + \omega_1' + \omega_2'$, (dotted curve) $\omega + \phi$, (dashed curve) ω_1', and (dash-dotted curve) ω_2' channels. The experimental data were taken from (□) [5], (■) [15], and (●) [16].

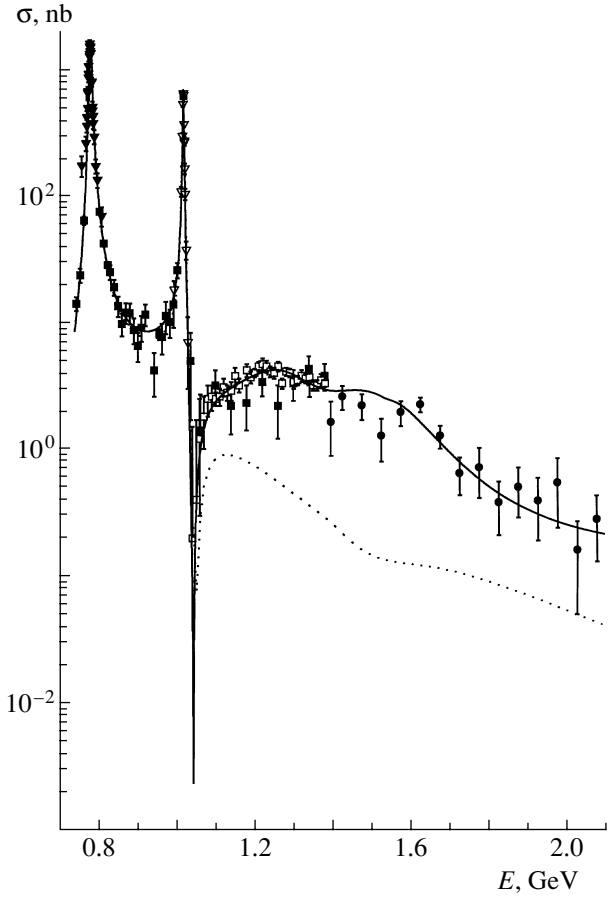

Fig. 2. Cross section for the reaction $e^+e^- \to \pi^+\pi^-\pi^0$ over the energy region containing the resonances of the ground-state vector nonet. The experimental data were taken from (□) [5], (■) [15], (●) [16], (▼) [17], and (▽) [4]. The notation for the curves is identical to that in Fig. 1.

reason, the resonance being discussed was not included in final data processing. The resulting description with allowance for the $\rho(770) + \rho_2'$ contribution is shown in Fig. 3. In visually comparing the contributions of the individual resonances in Figs. 1, 2, and 3 with the total contribution, it should be borne in mind that the last contribution is not directly related to the first ones. The point is that the resonances are strongly mixed by their common decay modes, and this mixing makes a substantial contribution to the cross section [2, 3]. We note that the central value of the parameter R appearing in the expression for the form factor

$$C_{\rho\omega\pi}(E) = \frac{1 + (Rm_\rho)^2}{1 + (RE)^2}, \qquad (4.3)$$

which was introduced to moderate an overly fast growth of the $\rho \to \omega\pi^0$ partial width with energy,

$$\Gamma_{\rho\omega\pi}(E) \to C^2_{\rho\omega\pi}(E)\Gamma_{\rho\omega\pi}(E),$$

proved to be zero in our data processing; more precisely, the experimental errors allow variations of this parameter in the range from 0 to 0.37 GeV^{-1}. Let us indicate the distinctions between our data analysis and that in [6]. First, we have taken into account the contributions of all known decay modes (see Tables 1 and 2), whereas the authors of [6] included only two decay modes, $\pi^+\pi^-$ and $\omega\pi^0$, in their analysis. Second, we have taken into account the mixing of the resonances that is due to the decay modes neglected in [6]. Third, the expression

$$C_{\rho\omega\pi}(E) = \left\{1 + [Rq_{\omega\pi}(E)]^2\right\}^{-1}$$

used in [6] for the form factor differs from ours. The expression for the form factor in [6] and that in (4.3) have the same asymptotic behavior for $E \to \infty$: $E\Gamma_{\rho\to\omega\pi}(E) \to \mathrm{const}$. However, it was assumed in [6] that the value of the parameter R is common both to the $\pi^+\pi^-$ and $\omega\pi^0$ modes and to ρ-like resonances; in our study these parameters were taken to be different, with the value of R for the $\pi^+\pi^-$ channel being set to zero because of a rather slow growth of the partial width with respect to this decay

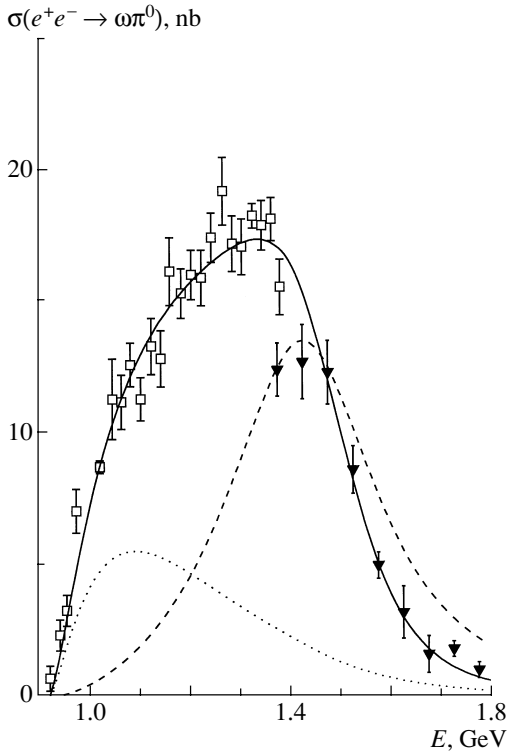

Fig. 3. Cross section for the reaction $e^+e^- \to \omega\pi^0$. Shown in the figure are the contributions of (solid curve) the $\rho(770) + \rho_2'$ state, (dotted curve) the $\rho(770)$ meson, and (dashed curve) the ρ_2' resonance. The experimental data were taken from (□) [6] and (▼) [19].

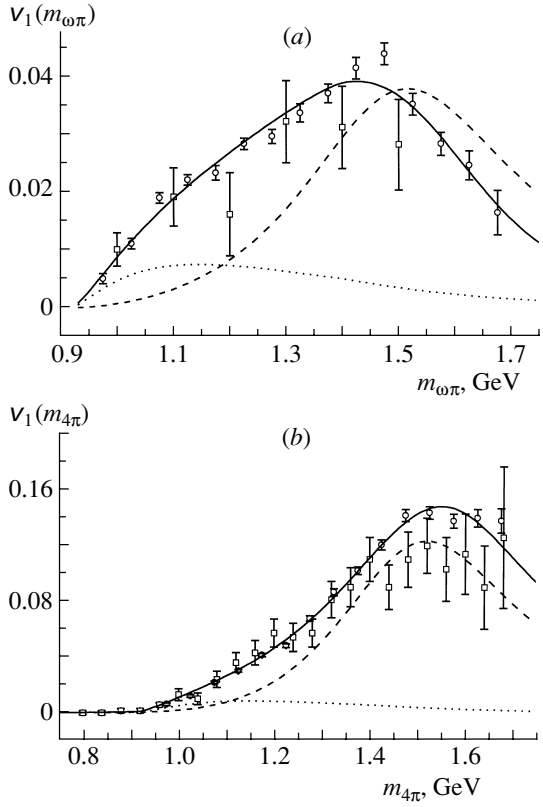

Fig. 4. Spectral function of the vector current according to measurements in the decays (*a*) $\tau^- \to \omega\pi^-\nu_\tau$ and (*b*) $\tau^- \to \pi^+2\pi^-\pi^0\nu_\tau$. The notation for the curves is identical to that in Fig. 3. The experimental data were taken from (○) [7] and (□) [20].

mode with increasing energy. The authors of [6] argue that R does not vanish.

In the present study, we performed a global analysis of new data on the decay $\tau^- \to \nu_\tau(4\pi)^-$ from the CLEO detector [7] (four pions in the final state, including $\omega\pi^-$). The high precision of these measurements makes it possible to improve the accuracy in determining the parameters of the ρ_2' resonance in relation to that in [2], where data from the ARGUS detector were used [20]. Our analysis of the new data has revealed that they can be adequately described by the contributions of the ρ_2' resonance and $\rho(770)$ meson without including the contribution of the ρ_1' resonance. The results are shown in Fig. 4. The shift of the peak toward smaller values of the invariant mass of the $(4\pi)^-$ system near 1500 MeV can be explained by the aforementioned shift of a resonance peak according to Eq. (2.7).

5. CONCLUSION

Our conclusions are as follows. First, the widths of the resonances $\rho_{1,2}'$ and $\omega_{1,2}'$ are very large. This naturally fits in the usual two-quark model, where these resonances are nothing but radial excitations of the mesons from the ground-state vector nonet. In view of the large uncertainties in determining the resonance parameters, we cannot rule out either the traditional spectroscopic identification[1)] of the ρ_1' and ω_1' resonances with the 2^3S_1 state in the $q\bar{q}$ model [1, 12] or some involved schemes of mixing that include exotic configurations [21]. At the same time, the

[1)]The fact that the central value of the width $\Gamma_{\rho_1'}$ in the channels $e^+e^- \to \rho\eta$ and $J/\psi \to \pi^+\pi^-\pi^0$ far exceeds its values obtained in the other channels considered here (see Table 1) can be explained by a large central value of the mass of the ρ_1' resonance. However, the uncertainties in determining this mass in the above channels are so large that it would be premature to state that our conclusions disagree with the predictions from [12], where $\Gamma_{\rho_S} \sim 500$ MeV. Note that the central value of $m_{\rho_1'}$ in the $\rho\eta$ channel should be taken to be preliminary because of large uncertainties in the experimental data; at the same time, a large central value of this mass in the channel $J/\psi \to \pi^+\pi^-\pi^0$ was obtained by requiring that the coupling constants determined for the resonances from different reactions be consistent (for details, see [2]).

fact that the central values of the widths of the ρ_2' and ω_2' resonances are large rules out the interpretation of these states as the 1^3D_1 orbital excitation of the ground-state vector nonet, because this excitation is relatively narrow [12]. However, this conclusion cannot be considered to be final because of large uncertainties in determining the above widths. Second, care should be taken in identifying a particular peak or some other structure in the energy dependence of the cross section with a specific spectroscopic state, since the concerted effect of such factors as a large resonance width, a fast increase in phase space with energy, and resonance mixing caused by common decay modes [2, 3] may result in a significant shift of the apparent peak with respect to the bare resonance mass. In a broader context, the fact that our analysis leads to very large widths of the resonances under study—in particular, of isoscalar ω-like states—suggests that either the available experimental data are inconsistent, or the description in terms of resonances exclusively is not adequate, in which case some nonresonance contributions must be included in the amplitudes of the processes being considered. However, the accuracy of the experimental data is not sufficient for specifying such contributions. One can hope that a more precise measurement of the cross sections over the energy range 1400–2000 MeV in future experiments would make it possible to isolate nonresonance contributions (if they do exist) and to check the interpretation of higher excitations of the vector nonet as resonances.

ACKNOWLEDGMENTS

We are grateful to V.P. Druzhinin, E.V. Pakhtusova, S.I. Serednyakov, and S.I. Eidel'man for discussions.

This work was supported in part by the Russian Foundation for Basic Research and the International Association for the Promotion of Cooperation with Scientists from the Independent States of the Former Soviet Union (grant no. IR-97-232).

REFERENCES

1. Particle Data Group (D. E. Groom *et al.*), Eur. Phys. J. C **15**, 1 (2000).
2. N. N. Achasov and A. A. Kozhevnikov, Yad. Fiz. **60**, 1131 (1997) [Phys. At. Nucl. **60**, 1011 (1997)]; Phys. Rev. D **55**, 2663 (1997).
3. N. N. Achasov and A. A. Kozhevnikov, Yad. Fiz. **60**, 2212 (1997) [Phys. At. Nucl. **60**, 2029 (1997)]; Phys. Rev. D **57**, 4334 (1998).
4. R. R. Akhmetshin *et al.,* Phys. Lett. B **434**, 428 (1998).
5. M. N. Achasov *et al.,* Phys. Lett. B **462**, 365 (1999).
6. M. N. Achasov *et al.,* Phys. Lett. B **486**, 29 (2000).
7. K. W. Edwards *et al.,* Phys. Rev. D **61**, 072003 (2000).
8. D. Aston *et al.,* in *Proceedings of the International Conference on Hadron Spectroscopy "Hadron 91," College Park, Maryland,* Ed. by S. Oneda and D. C. Peaslee (World Sci., Singapore, 1992), pp. 75, 410.
9. M. A. Shifman, A. I. Vainshtein, and V. I. Zakharov, Nucl. Phys. B **147**, 385, 448, 519 (1979).
10. V. M. Khatsimovskiĭ, Yad. Fiz. **41**, 814 (1985) [Sov. J. Nucl. Phys. **41**, 519 (1985)]; M. V. Mergvelashvili and M. E. Shaposhnikov, Z. Phys. C **38**, 467 (1988); V. M. Braun and I. E. Filyanov, Z. Phys. C **44**, 157 (1989); M. Lublinsky, Phys. Rev. D **55**, 249 (1997).
11. S. B. Gerasimov and A. B. Govorkov, Z. Phys. C **13**, 43 (1982).
12. S. Godfrey and N. Isgur, Phys. Rev. D **32**, 189 (1985).
13. M. K. Volkov and V. L. Yudichev, Fiz. Élem. Chastits At. Yadra **31**, 576 (2000) [Phys. Part. Nucl. **31**, 282 (2000)].
14. Y. S. Tsai, Phys. Rev. D **4**, 2871 (1971); F. J. Gilman and D. H. Miller, Phys. Rev. D **17**, 1846 (1978); F. J. Gilman and S. H. Rhye, Phys. Rev. D **31**, 1066 (1985).
15. S. I. Dolinsky *et al.,* Phys. Rep. **202**, 99 (1991).
16. A. Antonelli *et al.,* Z. Phys. C **56**, 15 (1992).
17. L. M. Barkov *et al.*, Pis'ma Zh. Éksp. Teor. Fiz. **46**, 132 (1987) [JETP Lett. **46**, 164 (1987)].
18. V. A. Novikov *et al.,* Phys. Rep. **41**, 1 (1978).
19. L. Stanco, in *Proceedings of the International Conference on Hadron Spectroscopy "Hadron 91," College Park, Maryland,* Ed. by S. Onega and D. C. Peaslee (World Sci., Singapore, 1992), p. 84.
20. H. Albrecht *et al.,* Phys. Lett. B **185**, 223 (1987).
21. A. Donnachie and Yu. S. Kalashnikova, Z. Phys. C **59**, 621 (1993); A. Donnachie, Yu. S. Kalashnikova, and A. B. Clegg, Z. Phys. C **60**, 187 (1993); A. Donnachie and A. B. Clegg, Z. Phys. C **62**, 455 (1994); A. Donnachie and Yu. S. Kalashnikova, Phys. Rev. D **60**, 114011 (1999).

Translated by E. Rogalyov

Physics of Atomic Nuclei, Vol. 65, No. 1, 2002, pp. 161–169. From Yadernaya Fizika, Vol. 65, No. 1, 2002, pp. 167–175.
Original English Text Copyright © 2002 by Chernavskaya, Feinberg, Royzen.

ELEMENTARY PARTICLES AND FIELDS
Theory

"Free" Constituent Quarks and Dilepton Production in Heavy-Ion Collisions*

O. D. Chernavskaya[**], **E. L. Feinberg**[***], **and I. I. Royzen**[****]

Lebedev Institute of Physics, Russian Academy of Sciences, Leninskiĭ pr. 53, Moscow, 117924 Russia

Received October 9, 2000

Abstract—An approach is suggested that invokes vitally the notion of constituent massive quarks (valons) that can survive and propagate rather than hadrons (except of pions) within hot and dense matter formed below the chiral-transition temperature in the course of heavy-ion collisions at high energies. This approach is shown to be quite good for describing the experimentally observed excess in the dilepton yield at masses $250 \leq M_{ee} \leq 700$ MeV over the prompt-resonance-decay mechanism (CERES cocktail) predictions. In certain aspects, it appears to be even more successful than conventional approaches: it seems to match the data somewhat better at dilepton masses below the two-pion threshold and below the ρ-meson peak, as well as at higher dilepton masses (beyond the ϕ-meson one). The approach implies no specific assumptions on the special features of phase transitions in expanding nuclear matter, and the ideal gas approximation is motivated to be still workable for describing the pion–valonic system under consideration. © *2002 MAIK "Nauka/Interperiodica".*

1. INTRODUCTION

A few years ago, experimental evidence was obtained [1] that e^+e^- pairs (below referred to as dileptons) with invariant masses of $250 \leq M \leq 700$ MeV produced in the course of heavy-ion collisions at high energies are by far more numerous (up to a factor of about 5–7) than what could be predicted by directly summing the contributions of known mesonic-resonance decays (CERES cocktail), although a similar treatment of the dilepton yield in the proton–nucleus collisions was quite successful. Since then, many attempts have been made [2] to put forward a reasonable theoretical explanation of such a distinction. Generally, most of these attempts were based on the thermodynamical approach [3] supplemented with some assumptions on the kinetics and in-medium properties of hadronic resonances (changes in their masses and widths [2, 4]) in hot and dense matter (fireball) formed in the course of the heavy-ion collisions at high energies. It was demonstrated in [2] that, for a proper choice of resonance modifications (predominantly, of the ρ-meson width), a seemingly satisfactory agreement between the above experimental data and their theoretical treatment can be achieved. Unfortunately, relevant models inevitably suffer from the well-known underlying ambiguities—first of all, from a large extent of freedom in choosing the equation of state (EoS) and the in-medium particle mass operator. That is why their predictions are not undeniable and the elaboration of some alternative approaches seems to be not out of place.

The approach we are to discuss below is based on a microscopic picture of hot-fireball evolution, which necessarily implies the important role of massive constituent quarks [5] (following Hwa [6], we refer to them below as valons) at a certain stage of evolution. The notion of a valon was quite fruitfully exploited at the early age of the quark model and was almost forgotten upon the advent of elegant QCD, which makes it possible to deduce and predict many phenomena in terms of current (pointlike) quarks and gluons. Attempts at embedding valons rigorously into the framework of QCD as some quasibound color states of quarks and gluons were not successful [7], but, being physically very attractive, the notion of a valon was exploited nevertheless to furnish qualitative motivations in favor of one or another statement. Among them, we would like to mention, first of all, attempts at distinguishing between the hadronic breakdown temperature [8] and the chiral-symmetry-restoration temperature by considering either two successive phase transitions [9, 10] or gradual valonic-mass decrease as the temperature rises, being above the former one [11].

More detailed attempts at incorporating valons as certain phenomenological entities were made [12, 13]

*This article was submitted by the authors in English.

** e-mail: chernav@lpi.ru
*** e-mail: feinberg@lpi.ru
**** e-mail: royzen@lpi.ru

within the bag-model EoS of nuclear matter. Two first-order phase transitions were considered (instead of one within conventional models) in the course of fireball expansion: first, from the short phase of quark–gluon plasma (QGP) to the intermediate one (chiral symmetry breaking at $T_{\rm ch} \simeq 200$ MeV), which is rather short too (it lasts until quick cooling down to the Hagedorn temperature, $T_{\rm H} \simeq 140$ MeV, is completed), and, second, long and nearly isothermic transition (which is referred to as a mixed pion–valonic state by analogy with the conventional mixed QGP–hadronic state) from this phase to the short hadronic phase that ends by freeze-out at slightly lower temperature, $T_f \simeq 120$ MeV.

Being undoubtedly different, all these models (including conventional ones) show one common feature: the (mixed) phase preceding color confinement lasts much longer than the other ones, irrespective of the special features of a specific model. That is why one can reasonably believe that the substantial deceleration of expansion and the corresponding prolongation of the pion–valonic phase is inherent not only in all versions of the bag model—this qualitative effect is, most probably, a general and inevitable consequence of the need for meeting color confinement at low densities. In what follows, we keep this pattern in mind as a guideline. Thus, within our approach, just the pion–valonic phase of expansion (not the QGP one) is expected to be responsible for "extra dileptons" with low masses (over the CERES cocktail sample) seen at SPS: they can indeed be produced during this long phase in the course of numerous successive collisions of particles within the fireball. Being quite short, the hadronic phase can provide a resonance background (CERES cocktail) only.

The physical meaning of these phases in fireball evolution seems quite transparent [5], irrespective of whether a sharp or a soft phase transitions occurs, as well as of the specific time profile of the fireball temperature or of some other model-dependent features: chiral symmetry breaking (restoration) and color confinement (deconfinement) are assumed to happen under substantially different thermodynamic conditions. The valon can be thought of as a quasiparticle in a sense that it absorbs the most part of strong color interaction to form (within a suitable range of temperatures and densities) a nearly ideal (color-screened) valonic gas that is equivalent, in its physical manifestations, to the gas of strongly interacting conventional (free) hadrons or QCD (pointlike) quarks and gluons. One can deal with either of the above representations, but, of these two options, the former is obviously by far more comfortable for a theoretical treatment. Indeed, within a medium of density about the nucleon density (in which the nucleon bodies themselves would occupy the entire volume), the "equivalent" set of valon bodies (whose radius is supposed [14, 15] to be about three times smaller than the nucleon one) would occupy about 10% of the volume only. Therefore, even at noticeably higher densities (say, at the density that is assumed to appear at the chiral phase transition—about twice as high as the nucleon one or about four times higher than the density of nuclei), a gaseous approach to the treatment of valonic matter still seems reasonable. As usual, one has to pay for this simplification: a poorly determined entity—the cross section for valon–valon interaction—enters into relevant formulas inevitably. Below, a semiquantitative approximation is suggested that makes it possible to overcome this unpleasant obstacle.

It is worthy of note that, because of what is said above, precise and complicated calculations are unnecessary even at those points where they could indeed be performed, when the problem we are interested in is considered. That is why rather crude approximations that we shall exploit below are suitable.

2. GENERAL DESCRIPTION OF THE APPROACH

The following picture of fireball evolution is adopted:

(i) After cooling down to the temperature $T = T_{\rm ch}$, the QGP fireball undergoes a rather quick phase transition,[1)] which results in the formation of two-component (valonic and pionic) quasi-ideal gases in an equilibrium state,[2)] the relative content of each species being controlled by the detailed-balance principle; the only interaction is taken into account that converts $Q\bar{Q}$ valons into pions, and vice versa.

(ii) This state is maintained sufficiently long for copiously producing dileptons via successive particle interactions. As for "macroscopic" patterns (longitudinal and transverse flows), they are subjected, as usual, to a relativistic thermo- and hydrodynamical treatment. What we need here of all that is an estimate of duration of the pion–valonic phase. So long as, in the end, the need for color confinement

[1)] Nothing, except of temperature and baryon density, prevents the transformation of pointlike quarks and antiquarks into "dressed" ones (i.e., into the valons and antivalons, Q and $\bar{Q}$). That is why valons are reasonably expected to appear, under proper conditions, almost instantly.

[2)] The pions are the only hadrons that have a good chance to survive within the medium at this stage because the binding energy of valons coupled to form a pion, $2m_Q - m_\pi \simeq 500$ MeV, substantially exceeds the temperature. Although the time of chemical equilibration within the fireball is, most probably, somewhat longer than that of the chiral phase transition itself, it is comparatively short too [16].

at low densities is motivated above to be responsible for its prolongation, no reasons seem to be put forward for the appearance of a substantial difference in this respect between the suggested approach and conventional or bag-model treatments. That is why the corresponding estimates given by the latter ones [12, 13, 17] will be quoted for orientation.

(iii) Mesonic resonances are expected to be nearly melted [18] over almost the entire duration of the pion–valonic phase in the sense that their effective widths are crucially influenced by the inverse mean free time $\bar{t}^{-1}$, which is undoubtedly greater than the relevant intrinsic widths Γ_i.[3)] That is why dileptons produced under such conditions in the reactions $\pi^+\pi^- \to e^+e^-$ and $Q\bar{Q} \to e^+e^-$ are to be treated reasonably as a kind of a nonresonance multicollision (transport) contribution (just what we are here to deal with), which should be added to dileptons originating from "normal" mesonic-resonance decays (CERES cocktail) at the final stage of expansion (when these resonances can survive). The heavier the colliding nuclei and the higher the degree of centrality of an observed collision, the greater the number of these transport dileptons.[4)]

The general strategy of the calculations looks as follows:

(i) The total numbers of pions, N_π, and valons, N_Q and $N_{\bar{Q}}$, within the fireball are linked by using the detailed-balance principle.

(ii) The rate of the reactions $\pi^+\pi^- \to e^+e^-$ and $Q\bar{Q} \to e^+e^-$ is estimated as a function of M and N_π. Being multiplied by the entire duration of fireball expansion from the temperature $T_{\rm ch}$ to the temperature T_f, it gives the total yield of dileptons produced via pionic and valonic collisions.

(iii) N_π is linked to $N_{\rm ch}$, the total number of charged hadrons coming from the fireball after freeze-out, and the general formula is adopted for comparing the results of the calculations and experimental data.

(iv) The results obtained are contrasted against available data on the production of low-mass dileptons, as well as against the results of some conventional approaches.

3. NOTATION

The following notation is used:

$d\nu_Q^w/dt$ is the rate of "white" $Q\bar{Q}$ collisions in which colors of Q and $\bar{Q}$ are canceled to produce a color-singlet state;

$d\nu_\pi/dt$ is the rate of $\pi^+\pi^-$ and $\pi^0\pi$ collisions;

$d\nu_Q^{w0}/dt$ and $d\nu_\pi^0/dt$ are the rates of collisions selected from the above ones in which the particles involved necessarily have opposite (and nonzero) electric charges;

$\lambda = [N_Q/N_{\bar{Q}}]^{1/2} \simeq \exp(\mu_Q/T)$, μ_Q being the chemical potential of u and d valons, is the valon fugacity;

$b = N_\pi/(N_Q + N_{\bar{Q}})$;

$\bar{t}$ and τ are, respectively, the mean free time of particles within fireball and the duration of fireball cooling from the temperature $T_{\rm ch}$ to the temperature $T_{\rm H}$.

4. CALCULATIONS

1. Being averaged over the particle distributions, the detailed-balance principle reads

$$\nu_Q^w(T)\overline{\Omega_\pi}(T) \simeq \nu_\pi(T)\overline{\Omega_Q}(T), \qquad (1)$$

where $\overline{\Omega_i}$ are the mean values of the corresponding final-state phase spaces. Below, the binary reactions are to be considered only because $2 \to 4$ reactions are substantially suppressed by scarcity of the typical thermal final-state phase space at $T < T_{\rm ch}$, and 3 (or more) $\to$ anything reactions are rather rare events at the typical particle densities under consideration (however, see the discussion below). Moreover, we restrict ourselves, for a while, to the two lightest flavors ($N_f = 2$) because of the low concentration of s quarks: their number is believed to be about [19] $(0.25–0.5)\exp[(m_{u,d} - m_s)/T] \simeq 10\%$ of the number of $(\bar{u} + \bar{d})$ quarks; thus, the relevant corrections are obviously within the very accuracy of the suggested approach.

Since each antiquark of certain color and flavor can encounter, with the same probability, λ^2 quarks and one antiquark ($2N_c$ species of each of them) and b pions for each of them, of which only two species are suitable to build a color singlet state,

$$d\nu_Q^w(T) = \frac{\lambda^2 N_{\bar{Q}}}{(\lambda^2+1)(1+b)N_c}\frac{dt}{\bar{t}(T)}. \qquad (2)$$

[3)] Since $T > T_{\rm H}$, the mean free time (path) must be shorter than or about 1 fm (the radius of valonic confinement or of hadronization); the effective width of each resonance thus decreases along with the evolution of the intermediate phase to become finally $(\bar{t}^{-1} + \Gamma_i) \simeq 200$ MeV $+ \Gamma_i$.

[4)] The dileptons originating from processes of the bremsstrahlung type make virtually no contribution to the part of the dilepton mass spectrum under discussion. Indeed, typical masses of bremsstrahlung virtual photons emitted by pions or u and d valons are wittingly lower than m_π or m_Q, respectively, thus being, in any case, lower than 300 MeV (in fact, only photons of much lower masses are noticeable). As for heavier valons, yes, they could emit such heavy photons (especially, c, b, and t ones), but their relative concentration itself is by far too low and one can undoubtedly disregard the relevant dilepton yield.

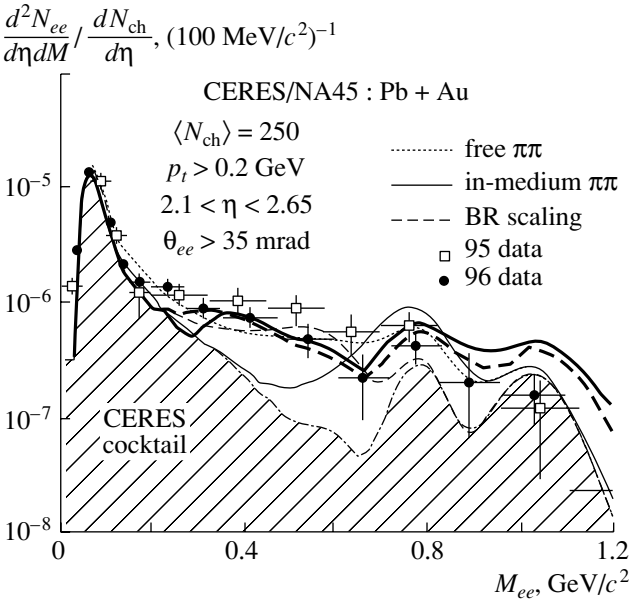

Fig. 1. Low-mass dilepton (e^+e^-) yield. Our results (bold solid and bold dashed curves refer to $m_\pi = 140$ MeV, $\tau/\bar{t} = 20$ and $m_\pi = 100$ MeV, $\tau/\bar{t} = 30$, respectively; $\sigma_0 = 10$ mb, $\Delta = 0.2$ GeV) are contrasted against the entire bulk of CERES dilepton data [1] and the predictions of thermal dilepton calculations quoted in [2, 24].

Quite similarly, a π^0 meson encounters another π meson with the probability $\dfrac{1}{(1+b^{-1})}\dfrac{dt}{\bar{t}}$, the total rate of $\pi^0\pi$ collisions being, therefore, $\dfrac{2N_\pi}{9(1+b^{-1})}\dfrac{dt}{\bar{t}}$ ($\pi^0\pi^\pm$ collisions) plus $\dfrac{N_\pi}{18(1+b^{-1})}\dfrac{dt}{\bar{t}}$ ($\pi^0\pi^0$ collisions); the rate of $\pi^+\pi^-$ collisions is obviously $\dfrac{N_\pi}{9(1+b^{-1})}\dfrac{dt}{\bar{t}}$. Of course, $\pi^+\pi^+$ and $\pi^-\pi^-$ collisions are out of the game in the detailed-balance equation (within the above approximation), since they never result in a two-valonic final state. Thus, for the total rate of $\pi\pi$ collisions to be taken into account, one gets

$$d\nu_\pi(T) = \frac{7}{18}\frac{bN_\pi}{1+b}\frac{dt}{\bar{t}(T)}. \qquad (3)$$

The valonic and pionic phase spaces are

$$\overline{\Omega_Q}(T) \simeq 4(2S_Q+1)^2 N_c \overline{p_Q^2}(T) \qquad (4)$$

(5)

and

$$\overline{\Omega_\pi}(T) \simeq (2I_\pi+1)^2 \overline{p_\pi^2}(T),$$

respectively, where S_Q is the valonic spin, I_π is the pionic isospin, $p_Q(p_\pi)$ is the valon (pion) momentum in the c.m. frame of two interacting valons (pions), and N_c appears here instead of N_c^2 since only the color-singlet sector of the total phase space of two valons is taken into account. Straightforward averaging over the Boltzmann distribution gives the mean value of the square of the energy of a particle of mass m,

$$\overline{E^2(m,T)} = T^2\left[3\frac{m}{T}\frac{K_1(m/T)}{K_2(m/T)} + 12 + \frac{m^2}{T^2}\right],$$

where $K_{1,2}$ are the corresponding Bessel functions. The c.m. value of $\overline{p_\pi^2}$ ($\overline{p_Q^2}$) for each particle in the pionic (valonic) final state is obtained obviously by inserting $m = m_Q$ into this expression ($m = m_\pi$), subtracting m_π^2 (m_Q^2), and taking half of this difference. Within the temperature range we are interested in, the ratio of these values varies slowly and it (namely, the ratio of the mean value of pion momentum squared to that of the valon momentum squared) is about two at the temperature of $\bar{T} \simeq 160$ MeV, which will be exploited in what follows as a certain effective mean temperature instead of the current one. Making use of the above notation and combining Eqs. (1)–(4), we obtain

$$b \simeq 0.6\frac{\lambda}{(\lambda^2+1)} \leq 0.3. \qquad (6)$$

Since the fraction of "large" pions (as compared to "small" valons) is relatively small (at the reasonable value of λ, $\lambda \simeq \sqrt{3}$, that refers to $\mu_Q \simeq 80$ MeV, one has $b \simeq 0.24$), the motivation in favor of the applicability of the gaseous approximation given above for the purely valonic medium remains valid. It is also worthy of note that this chemically equilibrium ratio of valons and pions corresponds to what would be obtained if they were considered as being ideal noninteracting gases. This fact makes it possible, at least, to be sure that the rather crude and idealized gaseous approach to the problem under consideration is not controversial.

2. The rates of "white" collisions with zero total electric charge, which can produce dileptons via the virtual photon intermediate state, are estimated quite similarly:

$$d\nu_Q^0 = 0.5 d\nu_Q, \quad d\nu_\pi^0 = \frac{b}{9(1+b)}\frac{dt}{\bar{t}}. \qquad (7)$$

It is easy to check that the probability dW/dM of a two-particle collision with the invariant mass (the total energy in their c.m. frame) M is (in the approximation of ideal Boltzmann gas [5)])

[5)] There is no reason to refine it by taking into account Bose and Fermi statistics of pions and valons, respectively, in view of a poor accuracy and specific kinematical selection (see below) of available experimental data.

$$\frac{dW}{dM} = \frac{M}{8}\int\limits_{M}^{\infty} e^{-\xi/T}d\xi \int\limits_{0}^{\sqrt{(\xi^2-M^2)(1-4m_i^2/M^2)}} (\xi^2-\eta^2)d\eta \Bigg/ \left[\int\limits_{0}^{\infty} p^2 e^{-\sqrt{p^2+m_i^2}/T}dp\right]^2, \quad (8)$$

where $i = Q, \pi$ and ξ and η are, respectively, the sum and difference of colliding particle energies.[6)]

3. To compare the above approach straightforwardly with experimental data on dilepton production, one should link the numbers of pions and valons within the fireball and the number of observed charged particles. This relation is suggested to be

$$N_{\rm ch} \simeq \frac{2}{3}N_\pi + 2N_{\bar{Q}} + 0.4N_B, \quad (9)$$

where

$$N_B = \frac{1}{3}(\lambda^2-1)N_{\bar{Q}}^{u+d} \simeq \frac{1}{3}(\lambda^2-1)N_{\bar{Q}}$$

is the fireball total baryon number and, thus, $0.4N_B$ is approximately equal to the proton outcome from the fireball (in accordance with the approximate ratio of protons and neutrons in heavy-ion collisions). Equation (8) also implies that, in course of thermally equilibrium hadronization, the number of decoupled pions emitted from the fireball is nearly equal to the number of pions coupled within it and that each $Q\bar{Q}$ pair produces about two charged pions (actually, about three pions, the third being neutral).

Now, combining Eqs. (5)–(8), we arrive at the basic formula for the excess in the dilepton yield, which is to be compared with observations:

$$\frac{1}{N_{\rm ch}}\frac{dN_{ee}}{dM} \simeq \frac{0.1\lambda^2(1+0.6\lambda+\lambda^2)^{-1}}{4.7+\lambda+0.33\lambda^2} \times \frac{\tau}{\bar{t}}\left[\frac{dW_{\pi\pi}}{dM}\frac{\sigma_{\pi\pi\to ee}}{\sigma_{\pi\pi}^{\rm tot}} + 4\frac{dW_{Q\bar{Q}}}{dM}\frac{\sigma_{Q\bar{Q}\to ee}}{\sigma_{Q\bar{Q}}^{\rm tot}} + \beta\times(\text{the previous term where } Q_s \text{ appears instead of } Q\equiv Q_{u,d})\right]. \quad (10)$$

Here, $\sigma_{Q\bar{Q}}$ stands for the half-sum of the cross sections for $Q_u\bar{Q}_u$ and $Q_d\bar{Q}_d$ annihilation into e^+e^-; $\sigma_{\pi\pi}^{\rm tot}$ and $\sigma_{Q\bar{Q}}^{\rm tot}$ stand for the corresponding total cross sections; and β takes into account the relative rate of strange-valon collisions, $\beta \simeq 0.1$ (see above). The relative effectiveness of the latter ones in dilepton production is still about 1.7 times lower,[7)] thus being about 6% of the light quark one. That is why the strange-valon contribution is neglected below. Of course, Eq. (9) could be reformulated to take a more traditional form (for the latter, see [20]), by making use of the above relations and the well-known definition $\sigma_i^{\rm tot}\bar{t}_i\sqrt{2} \simeq n_i^{-1}$, where n_i is the number density of the ith particle species and $\sigma_i^{\rm tot}$ and $\bar{t}_i$ are the relevant cross section and mean free time, respectively. The chosen way of description is preferred here deliberately to avoid unnecessary complications. Moreover, its physical meaning seems more transparent, whereas the drawbacks of two ways of description are essentially equivalent (poorly defined $\pi\pi$ and $Q\bar{Q}$ total cross sections in the one given here and equally poorly defined corresponding in-medium ρ-meson electromagnetic form factor which would enter inevitably into the usually exploited formulas).

Two general results can be deduced from Eq. (9) right away, before going into more detailed calculations. First, the mean number of successive interactions of a particle over the fireball evolution time, $\tau/\bar{t}$, is the only factor on the right-hand side of Eq. (9) that depends on $N_{\rm ch}$: $\tau \sim V \sim N_{\rm ch}$ and $\tau \sim V^{1/3} \sim N_{\rm ch}^{1/3}$ in the limiting cases of, respectively, one-dimensional (longitudinal) and three-dimensional (spherical) expansion of the fireball (V is the fireball volume at the freeze-out temperature); thus, Eq. (9) apparently admits the trend $N_{ee} \sim N_{\rm ch}^2$ observed in the SPS experiments [21]. Second, the predicted excess in the dilepton yield is almost insensitive to the choice of valon chemical potential within the range $0 \le \mu_Q \le 80$ MeV, since the corresponding variation of the λ-dependent factor on the right-hand side of Eq. (9) does not exceed 20%.[8)]

[6)]The nominator here is nothing but the product of the momentum distributions of two independent particles in the c.m. frame of a small volume dV (where they are assumed to be spherically symmetric) integrated with the factor $\delta[(p_1+p_2)^2-M^2]$, whereas the denominator takes into account the normalization.

[7)]This coefficient appears as the interplay of two factors: the ratio of quark electromagnetic charges squared, $(e_u^2+e_d^2)/2e_s^2 = 2.5$, and the ratio $\sigma_{Q\bar{Q}}^{\rm tot}/\sigma_{Q_s\bar{Q}_s}^{\rm tot}$ estimated, from a comparison of the πp and the Kp cross sections, to be nearly equal to 1.5.

[8)]However, at lower energies (AGS, SIS), when this potential is expected to be considerably higher, its influence should result in quite observable (about two times) reduction of the dilepton excess in collisions of the same nuclei as compared to the SPS one. At the same time, it should be noted that a similar effect comes from a decrease in the ratio $\tau/\bar{t}$ at overly low energies, when the fireball initial temperature T_i is lower than $T_{\rm ch}$.

The most vulnerable point of formula (9) is the ratio of the above cross sections. It can be estimated within the framework of the following reasoning. The resonance irregularities (mostly, the ρ-meson one) in the cross section of dilepton production and in the total one are expected to be of similar (the same within VDM) shape [22] and cancel each other to a considerable extent. That is why the background contributions (namely, they are meant under the letter σ below) are to be compared only. Thus, we have

$$\sigma_{\pi\pi\to ee} \simeq \frac{4\pi\alpha^2}{3M^2}, \quad \sigma_{Q\bar{Q}\to ee} \simeq \frac{10\pi\alpha^2}{27M^2}.$$

The total cross sections for $Q\bar{Q}$ and $\pi\pi$ interactions can be estimated, obviously, only in terms of plausibility and similarity to the known hadronic ones. We assume that, in spirit of the suggested approach, each of u and d valons (antivalons) interacts (strongly) as if it were "1/3 of the proton" (antiproton). Since the cross section for $p\bar{p}$ interaction [23] exhibits almost no resonance structure and can be fitted pretty well (at not overly high c.m. energies E_c) in terms of the simple phenomenological formula[9)]

$$\sigma_{p\bar{p}}(E_c) - 40\ \text{mb} \simeq \frac{24\ \text{mb}}{\sqrt{E_c/(2m_p) - 1}}, \qquad (11)$$

one can expect that the corresponding cross section for the interaction of a light valon and a light antivalon respects approximately the formula

$$\sigma_{Q\bar{Q}}(M) - 9\ \text{mb} \simeq \frac{5.4\ \text{mb}}{\sqrt{M/(2m_Q) - 1}}, \qquad (12)$$

where the $Q_{u,d}\bar{Q}_{u,d}$ cross section at the c.m. energy $M = E_c/3$ is estimated to be about 0.22 (instead of 1/9) of the $p\bar{p}$ one at the c.m. energy E_c, approximately 50% shadowing in the $p\bar{p}$ interaction being taken into account.[10)]

This way of reasoning is not applicable immediately to linking the shapes of the $p\bar{p}$ and $\pi^+\pi^-$ total cross sections, first of all, because the former reaction is exothermic[11)] (just like the $Q\bar{Q}$ one), whereas the latter one is not; therefore, the above cross sections differ substantially in their threshold behavior. Nevertheless, available experimental data show unambiguously a general trend of all the known hadronic cross sections (apart from their resonance structure, i.e., averaged with respect to it—namely, of their background components that are just relevant) to increase gradually toward the threshold (except for, maybe, a very narrow domain in the close vicinity of the threshold). Compiling the data, one can conclude that these cross sections show a two- to threefold decrease as the c.m. energy increases by about 1 GeV above the threshold and that they approach almost constant values as the energy exceeds substantially the sum of the interacting-particle masses. It seems reasonable to assume that the same is qualitatively true for the background component of the $\pi^+\pi^-$ cross section as well. That is why the following formula can be proposed:

$$\sigma_{\pi\pi}(M) - \sigma_0 \simeq \frac{3\sigma_0\Delta}{\sqrt{M/(2m_\pi) - 1} + \Delta}. \qquad (13)$$

Here, $\sigma_0 \simeq 10$–15 mb is the high-energy value of $\sigma_{\pi\pi}$ and $0.2 \le \Delta \le 1$, a somewhat low value of Δ from this interval seeming rather more suitable because of the relatively small pion mass.

4. After insertion of Eqs. (11)–(13) into the basic Eq. (9), we are almost ready to compare the approach with data. What remains to be done is to adapt formula (7) to the specific conditions of the measurements, i.e., to take into account the fact that only leptons, e^+ and e^-, with transverse momenta of $p_T > 200$ MeV were selected in all data and that a further selection of data into two groups incorporating events where the dilepton total transverse momenta are $200 < q_T < 500$ MeV and $q_T > 500$ MeV, respectively, was made. These restrictions are taken into account approximately: the limits of integration with respect to ξ in Eq. (7) are chosen to allow for the above conditions on average (i.e., these limits correspond to a "typical dilepton" built up of two leptons whose momenta are averaged over their relative directions and over their absolute values). As a result,

$$\max[M, p_T\sqrt{6} \simeq 0.5\ \text{GeV}], \quad p_T = 0.2\ \text{GeV},$$

appears instead of M for the lower limit and

$$\sqrt{M^2 + \frac{3}{2}q_T^2}, \quad q_T = 0.5\ \text{GeV},$$

stands for the upper (lower) limit for $q_T < 0.5$ GeV ($q_T > 0.5$ GeV) events.

Below, the results of the suggested approach are compared with the experimental data and with the theoretical predictions obtained within some conventional theoretical approaches.

[9)] This formula corrected by multiplying of its right-hand side by the factor $(E_c/2m_p)^{-0.4}$ (which is of no importance within the energy range of our interest here) smoothly interpolates between the threshold behavior of the total $p\bar{p}$ cross section and its high-energy parametrization [23] motivated by the Regge approach.

[10)] This qualitative estimate emerged from the observation that total πp and pp cross sections at the relevant energies are more likely in the ratio 5 : 6 [23] than in the ratio 2 : 3, which would be expected if there were no shadowing at all. By the way, Eq. (11) is coordinated pretty well with the (also qualitative) estimate that $Q\bar{Q}$ total cross section at c.m. energy of a few GeV should be on the order of the confinement radius squared, i.e., about 1 fm$^2 \simeq 10$ mb.

[11)] That is why the simplest interpolation of the form $\sim(E_c - 2m_p)^{-1/2}$ fits its cross section fairly well.

5. DISCUSSION AND CONCLUDING REMARKS

At first glance, a doubt could be expressed that the valons play a significant role in the production of dileptons with masses of $M \leq 2m_Q \simeq 660$ MeV, which are just of primary interest here, since they do not produce these dileptons directly. However, this is not correct: they do play this role because they directly affect the number of pions within the fireball and the number of charged particles in the final state; therefore, their influence on the ratio of dileptons to charged particles is quite unambiguous.

Unfortunately, we cannot extract, from our results, direct information about the duration of fireball expansion, τ, and about the mean free time $\bar{t}$ separately because the dilepton yield is proportional to their ratio only. The curves presented in Figs. 1 and 2 are obtained under the condition that $\tau/\bar{t} = 20$ or 30 for free pions ($m_\pi = 140$ MeV) or "in-medium" pions ($m_\pi = 100$ MeV), respectively. At the same time, a quadratic growth of the total dilepton yield in relation to the charged particle one, $N_{ee} \sim N_{\rm ch}^2$, which was drawn [21] from the CERES data, is a piece of evidence in favor of predominantly longitudinal fireball expansion at the SPS energies. The well-known estimates predict, in this case, a rather long expansion time [13, 17]. If one adopts a reasonable estimate for the mean free time, $\bar{t} \simeq 0.7$–1.0 fm, then the duration of the pion–valonic phase (which is nearly equal to the entire duration of fireball expansion) is $\tau \simeq 15$–20 or 20–30 fm for free or in-medium pions, respectively. These values are compatible with what was predicted, the latter seeming somewhat preferable.

At the same time, owing to a considerable enhancement of the pressure within the fireball, along with an increase in its energy density predicted within the hydrodynamical model, the role of transverse flow increases too; thus, the three-dimensional pattern of fireball expansion is expected to become substantially more pronounced in RHIC and LHC collisions. As a result, a certain modification in the functional form of the above correlation is expected to be observed, the degree of 2 there gradually decreasing toward that of 4/3 (which refers to spherical expansion). Thus, at RHIC, one can expect a noticeably slower rise of the excess in the dilepton yield over the CERES cocktail sample than would be predicted by a careless extrapolation of the longitudinal-expansion models (say, than approximately 4.5-fold in relation to SPS if one assumes that $N_{\rm ch} \sim E_c^{1/2}$).

Within the suggested approach, three-particle collisions were neglected. This approximation can be justified only if the mean interaction time (about the particle size) is much shorter than the mean free time (about the mean free path). One has to agree that the above estimate of a reasonable value of the mean free time, $\bar{t} \simeq 0.7$–1.0 fm, does not meet this requirement completely even for valons of size about 0.3 fm. A typical diagram that refers to three-particle collision is shown in Fig. 3. Intervention of a third particle (labeled as 3) results, apparently, in some dispersion of the dilepton mass around its only value that would be prescribed by the energy conservation law if only two particles collided. In turn, this results in smoothing the irregularities (kinks, dips, or bumps), if they are inherent in the dilepton mass spectrum predicted by two-particle collision kinematics. In particular, the dip in the spectrum below the two-pion threshold obtained in the two-particle collision approximation (see Fig. 2*a*) could be flattened, to some extent, by this smoothing. However, the relevant corrections are hardly sufficient to level this dip completely—we mean quite a probable minimum also seen there in the

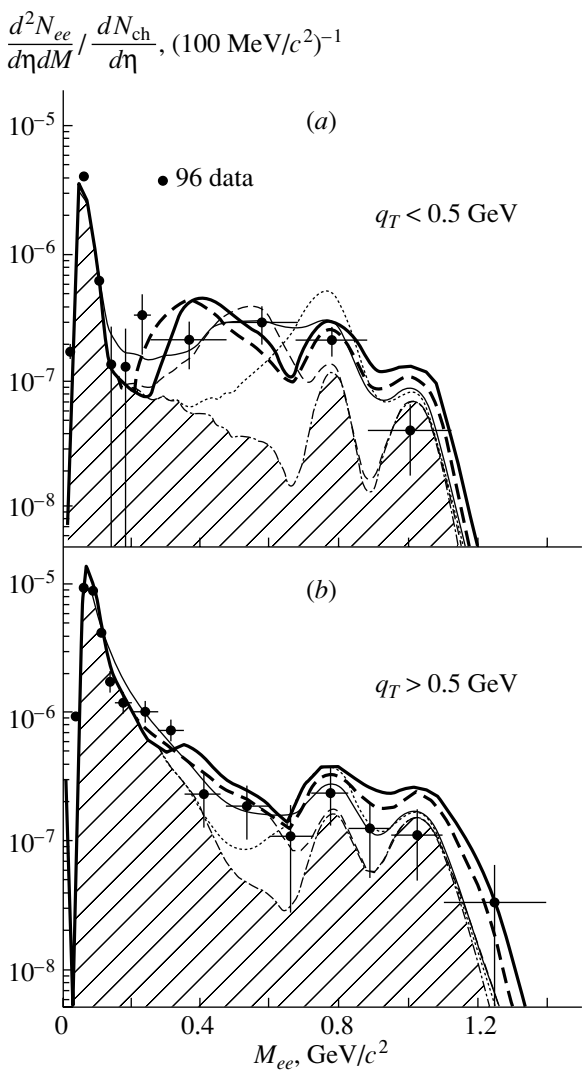

Fig. 2. As in Fig. 1, but for two q_T-selected groups of data.

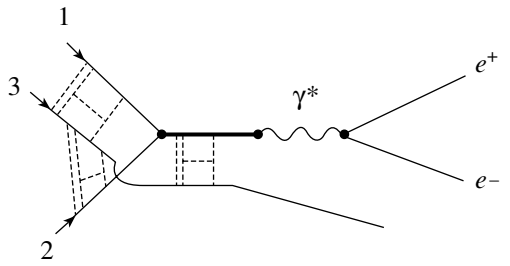

Fig. 3. A typical diagram of three-particle collision. It shows that intervention of the "third" particle can affect the mass of the produced dilepton pair to shift it up or down. In particular, this mass can occur below the physical threshold of the corresponding two-particle $(1+2)$ reaction. A very likely minimum before the two-pion threshold seen in Fig. 2*a* is indicative of the conclusion that the contribution of three-particle collisions to the dilepton yield is rather small.

data specially selected to emphasize the contribution of pion–pion collisions.

At the same time, Fig. 1 shows that the occurrence of a noticeable dip below the $2m_\pi$ threshold is apparently predicted in the entire bulk of data if the in-medium pion mass is equal to the free one, whereas virtually no visible dip is predicted if an effective lowering of this mass is qualitatively taken into account by setting it to 100 MeV. That is why a significant refinement of the data within this mass region is asked anxiously, because this can provide valuable information about the properties of dense and hot matter that might be even more important than the dilepton yield itself. In particular, it can be correlated with the properties of the chiral transition. As for the properly selected events, $q_T \leq 500$ MeV (see Fig. 2), we would like to point out again that this dip is quite apparently predicted by either of the above versions of the theoretical approach suggested, in contrast to the conventional ones. Again, allowance for a some decrease in the in-medium pion mass seems fruitful [although three-particle interaction could be responsible too (see above) for a slight shift to the left of the minimum suggested by the data from the position predicted by the free-pion-mass version of the approach presented].

The predicted yield of dileptons with $M_\rho \leq M \leq M_\phi$ looks slightly overestimated (see Figs. 1 and 2). However, this excess (if it can be taken seriously into consideration in view of overly poor accuracy of the data), which is undoubtedly due to $Q\bar{Q}$ annihilation, may be rather illusory: in particular, at the ϕ-meson peak, experimental points are even slightly lower than they are expected to occur according to the estimate of the prompt-resonance (CERES cocktail) contribution itself, which seems unreasonable. This disparity can be taken as a hint that something here may suffer from a systematic error. If this is so, then the agreement between our predictions and the data is improved, irrespective of what—data or CERES cocktail—is to be corrected, since what we have calculated is just the expected excess in the observed dilepton yield over the CERES cocktail sample. At still higher dilepton masses, both the data and our results (unlike the other ones) show a quite compatible excess over this sample (see Fig. 2*b*), which is undoubtedly due to $Q\bar{Q}$ annihilation.

An advantage of the suggested approach is that its physical meaning and internal structure are very transparent and open for discussion, tracing, and corrections, since no complicated generators are involved: almost all the calculations are quite simple to perform approximately by hand.

Summarizing what was said above, we conclude that the low-mass spectrum of dileptons produced in the course of heavy-ion collisions can be understood in quite a natural way in terms of the pion–valonic contents of expanding hot and dense matter (fireball) below the chiral transition temperature. The above consideration showed, however, that dilepton production is affected by a number of factors and that some of them could be estimated rather semiquantitatively. Thus, we are supplied again with an insight on fruitfulness of using the notion of a valon, although the suggested pieces of evidence in favor of its right to be acknowledged as a real physical object are still far from being decisive.

ACKNOWLEDGMENTS

The authors are indebted to N.G. Polukhina for her valuable help in composing the figures.

This work was supported by the Russian Foundation for Basic Research (project nos. 96-15-96798 and 00-02-17250).

REFERENCES

1. CERES Collab. (G. Agakichiev *et al.*), Phys. Rev. Lett. **75**, 1272 (1995); Phys. Lett. B **422**, 405 (1998).
2. R. Rapp, Nucl. Phys. A **661**, 33c (1999) and references therein.
3. E. L. Feinberg, Nuovo Cimento **34**, 391 (1976); Usp. Fiz. Nauk **139**, 3 (1983) [Sov. Phys. Usp. **26**, 1 (1983)] and references therein.
4. B. Friman, Nucl. Phys. A **610**, 358c (1996) and references therein.
5. E. L. Feinberg, in *Proceedings of the International Conference "Relativistic Heavy Ion Collisions,"* Ed. by L. P. Chernai and D. D. Strottman (World Sci., Singapore, 1991).
6. R. Hwa, Phys. Rev. D **20**, 2838 (1979).
7. K. G. Wilson, Phys. Rev. D **10**, 2245 (1974).
8. R. C. Hagedorn, Nuovo Cimento Suppl. **3**, 147 (1956).

9. O. K. Kalashnikov and V. V. Klimov, Phys. Lett. B **88B**, 328 (1979).
10. E. V. Shuryak, Phys. Lett. B **107B**, 103 (1981).
11. A. V. Bochkarev and M. E. Shaposhnikov, Nucl. Phys. B **268**, 220 (1986).
12. J. Cleymans, K. Redlich, H. Satz, and E. Suhonen, Z. Phys. C **33**, 151 (1986); D. V. Anchishkin, K. A. Bugaev, and M. I. Gorenstein, Z. Phys. C **45**, 687 (1990); S. P. Baranov and L. V. Fil'kov, Z. Phys. C **57**, 149 (1993).
13. O. D. Chernavskaya and E. L. Feinberg, in *Proceedings of International Conference "Hot Hadronic Matter: Theory and Experiment"*, Ed. by J. Letessier and J. Rafelski (Plenum, New York, 1995); J. Mosc. Phys. Soc. **6**, 37 (1996).
14. V. V. Anisovich *et al.*, Usp. Fiz. Nauk **143**, 501 (1984) [Sov. Phys. Usp. **27**, 901 (1984)].
15. B. L. Ioffe and V. A. Khoze, *Hard Processes* (North-Holland, Amsterdam, 1984), Vol. 1.
16. U. Heinz, Nucl. Phys. A **661**, 140c (1999).
17. R. Stock, Nucl. Phys. A **661**, 282c (1999) and references therein.
18. V. L. Eletsky *et al.*, Eur. Phys. J. A **3**, 381 (1998); Nucl. Phys. A **661**, 514c (1999).
19. J. Sollfrank *et al.*, Nucl. Phys. A **638**, 399c (1998).
20. G. Gale and J. Kapusta, Phys. Rev. C **35**, 2107 (1987).
21. J. Stachel, *Talk at the CERN Seminar*, Feb. 10, 2000.
22. F. M. Renard, *Basics of Electron-Positron Collisions* (Edition Frontières, Giv-surf Yvette, 1981), Chap. 6; H. Joss, in *Proceedings of the Heidelberg International Conference on the Elementary Particles, Amsterdam, 1967*.
23. Particle Data Group (R. M. Burnett *et al.*), Phys. Rev. D **54**, 1 (1996).
24. R. Rapp, *Talk at the International Conference "Quark Matter'99," Torino, Italy, 1999*.

Physics of Atomic Nuclei, Vol. 65, No. 1, 2002, pp. 170–181. Translated from Yadernaya Fizika, Vol. 65, No. 1, 2002, pp. 176–187.
Original Russian Text Copyright © 2002 by Rapoport, Turundaevsky, Shestoperov.

ELEMENTARY PARTICLES AND FIELDS
Theory

Comparison of Features of High-Energy Proton and Alpha-Particle Interactions with C, Fe, and Pb Nuclei in Various Models

I. D. Rapoport, A. N. Turundaevsky*, and V. Ya. Shestoperov

Institute of Nuclear Physics, Moscow State University, Vorob'evy gory, Moscow, 119899 Russia
Received October 25, 2000; in final form, March 30, 2001

Abstract—The results that the FLUKA, GHEISHA, and QGSM codes produce for the features of hadron interactions are compared with one another and with experimental data. Distinctions between hadronic cascades computed in lead and iron on the basis of the different codes are analyzed. The possibility of using model concepts underlying the codes in question at energies above 1 TeV is considered.
© *2002 MAIK "Nauka/Interperiodica".*

INTRODUCTION

The GEANT package [1], involving an exclusive description of cascade processes, which makes it possible to determine mean cascade features and their fluctuations, is extensively used to simulate nuclear cascades in matter. The existing GEANT versions include various codes generating inelastic nuclear interactions and relying on the results of accelerator experiments. However, advancements toward the region of higher energies present a challenge in testing these codes. In order to employ, for this purpose, data from collider experiments on proton–proton and proton–antiproton interactions, it is necessary to describe adequately intranuclear processes in hadron–nucleus and nucleus–nucleus interactions.

There are also difficulties in the region of accelerator energies proper. Frequently, accelerator experiments do not record neutral secondaries, with the result that many features that are of importance for simulating cascade processes—for example, the partial inelasticity factor K_γ, its fluctuations, and the spectrum of product photons—cannot be normalized to experimental data.

In view of this, it is advisable to perform a comparative analysis of conceptually different codes for generating hadron interactions, with reference to relevant energy dependences, because this aspect is of paramount importance for simulating cascades in matter and for comparing the results obtained from such simulations with available experimental data.

*e-mail: ant@eas.npi.msu.ru

1. COMPARISON OF FEATURES OF AN INTERACTION EVENT AT ACCELERATOR ENERGIES IN DIFFERENT MODELS

1.1. Model Concepts of Hadron Interactions

According to approaches to describing processes of hadron–nucleus interaction, the class of codes generating such processes can be partitioned, by convention, into two subclasses. The first includes generators employing phenomenological models based on approximations of experimental data on hadron–nucleus interactions at comparatively low energies (below 400 GeV) and on hadron–hadron interactions implemented at colliders (below $\sqrt{s} = 900$ GeV). Within models underlying generators that form the other subclass, an event of hadron–nucleus interaction is treated as a set of hadron–nucleon interactions described within various model concepts. The codes being discussed can consist of conceptually dissimilar parts employing different approaches to describe different processes.

In our comparative analysis, we consider the GHEISHA [1, 2] and the FLUKA [1, 3, 4] generators of hadron interactions (they are contained in the modern version of the GEANT 3.21 package) and the QGSM [5, 6], which belongs to a different class of codes.

The phenomenological code GHEISHA [1, 2], which is the fastest one, belongs to the first subclass. It is based on a direct approximation of accelerator data (multiplicity, inelasticity factor) on hadron–hadron and hadron–nucleus interactions. In this code, the number of secondaries generated in an interaction event is bounded by a value chosen by convention ($N < 100$). This is a purely technical feature,

but it imposes some limitations on the potential of the code.

The FLUKA code, which is based on the model of dual topological unitarization [1, 3, 4], belongs to the second subclass of models. According to this model, hadron–hadron collisions result in the formation of two strings, which then fragment into secondary hadrons. String fragmentation into hadrons is described by the special code BAMJET, which is based on an analysis of experimental data [7]. In the case of hadron–nucleus interaction, the impact parameter and the distribution of nucleons in the target nucleus are varied at random. The code determines the types of secondary hadrons and their momentum distributions, along with some sort of spacetime description of particle formation. A particle-formation time τ that is constant in the particle rest frame is introduced in the code; a secondary hadron can undergo interaction only at the distance $l = c\beta\gamma\tau$ from the production vertex ($\beta = v/c$, and γ is the Lorentz factor for a given particle). At the same time, the correlation between the multiplicity of low-energy nucleons knocked out in the developing intranuclear cascade, on one hand, and the number of nucleons hit by the incident hadron, on the other hand, is taken into account empirically [4]. The interactions of particles whose momenta lie in the region extending up to 5 GeV/c are simulated with the aid of the dedicated code HADRIN [8]. By varying the parameters of the code, it is possible to obtain secondary-particle distributions that are compatible with available experimental data [9].

It should be indicated that nucleus–nucleus interactions cannot be simulated on the basis of the GHEISHA and FLUKA versions that are contained in the GEANT 3.21 package.

The resort to the QGSM code, which makes it possible to simulate nucleus–nucleus interactions, was motivated by different model concepts. It is also based on the model of quark–gluon strings [5, 6], but the momentum distributions used in this code for constituents are somewhat different from that in the FLUKA code, the description of the spacetime evolution of the intranuclear cascade also being different. For the hadron-formation coordinate and time, one takes either the coordinate and time of the point where the trajectories of the quarks forming the secondary hadron in question intersect ("yo-yo" formation time) or the coordinate and time of the point at which the string is ruptured ("constituent" formation time). The hadron-formation time is then determined by the string tension κ (a free parameter that is taken to be $\kappa = 0.5$ or 0.9 GeV/fm in the different versions of this model). That secondaries can interact with one another ("hot cascading") is also taken into account.

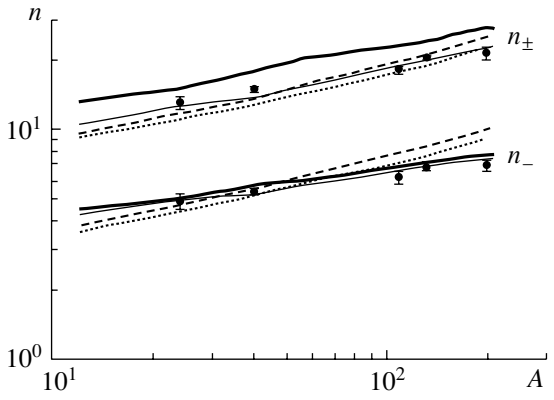

Fig. 1. Multiplicities of secondaries versus the target mass number ($E = 200$ GeV) according to simulations based on (thick solid curves) the FLUKA code, (thin solid curves) the GHEISHA code, or the QGSM code implemented (dashed curves) with the string tension of $\kappa = 0.9$ GeV/fm and the constituent formation time or (dotted curves) with the string tension of $\kappa = 0.5$ GeV/fm and the "yo-yo" time. Points represent experimental data from [11, 12].

The QGSM code satisfactorily describes basic features of all processes induced by high-energy hadron–nucleus and nucleus–nucleus collisions, with the exception of the evaporation process and the fragmentation of the residual nucleus. This code was tested by applying it to proton–nucleus collisions, as well as to pion–nucleus and kaon–nucleus collisions at 250 GeV [10].

1.2. Features of Hadron Interactions in Various Models

The multiplicity of secondaries is one of the important features of an inelastic-interaction event. The results of the calculations performed according to the various models for the multiplicity of all charged particles, $n_\pm$, and the multiplicity of negatively charged particles, n_-, generated in pMg, pAu, pAr, and pXe interactions (at an energy of 200 GeV), for which there are relevant experimental data [11, 12], are displayed in Table 1. The resulting multiplicities of secondaries are also shown in Fig. 1 versus the target mass number. The quantity $n_\pm$ takes into account hadrons generated in multiparticle-production processes and protons knocked out of the target nucleus. Here, the best agreement with experimental data is achieved within the GHEISHA model. The FLUKA model exaggerates the relevant multiplicity because of an excess of low-energy protons emitted in the nuclear-residue-evaporation process, which is taken into account in the model. The dependence of the multiplicity $n_\pm$ on the target mass number is stronger

Table 1. Multiplicity of secondaries ($E = 200$ GeV)

Code	Reaction			
	p^{24}Mg	p^{1}97Au	p^{40}Ar	p^{131}Xe
			$n_{\pm}$	
FLUKA	15.0	27.9	17.9	24.1
GHEISHA	12.6	22.8	13.8	20.2
QGSM, "yo-yo," $\kappa = 0.5$ GeV/fm	11.1	23.0	12.9	19.0
QGSM, constituent, $\kappa = 0.9$ GeV/fm	11.8	25.1	13.6	21.3
Experiment	13.1 ± 0.9	21.6 ± 1.2	14.98 ± 0.45	20.67 ± 0.40
			n_{-}	
FLUKA	5.0	7.8	5.7	7.2
GHEISHA	5.0	7.7	5.3	7.0
QGSM, "yo-yo," $\kappa = 0.5$ GeV/fm	4.4	9.2	5.2	7.7
QGSM, constituent, $\kappa = 0.9$ GeV/fm	4.7	10.0	5.5	8.5
Experiment	4.9 ± 0.4	7.0 ± 0.4	5.39 ± 0.17	6.84 ± 0.13

Table 2. Mean rapidity of secondaries ($E = 200$ GeV)

Code	Reaction	
	p^{40}Ar	p^{131}Xe
	$\langle y_{\pm} \rangle$	
FLUKA	1.88	1.63
GHEISHA	2.25	1.88
QGSM, "yo-yo," $\kappa = 0.5$ GeV/fm	2.43	2.06
QGSM, constituent, $\kappa = 0.9$ GeV/fm	2.34	1.92
Experiment	2.39 ± 0.04	2.00 ± 0.02
	$\langle y_{-} \rangle$	
FLUKA	2.45	2.32
GHEISHA	2.43	2.27
QGSM, "yo-yo," $\kappa = 0.5$ GeV/fm	2.51	2.22
QGSM, constituent, $\kappa = 0.9$ GeV/fm	2.41	2.06
Experiment	2.61 ± 0.08	2.42 ± 0.03

in the QGSM than in the other models and in experiments. This model disregards the evaporation and fragmentation processes, so that the emission of low-energy protons is governed exclusively by the intranuclear cascade. Still stronger distinctions between the results produced by the different models are observed for the analogous dependence of the multiplicity n_{-}. That the multiplicity n_{-} depends rather strongly, within the QGSM, on the target mass number is due to an exaggerated contribution of inelastic contributions in the intranuclear cascade.

For another feature of nuclear processes, we take the rapidity averaged over the inclusive distribution, $\langle y \rangle$. One can also consider the rapidity distribution of all charged particles and the rapidity distribution of only negatively charged particles, the corresponding mean values being $\langle y_{\pm} \rangle$ and $\langle y_{-} \rangle$. While the latter is due exclusively to multiparticle-production pro-

cesses, $\langle y_{\pm}\rangle$ also depends on the emission of protons knocked out of the target nucleus.

The $\langle y\rangle$ values calculated within the various models for pAr and pXe interactions at 200 GeV are given in Table 2, along with experimental data from [11, 12]. For the lighter nucleus of argon, the $\langle y_{-}\rangle$ value calculated within the QGSM is close to experimental data, but, for the heavier nucleus of xenon, the $\langle y_{-}\rangle$ value is noticeably underestimated, which suggests an excess of low-energy negative pions, in accordance with the above comment on an exaggerated contribution of the inelastic intranuclear cascade in this model. That the $\langle y_{\pm}\rangle$ values are underestimated in the FLUKA model is due to the inclusion of the nuclear-evaporation process and "black"-proton formation in the model that are not always detected experimentally.

The process of hadron–nucleus interaction can be represented as a set of interactions with individual intranuclear nucleons (Glauber approach [9]). Under the assumption that the cross section for hadron interaction with an intranuclear nucleon is equal to the cross section for the analogous interaction with a free nucleon, σ_{hn}, the mean number of hit nucleons, $\langle\nu\rangle$, is given by $\langle\nu\rangle = A\sigma_{hn}/\sigma_{hA}$ (σ_{hA} is the cross section for hadron–nucleus interaction). Individual interaction events differ in impact parameter and in the number ν of hit intranuclear nucleons. The quantity ν is not observed directly; as an estimate of it, some authors use the quantity ν_g, which depends on the multiplicity n_g of emitted "gray" protons: $\nu_g = (1.02 \pm 0.12)\langle\nu\rangle(n_g/\langle n_g\rangle)^{1/2}$ ($n_g > 0$) [11, 13, 14]. By and large, the estimate of hit nucleons on the basis of the number of gray protons corresponds to the true value of ν at a given value of n_g, but, in an individual case, there are fluctuations associated with unequal numbers protons and neutrons knocked out of the nucleus by the primary particle [13].

By gray protons, some authors mean all low-energy protons (of momentum less than 1 to 1.5 GeV/c) [13, 14], while others eliminate black protons (of momenta not greater than 0.3 GeV/c) from their number [11]. The elimination of these is motivated by the following consideration. For a first approximation, one can treat gray protons as low-energy products of incident-hadron interaction with intranuclear nucleons and black protons as the products of residual-nucleus evaporation. If these processes are weakly correlated [11], the elimination of black protons contributes to revealing the relationship between the number of observed protons, n_g (defined as is described above), and the number of hit intranuclear nucleons, ν. It should be noted that the different models describe differently the intranuclear cascade, which affects the yield of gray and black protons, and that the yield of inelastic-interaction products depends on the number of hit nucleons.

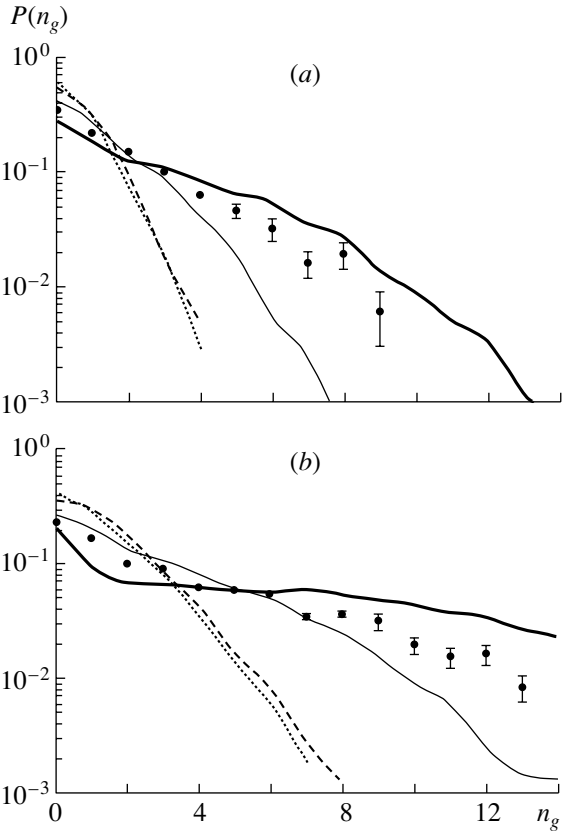

Fig. 2. Distribution with respect to the number of gray protons in (a) pAr and (b) pXe interactions at $E =$ 200 GeV [$P(n_g)$ is the fraction of events characterized by a given value of n_g]. The notation for the curves is identical to that in Fig. 1. Points represent experimental data from [14].

For pAr and pXe interactions at 200 GeV, the distributions with respect to the number of gray protons according to our calculations within the various models are displayed in Fig. 2, along with experimental data from [14]. Taking into account the conditions prevalent in that experiment, we included, in these distributions, protons with momenta in the range $0.1 < p < 0.6$ GeV/c. A deficiency of protons within the QGSM demonstrates that evaporation and fragmentation processes, which are disregarded in this model, are operative here.

For pAu and pMg interactions at 200 GeV, we have calculated the multiplicities of negatively charged secondaries, n_{-}, relying on the various models discussed above. The results of these calculations are presented in Fig. 3 versus n_g. Also shown in this figure are the relevant experimental data from [11]. In order to perform normalization to experimental data,

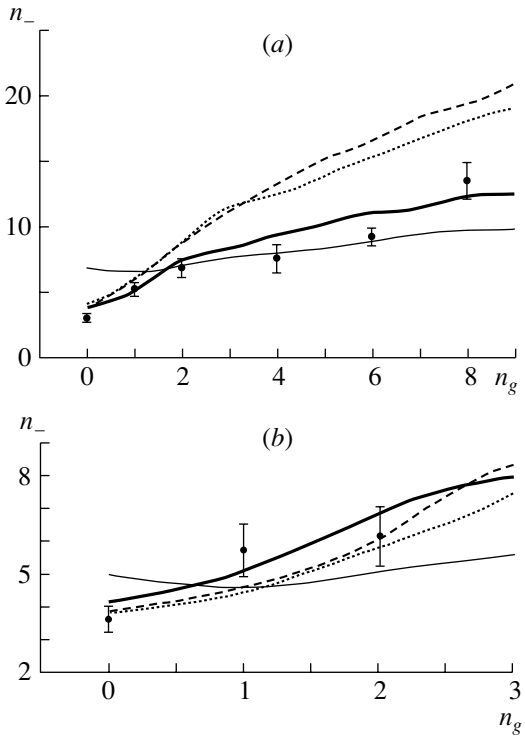

Fig. 3. Multiplicity of negatively charged secondaries versus the number of gray protons in (*a*) *p*Au and (*b*) *p*Mg interactions at $E = 200$ GeV. The notation for the curves is identical to that in Fig. 1. Points represent experimental data from [11].

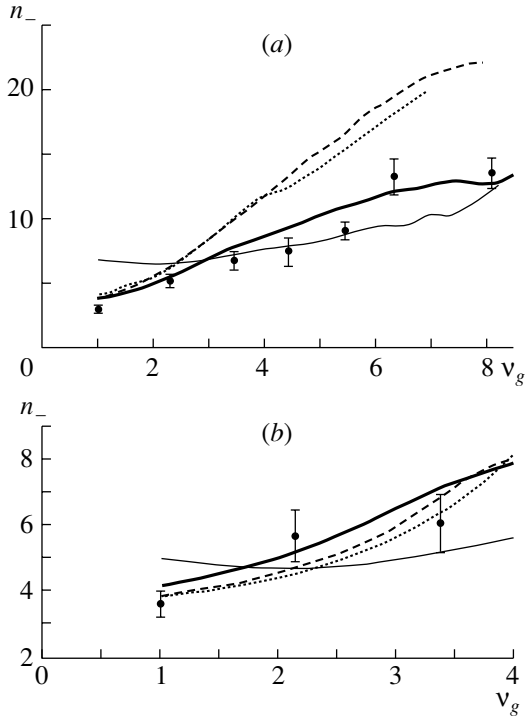

Fig. 4. Multiplicity of negatively charged secondaries versus the number of hit target nucleons (which is determined by the number of gray protons) in (*a*) *p*Au and (*b*) *p*Mg interactions at $E = 200$ GeV. The notation for the curves is identical to that in Fig. 1. Points represent experimental data from [11].

gray protons were selected according to the criterion $0.3 < p < 1.2$ GeV/c.

Figure 4 displays the corresponding dependences of n_- on the number of hit nucleons, ν_g, which was determined from the number n_g of gray protons. For the comparatively light nucleus of magnesium, all of the models considered above successfully describe experimental data, but, in dealing with interactions involving the heavier nucleus of gold, *p*Au, these models produce substantially different results. A stronger dependence of the multiplicity n_- on ν_g in the QGSM than in the other models results from the aforementioned special feature of the model, where gray protons originate only from the interactions of the primary particle and from the intranuclear cascade, since the evaporation and fragmentation processes are disregarded in this model. Because of a small fraction of central collisions, this circumstance has a less pronounced effect on the mean multiplicity (see Table 1).

Our analysis of inclusive and eventual features of hadron interactions that was based on various model concepts makes it possible to pinpoint the lines that one should follow in order to refine the models discussed above.

2. EXTRAPOLATION TO THE REGION OF HIGH ENERGIES AND SOME DATA FROM COSMIC-RAY EXPERIMENTS

2.1. High-Energy Hadron Interactions within Model Concepts

Discrepancies between the model concepts were analyzed above in the region of accelerator energies. The choice of the quantities to be subjected to a comparison was dictated by available data from accelerator experiments. A similar comparative analysis at higher energies can rely only on cosmic-ray experiments, the only source of information in this region. Information that is of importance for describing the cascade process in matter and which is employed in this case includes data on interaction cross sections, inelasticity factors, and spectral features of photons that are produced predominantly in neutral-pion and eta-meson decays over a wide energy range.

That the number of secondaries is bounded in the GHEISHA code—this feature of the code has already been discussed above—entails an underestimation of the multiplicity at high energies, especially for targets of large mass number (Table 3). Although the multiplicity of secondaries, which possess an exponentially

Table 3. Mean multiplicity $\langle n_{\pi^0} \rangle$

Code	E, TeV				
	0.125	0.5	2	8	32
			pC		
FLUKA	4.52	6.91	9.75	13.63	17.75
GHEISHA	3.96	6.39	9.61	12.61	13.76
QGSM, constituent, $\kappa = 0.9$ GeV/fm	4.09	5.96	8.16	10.48	15.72
			pFe		
FLUKA	6.21	9.72	13.67	20.38	27.57
GHEISHA	5.30	8.22	12.78	16.57	18.27
QGSM, constituent, $\kappa = 0.9$ GeV/fm	6.05	8.75	12.11	19.06	27.19
			pPb		
FLUKA	7.48	11.92	18.35	27.05	38.19
GHEISHA	7.13	10.95	15.79	21.37	23.87
QGSM, constituent, $\kappa = 0.9$ GeV/fm	9.31	13.68	21.01	33.68	46.72

Table 4. Partial inelasticity factor K_γ

Code	E, TeV				
	0.125	0.5	2	8	32
			pC		
FLUKA	0.182	0.182	0.179	0.194	0.194
GHEISHA	0.127	0.143	0.159	0.183	0.179
QGSM, constituent, $\kappa = 0.9$ GeV/fm	0.166	0.173	0.175	0.175	0.178
			pFe		
FLUKA	0.201	0.201	0.199	0.203	0.202
GHEISHA	0.140	0.152	0.178	0.187	0.196
QGSM, constituent, $\kappa = 0.9$ GeV/fm	0.197	0.200	0.196	0.209	0.201
			pPb		
FLUKA	0.207	0.203	0.203	0.209	0.214
GHEISHA	0.163	0.173	0.182	0.205	0.210
QGSM, constituent, $\kappa = 0.9$ GeV/fm	0.226	0.233	0.226	0.230	0.233

descending energy spectrum, is determined primarily by the low-energy component, calculations reveal that discrepancies between the estimates of the multiplicity of, say, neutral pions and of the corresponding yield of photons have a sizable effect on the energy-dependent features of the interaction (see Tables 3, 4). From Table 4, it can be seen that the mean partial inelasticity factor K_γ in the GHEISHA model is much less than the experimental value of 0.19 ± 0.01 ($E > 0.4$ TeV, Fe) [15]. Satisfactory agreement with experimental data is attained within the FLUKA and QGSM concepts.

For pN interaction at 100 TeV, the partial inelasticity factors K_γ and $K_{\pi^\pm}$ and the multiplicities n_γ and $n_{\pi^\pm}$ calculated according to the FLUKA, the GHEISHA, and the QGSM code are quoted in Table 5, along with the results of the calculations performed in [16] within different models relying on various versions of the model of quark–gluon strings and including DPMJET (which is a further devel-

Table 5. Partial inelasticity factors and multiplicities of secondaries along with data from [16] (for γ and $\pi^{\pm}$ from pN interaction at $E = 100$ TeV)

Code	K_γ	$K_{\pi^\pm}$	n_γ	$n_{\pi^\pm}$	$\langle E_\gamma \rangle$, GeV	$\langle E_{\pi^\pm} \rangle$, GeV
FLUKA	0.1949	0.3936	41.1	36.8	474	958
GHEISHA	0.1850	0.4735	29.1	30.1	636	1573
QGSM, constituent, $\kappa = 0.9$ GeV/fm	0.1777	0.2729	45.0	34.2	395	798
QGSM, "yo-yo," $\kappa = 0.5$ GeV/fm	0.1748	0.2736	43.2	32.8	405	834
VENUS	0.1697	0.3031	44.9	38.8	378	781
QGSJET	0.1901	0.3059	45.5	34.2	418	894
SIBYLL	0.1919	0.3018	37.8	28.1	508	1074
HDPM	0.1484	0.2673	47.8	36.7	310	728
DPMJET	0.2093	0.3409	46.3	38.4	452	888

Table 6. Fitted values of the parameters in the cross section for inelastic interactions

Reaction	σ_0, mb	b, mb	Reaction	σ_0, mb	b, mb
FLUKA			GHEISHA		
pC	252	11.1	pC	315	25.3
pFe	750	16.5	pFe	954	68.2
pPb	1927	18.7	pPb	2302	157.8
QGSM, constituent, $\kappa = 0.9$ GeV/fm					
pC	280	9.3	HeC	480	17.5
pFe	764	23.0	HeFe	1109	2208
pPb	1727	44.4	HePb	15.3	44.1

Table 7. Mean energy-absorption length (g/cm^2) in an iron and a lead absorber within various models

Model	E, TeV			
	0.5	2	8	32
Empirical formula	270	325	380	436
pFe, FLUKA	288	317	420	506
pFe, GHEISHA	325	397	458	391
pFe, QGSM (constituent, $\kappa = 0.9$ GeV/fm)	251	366	400	472
HeFe, QGSM (constituent, $\kappa = 0.9$ GeV/fm) + FLUKA	266	306	396	446
pPb, FLUKA	442	622	863	929
pPb, GHEISHA	387	528	569	679
pPb, QGSM (constituent, $\kappa = 0.9$ GeV/fm)	550	610	692	737
HePb, QGSM (constituent, $\kappa = 0.9$ GeV/fm) + FLUKA	429	489	715	828

opment of the FLUKA model), QGSJET (which is conceptually close to the QGSM), and VENUS. The phenomenological models SIBYLL and HDPM [16] are based on approaches that are close to the approach underlying the GHEISHA model. Data from Table 5 indicate that the different model descriptions of pN interaction lead to strongly different results for the features of the interaction. The phenomenolog-

ical codes stand out owing to some of their special features. The GHEISHA and SIBYLL models yield the lowest multiplicities of secondaries at the highest mean energy, while the HDPM model underestimates (in relation to the other models) the inelasticity factors and, accordingly, the mean energy of secondaries.

The main contribution to the energy release at the initial segment of the cascade curve comes from the products of the first inelastic interaction (these are predominantly photons originating from neutral-pion decays). For pC, pFe, and pPb interactions at $E = 5$, 8, and 8 TeV, respectively, the distributions of the inelastic-interaction cross section σ_{in} with respect to the partial inelasticity factor K_γ, $d\sigma_{\text{in}}/dK_\gamma$, according to the calculations within the various models are displayed in Fig. 5, along with experimental data from [17, 18]. Here, the best agreement is attained with the QGSM code.

The distinctions between the models are associated, to a considerable extent, with the character of the distribution in the small-K_γ region (an excess of events in this region is observed in the GHEISHA model). For the development of a cascade in matter, this is insignificant, because such interactions do not make sizable contributions to the cascade.

The shape of the spectrum of product photons has a profound effect on the development of the cascade: in the case of a harder spectrum, a considerable part of the energy is carried away by high-energy photons, the maximum of the electromagnetic cascade is shifted toward the interior of the absorber, and the energy release near the interaction vertex is reduced. The photon energy spectra computed on the basis of the models considered here are displayed in Fig. 6, along with experimental data from [17]. Within the experimental errors, all three models describe satisfactorily the spectrum of photons.

The distinctions between the codes generating hadron interactions are manifested in the energy dependence of the inelastic-interaction cross section σ_{in}. All of the models used assume a logarithmic growth of the cross section, $\sigma_{\text{in}} = \sigma_0 + b \ln E$ (here, σ_{in} and b are measured in mb, and E is taken in TeV), with various parameter values quoted in Table 6 for all three models in the case of pC, pFe, and pPb interactions and for the QGSM code in the case of HeC, HeFe, and HePb interactions. (For the models considered here, we present, in Tables 1–6, features that were obtained by generating about 10^4 interaction events according to the relevant models for each value of primary energy.)

As follows from Table 6, the GHEISHA model yields the sharpest energy dependence of the cross section for proton–nucleus interaction, the cross sections calculated within this model being in excess of experimental data for energies above a value of about 50 GeV. By way of example, we indicate that an interpolation of experimental data from [19] leads to $\sigma_{\text{in}}(p\text{Fe}) = 711 \pm 23$ mb at 200 GeV, while the result obtained at this energy value according to the GHEISHA model is 844 mb (calculations on the basis of the FLUKA and the QGSM code lead to the values of 723 and 727 mb, respectively). It should be noted, however, that this overestimation of the cross section does not mean a complete failure of the GHEISHA model in describing intranuclear cascades, since a significant contribution to the inelastic-interaction cross section comes from events characterized by a small inelasticity factor, in which case a small number of secondaries are produced.

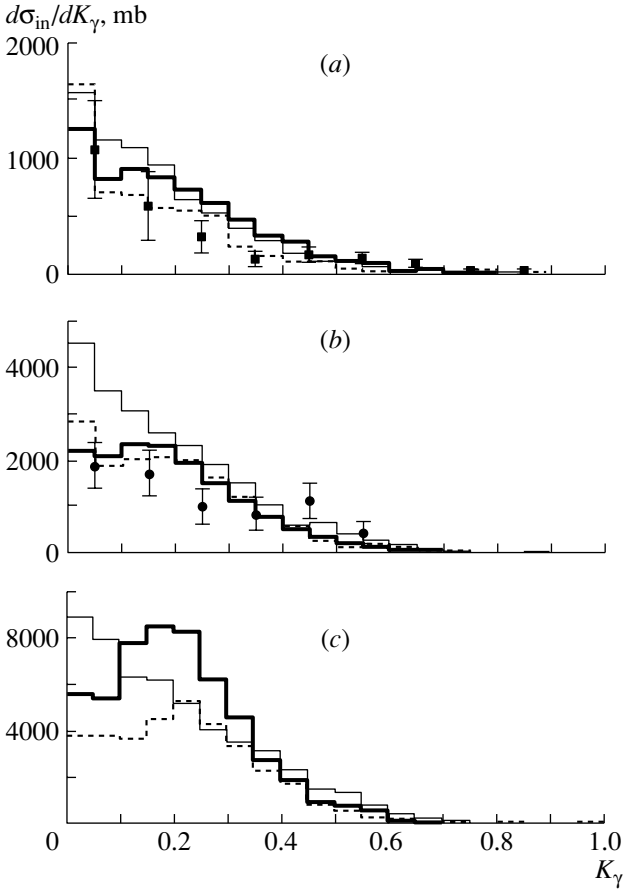

Fig. 5. Distributions of the inelastic-interaction cross sections in the partial inelasticity factor K_γ, $d\sigma_{\text{in}}/dK_\gamma$, for (*a*) pC, (*b*) pFe, and (*c*) pPb collisions at $E = 5$, 8, and 8 TeV, respectively. The thick solid, thin solid, and dashed curves represent the results obtained with the aid of, respectively, the FLUKA, the GHEISHA, and the QGSM code (in the last case, the string tension was set to $\kappa = 0.9$ GeV/fm and the constituent formation time was used). The experimental data displayed in this figure were borrowed from (closed boxes) [17] and (closed circles) [18].

Table 8. Mean energy-release fraction $\langle K_b \rangle$ and corresponding root-mean-square deviation $D = \langle (K_b - \langle K_b \rangle)^2 \rangle^{1/2} / \langle K_b \rangle$ versus the absorber thickness

X, cm	$\langle K_b \rangle$	D	$\langle K_b \rangle$	D	X, cm	$\langle K_b \rangle$	D	$\langle K_b \rangle$	D
	$E = 0.5$ TeV		$E = 32$ TeV			$E = 0.5$, TeV		$E = 32$ TeV	
	pFe, FLUKA					pPb, FLUKA			
15	0.050	1.41	0.015	1.72	10	0.079	1.60	0.045	1.99
30	0.23	0.81	0.15	0.90	15	0.15	1.21	0.11	1.36
45	0.41	0.53	0.34	0.54	30	0.33	0.70	0.28	0.75
60	0.55	0.38	0.48	0.36	45	0.49	0.46	0.43	0.50
75	0.65	0.28	0.60	0.24	60	0.61	0.31	0.54	0.36
	pFe, GHEISHA					pPb, GHEISHA			
15	0.056	1.27	0.015	1.40	10	0.069	1.46	0.063	1.75
30	0.22	0.80	0.16	0.80	15	0.13	1.12	0.14	1.20
45	0.38	0.52	0.34	0.49	30	0.30	0.62	0.33	0.63
60	0.50	0.35	0.49	0.31	45	0.44	0.42	0.46	0.38
75	0.60	0.26	0.59	0.21	60	0.54	0.29	0.55	0.27
	pFe, QGSM (constituent, $\kappa = 0.9$ GeV/fm)					pPb, QGSM (constituent, $\kappa = 0.9$ GeV/fm)			
15	0.056	1.44	0.015	1.78	10	0.071	1.74	0.046	1.99
30	0.24	0.82	0.14	0.96	15	0.14	1.26	0.11	1.40
45	0.41	0.56	0.32	0.62	30	0.34	0.70	0.29	0.71
60	0.55	0.40	0.47	0.40	45	0.50	0.47	0.44	0.48
75	0.66	0.29	0.60	0.29	60	0.62	0.35	0.56	0.33
HeFe, QGSM (constituent, $\kappa = 0.9$ GeV/fm) + FLUKA					HePb, QGSM (constituent, $\kappa = 0.9$ GeV/fm) + FLUKA				
15	0.077	1.11	0.021	1.43	10	0.086	1.50	0.053	1.59
30	0.27	0.61	0.16	0.76	15	0.16	1.08	0.12	1.08
45	0.44	0.38	0.33	0.46	30	0.37	0.58	0.30	0.56
60	0.58	0.25	0.48	0.30	45	0.54	0.36	0.46	0.36
75	0.68	0.17	0.60	0.21	60	0.66	0.24	0.58	0.25

2.2. Nuclear Cascade in Matter and Its Energy Features

Obviously, the distinctions between the codes generating hadron interactions must lead to distinctions between results obtained by simulating high-energy hadronic cascades in matter. For a quantity that characterizes a code, we can choose the energy release in matter (this quantity, which involves the integrated effect of many interactions, is determined by the development of the cascade), E_{rel}, or the dimensionless relative energy release $K_b = E_{\text{rel}}/E$. A simulation of hadronic cascades initiated by protons and He nuclei in the energy range 0.5–32 TeV was performed for iron and lead absorbers (of thickness up to 90 and 60 cm, respectively).

Cascades initiated by protons were simulated with the aid of the FLUKA, GHEISHA, and QGSM codes. In cascades initiated by He nuclei, the first interaction was computed on the basis of the QGSM, while subsequent interactions were treated by using the FLUKA code. Electromagnetic processes were described within the relevant GEANT package [1].

The absorption of the hadronic-cascade energy can be analyzed in two aspects. In the first of these, the mean fraction of the energy release, $\langle K_b \rangle$, and the relevant root-mean-square deviation $D = \langle (K_b - \langle K_b \rangle)^2 \rangle^{1/2} / \langle K_b \rangle$ are described as functions of the absorber thickness X, all cascades in the absorber being considered, irrespective of the position of the vertex of

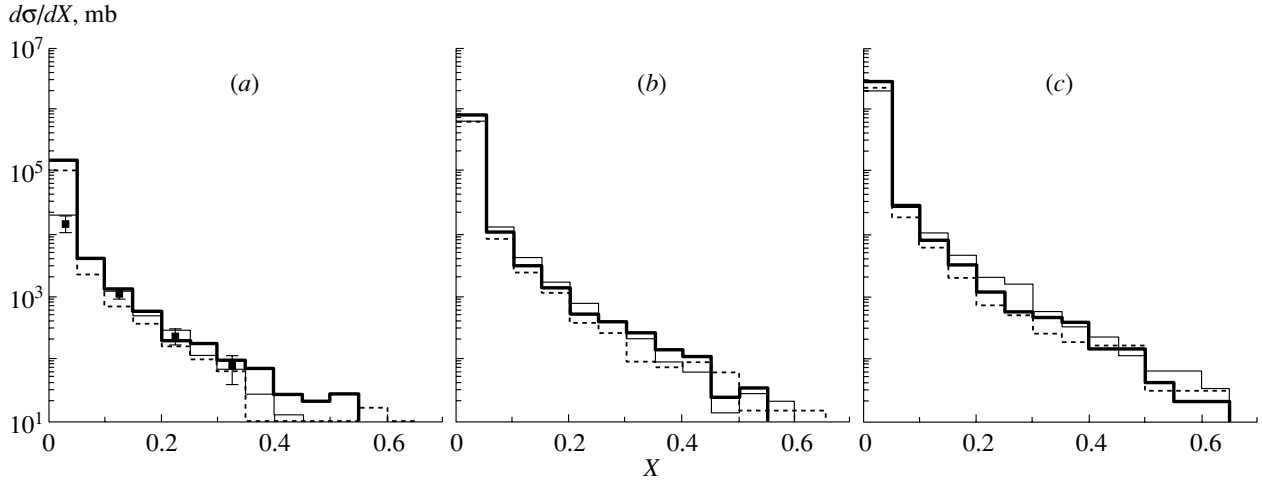

Fig. 6. Energy spectra of photons ($X = E_\gamma/E$) from (a) pC, (b) pFe, and (c) pPb interactions at $E = 5$, 8, and 8 TeV, respectively. The notation for the histograms is identical to that in Fig. 5. Points represent experimental data from [17].

the first inelastic interaction. In the second one, the mean fraction of the energy release, $\langle K_b \rangle$, and the relevant root-mean-square deviation D are investigated as functions of the depth of cascade development, $(X - X_{\text{int}})$ (X_{int} is the position of the vertex of the first interaction event). This makes it possible to study the development of a cascade by comparing the different models. The first approach corresponds to experiments that do not localize first-interaction events in matter, while the second approach simulates experiments featuring such detailed information [20, 21]. (Questions concerning the localization of the first events of inelastic interactions and the distinctions between the generators of inelastic interactions in describing the initial segment of the cascade curve are considered in [22].)

For an iron absorber, the results obtained within the various models for the quantity $\langle K_b \rangle$ as a function of the depth to which cascades initiated by protons and alpha particles of various energies penetrate are displayed in Fig. 7a, along with experimental data from [23, 24]. Figure 7b shows similar dependences for a lead absorber. In describing proton-initiated cascades, experimental points corresponding to depths in excess of 200 g/cm^2 are best reproduced with the aid of the FLUKA model. For this case, the QGSM predicts a greater energy release, while the GHEISHA model leads to a smaller value of it. At small depths, all of the models being considered overestimate somewhat $\langle K_b \rangle$.

Figure 8 displays fluctuations of the energy release at various cascade levels. If the absorber thickness is sufficiently large (greater than 200 g/cm^2 for iron), the dependence of these fluctuations on the cascade depth is close to an exponential dependence. It should be noted that an absorber of thickness in excess of 500 g/cm^2 is required for measuring K_b to a precision of 20%.

The exponential approximation $\langle dE/dX \rangle \sim \exp(-X/L)$ was proposed in [25] for describing the absorption of energy at the tail of the cascade curve. For the mean absorption length L (in t units), we take here the expression $L(E) = 21.4 + 6.6 \log E$ (E is measured in TeV), which was obtained as an approximation of accelerator and cosmic-ray data on proton-initiated cascades in iron over the energy range 0.02–20 TeV.

An analysis of experimental data reported in [23, 24] and of the results of simulations reveals that the exponential approximation is possible from the cascade depth of about 300 g/cm^2 for a primary proton and 400 g/cm^2 for a primary alpha particle in the energy range 1–100 TeV. The distinction is due to the fact that, in the case of a primary nucleus, fragments or individual spectator nucleons carry away, after the first interaction event, a considerable part of the energy, thereby smearing the cascade maximum.

For an iron absorber, the values of L that were calculated on the basis of the models considered here are quoted in Table 7. The results obtained by using the FLUKA and the QGSM model are in satisfactory agreement with the above empirical formula. The GHEISHA code produces somewhat overestimated values of the absorption length L at the energies of 0.5, 2, and 8 TeV and a considerably underestimated value of L at 32 TeV. The latter may stem from an inadequate description of inelastic interactions in the region $E > 10$ TeV within this model. The FLUKA model agrees best of all with experimental data from [26]: $L = 264 \pm 15$ g/cm^2 at $E = 0.6$ TeV and $L =$

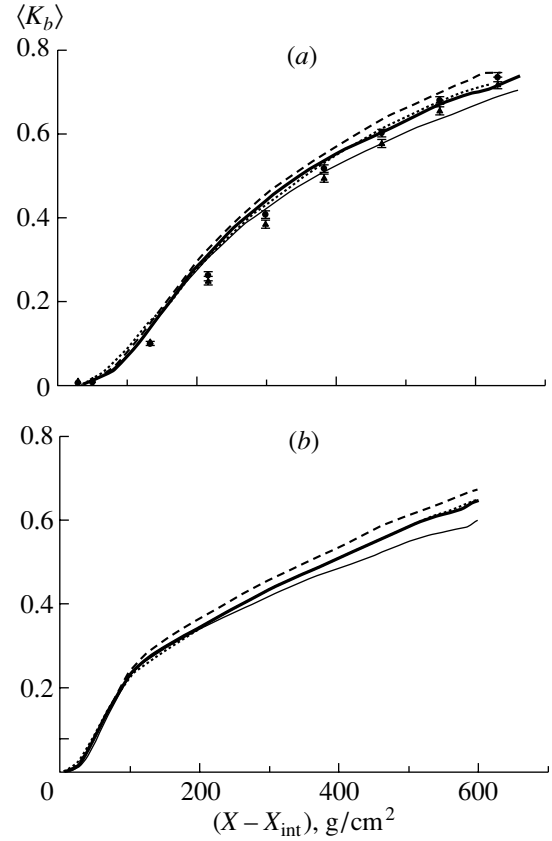

Fig. 7. Mean energy-release fraction $\langle K_b \rangle$ as a function of the depth to which the cascade develops and which is reckoned from the interaction vertex X_{int}. The curves in the figure are plotted for (*a*) *p*Fe, HeFe and (*b*) *p*Pb, HePb interactions at $E = 8$ TeV. The case of proton interactions is represented by thick solid, thin solid, and dashed curves, which were computed with the aid of, respectively, the FLUKA code, the GHEISHA code, and the QGSM code with the string tension of $\kappa = 0.9$ GeV/fm and the constituent formation time. The case of He interactions (dotted curves) was treated within the approach where the QGSM code with the string tension of $\kappa = 0.9$ GeV/fm and the constituent formation time is combined with the FLUKA code. The Sokol-2 experimental data [23, 24] in Fig. 7*a* are shown by closed circles and closed triangles for, respectively, *p*Fe and HeFe interactions.

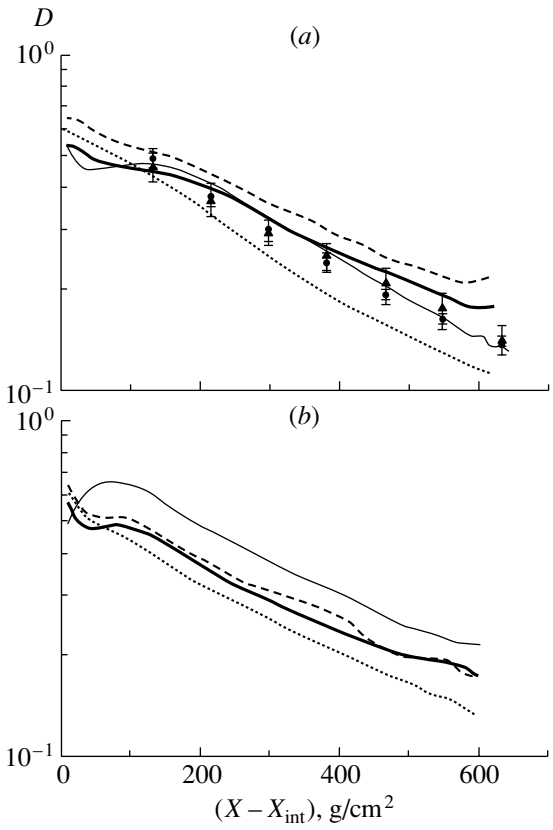

Fig. 8. Relative root-mean-square deviation of the energy-release fraction, $D = \langle (K_b - \langle K_b \rangle)^2 \rangle^{1/2} / \langle K_b \rangle$, as a function of the depth to which the cascade develops and which is reckoned from the interaction vertex X_{int}. The curves in the figure are plotted for (*a*) *p*Fe, HeFe and (*b*) *p*Pb, HePb interactions at $E = 8$ TeV. The Sokol-2 experimental data in Fig. 8*a* were borrowed from [23, 24]. The notation for the curves and points is identical to that in Fig. 7.

314 ± 24 g/cm^2 at $E = 1.4$ TeV. The model values of L for a lead absorber are also quoted in Table 7.

In addition to the dependence of $\langle K_b \rangle$ on the cascade-penetration depth, we have also investigated the dependence of $\langle K_b \rangle$ on the absorber thickness without fixing the vertex of the first inelastic interaction. The results of the simulation on the basis of the three models considered here are compiled in Table 8 ($\langle K_b \rangle$ and $D = \langle (K_b - \langle K_b \rangle)^2 \rangle^{1/2} / \langle K_b \rangle$ for *p*Fe and *p*Pb interactions) for $E = 0.5$ and 32 TeV. From Table 8, it can be seen that, for *p*Fe interactions, the three models lead to close values (within 10%) of $\langle K_b \rangle$ and D. For a lead absorber, close values are obtained for these quantities within the FLUKA and the QGSM approach; here, the GHEISHA model yields underestimated values of $\langle K_b \rangle$ at 0.5 TeV and overestimated values of this quantity at 32 TeV for small cascade-penetration depths. This is due to the energy dependence of the partial inelasticity factor K_γ within this model (see Table 4).

CONCLUSION

Some features of the FLUKA, GHEISHA, and QGSM codes generating hadron interactions have been compared with available experimental results (specifically, this has been done for cross sections, partial inelasticity factors, and rapidity distributions of interaction products). On this basis, we have been able to conclude that the model concepts underlying the FLUKA and the QGSM code closely correlate with experimental observations. Within

the GHEISHA model, the cross section for inelastic interaction is larger, while the inelasticity factor is smaller. This distorts, within 10%, the energy release in an iron absorber and substantially affects the character of the energy release in lead for $E > 10$ TeV. In view of this, it is preferable to use the FLUKA and QGSM codes in the region of higher energies. By comparing the dependences of the energy release and of its fluctuations on the depth of cascade propagation with the results of the Sokol-2 experiment, we have been able to assess the applicability of the models considered here to describing cascade processes in matter at high energies.

REFERENCES

1. GEANT User's Guide, CERN DD/EE/83/1 (1983)
2. H. C. Fesefeldt, Technical Report PITHA 85-02, III Physikalisches Institut, RWTH Aachen Physikzentrum (1985).
3. J. Ranft and S. Ritter, Z. Phys. C **20**, 347 (1983).
4. A. Fasso, A. Ferrari, J. Ranft, *et al.*, Nucl. Instrum. Methods Phys. Res. A **332**, 459 (1993).
5. N. S. Amelin, K. K. Gudima, S. Yu. Sivoklokov, and V. D. Toneev, Yad. Fiz. **52**, 272 (1990) [Sov. J. Nucl. Phys. **52**, 172 (1990)].
6. N. S. Amelin, K. K. Gudima, and V. D. Toneev, Yad. Fiz. **51**, 512 (1990) [Sov. J. Nucl. Phys. **51**, 327 (1990)].
7. S. Ritter, Z. Phys. C **16**, 27 (1982).
8. K. Hanßgen and J. Ranft, Nucl. Sci. Eng. **88**, 537 (1984).
9. J. Ranft, Preprint SSC-143 (1987).
10. Sh. M. Yandarbiev, A. M. Dunaevskiĭ, F. K. Rizatdinova, *et al.*, Yad. Fiz. **56** (10), 153 (1993) [Phys. At. Nucl. **56**, 1389 (1993)].
11. D. H. Brick, M. Widgoff, P. Beilliere, *et al.*, Phys. Rev. D **39**, 2484 (1989).
12. C. De Marzo, M. De Palma, A. Distante, *et al.*, Phys. Rev. D **26,** 1019 (1982).
13. W. Q. Chao, M. Q. Hegab, and J. Hufner, Nucl. Phys. A **395**, 482 (1983).
14. C. De Marzo, M. De Palma, A. Distante, *et al.*, Phys. Rev. D **29**, 2476 (1984).
15. V. V. Avakyan, S. R. Gevorkyan, V. M. Zhamkochyan, *et al.*, Vopr. At. Nauki Tekh., Ser.: Tekh. Fiz. Éksp. **4** (16), 56 (1983).
16. J. Knapp, D. Heck, and G. Schatz, Preprint No. 5828, Institut für Kernphysik (Karlsruhe, FZKA, 1996).
17. V. Ya. Shestoperov, Doctoral Dissertation in Physics and Mathematics (Nauchn. Issled. Inst. Yad. Fiz. Mosk. Gos. Univ., Moscow, 1981).
18. S. A. Azimov and T. S. Yuldashbaev, *Inelastic Collisions of High-Energy Particles with Nucleons and Nuclei* (Fan, Tashkent, 1974).
19. S. Fredriksson, G. Eilam, G. Berlad, *et al.*, Phys. Rep. **144**, 187 (1987).
20. N. L. Grigorov, I. P. Ivanenko, I. D. Rapoport, *et al.*, Vestn. Mosk. Univ., Ser. 3: Fiz., Astron. **29**, 44 (1988).
21. I. P. Ivanenko, I. D. Rapoport, V. Ya. Shestoperov, *et al.*, Vopr. At. Nauki Tekh., Ser.: Tekh. Fiz. Éksp. **4** (4), 40 (1989).
22. I. D. Rapoport, A. N. Turundaevsky, V. Ya. Shestoperov, and I. V. Yashin, Yad. Fiz. **62**, 1026 (1999) [Phys. At. Nucl. **62**, 959 (1999)].
23. I. P. Ivanenko, I. D. Rapoport, V. Ya. Shestoperov, *et al.*, Preprint NIIYaF MGU-89-29/106 (Institute of Nuclear Physics, Moscow State University, Moscow, 1989).
24. I. P. Ivanenko, I. D. Rapoport, V. Ya. Shestoperov, *et al.*, Preprint NIIYaF MGU-88-6/83 (Institute of Nuclear Physics, Moscow State University, Moscow, 1988).
25. F. Siohan, R. W. Ellsworth, A. S. Ito, *et al.*, Nucl. Instrum. Methods **167**, 371 (1979).
26. A. E. Morozov, S. A. Slavatinskiĭ, and I. N. Fetisov, Izv. Akad. Nauk SSSR, Ser. Fiz. **35**, 2022 (1971).

Translated by A. Isaakyan

Physics of Atomic Nuclei, Vol. 65, No. 1, 2002, pp. 18–37. From Yadernaya Fizika, Vol. 65, No. 1, 2002, pp. 20–39.
Original English Text Copyright © 2002 by Eremenko, Fotina, Giardina, Lamberto, Malaguti, Platonov, Taccone, Yuminov.

NUCLEI
Experiment

Fission Time in the ^{28}Si + ^{nat}Pt Reaction*

D. O. Eremenko, O. V. Fotina, G. Giardina[1)], A. Lamberto[1)], F. Malaguti[2)], S. Yu. Platonov, A. Taccone[1)], and O. A. Yuminov

Institute of Nuclear Physics, Moscow State University, Vorob'evy gory, Moscow, 119899 Russia

Received July 27, 2000; in final form, November 24, 2000

Abstract—The experimental fission times are analyzed for excited nuclei produced in the ^{28}Si + ^{nat}Pt reaction. Experimental lifetimes obtained by the crystal-blocking technique range between 10^{-17} and 10^{-18} s at bombarding energies between 140 and 170 MeV, respectively. Experimental data are analyzed within the statistical theory of nuclear reactions and the double-humped-fission-barrier model with allowance for preequilibrium processes and the nuclear-dissipation phenomenon. It is shown that fission barriers retain their double-humped structure for nuclear temperatures up to about 1.7–1.8 MeV and that the lifetimes of excited strongly deformed states in the second potential well contribute substantially to the observed delay times in the fission decay channel. © *2002 MAIK "Nauka/Interperiodica".*

1. INTRODUCTION

The potential-energy surfaces of heavy nuclei display two minima, whose nature is associated with the existence of shells even at anomalously large deformations [1]. Consequently, the fission barrier for heavy nuclei is double-humped, where the population of excited states in the second potential well is realized. At excitation energies near the barrier, the crossing of nuclei through the second minimum is noticeably influenced by the states in the second potential well. However, with increasing excitation energy, the penetrability of the fission barrier approaches unity and the sensitivity of the fission-cross-section structure to the second-well states becomes lower. Moreover, an increase in the excitation energy leads to a decrease in the shell correction values, so that the double-humped structure of the fission barriers tends to transform into a single-humped one: the liquid-drop barrier with only one class of excited states under equilibrium deformations.

The energy dependence of the shell effect on the fission-barrier structure can be experimentally investigated by measuring the delay time in the fission channel. In this way, it was shown in [2] that the existence of quasistationary transition states in the second well of heavy fissioning nuclei manifests itself in the dynamics of induced fission. It was demonstrated in [3, 4] that the existence of two classes of excited states in heavy nuclei is reflected in different time dependences of the decay yields for different channels. In particular, the fission delay time is due to the lifetimes of excited states in the first and second potential wells. They appear as an additional time delay in the fission channel in relation to the decay times in any other decay channel, like the emission of neutrons, light charged particles, or photons.

In the present study, we analyze the experimental fission times for excited nuclei produced in the ^{28}Si + ^{nat}Pt reaction. Experimental lifetimes have been obtained by the crystal-blocking technique at beam energies of 140 to 170 MeV. Experimental data have been compared with the results of statistical-model calculations that take into account the existence of both classes of excited states realized in the first and second potential wells of fissioning nuclei. The aim was to find evidence of an additional time delay in the fission decay channel, induced by the lifetime of the excited states in the second well, and to check whether the fission barrier retains or loses its double-humped structure at the excitation energies considered here. It is shown that the additional time delay in the fission decay channel does indeed exist, which is interpreted as the effect that excited states in the second potential well exert on the fission time. This also demonstrates that the fission barriers retain their double-humped structure for nuclear temperatures up to about 1.7–1.8 MeV.

*This article was submitted by the authors in English.

[1)]Istituto Nazionale di Fisica Nucleare, Sezione di Catania, and Dipartimento di Fisica, Università di Messina, Messina, Italy.

[2)]Istituto Nazionale di Fisica Nucleare, and Dipartimento di Fisica, Università di Bolognà, Viale C. Berti Pichat 6/2, I-40127 Bologna, Italy.

1063-7788/02/6501-0018$22.00 © 2002 MAIK "Nauka/Interperiodica"

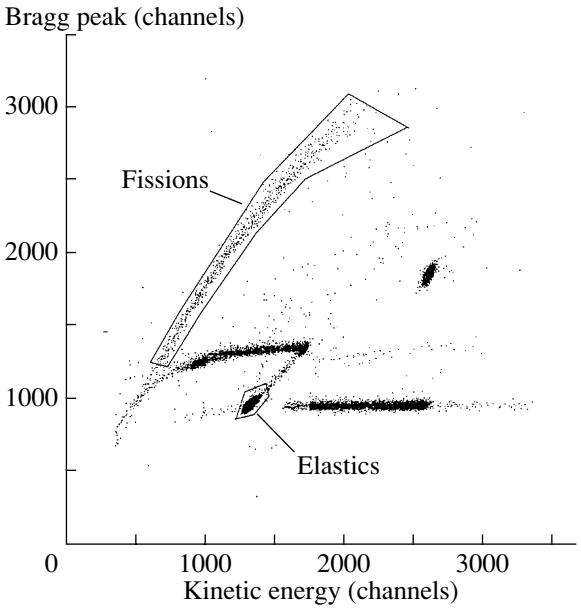

Fig. 1. Typical scatter plot from the Bragg chamber in the $E-Z$ plane, with no cut on x and y values, displaying "elastic events" and the "fission island." Individual Z values are not resolved.

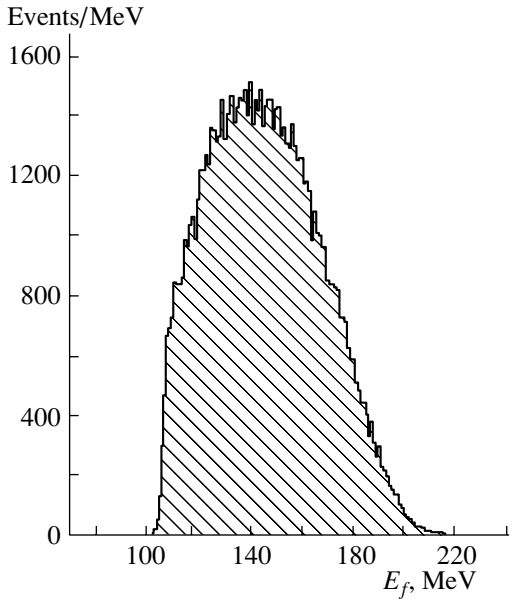

Fig. 2. Example of the experimental spectrum of initial kinetic energies of fission fragment for the case of a 150-MeV beam.

2. EXPERIMENTAL PROCEDURE

The crystal-blocking method [5–8] was used to measure fission times in the ^{28}Si + ^{nat}Pt reaction.

The measurements were carried out at the LLINFN (Italy) by using thin ($\sim$0.5 μm) self-sustaining ^{nat}Pt$\langle 100\rangle$ single-crystal targets of large area (diameter $\approx$5 mm). They were prepared at the Physics Institute, Århus University (Denmark), by epitaxial growth from the gaseous the phase on a NaCl crystal, later dissolved in water. This technique ensured a nearly perfect orthogonality between the crystal axis ($\langle 100\rangle$) and its surface.

A 140- to 170-MeV ^{28}Si beam was extracted from the Tandem-XTU accelerator and was successfully focused to less than 1 mm in diameter by using only magnetic steerers and lenses. Thus, no collimator was necessary, whereby the related "slit-scattering" effects and the consequent spoiling of the pattern quality were avoided. The focusing was achieved with magnets very far upstream of the target, in order to minimize the beam divergence.

A six-axis computerized goniometer was used to orient the crystals and to translate them to exploit "fresh" positions on the target when radiation damage appeared. This happened typically after approximately a 15-μC beam fluence at a current of about 2 nA.

Reaction products were observed at $\theta_{lab} = 25^\circ$ by using a detector telescope made from a multiwire gas proportional chamber followed by an axial Bragg chamber. The multiwire detector, 10×10 cm^2 in area and placed at a distance of 60 cm from the target, was a two-sector gas proportional counter with a common (1-μm thick) cathode and two anodes formed by wires orthogonal to each other to have both the x and y coordinates of the incident-ion position. The anodes were on the opposite sides of the cathode, and the wires (20 μm in diameter) were 1 mm away. Gas (isobutane at 14 mbar) was under continuous flux, and the total detector thickness was 5 mm.

The multiwire detector had a spatial resolution of 1 mm and was placed 60 cm from the target, with the result that the angular resolution was $\Delta\theta = 1.667$ mrad.

The Bragg chamber was a gas (CF_4) ionization chamber operating in an axial electric field. In this way, reaction products with atomic number $Z > 12$ were fully stopped in the chamber.

Events defined by the x, y spatial coordinates of the ion from the multiwire and by its kinetic energy E and charge Z from the Bragg chamber were collected individually on magtape for off-line data reduction.

For more details, the reader is referred to [9–11].

3. DATA REDUCTION

Figure 1 displays a typical scatter plot from the Bragg chamber in the $Z-E$ plane, with no cut on x and y values. The elastic peak and the island of fission fragments (FF) are clearly recognized. Individual Z

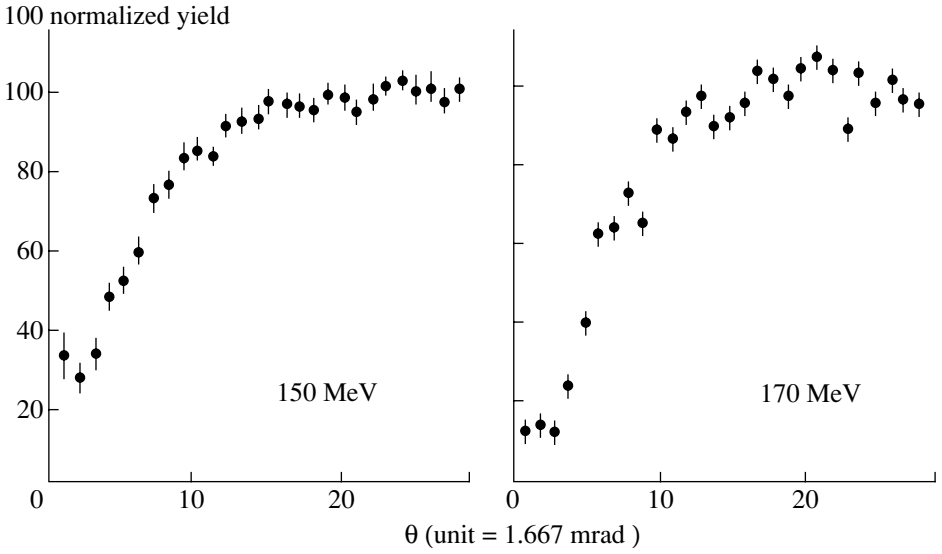

Fig. 3. Radial scans around the dip center for FF at beam energies of 150 and 170 MeV. The unit along the abscissa is the multiwire angular resolution, 5/3 mrad. The 170-MeV scan is used as the reference (prompt) dip.

values for FF are not resolved, because of their low kinetic energies, about 1.5 MeV per nucleon. As an example, Fig. 2 shows the experimental spectrum of initial kinetic energies of FF for the case of a 150-MeV beam. This spectrum was reconstructed from the energy distribution of fission events in the Bragg chamber.

Figure 3 displays the fission blocking dips at bombarding energies of 150 and 170 MeV. The FF blocking dips used hereafter are the sums over all experimental runs and correspond to the total beam fluence of about 250 μC.

Data reduction consisted in constructing separate blocking dips for FF. Their volume Ω [9], which is known [12, 13] to depend on the reaction time, was then evaluated. In order to avoid detection of possible nonexisting time delays simulated by crystal damage, we used, instead of Ω, the ratio

$$R = \Omega_D/\Omega_P \qquad (1)$$

of the delayed volume being considered and a reference (prompt) one extracted from a "zero delay blocking pattern" [9].

Since the dip also depends on the FF energy and charge, the delayed volumes must be corrected for their energy and charge difference from the prompt one by using an appropriate scaling law [14], stating that the transformed (reduced) volumes, viz.,

$$\Omega^* = \Omega \langle E^{-1} \rangle^{-1}/Z, \qquad (2)$$

are, to a good approximation, independent of the charge and kinetic energy of the channeled ion.

The calibration curve $R(v_\perp \tau)$ (see Fig. 4) relating changes in the blocking dip to the mean transverse displacement of the nucleus before decay was calculated for the mean mass and the mean kinetic energy of FF. Here, $v_\perp$ is the component of the compound-nucleus velocity in the direction orthogonal to the crystallographic axis, and τ is the mean lifetime of a decaying nucleus.

A common practice is to use the elastic dip (i.e., the one generated by elastically scattered projectiles) as a reference, but, because of a low (14 mbar) gas pressure in the multiwire detector, required to have the best possible resolution in the Bragg chamber (EZ plane), we had a poor quality of the 2-dimensional x–y scatter plot. Unfortunately, this had the undesirable consequence that elastic ^{28}Si events suffered from a low and unstable detection efficiency. As a result, the radial scan was not able to reach the "isotropic yield," rendering calculation of elastic dip volumes very ambiguous and useless for our purposes.

A way out of the difficulty is to observe (see Fig. 4) that the delayed volume (proportional to R) increases as $v_\perp \tau \equiv s^\perp$ decreases, reaching an asymptotic limit ($\sim$1.0) for $s_\perp < 0.025$ Å. Therefore, if two consequent beam energies generate two dips of the same volume, it seems quite reasonable to assume that they are in the asymptotic region. Then, they are prompt and can be used as a reference. In the present case, this happens for $E_{\rm beam} = 160$ and 170 MeV; therefore, we can take the FF dip at 170 MeV as our "reference." This assumption reinforces the observation that all

Summary of experimental results

E_{beam}, MeV	Ω, μsr	$\langle E\rangle^{theor}$, MeV	$\langle E\rangle^{expt}$, MeV	$\frac{\langle E\rangle^{theor}}{\langle E\rangle^{theor}_{170}}$	Ω^*, μsr	$R = \Omega^*/\Omega_{170}$	$s_\perp = v_\perp\tau$, Å	τ, 10^{-18} s
140	318.3 ± 13.6	138.6	138.6	0.95	302.3 ± 12.9	0.73 ± 0.03	$0.12^{+0.01}_{-0.02}$	$7.3^{+0.6}_{-1.2}$
147	353.8 ± 5.2	140.2	142.6	0.97	343.2 ± 5.0	0.82 ± 0.02	$0.084^{+0.008}_{-0.006}$	5.0 ± 0.4
150	393.7 ± 3.7	140.7	142.8	0.97	381.9 ± 3.6	0.91 ± 0.02	0.062 ± 0.004	3.6 ± 0.3
160	427.4 ± 4.4	142.9	142.9	0.98	418.8 ± 4.3	1.01 ± 0.02	<0.032	<1.8
170	417.0 ± 6.1	145.0	145.9	1.00	417.0 ± 6.1	1.0	0.0	0.0

Note: Ω values are the measured dip volumes. $\langle E\rangle^{theor}$ and $\langle E\rangle^{expt}$ represent the fragment mean kinetic energy evaluated by Viola systematics (see [15]) and the respective measured values. Ω^* displays the dip volumes scaled to a 170-MeV beam by multiplying them by the energy ratios of column 5. This is equivalent to the use of the scaling law (2) under the observation that Z has the same value for all detected fragments. From R values and from the calibration curve of Fig. 4, we get the mean transverse displacements $s_\perp$, where the $v_\perp$ stands for transverse recoil velocities for the respective incident beam energies. The last column shows the delay times τ.

our theoretical calculations of delay times result in $\tau \sim 0$ (not measurable) at 170 MeV (see Fig. 5).

In order to estimate FF energies, we used the well-known Viola systematics [15], and the result is displayed in column 3 of the table.

The table summarizes the experimental results: the last column contains the mean delay times for the five beam energies. Note that, at 160 MeV, we find $R \sim 1$; hence $\tau \sim 0$ (not measurable). This fact, suggesting that times at 160 MeV are already below the lowest sensitivity limit of the method, gives additional value to the choice of the 170-MeV dip as a reference one.

The resulting delay times in the fission channel due to nuclei produced in the ^{28}Si + ^{196}Pt reaction at different beam energies are displayed in Fig. 5. As one can see from Fig. 5, experimental fission times range between 10^{-18} and 10^{-17} s. It is useful to note that such long fission times were obtained for U-like nuclei at approximately the same excitation energy in [16] and [17] by means of the crystal-blocking

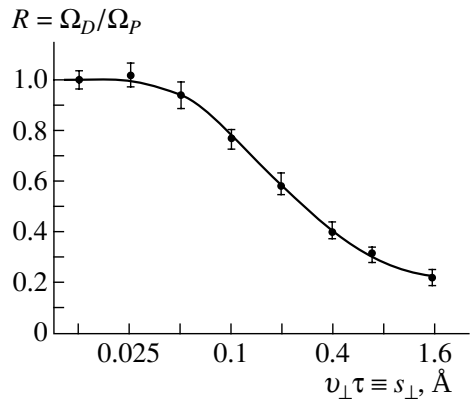

Fig. 4. Calibration curve $R(v_\perp\tau)$ from Monte Carlo blocking dips calculated for FF ^{112}Pd (of kinetic energy 145 MeV) traveling along the ⟨100⟩ axis of a ^{nat}Pt crystal, 0.25 μm thick (see [13] for details).

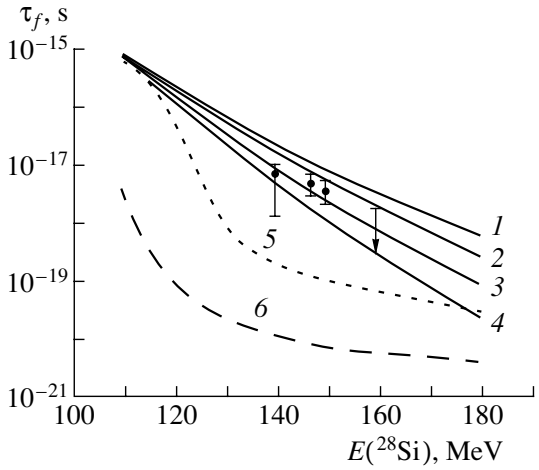

Fig. 5. Summary of the present experiment: delay times in the fission channel due to nuclei produced in the ^{28}Si+^{196}Pt reaction at different beam energies. Points represent experimental data. Dashed curves do not contain effects of neutron evaporation cascade. In detail, the dashed curves were computed (*5*) with or (*6*) without allowance for the delay times introduced by the excited states in the second potential well. The solid curves are the results of the calculations allowing for the delay due to the lifetime of excited states in the first and second potential wells and also for all possible fission chances. In calculating the solid curves, we took into account the temperature dependence of shell corrections with different values of the temperature parameter T_0: ∞ (*1*), 2.00 (*2*), 1.85 (*3*), and 1.75 MeV (*4*).

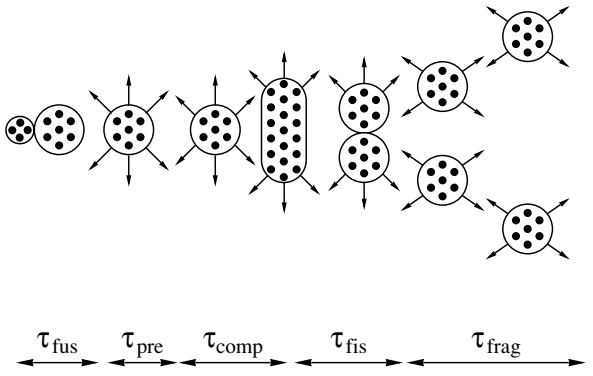

Fig. 6. Pictorial formulation of the dynamics of fusion–fission reactions: $\tau_{\rm fus}$ denotes the duration of the stage of the fusion of a bombarding particle with the target nucleus; $\tau_{\rm pre}$ is the duration of the stage of equilibration of the nuclear system; $\tau_{\rm comp}$ is the duration of the stage of compound-nucleus decay and the dynamical stage to build up the fission flux at the saddle point of the fission barrier; $\tau_{\rm fis}$ is the duration of the stage of the motion of the fissioning system from the saddle to the scission point; and $\tau_{\rm frag}$ is the duration of the stage of fission-fragment deexcitation.

technique and K-vacancy experimental method, respectively.

4. ANALYSIS OF EXPERIMENTAL LIFETIME RESULTS

The experimental data were analyzed under the assumption that the complete fusion of interacting nuclei that is followed by the fission of the compound nucleus and the formation of daughter nuclei upon neutron emission is the dominant channel of the reaction under study. This assumption was based, first of all, on the analysis of the experimental spectra of FF kinetic energies (see Fig. 2). The mean values of the kinetic energy of FF recorded at an angle of 25° in the laboratory frame nearly coincide with those that were evaluated for the case of symmetric complete fusion–fission reaction (see table, columns 3 and 4). As one can see from Fig. 2, the shape of the experimental spectra also favors the symmetric fission mode. Fast processes (like quasifission) make no substantial contribution to the reaction being investigated. In fact, the mean kinetic energies of fragments in these fast processes are approximately 10 MeV higher than in the case of the fusion–fission reaction (see, for example, [18]); on the other hand, the measured fission-time values favor slow processes, such as complete fusion followed by multichance fission. In our case, the fission of nuclei formed by the transfers of several nucleons should result in FF with energy significantly lower than 100 MeV. For example, the mean value of the FF kinetic energy in the laboratory frame should be about 69 MeV in the case of α-particle transfer. Events characterized by such values of the FF energy were not recorded by our detection system (see Fig. 2).

As a rule, the dynamical characteristics of nuclear reactions, like the nuclear lifetime, are analyzed on the basis of the well-known relation $\tau = \hbar/\Gamma$, where Γ is the total decay width of a given compound nucleus. Within this approach, the lifetimes of nuclear systems produced in the resonance reactions and fusion–fission reactions induced by heavy ions can be described satisfactorily for nuclear excitation energies $\leq$50 MeV. With increasing excitation energy, the lifetimes of compound nuclear systems decrease very promptly, and the dynamical stages of the evolution of nuclear systems begin to play a significant role at higher excitation energies. By way of example, we indicate that, by means of the "neutron clock" experimental technique, it was demonstrated in [19, 20] that the dynamical time scale of the motion of a fissioning nuclear system from the equilibrium deformation to the scission point is dominant in the total duration of the fusion–fission process.

In the experiments conducted by means of the crystal-blocking technique, we measure the delay time interval from the instant at which the momentum is transferred from the beam particle to the target nucleus to the instant at which the final fragment is formed (see Fig. 6). In this connection, we note that, to describe correctly the observable duration of the nuclear reaction under study, it is necessary to analyze all stages of the reaction that may contribute to the experimental fission lifetime: (i) the fusion of a bombarding particle with the target nucleus; (ii) the equilibration time at the initial stage of compound-nucleus formation; (iii) the lifetimes of the fissionable compound nuclei produced in the development of a neutron-emission cascade and the dynamical times to build up the fission flux at the saddle point of the fission barrier; (iv) the time it takes for the system to move from the saddle to the scission point; and, finally, (v) the time of FF deexcitation.

4.1. Analysis of the Influence of Preequilibrium Processes on the Duration of the Reaction

To describe the relaxation processes in the nuclear system produced in the fusion reaction being investigated, we use Griffin's exciton model [21].

In this model, the state of a nuclear system produced in a collision of a bombarding particle and a

target nucleus is determined by the exciton number $n = p + h$, where p is the number of particles above the Fermi energy and h is a number of holes below the Fermi energy, and by the excitation energy E^*.

We are interested only in the spectra of preequilibrium neutrons and in the equilibration time for the system under study; therefore, we can use the generalized kinetic master equation to analyze the probability P of finding the system in the n-exciton state at the time instant t [22],

$$\frac{dP(n,t)}{dt} = P(n-2,t)\lambda_+(n-2,E^*) + P(n+2,t)\lambda_-(n+2,E^*) - P(n,t)[\lambda_+(n,E^*) + \lambda_-(n,E^*) + W(n,E^*)], \quad (3)$$

with the initial condition

$$P(n,0) = \delta_{n,n_0} = \delta_{p,p_0}\delta_{h,h_0}, \quad (4)$$

where

$$W(n,E^*) = \sum_b W_b(n,E^*) = \sum_b \int_0^{E^*-B_b} \lambda_b(n,\epsilon_b)d\epsilon_b \quad (5)$$

is the probability of the emission of a particle b (neutron, proton, deuteron, triton, helion, or α particle) into a continuum.

The transition rate of the emission of a particle of energy ϵ_b into a continuum is

$$\lambda_b(n,\epsilon_b) = \frac{2s_b+1}{\pi^2\hbar^3}\mu_b\epsilon_b\sigma_{\rm inv}(\epsilon_b)R_b(p) \times \frac{\omega(p-p_b,h,E^*-B_b-\epsilon_b)}{\omega(p,h,E^*)}, \quad (6)$$

where s_b and μ_b are, respectively, the spin and the reduced mass of the projectile; B_b is the binding energy of the particle b; $R_b(p)$ is the term that takes into account charge conservation; and $\sigma_{{\rm inv},b}$ is the cross section for the inverse reaction.

The cross section for the inverse reaction, $\sigma_{{\rm inv},b}$, is determined by the penetrability factor in the optical model,

$$\sigma_{{\rm inv},b} = \sum_{l_b}\frac{\pi}{k^2}(2l_b+1)T_{b,l_b}, \quad (7)$$

where l_b is the angular momentum of the particle b and T_{b,l_b} is the respective transmission coefficient.

In our calculations, we used the density of exciton states suggested by Ericson and Strutinsky with the Williams corrections [23]:

$$\omega(p,h,E^*) = \frac{g(gE^*-A_{ph})^{p+h-1}}{h!p!(p+h-1)!}. \quad (8)$$

Here, A_{ph} is connected with the Pauli exclusion principle and is given by

$$A_{ph} = \frac{(p^2+h^2)+(p-h)-2h}{4}. \quad (9)$$

The single-particle level density g in (8) is related to the level-density parameter in the Fermi gas model by the equation $g = 6a/\pi^2$.

The rates of internal transitions are given by

$$\lambda_{0,\pm} = \frac{2\pi}{\hbar}\langle|M|^2\rangle\omega^{0,\pm}(E^*), \quad (10)$$

where the transition matrix element $\langle|M|^2\rangle$ is estimated by using the systematics from [24],

$$\langle|M|^2\rangle = \frac{kn}{A^3E^*}\times\begin{cases}\left(\dfrac{E^*}{7n}\right)^{1/2}\left(\dfrac{E^*}{2n}\right)^{1/2} & \text{for } E^*/n < 2\ \text{MeV}\\ \left(\dfrac{E^*}{7n}\right)^{1/2} & \text{for } 2 \le E^*/n < 7\ \text{MeV}\\ 1 & \text{for } 7 \le E^*/n \le 15\ \text{MeV}\\ \left(\dfrac{E^*}{15n}\right)^{1/2} & \text{for } E^*/n > 15\ \text{MeV},\end{cases} \quad (11)$$

where k is a free parameter.

The terms $\omega^{0,\pm}$ are determined by the expressions [23]

$$\omega^+ = \frac{g(gE-A_{ph})^2}{n+1}, \quad (12)$$

$$\omega^0 = g(gE-A_{ph})\frac{3n-2}{4}, \quad (13)$$

$$\omega^- = gph(n-2), \quad (14)$$

corrected by the Pauli exclusion principle.

To determine the free parameter k of the exciton model, we used experimental data on the yields of α particles in the ^{20}Ne + ^{197}Au reaction [25]. We fitted the parameter k with $g = A/13$ in (12)–(14) and (8) (see, for example, [26]). We chose these experimental data, because the excitation-energy range 50–

70 MeV considered here is close to that in the ^{28}Si + $^{\rm nat}$Pt reaction. We found the value of k in (11) to be 340 MeV^3.

The initial exciton configuration (p_0, h_0) from which the equilibration process starts is a free parameter of the model. In our calculations, we tested three versions of the initial exciton configurations: $n_0 = (30p, 1h)$, $(18p, 1h)$, and $(10p, 1h)$.

The criterion of equilibration was chosen to be [27]

$$\left|\frac{P(n,t) - P(n,t+\Delta t)}{P(n,t)}\right| \leq 0.05, \qquad (15)$$

where

$$\Delta t = \frac{1}{\lambda_+(n,E^*) + \lambda_-(n,E^*) + \lambda_0(n,E^*) + W(n,E^*)}. \qquad (16)$$

The preequilibrium fraction of neutron emission is determined as

$$p_n^{\rm pe} = \sum_n^{\bar{n}} \int_0^{\tau^{\rm pe}} dt P(n,t) W(n,E^*), \quad \bar{n} = 2\sqrt{2gE^*}, \qquad (17)$$

where $\tau^{\rm pe}$ is the equilibration time obtained from a solution to the master equation (3) with the equilibration criterion (15).

Figure 7 demonstrates the dependences of the equilibration time calculated for the above initial exciton configurations on the energy of bombarding particles in the ^{28}Si + ^{196}Pt reaction (taken as an example). As might have been expected, the equilibration times decrease smoothly as the beam energy increases and increase as the initial exciton configuration becomes more complicated. But as one can see, thermodynamic equilibration during the relaxation process occurs at times of 10^{-21}–10^{-20} s in any case. At this instant, the excitation energy has a random distribution over the degrees of freedom and the transition probabilities in more complex configurations become equal to the transition probabilities in less complex ones.

During the evolution of the nuclear system, the fraction of "hard" (preequilibrium) neutrons in the total neutron yield decreases as the exciton configuration becomes more complicated. The results obtained from an analysis of neutron emission at different stages of the equilibration process are presented in Fig. 8.

It should be noted that the emission of preequilibrium neutrons occurs even at the earliest stages of thermodynamic equilibration. The neutron energy spectrum then becomes "softer," and the "hard" component of the neutron spectrum may be considered to be formed within a time interval of about 10^{-20} s. After that, the "soft" part of the neutron spectrum is formed. Figure 9 demonstrates, as an example, the calculated total-energy spectra of neutrons emitted from the ^{224}U nucleus produced in the ^{28}Si + ^{196}Pt reaction.

As can be seen, the thermodynamic-equilibration time of about 10^{-20} s does not manifest itself in the experimental lifetime values because it is shorter than the lowest sensitivity limit of the blocking method (about 10^{-18} s in the case of the nuclear reaction under study). But as was demonstrated in [28], the emission of "hard" neutrons at the earliest stages of thermodynamic equilibration (see Fig. 10) leads to the formation of daughter nuclei "colder" than those formed upon the emission of evaporated neutrons. Because of a decrease in the excitation energy, the lifetimes of fissioning nuclei significantly increase; therefore, preequilibrium neutron emission can affect the experimental lifetime values. In view of this, it is necessary to evaluate the fraction of preequilibrium neutron emission in the total neutron yield from the compound nuclear system formed in the reaction being investigated.

The calculated preequilibrium fraction of neutron emission for various beam energies is presented in Fig. 11. One can see that the fraction of fissioning nuclei produced upon preequilibrium neutron emission is less than 15% for initial compound nuclei. But in the total neutron yield in the emission cascade, with the inclusion of neutron emission from the second potential well, the preequilibrium neutron fraction is less than 1.5%. In analyzing our experimental lifetime data, we can therefore neglect the mechanism of formation of "colder" fissioning daughter nuclei.

4.2. Time Decay Characteristics of Compound Nuclei with a Double-Humped Fission Barrier

In [2], the fission of compound nuclei that possess two classes of excited states realized in the first and second potential wells of a double-humped fission barrier was analyzed in terms of a statistical model. With reference to Fig. 12, we may identify the following two evolution stages in a fissioning nucleus:

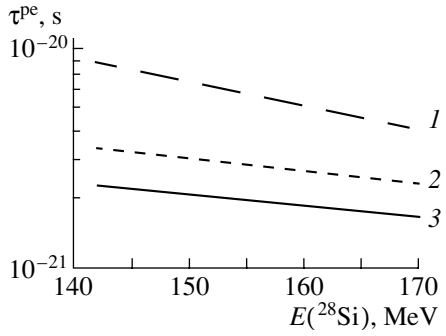

Fig. 7. Equilibration time as a function of the energy of bombarding particles in the $^{28}Si + {}^{196}Pt$ reaction according to the calculations for the (*1*) (10*p*, 1*h*), (*2*) (18*p*, 1*h*), and (*3*) (30*p*, 1*h*) initial exciton configurations.

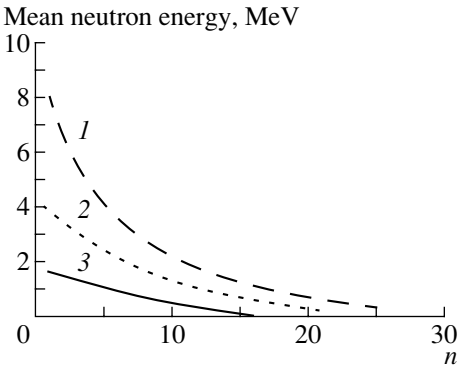

Fig. 8. Mean energy of preequilibrium neutrons emitted from the ^{224}U nucleus produced in the $^{28}Si + {}^{196}Pt$ reaction at the beam energy of 150 MeV according to the calculations for the (*1*) (10*p*, 1*h*), (*2*) (18*p*, 1*h*), and (*3*) (30*p*, 1*h*) initial exciton configurations.

(i) the formation and decay of excited states under equilibrium deformation [the excited states in the first potential well can decay either through the emission of particles or photons (or both) or through nonradiative transitions across the inner fission barrier to states in the second potential well];

(ii) decay of the second-well states [this can proceed either via the emission of particles or photons (or both), or via nonradiative transitions across the inner fission barrier into first-well states, or via transitions across the outer barrier, i.e., fission].

In this case, the populations of the states in the first and second potential wells [$n_1(t)$ and $n_2(t)$, respectively] are described by the set of "master" equations [2] ($\hbar = 1$)

$$\begin{cases} \dfrac{dn_1(t)}{dt} = -\Gamma_1 n_1(t) + \Gamma_{21} n_2(t) \\ \dfrac{dn_2(t)}{dt} = -\Gamma_2 n_2(t) + \Gamma_{12} n_1(t), \end{cases} \tag{18}$$

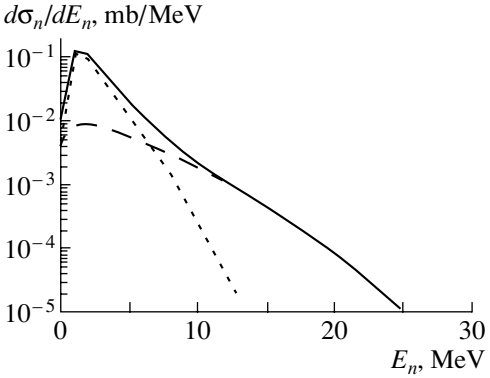

Fig. 9. Energy spectra of neutrons emitted from the ^{224}U nucleus produced in the $^{28}Si + {}^{196}Pt$ reaction at the beam energy of 150 MeV according to the calculations for the (18*p*, 1*h*) initial exciton configuration: (solid curve) total neutron spectrum, (dashed curve) spectrum of preequilibrium neutrons, and (short-dashed curve) spectrum of equilibrium (evaporated) neutrons.

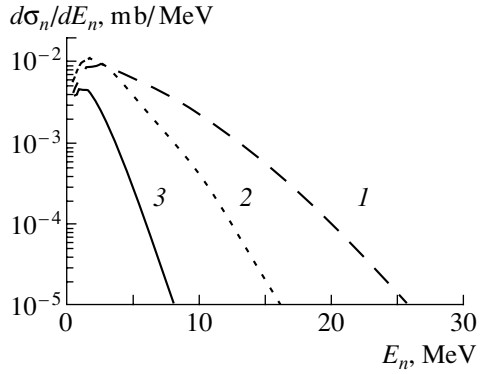

Fig. 10. Energy spectra of preequilibrium neutrons emitted from the ^{224}U nucleus produced in the $^{28}Si + {}^{196}Pt$ reaction (taken as an example) at the beam energy of 150 MeV according to the calculations for the (*1*) (10*p*, 1*h*), (*2*) (18*p*, 1*h*), and (*3*) (30*p*, 1*h*) initial exciton configurations.

where Γ_1 and Γ_2 are the total decay widths of first- and second-well states, respectively:

$$\Gamma_1 = \sum_i \Gamma_{1i} + \Gamma_{12}, \tag{19}$$

$$\Gamma_2 = \sum_i \Gamma_{2i} + \Gamma_{2f} + \Gamma_{21}. \tag{20}$$

Here, Γ_{1i} and Γ_{2i} are the partial widths with respect to the emission of particles and photons from the first and second potential wells, respectively; Γ_{12} and Γ_{21} are the widths with respect to nonradiative transitions through the inner fission barrier from one potential well to the other; and Γ_{2f} is the width with respect to the transitions through the outer barrier from the second well.

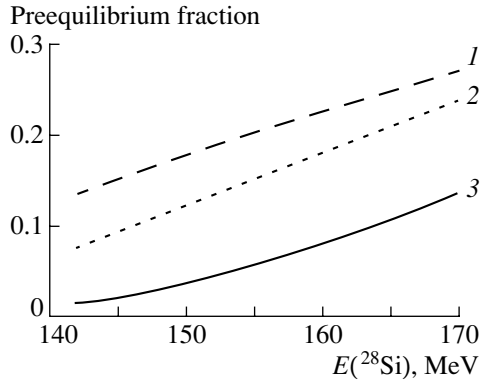

Fig. 11. Yield of the preequilibrium component of neutron emission for various energies of bombarding particles in the $^{28}\mathrm{Si} + {}^{196}\mathrm{Pt}$ reaction (taken as an example) according to the calculations for the (*1*) $(10p, 1h)$, (*2*) $(18p, 1h)$, and (*3*) $(30p, 1h)$ initial exciton configurations.

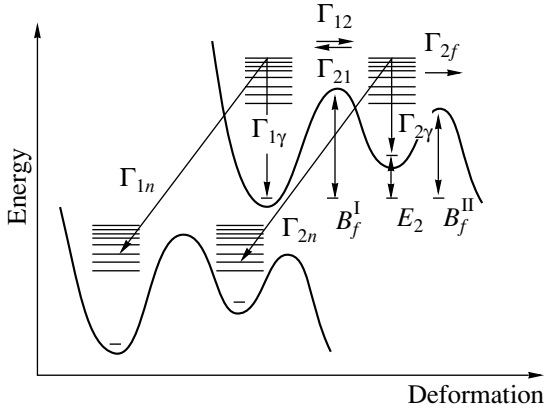

Fig. 12. Scheme of population and decay of excited states in the first and second potential wells of heavy fissionable nuclei. Here, B_f^{I} and B_f^{II} are the heights of the inner and outer fission barriers, respectively; E_2 is the second-potential-well depth, while the widths Γ are introduced in the text.

Assuming that, at the initial instant ($t = 0$), the populations of the states in the first and second potential wells are

$$n_1(0) = 1, \;\; n_2(0) = 0, \tag{21}$$

one can easily obtain [2] solutions to Eqs. (18), $n_1(t)$ and $n_2(t)$. Once they are known, the counting rate in any specific decay channel can easily be obtained.

For example, the counting rate in the induced-fission decay channel is

$$\frac{dn_f(t)}{dt} = \Gamma_{2f} n_2(t), \tag{22}$$

while, in decay channels associated with particle emission or in the γ-decay channel, we have

$$\frac{dn_i(t)}{dt} = \Gamma_{1i} n_1(t) + \Gamma_{2i} n_2(t). \tag{23}$$

A similar situation occurs for the mean decay times

$$\tau_j = \frac{\int_0^\infty t \frac{dn_j(t)}{dt} dt}{\int_0^\infty \frac{dn_j(t)}{dt} dt}, \tag{24}$$

which will also depend on the exit reaction channel.

It was shown in [3, 4] that the induced-fission time of decay

$$\tau_f = \frac{\Gamma_1 + \Gamma_2}{\Gamma_1\Gamma_2 - \Gamma_{12}\Gamma_{21}} \tag{25}$$

is longer than the time of decay of an excited nucleus via any other channel,

$$\tau_i = \left\{ \frac{\Gamma_1 + \Gamma_2}{\Gamma_1\Gamma_2 - \Gamma_{12}\Gamma_{21}} - \frac{\Gamma_{1i}}{\Gamma_{1i}\Gamma_2 + \Gamma_{2i}\Gamma_{12}} \right\}. \tag{26}$$

The additional time delay in the decay of an excited nucleus via the fission channel is determined by the expression

$$\Delta\tau = \tau_f - \tau_i = \frac{\Gamma_{1i}}{\Gamma_{1i}\Gamma_2 + \Gamma_{2i}\Gamma_{12}}. \tag{27}$$

Expressions (25)–(27) are especially pronounced if the coupling of excited states in the first and second potential wells is weak (i.e., $\Gamma_{21} \ll \Gamma_2$) and if the emission of particles and photons from excited states in the second potential well is neglected:

$$\tau_f \simeq \frac{\hbar}{\Gamma_1} + \frac{\hbar}{\Gamma_2}, \tag{28}$$

$$\tau_i \simeq \frac{\hbar}{\Gamma_1}, \tag{29}$$

$$\Delta\tau \simeq \frac{\hbar}{\Gamma_2} = 2\pi\hbar\frac{\rho_2}{N_2}. \tag{30}$$

Here, ρ_2 is the level density in the second potential well, and N_2 is the effective number of decay channels for second-well excited states.

It follows from (28)–(30) that the additional fission time delay is directly related to the lifetime of second-well excited states. Thus, the existence of two classes of quasistationary transition states in heavy nuclei leads to the differences of the dynamical characteristics of decay (such as mean decay times) through different exit channels. In this case, the decay times differ from the times of decay of excited nuclei featuring one class of excited states ($\tau_f = \tau_i = \hbar/\Gamma_1$) [4].

From (30), it can also be seen that the experimental determination of the additional time delay of the induced fission reaction, $\Delta\tau$, permits one to obtain information on the nuclear characteristics of strongly deformed excited states, such as the level density in the second potential well, the fission-barrier parameters, and shell corrections [29]. At the same time, it was demonstrated in [4] that traditional time-integrated decay characteristics, such as cross sections, are insensitive to the structure of excited states in the second potential well of fissioning nuclei in the above-barrier region of excitation energies.

4.3. Analysis of the Probability of Populating Second-Well States

As was noted above, transition excited states in the second potential well can greatly affect the fission dynamics of compound nuclei, increasing the mean time of decay via the fission channel in relation to any other decay channels. This effect is of importance only when these states are populated with a high probability, owing to the damping of collective motion [30].

In order to estimate this probability for the case of the nuclear reaction under study, we used the diffusion model [31], which permits us to take into account both thermal fluctuations in the fission mode and nuclear dissipation phenomena.

In the diffusion model [31], a fissioning system is described by a time-dependent distribution function $f(x,p,t)$. The function f depends on the collective variables x associated with the deformation of the system and its conjugate momentum p. The time evolution of the distribution function in phase space is described by the Fokker–Planck equation, which, in the case of one deformation degree of freedom, has the form

$$\frac{\partial f}{\partial t} = -\frac{p}{m}\frac{\partial f}{\partial x} + \frac{\partial U(x)}{\partial x}\frac{\partial f}{\partial p} + \frac{\gamma}{m}\frac{\partial}{\partial p}(fp) + D\frac{\partial^2 f}{\partial p^2}, \tag{31}$$

where $U(x)$ is the deformation potential, m is the reduced mass of the system, and γ is the friction constant that describes the coupling of the fission degree of freedom to the remainder of the system. The diffusion constant is given by $D = \gamma T^*$, where T^* is the effective temperature of the nuclear system.

In the present calculations, we used the quadratic approximation for the deformation potential $U(x)$,

$$U(x) = E_i \pm \frac{1}{2}m\omega_i^2(x - x_i)^2, \tag{32}$$

where $i = 1, 2, 3$; the positive sign applies to $i = 2$ (second potential well), and the negative sign corresponds to $i = 1, 3$ (inner and outer fission barriers, respectively); E_i represent the minima and maxima of the double-humped potential barrier; $\hbar\omega_i$ are their respective curvature energies; and x_i are the locations of extreme values of the deformation energy (fission coordinate).

We required that the parabolas representing the inner and outer fission barriers match smoothly with the parabola representing the second minimum at their points of intersection. This leads to four matching conditions. In order to specify the double-humped fission barrier, we used the translation invariance of the potential barrier along the x axis,

$$U(x) = E_2 \text{ at } x = x_2 = 0, \tag{33}$$

and six parameters. These are chosen to be three energies E_i and three curvature energies $\hbar\omega_i$. The values of these parameters were fixed on the basis of the well-known systematics of the parameters of double-humped fission barrier [32, 33].

In addition, we included a deep minimum for $x > x_3$ (corresponding to deformations near the scission point), which is identified with the completed fission process. In our calculations, we assumed that, at the temperatures considered here, the backflow through the outer fission barrier is absent.

For the inertia parameter m, we have taken the reduced mass corresponding to symmetric fission ($m = A/4$). The reduced dissipation coefficient $\beta = \gamma/m$ is treated as a coordinate-independent quantity.

For the effective temperature of a fissioning nuclear system, we took the value corresponding to the intrinsic excitation energy of the compound system. This temperature, which determines the equilibrium variance of the coordinate of a quantum oscillator according to the fluctuation–dissipation theorem and which makes it possible to take into account both thermal and quantum fluctuations, was found from the well-known relation [31, 34, 35]

$$T^* = \frac{\hbar\omega(\bar{x}(t))}{2\pi}\coth\frac{\hbar\omega(\bar{x}(t))}{2T}, \tag{34}$$

where

$$\bar{x}(t) = \frac{\int\limits_{-\infty}^{+\infty} dp \int\limits_{-\infty}^{+\infty} xf(x,p,t)dx}{\int\limits_{-\infty}^{+\infty} dp \int\limits_{-\infty}^{+\infty} f(x,p,t)dx} \tag{35}$$

and

$$T = \sqrt{\bar{E}_{\text{int}}(t)/(A/10)}. \tag{36}$$

The intrinsic excitation energy of the nucleus is represented as the difference

$$\bar{E}_{\text{int}}(t) = E^* - \bar{E}_{\text{coll}}(t), \tag{37}$$

where E^* is the total excitation energy and the kinetic energy of the collective motion of the fissioning compound system is

$$\bar{E}_{\text{coll}}(t) = \frac{\int\limits_{-\infty}^{\infty} dp \int\limits_{x_1}^{x_3} dx(p^2/2m + U(x))f(x,p,t)}{\int\limits_{-\infty}^{\infty} dp \int\limits_{-\infty}^{\infty} dx f(x,p,t)}. \tag{38}$$

The distribution function $f(x,p,t)$ obeys the initial condition

$$f(x,p,t=0) = f(p)\delta(x - x_1), \tag{39}$$

where x_1 is the value of the collective variable at the first saddle point. The initial collective-momentum

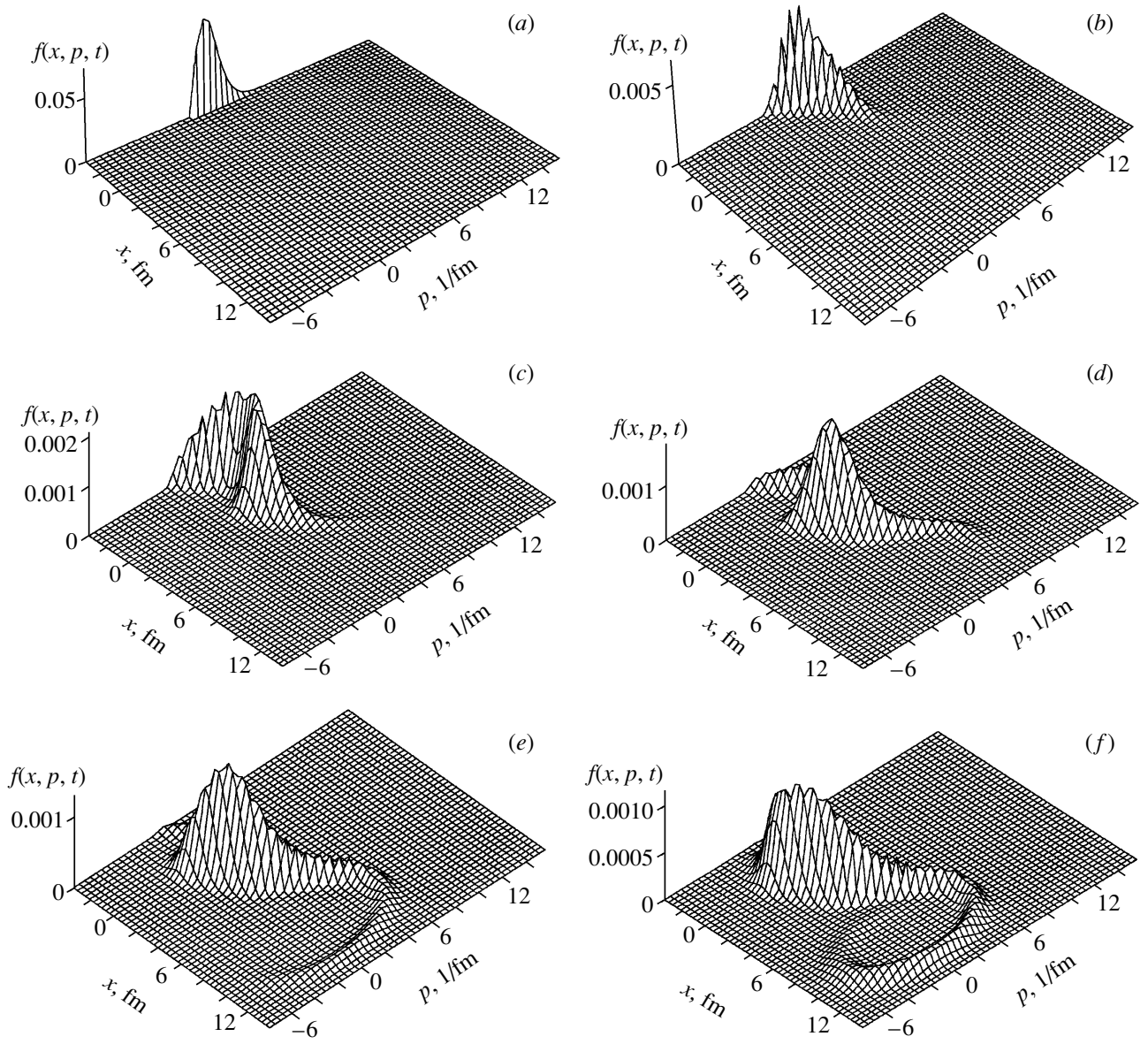

Fig. 13. Calculated spreading distribution $f(x,p,t)$ of the ^{224}U fissioning system for the reduced dissipation coefficient of $\beta = 0.2 \times 10^{21}$ s^{-1} and the excitation energy of $E^* = 60$ MeV at (*a*) $t_0 = 0$, (*b*) $t_1 = 2 \times 10^{-21}$ s, (*c*) $t_2 = 4 \times 10^{-21}$ s, (*d*) $t_2 = 6 \times 10^{-21}$ s, (*e*) $t_2 = 8 \times 10^{-21}$ s, and (*f*) $t_3 = 10 \times 10^{-21}$ s.

distribution $f(p)$ is related to the kinetic-energy distribution at the first saddle point and was calculated within the transition-state method [36]:

$$F(E_{\rm kin}) = C\frac{\rho(E^* - U(x_1) - E_{\rm kin})}{1 + \exp(2\pi E_{\rm kin}/\hbar\omega_1)}. \qquad (40)$$

Here, $\rho(E^* - U(x_1) - E_{\rm kin})$ is the level density at the first saddle point, and C is the normalization factor.

The Fokker–Planck equation was solved by means of the propagator method [34].

The spreading distribution $f(x,p,t)$ of the ^{224}U fissioning system produced upon the complete fusion of the ^{28}Si projectile nucleus with the ^{196}Pt target nucleus in phase space at various times is presented in Fig. 13 as an example of the results of our calculations.

The probability of the second-well-state population was determined by the relation

$$W(x_3, t_p) = \frac{\int\limits_{-\infty}^{\infty} dp \int\limits_{x_1}^{x_3} dx f(x,p,t_p)}{\int\limits_{-\infty}^{\infty} dp \int\limits_{-\infty}^{\infty} dx f(x,p,t_p)}, \qquad (41)$$

where t_p is the transient time required for fission events without trapping in the second well. The time

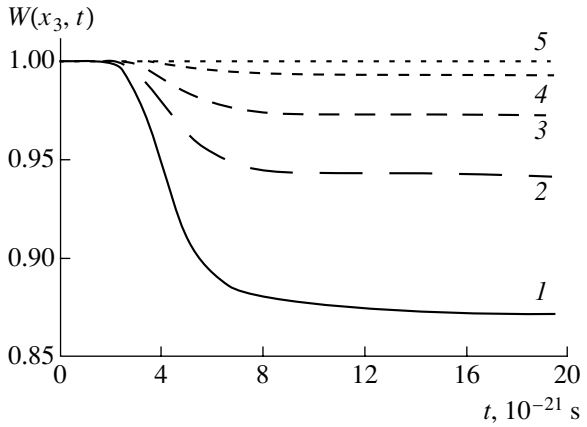

Fig. 14. Typical time dependence of the probability of finding the ^{224}U fissioning system to the left of the second saddle according to the calculations for $E^* = 60$ MeV and the β values of (*1*) 0.2×10^{21}, (*2*) 0.3×10^{21}, (*3*) 0.4×10^{21}, (*4*) 0.6×10^{21}, and (*5*) 1.0×10^{21} s^{-1}.

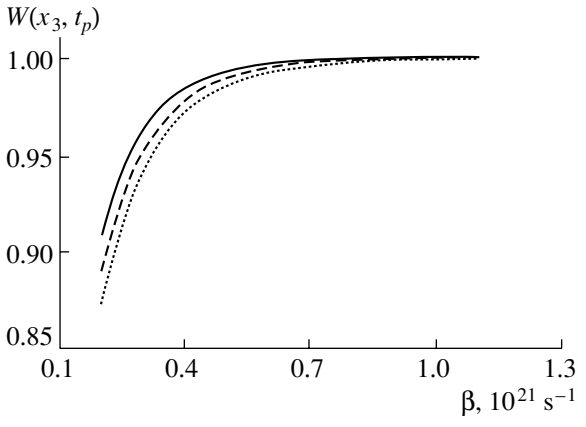

Fig. 15. Probabilities of populating second-well states versus the reduced dissipation coefficient β for the fissioning ^{224}U nucleus according to the calculations at the excitation energies of (solid curve) 50, (dashed curve) 60, and (dotted curve) 70 MeV.

dependence of the second-well-state population was used in order to determine t_p. Typical time dependences of $W(x_3, t)$ for ^{224}U are presented in Fig. 14. Here, the stepwise change in the time dependences of $W(x_3, t)$ is due to the completion of fission motion without trapping in the second well. In the present calculations, the value of t_p was taken to be 1.5×10^{-20} s.

The calculated probabilities of populating the second-well states versus the reduced dissipation coefficient β for the ^{224}U nucleus, chosen as an example, are presented in Fig. 15 at various excitation energies in the range achieved in experiments. In these dependences, a very fast saturation with increasing β attracts attention. It can be seen that the probability becomes close to unity at very low β values that are consistent with underdamped collective motion. It should be noted that, at present, all the deduced dissipation coefficients are consistent with an overdamped motion ($\beta \geq 2 \times 10^{21}$ s^{-1}) of a fissioning nucleus [19, 37]. It is significant that, by using any other value of the reduced dissipation coefficient, such estimates only lead to an increase in the probability.

Figure 16 shows the dependence of the population probability for the ^{224}U nucleus on the difference of the minimal fission barrier and the second-well depth $[\min(E_1, E_3) - E_2]$ at various values of the excitation energy and $\beta = 0.5 \times 10^{21}$ s^{-1}. It can be seen that, even for a very shallow second potential well $[\min(E_1, E_3) - E_2 \simeq 5$ MeV], the probability remains rather large (≥ 0.8). This fact is supposedly due to a small increase in the kinetic energy of the fission mode during the evolution from the first saddle point to the second potential well.

The calculated probabilities of populating second-well states in the ^{224}U fissioning nucleus versus the excitation energy are presented in Fig. 17. These calculations were also made for the cases of temperature-dependent and temperature-independent fission-barrier parameters. In the first case, we took into account the damping of shell effects with increasing nuclear temperature (for more details, see Subsection 4.4). As one can see from the data presented in Fig. 17, the inclusion of the temperature damping of shell effects in the potential surface of fissioning nucleus under study leads to a decrease in the population probabilities, especially at high excitation energies. This is due, first of all, to a decrease in the second-well depth {i.e., the parameter $[\min(E_1, E_3) - E_2]$—see Fig. 16}. However, it is necessary to emphasize that, even despite a decrease in the probability with increasing excitation energy, its magnitude exceeds 0.7 in the energy range being considered.

Thus, our calculations indicate that the probability of populating the second well remains close to unity for the energies to which fissioning nuclei are excited in the present experiments, even for small values of the reduced dissipation coefficient and even for a very shallow second well. This means that we must consider the lifetime of the excited states in the second potential well in the analysis of the experimental data on the fission lifetimes of actinide nuclei in this excitation-energy region.

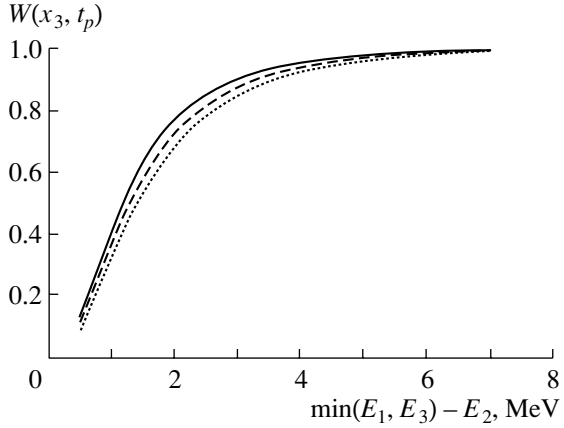

Fig. 16. Probability of populating second-well states in the ^{224}U fissioning nucleus as a function of the second-well depth according to the calculation for $\beta = 0.5 \times 10^{21}$ s^{-1} at the excitation energies of (solid curve) 50, (dashed curve) 60, and (dotted curve) 70 MeV.

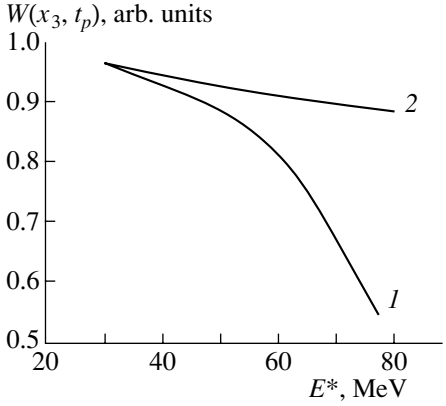

Fig. 17. Probability of populating second-well states in the ^{224}U fissioning nucleus as a function of the excitation energy according to the calculation at the reduced dissipation coefficient of $\beta = 0.5 \times 10^{21}$ s^{-1} for the cases of (*1*) temperature-dependent and (*2*) temperature-independent fission-barrier parameters.

4.4. Statistical Analysis of the Compound-Nuclei Decay Times

The experimental values of the fission decay time τ_f that were observed in the reaction under study are presented in Fig. 5. These values cover the range between 10^{-17} and 10^{-18} s, its specific value being dependent on the projectile energy.

Our theoretical analysis of the experimental data was made with reference to the statistical theory of nuclear reactions and with allowance for the fusion of bombarding nuclei with the natural isotopic mixture of target nuclei.

The statistical-model calculations were made by using the GFOT computer code [38], which was developed at the Institute of Nuclear Physics (Moscow State University) to analyze the dynamical decay characteristics of excited heavy nuclei. The GFOT code makes it possible to perform calculations both within a traditional approach, which assumes that the decay time of excited fissionable nuclei is determined exclusively by the lifetime of excited states at an equilibrium deformation, and within the approach that takes additionally into account the lifetime of excited nuclear states in the second potential well.

The cross section for compound-nucleus formation in the fusion of bombarding particles with target nuclei and also the distributions of the fissile nuclei with respect to the excitation energy and angular momentum at each step of the neutron-emission cascade were calculated within the optical model. The nuclear-potential parameters were taken from [39]. The Coulomb potential was treated in the parabola approximation.

According to (25), we calculated the fission decay times of excited compound nuclei within the statistical theory of nuclear reactions, taking into account the existence of two classes of excited states realized in the first and second potential wells:

$$\tau_f = 2\pi\hbar \frac{N_2\rho_1 + N_1\rho_2}{N_1N_2 - N_A^2}, \tag{42}$$

where ρ_1 and ρ_2 are the level densities in the first and the second potential well, respectively, and N_1 and N_2 are the total effective numbers of decay channels for first- and second-well excited states, respectively:

$$N_1 = N_A + \sum_i N_{1i}, \tag{43}$$

$$N_2 = N_A + N_B + \sum_i N_{2i}. \tag{44}$$

Here, i is the index of the emitted particle (neutron, proton, α particle) or of the emitted photon. The concrete form of N_{1i} was used as in [40], while N_{2i} was calculated by the same relation but with the level-density parameters in the second potential well. The effective number of channels of nonradiative transitions from the first to the second potential well was determined as

$$N_A = \int_{-B_f^I}^{E^*-B_f^I} \frac{\rho_A(E^* - B_f^I - \epsilon, J)d\epsilon}{1 + \exp(-2\pi\epsilon/(\hbar\omega_1))}. \tag{45}$$

It was assumed that it is equal to the effective number of channels of nonradiative transitions from the second to the first potential well. Analogously, it can

be found for the transitions through the outer fission barrier that

$$N_B = \int_{-B_f^{II}}^{E^*-B_f^{II}} \frac{\rho_B(E^* - B_f^{II} - \epsilon, J)d\epsilon}{1 + \exp(-2\pi\epsilon/(\hbar\omega_2))}, \qquad (46)$$

where ρ_A and ρ_B are the level densities at the first and at the second saddle point, respectively; B_f^{I} and B_f^{II} are the heights of the inner and the outer fission barrier, respectively; and J is the angular momentum.

In terms of the effective numbers of decay channels, the fission cross section and the cross section for the emission of the ith particle were expressed as

$$\sigma_f = \sigma_c \frac{N_A N_B}{N_1 N_2 - N_A^2}, \qquad (47)$$

$$\sigma_i = \sigma_{1i} + \sigma_{2i} = \sigma_c \frac{N_2 N_{1i} + N_A N_{2i}}{N_1 N_2 - N_A^2}, \qquad (48)$$

where σ_c is the cross section for compound-nucleus formation. It is necessary to emphasize that the probability of particle emission from excited first- and second-well states has been taken into account in the last expression.

In order to simulate the angular-momentum dependence of the double-humped fission barrier, we used the predictions of the advanced rotating liquid-drop model due to Sierk [41] that were corrected for shell effects,

$$B_f(J) = B_{\mathrm{ld}}(J) + \delta W_{\mathrm{add}}, \qquad (49)$$

where $B_{\mathrm{ld}}(J)$ is the liquid-drop part of the fission barrier and δW_{add} is the adiabatic value of the shell correction at the corresponding point of the potential surface.

In order to extract shell-correction values at the characteristic points of the fission barrier, i.e., at the first and second saddle points and in the second potential well, we took the difference of the liquid-drop part of the fission barrier and the real parameters of the double-humped fission barrier that were obtained by extrapolating the well-known systematics of experimental data [32].

The level density at the extreme points of the fission barrier was calculated within the level-density phenomenological model. The model allows one to take into account coherent collective excitations, correlation effects of the superconducting type, and shell effects [42].

In order to calculate the total level density within this model, we used the adiabatic approximation [43]

$$\rho(U, J) = \rho_{\mathrm{in}}(U, J) K_{\mathrm{coll}}(U), \qquad (50)$$

where $\rho_{\mathrm{in}}(U, J)$ is the intrinsic level density, which is associated with the internal degrees of freedom, and $K_{\mathrm{coll}}(U)$ is the collective-enhancement factor describing the effects of collective motions.

The density of internal nuclear states was calculated by the relation [44]

$$\rho_{\mathrm{in}}(U, J) = \frac{(2J+1)\sqrt{\pi}}{24\sqrt{2}\sigma_{\mathrm{eff}}^3\sqrt{a^3t^5}} \exp\left(2at - \frac{(J+\frac{1}{2})^2}{2\sigma_{\mathrm{eff}}^2}\right), \qquad (51)$$

where t is the nuclear temperature; a is the intrinsic level-density parameter; and σ_{eff} is the effective spin-cutoff parameter, which is related to the moments of inertia by the equation

$$\sigma_{\mathrm{eff}}^2 = I_\perp^{2/3} I_\parallel^{1/3} t. \qquad (52)$$

For the nuclear moments of inertia, we used the rigid-body values with the well-determined dependence on the quadrupole-deformation parameter ε [45],

$$I_\parallel = \frac{6}{\pi^2}\langle m^2\rangle a(1-\varepsilon^2)^{1/3}, \qquad (53)$$

$$I_\perp = \frac{2}{5} m_0 r_0^2 A^{5/3}(1-\varepsilon^2)^{-2/3}. \qquad (54)$$

The dependences in (53) and (54), which are distinct from the analogous dependences in [42], are suitable for any values of the quadrupole deformations.

For the mean square of the nuclear-magnetic-moment projection, we used the parametrization $\langle m^2\rangle = \xi A^{2/3}$, where $\xi = 0.19$ [45].

The values of the quadrupole-deformation parameter ε for the first and second potential wells were taken to be 0.2 and 0.6, respectively, and 0.4 and 0.8 for the first and second saddle points [46].

At nuclear temperatures above the critical point, the internal nuclear excitation energy has the form $U = at^2 - \Delta + E_{\mathrm{cond}}$. The condensation energy E_{cond}, which characterizes the decrease in the ground-state energy owing to the correlation interaction, was found from the parameter Δ [42]. The parameter Δ determines the odd–even difference of the nuclear binding energies (masses) in the ground state. It was chosen on the basis of the semiempirical estimate $\Delta_1 = 12/\sqrt{A}$ MeV [42]. In the second potential well, the corresponding parameter Δ_2 was chosen to be equal to the experimental value: $2\Delta_2 = 1.3$ MeV [32].

The phenomenological model parameter a, which allows for shell effects in the behavior of the level density within the shell-correction method, was taken above the critical temperature [42]:

$$a(U) = \tilde{a}\left(1 + f(U)\frac{\delta W}{U - E_{\mathrm{cond}} + \Delta}\right). \qquad (55)$$

Here,

$$f(U) = 1 - \exp(-\gamma(U - E_{\mathrm{cond}} + \Delta)) \qquad (56)$$

is the dimensionless universal function determining the energy dependence of the level-density parameter, and δW is the shell correction. For the parameter γ, we used the traditional value of $\gamma = 0.064$, which was obtained from the systematized data on the approximation of the experimental density of neutron resonances for heavy nuclei [47].

The asymptotic values of the level-density parameter $\tilde{a}$ at high excitation energies were calculated with allowance for the influence of the diffusivity of the surface layer of nuclei, according to [48], as

$$\tilde{a} \approx \alpha r_0^3 A + \beta r_0^2 A^{2/3} B_s + \gamma r_0 A^{1/3} B_k, \qquad (57)$$

where

$$B_s = \oint\limits_{\Sigma} d\sigma / 4\pi R^2 \qquad (58)$$

and

$$B_k = \oint\limits_{\Sigma} k d\sigma / 8\pi R \qquad (59)$$

are the surface area of a deformed nucleus and its integrated curvature (normalized to the corresponding values for the spherical nucleus), respectively; the symbol k represents the local curvature of the nuclear surface, which is defined in terms of the principal radii of curvature [48]; and $r_0 = 1.16$ fm is the "scale" parameter corresponding to the charge radius, which is determined from the experiments on elastic electron scattering. The numerical values of the parameters α, β, and γ were taken from [48]. The numerical values of the coefficients B_s and B_k for various values of the quadrupole and the hexadecapole deformation were taken from the calculations performed in [49].

Below the phase-transition point, the parametrization proposed in [42] was used to describe the above-listed level-density relations.

The collective enhancement factor has the form

$$K_{\rm coll}(U) = K_{\rm vibr}(U) K_{\rm rot}(U), \qquad (60)$$

where $K_{\rm vibr}(U)$ and $K_{\rm rot}(U)$ are the factors of vibrational and rotational enhancements, respectively.

In order to calculate the factor of vibrational enhancement, we used the liquid-drop estimate [42]

$$K_{\rm vibr}(U) = \exp\left\{1.69\left(\frac{3m_0 A}{4\pi\sigma_{\rm ld}}\frac{C_{\rm ld}}{C}\right)^{2/3} t^{4/3}\right\}, \qquad (61)$$

where $\sigma_{\rm ld} = 1.2$ MeV fm^{-2} is the surface tension in the liquid-drop model corresponding to the analogous phenomenological parameter in the mass formula. The ratio $C_{\rm ld}/C$ characterizes the difference of the rigidity coefficients between an excited nucleus and a liquid drop. In our calculations, we set $C = C_{\rm ld}$.

For the rotational enhancement factor, we used the following expression, which depends strongly on the type of nuclear-shape symmetry:

$$K_{\rm rot} = \begin{cases} 1 & \text{for spherical nuclei} \\ \sigma_\perp^2 & \text{for axisymmetric and mirror-symmetric nuclei} \\ 2\sigma_\perp^2 & \text{for axisymmetric and} \\ & \text{mirror-asymmetric nuclei} \\ \sqrt{\pi/2}\sigma_\perp^2\sigma_\parallel & \text{for ellipsoidal symmetry} \\ \sqrt{2\pi}\sigma_\perp^2\sigma_\parallel & \text{for axially asymmetric and} \\ & \text{mirror-symmetric nuclei} \\ \sqrt{8\pi}\sigma_\perp^2\sigma_\parallel & \text{for nuclei possessing no symmetry.} \end{cases} \qquad (62)$$

Here, $\sigma_\perp = I_\perp t/\hbar^2$ and $\sigma_\parallel = I_\parallel t/\hbar^2$, where $I_\perp$ and $I_\parallel$ are the nuclear moments of inertia with respect to the axes perpendicular and parallel to the symmetry axis, while t is the nuclear temperature.

Following common ideas of nuclear shapes (see, for example, [50]), we used the approximation of axial and reflection symmetry at an equilibrium deformation. According to traditional assumptions, axial asymmetry and reflection symmetry (axial symmetry and reflection asymmetry) were used at the first (second) saddle point. In the second potential well, the axial and reflection asymmetries of the nuclear shape were assumed according to [51, 52].

In Fig. 5, we present the results of the calculation of the fission decay times averaged over the isotopic composition of the initial compound nuclei ^{222}U, ^{223}U, and ^{224}U produced in the reaction investigated here.

As one can see, a simple calculation of the fission decay time within the advanced rotating liquid-drop model [41] taking into account only the lifetime of

excited states at an equilibrium deformation underestimates the experimental values by approximately three orders of magnitude. If we include the double-humped-fission-barrier model in the analysis with allowance for the lifetime of excited states in the second and first potential wells [4], the description of the experimental data is greatly improved.

The solid curves in Fig. 5 represent the results of the calculations performed within the double-humped-fission-barrier model that take into account all possible fission chances according to the expression

$$\tau_f = \sum_i \tau_{fi}\beta_i, \qquad (63)$$

where β_i is the contribution of the FF of the ith fission chance to the total yield of FF in the nuclear reaction under study and τ_{fi} is the fission decay time of the ith fission chance. Neutron emission leads to the cooling of nuclei before fission and, as a result, to an increase in the mean decay times in the fission channel.

In this case, the possibilities of neutron emission from the first and second potential wells were considered. Our analysis demonstrates that the probability of neutron emission from the second potential well, which leads to the population of the second-well states of daughter nuclei, is commensurate with or higher than the probability of neutron emission from the states at an equilibrium deformation. Therefore, the lifetimes of excited states in the second well play a significant role in the observed fission decay time.

The solid curve *1* in Fig. 5 was calculated without the damping of shell effects with increasing nuclear temperature. It can be seen that this curve overestimates the experimental τ_f values. To take into account the decrease in the shell-correction part (δW) of the fission-barrier parameters (heights of the inner and outer fission barriers and the second-well depth) with increasing nuclear temperature, we represented the shell correction as $\delta W = \delta W_{\rm add} F$, where F is a universal Fermi-type damping function $F(T)$ [53],

$$F(T) = \frac{1}{1+\exp((T-T_0)/d)}, \qquad (64)$$

where $d = 0.2$ MeV is the rate at which the shell correction decreases with increasing nuclear temperature and T_0 is an adjustable parameter. The best description of the experimental data can be achieved at $T_0 = 1.75$ MeV.

Thus, our experimental data indicate that the fission barriers retain their double-humped structure in the range of excitation energies considered here and that the lifetimes of transition excited states in the second potential well significantly contribute to the observed fission decay times.

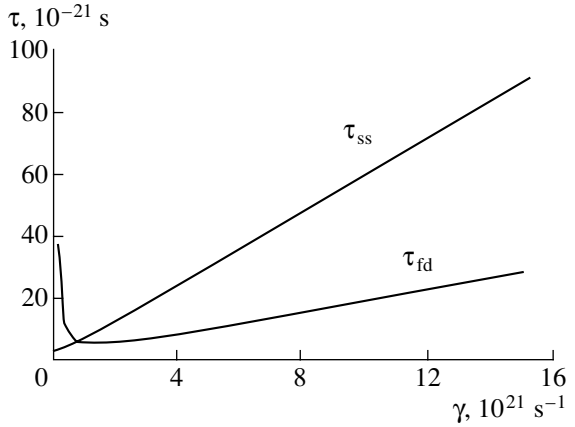

Fig. 18. Estimated time to build up the fission flux at the saddle point ($\tau_{\rm fd}$) and estimated time it takes for the system to move from the saddle to the scission point ($\tau_{\rm ss}$) versus the normalized nuclear-friction coefficient for the case of the ^{224}U fissioning nucleus with an excitation energy of 40 MeV.

4.5. Analysis of the Influence of Dynamical Processes on the Duration of Induced Fission Reaction

Compound-nucleus fission has two dynamical time scales: the time to build up the fission flux at the saddle point ($\tau_{\rm fd}$) and the time it takes for a fissioning system to move from the saddle to the scission point ($\tau_{\rm ss}$).

In the presence of the phenomenon of nuclear dissipation, the saddle–scission time is given by

$$\tau_{\rm ss} = \tau_{\rm ss}^0(\sqrt{(1+\gamma^2)}+\gamma), \qquad (65)$$

where $\tau_{\rm ss}^0 = (3\times 10^{-21})$ s [20, 54].

Usually, $\tau_{\rm fd}$ is estimated on the basis of the relation [19, 55]

$$\tau_{\rm fd} = \frac{\beta}{2\omega_{\rm gs}^2}\ln(10B_f/T) = \frac{\gamma}{\omega_{\rm gs}}\ln(10B_f/T) \qquad (66)$$

for $\beta > 2\omega_{\rm gs}^2$ or

$$\tau_{\rm fd} = \frac{1}{\beta}\ln(10B_f/T) = \frac{1}{2\gamma\omega_{\rm gs}}\ln(10B_f/T) \qquad (67)$$

for $\beta < 2\omega_{\rm gs}^2$.

In expressions (65)–(67), the parameter $\gamma = \beta/2\omega_{\rm gs}$ is the normalized friction coefficient [see (31)], β is the reduced dissipation coefficient, and $\hbar\omega_{\rm gs}$ is a characteristic energy in the local potential surface near the ground state.

It should be noted that $\tau_{\rm fd}$ plays an important role in the decay of a fissionable compound nucleus, since this time delay may substantially change the contributions of competitive decay channels at the early stage of the evolution of a fissioning nucleus.

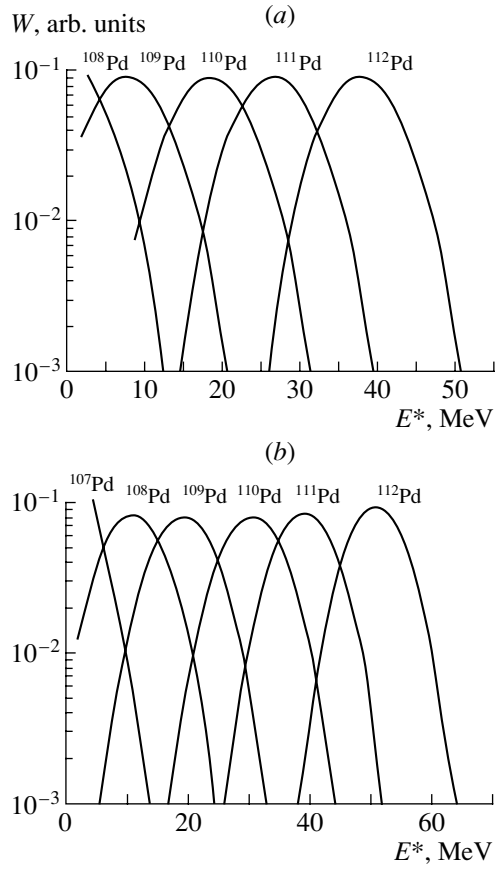

Fig. 19. Excitation function calculated for nuclei formed in the development of the neutron-evaporation cascade in excited FF produced in the reaction ^{196}Pt(^{28}Si, f) for beam energies of (*a*) 140 and (*b*) 170 MeV.

The results obtained by estimating $\tau_{\rm fd}$ and $\tau_{\rm ss}$ for the case of the ^{224}U fissioning nuclear system, chosen as an example, with an excitation energy of 40 MeV (which is minimal in our energy range) are presented in Fig. 18 versus the normalized friction coefficient γ. It should be noted that, in the estimations, we varied the γ values in the range given in the review of Hilscher and Rossner [19], who present all available data on the dissipation coefficient that were obtained from an analysis of various observables of heavy-ion-induced reactions. It is seen that these time scales are very short (not longer than 10^{-19} s) relative to the reaction time values observed in the present experiments.

4.6. Analysis of the Dechanneling Process due to the In-flight Decay of Observed FF

The phenomenon of the in-flight decay of the observed FF was first described by Karamyan [56], Gomez del Campo *et al.* [57], and Sellshop *et al.* [58] and is based on the observation that the reaction products are themselves excited nuclei that can decay by γ or particle emission during their flight within a crystal. The recoil associated with in-flight decay produces a random perturbation on the fragment path that fills the blocking dip, simulating a compound nucleus having a long lifetime.

In fact, it is possible to include this effect in the theory of channeling, and this results in a new method that is able to measure the lifetime of in-flight fragments [9, 13].

The dechanneling effect must be taken into account in interpreting the results of crystal-blocking experiments.

Let us assume, for the sake of simplicity, that the beam interacts with a lattice atom, producing a compound nucleus whose primary lifetime is $\tau_1 \approx 0$; i.e., it is below the sensitivity limit of the blocking method. The compound nucleus splits into excited FF, which eventually decay in flight after a secondary mean time τ_2. The distributions of recoil angles ψ can be calculated from reaction kinematics and can be introduced in our Monte Carlo code for channeling [13].

Under the assumption of isotropic emission from FF in the c.m. frame and of small deflection angles, the probability density for ψ is [58]

$$f(\psi) = \frac{\psi/\psi_m}{(\psi_m^2 - \psi^2)^{1/2}}, \quad \psi \in [0, \psi_m], \tag{68}$$

where the maximum deflection angle ψ_m is given by

$$\psi_m^2 = E_\gamma^2/(2Mc^2T) \tag{69}$$

for γ decay or by

$$\psi_m^2 = M_pT_p/(MT) \tag{70}$$

for particle decay. Here, M and T (M_p and T_p) are, respectively, the mass and the kinetic energy of the FF (emitted particle).

The deflection angles ψ can easily be sampled as

$$\psi = \psi_m\sqrt{1 - Ran^2}, \tag{71}$$

where *Ran* is a uniform [0, 1] variation. They can be introduced in the full three-dimensional Monte Carlo simulation, together with the azimuthal angle χ that is assumed to be uniform in the segment $[-\pi, +\pi]$. In this way, a new direction of propagation was generated for FF, whose subsequent path was calculated in the usual way [13].

Clearly, the effect on the whole blocking pattern will depend on the distribution of distances x_L traveled along its path by the FF before decay; hence, we find for exponential decay along the longitudinal mean displacement that

$$s_L = \langle x_L \rangle = v\tau_2, \tag{72}$$

where v is velocity of the FF.

In particular, the blocking pattern remains unchanged if $s_L = 0$. In fact, the angular distribution of FF due to decay has to be convoluted with that before decay, which is initially isotropic (and therefore remains isotropic) at small angles around the crystal axis.

If s_L now increases, the originally isotropic distribution evolves toward the blocking pattern, which is reached upon passing a few tenths of crystal planes. Correspondingly, the dechanneling effect due to in-flight decay ever becomes larger, and so does the modification to the final blocking pattern.

Detailed calculations performed with the Monte Carlo code have shown that the way in which the blocking pattern is strongly affected depends on the maximum deflection angle ψ_m [see (69) and (70)].

A simple kinematical consideration demonstrated that, in the case of heavy FF, the emission of photons cannot produce a considerable-secondary lifetime effect. In the decay of excited FF, the main decay mode is neutron emission (the α-decay yield is approximately two orders smaller). Assuming that $T_n = 0.5$ MeV and $T = 150$ MeV, we obtain the value of $\psi_m = 5.455$ mrad for FF. Therefore, $s_L = 0.05$ Å is necessary for the secondary lifetime to affect the blocking pattern. According to the values of the FF velocity that are realized in the reaction under study, the τ_2 values must be greater than about 10^{-16} s to have the effect of the secondary lifetime.

We used the GFOT computer code (see Subsection 4.4) to calculate the excitation functions for the FF, neutron-evaporation-cascade components, produced in the reaction investigated here (see Fig. 19) on the basis of the statistical theory of nuclear reactions. The calculations were made by using the level-density parameters from the well-known systematics of Dilg *et al.* [59]. We used the mean values of the excitation energy of FF (evaluated from the equation of reaction-energy balance): 38 and 51 MeV for the beam energies of 140 and 170 MeV, respectively. The shapes of the fission-fragment energy distributions were simulated by the Gaussian form with a variance of 10 MeV (FWHM). In this case, we have a six- or seven-neutron evaporation cascade from excited FF.

The values of τ_2 can be greater than 10^{-16} s in the range of 1 to 2 MeV around the neutron binding energy for the penultimate nucleus of the cascade (see Fig. 20). Since we extracted information about the primary lifetimes of compound nuclei from the ratio $R(E_{\mathrm{Si}}) = \Omega(E_{\mathrm{Si}})/\Omega(E_{\mathrm{Si}} = 170\,\mathrm{MeV})$, we must evaluate the fraction of FF having τ_2 greater than 10^{-16} s for beam energies of 140 and 170 MeV. We obtained this fraction as 6.8 and 6.6% for the cases of 140 and 170 MeV, respectively. Thus, we have demonstrated

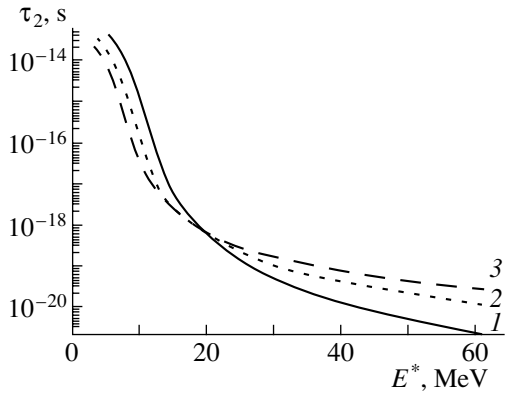

Fig. 20. Results of statistical calculations for the lifetime of the fission fragments (*1*) ^{108}Pd, (*2*) ^{107}Pd, and (*3*) ^{109}Pd produced in the reaction ^{196}Pt(^{28}Si, f) versus the excitation energy.

that the secondary-lifetime effect exists for the "delayed" blocking patterns and for the "prompt" one. But the influence of the secondary lifetimes is virtually the same for the beam energy used.

5. DISCUSSION AND CONCLUSIONS

We have measured delay times for induced fission in nuclei produced in the ^{28}Si + ^{nat}Pt reaction at bombarding energies of 140 to 170 MeV. Delay times induced in the fission channel by the compound nucleus (U isotopes with initial excitation energies of 40 to 70 MeV) vary from 10^{-17} to 10^{-18} s. This excitation-energy range is very interesting because, here, we can expect (from the energy dependence of the mass–energy distributions of FF [60] and other experimental data) that the influence of the nuclear-shell structure on the deformation energy of fissionable nuclei begins to decrease and that the double-humped fission barrier tends to transform into a single-humped one, so that nuclei have only one class of excited states.

The analysis of our experimental data has demonstrated that the time characteristics of fissioning heavy nuclei are very sensitive to the structure of the fission barrier. The rotating-liquid-drop-model calculation of τ_f underestimates the experimental data by approximately three orders of magnitude. In this case, a very low fission barrier (3.5 MeV) leads to a low probability of neutron emission by compound nuclei ($\Gamma_n/\Gamma_f \approx 0.01$) and, as a result, to a low probability of multichance fission.

The main goal of our investigations has been to find the energy range where shell effects totally disappear. The result has been that the experimental data

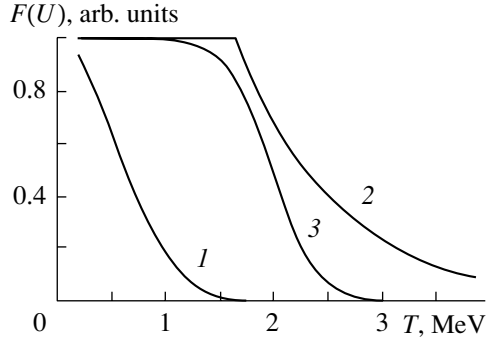

Fig. 21. Various types of damping functions discussed in the text. Curves *1* and *2* were obtained by using the damping from [42] and [61], respectively. Curve *3* represents the damping function of the Fermi type with $d = 0.2$ MeV and $T_0 = 1.75$ MeV.

can be understood only on the basis of the double-humped-fission-barrier model allowing for a time delay in the second well. In this case, they are successfully described by taking into account the damping of shell effects with increasing nuclear temperature. A phenomenological description of the temperature-dependent shell correction has been found by using the temperature parameter of the damping factor F, where $F = 1/2$ at $T = T_0 = 1.75$ MeV (see Fig. 21).

Indeed, an important property of the shell structure is that its influence on nuclear processes becomes less pronounced in highly excited nuclei and finally disappears at a certain temperature that was found by Strutinsky to be $t^* = \hbar\Omega/2\pi = 1.5 - 2$ MeV, where $\hbar\Omega$ is the intershell energy spacing [62]. The theoretical considerations by Bohr and Mottelson [63] also predict that shell effects should disappear at similar temperatures. In addition, our shell-correction damping used is very similar to the result from [61], where a semiempirical analysis was carried out for the temperature and spin dependences of shell corrections, but it is different from other results (see, for example, [42, 64]), which suggested a much faster decrease from a smaller energy. If we use the temperature damping function from [42], the analysis leads to fission-time values nearly identical to those in the case of the liquid-drop model (see the dashed curve *6* in Fig. 5). This result is a consequence of the fact that, at a beam energy of 120 MeV, the double-humped structure of the fission barrier completely disappears, whereupon the fission barrier becomes identical to that in the liquid-drop model. A decrease in the fission-barrier height leads to an increase in the fission probability and, consequently, to a reduction of the effect of fission after a few events of neutron emission in the course of deexcitation of the compound nucleus. Such behavior does not agree with our experimental results.

Figure 21 displays the various shell-correction damping functions discussed above.

In summary, we have shown that fission barriers retain their double-humped structure in the excitation-energy range considered here and that the times in the second potential well significantly contribute to the total observed delay time in the fission channel. This means that shell corrections are important up to a temperature of about 1.7–1.8 MeV.

This result may be very important for the synthesis of superheavy elements, since it extends the stabilizing effect of the shell structure to higher temperatures. One of the main problems in the synthesis of superheavy elements is to guarantee their stability against fission, which is supposed to be a predominant decay mode. If the temperature dependence of shell corrections obtained here holds for the superheavy "island of stability" as well, shell corrections to the fission barrier (hindering the rupture of a nucleus) may persist at excitation energies that are characteristic of heavy-ion-induced reactions near the Coulomb barrier.

ACKNOWLEDGMENTS

This work was supported in part by the Istituto Nazionale di Fisica Nucleare, the Ministero dell'Università e della Ricerca Scientifica e Tecnologica, the Russian Foundation for Basic Research (project nos. 98-02-16911 and 99-02-16992), and the State Program "Russian Universities" (grant no. 990602).

REFERENCES

1. V. M. Strutinsky, Nucl. Phys. A **95**, 420 (1967).
2. S. Bjørnholm and V. M. Strutinsky, Nucl. Phys. A **136**, 1 (1969).
3. O. A. Yuminov, in *Proceedings of the 15th All-Union Meeting on the Physics of Interaction between Charged Particles and Crystals* (Mosk. Gos. Univ., Moscow, 1985), p. 68.
4. O. A. Yuminov *et al.*, J. Phys. G **21**, 1243 (1995).
5. A. F. Tulinov, Usp. Fiz. Nauk **87**, 585 (1965) [Sov. Phys. Usp. **8**, 864 (1965)]; Dokl. Akad. Nauk SSSR **162**, 546 (1965) [Sov. Phys. Dokl. **10**, 463 (1965)].
6. D. S. Gemmel and R. E. Holland, Phys. Rev. Lett. **14**, 945 (1965).
7. S. A. Karamyan, Yu. V. Melikov, and A. F. Tulinov, Fiz. Élem. Chastits At. Yadra **4**, 456 (1973) [Sov. J. Part. Nucl. **4**, 196 (1973)].
8. S. A. Karamyan, Fiz. Élem. Chastits At. Yadra **17**, 753 (1986) [Sov. J. Part. Nucl. **17**, 333 (1986)].
9. E. Fuschini *et al.*, Phys. Rev. C **50**, 1964 (1994).
10. A. D'Arrigo *et al.*, in *Proceedings of the International Symposium "Large-Scale Collective Motion of Atomic Nuclei," Brolo (Messina), Italy, 1996,* Ed. by G. Giardina, G. Fazio, and M. Lattuada (World Sci., Singapore, 1997), p. 346.

11. D. O. Eremenko *et al.*, Izv. Akad. Nauk, Ser. Fiz. **62**, 896 (1998).
12. J. Lindhard, K. Dan. Vidensk. Selsk. Mat. Fys. Medd. **34**, 1 (1965).
13. F. Malaguti, Nucl. Instrum. Methods Phys. Res. B **34**, 157 (1988) and references therein.
14. E. Fuschini *et al.*, Nuovo Cimento A **10**, 177 (1972).
15. V. E. Viola, K. Kwiatkowski, and M. Walker, Phys. Rev. C **31**, 1550 (1985).
16. M. Morjean *et al.*, Phys. Rev. Lett. **82**, 5012 (1999).
17. J. D. Molitoris *et al.*, Phys. Rev. Lett. **70**, 537 (1993).
18. M. G. Itkis and A. Ya. Rusanov, Fiz. Élem. Chastits At. Yadra **29**, 299 (1998) [Phys. Part. Nucl. **29**, 160 (1998)].
19. D. Hilscher and H. Rossner, Ann. Phys. (Paris) **17**, 471 (1992).
20. P. Paul, Annu. Rev. Nucl. Sci. **44**, 65 (1994).
21. J. J. Griffin, Phys. Rev. Lett. **17**, 478 (1966).
22. C. Kalbach-Cline, Nucl. Phys. A **193**, 417 (1972).
23. Jr. Williams, Phys. Lett. B **31B**, 184 (1970).
24. C. Kalbach, Z. Phys. A **287**, 319 (1978).
25. F. P. Hessberger *et al.*, in *Proceedings of the International School–Seminar on Heavy Ion Physics, JINR, Dubna, 1993,* Vol. 2, p. 3.
26. J. M. Akkermans, H. Gruppelaar, and G. Reffo, Phys. Rev. C **22**, 73 (1980).
27. I. Ribansky, P. Oblozinsky, and E. Betak, Nucl. Phys. A **205**, 545 (1973).
28. O. V. Grusha, V. A. Khaimin, and O. A. Yuminov, Izv. Akad. Nauk SSSR, Ser. Fiz. **52**, 932 (1988).
29. D. O. Eremenko, S. Yu. Platonov, O. V. Fotina, and O. A. Yuminov, Yad. Fiz. **61**, 773 (1998) [Phys. At. Nucl. **61**, 695 (1998)].
30. D. O. Eremenko *et al.*, Nucl. Phys. A **589**, 395 (1995).
31. G. D. Adeev *et al.*, Fiz. Élem. Chastits At. Yadra **19**, 1229 (1988) [Sov. J. Part. Nucl. **19**, 529 (1988)].
32. J. E. Lynn and S. Bjørnholm, Rev. Mod. Phys. **52**, 725 (1980).
33. B. S. Bhandari and M. Khaliquzzaman, Phys. Rev. C **44**, 292 (1991).
34. F. Scheuter and H. Hofmann, Nucl. Phys. A **394**, 477 (1983).
35. K. Pomorski and H. Hofmann, J. Phys. (Paris) **42**, 381 (1981).
36. N. Bohr and J. Wheeler, Phys. Rev. **56**, 426 (1939).
37. P. Paul, Nucl. Phys. A **569**, 73c (1994).
38. O. V. Grusha, S. P. Ivanova, S. Yu. Platonov, and O. A. Yuminov, Izv. Akad. Nauk SSSR, Ser. Fiz. **51**, 2055 (1987).
39. T. D. Thomas, Phys. Rev. **116**, 703 (1959).
40. O. V. Grusha *et al.*, Nucl. Phys. A **429**, 313 (1984).
41. A. J. Sierk, Phys. Rev. C **33**, 2039 (1986).
42. A. V. Ignatyuk, G. N. Smirenkin, and A. S. Tishin, Yad. Fiz. **21**, 485 (1975) [Sov. J. Nucl. Phys. **21**, 255 (1975)].
43. S. Bjørnholm, A. Bohr, and B. Mottelson, in *Proceedings of the IAEA 3rd Symposium on Physics and Chemistry of Fission, IAEA, Vienna, 1973,* no. SM-174/367.
44. A. V. Ignatyuk, K. K. Istekov, and G. N. Smirenkin, Yad. Fiz. **29**, 875 (1979) [Sov. J. Nucl. Phys. **29**, 450 (1979)].
45. V. A. Ageev, V. Ya. Golovnya, E. A. Gromova, *et al.*, Yad. Fiz. **46**, 700 (1987) [Sov. J. Nucl. Phys. **46**, 392 (1987)].
46. P. Møller, Nucl. Phys. A **192**, 529 (1972).
47. A. V. Ignatyuk, A. B. Klepatskii, V. M. Maslov, and E. Sh. Sukhovitskii, Yad. Fiz. **42**, 569 (1985) [Sov. J. Nucl. Phys. **42**, 360 (1985)].
48. J. Toke and W. J. Swiatecki, Nucl. Phys. A **372**, 141 (1981).
49. W. D. Myers and W. J. Swiatecki, Ann. Phys. (N. Y.) **84**, 185 (1974).
50. A. Gavron *et al.*, Phys. Rev. C **13**, 2374 (1976).
51. S. Yu. Platonov, O. V. Fotina, and O. A. Yuminov, Nucl. Phys. A **503**, 461 (1989).
52. D. O. Eremenko *et al.*, Nuovo Cimento A **108**, 883 (1995).
53. G. Hansen and A. S. Jensen, Nucl. Phys. A **406**, 236 (1983).
54. J. R. Nix, Nucl. Phys. A **130**, 241 (1969).
55. K. H. Bhatt, P. Grangé, and B. Hiller, Phys. Rev. C **33**, 954 (1986).
56. S. A. Karamyan, Nucl. Instrum. Methods Phys. Res. B **51**, 534 (1990).
57. J. Gomez del Campo *et al.*, Phys. Rev. C **41**, 139 (1990).
58. R. F. A. Hoernle', R. W. Fearick, and J. P. F. Sellshop, Phys. Rev. Lett. **68**, 500 (1992).
59. W. Dilg, W. Schantl, H. Vonach, and M. Uhl, Nucl. Phys. A **217**, 269 (1973).
60. B. D. Wilkins, E. P. Steinberg, and R. R. Chasman, Phys. Rev. C **14**, 1832 (1976).
61. A. D'Arrigo *et al.*, J. Phys. G **20**, 365 (1994).
62. V. M. Strutinsky, Nucl. Phys. A **502**, 67c (1989).
63. A. Bohr and B. R. Mottelson, *Nuclear Structure* (Benjamin, New York, 1975; Mir, Moscow, 1977), Vols. I and II.
64. C. C. Sahm *et al.*, Nucl. Phys. A **441**, 316 (1985).

Physics of Atomic Nuclei, Vol. 65, No. 1, 2002, pp. 182–189. Translated from Yadernaya Fizika, Vol. 65, No. 1, 2002, pp. 188–195.
Original Russian Text Copyright © 2002 by Ladygin, Ladygina.

ELEMENTARY PARTICLES AND FIELDS
Theory

Polarization Effects in Inelastic Deuteron Scattering in the Region of Baryon-Resonance Excitation

V. P. Ladygin* **and N. B. Ladygina****

Joint Institute for Nuclear Research, Dubna, Moscow oblast, 141980 Russia

Received August 1, 2000; in final form, March 29, 2001

Abstract—Within the impulse approximation, polarization effects in inelastic deuteron scattering on nuclei are investigated in the region around the resonance of mass about 2190 MeV/c^2. It is shown that the spin-dependent part of the $NN \to NN^*(2190)$ amplitude plays a significant role at high momentum transfers. Predictions are obtained for some polarization observables and cross sections for various deuteron-spin-flip processes. © *2002 MAIK "Nauka/Interperiodica".*

1. INTRODUCTION

Investigation of nuclear reactions involving relativistic deuterons is an important line of research into intermediate- and high-energy physics. Here, reactions of deep-inelastic deuteron scattering on nuclei constitute one of the important subjects of such studies.

Since a deuteron loses a considerable part of its energy in such reactions, relevant observables must be sensitive to the structure of the deuteron at small distances, where nonnucleonic degrees of freedom can play a significant role. Thus, important information about the properties of the deuteron can be obtained not only from data on relativistic-deuteron fragmentation, elastic electron–deuteron and proton–deuteron scattering, the electro- and photodisintegration of deuterons, and other similar processes but also from data on deep-inelastic deuteron scattering on nuclei.

At the same time, inelastic deuteron scattering is traditionally used to investigate the mechanisms of formation of baryon resonances and their properties. Since the isospin of the deuteron is zero, $A(d,d)X$ reactions are selective with respect to the isospin of the unobservable system X (it must be equal to the isospin of the target A). Therefore, the $^1\mathrm{H}(d,d)X$ reactions, where a deuteron is inelastically scattered on hydrogen, is selective to the isospin of 1/2, and this process can be used to obtain important information about the production of baryon resonances like $N^*(1440)$, $N^*(1520)$, $N^*(1680)$, and $N^*(2190)$. In addition, it is of particular interest that the above reactions on nuclei are sensitive to processes of the $NN^* \to NN^*$ type, where a resonance produced on one nucleon is scattered on another one. For example, these properties of the $dp \to dX$ reactions made it possible to estimate, on the basis of data on the inelastic scattering of 9-GeV/c deuterons at angles of 103 and 139 mrad [1], the cross sections for the processes $dp \to dN^*(1440)$, $dp \to dN^*(1520)$, and $dp \to dN^*(1680)$, on one hand, and the corresponding amplitudes for $NN^* \to NN^*$ elementary processes, on the other hand.

The differential cross sections for inelastic deuteron scattering were measured in Saclay for hydrogen targets at a primary momentum of 2.95 GeV/c [2, 3], in Dubna for hydrogen and nuclear targets at primary-momentum values of up to 9 GeV/c [1, 4, 5], and at Fermilab for hydrogen targets at high momenta [6]. These investigations revealed that basic features of the processes in question can be explained rather well within the multiple-scattering model [7, 8].

The advent of polarized-deuteron beams has quickened interest in the reaction of inelastic deuteron scattering on nuclei, since the polarization observables of such reactions can furnish additional information about the properties of resonances in a nuclear medium.

So far, high-energy polarized deuterons have only been used, however, to study the tensor analyzing power T_{20} in the region of Roper resonance excitation $[P_{11}(1440)]$ for inelastic deuteron scattering on hydrogen and carbon targets in Dubna [9] and on hydrogen targets in Saclay [10], as well as for the reactions on hydrogen and carbon targets for the excitation of higher masses [11]. These experiments showed that, at momentum-transfer values satisfying the condition $-t \sim 0.3$–0.6 (GeV/c)^2, the tensor

*e-mail: ladygin@sunhe.jinr.ru
**e-mail: ladygina@sunhe.jinr.ru

analyzing power T_{20} takes negative values of large magnitude.

Within the model based on ω-meson exchange in the t channel [12], this behavior of the tensor analyzing power T_{20} was explained by the effect of a nonzero longitudinal isoscalar form factor for Roper resonance excitation [13].

In this article, experimental data on the tensor analyzing power A_{yy} and the vector analyzing power A_y for the inelastic scattering of 9-GeV/c deuterons on carbon nuclei at a secondary-deuteron detection angle of 85 mrad in the region around the 2190-MeV/c^2 resonance [14] are analyzed on the basis of the plane-wave impulse approximation. Polarization effects in inelastic deuteron scattering are considered in Section 2. In Section 3, we discuss the results obtained here. In the last section, we formulate the basic results of our investigation and the conclusions drawn from it.

2. POLARIZATION EFFECTS in $(d, d')X$ REACTIONS

Measurements of the tensor analyzing power T_{20} for forward inelastic deuteron scattering on hydrogen and carbon targets in the region of baryon-resonance excitation revealed that it is independent of the target mass number [9, 11]. This suggests that collective effects associated with target excitation are inoperative in this process and that data obtained for a nuclear target also furnish information predominantly about isospin-1/2 resonances. Moreover, we consider the case where the momentum transfers from the primary to the secondary deuteron are high [$|t| \sim 0.5$–1.0 (GeV/c)^2], so that the Fermi motion of nucleons in the nucleus can be neglected. Because of this, it seems reasonable to consider inelastic deuteron scattering on a carbon nucleus as the incoherent sum of inelastic deuteron-scattering processes on target nucleons, at least for polarization observables.

We consider the simplest impulse-approximation diagram (see Fig. 1) for inelastic deuteron scattering occurring on a nucleon and leading to the production of a resonance in the final state. The $dN \to dN^*$ amplitude, which is an element of the scattering matrix T, can be written in the form

$$\mathcal{F}_{M_d \to M_{d'}} = \langle d' N^* | T | dN \rangle \qquad (1)$$
$$= \int d^3\mathbf{p}'_0 \left\langle 1 M_{d'} \frac{1}{2} m'_{N^*} \middle| \psi_{d'}(\mathbf{p}'_0)[t_{pN}(\mathbf{q}) + t_{nN}(\mathbf{q})]\psi_d\left(\mathbf{p}'_0 - \frac{\mathbf{q}}{2}\right) \middle| 1 M_d \frac{1}{2} m_N \right\rangle,$$

where ψ_d is the deuteron wave function, $\mathbf{q} = \mathbf{k} - \mathbf{k}'$ is the 3-momentum transfer, and $t_{iN}(\mathbf{q})$ is the amplitude for the production of the resonance N^* on the ith nucleon.

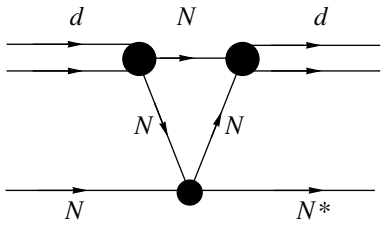

Fig. 1. Diagram for inelastic deuteron scattering in the plane-wave impulse approximation: (d) deuteron, (N) nucleon, and (N^*) $N^*(2190)$ resonance.

The deuteron wave function can be represented in the form

$$\psi_d(\mathbf{p})|1M_d\rangle = \sum_{L=0,2} \sum_{M_S=-1,0,1} \langle L M_L 1 M_S | 1 M_d \rangle \times |1 M_S\rangle Y_L^{M_L}(\hat{p}) u_L(p), \qquad (2)$$

where $Y_L^{M_L}$ is a spherical harmonic; $u_L(p)$ is the wave-function component corresponding to the orbital angular momentum L (it can take the values of 0 and 2); and M_d, M_L, and M_S are the projections of, respectively, the spin of the deutron, the orbital angular momentum of the deuteron, and the spin of the neutron–proton system onto the **z** axis. We choose the system of coordinates in such a way that the **z** axis is directed along the vector **q** and that the **y** axis is orthogonal to the scattering plane; that is,

$$\mathbf{z} = \frac{\mathbf{k} - \mathbf{k}'}{|\mathbf{k} - \mathbf{k}'|}, \quad \mathbf{y} = \frac{\mathbf{k} \times \mathbf{k}'}{|\mathbf{k} \times \mathbf{k}'|}, \quad \mathbf{x} = \mathbf{y} \times \mathbf{z}, \qquad (3)$$

where **k** and **k′** are, respectively, the primary- and the secondary-deuteron momentum in the c.m. frame.

In the impulse approximation, the nonzero vector analyzing power A_y obtained in [14] can be interpreted as follows: the spin-dependent part of the $NN \to NN^*$ elementary amplitude, where N^* is a baryon resonance of mass about 2.2 GeV/c^2, plays a significant role, and this must be taken into account in relevant calculations.

Let us write the $NN \to NN^*$ amplitude in the simplified form

$$t_{iN}(\mathbf{q}) = f_{iN}^{\mathrm{nf}}(q) + (\sigma \mathbf{n}) f_{iN}^{\mathrm{sf}}(q), \qquad (4)$$

where f_{iN}^{nf} and f_{iN}^{sf} are, respectively, the spin-independent and the spin-dependent part of the $NN \to NN^*$ amplitude and σ stands for the 2×2 Pauli matrix. The vector **n** is directed along the **y** axis. The form of the $NN \to NN$ elementary amplitude was simplified in a similar way in order to describe the data obtained in [15] for elastic pd scattering at 3.5 GeV because a partial-wave analysis for nucleon–nucleon scattering has not yet been performed at high energies.

It should be noted that, in general, the $NN \to NN^*$ amplitude is given by a more complicated expression involving a greater number of complex-valued amplitudes. For example, the matrix element for the process $NN \to NN^*$, where N^* is a 1440-MeV/c^2 resonance, generally depends on six complex-valued amplitudes. In order to reconstruct them even at a fixed primary energy, it is necessary to perform a large number of experiments measuring polarization observables over a wide range of angles. The $NN \to NN^*(2190)$ elementary amplitude was simplified here for want of experimental data on particle polarizations. We also assume that the production of the $N^*(2190)$ resonance in pp and np interactions is characterized by the same cross-section value and that the relevant amplitudes are both pure imaginary. This is done for the same reason: we do not have a sufficient amount of experimental data on the $NN \to NN^*(2190)$ elementary process at our disposal.

The amplitudes f_{iN}^{nf} and f_{iN}^{sf} can be parametrized as

$$f_{iN}^{\mathrm{nf}}(q) = i\sqrt{A_n/\pi}\exp(-B_n q^2/2), \qquad (5)$$
$$f_{iN}^{\mathrm{sf}}(q) = iq\sqrt{A_s/\pi}\exp(-B_s q^2/2),$$

where A_n, A_s, B_n, and B_s are constants. In principle, A_n and B_n can be determined on the basis of experimental data on the excitation of the $N^*(2190)$ resonance in pp interactions. However, such data were obtained only at proton momenta of 20 and 30 GeV/c [16]; at the same time, the proton momentum was 4.5 GeV/c in the experiment discussed here. Under the assumption that the $NN \to NN^*(2190)$ amplitude is weakly dependent on the primary energy, A_n and B_n can be estimated at 0.310 ± 0.058 mb $(\mathrm{GeV}/c)^{-2}$ and $5.12 \pm 0.48\,(\mathrm{GeV}/c)^{-2}$, respectively.

Because of the presence of the D wave in the deuteron wave function and the spin-dependent part of the amplitude for the elementary reaction, there are three independent amplitudes ($\mathcal{F}_{0\to0}$, $\mathcal{F}_{1\to1}$, and $\mathcal{F}_{1\to0}$). They are related to the remaining transitions by the equations

$$\mathcal{F}_{-1\to-1} = \mathcal{F}_{1\to1}, \qquad (6)$$
$$\mathcal{F}_{0\to-1} = -\mathcal{F}_{-1\to0} = -\mathcal{F}_{0\to1} = \mathcal{F}_{1\to0}.$$

In the impulse approximation, the independent amplitudes are given by

$$\mathcal{F}_{0\to0}(q) = 2f^{\mathrm{nf}}(q)T_{00}(q/2), \qquad (7)$$
$$\mathcal{F}_{1\to1}(q) = 2f^{\mathrm{nf}}(q)T_{11}(q/2),$$
$$\mathcal{F}_{1\to0}(q) = 2f^{\mathrm{sf}}(q)T_{10}(q/2),$$

where the amplitudes f^{nf} and f^{sf} are, respectively, the spin-independent and the spin-dependent part of the elementary amplitude for the production of a 2190-MeV/c^2 resonance, while the amplitudes T_{00}, T_{11}, and T_{10} are determined exclusively by the deuteron wave function. We have

$$T_{00} = S_0(q/2) + \sqrt{2}S_2(q/2), \qquad (8)$$
$$T_{11} = S_0(q/2) - \frac{1}{\sqrt{2}}S_2(q/2),$$

where S_0 and S_2 are, respectively, the spherical and quadrupole deuteron form factors, which can be represented as

$$S_0(q/2) = \int_0^\infty (u^2(r) + w^2(r))j_0(rq/2)dr, \qquad (9)$$

$$S_2(q/2) = \int_0^\infty 2w(r)\left(u(r) - \frac{1}{2\sqrt{2}}w(r)\right)j_2(rq/2)dr.$$

Here, $u(r)$ and $w(r)$ are, respectively, the S- and the D-wave component of the deuteron wave function in the coordinate representation and $j_0(rq/2)$ and $j_2(rq/2)$ are, respectively, a zero- and a second-order Bessel function.

The amplitude T_{10} is also expressed in terms of the S and the D wave; that is,

$$T_{10} = \frac{i}{\sqrt{2}}\int_0^\infty \left(u^2(r) - \frac{w^2(r)}{2}\right)j_0(rq/2)dr \qquad (10)$$
$$+ \frac{i}{2}\int_0^\infty w(r)\left(u(r) + \frac{w(r)}{\sqrt{2}}\right)j_2(rq/2)dr.$$

Let us define a second-order polarization observable that is related to the polarizations of the primary and the secondary deuteron by the equation

$$C_{i,j} = \frac{1}{|\mathcal{F}|^2}\sum\left\langle 1M_{d'}\frac{1}{2}m'|T|1M_d\frac{1}{2}m\right\rangle \qquad (11)$$
$$\times \langle 1M_d|Q_i|1M_d''\rangle\,\langle 1M_d''\frac{1}{2}m|T|1M_{d'}'\frac{1}{2}m'\rangle$$
$$\times \langle 1M_{d'}'|Q_j|1M_{d'}\rangle,$$

where summation is performed over all dummy indices; $|\mathcal{F}|^2$ is the quantity obtained by summing the square of the relevant matrix element over all possible states of both initial and final particles; the indices i and j are associated with the polarization of the initial and the final deuteron, respectively; and the matrices $Q_k = Q_0$, Q_y, and Q_{yy} are given by

$$Q_0 = \begin{pmatrix} 1 & 0 & 0 \\ 0 & 1 & 0 \\ 0 & 0 & 1 \end{pmatrix}, \quad Q_y = \begin{pmatrix} 0 & 0 & i \\ 0 & 0 & 0 \\ -i & 0 & 0 \end{pmatrix}, \qquad (12)$$

$$Q_{yy} = \begin{pmatrix} 1 & 0 & 0 \\ 0 & -2 & 0 \\ 0 & 0 & 1 \end{pmatrix}.$$

The identity matrix Q_0 corresponds to the case where the deuteron is unpolarized.

The basis spin functions for the deuteron are determined in the standard way as

$$|1+\rangle = -\frac{1}{\sqrt{2}} \begin{pmatrix} 1 \\ i \\ 0 \end{pmatrix}, \quad |1-\rangle = \frac{1}{\sqrt{2}} \begin{pmatrix} 1 \\ -i \\ 0 \end{pmatrix}, \quad (13)$$

$$|10\rangle = \begin{pmatrix} 0 \\ 0 \\ 1 \end{pmatrix}.$$

The tensor analyzing power A_{yy} and the vector analyzing power A_y; the polarizations of secondaries, P_{yy} and P_y; and the vector–vector and the tensor–tensor polarization transfer K_y^y and K_{yy}^{yy} determined in [17] are related to $C_{i,j}$ as follows:

$$A_{yy} = C_{yy,0}, \quad A_y = C_{y,0},$$
$$P_{yy} = C_{0,yy}, \quad P_y = C_{0,y},$$
$$K_y^y = C_{y,y}, \quad K_{yy}^{yy} = C_{yy,yy}.$$

By using (11), we can derive the expressions for the polarization observables in terms of the amplitudes that are given by the formulas in (7).

The tensor analyzing power A_{yy} and the vector analyzing power A_y can be represented as

$$A_{yy} = \frac{\mathcal{F}_{0\to0}^2 - \mathcal{F}_{1\to1}^2 + 4\mathcal{F}_{1\to0}^2}{\mathcal{F}_{0\to0}^2 + 2\mathcal{F}_{1\to1}^2 + 4\mathcal{F}_{1\to0}^2}, \quad (14)$$

$$A_y = -2\sqrt{2}\frac{\mathrm{Im}\,(\mathcal{F}_{0\to0} + \mathcal{F}_{1\to1})\mathcal{F}_{1\to0}^*}{\mathcal{F}_{0\to0}^2 + 2\mathcal{F}_{1\to1}^2 + 4\mathcal{F}_{1\to0}^2}. \quad (15)$$

The vector–vector polarization transfer from the primary to the secondary deuteron, K_y^y, is given by

$$K_y^y = 2\frac{2\mathcal{F}_{1\to0}^2 + \mathrm{Re}\,\mathcal{F}_{1\to1}\mathcal{F}_{0\to0}^*}{\mathcal{F}_{0\to0}^2 + 2\mathcal{F}_{1\to1}^2 + 4\mathcal{F}_{1\to0}^2}. \quad (16)$$

The tensor–tensor polarization transfer K_{yy}^{yy} is expressed in terms of the amplitudes squared as

$$K_{yy}^{yy} = \frac{\mathcal{F}_{0\to0}^2 + 5\mathcal{F}_{1\to1}^2 - 8\mathcal{F}_{1\to0}^2}{\mathcal{F}_{0\to0}^2 + 2\mathcal{F}_{1\to1}^2 + 4\mathcal{F}_{1\to0}^2}. \quad (17)$$

Within this approach, the vector and the tensor polarization of the secondary deuteron—P_y and P_{yy}, respectively—are equal to the corresponding analyzing powers; that is,

$$P_y = A_y, \quad P_{yy} = A_{yy}. \quad (18)$$

We note that relations (18) can be violated in general.

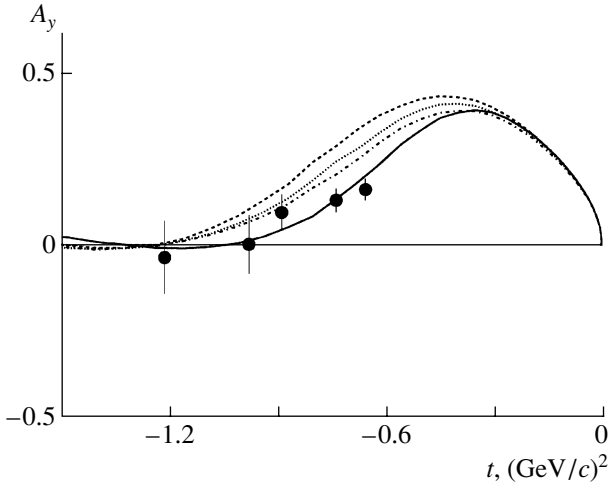

Fig. 2. Vector analyzing power A_y for the reaction $^{12}\mathrm{C}(d,d)X$ at a primary-deuteron momentum of 9 GeV/c and a detection angle of 85 mrad as a function of t. The experimental values (•) were borrowed from [14] and were reduced by a factor of 1.33 according to [20]. The solid curve represents the result of the calculation with the deuteron wave function for the Paris potential [18]; the dashed, the dotted, and the dash-dotted curve correspond to the results obtained by using the deuteron wave function for, respectively, the A, the B, and the C version of the Bonn potential [19]. The ratio of the spin-dependent to the spin-independent part of the $NN \to NN^*(2190)$ amplitude was taken in accordance with (22).

3. RESULTS

In order to simplify the above expressions for the polarization observables, we introduce the parameter $r(q)$,

$$r(q) = f^{\mathrm{sf}}(q)/f^{\mathrm{nf}}(q), \quad (19)$$

which is defined as the ratio of the spin-dependent and the spin-independent part of the $NN \to NN^*(2190)$ amplitude. If the slope parameters B_s and B_n coincide, $r(q)$ is a linear function of q. Since there is an insufficient amount of information about the elementary amplitude, it seems reasonable to set $B_s = B_n$.

The tensor analyzing power A_{yy} and the vector analyzing power A_y are expressed in terms of the quantities $T_{ij}(q/2)$, which were determined in formulas (8)–(10). Specifically, we have

$$A_{yy}(q) = \frac{T_{00}^2 - T_{11}^2 + 4r^2T_{10}^2}{T_{00}^2 + 2T_{11}^2 + 4r^2T_{10}^2}, \quad (20)$$

$$A_y(q) = 2\sqrt{2}r\frac{(T_{11} + T_{00})T_{10}}{T_{00}^2 + 2T_{11}^2 + 4r^2T_{10}^2}. \quad (21)$$

According to expression (21), the vector analyzing power A_y is proportional to the parameter $r(q)$. In Fig. 2, the data on the vector analyzing power A_y [14]

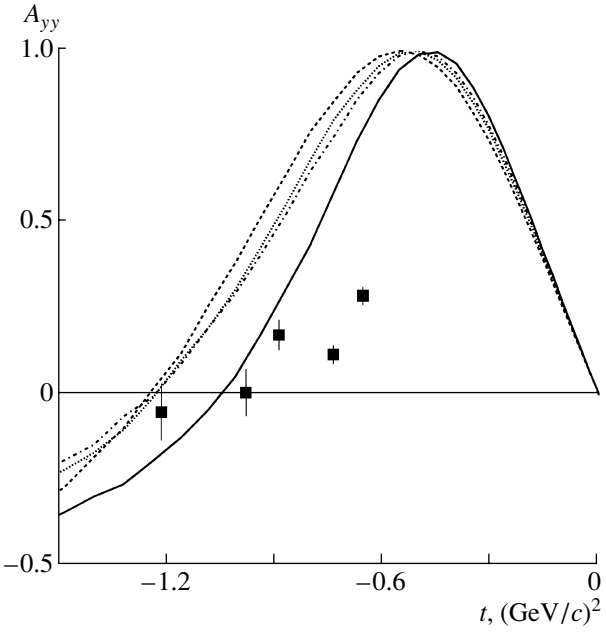

Fig. 3. Tensor analyzing power A_{yy} for the reaction $^{12}\mathrm{C}(d,d)X$ at a primary deuteron momentum of 9 GeV/c and a detection angle of 85 mrad as a function of t [14]. The curves were obtained under the same assumptions as in Fig. 2. The experimental data (■) were borrowed from [14].

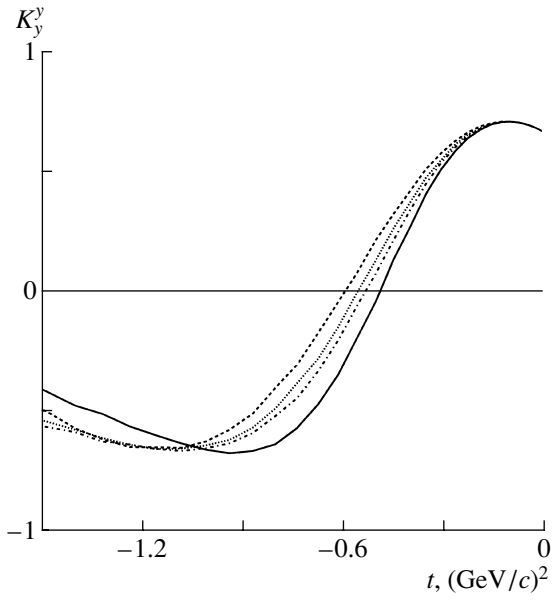

Fig. 4. Vector–vector polarization transfer K_y^y in the reaction $^{12}\mathrm{C}(d,d)X$ at a primary deuteron momentum of 9 GeV/c and a detection angle of 85 mrad as a function of t. The curves were obtained under the same assumptions as in Fig. 2.

are contrasted against the results of the calculations according to formula (21) by using standard deuteron wave functions [18, 19]. The corresponding experimental values [14] were reduced by a factor of 1.33 according to [20]. The solid curve represents the results of the calculation with the deuteron wave function for the Paris nucleon–nucleon potential [18]; the dashed, the dotted, and the dash-dotted curve correspond to the results obtained by using the deuteron wave functions for, respectively, the A, the B, and the C version of the Bonn potential [19]. The parameter $r(q)$ was taken in the form

$$r(q) = 0.4q. \qquad (22)$$

It can be seen that, by and large, the results of the calculations are in fairly good agreement with available experimental data, the use of the deuteron wave function for the Paris potential [18] providing a better description. If, however, we adopt $r \sim 0.3q$, the wave functions based on the Bonn potential [19] also make it possible to describe the experimental data reported in [14].

According to (20), the tensor analyzing power A_{yy} also depends on the parameter $r(q)$. However, this dependence is weaker than that for A_y. If the spin-dependent part of the amplitude of the elementary process is zero, the expression for A_{yy} takes the form

$$A_{yy}(q) = \frac{1}{2}\frac{S_2^2(q/2) + 2\sqrt{2}S_2(q/2)S_0(q/2)}{S_0^2(q/2) + S_2^2(q/2)}. \qquad (23)$$

From (23), it can be seen that, in the impulse approximation (Fig. 1), the tensor analyzing power A_{yy} is completely determined by the structure of the deuteron—it is independent of the properties of nucleon resonances. In Fig. 3, experimental data on A_{yy} [14] are presented along with the results of the calculations relying on formula (20) and employing the deuteron wave functions (solid curve) for the Paris potential [18] and (dashed, dotted, and dash-dotted curves) for various versions (A, B, and C, respectively) of the Bonn potential [19]. The parameter $r(q)$ was taken in the form (22), but the corresponding theoretical results are nearly coincident with the results of the calculations by formula (23). It can be seen that, by and large, the model yields results that are in qualitative agreement with experimental data—that is, it predicts positive values of A_{yy} at low $|t|$ and the passage through zero in the region of $-t = 1.0$–1.2 (GeV/c)^2. The deviation of the behavior of A_{yy} from the predictions of this model can be due both to the contribution of double rescatterings and to the presence of nonnucleonic degrees of freedom (for example, NN^* configurations [21, 22]) in the deuteron.

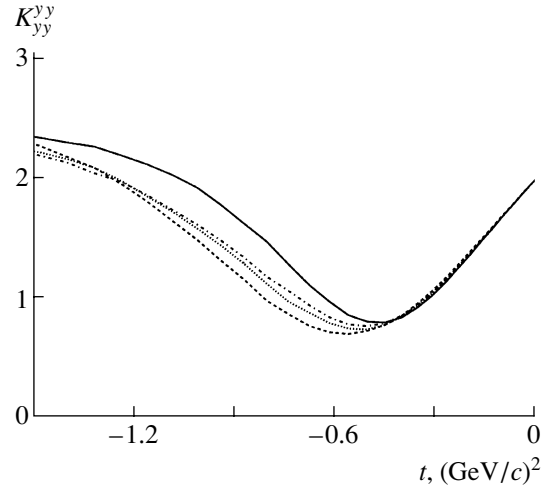

Fig. 5. Tensor–tensor polarization transfer K_{yy}^{yy} in the reaction $^{12}\mathrm{C}(d,d)X$ at a primary-deuteron momentum of 9 GeV/c and a detection angle of 85 mrad as a function of t. The curves were obtained under the same assumptions as in Fig. 2.

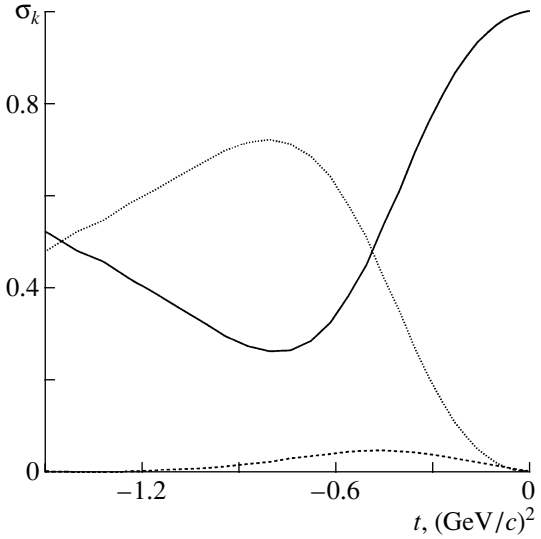

Fig. 6. Spin-flip cross sections for the reaction $^{12}\mathrm{C}(d,d)X$ at a primary deuteron momentum of 9 GeV/c and a detection angle of 85 mrad: (solid curve) σ_0, (dashed curve) σ_1, and (dotted curve) σ_2. The curves were obtained by using the deuteron wave function for the Paris potential [18] and the ratio of the spin-dependent to the spin-independent part of the $NN \to NN^*(2190)$ amplitude in the form (22).

The vector–vector and the tensor–tensor polarization transfer are given by

$$K_y^y(q) = 2\frac{T_{00}T_{11} + 2r^2T_{10}^2}{T_{00}^2 + 2T_{11}^2 + 4r^2T_{10}^2}, \qquad (24)$$

$$K_{yy}^{yy}(q) = \frac{5T_{11}^2 + T_{00}^2 - 8r^2T_{10}^2}{T_{00}^2 + 2T_{11}^2 + 4r^2T_{10}^2}. \qquad (25)$$

The predictions for the observables K_y^y and K_{yy}^{yy} are displayed in Figs. 4 and 5, respectively. The curves were obtained under the same assumptions as in Fig. 2. The parameter $r(q)$ was taken in the form (22). It can be seen that both these observables are sensitive to deuteron-wave-function values for $|t| \geq 0.5$ (GeV/c)^2. The vector–vector polarization transfer K_y^y is equal to $+2/3$ at low $|t|$, but it passes through zero in the region around $t \sim -0.6$ (GeV/c)^2, taking negative values at higher $|t|$. The tensor–tensor polarization transfer K_{yy}^{yy} is positive and takes a minimum value of about 0.8 to 1.0 in the region $-t \sim 0.4$–0.6 (GeV/c)^2.

Sometimes, it is convenient to use partial cross sections (or so-called spin-flip cross sections), being characterized by a specific spin flip. Since the deuteron spin is equal to unity, there are three such cross sections—σ_0, σ_1, and σ_2—which are expressed in terms of the polarization observables as [23]

$$\sigma_0 = \frac{1}{6}\left(2 + 3K_y^y + K_{yy}^{yy}\right), \qquad (26)$$

$$\sigma_1 = \frac{1}{9}\left(4 - (A_{yy} + P_{yy}) - 2K_{yy}^{yy}\right),$$

$$\sigma_2 = \frac{1}{18}\left(4 + 2(A_{yy} + P_{yy}) - 9K_y^y + K_{yy}^{yy}\right).$$

The sum of these cross sections is independent of t and is equal to unity. The results of the calculations with the deuteron wave function for the Paris potential [18] and the parameter $r(q)$ taken in the form (22) are shown in Fig. 6. The solid, the dashed, and the dotted curve represent the partial cross sections σ_0, σ_1, and σ_2, respectively. The cross section σ_0 is dominant at low values of $|t|$, but, even at $-t \sim 0.5$–0.6 (GeV/c)^2, it is the cross section σ_2 (which corresponds to spin-2 flip) that begins to dominate. The cross section σ_1 is small—in the region $-t \sim 0.3$–0.6 (GeV/c)^2, it does not exceed 5%.

It should be noted that, in the approach adopted in the present study, the polarization observables are functions of the square of the 4-momentum transfer, t. We also note that the expressions that we obtained can be applied not only to the $N^*(2190)$ resonance but also to other resonances. It goes without saying that, in this case, as well as in the case where the amplitude for the elementary process $NN \to \to NN^*$ depends strongly on the primary energy, the parameter $r(q)$ can have a different optimal value. Both the polarization observables and the spin-flip cross sections will then behave somewhat differently. Figure 7 displays the cross sections (solid curve) σ_0, (dashed curve) σ_1, and (dotted curve) σ_2. These

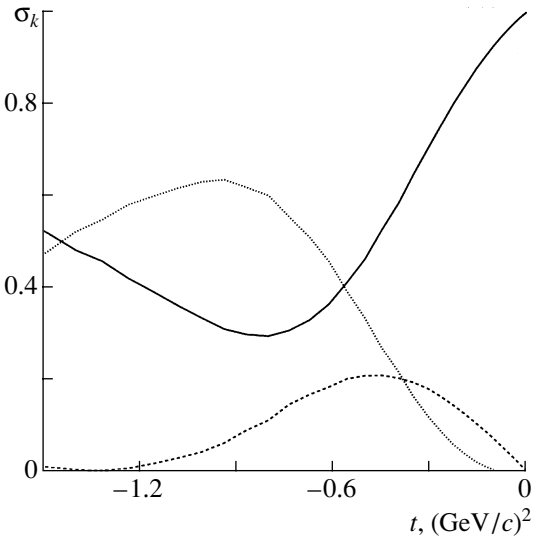

Fig. 7. Spin-flip cross sections for the reaction $^{12}\mathrm{C}(d,d)X$ at a primary-deuteron momentum of 9 GeV/c and a detection angle of 85 mrad: (solid curve) σ_0, (dashed curve) σ_1, and (dotted curve) σ_2. The curves were obtained by using the deuteron wave function for the Paris potential [18] and the ratio of the spin-dependent to the spin-independent part of the $NN \to NN^*(2190)$ amplitude in the form $r(q) = q$.

results were obtained by using the deuteron wave function for the Paris potential [18] and the relation $r = q$. It can be seen that, in this case, the spin-flip cross section σ_1 can become as large as some 20%.

4. CONCLUSION

The main results of our study can be formulated as follows.

Data on the vector analyzing power A_y for the inelastic scattering of 9-GeV/c deuterons on carbon nuclei [14] have been described in the plane-wave impulse approximation. It has been shown that the spin-dependent part of the amplitude for the $NN \to NN^*(2190)$ elementary process plays a significant role and that, at $-t = 1\,(\mathrm{GeV}/c)^2$, it is as large as 30 to 40% (its specific value depending on the choice of the deuteron wave function) of the spin-independent amplitude.

By and large, the data on the tensor analyzing power A_{yy} [14] can be qualitatively described within the plane-wave impulse approximation. The deviation of A_{yy} from the predictions of the model based on this approximation can be associated both with the presence of additional degrees of freedom in the deuteron [21, 22] and with the possible contribution of additional mechanisms of the double-rescattering type.

The predictions obtained for the vector–vector and the tensor–tensor polarization transfer—K_y^y and K_{yy}^{yy}, respectively—are sensitive both to the choice of deuteron wave function and to the choice of $NN \to NN^*(2190)$ elementary amplitude.

The cross sections σ_0, σ_1, and σ_2 for the various spin-flip processes have been estimated with the parameter $r(q)$ fixed on the basis of a fit to the experimental data on A_y from [14]. It has been shown that the cross section σ_0 is dominant at low $|t|$, but that, even at $-t \sim 0.5$–$0.6\,(\mathrm{GeV}/c)^2$, the cross section σ_2 begins to play the leading role. The cross section σ_1 is small—in the region $-t \sim 0.3$–$0.6\,(\mathrm{GeV}/c)^2$, it does not exceed 5%.

It should be emphasized, however, that, in calculating the process $^{12}\mathrm{C}(d,d)X$, many approximations have been made predominantly because of lack of necessary experimental data on the $NN \to NN^*(2190)$ elementary process. In view of this, it is important and interesting to perform polarization experiments aimed at reconstructing the matrix elements for baryon-resonance production in proton–proton and neutron–proton interactions.

Additionally, measurement of polarization observables in inelastic deuteron scattering on hydrogen and deuterium is of crucial importance for obtaining deeper insight into the effect of the target nucleus on the behavior of these observables.

ACKNOWLEDGMENTS

We are grateful to L.S. Azhgirey for stimulating discussions.

REFERENCES

1. L. S. Azhgireĭ, I. K. Vzorov, V. N. Zhmyrov, *et al.*, Yad. Fiz. **48**, 1758 (1988) [Sov. J. Nucl. Phys. **48**, 1058 (1988)].
2. J. Banaigs, J. Berger, L. Goldzahl, *et al.*, Phys. Lett. B **45B**, 535 (1973).
3. R. Baldini Celio, G. Bazini, F. L. Fabbri, *et al.*, Nucl. Phys. A **379**, 477 (1982).
4. L. S. Azhgireĭ, I. K. Vzorov, V. N. Zhmyrov, *et al.*, Yad. Fiz. **27**, 1027 (1978) [Sov. J. Nucl. Phys. **27**, 544 (1978)]; Yad. Fiz. **30**, 1578 (1979) [Sov. J. Nucl. Phys. **30**, 818 (1979)].
5. V. G. Ableev, G. G. Vorob'ev, L. Vizireva, *et al.*, Yad. Fiz. **37**, 348 (1983) [Sov. J. Nucl. Phys. **37**, 209 (1983)].
6. Y. Akimov, R. Cool, L. Golovanov, *et al.*, Phys. Rev. Lett. **35**, 763 (1975).
7. R.J. Glauber, in *Lectures in Theoretical Physics,* Ed. by W. E. Brittin and L. G. Dunham (Interscience, New York, 1959), Vol. 1, p. 315.
8. A. G. Sitenko, Ukr. Fiz. Zh. **4**, 152 (1959).

9. L. S. Azhgirey, E. V. Chernykh, A. P. Kobushkin, *et al.*, Phys. Lett. B **361**, 21 (1995).
10. M. Morlet, C. Djalali, E. Tomasi-Gustafsson, *et al.*, Saturne Exp. No. 250, data in progress.
11. L. S. Azhgirey, E. V. Chernykh, A. P. Kobushkin, *et al.*, JINR Rapid Commun., No. 2[88]-98, 17 (1998).
12. M. P. Rekalo and E. Tomasi-Gustafsson, Phys. Rev. C **54**, 3125 (1996).
13. E. Tomasi-Gustafsson, M. P. Rekalo, R. Bijker, *et al.*, Phys. Rev. C **59**, 1526 (1999).
14. L. S. Azhgirey, V. V. Arkhipov, S. V. Afanas'ev, *et al.*, Yad. Fiz. **62**, 1796 (1999) [Phys. At. Nucl. **62**, 1673 (1999)].
15. C. Ohmori, N. Horikawa, Y. Ishida, *et al.*, Phys. Lett. B **230**, 27 (1989).
16. E. W. Anderson, E. J. Bleser, G. B. Collins, *et al.*, Phys. Rev. Lett. **16**, 855 (1966).
17. H. O. Ohlsen, Rep. Prog. Phys. **35**, 717 (1972).
18. M. Lacombe, B. Loiseau, R. Vinh Mau, *et al.*, Phys. Lett. B **101B**, 139 (1981).
19. R. Machleidt, K. Holinde, and C. Elster, Phys. Rep. **149**, 1 (1987).
20. L. S. Azhgirey, V. N. Zhmyrov, V. P. Ladygin, and G. D. Stoletov, Kratk. Soobshch. Ob'edin. Inst. Yad. Inst., No. 3[95]-99, 20 (1999).
21. L. S. Azhgirey and N. P. Yudin, Yad. Fiz. **63**, 2280 (2000) [Phys. At. Nucl. **63**, 2184 (2000)].
22. A. P. Kobushkin, Phys. Lett. B **421**, 53 (1998).
23. T. Suzuki, Nucl. Phys. A **577**, 167 (1994).

Translated by A. Isaakyan

Physics of Atomic Nuclei, Vol. 65, No. 1, 2002, pp. 190–193. Translated from Yadernaya Fizika, Vol. 65, No. 1, 2002, pp. 196–200.
Original Russian Text Copyright © 2002 by Golokhvastov.

ELEMENTARY PARTICLES AND FIELDS
Theory

Interference Correlations of Pions and Elementary Cell of Phase Space

A. I. Golokhvastov*

Joint Institute for Nuclear Research, Dubna, Moscow oblast, 141980 Russia

Received July 17, 2000; in final form, November 17, 2000

Abstract—The amplitude-symmetrization procedure employed in studying interference correlations of identical pions is shown to be always valid only within one elementary cell $2\pi\hbar$ of phase space—that is, within one period of the interference cosine. However, this limitation does not lead to far-reaching consequences in using the interference method to determine the spacetime dimensions of the pion-generation volume. © *2002 MAIK "Nauka/Interperiodica".*

1. INTRODUCTION

The interference method for determining the spacetime dimensions of the pion-generation volume [1–5] is essentially based on two assumptions: (i) the possibility of averaging the amplitudes for two different ways of pion-pair emission at two different points of the pion-generation volume and (ii) the possibility of averaging the probabilities for various positions of these points within the generation volume.

In this study, it is shown that the first assumption is always valid only within one elementary cell $2\pi\hbar$ of phase space, which corresponds to one period of the interference cosine (Section 5). The second assumption is invalid if there is not this restriction (Section 6).

This does not impose stringent limitations on the use of the method, but the model assumption that single-particle pion sources undergo no recoil becomes redundant in view of this.

In Sections 2–4, we give a brief account of the method for nucleus–nucleus interactions, where noninterference kinematical and dynamical correlations of pions are expected to be negligible. In those sections, we use the system of units where $\hbar = 1$.

2. SYMMETRIZATION

We consider the case where, for example, π^- mesons are produced almost independently of each other by different "single-particle sources"—that is, in different nucleon–nucleon collisions, pion–nucleon rescatterings, and resonance decays at different spacetime points of the nuclear-collision region. The source position where the pion being considered was produced or underwent a significant rescattering for the last time prior to leaving the generation volume, whereupon it can be considered to be free, will be referred to as the pion-emission point.

The probability amplitude for an arbitrarily chosen pion to have a 4-momentum $p = (E, \mathbf{p})$ and to be emitted at a point $r=(t, \mathbf{r})$ is [5]

$$\phi(\mathbf{p}) \exp(-ipr), \qquad (1)$$

where $\phi(\mathbf{p})$ is the probability amplitude for the pion to have a momentum $\mathbf{p}$; $\exp(-ipr) \equiv \exp[-i(Et - \mathbf{p}\cdot\mathbf{r})]$ is the probability amplitude for the pion that has the momentum $\mathbf{p}$ to occur at the point $\mathbf{r}$ at the instant t [6, §5.1].

The probability density for the pion to have the momentum $\mathbf{p}$ and to be emitted by the source being considered is equal to the squared modulus of (1): $W(\mathbf{p}) = \phi^*(\mathbf{p})\phi(\mathbf{p})$.

Let us choose, at random, two successive π^- mesons from an arbitrary event. Since we assumed that pions are produced independently of one another, the amplitude of the probability that the first pion has a momentum $\mathbf{p}_1$ and is emitted at a point r_a and that the second pion has a momentum $\mathbf{p}_2$ and is emitted at a point r_b is equal to the product of the one-particle amplitudes,

$$A_{ab} = \phi_a(\mathbf{p}_1)\phi_b(\mathbf{p}_2) \exp[-i(p_1 r_a + p_2 r_b)]. \qquad (2)$$

Similarly, the probability amplitude for the first and the second π^- meson to be emitted at the points r_b and r_a, respectively, is

$$A_{ba} = \phi_b(\mathbf{p}_1)\phi_a(\mathbf{p}_2) \exp[-i(p_1 r_b + p_2 r_a)]. \qquad (3)$$

If these two cases are indistinguishable (see the relevant discussion in [2]; see also Section 5 of the present article)—that is, if they lead to the same final quantum state of all particles involved in the reaction—the probability density to choose two π^- mesons that have the momenta $\mathbf{p}_1$ and $\mathbf{p}_2$ and which are emitted by the sources at the points r_a and r_b is

*e-mail: golokhv@sunhe.jinr.ru

equal to one-half of the squared modulus of the sum of two amplitudes:

$$2W(\mathbf{p}_1,\mathbf{p}_2) = |A_{ab}+A_{ba}|^2 \qquad (4)$$
$$= |A_{ab}|^2 + |A_{ba}|^2 + 2\mathrm{Re}(A^*_{ab}A_{ba}).$$

A similar result is obtained in a famous experiment where one electron is scattered off two holes [6, §1.1] or two atoms [7, §XIX.25]. In just the same way as in those single-particle cases, one must average the probabilities rather than the amplitudes, provided that the points at which the pions were emitted can be determined with the aid of some detectors:

$$2W^{\mathrm{off}}(\mathbf{p}_1,\mathbf{p}_2) = W_a(\mathbf{p}_1)W_b(\mathbf{p}_2) \qquad (5)$$
$$+ W_b(\mathbf{p}_1)W_a(\mathbf{p}_2) = |A_{ab}|^2 + |A_{ba}|^2.$$

This background spectrum free from correlations (correlations off) is usually obtained in experiments from mixed pion pairs, where the pions are chosen at random from different events [4]. In the case of single-particle interference, the background is similarly obtained from events where only one hole is open [6, §1.1].

The correlation function for these two single-particle sources is equal to the ratio of the probabilities in (4) and (5):

$$C_{ab}(\mathbf{p}_1,\mathbf{p}_2) = 1 + \frac{2\mathrm{Re}(A^*_{ab}A_{ba})}{|A_{ab}|^2+|A_{ba}|^2}. \qquad (6)$$

The correlation function is not equal to unity, although it was obtained under the assumption of independent pion production and in the absence of any interaction between them. The reason is that we multiplied, in (2) and (3), the amplitudes rather than the probabilities of independent events and also averaged, in (4), the amplitudes and not the probabilities of different possibilities. The quantum theory of probabilities is different from the corresponding classical theory—the former is non-Laplacian [6, §1.1] and non-Kolmogorovian [8].

The numerator of the interference term in (6) is [see (2) and (3)]

$$2\mathrm{Re}\left\{\phi^*_a(\mathbf{p}_1)\phi^*_b(\mathbf{p}_2)\phi_b(\mathbf{p}_1)\phi_a(\mathbf{p}_2)\right. \qquad (7)$$
$$\left.\times \exp[i(p_1-p_2)(r_a-r_b)]\right\}.$$

Here, all the amplitudes are complex-valued functions, and we cannot simplify this expression without additional assumptions.

3. HOMOGENEITY CONDITION

Let us consider the case of a homogeneous volume of pion generation—that is, the case where all single-particle sources are identical:

$$\phi_a(\mathbf{p}) = \phi_b(\mathbf{p}) = \phi(\mathbf{p}). \qquad (8)$$

This condition is invalid for a generation volume where different parts (elements) move in different directions at different velocities and emit pions in different regions of the momentum spectrum. Such nonhomogeneity (momentum–coordinate correlation) is typical of almost all models of multiparticle production.

However, the equality in (8) seems valid in a certain approximation for an "individual" element of the volume—that is, for the subensemble of pions from the small part of the momentum spectrum where $p_1 \approx p_2$ [9]. For example, such an element, which is (virtually) homogeneous, could be formed by two Δ isobars (two single-pion sources) that move at close velocities and which are produced in different parts of the generation volume. In this example, the element may occupy the entire spacetime part of a nucleus collision—it is small only in momentum space.

With an eye to the application of such quasihomogeneous elements, we will adhere to condition (8). Under the condition in (8), the amplitudes $\phi(\mathbf{p})$ in (7) are combined into probabilities and are canceled by the denominator in (6):

$$C_{ab}(q) = 1 + \cos[(p_1-p_2)(r_a-r_b)]. \qquad (9)$$

The correlation function for the scattering of one electron off two holes (atoms) can be represented in the similar form

$$C_{ab}(\mathbf{k}) = 1 + \cos[(\mathbf{k}'-\mathbf{k})(\mathbf{r}_a-\mathbf{r}_b)], \qquad (10)$$

where $\mathbf{k}$ and $\mathbf{k}'$ are, respectively, the initial and the final momentum of the electron [7, §XIX. 25].

4. CORRELATION FUNCTION

If the shape of a homogeneous-generation volume (homogeneous element)—that is, the spacetime density of pion sources (more precisely, of their centers [3]), $\rho(r)$—is known, we can obtain the total correlation function by averaging the two-point correlation function (9) over all positions of these points ($qv \equiv p_1-p_2$):

$$C(q) = 1 + \int\int \rho(r_a)\rho(r_b)\cos[q(r_a-r_b)]d^4r_a d^4r_b. \qquad (11)$$

This procedure—that of averaging the probabilities rather than the amplitudes—assumes that different positions of the point r_a (or of r_b or of both) lead to different final quantum states of the particles involved

in the reaction (see the relevant discussion in [2]; see also Section 6).

Considering that $\cos[q(r_a - r_b)] = \mathrm{Re}[\exp(iqr_a) \times \exp(-iqr_b)]$, we arrive at

$$C(q) = 1 + \mathrm{Re}\left\{\int \rho(r_a)\exp(iqr_a)d^4r_a \times \int \rho(r_b)\exp(-iqr_b)d^4r_b\right\} = 1 + \left|\int \rho(r)\exp(iqr)d^4r\right|^2. \quad (12)$$

It is the basic formula of the interference method for determining the spacetime dimensions of the pion-generation volume.

Assuming that the spacetime shape of the generation volume in its rest frame is close to the Gaussian distribution

$$\rho(r) = \frac{1}{(2\pi)^2 R_x R_y R_z T} \times \exp\left(-\frac{r_x^2}{2R_x^2} - \frac{r_y^2}{2R_y^2} - \frac{r_z^2}{2R_z^2} - \frac{t^2}{2T^2}\right) \quad (13)$$

and substituting it into the square of the Fourier transform in (12), we obtain

$$C(q) = 1 + \exp\left(-q_x^2R_x^2 - q_y^2R_y^2 - q_z^2R_z^2 - q_t^2T^2\right), \quad (14)$$

where R_i is the root-mean-square scatter of pion-emission points and T is the root-mean-square scatter of pion-emission instants. We can determine the dimensions of the generation volume, R_i and T, from a fit to the experimental correlation function in terms of this (or any other) approximation.

5. AVERAGING OF AMPLITUDES

In (4), we averaged amplitudes (not probabilities) of two possible ways of pion-pair emission by two single-particle sources, assuming that the two ways lead to the same final quantum state of all particles involved in the reaction (for the same initial state) and that there are no spectators that preserved more detailed information.

However, a nucleus–nucleus interaction produces, in addition to the two π^- mesons being considered, many free particles that are emitted from various parts of the collision area. By measuring the coordinates and momenta of these particles immediately after their emission, we can try to pinpoint, without disturbing the two π^- mesons, the path realized in the event under study. Of course, this can be done only to a precision not higher than that which is allowed by the uncertainty relations. However, there is no need for performing actual measurements—the spectator particles themselves are detectors that can appear in a different quantum state upon the interchange of the pion momenta.

The emission of two pions from two different nucleus–nucleus collisions rather than from two regions of the same collision is a vivid example that does not differ radically from that considered here. If the spatial or time interval between these two collisions is large, the energy–momentum conservation laws are satisfied independently in either individual collision, thereby ruling out the possibility of pion-momentum exchange between the collisions (for $p_1 \neq p_2$). If this interval is small, this possibility appears: various groups of spectator particles can exchange the momentum of $p_1 - p_2$ simultaneously with pion-pair emission.

A quantitative estimate is obtained with the aid of the concept of a quantum (quantized) state in momentum–coordinate phase space for the system in the continuous part of the momentum spectrum [6, §4.3]. An elementary cell of size $2\pi\hbar$ per degree of freedom (equivalent to one discrete state) in phase space corresponds to a quantum state of any free particle (particle system) (see [10, §62] and [11, §7]).

The recoil momentum is redistributed among spectators upon the interchange of the pion momenta. The momentum increases by $q \equiv p_1 - p_2$ for those spectators that are emitted from the region around the point r_a and decreases by the same amount for those that are emitted from the region around the point r_b. In other words, a change occurs in the entire system of spectators: 4-momentum q is transferred to the 4-vector $s \equiv r_a - r_b$. Thus, the position of the system in phase space is shifted by $q_i s_i$ along each coordinate (i). If this shift significantly exceeds $2\pi\hbar$, the system of spectator particles occurs in a different quantum state. Therefore, the direct and the crossed reaction path are indistinguishable only for $q_i s_i < 2\pi\hbar$.

In this case, the two pions that we singled out must be emitted from one cell $q_i s_i < 2\pi\hbar$—that is, in one quantum state—and the effect is equivalent to the phenomenon of induced radiation [12, §§4.2–4.5].

It was shown in [2] that the interference contribution cannot be neglected even for $q_i s_i \gg \hbar$. Here, we have proven that, as soon as $q_i s_i > 2\pi\hbar$, this contribution can be small. In the intermediate case of $q_i s_i \sim 2\pi\hbar$, the amplitudes in (2) and (3) must obviously be averaged in (4) with different weights—this situation is analogous to that in single-particle interference where electrons behind the screen are irradiated with photons of wavelength on the order of the distance between the holes [12, §3.2].

Therefore, we can guarantee that the emission paths are indistinguishable only within one period of the cosine in (9). This is the point where our case

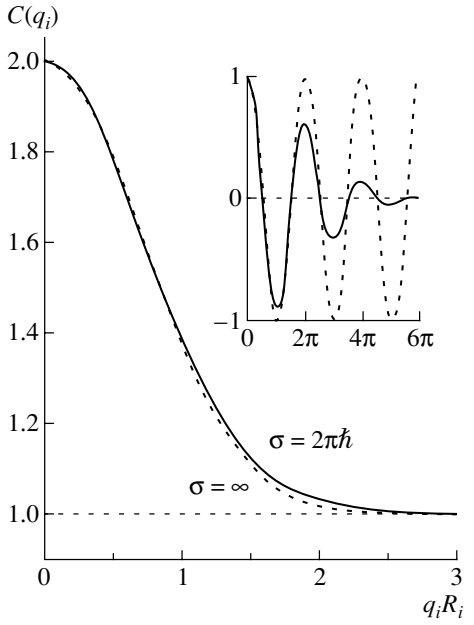

Dependence of the shape of the correlation function (in one dimension) on the corrections associated with the fact that the range of the cosine in (11) is bounded [the results are presented for the Gaussian generation volume (13)]. The solid curve was obtained by introducing the factor $\exp[-(q_i s_i)^2/2(2\pi\hbar)^2]$, with the variance $2\pi\hbar$ in the integrand in (11). The dashed curve is the usual Gaussian function (14) corresponding to the absence of this factor, or, which is equivalent, to an infinite variance in this factor. The inset displays the cosine before and after introducing the restriction.

differs from that of single-particle interference, where no constraint is imposed on the cosine (10). The reason is that an indefinite mass or, equivalently, a fixed position of two atoms [7, §XIX.24], mirrors [10, §3], or holes [13] (this rules out the possibility of determining the scatterer by the recoil momentum) is the condition of applicability of (10). In our case, the spectators are free particles.

Let us discuss the effect of this correction on the form of the correlation function for the Gaussian generation volume (13) (in one dimension). For this we introduce the fast decreasing factor $\exp[-(q_i s_i)^2/2(2\pi\hbar)^2]$, with the variance $2\pi\hbar$, in the integrand in (11). The solid curve in the figure illustrates the result obtained in this way. The dashed curve in the figure represents the usual Gaussian function (14). The fact that the upper curve depends only on the product q_iR_i is merely accidental—it is associated with the Gaussian character of both the factor and the shape of the volume.

Strictly speaking, the upper curve reduces to a hyperbola for large q_iR_i. However, the model condition requiring [2, 3] that single-pion sources have infinite masses and therefore undergo no recoil becomes redundant because of arbitrariness in choosing the approximation in (13) and because of indistinguishability of the two curves in experiments.

6. AVERAGING OF PROBABILITIES

In (11), we averaged the probabilities (rather than amplitudes) of various positions of the points r_a and r_b; that is, we assumed that different positions of the point r_a (or r_b or both) lead to different final quantum states of the particles involved in the reaction. However, the possibility of distinguishing different positions of the points is directly related to the above restriction on the indistinguishability of the direct and the crossed reaction path.

If different groups of spectator particles did not undergo recoil or, which is equivalent, if they could exchange momenta significantly exceeding $2\pi\hbar/(r_a - r_b)$ simultaneously with the emission of a pion pair, thereby rendering the direct and the crossed way indistinguishable for any spacing between the emission points, different positions of the points would also be indistinguishable. In this case, we should average the amplitudes [prior to squaring them in (4)] rather than the probabilities over the entire generation area. As a result, the interference peak would disappear (so-called coherent sources—see, for example, [14]).

REFERENCES

1. G. I. Kopylov and M. I. Podgoretskiĭ, Yad. Fiz. **15**, 392 (1972) [Sov. J. Nucl. Phys. **15**, 219 (1972)].
2. G. I. Kopylov and M. I. Podgoretskiĭ, Yad. Fiz. **18**, 656 (1973) [Sov. J. Nucl. Phys. **18**, 336 (1973)].
3. G. I. Kopylov and M. I. Podgoretskiĭ, Yad. Fiz. **19**, 434 (1974) [Sov. J. Nucl. Phys. **19**, 215 (1974)].
4. G. I. Kopylov, Phys. Lett. B **50B**, 472 (1974).
5. M. I. Podgoretskiĭ, Fiz. Élem. Chastits At. Yadra **20**, 628 (1989) [Sov. J. Part. Nucl. **20**, 266 (1989)].
6. R. P. Feynman and A. R. Hibbs, *Quantum Mechanics and Path Integrals* (McGraw-Hill, New York, 1965; Mir, Moscow, 1968).
7. A. Messiah, *Quantum Mechanics* (Interscience, New York, 1961; Nauka, Moscow, 1979).
8. D. N. Klyshko, Usp. Fiz. Nauk **168**, 975 (1998) [Phys. Usp. **41**, 885 (1998)].
9. M. Kh. Anikina *et al.,* Phys. Lett. B **397**, 30 (1997).
10. P. A. M. Dirac, *The Principles of Quantum Mechanics* (Clarendon, Oxford, 1958; Nauka, Moscow, 1979).
11. L. D. Landau and E. M. Lifshitz, *Course of Theoretical Physics,* Vol. 5: *Statistical Physics* (Nauka, Moscow, 1976; Pergamon, Oxford, 1980).
12. R. P. Feynman, R. B. Leighton, and M. Sands, *The Feynman Lectures on Physics* (Addison-Wesley, Reading, 1974; Mir, Moscow, 1978), Vol. 8.
13. N. Bohr, Usp. Fiz. Nauk **66**, 571 (1958).
14. D. H. Boal *et al.,* Rev. Mod. Phys. **62**, 553 (1990).

Translated by M. Kobrinsky

Physics of Atomic Nuclei, Vol. 65, No. 1, 2002, pp. 194–202. Translated from Yadernaya Fizika, Vol. 65, No. 1, 2002, pp. 201–209.
Original Russian Text Copyright © 2002 by Tyutin.

ELEMENTARY PARTICLES AND FIELDS
Theory

Once Again on the Equivalence Theorem

I. V. Tyutin

Lebedev Institute of Physics, Russian Academy of Sciences, Leninskiĭ pr. 53, Moscow, 117924 Russia

Received November 30, 2000; in final form, February 23, 2001

Abstract—The equivalence theorem in quantum field theory is proven on the basis of the field–antifield formalism. It is shown that the equivalence theorem does not contradict the well-known fact that, in quantum theory, some symmetries of the classical action functional are broken (anomalous). By way of example, a model is considered where natural finite counterterms can be chosen in different ways leading to physically nonequivalent quantum theories, but where the equivalence theorem remains valid.
© *2002 MAIK "Nauka/Interperiodica".*

1. INTRODUCTION

The equivalence theorem in Lagrangian quantum field theory [that is, the fact that physical observables in quantum theory—in particular, the S matrix—are independent of changes of field variables in the classical action functional (in other words, on the choice of parametrization of the classical action functional)] has a long history [1–11]. The first rigorous result belongs to Borchers [2], who proved that the S matrix for a Heisenberg field that has the form of a local normally ordered polynomial of a free field and a nonvanishing in-limit coincides with the S matrix that describes a free field and which is equal to unity (for a generalization of Borchers' results to theories involving interactions that is formulated within the axiomatic approach, the reader is referred to [11]). For models where there is a nonvanishing interaction, the first rigorous perturbative proof of the equivalence theorem on the basis of the quantum action principle was given in [8, 9]. In those studies, the authors considered theories for which the quantum action principle is valid in a form that coincides with the formal expression obtained, for example, from the representation of Green's functions in terms of a path integral. In general, however, the form of the quantum action principle differs from this formal expression by so-called local insertions (see Section 3).

For the equivalence theorem, we give here a perturbative proof that is valid in an arbitrary quantum theory renormalized with the aid of the Bogolyubov R operation [12] (see also [13] and references therein). The change in the classical action functional under a change of variables is interpreted as some kind of symmetry of this action functional. In this approach, the problem of proving the equivalence theorem reduces to the problem of exploring the possibility of conserving this symmetry in quantum theory. In order to solve this problem, we use a generalization of the field–antifield formalism [14] to the case of global symmetries [15–17] and the cohomologous method that was developed to study the structure of symmetries in a renormalized theory and which was successfully applied to gauge theories (see [18, 19] and references therein). We show that the equivalence theorem is valid in the sense that finite quantum corrections (counterterms depending on the parametrization of the action functional) to the classical action functional can always be chosen in such a way that physical observables and the S matrix are independent of the choice of parametrization of the classical action functional.

As is well known, a given classical action functional does not uniquely determine a quantum theory because there exists a wide arbitrariness in choosing finite counterterms, so that physically nonequivalent quantum theories can be obtained from the same classical action functional. From our results, it follows that the set of quantum theories that is generated by the family of classical action functionals related by changes of field variables is broken down into classes such that the equivalence theorem is valid within each individual class.

The validity of the equivalence theorem does not mean, however, that any symmetries of a classical theory, which are also formulated in terms of changes of variables, can be extended to the corresponding quantum theory. That a quantum theory has a symmetry implies that Green's functions must obey subsidiary conditions, Ward identities, which are independent of the conditions of the equivalence theorem. Conditions of these two types cannot always be satisfied simultaneously. By convention, we can say that the equivalence theorem means an on-shell

symmetry, while Ward identities mean an off-shell symmetry, which is stronger.

This article is organized as follows. In Section 2, we perform a formal consideration of the equivalence theorem. In Section 3, we derive a master equation for the generating functional for vertices and show that the equivalence theorem follows from this equation. In Section 4, we consider an example of theory where natural counterterms can be chosen in different ways leading to physically nonequivalent theories without violating the equivalence theorem. Within this theory, we also demonstrate that the validity of the equivalence theorem does not contradict the possible violation of some classical symmetries in the corresponding quantum theory.

2. FORMAL CONSIDERATION

In this section, we briefly recall a scheme according to which the equivalence theorem can be proven in a way that is convenient for our purposes. Suppose that the classical action functional has the form

$$S_0 = S_0(\varphi) = \int dx L(\varphi^i(x), \partial_\mu \varphi^i(x), \ldots).$$

For the sake of simplicity, we also assume that all fields (which will also be referred to as variables) $\varphi^i(x) \equiv \varphi^A$ are Bose fields and that the Lagrangian density L depends on a finite number of spatial derivatives of the fields $\varphi^i(x)$ (at least, perturbatively). We consider the family of the classical action functionals $S(\alpha, \varphi)$,

$$S(\alpha, \varphi) = S_0(\Phi(\alpha, \varphi)), \tag{1}$$

where the change of field variables $\Phi^A(\alpha, \varphi) = \Phi^i(\alpha, \varphi; x) = \Phi^i(\alpha, \varphi^j(x), \partial_\mu \varphi^j(x), \ldots) = \varphi^A + O(g)$,[1] $\Phi^i(0, \varphi; x) = \varphi^i(x)$, and the inverse change of variables $\tilde{\varphi}^A(\alpha, \Phi) = \Phi^A + O(g)$, $\Phi^A(\alpha, \tilde{\varphi}(\alpha, \Phi)) = \Phi^A$, $\tilde{\varphi}^A(\alpha, \Phi(\alpha, \varphi)) = \varphi^A$, are local (at least, perturbatively), the quantities

$$f^A = f^A(\alpha, \varphi) = f^i(\alpha, \varphi; x)$$
$$= -\frac{\partial \Phi^B(\alpha, \varphi)}{\partial \alpha} \frac{\delta \tilde{\varphi}^A(\alpha, \Phi)}{\delta \Phi^B} = \frac{\partial \tilde{\varphi}^A(\alpha, \Phi)}{\partial \alpha}$$

being (perturbatively) local functions of $\varphi^i(x)$. It is obvious that the following equality holds:

$$S(0, \varphi) = S_0(\varphi).$$

The fact that action functional $S(\alpha, \varphi)$ was derived from the action functional $S_0(\varphi)$ by a change of variables is reflected in the validity of the following equation (symmetry) for the action functional $S(\alpha, \varphi)$:

$$\frac{\partial S(\alpha, \varphi)}{\partial \alpha} + f^A(\alpha, \varphi) \frac{\delta S(\alpha, \varphi)}{\delta \varphi^A} = 0. \tag{2}$$

[1] Here, g denotes the complete set of coupling constants of the theory.

We note that Eq. (2) is satisfied by virtue of the fact that the change of variables itself obeys this equation:

$$\frac{\partial \Phi^A(\alpha, \varphi)}{\partial \alpha} + f^B(\alpha, \varphi) \frac{\delta \Phi^A(\alpha, \varphi)}{\delta \varphi^B} = 0.$$

Classical theories related by changes of variables are equivalent. Naively, the same is true in quantum field theory as well. Let us consider the family $Z(\alpha, J)$ of generating functionals for Green's functions in quantum field theory:

$$Z(\alpha, J) = e^{\frac{i}{\hbar} W(\alpha, J)}$$
$$= \int D\varphi \Delta(\alpha, \varphi) e^{\frac{i}{\hbar}\left(S(\alpha, \varphi) + J_A \varphi^A\right)}$$
$$= \int D\Phi e^{\frac{i}{\hbar}\left(S_0(\Phi) + J_A \tilde{\varphi}^A(\alpha, \Phi)\right)},$$
$$\Delta(\alpha, \varphi) = \mathrm{Det} \frac{\delta \Phi^A(\alpha, \varphi)}{\delta \varphi^B}.$$

By calculating the quantum expectation of the symmetry Eq. (2) and by formally performing integration by parts in the path integral, we obtain the equation for the generating functional for Green's functions,

$$\frac{\partial}{\partial \alpha} W(\alpha, J) - J_A \langle f^A \rangle(\alpha, J) = 0, \tag{3}$$
$$\langle f^A \rangle(\alpha, J) \equiv \frac{1}{Z(\alpha, J)}$$
$$\times \int D\varphi f^A(\alpha, \varphi) \Delta(\alpha, \varphi) e^{\frac{i}{\hbar}\left(S(\alpha, \varphi) + J_A \varphi^A\right)},$$

or, which is the same, the equation for the generating functional for vertex functions,

$$\frac{\partial \Gamma(\alpha, \varphi)}{\partial \alpha} + \langle f^A \rangle \frac{\delta \Gamma(\alpha, \varphi)}{\delta \varphi^A} = 0, \tag{4}$$
$$\Gamma(\alpha, \varphi) = W(\alpha, J) - J_A \varphi^A,$$
$$\varphi^A = \frac{\delta W(\alpha, J)}{\delta J_A}. \quad J_A = -\frac{\delta \Gamma(\alpha, \varphi)}{\delta \varphi^A}.$$

In Eq. (4), the quantity J is expressed in terms of φ in the functional $\langle f^A \rangle$. An equation of the type in (4) for the generating functional for vertex functions is referred to as a master equation.

We now assume that single-particle-irreducible components of skeleton diagrams (single-particle-irreducible skeleton subdiagrams not contained in any other single-particle-irreducible subdiagrams) have no single-particle pole singularities in the momentum conjugate to the coordinate of the vertex $f^i(\alpha, \varphi; x)$ (this assumption is correct at least when all fields are massive). From Eqs. (3) or (4), it then follows (see, for example, [7]) that particle masses and S-matrix elements are independent of α.

A drawback of this consideration is that none of the above expressions for quantities in quantum field theory (Z, W, Γ, $\langle f^A\rangle$) exists in view of known ultraviolet divergences. However, we can draw a useful conclusion from this formal consideration. As a matter of fact, the equivalence theorem is based on equations of the type in (3) or (4). If we prove that finite (renormalized) generating functionals satisfy equations of the type in (3) or (4), where $\langle f^A\rangle$ is the expectation value of a local operator, this will mean that masses and S-matrix elements are independent of α, but this is what we interpret as the equivalence theorem. In the next section, we will show that, in any theory that can be rendered finite with the aid of a renormalization similar to the Bogolyubov R operation, a master equation of the type in (4) can be obtained for the generating functional for vertex functions.

3. MASTER EQUATION

As was mentioned above, the fact that the action functional $S(\alpha,\varphi)$ is derived by a change of variables from the action functional $S_0(\varphi)$ can be interpreted as the presence of a global symmetry in the action functional $S(\alpha,\varphi)$, its infinitesimal form being

$$\delta\varphi^A = f^A\theta, \quad \delta\alpha = \theta,$$

where θ is a parameter of global symmetry transformations. In order to study global symmetries in quantum field theory, it is convenient to use the field–antifield formalism [15–17] developed by Batalin and Vilkovisky for the case of local (gauge) symmetries [14]. Here, we will follow this strategy.

In accordance with the presence of a global symmetry, we introduce an additional global ghost variable c, $\varepsilon(c)=1$, $c^2=0$; for the variables $\varphi^i(x)$, we introduce the antivariables $\varphi^*_i(x)$ of opposite Grassmann parity (we will not need the antivariables α^* and c^*). With each variable, we associate a ghost number gh,

$$gh(\varphi^A) = gh(\alpha) = 0, \quad gh(\varphi^*_A) = -1, \quad gh(c) = 1.$$

In the following, the complete set of variables will be denoted by η: $\eta=\{\varphi^A,\varphi^*_A,\alpha,c\}$; the set of variables φ^A, α will be denoted by ξ: $\xi=\{\varphi^A,\alpha\}$; and the dependence on these variables will be indicated explicitly.

For the master action functional $\mathcal{S}(\eta)$, $\varepsilon(\mathcal{S}) = gh(\mathcal{S}) = 0$, we take the expression

$$\mathcal{S}(\eta) = S(\xi) + \varphi^*_A f^A(\xi)c,$$

which satisfies the master equation

$$\frac{1}{2}(\mathcal{S}(\eta),\mathcal{S}(\eta)) + c\frac{\partial\mathcal{S}(\eta)}{\partial\alpha} \tag{5}$$
$$= \left(\frac{\partial S(\xi)}{\partial\alpha} + f^A(\xi)\frac{\delta S(\xi)}{\delta\varphi^A}\right)c = 0,$$

where the antibracket (F,G) of the functionals F and G is defined as

$$(F,G) = F\frac{\overleftarrow{\delta}}{\delta\varphi^A}\frac{\delta}{\delta\varphi^*_A}G - F\frac{\overleftarrow{\delta}}{\delta\varphi^*_A}\frac{\delta}{\delta\varphi^A}G.$$

The only corollary of the master Eq. (5) is Eq. (2) for the functional $S(\eta)|_{\varphi^*=0} = S(\xi)$; its general solution is

$$S(\xi) = S_0(\Phi(\xi)),$$

where S_0 is a functional. Thus, if $S(\xi)$ has the form (1), the master action functional $\mathcal{S}(\eta)$ satisfies the master equation, and vice versa: if we require that the master action functional $\mathcal{S}(\eta)$ satisfy the master Eq. (5), $S(\xi)$ has the form (1).

The generating functional for Green's functions is given by

$$Z(J) = e^{\frac{i}{\hbar}W(J)} = \left\langle \exp\left(\frac{i}{\hbar}(\mathcal{S}_{\rm int}(\eta) + J_A\varphi^A)\right)\right\rangle_{\rm ren},$$
$$\langle Q\rangle \equiv \frac{1}{Z(J)}\left\langle Q(\eta)\exp\left(\frac{i}{\hbar}(\mathcal{S}_{\rm int}(\eta) + J_A\varphi^A)\right)\right\rangle_{\rm ren},$$
$$\mathcal{S}_{\rm int}(\eta) = \mathcal{S}(\eta) - S_2(\varphi),$$

where $S_2(\varphi) = \mathcal{S}(\eta)|_{g=\varphi^*=0}$; $Q(\eta)$ is an arbitrary functional; and $\langle(\ldots)\rangle_{\rm ren}$ means that the expectation value of the expression in the parentheses over a free vacuum is calculated according to Feynman rules for free propagators determined by the action functional $S_2(\varphi)$, some regularization and renormalization procedure being employed in this calculation. We will not need an explicit form of the regularization scheme, but we assume that the quantum action principle is valid for finite Green's functions (see [18] and references therein; all schemes used at present satisfy this assumption). In particular, the generating functional $\Sigma(\eta)$ for vertices in the theory specified by the action functional $\mathcal{S}(\eta)$ possesses the following properties:

$$(i)\quad \frac{\partial}{\partial\lambda}\Sigma(\eta) = Q_\lambda(\hbar,\eta)\circ\Sigma(\eta), \quad Q_\lambda(\hbar,\eta)$$
$$= \frac{\partial}{\partial\lambda}\mathcal{S}(\eta) + \hbar Q^{(1)}_\lambda(\hbar,\eta),$$

where the operation (insertion) $Q_\lambda(\hbar,\eta)\circ\Sigma(\eta)$ means that vertex functions are calculated according to standard Feynman rules with the additional vertex $Q_\lambda(\hbar,\eta)$,[2)] λ is an arbitrary parameter of the theory, and $Q^{(1)}_\lambda(\hbar,\eta)$ is a local functional that is equal to

[2)] As a matter of fact, we have $Q(\hbar,\eta)\circ\Sigma(\eta)\equiv\langle Q\rangle$ (we use the notation adopted in the literature).

zero if the parameter λ does not appear in the free propagators (that is, if it appears only in $\mathcal{S}_{\rm int}$).

$$(ii)\quad \langle M^A\rangle \frac{\delta}{\delta\varphi^A}\Sigma(\eta) = Q_M(\hbar,\eta)\circ\Sigma(\eta),$$

$$Q_M(\hbar,\eta) = M^A(\eta)\frac{\delta}{\delta\varphi^A}\mathcal{S}(\eta) + \hbar Q_M^{(1)}(\hbar,\eta),$$

where $M^A = M^A(\eta)$ are local functions and $Q_M^{(1)}(\hbar,\eta)$ is a local functional.

(iii) The generating functional $\Sigma(\eta)$ for vertex functions is invariant under Poincaré transformations and possesses all linear homogeneous symmetries of the action functional $\mathcal{S}(\eta)$ that do not involve the spacetime coordinates and Lorentz indices. In particular, the generating functional for vertex functions conserves the ghost number in the case under consideration.

The regularization properties (i) and (ii) make it possible to prove [18] that, local insertions apart, the generating functional for vertex functions satisfies Eq. (5):

$$\frac{1}{2}(\Sigma(\eta),\Sigma(\eta)) + c\frac{\partial\Sigma(\eta)}{\partial\alpha} = -\hbar Q^{(1)}(\hbar,\eta)\circ\Sigma(\eta), \tag{6}$$

$$Q^{(1)}(\hbar,\eta) = Q_1^{(1)}(\eta) + O(\hbar).$$

Let us calculate the antibracket of the right- and the left-hand side of Eq. (6) with $\Sigma(\eta)$; on the left-hand side of the resulting relation, we will use the Jacobi identity for the antibracket, Eq. (6) itself, and the property $c^2 = 0$. As a result, we arrive at an equation that local insertions must obey and which is the consistency condition for Eq. (6):

$$(\Sigma(\eta), Q^{(1)}(\hbar,\eta)\circ\Sigma(\eta)) \tag{7}$$
$$+ c\frac{\partial}{\partial\alpha}(Q^{(1)}(\hbar,\eta)\circ\Sigma(\eta)) = 0.$$

In the one-loop approximation, we find from (6) that

$$\frac{1}{2}(\Sigma_{[1]}(\eta),\Sigma_{[1]}(\eta))_{[1]} + c\frac{\partial\Sigma_{[1]}(\eta)}{\partial\alpha} = -\hbar Q_1^{(1)}(\eta),$$
$$\Sigma(\eta) = \mathcal{S}(\eta) + \hbar\Sigma_1(\eta) + O(\hbar^2),$$

where the subscript $[n]$ on an arbitrary function G means that only the first $n+1$ terms of its Taylor series in $\hbar$ are taken into account:

$$G \equiv G_{[n]} + O(\hbar^{n+1}),\quad \frac{\partial^{n+1}}{\partial\hbar^{n+1}}G_{[n]} = 0.$$

Because the ghost number is conserved, the local functional $Q_1^{(1)}(\eta)$ has the ghost number of 1, so that it is linear in c and is independent of φ_A^*; that is,

$$Q_1^{(1)}(\eta) = cq^{(1)}(\xi).$$

In the one-loop approximation, the consistency condition for (7),

$$\omega Q_1^{(1)}(\eta) = 0,$$
$$\omega = \frac{\delta\mathcal{S}(\eta)}{\delta\varphi^A}\frac{\delta}{\delta\varphi_A^*} + \frac{\delta\mathcal{S}(\eta)}{\delta\varphi_A^*}\frac{\delta}{\delta\varphi^A} + c\frac{\partial}{\partial\alpha},\quad \omega^2 = 0,$$

is satisfied identically.

Lemma. The functional $Q_1^{(1)}$ can be represented in the form

$$Q_1^{(1)}(\eta) = \omega X^{(1)}(\eta),$$

where $X^{(1)}(\eta)$ is a local functional, $gh(X^{(1)}) = 0$.

In order to prove this lemma, it is convenient to go over from the variables η to the variables $\tilde\eta = \{\Phi^A, \Phi_A^* = \varphi_B^*(\partial\tilde\varphi^B(\alpha,\Phi)/\partial\Phi^A), \alpha, c\}$. For an arbitrary functional $G(\eta)$, we also introduce the functional $\tilde G(\tilde\eta)$,

$$\tilde G(\tilde\eta) = G(\eta(\tilde\eta)),\quad G(\eta) = \tilde G(\tilde\eta(\eta)).$$

We then have

$$\omega G(\eta) = \tilde\omega\tilde G(\tilde\eta),$$
$$\tilde\omega = \frac{\delta S_0(\Phi)}{\delta\Phi^A}\frac{\delta}{\delta\Phi_A^*} + c\frac{\partial}{\partial\alpha}.$$

In terms of the new variables, the statement of the lemma in the form of an equation for $X^{(1)}(\eta)$ can be represented as

$$\tilde Q_1^{(1)}(\tilde\eta) = \tilde\omega\tilde X^{(1)}(\tilde\eta). \tag{8}$$

In order to solve this equation, we introduce the operator $\gamma = \alpha\partial/\partial c$. The operators ω and γ form the algebra specified by the relations

$$\omega^2 = \gamma^2 = 0,\quad \omega\gamma + \gamma\omega = N,$$
$$[\omega, N] = [\gamma, N] = 0,\quad N = \alpha\frac{\partial}{\partial\alpha} + c\frac{\partial}{\partial c}.$$

A particular solution $\tilde X_p^{(1)}(\tilde\eta)$ to the nonhomogeneous Eq. (8) can be taken in the form

$$\tilde X_p^{(1)}(\tilde\eta) = \frac{1}{N}\gamma\tilde Q_1^{(1)}(\tilde\eta) = \int_0^\alpha d\alpha'\tilde q^{(1)}(\alpha',\Phi),$$

where the action of an arbitrary function $F(N)$ of the operator N is determined as follows:

$$F(N)\alpha^k c^l = F(k+l)\alpha^k c^l,\quad k,l \geq 0.$$

We note that, by construction, the functional $\tilde X_p^{(1)}(\tilde\eta)$ is local and is independent of φ^* and c: $\tilde X_p^{(1)} = \tilde X_p^{(1)}(\tilde\xi)$. A general solution to Eq. (8) is

obtained by adding, to $\tilde{X}_p^{(1)}(\tilde{\xi})$, a general solution $\tilde{X}_h^{(1)}(\tilde{\eta})$ to the homogeneous equation

$$\tilde{\omega}\tilde{X}_h^{(1)}(\tilde{\eta}) = 0. \qquad (9)$$

Let us represent $\tilde{X}_h^{(1)}(\tilde{\eta})$ in the form

$$\tilde{X}_h^{(1)}(\tilde{\eta}) = S_{01}(\Phi) + \tilde{X}_{h1}^{(1)}(\tilde{\eta}),$$
$$S_{01}(\Phi) = \tilde{X}_h^{(1)}(\tilde{\eta})|_{\alpha=c=0}$$

(since $gh(\tilde{X}_h^{(1)}) = 0$, the functional S_{01} depends only on Φ). The functional $S_{01}(\Phi)$ drops out of Eq. (9), and a standard argument leads to

$$\tilde{X}_{h1}^{(1)}(\tilde{\eta}) = \tilde{\omega}\tilde{Y}^{(1)}(\tilde{\eta}), \quad gh(\tilde{Y}^{(1)}) = -1,$$

where $\tilde{Y}^{(1)}(\tilde{\eta}) = \Phi_A^*\tilde{\Phi}_1^A(\tilde{\xi})$ is a local functional.

Going over to the original variables, we eventually obtain

$$X^{(1)}(\eta) = S_{01}(\Phi) + \frac{\delta S_0(\Phi)}{\delta\Phi^A}\Phi_1^A(\xi) \qquad (10)$$
$$+ \varphi_A^*\frac{\delta\tilde{\varphi}^A}{\delta\Phi_B}\left(\frac{\delta\Phi_1^B(\xi)}{\delta\varphi^C}\frac{\delta\tilde{\varphi}^C}{\delta\Phi^D}\frac{\partial\Phi^D(\xi)}{\partial\alpha} - \frac{\partial\Phi_1^B(\xi)}{\partial\alpha}\right)c$$
$$+ X_p^{(1)}(\xi).$$

Let us introduce the master action functional $\mathcal{S}^{(1)}(\eta)$

$$\mathcal{S}^{(1)}(\eta) = \mathcal{S}(\eta) + \hbar X^{(1)}(\eta) \equiv S^{(1)}(\xi)$$
$$+ \varphi_A^* f^{(1)A}(\xi)c,$$

where $f^{(1)A}(\xi) = f^A(\xi) + O(\hbar)$ is a local function. The master action functional $\mathcal{S}^{(1)}(\eta)$ does not satisfy the master Eq. (5):

$$(\mathcal{S}^{(1)}(\eta), \mathcal{S}^{(1)}(\eta)) + c\frac{\partial\mathcal{S}^{(1)}(\eta)}{\partial\alpha} = \hbar\Lambda^{(1)}(\hbar,\eta).$$

It is important, however, that $\Lambda^{(1)}(\hbar,\eta)$ is a local functional.

In the theory specified by the action functional $\mathcal{S}^{(1)}(\eta)$,[3)] the generating functional $\Sigma^{(1)}(\eta)$ for vertices again satisfies the master equation, apart from the local insertions. However, it is straightforward to verify that, in the one-loop approximation, there are no local insertions:

$$\Sigma_{[1]}^{(1)}(\eta) = \Sigma_{[1]}(\eta) + \hbar X^{(1)}(\eta),$$
$$\frac{1}{2}(\Sigma_{[1]}^{(1)}(\eta), \Sigma_{[1]}^{(1)}(\eta))_{[1]} + c\frac{\partial}{\partial\alpha}\Sigma_{[1]}^{(1)}(\eta)$$
$$= \frac{1}{2}(\Sigma_{[1]}(\eta), \Sigma_{[1]}(\eta))_{[1]} + c\frac{\partial}{\partial\alpha}\Sigma_{[1]}(\eta)$$
$$+ (\Sigma_{[1]}(\eta), \hbar X^{(1)}(\eta))_{[1]} + \hbar c\frac{\partial}{\partial\alpha}X^{(1)}(\eta)$$
$$= -\hbar Q_1^{(1)}(\eta) + \hbar\omega X^{(1)}(\eta) = 0.$$

Thus, the master equation for $\Sigma^{(1)}(\eta)$ fails from the two-loop approximation:

$$\frac{1}{2}(\Sigma^{(1)}(\eta), \Sigma^{(1)}(\eta)) + c\frac{\partial}{\partial\alpha}\Sigma^{(1)}(\eta)$$
$$= -\hbar^2 Q^{(2)}(\hbar,\eta)\circ\Sigma^{(1)}(\eta),$$
$$(\Sigma^{(1)}(\eta), Q^{(2)}(\hbar,\eta)\circ\Sigma^{(1)}(\eta))$$
$$+ c\frac{\partial}{\partial\alpha}(Q^{(2)}(\hbar,\eta)\circ\Sigma^{(1)}(\eta)) = 0.$$

The meaning of individual terms in expression (10) for $X^{(1)}$ now becomes clear: (i) The first term describes quantum corrections to the original classical action functional. (ii) The second and the third term take into account quantum corrections to the classical change of variables. (iii) The last term must compensate for the possible noncovariance (with respect to changes of field variables) of this regularization scheme.

By applying further the method of induction, we eventually find that there exists an action functional $\mathcal{S}^{(\infty)}(\eta)$,

$$\mathcal{S}^{(\infty)}(\eta) = \mathcal{S}(\eta) + \sum_{n=1}\hbar^n X^{(n)}(\eta) \equiv S^{(\infty)}(\xi)$$
$$+ \varphi_A^* f^{(\infty)A}(\xi)c,$$

where $f^{(\infty)A}(\xi)$ are local functions, such that the generating functional $\Sigma^{(\infty)}(\eta)$ for vertex functions that is associated with it satisfies the master equation

$$\frac{1}{2}(\Sigma^{(\infty)}(\eta), \Sigma^{(\infty)}(\eta)) + c\frac{\partial}{\partial\alpha}\Sigma^{(\infty)}(\eta) = 0.$$

By taking into account the relation [it is valid by virtue of property (i) for the regularization schemes used]

$$\frac{\delta}{\delta\varphi_A^*}\Sigma^{(\infty)}(\eta) = \langle f^{(\infty)A}\rangle_{(0)}(\xi)c,$$

where the subscript (0) on the angular bracket means that the relevant expectation value is calculated with the action functional $S_{\rm int}^{(\infty)}(\xi) = S^{(\infty)}(\xi) - S_2(\varphi)$, we obtain

$$\frac{\partial}{\partial\alpha}\Gamma^{(\infty)}(\xi) + \langle f^{(\infty)A}\rangle_{(0)}(\xi)\frac{\delta}{\delta\varphi^A}\Gamma^{(\infty)}(\xi) = 0,$$

where $\Gamma^{(\infty)}(\xi) \equiv \Sigma^{(\infty)}(\eta)|_{\varphi^*=0}$ is the generating functional for vertex functions in the theory specified by the renormalized action functional $S^{(\infty)}(\xi)$ (of course, it is straightforward to verify that the equality $\Sigma^{(\infty)}(\eta) = \Gamma^{(\infty)}(\xi) + \varphi_A^*\langle f^{(\infty)A}\rangle_{(0)}(\xi)c$ holds).

[3)] All expectation values $\langle(\ldots)\rangle_{\rm ren}$ must now be calculated with the action functional $\mathcal{S}_{\rm int}^{(1)}(\eta) = \mathcal{S}^{(1)}(\eta) - S_2(\varphi)$.

Thus, it has been established that, with the aid of adding appropriate counterterms to the original action functional, we can always arrive at a generating functional for vertex functions that satisfies the master Eq. (4)—that is, ensure fulfillment of the equivalence theorem.

We note that counterterms describing quantum corrections to the classical change of variables [in the one-loop approximation, these are the second and the third term in expression (10)] are arbitrary and can be set to zero. For this choice of counterterms, we have $f^{(\infty)A} = f^A$ and the master equation coincides in form with the naive Eq. (4).

We also note that the statement that we have proven does not contradict the well-known fact that some classical symmetries can be violated (anomalous) in quantum theory. Indeed, let the transformation $\varphi^A \to \Phi^A(\alpha, \varphi)$ be a symmetry of the classical action functional. In this case, $S(\alpha, \varphi) = S_0(\varphi)$, and we have, instead of Eq. (2), the stronger equations

$$\frac{\partial S(\alpha,\varphi)}{\partial \alpha} = 0, \quad f^A(\alpha,\varphi)\frac{\delta S(\alpha,\varphi)}{\delta \varphi^A} = 0, \qquad (11)$$

or, which is equivalent, two independent linear combinations of these equations,

$$\frac{\partial S(\alpha,\varphi)}{\partial \alpha} + a f^A(\alpha,\varphi)\frac{\delta S(\alpha,\varphi)}{\delta \varphi^A} = 0, \qquad (12)$$

$$\frac{\partial S(\alpha,\varphi)}{\partial \alpha} + b f^A(\alpha,\varphi)\frac{\delta S(\alpha,\varphi)}{\delta \varphi^A} = 0, \quad a \neq b \qquad (13)$$

(one of the coefficients—for example, a—can be equal to zero).

From the results of this section, it follows that one of the equations—for example, Eq. (12)—can be generalized to quantum theory. In this case, specific constraints [they must have the form (10)] are imposed on possible counterterms, with the result that it is impossible to verify analogously the possibility of simultaneously generalizing the second equation [that is, Eq. (13)] to quantum theory. This will be demonstrated explicitly in the next section.

4. EXAMPLE

As was indicated in the Introduction, arbitrariness in choosing counterterms $X_h^{(n)}(\eta)$—specifically the terms $S_{0n}(\varphi)$ [see (10)]—corresponds to the partition of renormalized theories into classes (in part, this arbitrariness is, of course, associated with redefining the original parameters of the theory). The validity of the equivalence theorem within a single class is ensured by the counterterms $X_p^{(n+1)}(\xi)$.

In this section, we will consider, by way of example, a family of classical models such that they are related by a change of variables and that the quantization of these leads to physically nonequivalent theories without violation of the equivalence theorem.

The model is specified by the action functional

$$S(\alpha,\psi) = S_0(\Psi(\alpha,\psi)) \qquad (14)$$

$$= \int dx\bar{\psi}\left(i\gamma^\mu\partial_\mu + \gamma^\mu V_\mu + \gamma^\mu\gamma^5 A_\mu + \alpha\frac{f_\pi}{m}\gamma^\mu\gamma^5\partial_\mu\varphi\right)\psi,$$

$$S_0(\psi) = \int dx\bar{\psi}(i\gamma^\mu\partial_\mu + \gamma^\mu V_\mu + \gamma^\mu\gamma^5 A_\mu)\psi,$$

$$\Psi(\alpha,\psi) = \exp\left(-i\alpha\frac{f_\pi}{m}\varphi\gamma^5\right)\psi,$$

where $\psi(x)$ is a quantum Dirac field; $V_\mu(x)$, $A_\mu(x)$, and $\varphi(x)$ are external vector, axial-vector, and pseudoscalar fields; $\gamma^5 = i\gamma^0\gamma^1\gamma^2\gamma^3$; and the metric is $\mathrm{diag}(+,-,-,-)$.

The action functional (14) satisfies the equation

$$\frac{\partial}{\partial\alpha}S + \frac{if_\pi}{m}\int dx\varphi(\gamma^5\psi\frac{\delta}{\delta\psi} + \bar{\psi}\gamma^5\frac{\delta}{\delta\bar{\psi}})S = 0. \qquad (15)$$

The generating functional for vertex functions must obey the equation

$$\frac{\partial}{\partial\alpha}\Gamma^{(1)} + \int dx(\langle f_\psi^{(1)}\rangle_{(0)}\frac{\delta}{\delta\psi} + \langle f_{\bar{\psi}}^{(1)}\rangle_{(0)}\frac{\delta}{\delta\bar{\psi}})\Gamma^{(1)} = 0, \qquad (16)$$

where the superscript (1) [instead of the superscript (∞)] means that the theory is exhausted by the one-loop approximation, $f_\psi^{(1)} = (i\frac{f_\pi}{m}\varphi\gamma^5 + O(\hbar))\psi$ and $f_{\bar{\psi}}^{(1)} = \bar{\psi}(i\frac{f_\pi}{m}\varphi\gamma^5 + O(\hbar))$.

The generating functional $\Gamma^{(1)}$ for vertex functions has the structure

$$\Gamma^{(1)} = S(\alpha,\psi) + \bar{\Gamma},$$

where $\bar{\Gamma} \equiv \Gamma^{(1)}|_{\psi=\bar{\psi}=0} = \bar{\Gamma}(\alpha, V_\mu, A_\mu, \varphi)$ corresponds to a set of vacuum diagrams that represent some example of physical observables; as a result, Eq. (16) takes the form

$$\frac{\partial}{\partial\alpha}\bar{\Gamma} = 0. \qquad (17)$$

At $\varphi = 0$, the expression for $\tilde{\Gamma}(V_\mu, A_\mu) \equiv \bar{\Gamma}|_{\varphi=0}$ is unambiguously {apart from the terms $\int dx[a(\partial_\mu V_\nu - \partial_\nu V_\mu)^2 + b(\partial_\mu A_\nu - \partial_\nu A_\mu)^2]$, which can be thought to be absorbed in $\hbar S_{\mathrm{counter}}(\alpha, V_\mu, A_\mu, \varphi)$ in expression (18) (see below)} determined by the requirements that the vector current be exactly conserved,

$$\partial_\mu\frac{\delta}{\delta V_\mu(x)}\tilde{\Gamma} = 0,$$

and that the axial current be "maximally" conserved (that is, conserved apart from terms associated with

diagrams involving three external legs). In this case, we have

$$\partial_\mu \frac{\delta}{\delta A_\mu(x)}\tilde{\Gamma} = -\frac{\hbar}{4\pi^2}(\varepsilon^{\mu\nu\lambda\sigma}\partial_\mu V_\nu(x)\partial_\lambda V_\sigma(x) + \frac{1}{3}\varepsilon^{\mu\nu\lambda\sigma}\partial_\mu A_\nu(x)\partial_\lambda A_\sigma(x))$$

with $\varepsilon^{0123} = 1$. For $\varphi \neq 0$, the expression for $\bar{\Gamma}$ is derived from the expression for $\tilde{\Gamma}$ by substituting $A_\mu + \alpha\frac{f_\pi}{m}\partial_\mu\varphi$ for A_μ and by adding the possible local counterterms (as before, the vector current must be conserved):

$$\bar{\Gamma}(\alpha, V_\mu, A_\mu, \varphi) = \tilde{\Gamma}\left(V_\mu, A_\mu + \alpha\frac{f_\pi}{m}\partial_\mu\varphi\right) + \hbar S_{\text{counter}}(\alpha, V_\mu, A_\mu, \varphi). \quad (18)$$

The dependence of $\tilde{\Gamma}$ on φ can be calculated explicitly (for example, by means of differentiation with respect to α):

$$\tilde{\Gamma}\left(V_\mu, A_\mu + \alpha\frac{f_\pi}{m}\partial_\mu\varphi\right) = \tilde{\Gamma}(V_\mu, A_\mu) + \frac{\alpha\hbar}{4\pi^2}\frac{f_\pi}{m}\int dx\left(\varphi(x)\varepsilon^{\mu\nu\lambda\sigma}\partial_\mu V_\nu(x)\partial_\lambda V_\sigma(x) + \frac{1}{3}\varphi(x)\varepsilon^{\mu\nu\lambda\sigma}\partial_\mu A_\nu(x)\partial_\lambda A_\sigma(x)\right).$$

As to $S_{\text{counter}}(\alpha, V_\mu, A_\mu, \varphi)$, the only term that will be isolated in it here is linear in φ and includes the tensor $\varepsilon^{\mu\nu\lambda\sigma}$ (terms corresponding to other independent structures are immaterial for our purposes and are not be written explicitly):

$$S_{\text{counter}}(\alpha, V_\mu, A_\mu, \varphi) = \frac{f_\pi}{m}\int dx\varphi\left(r_1'(\alpha)\varepsilon^{\mu\nu\lambda\sigma}\partial_\mu V_\nu\partial_\lambda V_\sigma + r_2'(\alpha)\varepsilon^{\mu\nu\lambda\sigma}\partial_\mu A_\nu\partial_\lambda A_\sigma\right) + S'_{\text{counter}}(\alpha, V_\mu, A_\mu, \varphi).$$

Thus, the general expression for $\bar{\Gamma}$ can be represented in the form

$$\bar{\Gamma}(\alpha, V_\mu, A_\mu, \varphi) = \tilde{\Gamma}(V_\mu, A_\mu) + \hbar\frac{f_\pi}{m}\int dx\varphi\left(r_1(\alpha)\varepsilon^{\mu\nu\lambda\sigma}\partial_\mu V_\nu\partial_\lambda V_\sigma + r_2(\alpha)\varepsilon^{\mu\nu\lambda\sigma}\partial_\mu A_\nu\partial_\lambda A_\sigma\right) + \hbar S'_{\text{counter}}(\alpha, V_\mu, A_\mu, \varphi), \quad (19)$$

$$r_1(\alpha) = \frac{\alpha}{4\pi^2} + r_1'(\alpha), \quad r_2(\alpha) = \frac{\alpha}{12\pi^2} + r_2'(\alpha).$$

Equation (17) is satisfied for the following choice of counterterms:

$$r_1'(\alpha) = -\frac{\alpha}{4\pi^2} + r_1, \quad r_2'(\alpha) = -\frac{\alpha}{12\pi^2} + r_2,$$
$$r_1, r_2 = \text{const},$$
$$S'_{\text{counter}} = S'_{\text{counter}}(V_\mu, A_\mu, \varphi),$$

where r_1, r_2, and S'_{counter} are independent of α.

As a result, we arrive at the following expression for $\bar{\Gamma}$:

$$\bar{\Gamma}(\alpha, V_\mu, A_\mu, \varphi) = \tilde{\Gamma}(V_\mu, A_\mu) + \hbar S'_{\text{counter}}(V_\mu, A_\mu, \varphi) + \hbar\frac{f_\pi}{m}\int dx\varphi\left(r_1\varepsilon^{\mu\nu\lambda\sigma}\partial_\mu V_\nu\partial_\lambda V_\sigma + r_2\varepsilon^{\mu\nu\lambda\sigma}\partial_\mu A_\nu\partial_\lambda A_\sigma\right) = \tilde{\Gamma}\left(V_\mu, A_\mu + \frac{f_\pi}{m}\partial_\mu\varphi\right) + \hbar S'_{\text{counter}}(V_\mu, A_\mu, \varphi) + \hbar\frac{f_\pi}{m}\int dx\varphi\left(\left(r_1 - \frac{1}{4\pi^2}\right)\varepsilon^{\mu\nu\lambda\sigma}\partial_\mu V_\nu\partial_\lambda V_\sigma + \left(r_2 - \frac{1}{12\pi^2}\right)\varepsilon^{\mu\nu\lambda\sigma}\partial_\mu A_\nu\partial_\lambda A_\sigma\right).$$

Obviously, this expression satisfies the equivalence theorem (it does not depend on the change of field variables in the classical action functional), but it still involves arbitrariness in choosing counterterms, which admits different types of treatment.

If one proceeds from the quantum theory that is constructed on the basis of the classical action functional (14) at $\alpha = 0$,

$$S(0, \psi) = S_0(\psi) = \int dx\bar{\psi}(i\gamma^\mu\partial_\mu + \gamma^\mu V_\mu + \gamma^\mu\gamma^5 A_\mu)\psi,$$

it seems natural to require that, at $\alpha = 0$ and, hence, at any value of α, the quantum theory be independent of the field φ on the fermion mass shell. For the functional $\bar{\Gamma}$, this requirement means that it is merely independent of φ; that is,

$$\bar{\Gamma} = \tilde{\Gamma}(V_\mu, A_\mu)$$

($r_1 = r_2 = S'_{\text{counter}} = 0$).

If one proceeds from the quantum theory that is constructed on the basis of the classical action functional (14) at $\alpha = 1$ (the case where any other nonzero value of α is taken for a normalization reduces to merely redefining the parameter f_π or m),

$$S(1, \psi) = \int dx\bar{\psi}\left(i\gamma^\mu\partial_\mu + \gamma^\mu V_\mu + \gamma^\mu\gamma^5 A_\mu + \frac{f_\pi}{m}\gamma^\mu\gamma^5\partial_\mu\varphi\right)\psi,$$

it seems natural to require that the field $\frac{f_\pi}{m}\partial_\mu\varphi$ interact with the same axial-vector current as the axial-vector field A_ν. In this case, we must set $r_1 = 1/4\pi^2$ and $r_2 = 1/12\pi^2$ (in addition, we assume for the sake of simplicity that $S'_{\text{counter}} = 0$), which yields

$$\bar{\Gamma} = \tilde{\Gamma}(V_\mu, A_\mu + \frac{f_\pi}{m}\partial_\mu\varphi).$$

Thus, the above example demonstrates that the requirement that the equivalence theorem be valid does not remove arbitrariness associated with the possibility of adding finite counterterms that lead to physically nonequivalent theories.

By considering the same model, we will now demonstrate that, in contrast to the equivalence theorem, all symmetries of the classical action functional cannot be generalized to the case of quantum theory.

We note that, in addition to (15), the action functional (14) possesses the local vector symmetry

$$\left(\partial_\mu \frac{\delta}{\delta V_\mu} - i\left(\psi\frac{\delta}{\delta\psi} - \bar\psi\frac{\delta}{\delta\bar\psi}\right)\right)S = 0 \qquad (20)$$

and the local axial symmetry

$$\left(\partial_\mu \frac{\delta}{\delta A_\mu} - \frac{if_\pi}{m}\left(\gamma^5\psi\frac{\delta}{\delta\psi} + \bar\psi\gamma^5\frac{\delta}{\delta\bar\psi}\right)\right)S = 0. \quad (21)$$

Let us explicitly write the equation that corresponds to the symmetry of the classical action functional (14) under global axial transformations and which is of course a limiting case of Eq. (21):

$$\int dx\left(\gamma^5\psi\frac{\delta}{\delta\psi} + \bar\psi\gamma^5\frac{\delta}{\delta\bar\psi}\right)S = 0. \qquad (22)$$

Instead of Eq. (21), we can consider the equation

$$\left(\frac{\partial}{\partial\alpha} - \frac{f_\pi}{m}\int dx\partial_\mu\varphi\frac{\delta}{\delta A_\mu}\right)S = 0, \qquad (23)$$

which, with allowance for (15), is equivalent to it.

As to the local vector symmetry, we assume (although this is immaterial for our purposes) that it preserves its form in quantum theory—that is, that the generating functional for vertex functions satisfies the equation

$$\left(\partial_\mu \frac{\delta}{\delta V_\mu} - i\left(\psi\frac{\delta}{\delta\psi} - \bar\psi\frac{\delta}{\delta\bar\psi}\right)\right)\Gamma^{(1)} = 0, \qquad (24)$$

or, which is equivalent, the equation

$$\partial_\mu\frac{\delta}{\delta V_\mu}\bar\Gamma = 0. \qquad (25)$$

In quantum theory, the analogs of Eqs. (21) and (23) of the local axial symmetry must take the form

$$\int dx\Bigg((\partial_\mu\varphi + O(\hbar))\frac{\delta}{\delta A_\mu} + \frac{if_\pi}{m}\Big[(\gamma^5\varphi + O(\hbar))\psi\frac{\delta}{\delta\psi} + \bar\psi(\gamma^5\varphi + O(\hbar))\frac{\delta}{\delta\bar\psi}\Big]\Bigg)\Gamma^{(1)} = 0; \qquad (26)$$

$$\left(\frac{\partial}{\partial\alpha} - \frac{f_\pi}{m}\int dx(\partial_\mu\varphi + O(\hbar))\frac{\delta}{\delta A_\mu}\right)\Gamma^{(1)} = 0, \quad (27)$$

or, which is equivalent,

$$\partial_\mu\frac{\delta}{\delta A_\mu}\bar\Gamma = 0; \qquad (28)$$

$$\left(\frac{\partial}{\partial\alpha} - \frac{f_\pi}{m}\int dx\partial_\mu\varphi\frac{\delta}{\delta A_\mu}\right)\bar\Gamma = 0 \qquad (29)$$

[we recall that the functional $\bar\Gamma$ is an $O(\hbar)$ quantity].

From the explicit expression (19) for the functional $\bar\Gamma$, it can be seen that either Eq. (17) can be satisfied, as was discussed above, or this is so for Eq. (29) [which means that the functional $\bar\Gamma$ depends on A_μ and φ only in the form of the combination $A_\mu + (\alpha f_\pi/m)\partial_\mu\varphi$], but that the two equations cannot be satisfied simultaneously. Equation (28) can never be valid [irrespective of whether Eqs. (17), (25), and (29) hold or whether they do not hold].

On the other hand, it can be seen from the explicit expression for the functional $\Gamma^{(1)}$ that it possesses a global axial symmetry,

$$\int dx\left(\gamma^5\psi\frac{\delta}{\delta\psi} + \bar\psi\gamma^5\frac{\delta}{\delta\bar\psi}\right)\Gamma^{(1)} = 0; \qquad (30)$$

that is, the global axial symmetry (22) of the classical action functional remains valid in quantum theory as well (in contrast to a local axial symmetry). This fact does not contradict the violation of (anomaly in) the law of axial-current conservation in quantum theory, since, in quantum theory, there is no direct analog of the Noether theorem, according to which the presence of a continuous symmetry of the local classical action functional leads to the existence of a conserved current.

ACKNOWLEDGMENTS

I am grateful to B.L. Voronov for a number of valuable critical comments.

This work was supported in part by the Russian Foundation for Basic Research (project nos. 99-01-00980, 99-02-17916, and 00-15-96566) and the Commission of the European Community (grant no. INTAS-96-0308).

REFERENCES

1. F. J. Dyson, Phys. Rev. **73**, 829 (1948).
2. H. I. Borchers, Nuovo Cimento **15**, 784 (1960).
3. S. R. Chisholm, Nucl. Phys. **26**, 469 (1961).
4. S. Kamefuchi, L. O'Raifeartaigh, and A. Salam, Nucl. Phys. **28**, 529 (1961).
5. S. Coleman, I. Wess, and B. Zumino, Phys. Rev. **177**, 2239 (1969).
6. G. 't Hooft and M. Veltman, *Combinatorics of Gauge Fields,* Preprint (Utrecht, 1972).
7. R. É. Kallosh and I. V. Tyutin, Yad. Fiz. **17**, 190 (1973) [Sov. J. Nucl. Phys. **17**, 98 (1973)].
8. Y. M. P. Lam, Phys. Rev. D **7**, 2943 (1973).
9. M. C. Bergere and Yuk-Ming P. Lam, Phys. Rev. D **13**, 3247 (1976).

10. I. V. Tyutin, Yad. Fiz. **35**, 222 (1982) [Sov. J. Nucl. Phys. **35**, 125 (1982)].
11. N. N. Bogolyubov, A. A. Logunov, A. I. Oksak, and I. T. Todorov, *General Principles of Quantum Field Theory* (Nauka, Moscow, 1987).
12. N. N. Bogoliubov and D. V. Shirkov, *Introduction to the Theory of Quantized Fields* (Nauka, Moscow, 1976; Wiley, New York, 1980).
13. O. I. Zav'yalov, *Renormalized Feynman Diagrams* (Nauka, Moscow, 1979).
14. I. A. Batalin and G. A. Vilkovisky, Phys. Lett. B **102**, 27 (1981).
15. B. L. Voronov and I. V. Tyutin, Yad. Fiz. **33**, 1137 (1981) [Sov. J. Nucl. Phys. **33**, 602 (1981)].
16. C. Becchi, A. Blasi, G. Bonneau, *et al.,* Commun. Math. Phys. **120**, 121 (1988).
17. F. Brandt, M. Henneaux, and A. Wilch, Nucl. Phys. B **510**, 640 (1998).
18. O. Piguet and S. P. Sorella, *Algebraic Renormalization* (Springer-Verlag, Berlin, 1995).
19. G. Barnich, F. Brandt, and M. Henneaux, Commun. Math. Phys. **174**, 57 (1995); hep-th/0002245.

Translated by A. Isaakyan

Physics of Atomic Nuclei, Vol. 65, No. 1, 2002, pp. 38–40. Translated from Yadernaya Fizika, Vol. 65, No. 1, 2002, pp. 40–43.
Original Russian Text Copyright © 2002 by Shpinel.

NUCLEI
Experiment

Electron–Phonon Multiplier Involving a Cascade of NIS Tunnel Junctions and Hot-Electron Microcalorimeters

V. S. Shpinel

Institute of Nuclear Physics, Moscow State University, Vorob'evy gory, Moscow, 119899 Russia

Received October 19, 2000

Abstract—A device for amplifying weak electric signals arising in a normal- or a superconducting-metal absorber upon the absorption of photons or phonons is proposed. The device consists of a cascade of normal-metal–insulator–superconductor (NIS) tunnel junctions, where the normal metal is used as an electrode and as a hot-electron microcalorimeter. Tunneling through the barrier, a particle transports energy of about Δ (energy gap in the superconductor) from one microcalorimeter to another and amplifies the current through the next NIS junction. The device operates as a solid-state electron multiplier at low temperatures. © *2002 MAIK "Nauka/Interperiodica".*

In this study, it is shown that the signal initiated by the emergence of hot electrons upon the absorption of, for example, the energy of x-ray and γ-ray photons or the energy of recoil nuclei in a metal can be detected and amplified by a device based on a chain of series microcalorimeters involving normal-metal–insulator–superconductor (NIS) tunnel junctions. Such a device has the $N_1I_1S_1N_2I_2S_2\ldots N_nI_nS_n$ structure formed by a cascade of microcalorimeters and NIS junctions (n), where the normal metal N is a microcalorimeter; simultaneously, part of its surface plays the role of the normal electrode of the tunnel junction. The second, superconducting, electrode S of this junction is in contact with the normal metal of the next calorimeter. Either the first microcalorimeter or, for enhancing the efficiency, the superconductor contacting it serves as the absorber.

The densities of electron states and transitions of quasielectrons through the tunnel junctions of the structure under consideration are shown in Fig. 1*a*. The direct tunnel current I through the NIS junction is given by

$$I = \frac{1}{2eR_n}(2\pi\Delta k_{\rm B}T)^{1/2}\exp\left(-\frac{\Delta - eV}{k_{\rm B}T}\right). \quad (1)$$

The bias voltage V applied to each junction has the same value and satisfies the condition $(\Delta - eV) \gg k_{\rm B}T$, where T is the absolute temperature; Δ is the energy gap in the superconductor; and R_n is the normal resistance, which is assumed to be identical for all junctions. Upon traversing the first junction, electrons arrive at the second microcalorimeter N_2 and release a power $\Delta \times I/e$ in it. In equilibrium, the heat coming to the calorimeter must be equal to the loss of heat by thermal conductivity. In this case, the following condition must be satisfied:

$$\Delta\frac{1}{e}I = -G\delta T. \quad (2)$$

Here, δT is the temperature difference between the electrons in the calorimeter and the ambient medium, while G is the thermal conductivity determined by two possible mechanisms, $G = g_{e-p} + g_t$. One of them, g_{e-p}, is the thermal conductivity associated with energy transfer to phonons by radiation, while the other, g_t, is the electron-energy transport during tunneling itself. The thermal conductivity g_{e-p} is given by $g_{e-p} = 5\Sigma UT^4$, where Σ is the electron–phonon coupling constant depending on the microcalorimeter material (for copper, $\Sigma = 2\times10^{-9}$ W K^{-5} μm^{-3}) and U and T are, respectively, the volume and the temperature of the microcalorimeter. The thermal conductivity g_t can be obtained by multiplying the energy carried by one electron, $\sim(\Delta - eV)$, by the current increment per 1 K of heating:

$$g_t = (\Delta - eV)\frac{1}{e}\frac{dI}{dT}. \quad (3)$$

Calculations reveal that the increase δT [Eq. (2)] in the microcalorimeter temperature due to the passage of the direct tunnel current of required magnitude is small because of the thermal conductivity of the electrodes, which are in thermal contact with the cool conductor of the refrigirator.

The absorption of energy E in the first microcalorimeter N_1 leads, above all, to the heating of electrons because the electron–phonon interaction g_{e-p} is very weak ($k_{\rm B}T \ll \Delta$) at low temperatures.

We assume that the time of electron heating is very short, in which case the further variation of the electron temperature is given by

$$\delta T_1(t) = \frac{E}{c_1}\exp\left(-\frac{t}{\tau_d}\right), \tag{4}$$

where the constant τ_d characterizes the time of cooling of the first microcalorimeter: $\tau_d = c_1/(g_{e-p} + g_1)$ (g_1 is the value of g_t for the first calorimeter and c_1 is its heat capacity). As soon as hot electrons appear in the normal electrode N_1 of the first NIS junction, the tunnel current through this junction increases by the quantity

$$\delta I_1(t) = \frac{dI_1}{dT}\delta T_1(t). \tag{5}$$

As a result, excess quasielectrons of energy about Δ appear in the superconducting electrode S_2 and, then, quickly penetrate into the microcalorimeter N_2, increasing its electron temperature by $\delta T_2(t)$. It should be emphasized that the inverse tunneling is suppressed here because the metal N_2 acts as a trap. The temperature $\delta T_2(t)$ is a function of time and can be found from the differential equation

$$\frac{d(\delta T_2)}{dt} = \frac{\Delta}{c_2}\frac{1}{e}\delta I_1 - \frac{g_2}{c_2}\delta T_2, \tag{6}$$

where c_2 is the heat capacity of the second microcalorimeter and g_2 is the thermal conductivity g_t due to tunneling through the second NIS junction. The thermal conductivity due to electron–phonon interaction is much less than g_t and is neglected here ($g_{e-p} \ll g_t$). Integrating Eq. (6), we obtain

$$\delta T_2(t) = \frac{a\Delta}{c_2 c_1}E\left[\frac{\exp(-\lambda_1 t)}{\lambda_2 - \lambda_1} + \frac{\exp(-\lambda_2 t)}{\lambda_1 - \lambda_2}\right]. \tag{7}$$

For the current δI_2 through the second microcalorimeter, we then have

$$\delta I_2(t) = \frac{a^2\Delta}{c_2 c_1}E\left[\frac{\exp(-\lambda_1 t)}{\lambda_2 - \lambda_1} + \frac{\exp(-\lambda_2 t)}{\lambda_1 - \lambda_2}\right], \tag{8}$$

where $a = 1/e \cdot dI/dT$ and $\lambda_i = g_i/c_i$. The subsequent penetration of electrons into the third microcalorimeter leads to a change in the temperature of this calorimeter. This change, $\delta T_3(t)$, can be found from an equation similar to (6).

$$\delta T_3(t) = \frac{a^2\Delta^2}{c_3 c_2 c_1}E\left[\frac{\exp(-\lambda_1 t)}{(\lambda_3 - \lambda_1)(\lambda_2 - \lambda_1)}\right. \tag{9}$$
$$\left. + \frac{\exp(-\lambda_2 t)}{(\lambda_3 - \lambda_2)(\lambda_1 - \lambda_2)} + \frac{\exp(-\lambda_3 t)}{(\lambda_1 - \lambda_3)(\lambda_2 - \lambda_3)}\right].$$

For the current, we obtain

$$\delta I_3(t) = \frac{a^3\Delta^2}{c_3 c_2 c_1}E\left[\frac{\exp(-\lambda_1 t)}{(\lambda_3 - \lambda_1)(\lambda_2 - \lambda_1)}\right. \tag{10}$$
$$\left. + \frac{\exp(-\lambda_2 t)}{(\lambda_3 - \lambda_2)(\lambda_1 - \lambda_2)} + \frac{\exp(-\lambda_3 t)}{(\lambda_1 - \lambda_3)(\lambda_2 - \lambda_3)}\right].$$

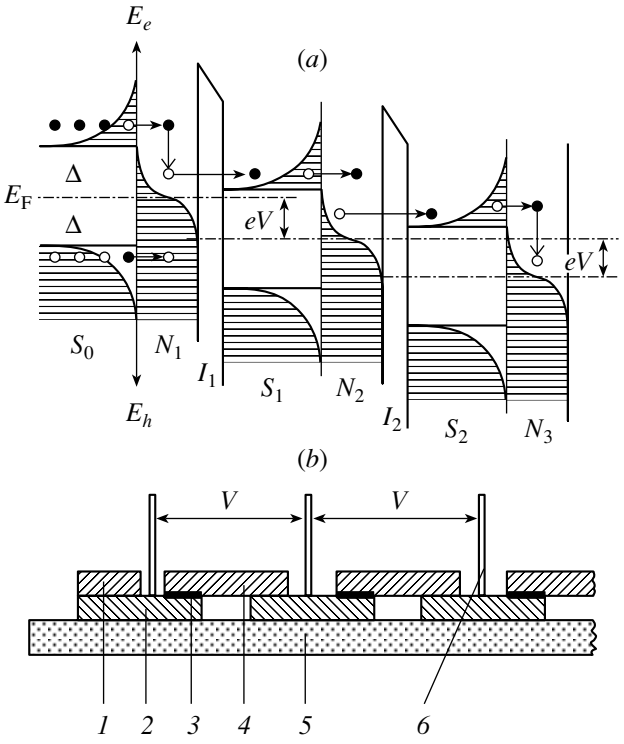

Fig. 1. *(a)* Diagram of electron states in the superconducting absorber (S_0) and in the electrodes of the electron multiplier (N_1S_1, $N_2S_2\ldots$). The notation used in the figure is the following: I_1, $I_2\ldots$, are insulating barriers; arrows indicate the directions of quasiparticle transitions; E_e and E_h are the energies of electrons and holes, respectively; E_F is the Fermi energy; and V is the bias voltage. *(b)* Layout of the multiplier structure: (*1*) absorber, (*2*) normal metal (Ag), (*3*) insulating barrier (Al_2O_3), (*4*) superconducting electrode (Nb), (*5*) substrate, and (*6*) electric contacts.

Using the same method, we find, for the nth calorimeter of the cascade, that

$$\delta I_n(t) = \frac{a^n\Delta^{n-1}}{c_n\cdots c_1}E\left[\frac{\exp(-\lambda_1 t)}{(\lambda_2 - \lambda_1)\cdots(\lambda_n - \lambda_1)}\right. \tag{11}$$
$$+ \frac{\exp(-\lambda_2 t)}{(\lambda_1 - \lambda_2)\cdots(\lambda_n - \lambda_2)} + \cdots$$
$$\left. + \frac{\exp(-\lambda_n t)}{(\lambda_1 - \lambda_n)\cdots(\lambda_{n-1} - \lambda_n)}\right].$$

These expressions show that the current-pulse shape is described by a superposition of exponentials and that its amplitude value $\delta I_n(\tau)$ increases with increasing number n of cascades. The amplification factor $K_n = \delta I_n(\tau)/\delta I_1(0)$ for the system involving only two series NIS junctions ($n = 2$) has the form

$$K_2 = \frac{\Delta}{c_2}\frac{1}{e}\frac{dI}{dT}\left(\frac{\exp(-\lambda_1\tau_2)}{\lambda_2 - \lambda_1} + \frac{\exp(-\lambda_2\tau_2)}{\lambda_1 - \lambda_2}\right), \tag{12}$$

where the constant τ_2 is the time it takes for the signal to pass an amplitude value:

$$\tau_2 = \frac{\ln\lambda_2 - \ln\lambda_1}{\lambda_2 - \lambda_1}. \quad (13)$$

To estimate K_n, we assume that, in expression (11), all the values of c_i are on the same order of magnitude and that all differences $(\lambda_1 - \lambda_k)$ there are about λ_1. We then have

$$K_n = \left(\frac{\Delta}{g}\frac{1}{e}\frac{dI}{dT}\right)^{n-1} f(\tau_n) = \left(\frac{\Delta}{\Delta - eV}\right)^{n-1} f(\tau_n), \quad (14)$$

where $f(\tau_n)$ is the value obtained by taking the function describing the time dependence of the pulse shape at the instant τ_n corresponding to its maximum.

The structure of the cascade of series NIS junctions is shown schematically in Fig. 1*b*. For microcalorimeters and normal electrodes, use is made there of silver films of area $40 \times 10\ \mu\text{m}^2$ and thickness $0.1\ \mu$m. The films were sputtered on a substrate $20\ \mu$m apart. On each film, an Al_2O_3 oxide layer is formed that covers only part of its surface. After that, Nb was sputtered on this oxide layer and on the surface of the neighboring silver film not covered with the oxide. In this way, we formed the superconducting electrode of the junction and implemented a Nb–Ag contact. In order to eliminate or to reduce heat losses into the substrate, it must be fabricated in the form of a thin membrane from Si_3N_4, as is recommended in the literature [1].

The volume of each microcalorimeter is $40\ \mu\text{m}^3$, and its heat capacity is $c = 7 \times 10^{-16}$ cal K^{-1}. Setting the parameters to $\Delta = 1.4 \times 10^{-3}$ eV, $(\Delta - eV)/k_\text{B}T = 2$, $R_n = 0.1\ \Omega$, and $T = 80 \times 10^{-3}$ K, we obtain the current of $I = 1.63 \times 10^{-4}$ A, the time constant of $\tau \sim 0.5 \times 10^{-7}$ s, the amplification factor of $K_2 = 10^2$, and a strong increase in the amplification with increasing number of cascades. Thus, the structure that is considered here and which is formed by a cascade of NIS tunnel junctions involving microcalorimeters has the properties of an electron multiplier that makes it possible to dispense with routinely used preamplifiers and SQUID amplifiers specially developed for detecting weak signals.

The energy resolution of such a multiplier is limited by thermal and electron noises. In our case, the thermodynamic limit on the resolution, $\Delta E = 2.35(k_\text{B}T^2c)^{1/2}$, is 0.25 eV. Electron noises caused by the shot effect of the direct tunnel current yield a value of $(I\tau/e)^{1/2} = 0.7 \times 10^4$ electrons for the fluctuation of the number of electrons over the time τ (it is equivalent to the absorption of energy of 0.16 eV). If we replace Nb by Al ($\Delta = 0.235 \times 10^{-3}$ eV) in such a multiplier, the amplification decreases for the adopted values of the parameters [R_n, T, and $(\Delta - eV)/k_\text{B}T = 2$], but it still remains reasonably high, $K_2 = 18$.

While the quantity g_{e-p} increases with increasing temperature, g_t decreases. For example, these quantities are on the same order of magnitude in our case of $Ag/Al_2O_3/Nb$ junctions at $T = 1.3$ K: $g_{e-p} = 2.8 \times 10^{-7}$ cal s^{-1} K^{-1} and $g_t = 0.58 \times 10^{-7}$ cal s^{-1} K^{-1}. For this reason, it is necessary to replace $\lambda = g_t/c$ by $\lambda = G/c = (g_{e-p} + g_t)/c$ in the formulas presented above. This will result in that the signal duration will become shorter, while the amplification factor will decrease to the value of $K_2 = 1.19$. Such a multiplier formed by ten cascades yields the total amplification factor of $K_{10} = 4.8$. It should be noted that an increase in g_{e-p} will lead to an increase in the noise associated with it.

The amplification of the signal by two cascades of tunnel NIS junctions was reported in [2], and the same principle of amplification was proposed in [3] for creating a low-temperature amplifier that would replace transistors and which was dubbed a "quatratran."

In summary, a new principle of the amplification of signals induced by hot electrons in a microcalorimeter operating as a high-resolution cryogenic detector of soft x rays and γ rays has been proposed in the present article. Owing to a low energy detection threshold in such a detector, it would become possible to measure the recoil energy of metal nuclei undergoing beta decay or capturing electrons.

ACKNOWLEDGMENTS

This work was supported by the Russian Foundation for Basic Research (project no. 99-02-18368).

REFERENCES

1. A. J. Manninen, M. M. Leivo, and J. P. Pekola, Appl. Phys. Lett. **70**, 1885 (1997).
2. V. S. Shpinel, in *Proceedings of the L International Conference on Nuclear Spectroscopy and Nuclear Structure: Clusters in Nuclear Physics, St. Petersburg, 2000,* p. 391; Izv. Akad. Nauk, Ser. Fiz. **64**, 2216 (2000).
3. N. E. Booth, P. A. Fisher, M. Nahum, and J. N. Ullom, Nucl. Instrum. Methods Phys. Res. A **444**, 33 (2000).

Translated by V. Bukhanov

Physics of Atomic Nuclei, Vol. 65, No. 1, 2002, pp. 41–48. Translated from Yadernaya Fizika, Vol. 65, No. 1, 2002, pp. 44–51.
Original Russian Text Copyright © 2002 by Rebane, Filinsky.

NUCLEI
Theory

Ground-State Energy and Stability of Three-Particle Coulomb Systems versus the Masses of the Particles Involved

T. K. Rebane and A. V. Filinsky[1)]

Institute of Physics (Petrodvorets Branch), St. Petersburg State University, Ul'yanovskaya ul. 1, Petrodvorets, 198904, Russia

Received May 23, 2000; in final form, March 5, 2001

Abstract—The ground-state energy of three-particle Coulomb systems (trions) is investigated versus the masses of the particles involved. Variational calculations are performed for 34 asymmetric trions $X^{\pm}Y^{\pm}Z^{\mp}$ consisting of electrons, muons, pions, kaons, nuclei of hydrogen isotopes and their antiparticles, as well as for more than 100 auxiliary three-particle systems involving particles of masses chosen arbitrarily. Wide bases of Laguerre exponential–polynomial functions depending on perimetric particle coordinates are used. Approximate analytic formulas for the ground-state energies of all trions $X^{\pm}Y^{\pm}Z^{\mp}$ with arbitrary particle masses are constructed on the basis of the values found here for the energies of asymmetric trions and the values calculated previously for the energies of symmetric trions $X^{\pm}X^{\pm}Z^{\mp}$. Particle-mass regions are determined where trions are stable with respect to dissociation. In addition to symmetric trions $X^{\pm}X^{\pm}Z^{\mp}$, which are stable at any particle masses, asymmetric trions $X^{\pm}X^{\pm}Z^{\mp}$ possess the stability property if the masses of the particles X and Y exceed the mass of the particle Z, where, by Z, we mean, for example, an electron, a muon, a pion, or a kaon. The $t^+d^+p^-$ and $t^+d^+d^-$ combinations of hydrogen nuclei and antinuclei are also stable with respect to dissociation. The general properties of the ground-state trion energy as a function of the particle masses are discussed. © *2002 MAIK "Nauka/Interperiodica".*

INTRODUCTION

Three-particle Coulomb systems (trions) are of interest for the theory of atoms and molecules, solid-state and nuclear physics, and elementary-particle theory. In view of a wide diversity of trions, which may consist of electrons, muons, pions, kaons, hydrogen nuclei, and other particles and antiparticles, it is highly desirable to perform a systematic analysis of their energies and properties versus the masses of the particles involved. The relevant dependences are determined by the dependence of the trion Hamiltonians on the particle masses, which can be treated by convention as continuous variables. The basic points of this approach were formulated in [1], where an approximate formula was proposed for the ground-state energy of $X^{\pm}X^{\pm}Z^{\mp}$ trions, which are symmetric with respect to two particles and which represent a series extending from the molecular hydrogen ion H_2^+ through various molecule-like and atomlike trions to the negative ion H^- of the hydrogen atom as one varies the particle masses. In [2], this approach was supplemented with detailed variational calculations performed for symmetric trions by using wide bases of Laguerre exponential–polynomial functions; also, precision analytic formulas were constructed there for predicting their energies. The results obtained along these lines demonstrate that the approach based on studying the parametric dependence of relevant Hamiltonians on particle masses possesses a rich potential.

It is of importance to generalize such an approach to a wide variety of particle-mass-asymmetric trions $X^{\pm}Y^{\pm}Z^{\mp}$, in which the charges of the particles involved are taken to be $q_1 = q_2 = -q_3 = \pm 1$, while the masses of the particles carrying identical charges are different: $m_1 \neq m_2$.

When the masses of all particles are changed by a factor of k, the energy of the Coulomb systems being considered changes by the same factor. The reduced energy of symmetric trions that arises upon separating this proportionality factor depends only on one parameter that is determined by the particle-mass ratio m_3/m_1; as to the reduced energy of asymmetric trions, it depends on two parameters determined by the particle-mass ratios m_3/m_1 and m_2/m_1. Because of this dependence on two variables, it is more difficult to investigate the reduced energy of asymmetric trions than the reduced energy of symmetric trions.

In contrast to symmetric trions $X^{\pm}X^{\pm}Z^{\mp}$, which are stable with respect to dissociation at any particle

[1)]Makarov State Marine Academy, St. Petersburg, Russia.

1063-7788/02/6501-0041$22.00 © 2002 MAIK "Nauka/Interperiodica"

masses, asymmetric trions $X^{\pm}Y^{\pm}Z^{\mp}$ become unstable as soon as the masses of the particles X and Y appear to be strongly different—as a result, such trions decay into the atom $X^{\pm}Z^{\mp}$ and the free particle $Y^{\pm}$.

PARAMETRIZATION OF THE PARTICLE-MASS DEPENDENCE OF THE TRION ENERGY

Trions formed by particles having unit charges and arbitrary masses are described by the Hamiltonian

$$H(\mathbf{r}_1,\mathbf{r}_2,\mathbf{r}_3) = -(1/2)[\Delta_1/m_1+\Delta_2/m_2+\Delta_3/m_3] + 1/r_{12}-1/r_{13}-1/r_{23}. \quad (1)$$

Here, we have used the system of Hartree atomic units ($\hbar = m_e = |e| = 1$). The likely charged particles 1 and 2 will be numbered in such a way that $m_1 \geqslant m_2$.

Introducing the relative particle coordinates

$$\mathbf{s} = \alpha(\mathbf{r}_1-\mathbf{r}_2), \quad \mathbf{t} = \alpha(\mathbf{r}_1+\mathbf{r}_2-2\mathbf{r}_3) \quad (2)$$

and separating the nonquantized motion of the center of mass, we find from (1) that the Hamiltonian can be recast into the form

$$H = \alpha h(\mathbf{s},\mathbf{t};\beta,\gamma), \quad (3)$$

where $h(\mathbf{s},\mathbf{t};\beta,\gamma)$ is the operator representing the reduced energy of the trion whose center of mass is at rest,

$$h(\mathbf{s},\mathbf{t};\beta,\gamma) = -\beta\Delta_s + 2\gamma\nabla_s\nabla_t - \Delta_t + 1/|\mathbf{s}| - 2/|\mathbf{s}+\mathbf{t}| - 2/|\mathbf{s}-\mathbf{t}|, \quad (4)$$

and where the parameters α, β, and γ depend on the particle masses as

$$\alpha = 2/(4/m_3+1/m_1+1/m_2), \quad (5)$$

$$\beta = (1/m_1+1/m_2)/[4/m_3+1/m_1+1/m_2], \quad (6a)$$

$$\gamma = (1/m_2-1/m_1)/[4/m_3+1/m_1+1/m_2]. \quad (6b)$$

The quantities β and γ are dimensionless and are bounded for any positive values of the particle masses:

$$0 \leqslant \beta \leqslant 1, \quad (7a)$$

$$0 \leqslant \gamma \leqslant \beta. \quad (7b)$$

They can vary within a right triangle whose legs are of unit length. Small values of the parameter β correspond to molecule-like systems consisting of heavy particles 1 and 2 and a light particle 3, while its values close to unity correspond to atomlike systems involving light particles 1 and 2 and a heavy particle 3.

Denoting by $\varepsilon(\beta,\gamma)$ the lowest eigenvalue of the operator $h(\mathbf{s},\mathbf{t};\beta,\gamma)$ (4), we find from (3) that the ground-state energy of a trion whose center of mass is at rest can be recast into the form

$$E(m_1,m_2,m_3) = \alpha\varepsilon(\beta,\gamma). \quad (8)$$

Thus, investigation of the ground-state energy of trions formed by particles of arbitrary masses amounts to considering the function $\varepsilon(\beta,\gamma)$ of two variables. We will show that this function increases monotonically with increasing β and decreases monotonically with increasing γ.

By applying the Feynman–Hellmann theorem to the β dependence of the eigenvalue of the reduced-energy operator (4), we arrive at

$$\partial\varepsilon(\beta,\gamma)/\partial\beta = \langle -\Delta_s\rangle \geqslant 0. \quad (9)$$

Here, the inequality sign takes into account nonnegativity of the expectation value of the operator $-\Delta_s$. From (9), it follows that the reduced energy of a trion increases monotonically with increasing β:

$$\varepsilon(\beta_2,\gamma) \geqslant \varepsilon(\beta_1,\gamma) \quad \text{for} \quad \beta_2 \geqslant \beta_1. \quad (10)$$

According to (6b), the reversal of the sign of γ corresponds to the interchange of the masses of the likely charged particles 1 and 2; since this does not affect the trion energy, the reduced energy ε is an even function of γ:

$$\varepsilon(\beta,\gamma) = \varepsilon(\beta,-\gamma), \quad \partial\varepsilon(\beta,\gamma)/\partial\gamma|_{\gamma=0} = 0. \quad (11)$$

From the basic equations of perturbation theory, it follows that the second derivative of the lowest energy eigenvalue with respect to a parameter that appears linearly in the Hamiltonian cannot be positive (see, for example, [3]):

$$\partial^2\varepsilon(\beta,\gamma)/\partial\gamma^2 \leqslant 0. \quad (12)$$

With allowance for (11), this means that the function $\varepsilon(\beta,\gamma)$ has a maximum at $\gamma = 0$ and decreases monotonically with increasing absolute value of γ. Therefore, we have

$$\varepsilon(\beta,\gamma_2) \leqslant \varepsilon(\beta,\gamma_1) < \varepsilon(\beta,0) \quad \text{for} \quad \gamma_2 \geqslant \gamma_1 > 0. \quad (13)$$

FORMULAS FOR TRION ENERGIES

Let us now construct analytic formulas for the energies of molecule-like and atomlike trions formed by particles of arbitrary masses. We denote by β_0 the value of β [recall that this parameter is given by Eq. (6a)] that separates the region of molecule-like trions ($0 \leqslant \beta \leqslant \beta_0$) and the region of atomlike trions ($1 \geqslant \beta \geqslant \beta_0$) and which can of course be chosen only by convention.

The quantity β (6a) can be represented in the form $\beta = 1/(1+4\mu_{12}/m_3)$, where $\mu_{12} = m_1m_2/(m_1+m_2)$, whence it follows that β is small if the ratio of the mass m_3 of particle 3 to the reduced mass μ_{12} of particles 1 and 2 is small. The case of $m_3 = 1$

Table 1. Variational values of the ground state energy E of asymmetric trions XYZ and their dissociation energy D

XYZ	E	D	XYZ	E	D
∞pe	−0.59879012	0.09879012	dpK	−384.336511	1.920730
∞Ke	−0.59728342	0.09728342	$dp\pi$	−135.752052	8.646704
$\infty \pi e$	−0.59226972	0.09226972	$dp\mu$	−106.012527	8.141724
$\infty \mu e$	−0.59061563	0.09061563	dpe	−0.59789797	0.09803415
tdd	−1101.36421	0.92422	$dK\pi$	−129.714658	2.609310
tdK	−429.800535	18.938568	$dK\mu$	−101.487236	3.616433
$td\pi$	−143.966185	13.866982	dKe	−0.59659347	0.09672966
$td\mu$	−111.364347	11.728063	$d\pi e$	−0.59186474	0.09200092
tde	−0.59913066	0.09922161	$pK\pi$	−122.833333	3.953225
tpK	−411.130254	0.268287	$pK\mu$	−97.4398216	4.5194127
$tp\pi$	−138.194810	8.0956969	$p\pi e$	−0.59147245	0.09174461
$tp\mu$	−107.494703	7.858419	$p\mu e$	−0.58990379	0.09017595
tpe	−0.59817613	0.09826708	$K\pi e$	−0.59079299	0.09130997
$tK\pi$	−132.371970	2.272768	$K\mu e$	−0.58928945	0.08980643
$tK\mu$	−103.014124	3.377840	$\pi\mu\pi$	−68.4438759	0.1621304
tKe	−0.59681456	0.09690551	$\pi\mu\mu$	−59.1982179	0.3583052
$t\pi e$	−0.59199787	0.09208881	$\pi\mu e$	−0.58632206	0.08814603

Note: The calculations were performed for the following particle-mass values: $m_e = 1$, $m_\mu = 206.768262$, $m_\pi = 273.12695$, $m_K = 966.1521$, $m_p = 1836.152701$, $m_d = 3670.483014$, and $m_t = 5496.92158$. The symbol "∞" stands for an infinitely heavy particle. The energy values are given in Hartree atomic units.

and $\mu_{12} = \infty$ ($\beta = 0$) corresponds to the energy of the molecular hydrogen ion H_2^+ formed by immobile nuclei occurring at equilibrium distances from each other. The first correction to this energy due to a deviation of β from zero is a quantum of zero-point oscillations and is of order $(m_3/\mu_{12})^{1/2}$ (first order in $\beta^{1/2}$). In view of this, we assume that, at small β, the lowest eigenvalue $\varepsilon(\beta, \gamma)$ of the operator given by (4) can be expanded in a series in powers of $\beta^{1/2}$. By virtue of (11), the expansion of $\varepsilon(\beta, \gamma)$ in γ involves only even powers of γ. As a result, we have

$$\varepsilon(\beta, \gamma) = \sum_{k,l=0} C_{kl} \beta^{k/2} \gamma^{2l} \quad (0 \leqslant \beta \leqslant \beta_0). \quad (14)$$

Taking into account Eq. (8), we find that the energy of molecule-like trions ($0 \leqslant \beta \leqslant \beta_0$) can be represented as

$$E(m_1, m_2, m_3) = \alpha(m_1, m_2, m_3) \quad (15)$$
$$\times \sum_{k,l=0} C_{kl} \beta(m_1, m_2, m_3)^{k/2} \gamma(m_1, m_2, m_3)^{2l}.$$

The dependence of α, β, and γ on the particle masses is specified by Eqs. (5), (6a), and (6b).

In the case of atomlike trions ($1 \geqslant \beta \geqslant \beta_0$), it is of importance to study the behavior of the function $\varepsilon(\beta, \gamma)$ in the vicinity of the point $\beta = 1$. In describing such trions, it is convenient to use, instead of the coordinates given by Eq. (2), the different relative coordinates

$$\mathbf{u} = 2m_1 m_2 m_3 (\mathbf{r}_1 - \mathbf{r}_3)/[2m_1 m_2 + (m_1 + m_2) m_3], \quad (16)$$
$$\mathbf{v} = 2m_1 m_2 m_3 (\mathbf{r}_2 - \mathbf{r}_3)/[2m_1 m_2 + (m_1 + m_2) m_3].$$

In terms of these coordinates, the Hamiltonian for a trion whose center of mass is immobile takes the form

$$H(\mathbf{u}, \mathbf{v}) = [2\alpha/(1+\beta)] [-(\Delta_u + \Delta_v)/2 \quad (17)$$
$$+ \gamma(\Delta_u - \Delta_v)/(1+\beta) - (1-\beta)\nabla_u \nabla_v/(1+\beta)$$
$$+ 1/|\mathbf{u} - \mathbf{v}| - 1/|\mathbf{u}| - 1/|\mathbf{v}|].$$

Its eigenvalues are proportional to $2\alpha/(1+\beta)$ and depend on $(1-\beta)/(1+\beta)$ and $\gamma/(1+\beta)$, these eigenvalues being even functions of the latter. In accordance with this, we find that the energy of atomlike trions ($1 \geqslant \beta \geqslant \beta_0$) can be represented as

$$E(m_1, m_2, m_3) = 2\alpha(m_1, m_2, m_3) \quad (18)$$
$$\times \sum_{k,l=0} D_{kl} \frac{[1 - \beta(m_1, m_2, m_3)]^k \gamma(m_1, m_2, m_3)^{2l}}{[1 + \beta(m_1, m_2, m_3)]^{1+k+2l}}.$$

Table 2. Coefficients C_{kl} in expression (15) for the ground-state energies of molecule-like trions formed by particles of arbitrary masses

$k\backslash l$	0	1	2	3	4
0	-1.20526928	$+1.51242531\times10^{-6}$	$+3.16620400\times10^{-5}$	-2.99544647×10^{-4}	$+2.60965753\times10^{-4}$
1	$+6.41792883\times10^{-1}$	-3.97265783×10^{-4}	-3.34351306×10^{-3}	$+3.69621461\times10^{-2}$	-3.20288790×10^{-2}
2	$+2.84533332\times10^{-1}$	$+2.58994774\times10^{-2}$	$+1.42668705\times10^{-1}$	-1.64771021	$+1.38281792$
3	-1.68692736×10^{-1}	-9.46297876×10^{-1}	-2.61150278	$+3.11319673\times10$	-2.43842847×10
4	-2.31688557×10^{-1}	-3.90717332	$+1.27581061\times10$	-2.28777592×10^{2}	$+1.51267584\times10^{2}$
5	$+5.15901631\times10^{-1}$	-4.21275017×10	-2.53003514	$+7.64003373\times10^{2}$	-3.40806411×10^{-2}
6	-9.65653999×10^{-1}	$+6.49728994\times10$	-1.04401088×10^{2}	-1.17529236×10^{3}	$+9.34085320\times10$
7	$+6.92626729\times10^{-1}$	-1.52826472×10	$+2.03656867\times10^{2}$	$+6.78822845\times10^{2}$	$+3.62074191\times10^{2}$

Table 3. Coefficients D_{kl} in expression (18) for ground-state energies of atomlike trions formed by particles of arbitrary masses

$k\backslash l$	0	1	2	3	4
0	-5.27751026×10^{-1}	-1.13168929×10	$+7.57548297$	$+2.04115176\times10^{3}$	$+3.12236903\times10^{5}$
1	$+3.28858696\times10^{-2}$	-1.10733733×10	$+2.82168215\times10^{2}$	-2.42035309×10^{4}	$+1.10089366\times10^{6}$
2	-5.99730266×10^{-2}	$+7.14241581$	-1.18146825×10^{3}	$+1.19192854\times10^{6}$	-2.78805701×10^{8}
3	$+3.71230296\times10^{-2}$	$+1.08208407\times10$	$+1.59135593\times10^{4}$	-1.15845842×10^{7}	$+2.87030990\times10^{9}$
4	-4.66442081×10^{-2}	$+4.85297705\times10$	-6.83844656×10^{4}	$+4.84275484\times10^{7}$	-1.23371748×10^{10}
5	$+3.38522644\times10^{-2}$	-1.01678037×10^{2}	$+1.22934741\times10^{5}$	-9.07993966×10^{7}	$+2.31729541\times10^{10}$
6	-3.14792151×10^{-2}	$+5.54377099\times10$	-8.13036181×10^{4}	$+6.21813140\times10^{7}$	-1.57911719×10^{10}

Expressions (15) and (18) are generalizations of the corresponding expressions for the energies of symmetric trions from [2] to the case of asymmetric trions formed by particles of arbitrary masses and reduce to them at $\gamma = 0$.

The coefficients C_{kl} and D_{kl} in expressions (15) and (18), respectively, were determined from a least squares fit to the results of our variational calculations performed for the energies of 206 trions by using wide bases of up to 3000 Laguerre exponential–polynomial functions of perimetric particle coordinates. In order to obtain a denser coverage of triangle (7) in the plane spanned by the parameters β and γ with reference points, these calculations were performed both for sets of the particle masses m_1, m_2, and m_3 corresponding to actual trions and for hypothetical sets of masses.

The variational values that we calculated for the energies of 34 actual asymmetric trions are presented in Table 1, along with the corresponding dissociation energies. These values comply with the results of the calculations from [4] to within seven to eight significant digits for the energies of asymmetric muonic molecules and to within eight to nine significant digits for the energies of asymmetric kaonic molecules. At the same time, the variational values that we found for the ground-state energies of two systems formed by particles of close masses ($\pi^+\mu^+\mu^-$ and $\pi^+\mu^+\pi^-$) are well below the values of -59.19816 and -68.44278 quoted in [4] (see Table 1).

Choosing an ad hoc boundary between molecule-like and atomlike trions at $\beta_0 = 0.3$, we found that the 40-term formula (15) with the coefficients C_{kl} from Table 2 reproduces the ground-state energies for all 85 reference molecule-like trions with a relative root-mean-square uncertainty of 9×10^{-8} and that the 35-term formula (18) with the coefficients D_{kl} from Table 3 reproduces the ground-state energies for all 121 reference atomlike trions with a relative root-mean-square uncertainty of 2×10^{-8}. These formulas make it possible to predict, to a precision of a few units at the seventh decimal place, the energies of all trions formed by particles of arbitrary masses. At $\gamma = 0$, they approximate the ground-state energies of symmetric trions. (The values found here for the coefficients C_{k0} and D_{k0} differ somewhat from those that were reported in [2] for symmetric trions; this is because the numbers of terms in the sums over k here and in [2] are different.)

ON THE STABILITY OF TRIONS

The problem of stability of trions consisting of particles that have unit charges was considered in [5–10]. Here, we are going to demonstrate that the particle-mass region where trions are stable with respect to dissociation can be considerably extended by combining the results of our variational calculations with the quantum-mechanical convexity relation for energy.

The lowest eigenvalue $E(\lambda)$ of the operator

$$\mathcal{H} = T + V + \lambda W, \tag{19}$$

where the operators T, V, and W are homogeneous functions of coordinates, their degrees of homogeneity being, respectively, -2, $-p$, and $-q$, and where λ is a parameter, which is seen to appear linearly in (19), was considered in [11, 12]. By varying the scale of the wave function, it can be proven that the following inequality is valid for the derivatives of $\mathcal{E}(\lambda)$:

$$\mathcal{E}''(\lambda) \leqslant q^2\mathcal{E}'(\lambda)^2/[2p\mathcal{E}(\lambda) + (q-p)(2-q)\lambda\mathcal{E}'(\lambda)]. \tag{20}$$

We now draw the straight line passing through two points (β_1, γ_1) and (β_2, γ_2) in the $\beta\gamma$ plane:

$$\beta(\lambda) = \beta_1 + \lambda(\beta_2 - \beta_1), \tag{21}$$
$$\gamma(\lambda) = \gamma_1 + \lambda(\gamma_2 - \gamma_1).$$

Let us consider the family of trions that is represented by the points $(\beta(\lambda), \gamma(\lambda))$ lying on this straight line. Substituting (21) into (4), we obtain the reduced-energy operator for the members of this family. It has the form (19), where $p = 1$ and $q = 2$ and where

$$T = -\beta\Delta_s + 2\gamma\nabla_s\nabla_t - \Delta_t, \tag{22}$$
$$V = 1/|\mathbf{s}| - 2/|\mathbf{s}+\mathbf{t}| - 2/|\mathbf{s}-\mathbf{t}|,$$
$$W = (\beta_1 - \beta_2)\Delta_s + 2(\gamma_2 - \gamma_1)\nabla_s\nabla_t.$$

Therefore, the reduced ground-state energy of trions belonging to this family,

$$\mathcal{E}(\lambda) = \varepsilon(\beta(\lambda), \gamma(\lambda)), \tag{23}$$

satisfies the inequality in (20) with $p = 1$ and $q = 2$:

$$\mathcal{E}''(\lambda) \leqslant 2\mathcal{E}'(\lambda)^2/\mathcal{E}(\lambda). \tag{24}$$

Since $\mathcal{E}(\lambda) < 0$ for a Coulomb system, it follows from (24) that

$$[-1/\mathcal{E}(\lambda)]'' \leqslant 0. \tag{25}$$

This inequality demonstrates that the graph representing the dependence of $-1/\mathcal{E}(\lambda)$ on λ is convex upward. A linear approximation of such a function on the basis of its values at the points $\lambda = 0$ and $\lambda = 1$ determines the boundary of its values at any point λ:

$$-1/\mathcal{E}(\lambda) \gtrless -1/\mathcal{E}(0) - \lambda[1/\mathcal{E}(1) - 1/\mathcal{E}(0)]. \tag{26}$$

Here, the upper (lower) inequality sign corresponds to λ within (off) the interval $0 < \lambda < 1$. Returning, with allowance for (23), from the quantity $\mathcal{E}(\lambda)$ to the function $\varepsilon(\beta(\lambda), \gamma(\lambda))$, we find from (26) that the reduced energies of the family of trions occurring on the straight line (21) satisfy the inequalities

$$\varepsilon(\beta(\lambda), \gamma(\lambda)) \gtrless \varepsilon(\beta_1, \gamma_1)\varepsilon(\beta_2, \gamma_2)/[(1-\lambda) \times \varepsilon(\beta_2, \gamma_2) + \lambda\varepsilon(\beta_1, \gamma_1)], \tag{27}$$

with the same conventions for the inequality signs as in (26). The inequalities in (27) specify a lower bound on the reduced energy $\varepsilon(\beta(\lambda), \gamma(\lambda))$ at the points lying on the straight-line segment between the points (β_1, γ_1) and (β_2, γ_2) and an upper bound on it at the points occurring off this segment.

If, of the two likely charged particles, the lighter (particle 2) is removed from the trion, there arises a $(1, 3)$ atom whose ground-state energy is

$$E_{\text{at}}(m_1, m_3) = -m_1m_3/2(m_1 + m_3). \tag{28}$$

By virtue of the variational principle, the ground-state energy of the trion is either below the energy of this atom,

$$E(m_1, m_2, m_3) < E_{\text{at}}(m_1, m_3), \tag{29a}$$

or equal to it,

$$E(m_1, m_2, m_3) = E_{\text{at}}(m_1, m_3). \tag{29b}$$

The trion is stable (unstable) with respect to dissociation in the first (second) case. By using relations (5), (6), and (8), the conditions under which the triton is stable or unstable [(29a) or (29b), respectively] reduce to the following inequalities for its reduced energy:

$$\varepsilon(\beta, \gamma) < 1/(2\gamma - \beta - 1), \tag{30a}$$

$$\varepsilon(\beta, \gamma) = 1/(2\gamma - \beta - 1). \tag{30b}$$

At the boundary of the stability region given by (30b), the reduced energy $\varepsilon(\beta, \gamma)$ changes continuously, but its derivative along the normal to the boundary undergoes a discontinuity, taking unequal values on the two sides of the boundary. Therefore, expressions (14), (15), and (18), which are continuously differentiable with respect to β and γ, approximate the energy of trions only in the region of their stability.

STABILITY OF SYMMETRIC TRIONS

All symmetric trions such that the likely charged particles have identical masses ($m_1 = m_2$) are stable with respect to dissociation [5]. This follows, for example, from the properties of the positronium ion $e^-e^-e^+$ ($m_1 = m_2 = m_3 = 1$), for which the ground-state energy and the mean values of the kinetic energies of the individual constituent particles are [13] (in Hartree atomic units)

$$E(1, 1, 1) = -0.262005;$$

$$\langle -\Delta_1/2\rangle = \langle -\Delta_2/2\rangle = 0.066619$$
$$\text{and} \quad \langle -\Delta_3/2\rangle = 0.128767.$$

Let us now consider a symmetric trion formed by particles of masses $m_1 = m_2 = M$ and $m_3 = m$. We take the expectation value of its energy for the positronium-ion eigenfunction where the scale of the coordinates of all particles is changed by a factor k. By using the variational principle and the virial theorem and considering that the operators of the kinetic and the Coulomb potential energy are homogeneous, we obtain the inequality

$$E(M,M,m) \leqslant k^2[(\langle -\Delta_1/2\rangle + \langle -\Delta_2/2\rangle)/M + \langle -\Delta_3/2\rangle/m] + 2kE(1,1,1), \quad (31)$$

where angular brackets denote expectation values for the positronium ion. By determining the optimum value of the scale factor k from the requirement that the right-hand side of the inequality in (31) be minimal and taking into account the numerical values of $\langle -\Delta_1/2\rangle$, $\langle -\Delta_2/2\rangle$, and $\langle -\Delta_3/2\rangle$, we obtain an upper bound on the energy of a symmetric trion formed by particles of masses $m_1 = m_2 = M$ and $m_3 = m$:

$$E(M,M,m) \leqslant -mM/(1.9409m + 1.8758M). \quad (32)$$

At all values of M and m, the upper bound given by (32) is below the energy $E_{\text{at}}(M,m) = -mM/2(m + M)$ of the atom that is produced upon the decay of the symmetric trion being considered. Thus, all symmetric trions are stable with respect to dissociation. By virtue of continuity, asymmetric trions in which the difference of m_1^{-1} and m_2^{-1} is small [that is, the asymmetry parameter γ as given by (6b) is small] are also stable. If, however, the asymmetry becomes greater, the trion can lose stability, in which case it decays into an atom that consists of two particles, 1 and 3, and the free light particle 2, which is not confined in the potential well of its polarization interaction with this atom.

CONVEXITY OF INSTABILITY REGION

We will now show that, if two trions corresponding to two points in the $\beta\gamma$ plane that have coordinates (β_1, γ_1) and (β_2, γ_2) are unstable, all trions corresponding to the straight-line segment (21), which connects these two points, are also unstable.

By virtue of (30b), the reduced energy of unstable trions is given by

$$\varepsilon(\beta_1,\gamma_1) = 1/(2\gamma_1 - \beta_1 - 1), \quad (33)$$
$$\varepsilon(\beta_2,\gamma_2) = 1/(2\gamma_2 - \beta_2 - 1).$$

Substituting these values into (27), we find that the reduced energy of a trion that corresponds to any point (β (λ),γ(λ)) of the straight-line segment (21) satisfies the inequality

$$\varepsilon(\beta(\lambda),\gamma(\lambda)) \geqslant 1/[\lambda(2\gamma_2 - \beta_2 - 1) - (\lambda - 1)(2\gamma_1 - \beta_1 - 1)] = 1/(2\gamma(\lambda) - \beta(\lambda) - 1). \quad (34)$$

This means that trions are unstable at all points of the straight-line segment connecting the points (β_1, γ_1) and (β_2, γ_2). Therefore, the region of instability of trions is convex [10].

REGION WHERE THE INSTABILITY OF TRIONS CAN BE FIRMLY ESTABLISHED

An exact determination of the boundary separating, in the $\beta\gamma$ plane, the region where trions are stable from the region where trions are unstable is a problem that has yet to be solved: variational calculations furnish an upper bound on the ground-state energy and make it possible to demonstrate stability for one system or another, but special methods are required to prove instability of such systems. Presently, a reliable proof of instability has been obtained only for trions with $m_1 = \infty$, $m_2 \leqslant 1.51$, and $m_3 = 1$ ($\beta = \gamma > 0.142$) [14,15], whence it follows, among other things, that a positron cannot form a bound state with a hydrogen atom, and for trions with $m_1 \geqslant 1.57$, $m_2 = 1$, and $m_3 = \infty$ ($\beta = 1$, $\gamma > 0.222$), which corresponds to instability of an analog of the negative ion of the hydrogen atom where one "electron" is heavier than the other one by a factor of 1.57 [16].

Let us now consider the region of β and γ values where stability of trions can be reliably established. The dimensions of such a region depend on the approach used and grow as this approach is refined. The simplest approach is based on employing the monotonic dependence of the reduced energy on γ. Suppose that, for some trion, the parameters β and γ satisfy the equation

$$1/(2\gamma - \beta - 1) = \varepsilon(\beta, 0), \quad (35)$$

where ε(β,0) is the reduced energy of a symmetric trion that is characterized by the same value of the parameter β. With allowance for (13), it can then be shown that inequality (30a) holds and that the trion is stable at these values of the parameters β and γ.

In Fig. 1, the region in which the stability of trions can be reliably established and which was constructed on the basis of solving Eq. (35) is below the broken line formed by curve *3* and a segment of the hypotenuse of the right triangle (7).

The region where stability can be definitively proven can be extended on the basis of direct variational calculations of asymmetric trions. Such calculations performed by using a basis of 50 exponential functions of interparticle distances reliably established [7] stability in the region that, in Fig. 1,

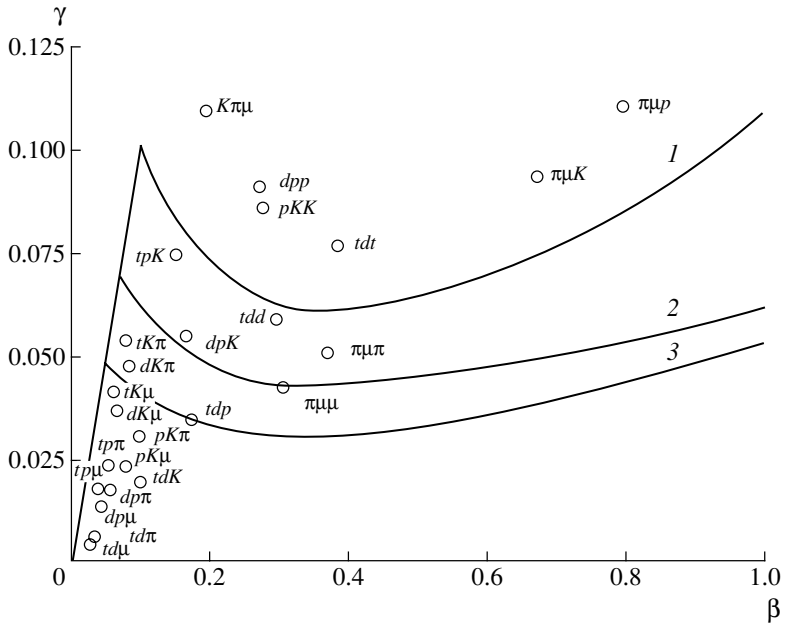

Fig. 1. Boundaries of the region where stability of $X^{\pm}X^{\pm}Z^{\mp}$ trions can be reliably established: (*1*) results of variational calculations performed by using wide bases of Laguerre functions, (*2*) results of the calculations from [7], and (*3*) results of the calculations based on Eq. (35). Stable symmetric trions lying on the β axis and stable trions bound by an electron, which are represented by points occurring very closely to the origin of coordinates are not shown in the figure.

lies below curve *2* and a segment of the hypotenuse of the triangle given by (7).

With the aid of variational calculations performed by using wide bases of Laguerre functions of perimetric particle coordinates, we have refined the region where trions are definitively stable: in Fig. 1, this region lies below curve *1* and the corresponding segment of triangle (7).

In Fig. 2, points represent all trions that can be composed of tritons (t), deuterons (d), protons (p), kaons (K), pions (π), muons (μ), and electrons (e) (in all, seven particle species) and their antiparticles and which include 49 symmetric systems $X^{\pm}X^{\pm}Z^{\mp}$ and 147 asymmetric systems $X^{\pm}Y^{\pm}Z^{\mp}$. All symmetric trions are stable. Of the aforementioned 147 asymmetric trions, 34 are definitively stable. These include asymmetric molecule-like trions bound by an electron ($t^+d^+e^-$, $t^+p^+e^-$, $d^+p^+e^-$, $t^+K^+e^-$, $d^+K^+e^-$, $p^+K^+e^-$, $t^+\pi^+e^-$, $d^+\pi^+e^-$, $p^+\pi^+e^-$, $K^+\pi^+e^-$, $t^+\mu^+e^-$, $d^+\mu^+e^-$, $p^+\mu^+e^-$, $K^+\mu^+e^-$, $\pi^+\mu^+e^-$), a muon ($t^+d^+\mu^-$, $t^+p^+\mu^-$, $d^+p^+\mu^-$, $t^+K^+\mu^-$, $d^+K^+\mu^-$, $p^+K^+\mu^-$, $\pi^+\mu^+\mu^-$), a pion ($t^+d^+\pi^-$, $t^+p^+\pi^-$, $d^+p^+\pi^-$, $t^+K^+\pi^-$, $d^+K^+\pi^-$, $p^+K^+\pi^-$, $\pi^+\mu^+\pi^-$), or a kaon ($t^+d^+K^-$, $d^+p^+K^-$, $t^+p^+K^-$). Two asymmetric combinations of hydrogen nuclei and antinuclei ($t^+d^+p^-$ and $t^+d^+d^-$) are also stable.

The straight-line segment *2* in Fig. 2 connects the aforementioned trion-instability points ($\beta_1 = 0.142$, $\gamma_1 = 0.142$) and ($\beta_2 = 1$, $\gamma_2 = 0.222$). Since the region of instability is convex, all trions occurring above this line are unstable. The remaining 16 trions ($p^+K^+K^-$, $t^+d^+t^-$, $d^+p^+p^-$, $\pi^+\mu^+K^-$, $K^+\pi^+\mu^-$,

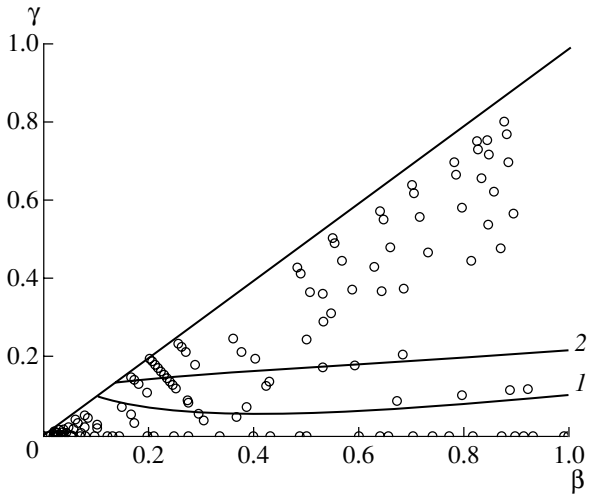

Fig. 2. Points that, in the plane spanned by the parameters $\beta = (1/m_1 + 1/m_2)/[4/m_3 + 1/m_1 + 1/m_2]$ and $\gamma = (1/m_2 - 1/m_1)/[4/m_3 + 1/m_1 + 1/m_2]$, correspond to 196 trions $X^{\pm}Y^{\pm}Z^{\mp}$ obtained by taking all possible combinations of the following particle species and their antiparticles: t, d, p, K, π, μ, and e. Symmetric trions $X^{\pm}X^{\pm}Z^{\mp}$, which are stable with respect to dissociation, lie on the β axis. Asymmetric trions $X^{\pm}Y^{\pm}Z^{\mp}$ whose stability (instability) can be definitively proven lie below curve *1* (above the straight line *2*). The condensation of points near the origin of coordinates corresponds to trions bound by an electron, a muon, a pion, or a kaon.

$\pi^+\mu^+p^-$, $\pi^+\mu^+d^-$, $t^+p^+p^-$, $\pi^+\mu^+t^-$, $p^+K^+p^-$, $p^+\pi^+\mu^-$, $K^+\pi^+\pi^-$, $d^+K^+K^-$, $d^+p^+d^-$, $d^+p^+t^-$, and $p^+K^+d^-$) occurring between this line and the boundary of the region where the trions in question are definitively stable either are unstable or are characterized by very low dissociation energies.

CONCLUSION

The results obtained here have revealed that, by combining precision variational calculations of the ground-state energies of reference trions with an analysis of the parametric dependence of the relevant Hamiltonian on the masses of the particles involved, one can determine, to a fairly high precision, the ground-state energies of all possible trions formed by particles of arbitrary masses and unit charges. The ground-state energies have been approximated by expression (15) for all molecule-like trions and by expression (18) for all atomlike trions. The same approach has enables us to establish that, of 196 trions that can be composed of seven particle and antiparticle species, 49 symmetric and 34 asymmetric trions are stable.

ACKNOWLEDGMENTS

This work was supported by the Russian Foundation for Basic Research (project no. 97-02-16126).

REFERENCES

1. A. V. Gur'yanov and T. K. Rebane, Zh. Éksp. Teor. Fiz. **83**, 1698 (1982) [Sov. Phys. JETP **56**, 980 (1982)].
2. T. K. Rebane and A. V. Filinsky, Yad. Fiz. **60**, 1985 (1997) [Phys. At. Nucl. **60**, 1816 (1997)].
3. L. D. Landau and E. M. Lifshitz, *Course of Theoretical Physics,* Vol. 3: *Quantum Mechanics: Non-Relativistic Theory* (Fizmatgiz, Moscow, 1963; Pergamon, New York, 1977).
4. A. M. Frolov and A. J. Thakkar, Phys. Rev. A **46**, 4418 (1992); D. M. Bishop, A. M. Frolov, and V. H. Smith, Phys. Rev. A **51**, 3636 (1995).
5. R. N. Hill, J. Math. Phys. **18**, 2316 (1977).
6. R. D. Poshusta, J. Phys. B **18**, 1887 (1985).
7. A. V. Gur'yanov and T. K. Rebane, Zh. Éksp. Teor. Fiz. **98**, 65 (1990) [Sov. Phys. JETP **71**, 34 (1990)].
8. A. V. Gur'yanov and T. K. Rebane, Opt. Spektrosk. **70**, 721 (1991) [Opt. Spectrosc. **70**, 419 (1991)].
9. A. M. Frolov and D. M. Bishop, Phys. Rev. A **45**, 6236 (1992).
10. A. Martin, J.-M. Richard, and Tsun Wu Tai, Preprint CERN-TH 6227/91 (Geneva, 1991); A. Martin, Preprint CERN-TH 6376/92 (Geneva, 1992); A. Martin, J.-M. Richard, and T. T. Wu, Phys. Rev. A **46**, 3697 (1992).
11. T. K. Rebane, Teor. Mat. Fiz. **56**, 432 (1983).
12. T. K. Rebane and N. N. Penkina, *Scale Transformation in the Quantum Theory of Atoms and Molecules* (Leningr. Gos. Univ., Leningrad, 1985), p. 163.
13. A. M. Frolov, Phys. Rev. A **57**, 2436 (1998).
14. M. Rotenberg and J. Stein, Phys. Rev. **182**, 1 (1969).
15. E. A. G. Armour and D. M. Schrader, Can. J. Phys. **60**, 581 (1982).
16. V. Glaser, H. Grosse, A. Martin, and W. Thirring, *Mathematical Problems in Theoretical Physics* (Springer-Verlag, Berlin, 1980), Lectures Notes in Physics, Vol. 116.

Translated by A. Isaakyan

Physics of Atomic Nuclei, Vol. 65, No. 1, 2002, pp. 49–57. Translated from Yadernaya Fizika, Vol. 65, No. 1, 2002, pp. 52–60.
Original Russian Text Copyright © 2002 by Varlamov, Stepanov.

NUCLEI
Theory

Main Channels of the Decay of the Giant Dipole Resonance in the ^{20,22}Ne Nuclei and Isospin Splitting of the Giant Dipole Resonance in the ^{22}Ne Nucleus

V. V. Varlamov* **and M. E. Stepanov****

Center of Data from Photonuclear Experiments, Institute of Nuclear Physics, Moscow State University, Vorob'evy gory, Moscow, 119899 Russia

Received September 15, 2000; in final form, December 27, 2000

Abstract—Data published in the literature on various photonuclear reactions for the ^{20,22}Ne isotopes and for their natural mixture are analyzed with the aim of exploring special features of the decay of giant-dipole-resonance states in these two isotopes. With the aid of data on the abundances of the isotopes and on the energy reaction thresholds, the cross sections for the reactions $^{20,22}\mathrm{Ne}[(\gamma,n)+(\gamma,np)]$ and $^{20,22}\mathrm{Ne}[(\gamma,p)+(\gamma,np)]$ are broken down into the contributions from the one-nucleon reactions (γ,n) and (γ,p) and the contributions from the reactions (γ,np). The cross sections for the reactions $^{20,22}\mathrm{Ne}(\gamma,n)^{19,21}\mathrm{Ne}$ and $^{20,22}\mathrm{Ne}(\gamma,p)^{19,21}\mathrm{F}$ in the energy range $E_\gamma = 16.0$–28.0 MeV and the cross sections for the reactions $^{20,22}\mathrm{Ne}(\gamma,np)^{18,20}\mathrm{F}$ in the energy range $E_\gamma = 23.3$–28.0 MeV are estimated. The behavior of the cross-section ratio $r = \sigma(\gamma,p)/\sigma(\gamma,n)$ for the ^{22}Ne nucleus as a function of energy is analyzed, and the isospin components of the giant dipole resonance in the ^{22}Ne nucleus are identified. The contributions of the isospin components of the giant dipole resonance in the ^{22}Ne nucleus to the cross sections for various photonuclear reactions are determined on the basis of an analysis of the diagram of the excitation and decay of pure isospin states in the ^{22}Ne nucleus and in nuclei neighboring it, which are members of the corresponding isospin multiplets. The isospin splitting of the giant dipole resonance and the ratio of the intensities of the isospin components are determined to be $\Delta E = 4.57 \pm 0.69$ MeV and $R = 0.24 \pm 0.04$, respectively. © *2002 MAIK "Nauka/Interperiodica".*

INTRODUCTION

Experimental data on the isospin splitting

$$\Delta E = E_{\mathrm{c.g.}}(T_>) - E_{\mathrm{c.g.}}(T_<), \qquad (1)$$

where $E_{\mathrm{c.g.}}$ stands for the energy centers of gravity of the cross sections $\sigma^>$ and $\sigma^<$ for the reactions contributing to the corresponding components of the giant dipole resonance (GDR) that are characterized by the isospin values $T_> = T_0 + 1$ and $T_< = T_0 = (N-Z)/2$ (the latter being the isospin of the ground state of the nucleus being considered), and experimental data on the ratio R of the intensities of the isospin GDR components,

$$R = \sigma^>_{-1}/(\sigma^>_{-1} + \sigma^<_{-1}), \qquad (2)$$

where $\sigma_{-1} = \int \sigma E^{-1} dE$ is the first moment of the integrated cross section for the GDR, were analyzed in [1] for a large number of nuclei.

For many nuclei (such as ^{14}C, ^{44,48}Ca, ^{48,54}Ti, ^{54}Cr, ^{54}Fe, ^{65}Cu, and ^{55}Co), it was found that experimental data deviate considerably from the predictions of the traditional theoretical models proposed in [2–5] for relatively heavy nuclei ($A > 90$). According to these models,

$$\Delta E^{\mathrm{theor}} = U(T_0+1)/T_0 = U_0(T_0+1)/A, \qquad (3)$$

where $U = (U_0/A)T_0$, U_0 being the energy of nuclear symmetry, and

$$R^{\mathrm{theor}} = 1/(T_0+1). \qquad (4)$$

It was shown that these discrepancies reflect the individual character of the manifestations of isospin GDR components in different nuclei and are due to the effect [6, 7] of the energy and isospin constraints on the decay of isobar-analog states of such nuclei through the neutronic channel. These constraints manifest themselves in many experiments [8–12], but they are disregarded by simple models.

It is not always possible to separate, on the basis of data from photonuclear experiments, information about the photoneutron from information about the photoproton channel of the decay of highly

*e-mail: varlamov@depni.npi.msu.su
**e-mail: stepanov@depni.npi.msu.su

Table 1. Abundances of neon isotopes and thresholds for some photonuclear reactions

Isotope	Abundance, %	Particle-separation energy in reactions, MeV				
		(γ, n)	(γ, p)	(γ, np)	$(\gamma, 2n)$	$(\gamma, 2p)$
^{20}Ne	90.51	16.9	12.8	23.3	28.5	20.8
^{21}Ne	0.27	6.3	13.0	19.6	23.6	23.6
^{22}Ne	9.22	10.4	15.3	23.4	17.1	26.4

Table 2. Information about the energy dependences of the cross sections for photoneutron and photoproton reactions

Isotope	Reaction	Energy range, MeV	References	Code
^{nat}Ne	$(\gamma, n) + (\gamma, np) + (\gamma, 2n)$[a)]	16–26	[15]	σ^{V}
	$(\gamma, n_0 + n_1 + n_2)$[b)]	17–31	[16]	
^{20}Ne	$(\gamma, n) + (\gamma, np)$	16–28	[17]	σ^{A}
	$(\gamma, p) + (\gamma, np)$[c)]	16–28	[18]	
^{22}Ne	$(\gamma, 2n)$[a)]	16–26	[15]	
	$(\gamma, p) + (\gamma, np)$[c)]	18–30	[18]	
	$(\gamma, n) + (\gamma, np)$ (estimate)	16–26	[14]	σ^{X}

[a)] Below the energy threshold for the reaction ^{20}Ne$(\gamma, 2n)$ ($E_{\text{thr}} = 28.5$ MeV), the cross sections for the reactions ^{nat}Ne$(\gamma, 2n)$ and ^{22}Ne$(\gamma, 2n)$ are identical.

[b)] Presented in this case is the differential reaction cross section that was obtained from the energy spectrum of photoneutrons emitted at an angle of 90° and which was multiplied by 4π.

[c)] Presented in this case is the differential reaction cross section that was obtained from the energy spectrum of photoprotons emitted at an angle of 90° and which was multiplied by 4π.

excited states forming a GDR. Without invoking the coincidence method, whose application runs into considerable difficulties under the conditions where the majority of the cross sections for photonuclear reactions are moderately small, one can obtain information only about the sums of some reactions—for example, $[(\gamma, n) + (\gamma, np)]$ or $[(\gamma, p) + (\gamma, np)]$—rather than about the one-neutron or the one-proton reaction individually. In many cases, the use of alternative experimental methods—above all, the popular induced-activity method, where the final nucleus of the specific reaction being studied is fixed—does not produce the desired effect either. By way of example, we indicate that, in the case of the ^{20,22}Ne nuclei, which are considered in the present study, only the final nucleus in the reaction ^{20}Ne$(\gamma, np)^{18}$F has a half-life value ($T_{1/2} = 109.77$ min) that is more or less appropriate for measuring induced activities; at the same time, nuclei produced in the other reactions that are discussed here have the half-life values indicated immediately below: ^{20}Ne$(\gamma, n)^{19}$Ne ($T_{1/2} =$ 17.22 s), ^{22}Ne$(\gamma, n)^{21}$Ne (stable), ^{20}Ne$(\gamma, p)^{19}$F (stable), ^{22}Ne$(\gamma, p)^{21}$F ($T_{1/2} = 4.158$ s), and ^{22}Ne$(\gamma, np)^{20}$F ($T_{1/2} = 11.00$ s). A similar situation can also be observed for a considerable number of other nuclei [1], since, for many of these, the reactions being discussed have relatively low energy thresholds.

At the same time, it is quite obvious that, without having detailed information about the energy dependences of the cross sections for all reactions being studied, it is rather difficult to analyze mechanisms that may be responsible for the formation and decay of GDR states, to consider effects that determine the resonance width (for example, configuration and isospin splittings), and to test various theoretical predictions for the magnitude and shape of the GDR.

The present article, which reports on a continuation of our previous studies, describes investigations into the isospin splitting of the GDR in the ^{22}Ne nucleus that have been performed by using new data on the cross sections for the one-nucleon reactions on ^{20,22}Ne nuclei. In [13, 14], we analyzed available experimental information about the cross sections for various photonuclear reactions on ^{20,22}Ne nuclei and on targets from a natural mixture of stable isotopes and estimated the energy dependences of the cross sections for the one-neutron (γ, n) and one-proton (γ, p) reactions, as well as for the (γ, np) reactions, on these nuclei.

1. ESTIMATING CROSS SECTIONS FOR THE REACTIONS ^{20,22}Ne$(\gamma, n)^{19,21}$Ne, ^{20,22}Ne$(\gamma, p)^{19,21}$F, AND ^{20,22}Ne$(\gamma, np)^{18,20}$F

1.1. Experimental Data

The energy thresholds for the reactions under study on three stable neon isotopes are presented in Table 1, along with data on the isotope abundances (percentage in a natural mixture of the isotopes). In the following, we disregard the presence of the ^{21}Ne isotope, whose abundance in a natural mixture is 0.27% .

Information about basic experimental data on the energy dependences of the cross sections for various photonuclear reactions on neon isotopes and on their natural mixture in the GDR energy region is displayed in Table 2.

1.2. Principles behind the Procedures for Estimating the Cross Sections for the Reactions ^{20,22}Ne$(\gamma, n)^{19,21}$Ne, ^{20,22}Ne$(\gamma, p)^{19,21}$F, and ^{20,22}Ne$(\gamma, np)^{18,20}$F

The estimates of the cross sections and the procedures used to derive them are described in detail elsewhere [13]. Below, we give a brief account of the basic principles behind these procedures and of the results obtained.

(i) The cross section $\sigma^{\mathrm{A}} = \sigma\{^{20}\mathrm{Ne}[(\gamma, n) + (\gamma, np)]\}$ [16], which was obtained by means of a nontraditional, rather involved procedure, was normalized to σ^{V} [15]. The resulting value of $\sigma^{\mathrm{A\text{-}pn}}$ was used to estimate the cross section $\sigma^{X} = \sigma\{^{22}\mathrm{Ne}[(\gamma, n) + (\gamma, np)\}$ for the ^{21}Ne isotope by means of the relation

$$\sigma^{\mathrm{V}} = 90.51\sigma^{\mathrm{A\text{-}pn}} + 9.22\sigma^{X}, \qquad (5)$$

which takes into account the abundances of the isotopes (as was indicated above, the presence of the ^{21}Ne isotope in a natural mixture was disregarded). The renormalized cross section $\sigma^{\mathrm{A\text{-}pn}}$ for the reaction $^{20}\mathrm{Ne}[(\gamma, n) + (\gamma, np)]$ and the estimated cross section (σ^{X}) for the reaction $^{22}\mathrm{Ne}[(\gamma, n) + (\gamma, np)]$ were used to assess the cross sections for the reactions ^{20,22}Ne$(\gamma, n)^{19,21}$Ne and ^{20}Ne$(\gamma, np)^{18}$F. The contributions of these two reactions were singled out (this corresponds to separating the contributions of the corresponding two giant resonances) by means of the procedure where the cross sections for the reactions $^{20,22}\mathrm{Ne}[(\gamma, n) + (\gamma, np)]$ are approximated by Gaussian functions:

$$\mathrm{Gauss}(E_\gamma) = \sigma^{\max}\exp\{-0.5[(E_\gamma - E^{\max})/\Gamma]^2\}. \qquad (6)$$

Here, $E^{\max}$ is the energy position of the maximum value $\sigma^{\max}$ of a Gaussian function of width Γ. In order to separate the contributions of the (γ, n) and (γ, np) reactions, use was made of the Gaussian functions centered in the energy regions below and above the thresholds for the (γ, np) reactions [the energy values of $E_\gamma = 23.3$ and 23.4 MeV for, respectively, the ^{20}Ne and the ^{22}Ne nucleus (see Table 1)]. In the case of the ^{20}Ne nucleus, this procedure was implemented with the inclusion of additional information [18] about the cross section for the reaction $^{20}\mathrm{Ne}[(\gamma, p) + (\gamma, np)]$, since, for the self-conjugate nucleus ^{20}Ne ($N = Z = 10$), the cross sections for the (γ, n) and (γ, p) reactions caused by the decays of the same GDR states through the neutronic and the protonic channel, respectively, must have the same shape {an investigation [19] of the cross-section ratio for the (γ, p) and (γ, n) reactions on a large number of $1d$–$2s$-shell self-conjugate nuclei revealed that, for the $N = Z = 10$ nucleus, the absolute values of these cross sections can differ by a factor of 1.5 to 2.5 because of the distinctions between the energy thresholds}. We have also taken into account the circumstance that protons of energy in excess of 2 MeV were recorded in [18]; as a result, the effective threshold for the reaction $^{20}\mathrm{Ne}(\gamma, np)^{18}\mathrm{F}$ was higher in the protonic than in the neutronic channel by precisely this value—it amounted to $E_\gamma = 25.3$ MeV—and the corresponding resonance occurred at an energy of $E_\gamma = 27.58$ MeV.

(ii) In estimating the cross section for the reaction $^{20}\mathrm{Ne}(\gamma, p)^{19}\mathrm{F}$,

(a) use was also made of the assumption that, for the self-conjugate ($N = Z$) nucleus ^{20}Ne, the same states of the compound nucleus ^{20}Ne decay through the neutronic and through the protonic channel;

(b) the experimental cross section for the reaction $^{20}\mathrm{Ne}[(\gamma, p) + (\gamma, np)]$ [18] and the cross section estimated previously for the reaction $^{20}\mathrm{Ne}(\gamma, n)^{19}\mathrm{Ne}$ were smoothed by Gaussian functions of width 3.0 MeV in order to eliminate the effect of structural features on their general behavior;

(c) the aforementioned two cross sections were normalized to data on the integrated cross sections that were computed for the energy range from the GDR maximum in the photoneutron channel ($E_\gamma =$ 20 MeV) to the effective threshold of the detection of protons from the (γ, np) channel ($E_\gamma = 25.3$ MeV)—they must coincide in shape in this region;

(d) the difference of the normalized cross sections was interpreted as the contribution of protons from the reaction $^{20}\mathrm{Ne}(\gamma, np)^{18}\mathrm{F}$;

(e) the cross section for the reaction $^{20}\mathrm{Ne}(\gamma, p)^{19}\mathrm{F}$ was determined as the difference of the experimental cross section for the reaction $^{20}\mathrm{Ne}[(\gamma, p) + (\gamma, np)]$

Table 3. Parameters of the Gaussian functions (energy E^{max}, amplitude σ^{max}, and width Γ of the maximum) approximating the cross sections for the reactions ^{22}Ne$[(\gamma,n)+(\gamma,np)]$ and ^{22}Ne$[(\gamma,p)+(\gamma,np)]$

E^{max}, MeV	σ^{max}, mb	Γ, MeV
^{22}Ne$[(\gamma,n)+(\gamma,np)]$, $\chi^2=0.22$		
21.21	19.70	1.73
25.56	9.34	0.41
^{22}Ne$[(\gamma,p)+(\gamma,np)]$, $\chi^2=0.48$		
20.26	10.99	1.46
24.23	5.87	1.52
27.75	2.18	1.38

and the cross section that corresponds to the contribution of protons from the reaction ^{20}Ne$(\gamma,np)^{18}$F and which was estimated according to the procedure described above.

(iii) In estimating the cross section for the reaction ^{22}Ne$(\gamma,p)^{21}$F,

(a) use was also made of the approach based on determining the contribution of the cross section for the reaction ^{22}Ne$(\gamma,np)^{20}$F to the cross section for the reaction ^{22}Ne$[(\gamma,p)+(\gamma,np)]$ [18] and on employing the procedure of approximations in terms of Gaussian functions in the energy regions below and above the effective energy thresholds for the (γ,np) reactions in the neutronic ($E_\gamma=23.4$ MeV) and the protonic ($E_\gamma=25.4$ MeV) channel;

(b) three maxima (at energies of $E_\gamma=20.26$, 24.23, and 27.75 MeV), and not two (as in the situation for the ^{20}Ne nucleus), were reliably identified in the cross section for the reaction ^{22}Ne$[(\gamma,p)+(\gamma,np)]$ (the procedure of approximating this cross section by three Gaussian functions was characterized by a much higher stability than the procedure employing two Gaussian functions);

(c) the only Gaussian function that occurs in the energy region above the effective proton-detection threshold ($E_\gamma=25.4$ MeV)—it peaks at an energy of $E_\gamma=27.75$ MeV (see Table 3)—was interpreted as that which corresponds to the contribution of protons from the reaction ^{22}Ne$(\gamma,np)^{20}$F, data on the relation between the cross section for this reaction and its effective contribution to the cross section for the reaction $[(\gamma,p)+(\gamma,np)]$ [18] on the ^{20}Ne isotope being used in doing this.

The cross sections estimated for the reactions ^{20,22}Ne$(\gamma,n)^{19,21}$Ne, ^{20,22}Ne$(\gamma,p)^{19,21}$F, and ^{20,22}Ne$(\gamma,np)^{18,20}$F on the basis of the procedures outlined above—these cross sections were obtained for the first time—are displayed in Fig. 1.

For the sake of comparison and for the purposes of the subsequent discussion, the cross section that describes the reaction ^{22}Ne$(\gamma,2n)^{20}$Ne [15] and which receives a contribution (see below) only from the $T_<$ component of the GDR in the ^{22}Ne nucleus is shown in Fig. 1*b*.

2. ISOSPIN SPLITTING OF THE GIANT DIPOLE RESONANCE IN THE ^{22}Ne NUCLEUS

In [13], we showed that the cross section for the reaction ^{22}Ne$[(\gamma,n)+(\gamma,np)]$ can be reliably approximated by the sum of two Gaussian functions (Table 3) centered at energies below (one) and above (the other) $E_\gamma=23.4$ MeV and that the cross section for the reaction ^{22}Ne$[(\gamma,p)+(\gamma,np)]$ can be approximated by the sum of three Gaussian functions. In the latter case, one is centered in the energy region $E_\gamma<23.4$ MeV, while the other two are centered in the energy region $E_\gamma>23.4$ MeV.

From the data in Table 3, it can be seen that the position ($E_\gamma=21.21$ MeV) of one of the Gaussian functions approximating the cross section for the reaction ^{22}Ne$[(\gamma,n)+(\gamma,np)]$ is very close to the position ($E_\gamma=20.26$ MeV) of the first of the three Gaussian functions approximating the cross section for the reaction ^{22}Ne$[(\gamma,p)+(\gamma,np)]$. This means that they are due to the decay of ^{22}Ne states of the same origin. For the ^{22}Ne nucleus, whose ground-state isospin is $T_0=(N-Z)/2=(12-10)/2=1\neq0$, these are presumably the states of the $T_<=T_0=1$ GDR component [2–5]. States of the GDR that are manifested in the protonic channel, but which are not manifested in the neutronic channel and which are shifted with respect to the isospin-$T_<$ states toward higher energies by about 5 MeV, may be only states of isospin $T_>=T_0+1=2$ [2–5].

A more detailed analysis of the excitation and decay of the GDR states in the ^{22}Ne nucleus is required

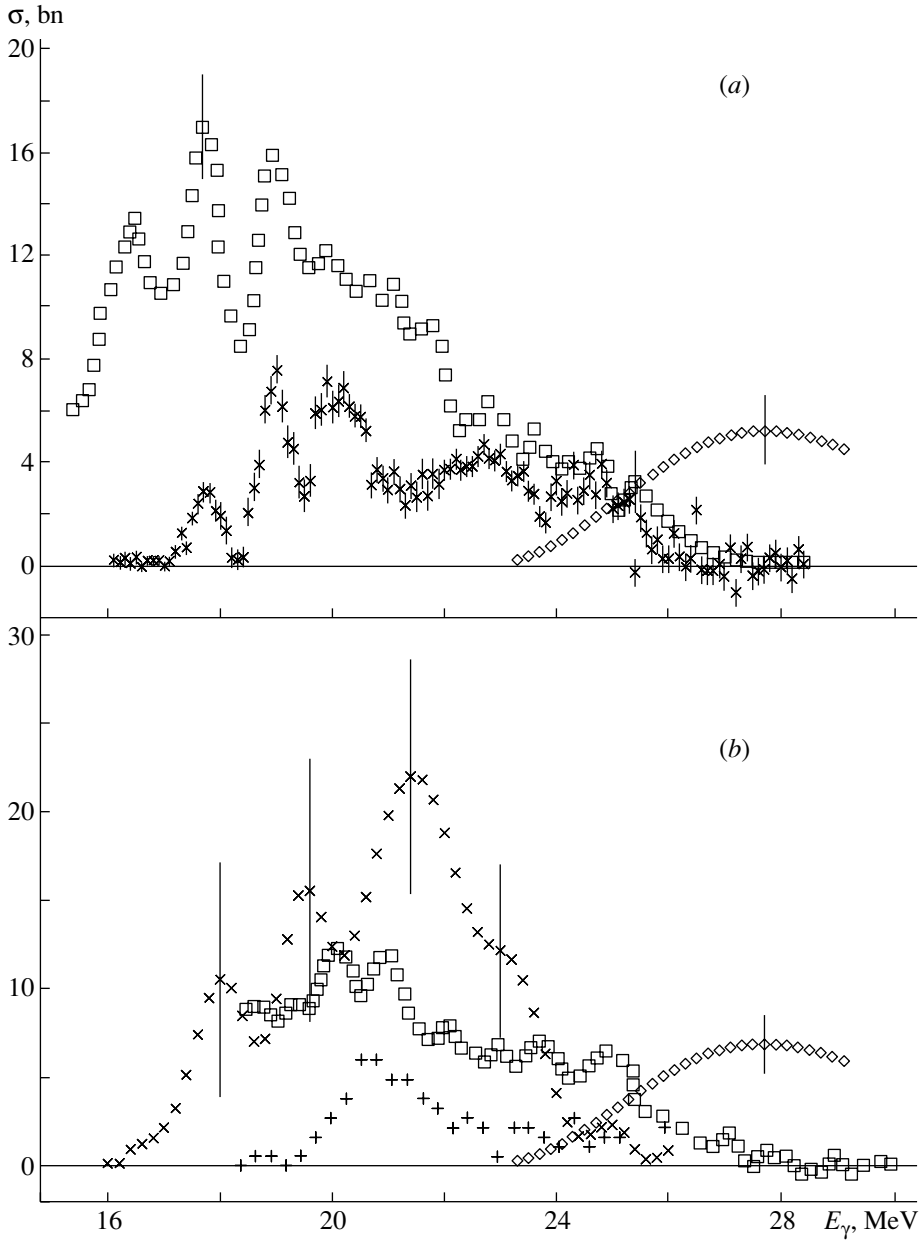

Fig. 1. Estimated cross sections for the reactions (*a*) $^{20}\mathrm{Ne}(\gamma, n)^{19}\mathrm{Ne}$ (×), $^{20}\mathrm{Ne}(\gamma, p)^{19}\mathrm{F}$ (□), and $^{20}\mathrm{Ne}(\gamma, np)^{18}\mathrm{F}$ (◇) and (*b*) $^{22}\mathrm{Ne}(\gamma, n)^{21}\mathrm{Ne}$ (×), $^{22}\mathrm{Ne}(\gamma, p)^{21}\mathrm{F}$ (□), and $^{22}\mathrm{Ne}(\gamma, np)^{20}\mathrm{F}$ (◇). For the sake of comparison, the cross section for the reaction $^{22}\mathrm{Ne}(\gamma, 2n)^{20}\mathrm{Ne}$ (+) [15] is additionally shown in the figure; for the clarity of the presentation, it is magnified by a factor of 5.

in order to interpret more reliably the relationship that we revealed between the neutronic and the protonic channel of the decay of its highly excited states.

2.1. Analysis of the Cross-Section Ratio for the Reactions $^{22}\mathrm{Ne}(\gamma, p)^{21}\mathrm{F}$ and $^{22}\mathrm{Ne}(\gamma, n)^{21}\mathrm{Ne}$ as a Function of Energy

Numerous previous investigations (see, for example, [7, 10, 20]) revealed the following: since, according to the concept of isospin splitting [2–5], isospin-$T_>$ states decay predominantly via proton emission, a significant growth of the ratio $r = \sigma(\gamma, p)/\sigma(\gamma, n)$ with energy is a manifestation of isospin-$T_>$ states against the background of isospin-$T_<$ states. The energy dependence $r(E_\gamma)$ obtained for the ^{22}Ne nucleus on the basis of data on the corresponding reaction cross sections smoothed with the aid of Gaussian functions of width 2 MeV is displayed in Fig. 2. The

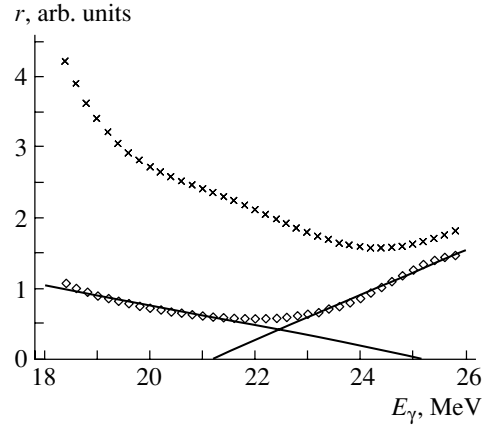

Fig. 2. Energy dependences of the cross-section ratio $r = \sigma(\gamma,p)/\sigma(\gamma,n)$ for (×) ^{20}Ne and (◇) ^{22}Ne nuclei. The straight lines represent least squares fits to the segments of the ratio r for the ^{22}Ne nucleus in the energy ranges 18.4–21.8 and 22.8–25.8 MeV.

analogous dependence for the ^{20}Ne nucleus is presented for the sake of comparison.

From Fig. 2, we can clearly see that the cross-section ratio $r = \sigma(\gamma,p)/\sigma(\gamma,n)$ for the ^{22}Ne nucleus remains approximately constant in the excitation-energy region below $E_\gamma \sim 22.5$ MeV, but it begins to grow quite fast at higher energies. In the case of the ^{20}Ne nucleus, where there is no isospin splitting of the GDR, the cross-section ratio $\sigma(\gamma,p)/\sigma(\gamma,n)$ shows a relatively slow growth only at substantially higher energies, in excess of $E_\gamma \sim 25.5$ MeV. On the basis of the data in Fig. 2, we can assume that the formation and decay of the GDR states in the ^{22}Ne nucleus proceeds in such a way that its $T_<$ states are concentrated predominantly at excitation energies below $E_\gamma \sim 22.5$ MeV, while the $T_>$ states are concentrated at higher energies.

As was indicated above, the position of one of the two Gaussian functions (with a maximum at $E_\gamma = 20.26$ MeV) approximating the cross section for the reaction $^{22}\mathrm{Ne}(\gamma,p)^{21}\mathrm{F}$ (see Table 3) is very close to the position ($E_\gamma = 21.21$ MeV) of the Gaussian function approximating the cross section for the reaction $^{22}\mathrm{Ne}(\gamma,n)^{21}\mathrm{Ne}$ (Table 3). This means that these two maxima are associated with the decay of GDR states of the ^{22}Ne nucleus that are of the same origin—these states are the GDR components of isospin $T_< = T_0 = 1$ [2–5].

More reliable information can be given only upon comprehensively examining the diagrams of the excitation and decay of states in the ^{22}Ne nucleus that are characterized by various isospin values and in nuclei neighboring it that are members of the corresponding isospin multiplets.

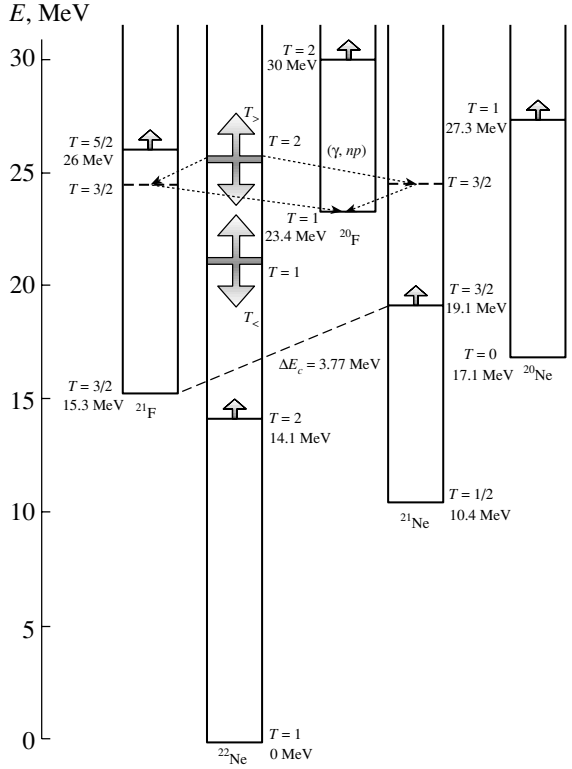

Fig. 3. Diagram of the excitation and decay of levels in the ^{22}Ne nucleus that are characterized by various isospin values and in nuclei neighboring it. Shown by the dashed line is the shift of the isospin-3/2 lowest level of the ^{21}Ne nucleus by the Coulomb energy $\{\Delta E_c = [1.444(Z-1/2)A^{-1/3} - 1.131] = 3.77$ MeV$\}$ with respect to the ground state of the ^{21}F nucleus (the ^{21}F and the ^{21}Ne nuclei are members of an isospin multiplet). Also displayed (wide arrows) are the energy positions [21] of the first levels of nuclei whose isospin is greater than the ground-state isospin by unity. The dotted lines with arrows indicate realizable (two of the four possible ones) channels of the reaction $^{22}\mathrm{Ne}(\gamma,np)^{20}\mathrm{F}$.

2.2. Analysis of the Diagrams of the Excitation and Decay of States in the ^{22}Ne Nucleus That Are Characterized by Various Isospin Values and in Nuclei Neighboring It

Information about the thresholds of various reactions and about the energy positions of ^{20,21,22}Ne and ^{20,21}F levels characterized by various isospin values that is necessary for performing such an analysis can be found in Fig. 3 (use is made here of data obtained in [21] by estimating the energy positions of the first levels whose isospin is greater than the ground-state isospin by unity).

From Fig. 3, we can see that, of the transitions that could occur, according to isospin-selection rules, between the corresponding states in the ^{22}Ne, ^{21}Ne, ^{20}Ne, ^{21}F, and ^{20}F nuclei, some are forbidden by

energy constraints. In the diagrams presented below for the possible transitions, those that are allowed both in isospin and in energy are labeled with the word "**yes**" and are printed in boldface.

Data in Fig. 3 indicate that none of the aforementioned constraints is operative for transitions that form the (γ, n) and the (γ, p) channel of GDR decay. The contributions of both isospin GDR components can manifest themselves in these channels:

$$\mathbf{^{22}Ne[}T_< = 1\mathbf{](}\gamma, n\mathbf{)^{21}Ne[}T = 1/2, 3/2\mathbf{]}\text{, yes;}$$

$$\mathbf{^{22}Ne[}T_> = 2\mathbf{](}\gamma, n\mathbf{)^{21}Ne[}T_> = 3/2\mathbf{]}\text{, yes;}$$

$$\mathbf{^{22}Ne[}T_< = 1\mathbf{](}\gamma, p\mathbf{)^{21}F[}T_< = 3/2\mathbf{]}\text{, yes;}$$

$$\mathbf{^{22}Ne[}T_> = 2\mathbf{](}\gamma, p\mathbf{)^{21}F[}T = 3/2, 5/2\mathbf{]}\text{, yes.}$$

It should only be emphasized that the decay of the $T_>(=2)$ states of the ^{22}Ne nucleus into the $T_>(=5/2)$ states of the ^{21}F nucleus does not seem to occur because energies at which $T_> = 5/2$ states appear in the ^{21}F nucleus are overly high for this (see Fig. 3).

Obviously, the (γ, np) reaction proceeds in two steps. According to the diagram considered above, there are no energy constraints at the first (neutron) step for the channels $^{22}\mathrm{Ne}[T_< = 1](\gamma, n)^{21}\mathrm{Ne}[T_< = 1/2]$ and $^{22}\mathrm{Ne}[T_< = 1](\gamma, n)^{21}\mathrm{Ne}[T_> = 3/2]$. Because of the high reaction thresholds at the second (proton) step—$^{21}\mathrm{Ne}[T_< = 1/2](\gamma, p)^{20}\mathrm{F}[T_< = 1]$ and $^{21}\mathrm{Ne}[T_> = 3/2](\gamma, p)\times{}^{20}\mathrm{F}[T = 1, 2]$—such transitions are impossible:

$$^{22}\mathrm{Ne}[T_< = 1](\gamma, np)^{20}\mathrm{F}[T = 1, 2] \to \begin{cases} ^{22}\mathrm{Ne}[T_< = 1](\gamma, n)^{21}\mathrm{Ne}[T_< = 1/2](\gamma, p)^{20}\mathrm{F}[T_< = 1], \text{ no;} \\ ^{22}\mathrm{Ne}[T_< = 1](\gamma, n)^{21}\mathrm{Ne}[T_> = 3/2](\gamma, p)^{20}\mathrm{F}[T = 1, 2], \text{ no;} \end{cases}$$

$$\mathbf{^{22}Ne[}T_> = 2\mathbf{](}\gamma, np\mathbf{)^{20}F[}T = 1, 2\mathbf{]} \to \begin{cases} \mathbf{^{22}Ne[}T_> = 2\mathbf{](}\gamma, n\mathbf{)^{21}Ne[}T_> = 3/2\mathbf{](}\gamma, p\mathbf{)^{20}F[}T_< = 1\mathbf{]}\text{, yes;} \\ ^{22}\mathrm{Ne}[T_> = 2](\gamma, n)^{21}\mathrm{Ne}[T_> = 3/2](\gamma, p)^{20}\mathrm{F}[T_> = 2], \text{ no.} \end{cases}$$

The excitation of the $T_>$ states in the ^{22}Ne nucleus above the $T_<$ states by a few MeV reduces the effect of the high threshold at the second reaction step and renders the probability of the decay $^{21}\mathrm{Ne}[T_> = 3/2](\gamma, p)^{20}\mathrm{F}[T_< = 1]$ nonzero, albeit small. In Fig. 3, this channel of the (γ, np) reaction is shown by the dotted line with arrows.

On the basis of similar considerations, only the decay $^{22}\mathrm{Ne}[T_> = 2](\gamma, p)^{21}\mathrm{F}[T_> = 3/2](\gamma, n)^{20}\mathrm{F}[T_< = 1]$ can be singled out as a feasible one in the decay diagrams for the (γ, np) reaction that are presented below:

$$^{22}\mathrm{Ne}[T_< = 1](\gamma, np)^{20}\mathrm{F}[T = 1, 2] \to {}^{22}\mathrm{Ne}[T_< = 1](\gamma, p)^{21}\mathrm{F}[T_< = 3/2](\gamma, n)^{20}\mathrm{F}[T = 1, 2], \text{ no;}$$

$$\mathbf{^{22}Ne[}T_> = 2\mathbf{](}\gamma, np\mathbf{)^{20}F[}T = 1, 2\mathbf{]} \to \begin{cases} \mathbf{^{22}Ne[}T_> = 2\mathbf{](}\gamma, p\mathbf{)^{21}F[}T_> = 3/2\mathbf{](}\gamma, n\mathbf{)^{20}F[}T_< = 1\mathbf{]}\text{, yes;} \\ ^{22}\mathrm{Ne}[T_> = 2](\gamma, p)^{21}F[T_> = 5/2](\gamma, n)^{20}\mathrm{F}[T_> = 2], \text{ no.} \end{cases}$$

In just the same way as the (γ, np) reaction, the $(\gamma, 2n)$ reaction occurs in two steps, the only difference being that, at the second step, the decay proceeds through the neutronic rather than through the protonic channel.

In Fig. 3, it can clearly be seen that the conditions for the decay of the $T_<$ states of the ^{22}Ne nucleus with the successive emission of two neutrons are much more favorable (the difference of the corresponding thresholds is about 6 MeV) than the conditions for the successive emission of a neutron and a proton. At the same time, the $T_>$ states of the ^{22}Ne nucleus can decay, according to isospin selection rules, only into the $T_> = 1$ states of the ^{20}Ne nucleus that occur (see Fig. 3) at energies in the region $E_\gamma > 27.3$ MeV:

$$\mathbf{^{22}Ne[}T_< = 1\mathbf{](}\gamma, 2n\mathbf{)^{20}Ne[}T_< = 0\mathbf{]} \to {}^{22}\mathbf{Ne[}T_< = 1\mathbf{](}\gamma, n\mathbf{)^{21}Ne[}T_< = 1/2\mathbf{](}\gamma, n\mathbf{)^{20}Ne[}T_< = 0\mathbf{]}\text{, yes;}$$
$$^{22}\mathrm{Ne}[T_> = 2](\gamma, 2n)^{20}\mathrm{Ne}[T_> = 1] \to {}^{22}\mathrm{Ne}[T_> = 2](\gamma, n)^{21}\mathrm{Ne}[T_> = 3/2](\gamma, n)^{20}\mathrm{Ne}[T_> = 1], \text{ no.}$$

The above diagrams of the possible transitions make it possible to draw the following conclusions:

(i) The (γ, n) and (γ, np) cross sections receive contributions from both GDR components.

Table 4. Parameters of the $T_<$ and $T_>$ isospin components of the GDR in the ^{22}Ne nucleus (energy center of gravity $E_{\text{c.g.}}$, integrated cross section σ^{int}, first moment σ_{-1} of the integrated cross section)

Component	$E_{\text{c.g.}}$, MeV	σ^{int}, MeV mb	σ_{-1}, mb
$T_<$	21.14 ± 1.90	125.00 ± 0.04	5.94 ± 0.53
$T_>$	25.71 ± 2.32	40.00 ± 0.01	1.92 ± 0.17

(ii) The cross section for the $(\gamma, 2n)$ reaction receives a contribution only from the $T_<$ GDR component; this result of the analysis that we performed is supported by the experimental cross section for the reaction $^{22}\text{Ne}(\gamma, 2n)^{20}\text{Ne}$ [15] (it is displayed in Fig. 1*b*): as was indicated in [21] and as is directly confirmed by our analysis, the decays of the $T_>$ states can be manifested in this cross section only at energies in the region $E_\gamma > 27$ MeV.

(iii) The cross section for the (γ, np) reaction receives a contribution only from the $T_>$ GDR component, this contribution being relatively small: only two decay channels of the possible four are realized; the energy thresholds of the two channels that are realized appear to be (Fig. 3) quite high [$E_{\text{thr}}(\gamma, np) = 23.4$ MeV].

The transitions that are singled out in the decay diagrams presented here as realizable ones can be used to interpret the contributions from the various isospin components of the GDR in the ^{22}Ne nucleus to various channels of its decay. Taking into account the way in which the $T_<$ and $T_>$ GDR components in the ^{22}Ne nucleus contribute to the (γ, n), (γ, p), (γ, np), and $(\gamma, 2n)$ cross sections, we can interpret the isospin components $\sigma^<$ and $\sigma^>$ as

$$\sigma^< = \sigma^<(\gamma, n) + \sigma^<(\gamma, p) + \sigma(\gamma, 2n), \qquad (7)$$
$$\sigma^> = \sigma^>(\gamma, n) + \sigma^>(\gamma, p) + \sigma(\gamma, np).$$

Table 3 displays the parameters of the Gaussian functions that approximate the estimated cross sections for the reactions $^{22}\text{Ne}(\gamma, n)^{21}\text{Ne}$ and $^{22}\text{Ne}(\gamma, p)^{21}\text{F}$; these approximations can be associated with the components $\sigma^<(\gamma, n)$ and $\sigma^>(\gamma, n)$, as well as with $\sigma^<(\gamma, p)$ and $\sigma^>(\gamma, p)$. By using them and relations (7), we have calculated the parameters of the isospin GDR components in the ^{22}Ne nucleus (the results are presented in Table 4). These data make it possible to estimate the isospin splitting ΔE (1),

$$\Delta E = E_{\text{c.g.}}(T_>) - E_{\text{c.g.}}(T_<)$$
$$= 25.71 - 21.14 = 4.57 \pm 0.69 \text{ MeV},$$

and the ratio R (2) of the intensities of the isospin GDR components,

$$R = \sigma^>_{-1}/(\sigma^>_{-1} + \sigma^<_{-1})$$
$$= 1.92/(1.92 + 5.94) = 0.24 \pm 0.04.$$

These estimates deviate considerably from the theoretical values of $\Delta E^{\text{theor}} = 5.45$ MeV (3) and $R^{\text{theor}} = 0.5$ (4). From the above results of the analysis of the diagrams of the excitation and decay of states characterized by various isospin values, it is clear that these discrepancies are due above all to the special features of the decay of the ^{22}Ne GDR through the (γ, np) channel. In [1], it was shown that manifestations of the isospin GDR components in the cross sections for various reactions are highly individual and that the parameters of isospin GDR splitting differ considerably from the predicted values in (3) and (4); the latter was observed in many experiments (see [8–12]). It was indicated that, for heavy nuclei, there are sufficient grounds to believe that the $T_>$ GDR branch manifests itself primarily in the photoproton channel, while the $T_<$ manifests itself in the photoneutron channel. This is not so for lighter nuclei because the thresholds for the isospin-allowed neutronic decay of $T_>$ states are insufficiently high in such nuclei and because the Coulomb nuclear barrier impedes the protonic decay of $T_<$ states in them less than in heavier nuclei. In addition, isospin splitting plays a much more important role in light and intermediate-mass nuclei than in heavy nuclei. In the specific case of the ^{22}Ne nucleus, the individual character of the isospin splitting of the GDR manifests itself in that, because of a very high threshold (see Table 1), in relation to the thresholds for the (γ, n) and (γ, p) reactions, the contribution to this channel from the $T_>$ GDR component proves to be significantly reduced, which is disregarded in the model considered in [2–5].

CONCLUSION

By performing a global analysis of the cross sections for various photonuclear reactions on the ^{20,22}Ne isotopes and on their natural mixture and by invoking data on the abundances of the isotopes and on the energy thresholds for the reactions being considered, we have been able to estimate, for the first time, the cross sections for the reactions $^{20,22}\text{Ne}(\gamma, n)^{19,21}\text{Ne}$ and $^{20,22}\text{Ne}(\gamma, p)^{19,21}\text{F}$ in the energy range $E_\gamma = 16.0$–28.0 MeV and for the reactions $^{20,22}\text{Ne}(\gamma, np)^{18,20}\text{F}$ in the energy range $E_\gamma = 23.3$–28.0 MeV.

For the ^{22}Ne nucleus, we have analyzed the ratio $r = \sigma(\gamma, p)/\sigma(\gamma, n)$ of the cross sections for the photoproton and the photoneutron reaction and identified the isospin GDR components. We have also analyzed the diagram of the excitation and decay of states in the ^{22}Ne nucleus that are characterized

by various isospin values and in nuclei neighboring it, which are members of the corresponding isospin multiplets. We have identified the contributions of the GDR components of isospins $T_< = 1$ and $T_> = 2$ in the ^{22}Ne nucleus to the cross sections for various photonuclear reactions. The isospin splitting of the GDR and the ratio of the intensities of its isospin components have been determined to be, respectively, $\Delta E = 4.57 \pm 0.69$ MeV and $R = 0.24 \pm 0.04$.

REFERENCES

1. V. V. Varlamov, B. S. Ishkhanov, and M. E. Stepanov, Izv. Akad. Nauk, Ser. Fiz. **62**, 1035 (1998).
2. S. Fallieros, B. Goulard, and R. H. Ventor, Phys. Lett. **19**, 398 (1965).
3. S. Fallieros and B. Goulard, Nucl. Phys. A **147**, 593 (1970).
4. R. O. Akyuz and S. Fallieros, Phys. Rev. Lett. **27**, 1016 (1971).
5. H. Morinaga, Phys. Rev. **97**, 444 (1955).
6. V. V. Varlamov, N. G. Efimkin, B. S. Ishkhanov, *et al.*, Yad. Fiz. **58**, 387 (1995) [Phys. At. Nucl. **58**, 337 (1995)].
7. V. V. Varlamov, N. G. Efimkin, B. S. Ishkhanov, *et al.*, Izv. Akad. Nauk, Ser. Fiz. **59** (5), 223 (1995).
8. K. G. McNeil, M. N. Thompson, A. D. Bates, *et al.,* Phys. Rev. C **47**, 1108 (1993).
9. V. V. Varlamov, B. S. Ishkhanov, I. M. Kapitonov, *et al.,* Nucl. Phys. A **222**, 548 (1974).
10. B. S. Ishkhanov, I. M. Kapitonov, V. G. Shevchenko, *et al.,* Nucl. Phys. A **283**, 307 (1977).
11. V. V. Varlamov, B. S. Ishkhanov, I. M. Kapitonov, *et al.*, Vestn. Mosk. Univ., Ser. 3: Fiz., Astron., No. 3, 297 (1976).
12. V. V. Varlamov, B. S. Ishkhanov, I. M. Kapitonov, *et al.*, Izv. Akad. Nauk SSSR, Ser. Fiz. **39**, 1744 (1975).
13. V. V. Varlamov and M. E. Stepanov, Preprint NIIYaF MGU-99-40.598 (Institute of Nuclear Physics, Moscow State University, Moscow, 1999).
14. V. V. Varlamov and M. E. Stepanov, Izv. Akad. Nauk, Ser. Fiz. **64**, 615 (2000).
15. A. Veyssière, H. Beil, R. Bergère, *et al.*, Nucl. Phys. A **227**, 513 (1974).
16. J. G. Woodworth, J. W. Jury, K. H. Lokan, and N. K. Sherman, Can. J. Phys. **53**, 795 (1975).
17. P. D. Allen, E. G. Muirhead, and D. V. Webb, Nucl. Phys. A **357**, 171 (1981).
18. W. Hoffman, R. Koziek, G. Kraft, and R. Mundenke, Z. Phys. **225**, 303 (1969).
19. B. S. Ishkhanov, I. M. Kapitonov, and V. I. Mokeev, Izv. Akad. Nauk SSSR, Ser. Fiz. **50**, 1974 (1986).
20. K. Shoda, H. Miyase, M. Sugawara, *et al.*, Nucl. Phys. A **239**, 397 (1975).
21. I. N. Boboshin, V. V. Varlamov, and B. S. Ishkhanov, in *Proceedings of the International Conference on Nuclear Physics: "Cluster Phenomena in Atomic Nuclei" (50th Conference on Nuclear Spectroscopy and Nuclear Structure), St. Petersburg, 2000* (Nauka, St. Petersburg, 2000), p. 287.

Translated by A. Isaakyan

Physics of Atomic Nuclei, Vol. 65, No. 1, 2002, pp. 58–64. From Yadernaya Fizika, Vol. 65, No. 1, 2002, pp. 61–67.
Original English Text Copyright © 2002 by Balbutsev.

NUCLEI
Theory

Large-Amplitude Motion in the Suzuki Model*

E. B. Balbutsev

Joint Institute for Nuclear Research, Dubna, Moscow oblast, 141980 Russia

Received November 22, 2000; in final form, February 19, 2001

Abstract—The classical and quantum aspects of the analytically solvable one-dimensional purely monopole Suzuki model are studied to clarify the problem of quantization of classical collective motion. A set of nonlinear dynamical equations for the monopole moment of a nucleus are derived from the time-dependent Hartree-Fock equation by using the Wigner function moments. It provides a description of large-amplitude monopole vibrations. The corresponding collective Hamiltonian is constructed and quantized. The anharmonicity of the collective spectra is analyzed in detail. © *2002 MAIK "Nauka/Interperiodica".*

1. INTRODUCTION

A one-dimensional harmonic-oscillator model with a monopole–monopole residual interaction was suggested by Suzuki [1] in 1973. Using the mean-field approach and the small-amplitude approximation, he gave a qualitative explanation of the nature of the recently discovered giant monopole resonance. However, the main interest in this model is connected with the fact that it has an exact solution. It is known that, in the Hartree approximation, the model reduces to the time-dependent Schrödinger equation with a harmonic-oscillator Hamiltonian, whose frequency is time-dependent. Its analytic solution was found by Popov and Perelomov [2]. Thus, we have here a rare example of a nonlinear problem having an analytic solution. That is why the Suzuki model is widely used as a test for various approximate methods for describing large-amplitude nuclear collective motion [3–5]. The first attempt at treating this model beyond the small-amplitude approximation was made by Kirson [6], who gave its algebraic analysis and found numerically its "exact" solution. Interest in investigating a collective motion beyond the usual random-phase approximation (small-amplitude approach) has been quickened since the experimental discovery of high-energy structures in heavy-ion grazing collisions and their interpretation in terms of multiphonon excitations of giant quadrupole resonances [7–9]. We consider this model with the aim of verifying the potential of the method of the Wigner function moments (WFM) in studying large-amplitude motion and nonlinear effects accompanying it. The simplicity of the model allows one to observe the appearance of anharmonicity in the collective spectra and to clarify some problems of quantization of classical equations of motion for collective variables describing giant resonances. In addition, using the WFM method, one is able to perform more extensive analysis of the collective aspects of the Suzuki model.

2. FORMULATION OF THE METHOD

The basis of our method for describing collective nuclear dynamics is the equation of motion for the one-body density matrix $\rho(\mathbf{r}_1, \mathbf{r}_2, t) = \langle \mathbf{r}_1 | \hat{\rho}(t) | \mathbf{r}_2 \rangle$,

$$i\hbar \frac{\partial \hat{\rho}}{\partial t} = \left[\hat{H}, \hat{\rho} \right], \tag{1}$$

where $\hat{H}$ is the self-consistent one-body Hamiltonian depending implicitly on the density matrix.

This equation is modified by applying the Wigner transform of the density matrix [10],

$$f(\mathbf{r}, \mathbf{p}, t) = \int d^3 s \exp(-i\mathbf{p} \cdot \mathbf{s}/\hbar) \times \rho\left(\mathbf{r} + \frac{\mathbf{s}}{2}, \mathbf{r} - \frac{\mathbf{s}}{2}, t\right), \tag{2}$$

and of the Hamiltonian,

$$H^{\mathrm{W}}(\mathbf{r}, \mathbf{p}) = \int d^3 s \exp(-i\mathbf{p} \cdot \mathbf{s}/\hbar) \times \left(\mathbf{r} + \frac{\mathbf{s}}{2} \middle| \hat{H} \middle| \mathbf{r} - \frac{\mathbf{s}}{2}\right). \tag{3}$$

Using (2) and (3), one arrives at [11, 12]

$$\frac{\partial f}{\partial t} = \frac{2}{\hbar} \sin\left(\frac{\hbar}{2}(\nabla_{\mathbf{r}}^H \cdot \nabla_{\mathbf{p}}^f - \nabla_{\mathbf{p}}^H \cdot \nabla_{\mathbf{r}}^f)\right) H^{\mathrm{W}} f, \tag{4}$$

where the upper index on the nabla operator stands for the function on which this operator acts. The right-hand side is just the brief notation for the infinite series corresponding to the expansion of the sine function. When one takes into account only the first term of this expansion, one obtains the equation equivalent to the Vlasov equation for the distribution function.

*This article was submitted by the author in English.

1063-7788/02/6501-0058$22.00 © 2002 MAIK "Nauka/Interperiodica"

If the Hamiltonian is the sum of a kinetic term and a local potential $V(\mathbf{r})$, its Wigner transform is just the classical version of the same Hamiltonian,

$$H^{\mathrm{W}} = p^2/2m + V(\mathbf{r}). \quad (5)$$

Then, Eq. (4) becomes

$$\frac{\partial f}{\partial t} + \frac{1}{m}\mathbf{p}\cdot\nabla_{\mathbf{r}} f = \frac{2}{\hbar}\sin\left(\frac{\hbar}{2}\nabla^V_{\mathbf{r}}\cdot\nabla^f_{\mathbf{p}}\right) Vf. \quad (6)$$

Now, we apply the WFM method to derive a closed set of dynamical equations for Cartesian tensors of second rank. This method was suggested in [13] and is described in detail in [14]. Its idea is based on the virial theorems of Chandrasekhar and Lebovitz [15]. Thus, without going into details, we integrate Eq. (6) over the phase space $\{\mathbf{p},\mathbf{r}\}$ with the weights $x_i x_j$, $p_i x_j$, and $p_i p_j$ to get the set of equations

$$\begin{aligned}
&\frac{d}{dt}J_{ij}(t) - \frac{1}{m}(L_{i,j} + L_{j,i}) = 0, \quad (7)\\
&\frac{1}{2}\frac{d}{dt}L_{i,j}(t) + \frac{1}{2}\int d\{\mathbf{p},\mathbf{r}\}x_i\frac{\partial V}{\partial x_j}f(\mathbf{r},\mathbf{p},t)\\
&\qquad - \Pi_{ij}(t) = 0,\\
&\frac{d}{dt}\Pi_{ij}(t) + \frac{1}{2m}\int d\{\mathbf{p},\mathbf{r}\}\left[p_i\frac{\partial V}{\partial x_j}\right]_{ij} f(\mathbf{r},\mathbf{p},t) = 0,
\end{aligned}$$

where $\int d\{\mathbf{p},\mathbf{r}\} \equiv 4/(2\pi\hbar)^3 \int d^3p \int d^3r$ and $[\ldots]_{ij}$ means symmetrization with respect to the indices i and j ($[a_i b_j]_{ij} = a_i b_j + a_j b_i$). We have introduced the notation

$$J_{ij}(t) = \int d\{\mathbf{p},\mathbf{r}\}\; x_i x_j f(\mathbf{r},\mathbf{p},t)$$

for an inertia tensor,

$$L_{i,j}(t) = \int d\{\mathbf{p},\mathbf{r}\} x_i p_j f(\mathbf{r},\mathbf{p},t)$$

for a mixed momentum–position tensor, and

$$\Pi_{ij}(t) = \frac{1}{2m}\int d\{\mathbf{p},\mathbf{r}\} p_i p_j f(\mathbf{r},\mathbf{p},t)$$

for the integral kinetic energy tensor.

We have thus derived the set of three dynamical equations for three collective variables $J_{ij}(t)$, $L_{i,j}(t)$, and $\Pi_{ij}(t)$. It is necessary to stress that these equations are exact because, up to this moment, we have not made any approximations. To close this set of equations, it is necessary to express the integrals involving derivatives of the potential $V(\mathbf{r})$ in terms of the three variables mentioned above. This problem can be solved rigorously in the case of V with quadratic coordinate dependence (which is the subject of this study).

3. SUZUKI MODEL

The microscopic Hamiltonian of the Suzuki model [1] is

$$\begin{aligned}
H = &\sum_{i=1}^{A}\left(\frac{p_i^2}{2m} + \frac{1}{2}m\omega^2 x_i^2\right) \quad (8)\\
&+ \frac{1}{2}\kappa\sum_{i\neq j}^{A}(x_i^2 - x_0^2/A)(x_j^2 - x_0^2/A),
\end{aligned}$$

where x_0^2 is the value of the tensor J_{11} for the oscillator ground state. Usually, it is studied in the Hartree approximation. The time-dependent mean field of the model is

$$V(x,t) = \frac{m}{2}\omega^2 x^2 + \kappa(J - x_0^2)(x^2 - x_0^2/A), \quad (9)$$

where $J = J_{11}(t)$. It looks like a harmonic-oscillator potential with the time-dependent frequency $\omega^2(t) = \omega^2 + \frac{2}{m}\kappa(J - x_0^2)$. An exact solution to the Schrödinger equation with such a potential was found by Popov and Perelomov [2]. Roughly speaking, it is the usual oscillator wave function whose arguments are modified by the linearly independent solutions Z_1 and Z_2 to the classical equation

$$\ddot{Z} + \omega^2(t)Z = 0. \quad (10)$$

One can write Z_1 and Z_2 in the form

$$Z_1 = r(t)e^{i\gamma(t)}, \quad Z_2 = Z_1^*,$$

with $r(t)$ and $\gamma(t)$ obeying the differential equations

$$\begin{aligned}
&\ddot{r} - \frac{W^2}{r^3} + \omega^2(t)r = 0, \quad (11)\\
&\dot{\gamma} - W/r^2 = 0.
\end{aligned}$$

The constant W, being proportional to the Wronskian of Eq. (10),

$$2iW = \dot{Z}_1 Z_2 - \dot{Z}_2 Z_1,$$

is determined by the initial conditions.

Suzuki estimated the energy of the giant monopole resonance in the small-amplitude approximation, neglecting nonlinear effects of the model. They were considered in [3–5], where this model was used to test various approaches to investigating large-amplitude collective motion. We pursue just the same goal with our method.

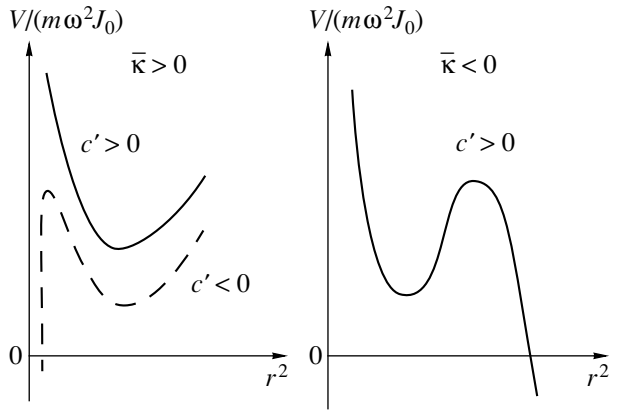

Fig. 1. Potential $V(r)$ (19) as a function of r for various values of $\bar\kappa$ and c'.

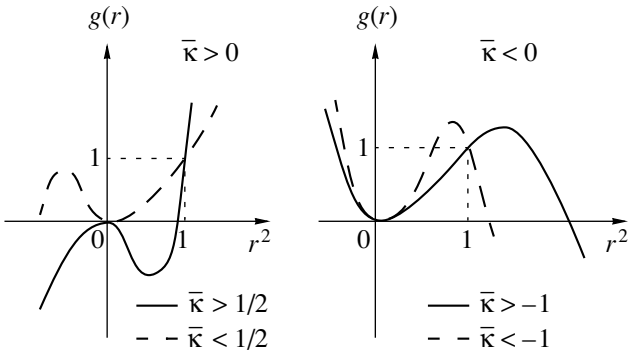

Fig. 2. Function $g(r)$ for various values of $\bar\kappa$.

3.1. Equations of Motion

For the potential (9), Eqs. (7) become

$$\frac{m}{4}\ddot J + J\left[\frac{m}{2}\omega^2 + \kappa(J - J_0)\right] - \Pi = 0, \qquad (12)$$
$$\dot\Pi + \dot J\left[\frac{m}{2}\omega^2 + \kappa(J - J_0)\right] = 0,$$

with $J_0 \equiv x_0^2$ and $\Pi = \Pi_{11}(t)$. The time dependence of the tensors is omitted for the sake of simplicity. The second equation of this set reduces to the integral of the motion

$$\Pi + \frac{m}{2}\omega^2 J + \frac{\kappa}{2}(J - J_0)^2 = E, \qquad (13)$$

whose physical meaning is that the total energy of the system is a conserved quantity. It is indeed easy to see that it is equal to the Hartree–Fock average of the microscopic Hamiltonian (8)—that is, $E = \langle\Psi \mid H \mid \Psi\rangle$. Another integral can be found by multiplying the second equation in (12) by J and by subtracting the result from the first equation multiplied by $\dot J$,

$$J(t)\Pi(t) - \frac{m}{8}\dot J(t)^2 = c, \qquad (14)$$

where the constant c is determined by the initial conditions. With the aid of Eq. (14), one is able to reduce the set of Eqs. (12) to the single equation

$$\frac{m}{4}\ddot J + \frac{m}{2}\omega^2 J + \kappa(J - J_0)J - \frac{c}{J} - \frac{m}{8J}\dot J^2 = 0. \qquad (15)$$

Upon the change of variable $J = J_0 r^2$, this equation can be written in the form

$$\ddot r + \omega^2(t) r - \omega^2\frac{c'}{r^3} = 0, \qquad (16)$$

where $\omega^2(t) = \omega^2[1 + 2\bar\kappa(r^2 - 1)]$, $\bar\kappa = \kappa J_0/(m\omega^2)$, and $c' = 2c/(m\omega^2 J_0^2)$. In this equation, one immediately recognizes one of the above equations written in (11), the constants W and c' being related by the equation $W^2 = \omega^2 c'$. If one supposes here that $c' = 1$, this equation becomes identical to the corresponding equations from [3, 4]. This choice of c' was dictated by their choice of the initial condition $\omega(t = -\infty) = \omega$, which is not accidental—just this initial condition was used in [2] to find an exact solution to the problem. The analysis of the c' dependence of Eq. (16) allows one to find new properties of the model.

Solving Eqs. (13) and (14) with respect to Π, one can rewrite the energy in a more traditional form, as a sum of kinetic and potential energies,

$$E = \frac{m}{8J}\dot J^2 + \frac{c}{J} + \frac{m}{2}\omega^2 J + \frac{\kappa}{2}(J - J_0)^2, \qquad (17)$$

or in terms of r,

$$E = \frac{m}{2}J_0\{\dot r^2 + \omega^2[r^2 + c'/r^2 + \bar\kappa(r^2 - 1)^2]\}. \qquad (18)$$

The r dependence of the potential

$$V(r) = \frac{m}{2}\omega^2 J_0[r^2 + c'/r^2 + \bar\kappa(r^2 - 1)^2] \qquad (19)$$

for various values of $\bar\kappa$ and c' is schematically illustrated in Fig. 1.

3.2. Equilibrium State and Small-Amplitude Approximation

By definition, the kinetic energy at equilibrium is equal to zero and the potential energy is at its minimum. The equation determining the extrema of $V(r)$ is

$$g(r) - c' = 0, \qquad (20)$$

where $g(r) = r^4[1 + 2\bar\kappa(r^2 - 1)]$. The function $g(r)$ is sketched in Fig. 2.

It is seen that, in the case of $\bar\kappa > 0$, the polynomial in (20) has only one positive root for $c' > 0$, which corresponds to the minimum of the potential (see Fig. 1). It describes the stable equilibrium state, which is more compressed ($J_{\rm eq} < J_0$) than that of the harmonic oscillator when $c' < 1$ and less compressed

($J_{\rm eq} > J_0$) when $c' > 1$. Using an analogy with an equilibrium deformation, one can say that the system has a positive static compression for $c' < 1$ and a negative static compression (dilatation) for $c' > 1$ if one assumes that the oscillator ground state has zero static compression.

There is no need for analyzing the situation with $c' < 0$ (see, however, the next section) because this integral of the motion cannot be negative in the state of equilibrium. Indeed, substituting $\dot{J} = 0$ into (14), we obtain

$$c_{\rm eq} = J_{\rm eq}\Pi_{\rm eq}, \tag{21}$$

J and Π being positive by definition; hence, $c_{\rm eq}$ and $c'_{\rm eq}$ are positive definite.

In the case of $\bar{\kappa} < 0$, the polynomial in (20) has two positive roots if $0 \le c' < (1-2\bar{\kappa})^3/(27\bar{\kappa}^2)$. The smaller root corresponds to the minimum of the potential well, and the larger one corresponds to the maximum of the barrier. The latter equilibrium state is metastable due to a finite value of the barrier height. For $\bar{\kappa} \le -1$, the equilibrium state has a positive static compression independent of the c' value. For $\bar{\kappa} > -1$, the equilibrium state has a positive static compression when $c' < 1$ and a negative one when $c' > 1$. The potential has no extrema when $c' \ge (1-2\bar{\kappa})^3/(27\bar{\kappa}^2)$, possessing only an inflection point at $r^2 = (-c'/\bar{\kappa})^{1/3}$.

To find the energy of small vibrations about the equilibrium state, we apply a linearization procedure. Writing Eq. (16) in terms of the new variable $y = r - r_{\rm eq}$ and neglecting y^2 terms, we find

$$\ddot{y} + y\omega^2\left[1 + 3c'/r_{\rm eq}^4 + 2\bar{\kappa}(3r_{\rm eq}^2 - 1)\right] + \omega^2\left[r_{\rm eq} - c'/r_{\rm eq}^3 + 2\bar{\kappa}(r_{\rm eq}^3 - r_{\rm eq})\right] = 0. \tag{22}$$

This equation is transformed into

$$\ddot{y} + 4\omega^2[1 + \bar{\kappa}(3r_{\rm eq}^2 - 2)]y = 0 \tag{23}$$

after taking into account Eq. (20), which is satisfied by $r_{\rm eq}$. The corresponding eigenfrequency is

$$\tilde{\Omega} = 2\omega\sqrt{1 + \bar{\kappa}(3r_{\rm eq}^2 - 2)}. \tag{24}$$

Assuming here that $J_0 = 0$, we reproduce the result from [5]:

$$\tilde{\Omega} = 2\omega\sqrt{1 + \frac{3\kappa}{m\omega^2}J_{\rm eq}}.$$

Equation (20) can easily be solved at $c' = 1$. One positive extremum lies at $r^2 = 1$. It corresponds to the maximum of the barrier for $\bar{\kappa} < -1$ and to the minimum of the potential for $\bar{\kappa} > -1$. Only this minimum was analyzed in [3, 4]. From (24), one obtains the corresponding expression for the frequency in the random-phase approximation (RPA)

$$\tilde{\Omega} = 2\omega\sqrt{1 + \bar{\kappa}}. \tag{25}$$

Another positive extremum lies at $r^2 = -(1 + \sqrt{1 - 8\bar{\kappa}})/(4\bar{\kappa})$. It corresponds to the maximum of the barrier for $0 > \bar{\kappa} > -1$ and to the minimum of the potential for $\bar{\kappa} < -1$. The corresponding expression for the RPA frequency is

$$\tilde{\Omega}^2 = \omega^2(1 - 8\bar{\kappa} - 3\sqrt{1 - 8\bar{\kappa}}). \tag{26}$$

The strength constant $\bar{\kappa} = -1$ is the critical one. With this $\bar{\kappa}$, the potential has neither a minimum nor a maximum and the point $r^2 = 1$ proves to be its inflection point.

3.3. Analysis of the Exact Solution

To find an exact expression for the function $J(t)$, it is convenient to use Eq. (17). Its solution can be expressed in terms of the Jacobian elliptic function [16],

$$J(t) = \eta_1 + (\eta_2 - \eta_1)\mathrm{sn}^2(\bar{\omega}t + \chi). \tag{27}$$

Here, $\bar{\omega} = \sqrt{(\eta_1 - \eta_3)\kappa/m}$ and η_i are the real roots of the polynomial

$$P(J) = -J^3 + a_2J^2 + a_1J + a_0 \tag{28}$$

with $a_2 = 2J_0 - m\omega^2/\kappa$, $a_1 = 2E/\kappa - J_0^2$, and $a_0 = -2c/\kappa$. The roots satisfy the condition $\eta_1 > \eta_2 > \eta_3$ for $\kappa > 0$ and the condition $\eta_1 < \eta_2 < \eta_3$ for $\kappa < 0$. The phase χ is determined by the initial conditions. The function $\mathrm{sn}(\phi)$ is periodic with period $\Delta\phi = 4\mathbf{K}$, where

$$\mathbf{K}(k) = \int_0^{\pi/2} \frac{d\phi}{\sqrt{1 - k^2\sin^2\phi}} \tag{29}$$

is a complete elliptic integral of the first kind with $k^2 = (\eta_2 - \eta_1)/(\eta_3 - \eta_1)$. There exists an analytic expression for the Fourier expansion of this function [17],

$$\mathrm{sn}(\bar{\omega}t) = \frac{2\pi}{k\mathbf{K}}\sum_{n=1}^{\infty}\frac{q^{n-1/2}}{1 - q^{2n-1}}\sin(2n-1)\frac{\bar{\omega}\pi}{2\mathbf{K}}t,$$

where $q = \exp(-\pi\mathbf{K}'/\mathbf{K})$, $\mathbf{K}'(k) = \mathbf{K}(\sqrt{1-k^2})$. This formula involves only frequencies that are proportional to odd numbers of the basic frequency $\Omega = \dfrac{\bar{\omega}\pi}{2\mathbf{K}}$. It is obvious that sn^2 includes the frequencies $n\Omega$ with n even only. Thus, the Fourier expansion of the function $J(t)$ will involve only one basic frequency 2Ω and its satellites 4Ω, 6Ω, etc. Numerically, the frequency $2\Omega = \dfrac{\bar{\omega}\pi}{\mathbf{K}}$ can be rather different from the result of the harmonic problem (24). Thus, the

Table 1. Dependence of eigenfrequencies on the initial conditions

I	c'	0	0.01	0.1	0.5	1
	$\hbar\Omega$	9.25	14.13	17.91	21.84	23.98
II	c'	−0.0001	−0.04	−0.08	−0.1	−0.11
	$\hbar\Omega$	16.89	15.96	14.55	13.31	12.18
III	c'	0.94	0.945	0.95	1	1.005
	$\hbar\Omega$	5.53	7.04	7.58	9.50	9.60
IV	c'	0.47	0.5	0.7	0.75	0.755
	$\hbar\Omega$	10.66	14.68	18.90	19.42	19.46

Note: (I) $\bar\kappa = 2$, $E = 24$ MeV, $r^2_{\rm eq} = 1$; (II) $\bar\kappa = 2$, $E = 24$ MeV, $r^2_{\rm eq} = 0.752$; (III) $\bar\kappa = -0.5$, $E = 9.5$ MeV, $r^2_{\rm eq} = 1$; (IV) $\bar\kappa = -2$, $E = 15$ MeV, $r^2_{\rm eq} = 0.5$.

effect of including the anharmonic term $\sim J^2(t)$ in the system (12) is the transformation of the basic frequency $\tilde\Omega$ into 2Ω and the appearance of satellites $n2\Omega$. The equidistance of such a spectrum is evident, characteristic of a bounded classical motion.

It is necessary to note the dependence of Ω on the initial conditions (also characteristic of classical motion). The roots of the polynomial in (28) depend on c and E. These constants, together with the phase χ, are determined by $J(0)$, $\dot J(0)$, and $\Pi(0)$. Examples of such a dependence are demonstrated in Table 1.

A very interesting situation arises at a sufficiently large value of $\dot J(0)$, in which case the constant c' becomes negative. If $\bar\kappa > 1/2$ and $0 > c' > (1 - 2\bar\kappa)^3/(27\bar\kappa^2)$, the polynomial in (20) has two positive roots (Fig. 2) with $r^2 < 1$: the larger one corresponds to the minimum of the potential well, and the smaller one corresponds to the top of the barrier. In this case, the time-dependent single-particle potential (9) is always repulsive. This fact becomes obvious after rewriting (9) as

$$V(x,t) = \frac{m}{2}\omega^2[1 + 2\bar\kappa(r^2 - 1)]x^2 - m\omega^2\bar\kappa(r^2 - 1)x_0^2/A$$

and noting that $[1 + 2\bar\kappa(r^2 - 1)] < 0$ for the region $0 < r^2 < (2\bar\kappa - 1)/(2\bar\kappa)$ being considered. Nevertheless, the system can possess a collective dynamical potential whose bottom is lower than that of the equilibrium state. The corresponding condition $V_{\rm bot} < V_{\rm eq}$ can be written as

$$2r^2_{\rm bot} + \bar\kappa(3r^2_{\rm bot} - 1)(r^2_{\rm bot} - 1) < 2r^2_{\rm eq} + \bar\kappa(3r^2_{\rm eq} - 1)(r^2_{\rm eq} - 1),$$

where $r_{\rm bot}$ is the position of the minimum of the dynamical potential. After simple transformations, one gets

$$(r^2_{\rm bot} - r^2_{\rm eq})\{2 + \bar\kappa[3(r^2_{\rm bot} + r^2_{\rm eq}) - 4]\} < 0.$$

Considering that $r^2_{\rm bot}$ is determined by $c' < 0$ and that $r^2_{\rm eq}$ is determined by $c' > 0$, it is easy to see from Fig. 2 (the case of $\bar\kappa > 1/2$) that $r^2_{\rm bot}$ is always smaller than $r^2_{\rm eq}$. Hence, one has

$$2 + \bar\kappa[3(r^2_{\rm bot} + r^2_{\rm eq}) - 4] > 0.$$

Substituting the minimal values of $r^2_{\rm bot}$ and $r^2_{\rm eq}$,

$$r^2_{\rm bot}({\rm min}) = \frac{2\bar\kappa - 1}{3\bar\kappa}, \quad r^2_{\rm eq}({\rm min}) = \frac{2\bar\kappa - 1}{2\bar\kappa},$$

into this formula, one finally obtains the condition $\bar\kappa > 1/2$, which is just our case.

In an analogous way, one can derive the condition for the top of the barrier $V_{\rm top}$ to be higher than $V_{\rm eq}$:

$$(r^2_{\rm top} - r^2_{\rm eq})\{2 + \bar\kappa[3(r^2_{\rm top} + r^2_{\rm eq}) - 4]\} > 0.$$

It is obvious that $r^2_{\rm top} < r^2_{\rm eq}$. Therefore, one has

$$2 + \bar\kappa[3(r^2_{\rm top} + r^2_{\rm eq}) - 4] < 0.$$

Considering that $r^2_{\rm top} \sim 0$, one obtains the condition

$$r^2_{\rm eq} < \frac{4}{3}\frac{2\bar\kappa - 1}{2\bar\kappa} = \frac{4}{3}r^2_{\rm eq}({\rm min}).$$

Such a potential is shown in Fig. 1 by the dashed curve. The eigenfrequencies calculated for this potential well are given in Table 1. The limits of variation of c' are determined by the input excitation energy E: at some value of c', the energy $E_{\rm eq} + E$ proves to be lower than the bottom of the potential well or higher than the top of the potential barrier.

3.4. Quantization

Solving nonlinear equations of motion, one expects to find anharmonicity effects. We have already observed the main effect of anharmonicity—the emergence of satellites of the basic frequency that form the equidistant spectrum. However, this result contradicts the practice of quantum-mechanical calculations, where one usually has some deviation from precise equidistance. In order to obtain anharmonicity of the spectrum, it is therefore necessary to quantize this model.

Its quantization is straightforward because we already have the expression for the energy of vibrations (17). Choosing $q = J$ and $p = (m\dot J)/(4J)$ as the canonically conjugate variables, one can represent the Hamiltonian in the form

$$H = \frac{p^2}{2m^*} + V(q) \qquad (30)$$

with

$$V(q) = \frac{m}{2}\omega^2 q + \frac{c}{q} + \frac{\kappa}{2}(q - J_0)^2, \;\; m^* = \frac{m}{4q}. \quad (31)$$

It is easy to see that the first Hamilton's equation $\dot{p} = -\partial H/\partial q$ coincides with Eq. (15), while the second Hamilton's equation $\dot{q} = \partial H/\partial p$ reproduces our definition of p.

The quantum Hamiltonian can be produced by following the Pauli [18, 19] prescription:

$$H = -\frac{\hbar^2}{m}\left(\frac{\partial}{\partial q} + 2q\frac{\partial^2}{\partial q^2}\right) + V(q).$$

This operation, however, does not complete the construction of the quantum Hamiltonian because it is necessary to solve the initial-condition problem. Our quantum Hamiltonian will contain the constant c, which is determined by the initial conditions. Thus, the variety of initial conditions of the classical problem will generate a variety of quantum Hamiltonians. However, the Hamiltonian that ideally describes the dynamics of the nucleus should be unique.

We suppose that the solution to this problem can be found by taking into account the fundamental difference between the classical and quantum descriptions of excitations. Being an integral of the motion (energy), the classical Hamiltonian changes each time when the initial conditions are changed. Hence, strictly speaking, all excited states and the equilibrium (ground) state are described by different Hamiltonians. An absolutely different situation prevails in a quantum case. Here, all states (ground and excited) are obtained as eigenstates of only one Hamiltonian. The ground state is the only state that is described by the same Hamiltonian in both cases. Therefore, it is natural to use, for quantization, the classical Hamiltonian derived for the initial conditions that correspond to the ground state. This means that, for our model, we have to take the equilibrium value of the constant c. This statement agrees with the conclusion of Klein [5] that "the value of c is related to the equilibrium value of q." Furthermore, it bears a strong resemblance to the stationarity conditions of Kan [20].

Two methods will be used to analyze the spectrum. The first one is the Bohr–Sommerfeld quantization rule

$$\int_{q_1}^{q_2} P(q)\,dq = \pi\hbar\left(n + \frac{1}{2}\right), \quad (32)$$

where q_1 and q_2 are the classical turning points and $P(q) = \sqrt{2m^*(E - V)}$.

The other method was suggested by Cambiaggio [21]. Its idea is in the self-consistency prescription: the input energies must coincide with the Fourier spectrum of the action.

Table 2. Spectra calculated by the Bohr–Sommerfeld (B) and Cambiaggio (C) methods

		$E_1 - E_0$	$E_2 - E_1$	$E_3 - E_2$	$E_4 - E_3$
IIa	B	9.489	9.151	8.749	8.243
	C	9.496	9.166	8.777	8.299
IIb	B	8.557	8.032	–	–
	C	8.572	8.073	–	–
III	B	14.339	13.686	12.858	11.657
	C	14.355	13.723	12.939	11.870

Note: (IIa) $c' = 1$, $\bar{\kappa} = -0.5$, $E_{\mathrm{RPA}} = 9.786$ MeV, $r^2_{\mathrm{eq}} = 1$; (IIb) $c' = 1.05$, $\bar{\kappa} = -0.5$, $E_{\mathrm{RPA}} = 8.975$ MeV, $r^2_{\mathrm{eq}} = 1.053$; (III) $c' = 1$, $\bar{\kappa} = -2$, $E_{\mathrm{RPA}} = 14.891$ MeV, $r^2_{\mathrm{eq}} = 0.64$.

The results strongly depend on the values of c_{eq} and $\bar{\kappa}$. In accordance with the results of the previous analysis, three domains of $\bar{\kappa}$ values must be considered separately: $\bar{\kappa} > 0$, $-1 < \bar{\kappa} < 0$, and $\bar{\kappa} < -1$.

Let us first consider the case of $\bar{\kappa} > 0$. Here, the potential well has infinite walls and a minimum at the point $J = J_0$ (for $c'_{\mathrm{eq}} = 1$), which corresponds to an equilibrium state of a harmonic oscillator; i.e., the inclusion of the residual interaction does not change the equilibrium state of the system that is characterized by the inertia tensor $J_{\mathrm{eq}} = J_0$ and by the energy $E_{\mathrm{eq}} = m\omega^2 J_0$. The spectrum, being infinite, has a very small anharmonicity. The calculations with $\bar{\kappa} = 2$ show that the levels E_n are positioned equidistantly to a good accuracy up to a rather large n. For example, the difference $E_1 - E_0 = 23.984$ MeV nearly coincides with $E_{\mathrm{RPA}} = 23.971$ MeV. A small anharmonicity can be noticed at $n \approx 100$. Thus, the difference $E_{101} - E_{100} = 26.017$ MeV demonstrates the anharmonicity $\mathrm{Anh} = (E_{101} - E_{100} - E_{\mathrm{RPA}})/E_{\mathrm{RPA}} \approx 8\%$.

The second case ($-1 < \bar{\kappa} < 0$) is more interesting. Here, the potential (31) has a minimum at the same point $J = J_0$ (for $c'_{\mathrm{eq}} = 1$), which also corresponds to an equilibrium state of a harmonic oscillator. However, this state is metastable because, now, the potential has a finite-height barrier whose top lies at the point $J = -J_0(1 + \sqrt{1 - 8\bar{\kappa}})/(4\bar{\kappa}) > J_0$. Therefore, the inclusion of the residual interaction with $-1 < \bar{\kappa} < 0$ changes the equilibrium state of the system qualitatively without changing its quantitative characteristics J_{eq} and E_{eq}. The barrier height decreases from ∞ to 0 when $\bar{\kappa}$ changes from 0 to -1. Hence, the anharmonicity can be rather large when $\bar{\kappa}$ is close to -1. For example, the barrier height is about 50 MeV

at $\bar{\kappa} = -0.5$ and $c'_{\rm eq} = 1$. The potential well has four bound states, and the deviation of the spectrum from an equidistant one is appreciable right from the beginning (Table 2). Taking $c'_{\rm eq} = 1.05$, one obtains the barrier of height about 22 MeV. The potential has only two bound states and the anharmonicity slightly increases (Table 2).

The third case ($\bar{\kappa} < -1$) is of special interest because this potential has a maximum at $J = J_0$ (for $c'_{\rm eq} = 1$). Its minimum lies at $J = J_{\rm eq} = -J_0(1 + \sqrt{1 - 8\bar{\kappa}})/(4\bar{\kappa}) < J_0$. The well depth (or barrier height) increases from 0 to ∞ when $\bar{\kappa}$ changes from -1 to $-\infty$. Hence, a remarkable anharmonicity can be observed in the vicinity of $\bar{\kappa} = -1$. For example, the well depth is about 67 MeV at $\bar{\kappa} = -2$. Here, there are four bound states, and the deviation of the spectrum from an equidistant one is strong, precisely as in the preceding case, even for low-lying states (Table 2).

It is seen from Table 2 that the results found by the Bohr–Sommerfeld and Cambiaggio methods are quite close, the difference between them increasing together with the anharmonicity. This behavior is naturally explained by the fact that both methods are approximate ones.

4. CONCLUSION

Let us list the main results of this study.

The classical and quantum aspects of the analytically solvable one-dimensional monopole model of Suzuki have been revisited. The set of nonlinear dynamical equations for monopole collective characteristics of a nucleus has been derived from the time-dependent Hartree–Fock equation by using the method of the Wigner function moments. This method reproduces the exact results for the collective properties of the model. It allows one to perform a more extensive analysis of the classical aspects of the problem and to look at the model from new sides (c dependence of the solutions of the equations of motion). The collective Hamiltonian that generates these equations has been constructed. It has been shown that the anharmonicity of the collective spectrum, being a specific property of quantum systems, cannot be observed in classical ones. The Hamiltonian has been quantized by two methods. The choice of initial conditions that is necessary for quantization of the model has been established. The calculations have shown that the anharmonicity of quantum spectra depends strongly on the strength constant of the residual interaction, being negligible for $\kappa > 0$ and rather large for $\kappa < 0$.

REFERENCES

1. T. Suzuki, Nucl. Phys. A **217**, 182 (1973).
2. V. S. Popov and A. M. Perelomov, Zh. Éksp. Teor. Fiz. **56**, 1375 (1969) [Sov. Phys. JETP **29**, 738 (1969)].
3. J. P. Blaizot and H. Schulz, Nucl. Phys. A **377**, 237 (1982).
4. H. Reinhardt and H. Schulz, Nucl. Phys. A **391**, 36 (1982).
5. A. Klein, Nucl. Phys. A **431**, 90 (1984).
6. M. W. Kirson, Nucl. Phys. A **317**, 388 (1979).
7. N. Frascaria, Nucl. Phys. A **482**, 245c (1988).
8. Ph. Chomaz and N. Frascaria, Phys. Rep. **252**, 278 (1995).
9. H. Emling, Prog. Part. Nucl. Phys. **33**, 729 (1994).
10. E. Wigner, Phys. Rev. **40**, 749 (1932).
11. P. Ring and P. Schuck, *The Nuclear Many Body Problem* (Springer-Verlag, Berlin, 1980).
12. H. J. Groenewold, Physica **12**, 405 (1946); J. E. Moyal, Proc. Cambridge Philos. Soc. **45**, 99 (1949).
13. E. B. Balbutsev *et al.,* Phys. Lett. B **105B**, 84 (1981).
14. E. B. Balbutsev, Fiz. Élem. Chastits At. Yadra **22**, 333 (1991) [Sov. J. Part. Nucl. **22**, 159 (1991)].
15. S. Chandrasekhar, *Ellipsoidal Figures of Equilibrium* (Yale Univ. Press, New Haven, 1969; Mir, Moscow, 1973).
16. V. I. Smirnov, *Course of Higher Mathematics* (Fizmatgiz, Moscow, 1958; Addison-Wesley, Reading, 1964), Vol. 3, Part 2.
17. I. S. Gradshteyn and I. M. Ryzhik, *Table of Integrals, Series, and Products* (Fizmatgiz, Moscow, 1962; Academic, New York, 1980).
18. W. Pauli, in *Handbuch der Physik* (Springer-Verlag, Berlin, 1933), Vol. 24, Part 1.
19. A. Bohr, K. Dan. Vidensk. Selsk. Mat. Fys. Medd. **26**, 14 (1952).
20. Kit-Keung Kan, Phys. Rev. A **24**, 2831 (1981).
21. M. C. Cambiaggio, in *Proceedings of International Conference "The Building Blocks of Nuclear Structure," Amalfi, Italy, 1992,* Ed. by A. Covello (World Sci., Singapore, 1993), p. 293.

Physics of Atomic Nuclei, Vol. 65, No. 1, 2002, pp. 65–68. From Yadernaya Fizika, Vol. 65, No. 1, 2002, pp. 68–72.
Original English Text Copyright © 2002 by Kolomietz, Shlomo.

NUCLEI
Theory

Surface Instability of a Nuclear Fermi Liquid Drop*

V. M. Kolomietz and S. Shlomo[1)]

Institute for Nuclear Research, National Academy of Sciences of Ukraine, pr. Nauki 47, Kiev, 252028 Ukraine

Received November 29, 2000

Abstract—A mechanical instability of an incompressible Fermi liquid drop with respect to surface distortions is considered. It is shown that the Fermi surface distortion (FSD) reduces the instability-growth rate for surface fluctuations due to its effects on both the viscosity and the increase in the stiffness coefficient. The dependence of the limiting temperature $T_{\rm lim}$ on the mass number and the multipolarity of the nuclear-surface distortion is calculated. It is shown that $T_{\rm lim}$ is not influenced by the FSD effect.
© *2002 MAIK "Nauka/Interperiodica".*

1. INTRODUCTION

With increasing internal excitation energy (temperature), an incompressible liquid drop reaches the region of mechanical instability with respect to shape fluctuations. The process of instability development is a complicated one. Both finite-size and memory and temperature effects in the collision integral influence strongly the rate of instability growth in a nuclear liquid drop [1, 2]. A realistic charged nuclear liquid drop becomes unstable at a limiting temperature $T_{\rm lim}$ that is significantly lower than the critical temperature T_c of the liquid–gas phase transition [3–8]. In the case of an incompressible and charged liquid, the limiting temperature is derived by the balance of the Coulomb and the surface energy and depends on the temperature behavior (critical exponent) of the surface tension in the vicinity of the critical temperature. In the present study, we analyze the instability-growth rate and the limiting temperature using a simple Fermi liquid–drop model with a sharp edge. The limiting temperature and the transition to an unstable regime are derived by the condition of the disappearance of the stiffness coefficient with respect to a small surface distortion of multipolarity L. In our model for the surface instability of finite nuclei, we assume an incompressible and uniformly charged liquid drop with temperature-dependent surface and Coulomb energies. This model is adequate to give general information about the A and L dependence of the limiting temperature and about the role of Fermi surface–distortion effects on the surface instability of finite nuclei. In Section 2, we derive the instability-growth rate for a hot and viscous Fermi liquid drop. In Section 3, we calculate the A dependence of the limiting temperature for various multipolarities L of the surface distortion and for various values of the surface critical exponent.

2. INSTABILITY-GROWTH RATE FOR SURFACE DISTORTIONS

We will consider small surface fluctuations of an incompressible Fermi liquid drop, assuming a time variation of the particle density in the form

$$\rho(t) = \rho_0 \Theta(R(t) - r), \tag{1}$$

where ρ_0 is the bulk density and the nuclear radius $R(t)$ is given by

$$R(t) = R_0 \left[1 + \sum_{LM} \beta_{LM}(t) Y_{LM} \right], \tag{2}$$

with $\beta_{LM}(t)$ being a small dimensionless parameter. In the present study, we concentrate on the surface instability with respect to small isoscalar fluctuations of the shape parameter $\beta_{LM}(t)$ only. Such a kind of instability is related to the surface stiffness coefficient of a nuclear liquid drop. We will not consider here the isovector mode and the corresponding instability, which are related to the symmetry energy. The linearized equation of motion for the collective variables $\beta_{LM}(t)$ can be directly derived from the collision kinetic equation under the assumption of a quadrupole distortion of the Fermi surface (fluid-dynamics approximation) and has the form (see [9–11])

$$-\omega^2 B_L \beta_{LM,\omega} + \left(C_L^{(\rm LD)} + \widetilde{C}_L(\omega) \right) \beta_{LM,\omega} = 0. \tag{3}$$

The collective mass B_L and the stiffness coefficient $C_L^{(\rm LD)}$ are given by the traditional liquid-drop model [12, 13]. Namely,we have

$$B_L = \frac{3}{4\pi L} A m R_0^2, \tag{4}$$

*This article was submitted by the authors in English.

[1)]Cyclotron Institute, Texas A&M University, College Station, TX 77843-4242 USA.

$$C_L^{(\mathrm{LD})} = \frac{1}{4\pi}(L-1)(L+2)b_S A^{2/3} - \frac{5}{2\pi}\,\frac{L-1}{2L+1}b_{\mathrm{C}}\frac{Z^2}{A^{1/3}},$$

where b_S and b_{C} are, respectively, the surface-energy and Coulomb energy coefficients appearing in the nuclear-mass formula and R_0 is the radius of the nucleus. The additional contribution $\widetilde{C}_L(\omega)$ to the stiffness coefficient in Eq. (3) is due to the dynamical Fermi surface distortion. It is given by [9]

$$\widetilde{C}_L(\omega) = \frac{-i\omega\tau}{1-i\omega\tau}d_L P_{\mathrm{eq}}, \tag{5}$$

where information about the multipolarity is in

$$d_L = 2\frac{(L-1)(2L+1)}{L}R_0^3. \tag{6}$$

Here, τ is the relaxation time and P_{eq} the equilibrium pressure of a Fermi gas,

$$P_{\mathrm{eq}} \approx \rho_0 p_{\mathrm{F}}^2/5m,$$

where p_{F} is the Fermi momentum.

We point out that Eqs. (3) and (5) can be established by means of a direct algebraic transformation of the collision kinetic equation in the case of an incompressible and irrotational liquid (see [9, 10]). The ω dependence of the stiffness coefficient $\widetilde{C}_L(\omega)$ in Eq. (5) reflects memory effects due to the collision integral. In the rare-collision regime, $\omega\tau \gg 1$, the contribution of $\widetilde{C}_L(\omega)$ exceeds significantly the liquid drop term $C_L^{(\mathrm{LD})}$ in Eq. (3) and provides a correct description of the isoscalar multipole giant resonances in cold nuclei (see [10]) and a correct zero-to-first-sound transition in heated nuclei (see [9, 11, 14]). In this respect, our approach is applicable to nuclei. Notice also that, from the point of view of quantum theory, like the random-phase approximation (RPA) or the time-dependent Hartree–Fock (TDHF) approximation, the terms $C_L^{(\mathrm{LD})}$ and $\widetilde{C}_L(\omega)$ are both caused (at $\omega\tau \gg 1$) by the long-range (zero-sound) correlations through a self-consistent mean field. That the term $\widetilde{C}_L(\omega)$ appears owing to the Fermi surface–distortion effect only and that it disappears in the frequent-collision limit at $\omega\tau \ll 1$ are, however, important features of this term. We want to stress that Eqs. (3) and (5) are valid for arbitrary relaxation times τ and describe both the rare- and the frequent-interparticle-collision limit, as well as the intermediate case. Thus, the term $\widetilde{C}_L(\omega)$ takes into account long-range (mean-field) correlations in the case of pure zero-sound regime, $\omega\tau \gg 1$, and the collision (two-body) viscosity in all intermediate cases of $\omega\tau$. Moreover, depending on the derivation of the relaxation time τ in Eq. (5), the term $\widetilde{C}_L(\omega)$ takes into account one- or two-body dissipation, temperature effects, etc. (see [14]). The equations of motion (3) and Eq. (5) are obtained as the semiclassical and fluid-dynamics [15] approximation to the collision kinetic equation for an incompressible Fermi liquid (see [9]).

In the case of a stable mode, $\mathrm{Im}(\omega) > 0$, Eq. (3) describes a damped capillary excitation at the surface of the Fermi liquid drop. The corresponding secular equation has the form [9]

$$-\omega^2 B_L + C_L^{(\mathrm{LD})} + C'_L(\omega) - i\omega\gamma_L(\omega) = 0, \tag{7}$$

where $\gamma_L(\omega)$ is the friction coefficient,

$$\gamma_L(\omega) = \mathrm{Re}\Big(\frac{\tau}{1-i\omega\tau}\Big)d_L P_{\mathrm{eq}}, \tag{8}$$

and

$$C'_L(\omega) = \mathrm{Im}\Big(\frac{\omega\tau}{1-i\omega\tau}\Big)d_L P_{\mathrm{eq}}. \tag{9}$$

The additional contribution $C'_L(\omega)$ to the stiffness coefficient in Eq. (7) disappears in the frequent-collision (first-sound) regime for $\mathrm{Re}(\omega)\tau \to 0$.

Important information concerning the instability of hot nuclei can be obtained from a thermodynamic consideration through the evaluation of the free energy and the equation of state in some appropriate models (see [4] and references therein). In the present study, we use the dynamical approach to instability, considering a mechanical instability with respect to surface fluctuations. An advantage of this approach is that we are able to take into consideration several important aspects of nuclear instability that cannot be studied within thermodynamic approaches—namely, (i) the influence of Fermi surface–distortion effects on the instability-growth rate, (ii) the influence of memory effects in nuclear friction on the development of instability, and (iii) the dependence of the limiting temperature on the multipolarity L of the deformation of the nuclear surface. Let us consider the surface-instability regime, $C_L^{(\mathrm{LD})} < 0$. The growth rate $\Gamma = -i\omega$ (Γ is real, $\Gamma > 0$) can be found from Eq. (7) and is given by

$$\Gamma_L^2 = {\Gamma_L^{(\mathrm{LD})}}^2 - \zeta_L(\Gamma_L), \tag{10}$$

where

$$\Gamma_L^{(\mathrm{LD})} = \sqrt{|C^{(\mathrm{LD})}|/B_L} \tag{11}$$

and

$$\zeta_L(\Gamma_L) = \frac{\Gamma_L\tau}{1+\Gamma_L\tau}\frac{d_L P_{\mathrm{eq}}}{B_L}. \tag{12}$$

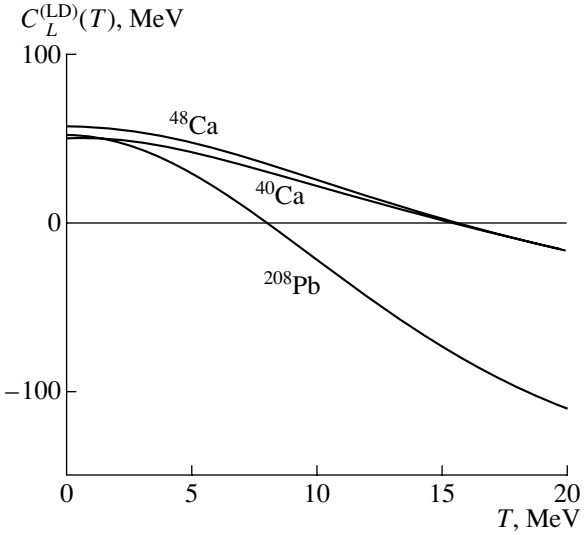

Fig. 1. Temperature dependence of the LDM stiffness coefficient $C_L^{(\mathrm{LD})}$ for a quadrupole surface deformation ($L = 2$). The nuclei being considered are indicated near the corresponding curves.

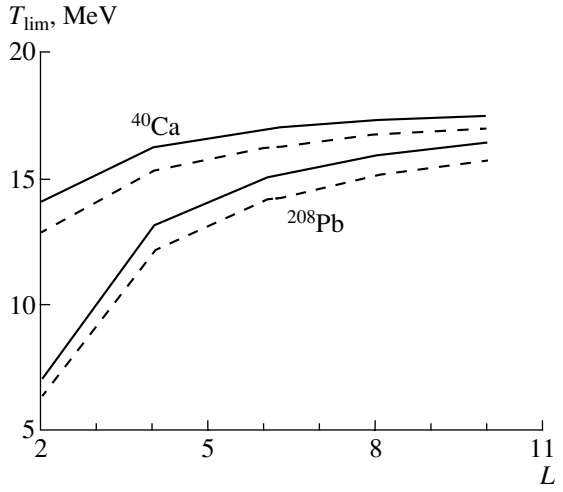

Fig. 2. Limiting temperature T_{lim} as a function of the multipolarity L of the surface deformation for the ^{208}Pb and ^{40}Ca nuclei. The solid curve is for the critical exponent of $\nu = 1.25$, and the dashed curve is for $\nu = 1.5$.

2.1. Frequent-Collision Regime: $\tau\Gamma_L \to 0$

The perturbation-theory solution to Eq. (10) has the form

$$\Gamma_L \approx \Gamma_L^{(\mathrm{LD})}\left(1 - \frac{\tau d_L P_{\mathrm{eq}}}{2B_L\Gamma_L^{(\mathrm{LD})}}\right). \qquad (13)$$

Thus, in the frequent-collision regime, the Fermi surface distortion influences the instability-growth rate Γ_L through interparticle collisions only. As can be seen from Eqs. (13), (11), (6), and (4), the instability-growth rate decreases with increasing L. Relaxation processes reduce slightly the surface instability due to the second term on the right-hand side of Eq. (13).

2.2. Rare-Collision Regime: $\tau\Gamma_L \to \infty$

The secular Eq. (10) reduces to the form

$$\Gamma_L^2 = \Gamma_L^{(\mathrm{LD})^2} - \frac{d_L P_{\mathrm{eq}}}{B_L}. \qquad (14)$$

We point out that the second term on the right-hand side of Eq. (14) is due to the Fermi surface–distortion effects. This term reduces significantly the instability-growth rate Γ_L with respect to that, $\Gamma_L^{(\mathrm{LD})}$, given by the liquid-drop model.

3. LIMITING TEMPERATURE: NUMERICAL ILLUSTRATIONS AND DISCUSSION

For the numerical calculations performed in this study, we assume a temperature dependence of the surface and Coulomb parameters in the liquid-drop stiffness coefficient $C_L^{(\mathrm{LD})}$ of Eq. (4) [16, 17]:

$$b_S = 17.2\frac{16 + C_i}{x_i^{-3} + C_i + (1 - x_i)^{-3}} \times \left(\frac{T_c^2(x_i) - T^2}{T_c^2(x_i) + a(x_i)T^2}\right)^{\nu} \ (\mathrm{MeV}), \qquad (15)$$

$$b_c = 0.7(1 - x_{\mathrm{C}}T^2) \ (\mathrm{MeV}),$$

where (see [17]) $a(x_i) = a_0 + a_2y^2 + a_4y^4$, $y = 0.5 - x_i$, $C_i = 24.4$, $a_0 = 0.935$, $a_2 = -5.1$, $a_4 = -1.1$, and the parameter x_{C} was chosen to be $x_{\mathrm{C}} = 0.76 \times 10^{-3}$ MeV^{-2} [16]. The dependence of the critical temperature $T_c(x_i)$ on the asymmetry parameter x_i was taken in the form $T_c(x_i) = T_c[1 - cy^2 - dy^4]$, with $c = 3.31$ and $d = 7.36$, and $T_c = 18$ MeV is the critical temperature for infinite nuclear Fermi liquid [17]. We performed our numerical calculations for two values of the surface critical exponent, $\nu = 1.25$ and $\nu = 1.5$. The corrected asymmetry parameter $x_i \approx Z/A$ for certain nuclei was taken from [17]. We point out that, due to the temperature dependence of the surface and Coulomb parameters b_S and b_{C} in Eq. (15), our model takes into consideration the temperature dependence of the bulk particle density ρ_0. Indeed, the temperature dependence of both parameters b_S and b_{C} has been established from a fit to the self-consistent calculations of the free energy in the temperature-dependent Thomas–Fermi model,

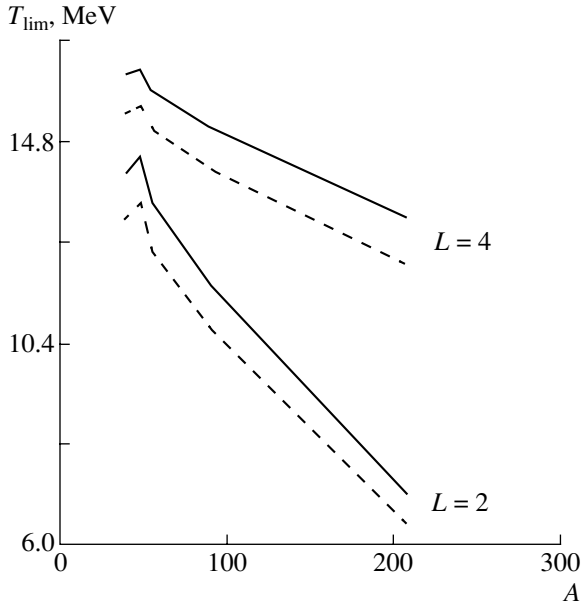

Fig. 3. Limiting temperature $T_{\rm lim}$ as a function of the mass number A for $L = 2$ and $L = 4$ deformations of the nuclear surface. The solid curve is for the critical exponent of $\nu = 1.25$, and the dashed curve is for $\nu = 1.5$.

where the temperature dependence of the particle density is taken into account automatically. Moreover, the temperature dependence of the Coulomb parameter b_C in Eq. (15) is in fact due to the radial blow up of the nucleus by temperature.

The temperature dependence of the LDM stiffness coefficient $C_L^{(\rm LD)}$ is shown in Fig. 1 for a quadrupole surface distortion ($L = 2$). The T dependence of $C_L^{(\rm LD)}$ is significantly stronger for heavy nuclei because of the balance of the larger surface and Coulomb terms in Eq. (4) in these nuclei.

Using Eq. (15), one can find the limiting temperature $T_{\rm lim}$ at which the liquid-drop contribution $C_L^{(\rm LD)}$ to the stiffness coefficient vanishes:

$$C_L^{(\rm LD)} \equiv C_L^{(\rm LD)}(T)\Big|_{T=T_{\rm lim}} = 0.$$

For temperatures $T > T_{\rm lim}$, the nucleus is unstable with respect to surface distortions. The limiting temperature $T_{\rm lim}$ depends on the mass number A and on the multipolarity L of the surface distortion. In Fig. 2, the L dependence of $T_{\rm lim}$ is shown for the ^{208}Pb and ^{40}Ca nuclei. An increase in the limiting temperature with L means that the yield of small clusters (high L) caused by the surface instability of the nucleus increases with T. The A dependence of the limiting temperature $T_{\rm lim}$ for $L = 2$ and $L = 4$ and for two values of the surface critical exponent ν is plotted in Fig. 3. This A dependence becomes weaker with increasing L.

We point out that Figs. 2 and 3 were obtained within the liquid-drop model, Fermi surface–distortion effects being neglected. However, as can be seen from Eqs. (10) and (12), the general condition of the development of the instability given by $\Gamma_L = 0$ coincides with the same condition $\Gamma_L^{(\rm LD)} = 0$ for the liquid-drop model. Therefore, the limiting temperature $T_{\rm lim}$ should be the same in both cases, and Figs. 2 and 3 are applicable to the Fermi liquid drop as well.

ACKNOWLEDGMENTS

V.M. Kolomietz thanks the Cyclotron Institute at the Texas A&M University for the kind hospitality.

This work was supported in part by the US Department of Energy under grant no. DOE-FG03-93ER40773 and by INTAS under grant no. 93-0151.

REFERENCES

1. C. J. Pethick and D. G. Ravenhall, Nucl. Phys. A **471**, 19c (1987).
2. V. M. Kolomietz and S. Shlomo, Phys. Rev. C **60**, 044612 (1999).
3. P. Bonche, S. Levit, and D. Vautherin, Nucl. Phys. A **436**, 265 (1985).
4. S. Levit and P. Bonche, Nucl. Phys. A **437**, 426 (1985).
5. D. Bandyopadhyay, J. N. De, S. K. Samaddar, and D. Sperber, Phys. Lett. B **218**, 391 (1989).
6. J. N. De, D. Bandyopadhyay, S. K. Samaddar, and N. Rudra, Nucl. Phys. A **534**, 294 (1991).
7. H. Q. Song and R. K. Su, Phys. Rev. C **44**, 2505 (1991).
8. Y. J. Zhang, R. K. Su, H. Q. Song, and F. M. Lin, Phys. Rev. C **54**, 1137 (1996).
9. D. Kiderlen, V. M. Kolomietz, and S. Shlomo, Nucl. Phys. A **608**, 32 (1996).
10. J. R. Nix and A. J. Sierk, Phys. Rev. C **21**, 396 (1980).
11. V. M. Kolomietz, V. A. Plujko, and S. Shlomo, Phys. Rev. C **52**, 2480 (1995).
12. H. Lamb, *Hydrodynamics* (Dover, New York, 1945).
13. A. Bohr and B. R. Mottelson, *Nuclear Structure*, Vol. 2: *Nuclear Deformations* (Benjamin, New York, 1975; Mir, Moscow, 1977).
14. V. M. Kolomietz, V. A. Plujko, and S. Shlomo, Phys. Rev. C **54**, 3014 (1996).
15. G. Holzwarth and G. Eckart, Z. Phys. A **284**, 291 (1978).
16. C. Guet, E. Strumberger, and M. Brack, Phys. Lett. B **205**, 427 (1988).
17. D. G. Ravenhall, C. J. Pethick, and J. M. Lattimer, Nucl. Phys. A **407**, 571 (1983).

Physics of Atomic Nuclei, Vol. 65, No. 1, 2002, pp. 69–74. Translated from Yadernaya Fizika, Vol. 65, No. 1, 2002, pp. 73–78.
Original Russian Text Copyright © 2002 by Filippov, Lashko.

NUCLEI
Theory

Energy and Angular Distributions in ^{6}He Photodisintegration

G. F. Filippov* **and Yu. A. Lashko**

Bogolyubov Institute for Theoretical Physics, National Academy of Sciences of Ukraine, Metrologicheskaya ul. 14b, Kiev, 252143 Ukraine

Received September 28, 2000

Abstract—Energy and angular distributions of the neutrons and the α particle from the reaction ^{6}He(γ, 2n)^{4}He is examined in the minimal approximation of the hyperspherical-function method in the algebraic version of the resonating-group method. The differential cross section for ^{6}He photodisintegration is calculated as a function of the energies of the product particles, the angles between their momenta, and their emission angles with respect to the incident-photon momentum. © *2002 MAIK "Nauka/Interperiodica".*

1. INTRODUCTION

Since facilities employing intense beams of ^{6}He ions are expected to be commissioned in the near future and are planned to be used to study ^{6}He photodisintegration into an α particle and two neutrons, it is of current interest to analyze theoretically the reaction ^{6}He$(\gamma, 2n)^4$He in order to predict the behavior of the energy and angular distributions of three final particles and to reveal basic factors that control the dependence of the differential cross section on the energies of emitted particles and on the direction of their motion.

Three-body ^{6}He disintegration was experimentally observed in various reactions—for example, in the reaction $^6\mathrm{He} \to {}^4\mathrm{He} + n + n$ in the Coulomb field of a lead target [1]. It should be borne in mind that we examine nuclear disintegration by a dipole photon rather than Coulomb excitation in the field of a heavy nucleus, in which case there can occur $E\lambda$, $\lambda \geq 1$, transitions.

Previously, ^{6}He photodisintegration was investigated theoretically in [2] and in [3], where the photon-energy dependence of the $E1$-transition matrix element was found among other things. In this study, we aim at determining the photodisintegration cross section as a function of the energies of final particles and their emission angles with respect to the incident-photon momentum, as well as of the angles between the final-particle momenta.

As in [3], we apply the algebraic version of the resonating-group model and the asymptotic-potential approximation. The ^{6}He nucleus is treated as a system of three loosely bound clusters into which it decays above the $^6\mathrm{He} \to \alpha + n + n$ threshold. For its ground (0^+) state, the wave function is represented as a superposition of the hyperspherical harmonics corresponding to the grand-orbital values of $K = 0$ and 2 that is allowed by the Pauli exclusion principle; the wave functions for the 1^- continuum states into which the $E1$ transitions occur are constructed as an allowed superposition of the $K = 1$ and 3 hyperspherical harmonics.

First, we discuss some features of the three-body decay of a nuclear system that distinguish it from two-body decays. In the latter case, the angular distribution with respect to a specified direction is the only characteristic of the system at a given energy. In analyzing a three-body decay process at a given energy of the system being considered, it is necessary to determine not only the emission probability for each of the three product particles as a function of the direction of its momentum with respect to both a specified direction and directions of the momenta of the remaining final particles but also the energy distribution of this particle.

To answer the questions that arise in analyzing three-body decay, we first consider phase space and, taking into account all constraints imposed by conservation laws, find the region of allowed values of the momenta and energy of the emitted particles; after that, we represent the phase-space element in a form that is the most convenient for practical applications (Section 2). As a result, we obtain the contribution of the phase-space volume to the energy and angular distributions, a factor that is indeed of importance for further calculations.

The second factor that must be taken into account is the squared matrix element of the electric-dipole-transition operator. This matrix element relates the

*e-mail: gfilippov@gluk.apc.org

wave function for the ^{6}He ground state to continuum-state wave functions. For this reason, the next stage of the calculations (Section 3) is devoted to analyzing the wave functions constructed for the 1^- continuum states of the ^{6}He nucleus as an expansion in the harmonic-oscillator basis. The simple example of a six-dimensional plane wave demonstrates that not only the functions of the harmonic-oscillator basis but also the coefficients in the expansion of solutions to the Schrödinger equation in this basis are expressed in terms of hyperspherical functions and depend on the momenta of diverging particles. The reduction of hyperspherical harmonics to bispherical functions is a means to separate the variables that specify the spatial orientation of the entire three-cluster system from variables characterizing both the absolute value of the momentum of each cluster and the direction of this momentum with respect to the momenta of the other two clusters. As a result, we reveal the importance of the hyperspherical harmonics for determining the angular and energy distributions.

2. MOMENTA OF CLUSTERS IN THEIR c.m. FRAME

Let us begin by considering the kinetic energy T of the system formed by an alpha particle and two neutrons. We denote by $\mathbf{p}_1$ the momentum of the alpha particle and by $\mathbf{p}_2$ and $\mathbf{p}_3$ the momenta of the two neutrons. We then have

$$T = \frac{\mathbf{p}_1^2}{8} + \frac{\mathbf{p}_2^2}{2} + \frac{\mathbf{p}_3^2}{2}, \tag{1}$$

where the neutron mass is set to unity, whereupon the alpha-particle mass takes the value of 4. Since ^{6}He photodisintegration is analyzed here above the threshold for three-body decay, the energy E is fixed and equal to T at long distances between the particles. This energy is defined in the c.m. frame, where

$$\mathbf{p}_1 + \mathbf{p}_2 + \mathbf{p}_3 = 0. \tag{2}$$

It is appropriate to exclude $\mathbf{p}_3$ from the right-hand side of Eq. (1) by using Eq. (2) and substitute E for T on the left-hand side of Eq. (1). The remaining two vector variables are related as

$$E = \frac{\mathbf{p}_1^2}{8} + \frac{\mathbf{p}_2^2}{2} + \frac{(\mathbf{p}_1 + \mathbf{p}_2)^2}{2}. \tag{3}$$

In order to calculate the energy and angular distributions, it is necessary to determine the density $d\rho_f$ of states per unit energy in phase space. It is convenient to introduce the vectors

$$\mathbf{k}_1 = \frac{1}{\sqrt{3}}\left(\frac{\mathbf{p}_1}{2} - \mathbf{p}_2 - \mathbf{p}_3\right) = \frac{\sqrt{3}}{2}\mathbf{p}_1,$$

$$\mathbf{k}_2 = \frac{1}{\sqrt{2}}(\mathbf{p}_2 - \mathbf{p}_3) = \frac{1}{\sqrt{2}}(\mathbf{p}_1 + 2\mathbf{p}_2)$$

in the c.m. frame, which are defined in such a way that the reduced masses corresponding to them are equal to unity. In terms of these vectors, the energy is expressed as

$$\frac{\mathbf{k}_1^2}{2} + \frac{\mathbf{k}_2^2}{2} = E = \frac{k^2}{2}. \tag{4}$$

As a result, many relations are simplified. In particular, we have

$$d\rho_f = \frac{d\,\mathbf{k}_1 d\,\mathbf{k}_2}{(2\pi)^6 dE}. \tag{5}$$

It follows from Eq. (4) that

$$k_1 = k\cos\alpha, \quad k_2 = k\sin\alpha, \quad 0 \le \alpha \le \pi/2. \tag{6}$$

We also note that

$$\mathbf{p}_1 = \frac{2}{\sqrt{3}}\,\mathbf{k}_1, \quad \mathbf{p}_2 = \frac{1}{\sqrt{2}}\,\mathbf{k}_2 - \frac{1}{\sqrt{3}}\mathbf{k}_1. \tag{7}$$

The quantities p_1 and p_2 are related to α and t as

$$p_1 = \frac{2}{\sqrt{3}}\,k\cos\alpha, \tag{8}$$

$$p_2 = k\sqrt{\frac{5 - \cos 2\alpha}{12} - \frac{1}{\sqrt{6}}\,\sin 2\alpha \times t},$$

where $t = (\mathbf{k}_1 \cdot \mathbf{k}_2)/k_1 k_2$. Therefore, the α-particle energy E_1 and the energy E_2 of one of the neutrons can be represented as

$$E_1 = \frac{k^2}{6}\cos^2\alpha, \tag{9}$$

$$E_2 = \frac{k^2}{24}(5 - \cos 2\alpha - 2\sqrt{6}\,t\sin 2\alpha).$$

From (9), it immediately follows that the domain of the allowed E_1 and E_2 values is within a loop referred to as a "kinematical locus" or a Dalitz plot [4]. This region, whose lower and upper boundaries correspond to $t = 1$ and -1, respectively, is specified by the inequalities

$$0 \le E_1 \le \frac{k^2}{6},$$

$$\frac{5k^2}{12}\sin^2(\alpha - \alpha_0) \le E_2 \le \frac{5k^2}{12}\sin^2(\alpha + \alpha_0),$$

where $\sin\alpha_0 = \sqrt{2/5}$ and $\cos\alpha_0 = \sqrt{3/5}$.

Figure 1 shows that the locus in the (E_1, E_2) plane is an oval tangent to the E_2 and the E_1 axis at the points where $\alpha = \pi/2$ and α_0, respectively.

From the energy-conservation law

$$k_1^2 + k_2^2 = \frac{5}{4}p_1^2 + 2p_2^2 + 2(\mathbf{p}_1 \cdot \mathbf{p}_2) = k^2,$$

it follows that the cosine of the angle between the vectors $\mathbf{p}_1$ and $\mathbf{p}_2$ is

$$\tau = \frac{(\mathbf{p}_1 \cdot \mathbf{p}_2)}{p_1 p_2} = \frac{k^2 - 5/4 \times p_1^2 - 2p_2^2}{2p_1 p_2} \tag{10}$$

$$= \frac{-2\cos\alpha + \sqrt{6}\sin\alpha \times t}{\sqrt{5 - 2\cos 2\alpha - 2\sqrt{6}\sin 2\alpha \times t}}.$$

Each point in the locus corresponds to specific values of the momentum and energy of the α particle and each of the two neutrons. In particular, the point a, where $\alpha = \pi/2$, corresponds to the alpha particle at rest and the neutrons having the energy $k^2/4$ and moving in opposite directions. A neutron has the maximum energy of $5k^2/12$ at $\alpha = \pi/2 - \alpha_0$ (point b). In this case, $\tau = -1$; that is, the alpha particle, whose energy is $k^2/15$, and the second neutron move in the opposite direction. Yet another noteworthy point is c, where $\alpha = 0$. In this case, the alpha-particle energy attains its maximum value of $k^2/6$ and is equal to the energy of each of the two neutrons moving together in the direction opposite to that of the alpha particle ($\tau = -1$ again). In the situation corresponding to the point d, where $\alpha = \alpha_0$, one neutron is at rest and the energies of the alpha particle and the second neutron are $k^2/10$ and $2k^2/5$, respectively.

As a result, the number of states per unit phase-space volume is

$$d\rho_f = \left(\frac{3}{2}\right)^{3/2} \frac{d\mathbf{p}_1 d\mathbf{p}_2}{(2\pi)^6 dE}$$

$$= \left(\frac{3}{2}\right)^{3/2} \frac{p_1^2 dp_1 p_2^2 dp_2 d\Omega_1 d\Omega_2}{(2\pi)^6 dE},$$

where Ω_1 and Ω_2 are the angles specifying the directions of the vectors $\mathbf{p}_i$ and $\mathbf{p}_2$, respectively. We define these angles in the coordinate system where the z axis is aligned with the vector $\mathbf{p}_1$. Therefore, we have

$$d\Omega_2 = d\tau d\phi_2,$$

where the angle ϕ_2 specifies the rotation of the plane spanned by the vectors $\mathbf{p}_1$ and $\mathbf{p}_2$ about the vector $\mathbf{p}_1$. We then have

$$d\rho_f = \left(\frac{3}{2}\right)^{3/2} \frac{p_1 dp_1 p_2 dp_2}{(2\pi)^6} d\Omega_1 d\phi_2 \qquad (11)$$

$$= 4\left(\frac{3}{2}\right)^{3/2} \frac{dE_1 dE_2}{(2\pi)^6} \sin\theta_1 d\theta_1 d\phi_1 d\phi_2.$$

The angular distributions in the three-body decay of ^{6}He will be analyzed in terms of the angles θ_1, ϕ_1, and ϕ_2, which specify the spatial orientations of the set of the vectors $\mathbf{p}_1$ and $\mathbf{p}_2$, and the cosine τ of the angle between these vectors. The energy distribution is characterized by a function that depends on the above angle α and which is to be determined. As a matter of fact, these are five independent variables of hyperspherical harmonics in the momentum representation. In order to determine the angular and energy distributions in question, it is therefore sufficient

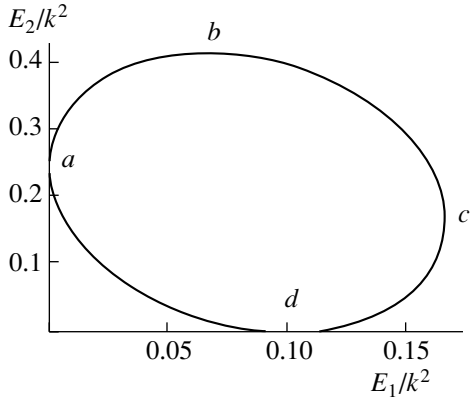

Fig. 1. Region of allowed values of the energies E_1 and E_2 (points a, b, c, and d correspond to $\alpha = \pi/2, \pi/2 - \alpha_0, 0$, and α_0, respectively).

to find the weight coefficients of the hyperspherical harmonics entering into the wave functions for those 1^- states of the ^{6}He continuum that are related to the ground state by the $E1$-transition operator.

Later, we will return to the expression for $d\rho_f$; for now, we proceed to analyze the wave functions for the states of our interest and the matrix elements of the $E1$-transition operator.

3. WAVE FUNCTION FOR THE ^{6}He GROUND STATE

As in [3], the wave function $\Psi(0^+)$ for the ^{6}He ground state is represented as an expansion in the harmonic-oscillator basis states $\Psi_\nu(0^+)$. Each of these is a superposition of the $K = 0$ and 2 hyperspherical harmonics:

$$\Psi(0^+) = \sum_{\nu=0}^{\infty} C_\nu(0^+)\Psi_\nu(0^+), \qquad (12)$$

$$\Psi_\nu(0^+) = N_\nu^+(3a^2 - 2b^2)(a^2 + b^2)^\nu,$$

$$N_\nu^+ = \frac{1}{2^\nu}\sqrt{\frac{4}{(29\nu + 104)\nu!(\nu + 3)!}}.$$

Here, ν is the number of oscillator excitation quanta of the basis function (this number is measured from the minimal number equal to two; that is, $\nu = 0$ corresponds to two oscillator quanta), and a and b are the lengths of the Jacobi vectors $\mathbf{a}$ and $\mathbf{b}$ that are defined in the c.m. frame in Fock–Bargmann space and which are related to the complex vector parameters $\mathbf{R}_i$, $i = 1, 2, 3$, of the Bloch–Brink orbitals as

$$\mathbf{a} = \sqrt{\frac{2}{3}}\left(\mathbf{R}_1 - \frac{\mathbf{R}_2 - \mathbf{R}_3}{2}\right);$$

$$\mathbf{b} = \frac{1}{\sqrt{2}}(\mathbf{R}_2 - \mathbf{R}_3).$$

The expansion coefficients $C_\nu(0^+)$ were determined by solving the set of the algebraic equations of the asymptotic-potential approximation [3].

4. STRUCTURE OF THE WAVE FUNCTIONS FOR THE 1^- CONTINUUM STATES

In order to analyze the distributions in the energy and the angles of the alpha particle and two neutrons diverging after ^{6}He photodisintegration, we represent the wave functions for the $L^\pi = 1^-,\ S = 0$ continuum states of this nucleus as

$$\Psi(1^-, m) = \sum_{\nu=0}^{\infty} C_\nu(1^-, m; \mathbf{k}_1, \mathbf{k}_2)\Psi_\nu(1^-, m; \mathbf{a}, \mathbf{b}), \tag{13}$$

where the harmonic-oscillator basis functions

$$\begin{aligned}\Psi_\nu(1^-, m; \mathbf{a}, \mathbf{b}) \qquad (14)\\ = N_\nu^-(3a^2 - 2b^2)a_m(a^2 + b^2)^\nu\\ = N_\nu^-(a^2 + b^2)^{\nu+3/2}(3\cos^2\beta\\ - 2\sin^2\beta)\cos\beta\frac{4\pi}{3}Y_{1m}(\Omega_{\mathbf{a}}),\end{aligned}$$

$$N_\nu^- = \frac{1}{2^\nu}\sqrt{\frac{4!}{(13\nu + 38)\nu!(\nu + 4)!}}$$

defined in Fock–Bargmann space are superpositions of the hyperspherical harmonics that are specified by the grand-orbital value of $K = 1$ and 3, the orbital angular momentum of $L = 1$, and its projection m and which are allowed by the Pauli exclusion principle:

$$\begin{aligned}\Psi_\nu(1^-, m; \mathbf{a}, \mathbf{b}) = \frac{1}{2\sqrt{13\nu + 38}}\Big(5\sqrt{\nu + 5}\Psi_{\nu,K=3}^{L=1,m}\\ + 3\sqrt{3(\nu + 1)}\Psi_{\nu+1,K=1}^{L=1,m}\Big).\end{aligned}$$

The angle β is defined in such a way that

$$a^2 = (a^2 + b^2)\cos^2\beta, \quad b^2 = (a^2 + b^2)\sin^2\beta. \tag{15}$$

In turn, we have

$$\begin{aligned}\Psi_{\nu,K=3}^{L=1,m}(\mathbf{a}, \mathbf{b})\\ = \frac{1}{2^\nu}\sqrt{\frac{5!}{(\nu + 5)!\nu!}}\,\frac{1}{4\sqrt{15}}(a^2 + b^2)^\nu(3a^2 - 5b^2)a_m,\end{aligned}$$

$$\begin{aligned}\Psi_{\nu+1,K=1}^{L=1,m}(\mathbf{a}, \mathbf{b})\\ = \frac{1}{2^\nu}\sqrt{\frac{4!}{(\nu + 4)!(\nu + 1)!}}\,\frac{1}{4}(a^2 + b^2)^{\nu+1}a_m.\end{aligned}$$

In [3], use was made of two 1^- states characterized by different sets of grand-orbital values. Here, we restrict ourselves to the simpler single-channel case. The basis wave function (14) is a linear superposition of the basis functions presented in [3].

The coefficients in the expansion in the harmonic-oscillator basis,

$$\begin{aligned}C_\nu(1^-, m; \mathbf{k}_1, \mathbf{k}_2) \qquad (16)\\ = C_\nu(1^-, E)\phi_{1^-,m}(\alpha, \Omega_{\mathbf{k}_1}, \Omega_{\mathbf{k}_2}),\end{aligned}$$

are expressed in terms of the Jacobi momenta $\mathbf{k}_1$ and $\mathbf{k}_2$ and possess the same transformation properties as the basis functions $\Psi_\nu(1^-, m; \mathbf{a}, \mathbf{b})$. In particular, the factor

$$\begin{aligned}\phi_{1^-,m}(\alpha, \Omega_{\mathbf{k}_1}, \Omega_{\mathbf{k}_2}) \qquad (17)\\ = \sqrt{\frac{512}{117\pi}}(3\cos^2\alpha - 2\sin^2\alpha)\\ \times \cos\alpha Y_{1m}^*(\Omega_{\mathbf{k}_1})Y_{00}(\Omega_{\mathbf{k}_2}),\end{aligned}$$

which appears in the expansion coefficients, is a superposition of the $K = 1$ and 3 hyperspherical harmonics in the momentum representation. It differs only in notation from the analogous factor in the basis functions (14) and provides information on the energy and angular distributions of particles. By analogy with Eq. (15), we write

$$k_1 = k\cos\alpha, \quad k_2 = k\sin\alpha, \quad k^2 = k_1^2 + k_2^2, \tag{18}$$

where α is the hyperspherical angle and k is the hyperradius in momentum space. The superposition of hyperspherical harmonics in (17) is normalized in such a way that

$$\begin{aligned}\sum_m \int_0^{\pi/2} \sin^2\alpha\cos^2\alpha d\alpha \qquad (19)\\ \times \int d\Omega_{\mathbf{k}_1}\int d\Omega_{\mathbf{k}_2}|\phi_{1^-,m}(\alpha, \Omega_{\mathbf{k}_1}, \Omega_{\mathbf{k}_2})|^2 = 1.\end{aligned}$$

We now can obtain the differential cross section for the electric-dipole photodisintegration of the ^{6}He nucleus.

5. DIFFERENTIAL CROSS SECTION FOR THE $E1$ PHOTODISINTEGRATION OF THE ^{6}He NUCLEUS

The differential cross section for ^{6}He photodisintegration is given by

$$d\sigma_f = \frac{4\pi^3}{9c}d\rho_f\omega \times B(E1), \tag{20}$$

where $\hbar\omega$ is the energy of the photon absorbed by the nucleus. As was shown in Section 2, the density $d\rho_f$ of states depends trivially on the energies of the final particles; that is, all the values of the energies E_1 and E_2 are equiprobable in their allowed domain. The nontrivial dependence of the cross section for nuclear photodisintegration on the energies of the

alpha particle and one of the neutrons is determined by the reduced transition probability

$$B(E1) = r_0^2 \frac{(2\pi)^6}{k^5} \times \sum_{m,\mu} \Big(\Psi(1^-,m)|\hat{\mathrm{M}}_\mu|\Psi(0^+,0)\Big)^2. \tag{21}$$

In Fock–Bargmann space, the electric-dipole-transition operator can be represented as [3]

$$\hat{\mathbf{M}}(E1) = \frac{e}{\sqrt{8\pi}}(\mathbf{a} + \mathbf{a}^*).$$

The matrix element of the $E1$-transition operator has the form

$$\Big(\Psi(1^-,m)|\hat{M}_\mu|\Psi(0^+,0)\Big) = \sum_{\nu=0}^{\infty} C_\nu(1^-,m;\mathbf{k}_1,\mathbf{k}_2) \times \Big(\langle\nu,1^-,m|\hat{M}_\mu|\nu,0^+,0\rangle C_\nu(0^+) + \langle\nu,1^-,m|\hat{M}_\mu|\nu+1,0^+,0\rangle C_{\nu+1}(0^+)\Big),$$

where the partial matrix elements are given by

$$\langle\nu,1^-,m|\hat{M}_\mu|\nu,0^+,0\rangle = C^{1,m}_{00;1\mu}\frac{e}{\sqrt{8\pi}}\frac{N_\nu^+}{N_\nu^-} = C^{1,m}_{00;1\mu}\frac{e}{\sqrt{8\pi}}\frac{1}{\sqrt{6}}\sqrt{\frac{(13\nu+38)(\nu+4)}{29\nu+104}},$$

$$\langle\nu,1^-,m|\hat{M}_\mu|\nu+1,0^+,0\rangle = C^{1,m}_{00;1\mu}\frac{e}{9\sqrt{8\pi}}\frac{N_\nu^-}{N_{\nu+1}^+} = C^{1,m}_{00;1\mu}\frac{e\times\sqrt{6}}{9\sqrt{8\pi}}\sqrt{\frac{(29\nu+133)(\nu+1)}{13\nu+38}}.$$

Taking into account the dependence (17) of the expansion coefficients on the hyperspherical angles, we eventually obtain

$$\sum_{m,\mu}\Big(\Psi(1^-,m)|\hat{M}_\mu|\Psi(0^+,0)\Big)^2 = \frac{e^2}{\pi^3}\frac{2}{117}\sin^2\theta_1\cos^2\alpha(3\cos^2\alpha - 2\sin^2\alpha)^2 \times\Bigg(\sum_{\nu=0}^{\infty} C_\nu(1^-,E)\Bigg(\sqrt{\frac{(13\nu+38)(\nu+4)}{29\nu+104}}C_\nu(0^+) + \frac{4}{3}\sqrt{\frac{(\nu+1)(29\nu+133)}{13\nu+38}}C_{\nu+1}(0^+)\Bigg)\Bigg)^2.$$

The differential cross section for ^{6}He photodisintegration can be represented as

$$d\sigma_f = \sigma_0(E)\frac{2^{19/2}\times 3^{5/2}}{13\pi}\tilde{E}_1(15\tilde{E}_1 - 1)^2 \times \sin^3\theta_1 d\theta_1 d\tilde{E}_1 d\tilde{E}_2, \tag{22}$$

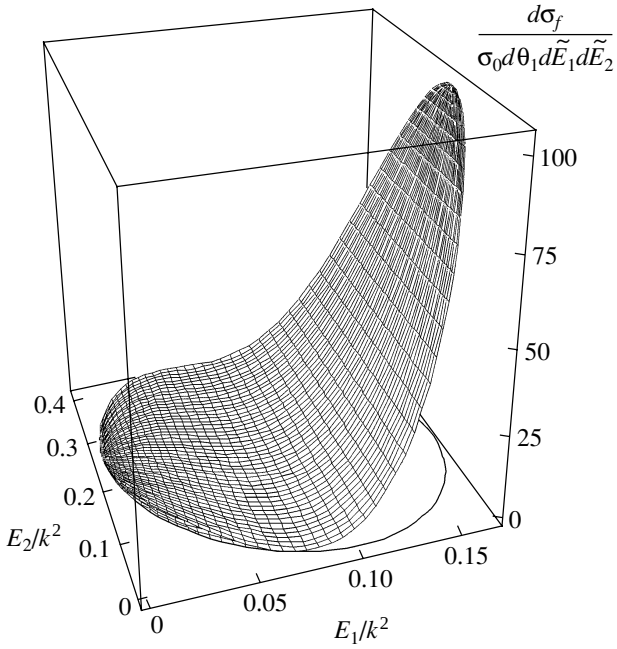

Fig. 2. Differential cross section for ^{6}He photodisintegration at a fixed photon energy E and $\theta_1 = \pi/2$. The locus is shown in the (E_1, E_2) plane.

where $E_1 = k^2\tilde{E}_1$ and $E_2 = k^2\tilde{E}_2$. The coefficient in Eq. (22) is chosen in such a way that

$$\int d\tilde{E}_1 \int d\tilde{E}_2 \int d\theta_1 d\sigma_f = \sigma_0(E).$$

The total cross section $\sigma_0(E)$ depends only on the photon energy:

$$\sigma_0(E) = \frac{\pi^2}{162}\frac{e^2 r_0^2}{c}\frac{\omega}{k}\Bigg(\sum_{\nu=0}^{\infty} C_\nu(1^-,E) \times\Bigg(\sqrt{\frac{(13\nu+38)(\nu+4)}{29\nu+104}}C_\nu(0^+) + \frac{4}{3}\sqrt{\frac{(\nu+1)(29\nu+133)}{13\nu+38}}C_{\nu+1}(0^+)\Bigg)\Bigg)^2.$$

Upon specifying this energy, we can therefore determine the differential cross section as a function of the energies and angles between the final-particle momenta.

The θ_1 dependence of the cross section is identical to that for the deuteron because this anisotropy is due to the transverse photon polarization. The differential cross section $d\sigma_f$ will obviously peak at $\theta_1 = \pi/2$ (the alpha particle is emitted perpendicularly to the photon momentum). Figure 2 shows $d\sigma_f/\sigma_0 d\theta_1 d\tilde{E}_1\, d\tilde{E}_2$ as a function of E_1 and E_2 at fixed θ_1. The photodisintegration cross section is maximal at $\alpha = 0$. As was shown in Section 2, this α value corresponds

to $\tau = -1$; that is, the decay process in which the momentum of the alpha particle and the momentum of the pair of neutrons are opposite to each other is the most probable. In this case, the energies of all the three particles are equal to one another and the alpha-particle energy attains its maximum possible value ($E_1 = E_2 = E_3 = k^2/6$). The cross section is minimal when two neutrons move in opposite directions and the alpha particle is at rest.

6. CONCLUSION

By considering the example of ^{6}He photodisintegration, we have demonstrated that the angular and energy distributions are completely determined by the wave function for the final nuclear state—more precisely, by the coefficients in the wave-function expansion in allowed basis functions. Using hyperspherical functions, one can easily obtain the differential cross section for ^{6}He disintegration as a function of the energies of the final particles and the angles between their momenta.

It is important that our results are independent of the asymptotic-potential approximation used here. Even beyond this approximation, we would arrive at the same conclusions because a resort to a more precise potential would affect only the coefficients $C_\nu(1^-, E)$, which can change solely the total cross section $\sigma_0(E)$. However, the form of the functions in (17) is dictated by the use of the minimal approximation of the hyperspherical-harmonic method. If hyperspherical harmonics of higher grand orbitals K were included, the energy and angular distributions of final particles would be somewhat different.

As can be seen from Eq. (22), the energy and angular distributions are similar for different photon energies. However, this is so only for low photon energies. As the energy increases, other reaction channels open, with the result that the distributions become energy-dependent.

Thus, ^{6}He disintegration is most probably accompanied by the emission of the alpha particle and valence neutrons in opposite directions in the plane orthogonal to the photon momentum. This behavior is explained by the following mechanism. The electric dipole moment of the ^{6}He nucleus is zero in the ground state. Following the $E1$ transition, the nucleus occurs in a state whose dipole moment is determined by the configuration of the excited nuclear state in the c.m. frame of the nucleus. Two limiting configurations can in principle be realized at given ^{6}He energy. One of these corresponds to the alpha particle at rest and the neutrons moving in opposite directions and has zero electric dipole moment. Therefore, the effective differential cross section for the transition to this configuration is also equal to zero. The second configuration is realized when the α particle and the neutron pair move in opposite directions. The electric dipole moment of the system is maximal in this configuration; therefore, the probability of exciting this configuration is also maximal.

According to the experimental data of Aumann *et al.* [1], who measured the energy distribution of neutrons emitted in three-body ^{6}He disintegration in the Coulomb field of a lead nucleus and who employed the relative energies equivalent to the energies $E_1 = k_1^2/2$ and $E_2 = k_2^2/2$, very small values of both the relative energy of the neutrons and the angle between their momenta are the most probable. This result agrees with our conclusions based on an expression for the cross section in terms of the c.m. cluster energies.

REFERENCES

1. T. Aumann *et al.*, Phys. Rev. C **59**, 1252 (1999).
2. B. V. Danilin *et al.*, Phys. Rev. C **55**, R577 (1997).
3. G. F. Filippov, Yu. A. Lashko, and L. P. Shvedov, Yad. Fiz. **62**, 1772 (1999) [Phys. At. Nucl. **62**, 1651 (1999)].
4. O. F. Nemets and K. O. Terenetskiĭ, *Nuclear Reactions* (Vishcha Shkola, Kiev, 1977).

Translated by R. Tyapaev

Physics of Atomic Nuclei, Vol. 65, No. 1, 2002, pp. 75–81. Translated from Yadernaya Fizika, Vol. 65, No. 1, 2002, pp. 79–86.
Original Russian Text Copyright © 2002 by Orlin.

NUCLEI
Theory

Shell-Model Description of the Noncompound Component of Nucleon-Induced Reactions on Light and Medium-Mass Nuclei at Incident-Nucleon Energies of up to 12 MeV

V. N. Orlin

Institute of Nuclear Physics, Moscow State University, Vorob'evy gory, Moscow, 119899 Russia
Received July 12, 2000; in final form, October 19, 2000

Abstract—The coupled-channel method as implemented within the intermediate-coupling scheme of the shell model is used to describe the noncompound component of nucleon–nucleus reactions. The proposed model is aimed at taking into account the effect of collective doorway states (giant resonances) on the properties of nucleon-induced reactions on light and medium-mass nuclei at incident-nucleon energies of up to 12 MeV. © *2002 MAIK "Nauka/Interperiodica"*.

1. INTRODUCTION

Over the past 10–15 years, the Feshbach–Kerman–Koonin statistical theory of multistep reactions [1–3] has been widely used to describe nucleon-induced reactions. In many aspects, this quantum-mechanical theory is equivalent to the semiclassical exciton model proposed by Griffin [4], despite obvious distinctions between the formalisms adopted in the two approaches (see the relevant discussion in [5]); however, the former provides a considerably better description of angular distributions of reaction products, because it takes explicitly into account the presence of configurations of the compound system that involve a particle in a continuum.

Calculations based on Feshbach–Kerman–Koonin theory reproduce fairly well available experimental data, including experimental nucleon spectra integrated with respect to angles and experimental angular distributions of nucleons. However, an analysis of these calculations reveals a strong scatter of the resulting estimates for the contributions of various possible processes [multistep direct, multistep compound, and equilibrium (evaporation) processes] for identical reactions on the same target nuclei at the same incident-nucleon energies; this indicates that there are too many adjustable parameters in the theory and casts some doubt on the physical meaning of the results it yields (see the discussion of this question in [6]). The problem in question is especially important at moderate energies of nucleons inducing the reactions being considered ($\varepsilon < 30$ MeV), in which case various processes strongly compete. In [7], it was assumed that difficulties arising in Feshbach–Kerman–Koonin theory are due to the disregard of processes involving the excitation of collective degrees of freedom of the final nucleus. The inclusion of such collective nuclear processes [8, 9] does indeed render the description of various reactions more consistent, but it was shown in [6] that this does not solve completely the problem of unifying the parameters of the theory.

In all probability, this difficulty is inherent in Feshbach–Kerman–Koonin theory, which is based on the assumption that the amplitudes of various multistep processes leading to the same final state contribute to the total amplitude incoherently, whence it follows that the total reaction cross section can be represented as the sum of contributions from individual processes. However, this approximation, which is correct at high energies ε of nucleons incident on a target, becomes invalid in the energy region $\varepsilon \leq 20$ MeV, where coherent doorway states corresponding to the giant dipole resonance and, possibly, to some other eigenstates of the compound system are formed at initial reaction stages. It therefore comes as no surprise that the predictions of the theory are quite ambiguous at moderate values of the energy ε.

If the giant dipole resonance of a compound system has an intermediate structure—this is characteristic of many light and medium-mass nuclei ($A \leq 80$) featuring unfilled shells—it modulates the dependence of the cross section for a nucleon–nucleus reaction on the incident-nucleon energy ε. This can be seen, for example, from the data presented in [10], where the partial cross sections $\sigma(p, n)$ corresponding to a fixed state of the final nucleus were measured for some $1f2p$-shell vibrational nuclei. For the incident-proton energy varied from

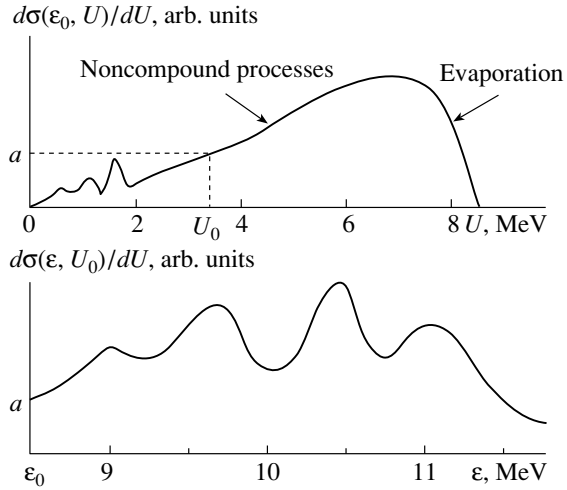

Schematic representation of the reaction cross section $d\sigma(\varepsilon, U)/dU$ integrated with respect to angles as a function of (upper part of the figure) the excitation energy U of the final nucleus and (lower part of the figure) the energy ε of the nucleon incident on a target for the case where the giant dipole resonance formed in the compound system has an intermediate structure. The segments of the cross-section graph that are dominated by evaporation and noncompound processes are indicated in the upper part of the figure.

the reaction threshold to $\varepsilon_p \sim 12$–14 MeV, the cross sections found in [10] reveal a pronounced resonance structure that can be interpreted as the intermediate structure of the giant dipole resonance of a compound system. It should be emphasized that Feshbach–Kerman–Koonin theory is unable to account for such a structure.

The figure illustrates the role of coherent doorway states. For nucleon-induced reactions, the cross section $d\sigma(\varepsilon, U)/dU$ integrated with respect to angles as a function of the excitation energy U of the final nucleus and as a function of the incident-nucleon energy ε is depicted schematically for the case where the giant dipole resonance formed in a compound system has an intermediate structure.

Because of a nonuniform (shell) distribution of single-particle nuclear levels, a significant part of the total excitation energy of the compound system formed in reactions induced by a projectile nucleon of moderate energy is absorbed, at the first stage (within which nonequilibrium processes develop), either by a particle occupying a quasidiscrete level in a continuum or by a hole in a totally filled shell. The remaining part of the energy of the system is quickly distributed among the eigenstates of valence nucleons (this is so at least in light and medium-mass nuclei with unfilled outer shells, in which case the ground state is strongly degenerate). Owing to this, the noncompound component of nucleon-induced reactions that takes into account multistep direct, multistep compound, and collective nuclear processes of Feshbach–Kerman–Koonin theory can be described on the basis of the coupled-channel method employing $|\alpha\rangle|\Psi_i\rangle$ and $|\gamma^{-1}\rangle|\Psi_i\rangle$ basis configurations, where $|\alpha\rangle$ is a nucleon state on a free level α, $|\gamma^{-1}\rangle$ is a nucleon-hole state on a filled level γ, and $|\Psi_i\rangle$ stands for low-lying eigenstates of the nuclear core.

The formalism proposed in this study is similar to the formalism developed in [11–14] to describe giant multipole resonances in light and medium-mass nuclei. However, there are two important distinctions: (i) In describing the noncompound component of nucleon-induced reactions, an absorbing optical potential must be used for the particle α and the hole γ^{-1} in order to consider that doorway states die out in the course of formation of compound nuclear states. (ii) In relation to the calculations of giant resonances, it is necessary to extend the basis $\{|\Psi_i\rangle\}$ by including in it low-lying states of anomalous parity since a specific particle or a specific hole can execute transitions between opposite-parity levels.

By successively adding nucleons to a nuclear system [15], the wave functions for low-lying states of light and medium-mass nuclei can be calculated up to excitation energies of $U \sim 10$–12 MeV. This makes it possible to describe the noncompound component of the energy spectrum of emitted nucleons at incident-nucleon energies in the region $\varepsilon \leq 12$ MeV and the ε dependence of this component (see figure) over the entire region of the giant dipole resonance for excitation energies of the final nucleus that satisfy the condition $U \leq 10$–12 MeV.

The model employed in the present article is described in Sections 3–5: An account of the basic concepts of the formalism developed here is given in Section 3. The procedure used to discretize a continuum is outlined in Section 4. The on-shell elements of the scattering matrix are calculated in Section 5.

2. FORMAL EXPRESSION FOR THE CROSS SECTION FOR NUCLEON–NUCLEUS REACTIONS

For a reaction where a two-particle system goes over from the τi to the $\tau' i'$ nucleon–nucleus channel, the differential cross section obtained upon averaging over initial magnetic numbers and summation over final magnetic numbers is given by

$$\frac{d\sigma_{\tau i\to\tau' i'}(\varepsilon,\varepsilon',\theta)}{d\Omega} = \frac{\hbar^2}{4\varepsilon\mu(2J_i+1)} \times \sum_{L=0}^{L_{\max}} B_L(\tau i\to\tau' i';\varepsilon,\varepsilon')P_L(\cos\theta), \quad (1)$$

where μ, τ, and ε (μ', τ', and ε') are, respectively, the reduced mass, the z projection of the isospin, and the

energy of the relative motion of the incident (emitted) nucleon; $i \equiv E_i, J_i, \ldots$ ($i' \equiv E_{i'}, J_{i'}, \ldots$) stands for the set of quantum numbers that characterize the internal state of the target nucleus (final nucleus); and θ is the angle between by the wave vectors of the incident and the emitted nucleon.

The coefficients in the expansion of the cross section $d\sigma/d\Omega$ in Legendre polynomials have the form

$$B_L(\tau i \to \tau' i'; \varepsilon, \varepsilon') = \frac{\pi^2}{2(2L+1)} \tag{2}$$
$$\times \sum_{ll'} \sum_{l''l'''} \sum_{jj'} \sum_{j''j'''} \sum_{JJ'} (-1)^{j-j'}(2J'+1)$$
$$\times [(2j+1)(2j'+1)(2l+1)$$
$$\times (2l'+1)(2l''+1)(2l'''+1)]^{1/2}$$
$$\times (l0l''0|L0)(l'0l'''0|L0) U(ll''jj''; L1/2)$$
$$\times U(l'l'''j'j'''; L1/2) U(jJ_iLJ'; Jj'')$$
$$\times U(j'J_{i'}LJ'; Jj''') \times \left\langle (\varepsilon' l'j'\tau', i')_J | \mathcal{T} | (\varepsilon l j \tau, i)_J \right\rangle$$
$$\times \left\langle (\varepsilon' l'''j'''\tau', i')_{J'} | \mathcal{T} | (\varepsilon l'' j'' \tau, i)_{J'} \right\rangle^*,$$

where $\langle (\varepsilon' l'j'\tau', i')_J | \mathcal{T} | (\varepsilon l j \tau, i)_J \rangle$ are the elements of the transition matrix in the representation specified by the quantum numbers $\varepsilon l j \tau i J$ (l is the orbital angular momentum of the nucleon, j is its total angular momentum, and J is the total angular momentum of the reaction channel).

The matrix $\mathcal{T}$, which is related to the scattering matrix S by the equation

$$S = 1 - 2\pi i \mathcal{T}, \tag{3}$$

is calculated on the energy shell

$$\varepsilon + m_\tau c^2 + E_i = \varepsilon' + m_{\tau'} c^2 + E_{i'}, \tag{4}$$

where E_i ($E_{i'}$) is the energy of the internal state of the target nucleus (final nucleus) and $m_\tau c^2$ ($m_{\tau'} c^2$) is the rest energy of the incident (emitted) nucleon.

In the $C \equiv \alpha i J \equiv \varepsilon l j \tau i J$ representation, the on-shell elements of the scattering matrix can be represented in the form

$$\langle C' | S | C \rangle = \lim_{\eta \to 0} \int_{E_C - \eta}^{E_C + \eta} \langle C'^{(-)} | C^{(+)} \rangle \, dE_{C'}, \tag{5}$$

where $|C^{(\pm)}\rangle$ are eigenstates of the nuclear Hamiltonian H ($H|C^{(\pm)}\rangle = E_C |C^{(\pm)}\rangle$, $E_C = \varepsilon_C + m_{\tau_C} c^2 + E_{i_C}$) that satisfy the boundary conditions

$$|C^{(\pm)}\rangle \longrightarrow (|\alpha_C\rangle_{\text{free}} |\Psi_{i_C}\rangle)_{J_C} \tag{6}$$
$$+ \text{diverging (converging) spherical waves}$$
$$\text{for } r \to \infty.$$

Here, r is the distance between the nucleon and the residual nucleus, and $|\alpha_C\rangle_{\text{free}}$ and $|\Psi_{i_C}\rangle$ are the wave functions describing, respectively, the free motion of the nucleon and the internal state of the residual nucleus.

3. BASIC CONCEPTS OF THE MODEL

Let us consider the problem of describing the noncompound component of nucleon-induced reactions on light and medium-mass nuclei at incident-nucleon energies corresponding to the region of the excitation of the giant dipole resonance in the compound system. As was indicated in the Introduction, the main contribution to the noncompound component of such reactions comes from *particle on a free level + nuclear core in a low-lying excited state* and *hole on a completely filled level + nuclear core in a low-lying excited state* configurations. Therefore, the nucleon–nucleus scattering states $|C^{(\pm)}\rangle$ that involve diverging (+) or converging (−) waves at infinity can be represented in the form

$$|C^{(\pm)}\rangle = \sum_W \langle W/C^{(\pm)}\rangle |W\rangle, \tag{7}$$

where $|W\rangle$ are basis states corresponding to particle ($|\alpha, i\rangle \equiv a_\alpha^+ |\Psi_i(A)\rangle$) and hole ($|\gamma, i\rangle \equiv a_{-\gamma} |\Psi_i(A+2)\rangle$) reaction channels [in order to simplify the presentation, the quantum numbers J characterizing the total angular momentum of the p (h) channel are omitted here and below]; $\langle W/C^{(\pm)}\rangle$ are coefficients in the expansion of the scattering states in the basis configurations; a_α^+ is the operator that creates a nucleon in the free single-particle state $|\alpha\rangle \equiv |\varepsilon l j m \tau\rangle$ of the mean nuclear field $u(r)$; $a_{-\gamma}$ is the hole creation operator corresponding to the absorption of a nucleon from the filled single-particle state $|-\gamma\rangle \equiv (-1)^{j+m} |\varepsilon l j - m \tau\rangle$; $|\Psi_i(A)\rangle$ and $|\Psi_i(A+2)\rangle$ are low-lying eigenstates of, respectively, the A and the $A+2$ nucleus (A is the mass number of target nucleus); and the symbol $\sum_x$ denotes summation over discrete and integration with respect to continuous quantum numbers x [in (7), integration is performed with respect to single-particle energies $\varepsilon > 0$ of the continuous spectrum].

The expansion in (7) corresponds to the intermediate-coupling approximation. The aforementioned low-lying states $|\Psi_i(A)\rangle$ and $|\Psi_i(A+2)\rangle$ (at excitation energies of $U \leq 10$–12 MeV), which are necessary for implementing this approximation, can be computed on the basis of the method proposed in [15].

In order to obtain a correct absolute value of the noncompound component of the reaction cross section, we must consider that the doorway states $|W\rangle$ die out in the process of formation of a compound nuclear state. This can be done by introducing a complex-valued optical potential $u(r)$ for the particle α and the hole γ^{-1}.

Generally speaking, the basis $|W\rangle$ is not orthonormalized since $a_\alpha |\Psi_i\rangle \neq 0$ and $a_{-\gamma}^+ |\Psi_i\rangle \neq 0$ for the

anomalous-parity state $|\Psi_i\rangle$. This basis is characterized by the metric tensor

$$\langle\widetilde{W}|W'\rangle = \delta_{WW'} + \langle\widetilde{W}|W'\rangle_{\rm reg}, \qquad (8)$$

where the symbol tilde over a state indicates that it is defined for the complex-conjugate single-particle potential $u^*(r)$;

$$\langle\widetilde{W}|W'\rangle_{\rm reg} = -\begin{cases} \langle\Psi_{i_W}(A)|a^+_{\alpha_{W'}}a_{\alpha_W}|\Psi_{i_{W'}}(A)\rangle & \text{for } W, W' \in p \text{ channels} \\ \langle\Psi_{i_W}(A+2)|a_{-\gamma_{W'}}a^+_{-\gamma_W}|\Psi_{i'_W}(A+2)\rangle & \text{for } W, W' \in h \text{ channels} \\ 0 & \text{in the remaining cases} \end{cases} \qquad (9)$$

is the regular part of the scalar product $\langle\widetilde{W}|W'\rangle$; and $\delta_{WW'}$ is a Kronecker delta symbol for discrete quantum numbers and a Dirac delta function for continuous quantum numbers.

The expansion coefficients $\langle W/C^{(\pm)}\rangle$ determine the contravariant coordinates of the state $|C^{(\pm)}\rangle$ in the nonorthonormalized basis $\{|W\rangle\}$, while the scalar products

$$\langle\widetilde{W}|C^{(\pm)}\rangle = \sum_{\widetilde{W}}\langle W/C^{(\pm)}\rangle\langle\widetilde{W}|W\rangle \qquad (10)$$

determine the covariant coordinates of this state.

The scattering states $|C^{(\pm)}\rangle$ satisfy the time-independent Schrödinger equation

$$H|C^{(\pm)}\rangle = E_C|C^{(\pm)}\rangle, \qquad (11)$$

where $H = H_0 + V_{\rm res}$ is the nuclear Hamiltonian; $H_0 = \sum_k[-\frac{\hbar^2}{2m_{\tau_k}}\Delta_k + m_{\tau_k}c^2 + u(r_k)]$ is the single-particle shell-model Hamiltonian describing the motion of nucleons in a finite spherically symmetric potential $u(r)$ (which is complex-valued for open and closed reaction channels W); $V_{\rm res}$ is the residual nucleon–nucleon interaction (its choice is discussed in [12, 13]); and $E_C = \varepsilon_C + m_{\tau_C}c^2 + E_{i_C}(A)$ is the energy of the scattering states $|C^{(\pm)}\rangle$ corresponding to the reaction channel $C = \alpha_C i_C = \varepsilon_C l_C j_C \tau_C i_C$.

We multiply this equation by $\langle\widetilde{W}|$ from the left and substitute the expansion given by (7) into the result. We then obtain the following set of homogeneous integral equations for the amplitudes $\langle W'/C^{(\pm)}\rangle$ of coupled reaction channels:

$$\sum_{W'}\left(\langle\widetilde{W}|H|W'\rangle - E_C\langle\widetilde{W}|W'\rangle\right)\langle W'/C^{(\pm)}\rangle = 0. \qquad (12)$$

The matrix elements $\langle\widetilde{W}|H|W'\rangle$ can be represented in the form

$$\langle\widetilde{W}|H|W'\rangle = E_W\langle\widetilde{W}|W'\rangle + \langle\widetilde{W}|\mathcal{V}|W'\rangle, \qquad (13)$$

where

$$E_W = \begin{cases} \varepsilon_W + m_{\tau_W}c^2 + E_{i_W}(A) & \text{for } W \in p \text{ channels} \\ -\varepsilon_W - m_{\tau_W}c^2 + E_{i_W}(A+2) & \text{for } W \in h \text{ channels} \end{cases} \qquad (14)$$

and the operator $\mathcal{V}$ is defined as

$$\langle\widetilde{W}|\mathcal{V} = \begin{cases} \langle\Psi_{i_W}(A)|[a_{\alpha_W}, V_{\rm res}] & \text{for } W \in p \text{ channels} \\ \langle\Psi_{i_W}(A+2)|[a^+_{-\gamma_W}, V_{\rm res}] & \text{for } W \in h \text{ channels.} \end{cases} \qquad (15)$$

In deriving Eqs. (13)–(15), we have considered that $|\Psi_i(A)\rangle$ and $|\Psi_i(A+2)\rangle$ are eigenstates of the nuclear Hamiltonian H and that $|\alpha\rangle$ and $|-\gamma\rangle$ are eigenstates of the Hamiltonian H_0.

By substituting expressions (13) into Eqs. (12), we can recast the coupled-channel equations into the form

$$(E_C - E_W)\sum_{W'}\langle\widetilde{W}|W'\rangle\langle W'/C^{(\pm)}\rangle = \sum_{W'}\langle\widetilde{W}|\mathcal{V}|W'\rangle\langle W'/C^{(\pm)}\rangle. \qquad (16)$$

In order to take into account the boundary conditions (6), we replace the homogeneous set of Eqs. (16) by the nonhomogeneous set of equations

$$\sum_{W'}\langle\widetilde{W}|W'\rangle\langle W'/C^{(\pm)}\rangle = \exp\{\pm i\delta_C\}\delta_{W,C} + \frac{1}{E_C - E_W \pm i\rho}\sum_{W'}\langle\widetilde{W}|\mathcal{V}|W'\rangle\langle W'/C^{(\pm)}\rangle, \qquad (17)$$

where $\rho \to 0^+$ and δ_C is the phase shift associated with nucleon scattering on the complex potential $u(r)$.

It is obvious that solutions to the set of Eqs. (17) are also solutions to the homogeneous set of Eqs. (16). We will now show that they satisfy the necessary boundary conditions. To do this, it is sufficient to prove that, in the limit $t \to \mp\infty$, the wave packet

$$|C^{(\pm)}(t)\rangle\rangle = \int_{-\infty}^{+\infty} \rho_\eta(\varepsilon_C - \varepsilon_C^{(0)})|C^{(\pm)}\rangle \times \exp\left\{-\frac{i}{\hbar}[\varepsilon_C + E_{i_C}(A)]t\right\} d\varepsilon_C, \quad (18)$$

which is constructed from solutions to Eqs. (17) with the weight function

$$\rho_\eta(\varepsilon) = \frac{\eta/\pi}{\varepsilon^2 + \eta^2}, \quad (19)$$

is transformed into a wave packet that describes the free motion of a nucleon relative to the residual nucleus.

From Eqs. (8) and (17), we obtain

$$\langle W/C^{(\pm)}\rangle = \exp\{\pm i\delta_C\}\delta_{W,C} - \sum_{W'}\langle\widetilde{W}|W'\rangle_{\rm reg}\langle W'/C^{(\pm)}\rangle + \frac{1}{E_C - E_W \pm i\rho}\sum_{W'}\langle\widetilde{W}|\mathcal{V}|W'\rangle\langle W'/C^{(\pm)}\rangle. \quad (20)$$

By substituting this expression into the expansion in (7) and by using the definition (18) of the wave packet, we arrive at

$$\langle W/C^{(\pm)}(t)\rangle\rangle \simeq \int_{-\infty}^{+\infty} \rho_\eta(\varepsilon_C - \varepsilon_C^{(0)}) \times \exp\{\pm i\delta_C\}\delta_{W,C}\exp\left\{-\frac{i}{\hbar}[\varepsilon_C + E_{i_C}(A)]t\right\} d\varepsilon_C - \left(\sum_{W'}\langle\widetilde{W}|W'\rangle_{\rm reg}\langle W'/C^{(\pm)}\rangle\right)\Bigg|_{\varepsilon_C=\varepsilon_C^{(0)}} \times \int_{-\infty}^{+\infty}\rho_\eta(\varepsilon_C - \varepsilon_C^{(0)})\exp\left\{-\frac{i}{\hbar}[\varepsilon_C + E_{i_C}(A)]t\right\} d\varepsilon_C + \left(\sum_{W'}\langle\widetilde{W}|\mathcal{V}|W'\rangle\langle W'/C^{(\pm)}\rangle\right)\Bigg|_{\varepsilon_C=\varepsilon_C^{(0)}} \times \int_{-\infty}^{+\infty}\rho_\eta(\varepsilon_C - \varepsilon_C^{(0)})\frac{\exp\left\{-\frac{i}{\hbar}[\varepsilon_C + E_{i_C}(A)]t\right\}}{E_C - E_W \pm i\rho} d\varepsilon_C. \quad (21)$$

[In deriving Eq. (21), it was assumed that the wave-packet width η is much smaller than the width of resonances in the nuclear matrix elements.]

For $t \to \mp\infty$, the second and the third term on the right-hand side of Eq. (21) tend to zero in proportion to $\exp\{-\eta|t|/\hbar\}$. It follows that, for $t \to \mp\infty$, we have

$$|C^{(\pm)}(t)\rangle\rangle \to \left[\int_{-\infty}^{+\infty}\rho_\eta(\varepsilon_C - \varepsilon_C^{(0)}) \times \exp\{\pm i\delta_C\}\, a^+_{\alpha_C}\exp\left\{\frac{-i\varepsilon_C t}{\hbar}\right\} d\varepsilon_C\right] \times |\Psi_C(A)\rangle\exp\left\{\frac{-iE_{i_C}(A)t}{\hbar}\right\} \to \int_{-\infty}^{+\infty}\rho_\eta(\varepsilon_C - \varepsilon_C^{(0)})a^+_{\alpha_C}({\rm free})|\Psi_C(A)\rangle \times \exp\left\{-\frac{i}{\hbar}[\varepsilon_C + E_{i_C}(A)]t\right\} d\varepsilon_C, \quad (22)$$

but this is precisely the statement that we wanted to prove [$a^+_{\alpha_C}$(free) is the operator that creates a nucleon in the free state $|\alpha_C\rangle_{\rm free}$].

4. DISCRETIZATION OF A CONTINUUM

The matrix elements $\langle\widetilde{W}|W'\rangle_{\rm reg}$ and $\langle\widetilde{W}|\mathcal{V}|W'\rangle$ appearing in Eqs. (20) depend on the behavior of the continuum single-particle states $|\alpha\rangle$ only in the internal region of the reaction ($r \le R_0 \approx 1.5A^{1/3}$ fm), since it is the region where these states overlap the bound configurations $|\Psi_i(A)\rangle$ and $|\Psi_i(A+2)\rangle$. But in a finite spatial region, the following expansion is valid:

$$|\alpha\rangle = \sum_n \langle n\hat{\alpha}|\alpha\rangle|n\hat{\alpha}\rangle \text{ for } r \le R_0. \quad (23)$$

Here, $|\alpha\rangle = |\varepsilon ljm\tau\rangle$ is that continuum or bound nucleon state in the field of the potential $u(r)$ which corresponds to a free level, and $|n\hat{\alpha}\rangle \equiv |nljm\tau\rangle$ is the wave function for a spherical oscillator involving n oscillator quanta ($\hat{\alpha} \equiv ljm\tau$).

By using the expansion in (23), we recast Eqs. (20) into the form

$$\langle W/C^{(\pm)}\rangle = \exp\{\pm i\delta_C\}\delta_{W,C} - \sum_{w'}\langle\widetilde{W}|w'\rangle_{\rm reg}\langle w'/C^{(\pm)}\rangle + \frac{1}{E_C - E_W \pm i\rho}\sum_{w'}\langle\widetilde{W}|\mathcal{V}|w'\rangle\langle w'/C^{(\pm)}\rangle, \quad (24)$$

where

$$|w'\rangle = \begin{cases} |n_{w'}\hat{\alpha}_{w'}i_{w'}\rangle = a^+_{n_{w'}\hat{\alpha}_{w'}}|\Psi_{i_{w'}}(A)\rangle & \text{for } |w'\rangle \in p \text{ channels} \\ |W'\rangle & \text{for } |w'\rangle \in h \text{ channels} \end{cases} \quad (25)$$

are discrete states that determine the basis for $r \le R_0$ ($a^+_{n_{w'}\hat{\alpha}_{w'}}$ is the operator that creates the oscillator state $|n_{w'}\hat{\alpha}_{w'}\rangle$) and

$$\langle w'/C^{(\pm)}\rangle = \begin{cases} \sum\limits_{\varepsilon_{W'}} \langle n_{w'}\hat{\alpha}_{w'}|\alpha_{W'}\rangle\langle W'/C^{(\pm)}\rangle & \text{for } w' \in p \text{ channels} \\ \langle W'/C^{(\pm)}\rangle & \text{for } w' \in h \text{ channels} \end{cases} \quad (26)$$

are the contravariant components of the scattering state that characterize its configuration composition in the internal region of the reaction [in (26), integration (summation) is performed with respect to the single-particle energies $\varepsilon_{W'}$].

Equations (24) reduce the problem of calculating scattering states to calculating a finite number of internal components $\langle w'/C^{(\pm)}\rangle$. For these components, we can derive a compact set of linear algebraic equations. By multiplying Eqs. (17) with $W = \alpha_W i_W$ by $\langle n_w\hat{\alpha}_w|\alpha_W\rangle$ from the left and by integrating (summing) the result with respect to the single-particle energies ε_W, we obtain

$$\sum_{w'}\left\{\langle\widetilde{w}|w'\rangle - U_+(w)\sum_k f^{(\pm)}_{kw}(E_C)\right. \quad (27)$$
$$\times\langle k\hat{\alpha}_w i_w|\mathcal{V}|w'\rangle - (1-U_+(w))$$
$$\left.\times\frac{1}{E_C - E_W \pm i\rho}\langle\widetilde{w}|\mathcal{V}|w'\rangle\right\}\langle w'/C^{(\pm)}\rangle$$
$$= U_+(w)\exp\{\pm i\delta_C\}\delta_{\hat{\alpha}_c\hat{\alpha}_w}\delta_{i_C i_W}\langle n_w\hat{\alpha}_w|\alpha_C\rangle,$$

where $U_+(w)$ is a step function equal to unity for $w \in$ particle channels and zero for $w \in$ hole channels and the function $f^{(\pm)}_{kw}(E_C)$ can be represented in the form

$$f^{(\pm)}_{kw}(E_C) = \sum_{\varepsilon_W}\frac{\langle n_w\hat{\alpha}_w|\alpha_W\rangle\langle k\hat{\alpha}_w|\alpha_W\rangle}{E_C - E_W \pm i\rho} \quad (28)$$
$$= \int_0^{\varepsilon_{\max}}\frac{\langle n_w\hat{\alpha}_w|\alpha_W\rangle\langle k\hat{\alpha}_w|\alpha_W\rangle}{E_C - E_W \pm i\rho}d\varepsilon_W$$
$$+ \text{ discrete terms}$$

($\varepsilon_{\max} > 50$ MeV is the maximal single-particle energy up to which we take into account the continuum).

From Eqs. (27) and (28), it can be seen that the problem of taking into account the continuum reduces to calculating the principal values of the improper integrals in (28). The matrix of the set of Eqs. (27) depends on the energy E_C, the angular momentum J_C, and the parity of the compound nucleus, but it is independent of whether the channel αi to which the scattering state $|C^{(\pm)}\rangle$ under consideration corresponds is an input or an output one. For a realistic choice of oscillator states, the sum in (23) converges fast, so that the dimension of the set of Eqs. (27) is not very large in general. A conventional technique of shell-model calculations can be used to compute the nuclear matrix elements $\langle\widetilde{w}|\mathcal{V}|w'\rangle$ on the basis of the known low-lying states $|\Psi_i(A)\rangle$ and $|\Psi_i(A+2)\rangle$.

5. CALCULATION OF ON-SHELL SCATTERING-MATRIX ELEMENTS

Since a complex-valued potential is used in this model, expression (5) for the on-shell elements of the scattering matrix must be recast into the form

$$\langle C'|S|C\rangle = \lim_{\eta\to 0}\int_{E_C-\eta}^{E_C+\eta}\langle\widetilde{C}'^{(-)}|C^{(+)}\rangle\,dE_{C'}, \quad (29)$$

where $|\widetilde{C}'^{(-)}\rangle$ is the scattering state found for the complex-conjugate potential $u^*(r)$.

By using the expansion in (7), we obtain

$$\langle C'|S|C\rangle = \lim_{\eta\to 0}\int_{E_C-\eta}^{E_C+\eta}\sum_W\sum_{\widetilde{W}'}\langle W/C^{(+)}\rangle \quad (30)$$
$$\times\langle\widetilde{W}'/\widetilde{C}'^{(-)}\rangle^*\langle\widetilde{W}'|W\rangle\,dE_{C'}.$$

Further, we substitute relations (8) and (24) into (30) and perform some simple transformations. In this way, we find that the on-shell elements of the scattering matrix can be represented in the form

$$\langle C'|S|C\rangle = \exp\{2i\delta_C\}\delta_{\hat{\alpha}_c\hat{\alpha}_{c'}}\delta_{i_C i_{C'}} \quad (31)$$
$$- i\pi\exp\{i\delta_{C'}\}\sum_{w'}\langle\widetilde{C}'|\mathcal{V}|w'\rangle\langle w'/C^{(+)}\rangle$$
$$- i\pi\exp\{i\delta_C\}\sum_{\widetilde{w}'}\langle C|\mathcal{V}|\widetilde{w}'\rangle^*\langle\widetilde{w}'/\widetilde{C}'^{(-)}\rangle^*,$$

where it is assumed that $E_C = E_{C'}$.

From Eq. (31), it can be seen that the on-shell scattering matrix can be expressed in terms of a finite

number of the internal components of the scattering states $|C^{(+)}\rangle$ and $|\widetilde{C}'^{(-)}\rangle$, for which we have derived above a compact set of algebraic equations [see formula (27)].

6. DISCUSSION

Let us summarize some results of this investigation.

(i) First and foremost, we note that the formalism proposed here is a two-component one. The coupled-channel Eqs. (27) make it possible to calculate both the proton ($\langle lj\tau = -1/2, i|C^{(\pm)}\rangle$) and the neutron ($\langle lj\tau = +1/2, i|C^{(\pm)}\rangle$) components of scattering states, whereby one can simultaneously investigate (n, n'), (n, p), (p, n), and (p, p') reactions.

(ii) The model enables one to describe correctly collective nuclear processes [7], since the basis states $a^+_\alpha|\Psi_i(A)\rangle$ include low-lying collective states $|\Psi_i(A)\rangle$ of the final nucleus. It should be emphasized that, in contrast to the analyses performed in [8, 9], this description is fully microscopic and is not based on the distorted-wave approximation.

(iii) At moderate energies of incident nucleons ($\varepsilon \leq 12$ MeV), it is sufficient to take into account, in the single-particle basis $\{|\alpha\rangle, |-\gamma\rangle\}$ used in relevant calculations, only two shells, one above the valence shell and one below it.

(iv) In order to obtain a correct absolute value of the noncompound reaction component, it is necessary to use a complex-valued single-particle potential $u(r)$ (see above). This potential must be absorbing for particle states above the Fermi surface and generating for particle states below the Fermi surface (in order to ensure the absorption of a hole). The surface potential found in the global optical model [16] from an analysis of data on the scattering of $\varepsilon \leq 15$ MeV neutrons possesses the required property. It seems that the potential from [16] cannot be used directly, since Eqs. (27) take partly into account inelastic processes that determine the imaginary part of the optical potential. However, one can make use of the form of this potential, considering its amplitude as a model parameter.

(v) In contrast to Feshbach–Kerman–Koonin theory, the model being considered does not separate the contributions of multistep direct, multistep compound, and collective nuclear processes to the noncompound component of a nucleon-induced reaction. Such a partition is probably meaningful at high projectile energies ($\varepsilon > 30$ MeV), but it is hardly possible in the energy region where collective states (giant resonances) are formed in input channels. For nucleon-induced reactions, a detailed investigation of the behavior of partial cross sections corresponding to a fixed state (or a fixed group of states) of the final nucleus versus the incident-nucleon energy ε or versus the excitation energy of the compound system (see figure) could be a good test of advantages of the two approaches. This test would reveal the role of collective doorway states in nucleon-induced reactions.

ACKNOWLEDGMENTS

I am grateful to B.S. Ishkhanov, who suggested that I address this problem.

REFERENCES

1. H. Feshbach, A. Kerman, and S. Koonin, Ann. Phys. (N.Y.) **125**, 429 (1980).
2. R. Bonetti, M. B. Chadwick, P. E. Hodgson, *et al.,* Phys. Rep. **202**, 171 (1991).
3. R. Bonetti, J. M. Akkermans, A. J. Koning, *et al.,* Phys. Rep. **247**, 1 (1994).
4. J. J. Griffin, Phys. Rev. Lett. **17**, 478 (1966).
5. M. Herman and G. Reffo, in *Proceedings of the 5th International Conference on Nuclear Reaction Mechanisms, Varenna, Italy, 1988,* p. 83.
6. P. Demetriou, P. E. Hodgson, A. Marcinkowski, *et al.,* J. Phys. G **22**, 629 (1996).
7. A. Marcinkowski, P. Demetriou, and P. E. Hodgson, J. Phys. G **21**, 1089 (1995).
8. A. Marcinkowski, B. Marianski, P. Demetriou, *et al.,* Phys. Rev. C **52**, 2021 (1995).
9. P. Demetriou, A. Marcinkowski, and P. E. Hodgson, Nucl. Phys. A **596**, 67 (1996).
10. F. Folkmann and C. Gaarde, Nucl. Phys. A **252**, 343 (1975).
11. E. N. Golovach and V. N. Orlin, Yad. Fiz. **62**, 247 (1999) [Phys. At. Nucl. **62**, 212 (1999)].
12. E. N. Golovach, B. S. Ishkhanov, and V. N. Orlin, Nucl. Phys. A **653**, 45 (1999).
13. E. N. Golovach, B. S. Ishkhanov, and V. N. Orlin, Yad. Fiz. **63**, 444 (2000) [Phys. At. Nucl. **63**, 377 (2000)].
14. E. N. Golovach and V. N. Orlin, Nucl. Phys. A **662**, 267 (2000).
15. E. N. Golovach and V. N. Orlin, Yad. Fiz. **59**, 1948 (1996) [Phys. At. Nucl. **59**, 1879 (1996)].
16. J. Rapaport, Phys. Rep. **87**, 25 (1982).

Translated by A. Isaakyan

Physics of Atomic Nuclei, Vol. 65, No. 1, 2002, pp. 82–84. Translated from Yadernaya Fizika, Vol. 65, No. 1, 2002, pp. 87–89.
Original Russian Text Copyright © 2002 by Litvinsky, Rusinko.

NUCLEI
Theory

ARC Spectra from the Reaction ^{115}In(n,γ) and Temperature Dependence of the Width of the Giant Magnetic Resonance

L. L. Litvinsky and P. M. Rusinko

State Research and Engineering Center for Control Systems and Emergency Response, pr. Geroev Stalingrada 64/56, Kiev, 04213 Ukraine

Received September 5, 2000; in final form, January 14, 2001

Abstract—The resonance-averaged spectra of primary γ transitions in the reaction ^{115}In(n,γ) are analyzed at the average neutron energies of $E_n = 1.9$, 24.3, and 134 keV. The temperature dependence of the width of the giant magnetic resonance is found by parametrizing the observed intensities of $M1$ transitions.
© *2002 MAIK "Nauka/Interperiodica".*

1. INTRODUCTION

Investigation of γ-ray spectra from neutron capture that are averaged over neutron resonances (ARC spectra) indicates that giant resonances manifest themselves in the energy dependence of $E1$ and $M1$ radiative strength functions $S_\gamma^{E1,M1}(E_\gamma)$ [1]. Radiative strength functions S_γ^{PL} are determined by parametrizing the experimental mean values of the partial widths of primary γ transitions in (n,γ) reactions as

$$\Gamma_{\gamma i}^{J}(E_{\gamma i}) = \sum S_\gamma^{PL} D_J (E_{\gamma i})^{2L+1}, \qquad (1)$$

where D_J is the mean spacing between resonances of spin J, $E_{\gamma i}$ is the γ-transition energy, and summation is performed over all P types (electric and magnetic) and multipole orders L contributing to ith γ transition.

Recent experimental data provide information predominantly about the $E1$ component, which makes the main contribution to γ spectra. As was shown in [2–4], $E1$-transition intensities observed for spherical nuclei cannot be satisfactorily approximated on the basis of the Brink hypothesis, which predicts the Lorentzian energy dependence

$$S_\gamma^{E1}(E_\gamma) \sim \Gamma_G E_\gamma / ((E_\gamma^2 - E_G^2)^2 + (E_\gamma \Gamma_G)^2), \quad (2)$$

where E_G and Γ_G are the energy and width of the giant electric dipole resonance (GEDR) observed in (γ, n) reactions.

The energy dependence $S_\gamma^{E1}(E_\gamma)$ experimentally observed in ARC spectra and in γ spectra from $(n,\gamma\alpha)$ reactions on spherical nuclei is satisfactorily approximated by introducing a temperature-dependent GEDR width. This approach was most consistently justified within the Kadmensky–Markushin–Furman model [4], where the $E1$ strength function is parametrized as

$$S_\gamma^{E1}(E_\gamma) \sim E_\gamma \Gamma_t(E_\gamma, T)/(E_\gamma^2 - E_G^2)^2. \qquad (3)$$

Here, the spreading GEDR width Γ_t associated with the residual-nucleus temperature T has the form

$$\Gamma_t(E_\gamma, T) = \Gamma_G(E_\gamma^2 + 4\pi T^2)/E_G, \qquad (4)$$

where

$$T = ((E_n + B_n - E_\gamma)/a)^{1/2}, \qquad (5)$$

with B_n and a being the binding energy and the level-density parameter, respectively.

Experimental data on the energy dependence of the $M1$ radiative strength function $S_\gamma^{M1}(E_\gamma)$ are scanty. Kopecky and Chrien [5] showed that the intensities of $M1$ transitions in the ARC spectra from the reaction ^{105}Pd(n,γ) are consistent with the predictions of the spin-flip model [6], where a giant magnetic resonance (GMR) is associated with transitions between the components of the single-particle spin–orbit doublet. The energy dependence $S_\gamma^{M1}(E_\gamma)$ is approximated by the Lorentzian profile (2) with a width Γ_G^{M1} of about the single-particle fragmentation width,

$$\Gamma_G^{M1} \approx \Gamma \downarrow \approx 4 \text{ MeV}. \qquad (6)$$

The GMR energy predicted by the spin-flip model for $A \sim 100$ nuclei is [6]

$$E_G^{M1} \approx 8 \text{ MeV}. \qquad (7)$$

In analyzing the ARC spectra from the reaction ^{113}Cd(n,γ), one of the present authors [7, 8] estimated the parameters of the GMR at

$$E_G^{M1} = 8.8 \pm 1.6 \text{ MeV}, \quad \Gamma_G^{M1} = 4.7 \pm 2.6 \text{ MeV}, \qquad (8)$$

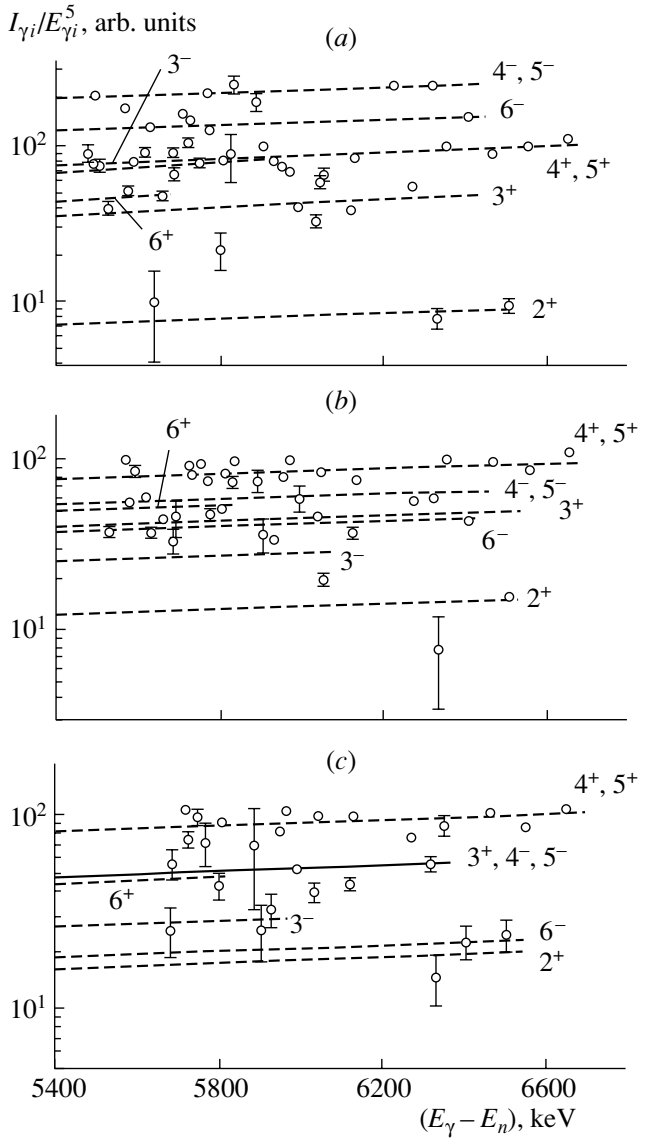

Fig. 1. Reduced relative intensities of primary γ transitions in the reaction ^{115}In(n,γ) at the mean neutron energies of (*a*) 1.9, (*b*) 24.3, and (*c*) 134 keV [9]: (points) experimental data and (solid and dashed lines) mean intensities of the transitions to final states of spin–parities indicated in the figure.

in accord with the model results in (6) and (7).

At the same time, large statistical and fluctuation errors in the experimental data analyzed in [5, 7, 8] gave no way to examine reliably the possible temperature dependence of the GMR width or to disprove its presence. Here, we analyze the ARC spectra from the reaction ^{115}In(n,γ) that were measured in [9] with a higher statistical accuracy and a lower fluctuation error in relation to the data analyzed in [5, 7, 8].

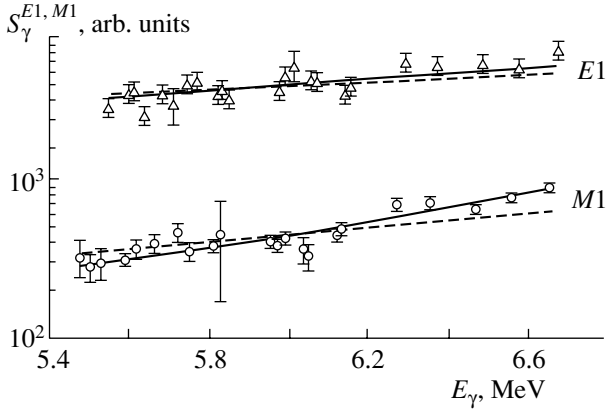

Fig. 2. Energy dependence of the $E1$ and $M1$ radiative strength functions: (points) experimental data and (solid and dashed lines) their approximations by Eqs. (3) and (2), respectively.

2. ENERGY DEPENDENCE OF THE $E1$ AND $M1$ RADIATIVE STRENGTH FUNCTIONS

Figure 1 shows the energy dependence of the reduced relative intensities $I_{\gamma i}^0$ determined for the reaction ^{115}In(n,γ) in [9] for the neutron energies of $E_n = 1.9$, 24.3, and 134 keV as

$$I_{\gamma i}^0 = I_{\gamma i}/E_{\gamma i}^5, \qquad (9)$$

where $I_{\gamma i}$ are the relative intensities of the γ transitions directly observed in the ARC spectra. The method used to process and analyze the spectra was described in detail elsewhere [10].

The intensities $I_{\gamma i}^0$ were analyzed by the method outlined in [7, 8]. The contributions of the d and the f wave and corrections for resonance self-shielding were taken into account in data analysis, but these effects are not crucial. At $E_n = 1.9$ keV, the $E1$ transitions from $J^\pi = 4^+$ and 5^+ s-wave resonances make a dominant contribution to the intensities of primary transitions to the $J^\pi = 3^- – 6^-$ final states. The intensities of the transitions to the $J^\pi = 3^+ – 6^+$ states for $E_n = 1.9$ keV are determined not only by $M1$ transitions from s-wave resonances but also by a sizable contribution of $E1$ transitions from p-wave resonances. At $E_n = 24.3$ and 134 keV, the p-wave contribution increases, whereas the s-wave contribution decreases noticeably.

To investigate the energy dependence of $S_\gamma^{E1}(E_\gamma)$ and $S_\gamma^{M1}(E_\gamma)$, we analyzed transitions to positive-parity states for $E_n = 24.3$ and 134 keV and $E_n = 1.9$ keV, respectively. The contribution from the opposite-parity component was taken into account by the method of successive approximations. Our calculations also included the contribution from $E2$

transitions. Figure 2 shows the results that we obtained.

3. PARAMETERS OF THE GIANT ELECTRIC AND MAGNETIC RESONANCES

The resulting radiative strength functions $S_\gamma^{E1}(E_\gamma)$ and $S_\gamma^{M1}(E_\gamma)$ were approximated by two methods:

(i) as the Lorentzian profile (2) with a constant width $\Gamma_G(\Gamma_G^{M1})$;

(ii) within the Kadmensky–Markushin–Furman model specified by expression (3) with a temperature-dependent width.

The estimates in (6) and (7) were taken as the input values of the GMR parameters. For the GEDR parameters, we adopted the estimates

$$E_G = 16\ \text{MeV}, \quad \Gamma_G = 7\ \text{MeV}, \tag{10}$$

which were based on data for neighboring nuclei [1].

Figure 2 shows the resulting parametrizations. Experimental data on S_γ^{E1} proved to be insufficiently sensitive for reliably determining the GEDR parameters. The χ^2 values for the parametrizations of $S_\gamma^{E1}(E_\gamma)$ with the parameters fixed at the values in (10) are the following:

$$\text{for the Lorentzian profile (2)}, \quad \chi = 1.3; \tag{11}$$

$$\text{for the Kadmensky–Markushin–Furman model [expression (3)]}, \quad \chi = 0.92.$$

In accord with other data for spherical nuclei [1], the results in (11) indicate that the approach based on (3) is preferable.

Our analysis of data on S_γ^{M1} has revealed that E_G^{M1} and Γ_G^{M1} cannot be determined simultaneously because of their strong correlation. For χ^2 and E_G^{M1}, the calculations that were performed with Γ_G^{M1} fixed at the value in (6) yielded the following results:

$$\text{for the Lorentzian profile (2)}, \quad \chi^2 = 2.3, \tag{12}$$

$$E_G^{M1} = 9 \pm 6\ \text{MeV};$$

for expression (3), $\chi^2 = 0.93$,

$$E_G^{M1} = 8.6 \pm 0.4\ \text{MeV}.$$

From these results, it follows that the quality of the fit is much higher in the case of the temperature-dependent GMR width. A similar improvement is also achieved by using the Lorentzian profile (2) with the invariable parameter Γ_G^{M1} reduced to values

$$\Gamma_G^{M1} < 1\ \text{MeV}. \tag{13}$$

However, these values of the width Γ_G^{M1} are much less than the single-particle estimate (6) and the experimental results for neighboring nuclei [5, 7, 8]. In contrast to the results reported in [5, 7, 8], the data obtained in this study refer to an energy range far off the GMR energy. For this reason, the required small Γ_G^{M1} value (13) can also be treated as a manifestation of the strong temperature dependence of the GMR width.

REFERENCES

1. B. J. Allen, I. Bergqvist, R. E. Chrien, *et al., Neutron Radiative Capture* (Pergamon, Oxford, 1984).
2. V. A. Vtyurin, Yu. P. Popov, and V. I. Furman, in *Neutron Physics* (TsNIIatominform, Moscow, 1984), Vol. 1, p. 144.
3. J. Kopecky and M. Uhl, Phys. Rev. C **41**, 1941 (1990).
4. S. G. Kadmenskiĭ, V. P. Markushev, and V. I. Furman, Yad. Fiz. **37**, 277 (1983) [Sov. J. Nucl. Phys. **37**, 165 (1983)].
5. J. Kopecky and R. E. Chrien, Nucl. Phys. A **468**, 285 (1987).
6. A. Bohr and B. Mottelson, *Nuclear Structure*, Vol. 2: *Nuclear Deformations* (Benjamin, New York, 1975; Mir, Moscow, 1977).
7. L. L. Litvinsky, in *Proceedings of the II International Seminar on Interaction of Neutrons with Nuclei, Dubna, 1994* (JINR, Dubna, 1994), p. 32.
8. L. L. Litvinsky, Z. Phys. A **349**, 147 (1994).
9. L. L. Litvinsky, V. G. Krivenko, *et al.*, Preprint No. 94-15, KIYaI (Kiev Inst. for Nuclear Research, Kiev, 1994).
10. L. L. Litvinskiĭ, V. A. Libman, *et al.*, Preprint No. 94-12, KIYaI (Kiev Inst. for Nuclear Research, 1994).

Translated by R. Tyapaev

Physics of Atomic Nuclei, Vol. 65, No. 1, 2002, pp. 85–89. Translated from Yadernaya Fizika, Vol. 65, No. 1, 2002, pp. 90–94.
Original Russian Text Copyright © 2002 by Belov, Lutpullaev, Olimov, Yuldashev.

ELEMENTARY PARTICLES AND FIELDS
Experiment

Rapidity and Azimuthal Correlations in $\pi^- p$ and π^-C Collisions at 40 GeV/c

M. A. Belov[1)], S. L. Lutpullaev, K. Olimov[*], and B. S. Yuldashev[1)]

Institute for Physics and Technology, Fizika–Solntse Research and Production Association, ul. Timiryazeva 2b, Uzbek Academy of Sciences, Tashkent, 700084 Republic of Uzbekistan

Received November 13, 2000; in final form, April 3, 2001

Abstract—New results are presented that were obtained from an analysis of experimental data on rapidity and azimuthal correlations in $\pi^- p$ and π^-C collisions at 40 GeV/c. Some nonstandard methods for seeking correlations are developed. Dynamical correlations associated with fluctuations of the number of intranuclear collisions at a given multiplicity are discovered in π^-C collisions. It is shown that the Lund model cannot describe the experimental data being discussed. © *2002 MAIK "Nauka/Interperiodica".*

1. INTRODUCTION

The multiparticle production of hadrons dominates strong interactions at high energies. Numerous models, including those based on the quark-parton structure of hadrons, are developed to describe this complicated process. However, existing experimental data and standard methods for their treatment do not favor any of the competing models. In the present study, correlations are analyzed by the nonstandard statistical methods proposed in [1–4]. The exposition is organized as follows. In Section 2, we briefly describe these methods and a further development [3] of the method for an analysis of variances of rapidities. In Section 3, the methods described in the preceding section are used to investigate $\pi^- p$ and π^-C interactions at 40 GeV/c.

In order to find out whether any of the methods proposed below are sensitive to the interaction mechanism and to choose between various theoretical approaches, experimental data are contrasted against the results of calculations based on the Lund quark-fragmentation model [5], which describes successfully the multiplicities and other inclusive features of secondaries from high-energy hadron–nucleon and hadron–nucleus collisions. In the model version [5] tested here, a string is stretched between a quark and a diquark (in the case where a nucleon is used as a projectile) separately for the target and the projectile. The interaction occurs via momentum exchange when two colliding hadrons approach each other at a distance $d \le \sqrt{\sigma_{hh}}$ (where σ_{hh} is the inelastic cross section for the colliding hadrons). As a result, there arise two longitudinally extended excited objects, which then fragment independently. For hadron–nucleus interactions, it is assumed that the projectile traversing the nucleus can interact with ν target nucleons and that the mass of the projectile string increases upon each successive interaction event. If the projectile mass after n subcollisions became m_n, the next subcollision is considered as a collision of two hadrons having the mass equal to that of the nucleon and the mass m_n. Eventually, we obtain ν target strings and one projectile string. The string-fragmentation time substantially exceeds the internucleon time of flight; therefore, the projectile string fragments outside the nucleus. The number of intranuclear collisions is usually calculated by the Glauber method.

2. STATISTICAL CORRELATION METHODS

χ^2 criterion. The χ^2 criterion is applicable for arbitrary multiplicities. The azimuthal angle φ (the angle of particle emission in the plane orthogonal to the direction of the incident beam) varies in the interval from 0 to 2π. We break down this interval into m equal bins and compose the well-known quantity

$$\chi^2 = \frac{m}{n}\sum_{k=1}^{m}\left[n_k - \frac{n}{m}\right]^2 = \frac{m}{n}\sum_{k=1}^{m} n_k^2 - n, \qquad (1)$$

where n_k is the number of particles in the kth bin and $n = \sum_{k=1}^{m} n_k$ is the number of charged secondaries in one event. The azimuthal angles φ_1, φ_2, …, φ_n have the same distributions in events characterized by a given multiplicity n. Assuming that these angles are

[1)]Institute of Nuclear Physics, Uzbek Academy of Sciences, pos. Ulughbek, Tashkent, 702132 Republic of Uzbekistan.
[*]e-mail:olimov@physic.uzsci.net

mutually independent, we write the multidimensional probability in the form

$$p(\varphi_1, \varphi_2, \ldots, \varphi_n)d\varphi_1 d\varphi_2 \ldots d\varphi_n = \prod_{i=1}^{n} p(\varphi_i)d\varphi_i. \quad (2)$$

The mean value of the quantity $\alpha = \chi^2/(m-1)$ is then given by

$$\langle\alpha\rangle = 1 + (n-1)\frac{m}{m-1}\sum_{k=1}^{m}\left[p_k - \frac{1}{m}\right]^2, \quad (3)$$

where p_k is the probability for φ to fall within the kth bin and angular brackets denote averaging over events. It can easily be shown that, in the presence of dynamical (kinematical) correlations, the value $\langle\alpha\rangle$ is maximal (minimal) at $m = 2$ and that $\langle\alpha\rangle \to 1$ for $m \to \infty$. If both the projectile and the target are unpolarized, the density of the one-dimensional distribution is

$$p(\varphi) = 1/2\pi, \quad (4)$$

so that the mean value of α is

$$\langle\alpha\rangle = 1, \quad (5)$$

its variance being

$$\sigma^2[\alpha] = \frac{2(n-1)}{(m-1)n} < \frac{2}{m-1}. \quad (6)$$

The equality in (5) and the inequality in (6) can easily be generalized to events where n can take different values. According to the central limit theorem of probability theory, α averaged over a large number N of events must fall within the interval

$$\left[1 - \frac{2\sqrt{2}}{\sqrt{(m-1)\,N}}\right] < \frac{1}{N}\sum_{i=1}^{N}\alpha_i < \left[1 + \frac{2\sqrt{2}}{\sqrt{(m-1)\,N}}\right] \quad (7)$$

with a probability over 95%. Otherwise, we can conclude that there are azimuthal correlations.

The χ^2 criterion can be applied to searches for rapidity correlations if, from the rapidity y, we go over to the uniformly distributed quantity

$$z = \int_{-\infty}^{y} p_n(y')dy', \quad (8)$$

where $p_n(y)$ is the density of the rapidity distribution in events characterized by a fixed multiplicity n. According to (8), one can associate, with each value of the rapidity y, the quantity z equal to the ratio of the number of rapidities lower than y to the total number of rapidities characterized by identical multiplicities. We break down the range of z between 0 and 1 into m equal bins and calculate the value of χ^2 (1) for each event. If the inequality in (7) is violated, rapidity correlations are present.

***β* criterion.** To study azimuthal correlations at large n, P. Zelinskii (private communication, 1962) used the quantity

$$\beta = \frac{\mathbf{r}^2}{n} = \frac{\left(\sum_{i=1}^{n}\cos\varphi_i\right)^2 + \left(\sum_{i=1}^{n}\sin\varphi_i\right)^2}{n}, \quad (9)$$

where $\mathbf{r}$ is the sum of unit vectors directed along the transverse momenta of n secondaries. In contrast to α, β is independent of the choice of reference axis for azimuthal angles. Let us show that this criterion is applicable at any n. We have

$$\langle\beta\rangle = 1 + (n-1)[\langle\cos\varphi\rangle^2 + \langle\sin\varphi\rangle^2], \quad (10)$$

$$\langle\cos\varphi\rangle = \int_0^{2\pi}\cos\varphi p(\varphi)d\varphi,$$

$$\langle\sin\varphi\rangle = \int_0^{2\pi}\sin\varphi p(\varphi)d\varphi.$$

It follows from (2) and (4) that

$$\langle\beta\rangle = 1, \quad \sigma^2[\beta] = \frac{n-1}{n} < 1. \quad (11)$$

Therefore, β averaged over a large number N of events must fall within the interval

$$\left[1 - \frac{2}{\sqrt{N}}\right] < \frac{1}{N}\sum_{i=1}^{N}\beta_i < \left[1 + \frac{2}{\sqrt{N}}\right] \quad (12)$$

with a probability over 95%. Otherwise, azimuthal correlations are present.

Analysis of variances of rapidities. In the theory of the analysis of variance, use is made of the quantity

$$F = \frac{nS_1^2}{S_2^2}, \quad (13)$$

where

$$S_1^2 = \frac{1}{N-1}\sum_{i=1}^{N}\left[\bar{y}_i - \langle y\rangle\right]^2, \quad (14)$$

$$S_2^2 = \frac{1}{N}\sum_{i=1}^{N}\left[\frac{1}{n-1}\sum_{j=1}^{n}(y_{ij} - \bar{y}_i)^2\right]$$

with

$$\bar{y}_i = \frac{1}{n}\sum_{j=1}^{n} y_{ij}, \quad \langle y\rangle = \frac{1}{N}\sum_{i=1}^{N} y_i.$$

Here, N is the number of events characterized by the same multiplicity n and y_{ij} is the rapidity of the jth particle in the ith event. If n quantities y_j are independent, then $F \to 1$ for $N \to \infty$.

Let us consider a nonhomogeneous ensemble of events; it can easily be broken down into subensembles having different rapidity distributions of secondaries. If the quantities y_j ($j = 1, 2, \ldots, n$) are independent in each subensemble and if the number N of events in the ensemble is infinitely large, the ratio of variances is

$$F = 1 + n\sum_k \omega_k(\upsilon_k - \upsilon)^2 / \sum_k \omega_k\sigma_k^2, \qquad (15)$$
$$\upsilon = \sum_k \omega_k\upsilon_k,$$

where υ_k and σ_k^2 are, respectively, the expectation value and the variance of y_j in the kth subensemble and ω_k is the fraction of the events from the kth subensemble in the ensemble.

We group the events of the ensemble into complex trials, each consisting of N events, and consider the distribution of the quantity F in these complex trials. If the quantities y_j ($j = 1, 2, \ldots, n$) in the ensemble are independent and have arbitrary distributions and if n is large, the ratio of variances assumes the form

$$F \approx \chi^2_{N-1}/(N-1), \qquad (16)$$

where the quantity χ^2_{N-1} has a χ^2 distribution with $(N-1)$ degrees of freedom. According to (16), the expectation value and the variance of the quantity F are

$$\upsilon[F] = 1, \quad \sigma^2[F] = 2/(N-1). \qquad (17)$$

At N exceeding 30, the χ^2 distribution reduces to a normal distribution. Therefore, the quantity F must fall within the interval

$$\left[1 - \frac{2\sqrt{2}}{\sqrt{N-1}}\right] < F < \left[1 + \frac{2\sqrt{2}}{\sqrt{N-1}}\right] \qquad (18)$$

with a probability of about 95%. Otherwise, there are rapidity correlations.

In relation to the χ^2 criterion, the analysis of variances is advantageous in that it does not require determining the values of z from the rapidities. This procedure is incorrect for a small number of events and is cumbersome for a large number of events.

The problem of assessing values of n at which formulas (16) and (18) are valid was not discussed in [3]. It is difficult to solve this problem in general. Let us consider it for the example of a normal rapidity distribution. In this case, we have

$$nS_1^2/\sigma^2 = \chi^2_{N-1}/(N-1), \qquad (19)$$
$$S_2^2/\sigma^2 = \chi^2_{N(n-1)}/N(n-1),$$

where σ^2 is the variance of rapidities. The two quantities in (19) are independent. At large values of N, these quantities have narrow distributions; therefore, the ratio of variances assumes the form

$$F \approx 1 + nS_1^2/\sigma^2 - S_2^2/\sigma^2. \qquad (20)$$

It follows from (19) and (20) that the quantity F has an approximately normal distribution with the parameters

$$\upsilon[F] = 1, \quad \sigma^2[F] = \frac{2}{N-1} + \frac{2}{N(n-1)}. \qquad (21)$$

Neglecting the second term in the second formula in (21) for $n > 5$, we arrive at the approximation in (16).

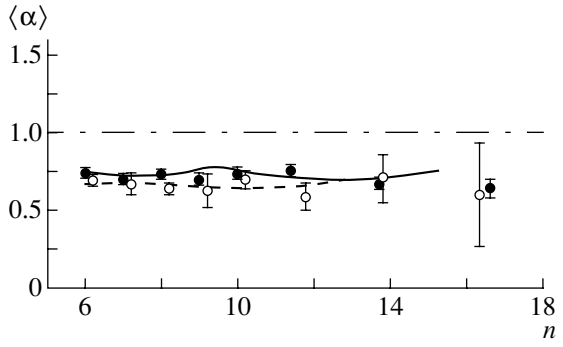

Fig. 1. $\langle\alpha\rangle$ as a function of the number n of secondary pions for azimuthal angles at $m = 2$ (experimental points and theoretical curves calculated on the basis of the Lund model): (closed circles) experimental data for π^-C, (open circles) experimental data for π^-p, (solid curve) theoretical results for π^-C, and (dashed curve) theoretical results for π^-p.

3. ANALYSIS OF EXPERIMENTAL DATA

Here, we analyze experimental data obtained by a collaboration that processes films from the 2-m propane (C_3H_8) bubble chamber installed at the Joint Institute for Nuclear Research (JINR, Dubna). The chamber was irradiated with 40-GeV/c π^- mesons. We studied 5336 π^-p and 5576 π^-C collisions featuring more than five charged secondaries. We excluded unambiguously identified protons from secondaries. Events that did not satisfy selection criteria for π^-N collisions were identified as those of π^-C interactions. The details of the experiment are described in [6]. We determined the rapidity using the pion mass. Events characterized by close values of n were combined into groups, and groups containing less than 50 events were discarded.

Azimuthal correlations. Figure 1 displays the mean value of α ($m = 2$), which characterizes azimuthal correlations, as a function of the number n of secondary pions. The statistical error is assumed to be $\sqrt{1/(m-1)N}$. Correlations in π^-p

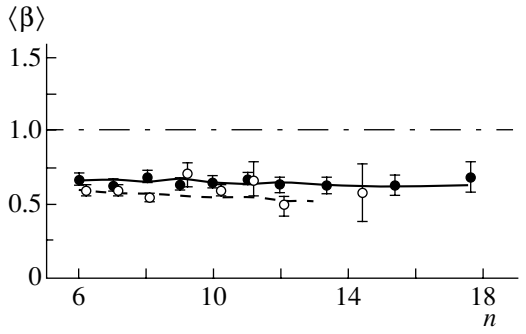

Fig. 2. $\langle\beta\rangle$ as a function of the number n of secondary pions. The notation is identical to that in Fig. 1.

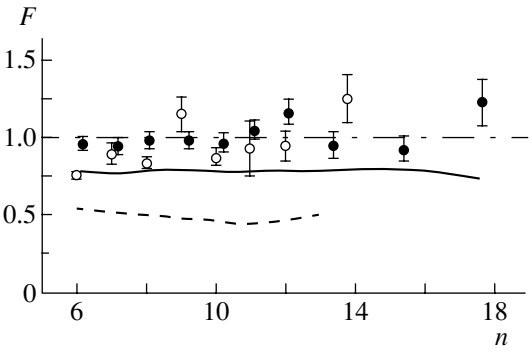

Fig. 3. Ratio F of variances as a function of the number n of secondary pions for azimuthal angles at $m = 2$. The notation is identical to that in Fig. 1.

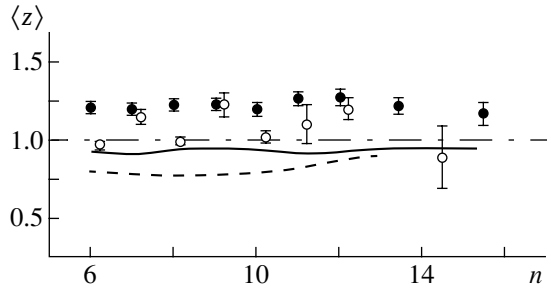

Fig. 4. $\langle z\rangle$ as a function of the number n of secondary pions for rapidities at $m = 2$. The notation is identical to that in Fig. 1.

and π^-C collisions have a kinematical character. The momentum-conservation law suppresses asymmetric configurations of the transverse momenta, with the result that the mean value of α is reduced. Within the statistical errors, $\langle\alpha\rangle(m = 2)$ does not depend on the number of secondary pions, and we did not observe positive correlations associated with the dynamics of particle production. The calculations on the basis of the Lund model satisfactorily describe the experimental data in question.

Figure 2 presents the mean value of β as a function of the multiplicity n. In this case, we also confirm the kinematical character of azimuthal correlations. The conservation of the transverse momentum reduces the length of the vector **r** in (9). At the same time, the development of the intranuclear cascade could lead to an excess of asymmetric configurations of azimuthal angles and to fulfillment of the inequality $\langle\beta\rangle > 1$ in π^-C collisions.

In either dependence, the kinematical correlations are more pronounced in π^-p collisions than in π^-C collisions.

Rapidity correlations. The quantity $F(m = 2)$, which characterizes rapidity correlations, is displayed in Fig. 3 as a function of the number of secondary pions. As in the two dependences considered above, we do not observe here any positive correlations. Dynamical correlations are likely to be compensated by kinematical ones [$F(m = 2) \approx 1$]. Within the statistical errors, $F(m = 2)$ does not depend on n. In the Lund model, kinematical correlations are stronger than dynamical.

Figure 4 presents the mean value of z ($m = 2$) as a function of the number of secondary pions. Clear rapidity correlations in π^-C interactions can be explained in the following way. The number of intranuclear nucleons that participate in collision events characterized by the same multiplicity n fluctuates, whence it follows that the ensemble of events can be broken down into subensembles. The partial rapidity distributions of secondaries and the quantity z are different in the subensembles, and the partial distribution of z differs from a uniform one. By applying formula (1) to the subensembles, we obtain

$$z = \chi^2(m-1),$$

$$\langle z\rangle = 1 + (n-1)\,\frac{m}{m-1}\sum_{k=1}^{m}\left[p_k - \frac{1}{m}\right]^2,$$

where p_k is the probability for z to fall within the kth bin. On this basis, we conclude that the inequality $\langle z\rangle > 1$ is valid in the subensembles and, hence, over the entire ensemble. In π^-p interactions, dynamical and kinematical correlations compensate each other. The occurrence of moderate positive correlations at odd n is due to the admixture of diffraction events. In the Lund model, dynamical correlations are strongly suppressed by kinematical correlations.

From the above data analysis, we can draw the conclusion that the quantity z is the most sensitive to the presence of correlations and to distinction between various models. The quantities α and β, which depend on the azimuthal angle of particle emission,

seem insensitive to either the mechanism of multiparticle production or the choice between various theoretical approaches.

ACKNOWLEDGMENTS

We are grateful to V.M. Chudakov for assistance in developing the method of analysis of variances and for an enlightening discussion on our results.

REFERENCES

1. V. M. Chudakov, Zh. Éksp. Teor. Fiz. **40**, 156 (1961) [Sov. Phys. JETP **13**, 107 (1961)].
2. Sh. Abduzhamilov, S. A. Azimov, L. P. Chernova, *et al.*, Zh. Éksp. Teor. Fiz. **45**, 407 (1963) [Sov. Phys. JETP **18**, 281 (1964)].
3. S. A. Azimov, Yu. P. Kratenko, N. Sh. Saidkhanov, and V. M. Chudakov, Izv. Vyssh. Uchebn. Zaved., Fiz., No. 1, 120 (1977).
4. A. Zhumanov, V. Sh. Navotnyi, K. Olimov, and V. M. Chudakov, Yad. Fiz. **57**, 1462 (1994) [Phys. At. Nucl. **57**, 1389 (1994)].
5. B. Andersson, G. Gustafson, and B. Nilsson-Almqvist, Nucl. Phys. B **281**, 289 (1987); Lund University Report LU TP 86-3 (1986), p. 15.
6. A-ABBVDKMSSTTU-BKh Collab. (A. U. Abdurakhimov, N. Angelov, K. P. Vishnevskaya, *et al.*), Yad. Fiz. **18**, 545 (1973) [Phys. At. Nucl. **18**, 281 (1973)].

Translated by M. Kobrinsky

Physics of Atomic Nuclei, Vol. 65, No. 1, 2002, pp. 90–101. Translated from Yadernaya Fizika, Vol. 65, No. 1, 2002, pp. 95–106.
Original Russian Text Copyright © 2002 by A. Bondarenko, R. Bondarenko, Galoyan, Kladnitskaya, Rogachevsky, Uzhinskii.

ELEMENTARY PARTICLES AND FIELDS
Experiment

Features of CC Interactions at a Momentum of 4.2 GeV/c per Nucleon for Various Degrees of Nuclear-Collision Centrality

A. I. Bondarenko, R. A. Bondarenko, A. S. Galoyan, E. N. Kladnitskaya*, O. V. Rogachevsky, and V. V. Uzhinskii

Joint Institute for Nuclear Research, Dubna, Moscow oblast, 141980 Russia

Received July 5, 2000; in final form, November 29, 2000

Abstract—The multiplicity, rapidity, and transverse-momentum distributions of secondaries (negative pions and protons) from CC interactions characterized by various numbers of participant protons are presented. It is shown that, in contrast to the mean transverse momenta of protons, the mean transverse momenta of pions depend only slightly on the degree of collision centrality. The shape of the rapidity distributions of negative pions is also weakly dependent on the degree of collision centrality. With decreasing impact parameter, the product protons are found to concentrate in the central rapidity region. The data in question are analyzed within the modified version of the FRITIOF model. It is shown that, as soon as elastic nucleon rescatterings are taken into account, the model describes satisfactorily the experimental features of negative pions and fast protons. The spectra of slow protons are described only qualitatively because of limitations of the evaporation model used here to treat the deexcitation of residual nuclei. © *2002 MAIK "Nauka/Interperiodica".*

INTRODUCTION

The idea of a cascade of elementary-particle interactions in hadron–nucleus and nucleus–nucleus collisions forms a basis of the popular cascade–evaporation model [1, 2].[1)] It is believed that only within this framework is it possible to explain the yield of fast nucleons. An alternative point of view according to which a large yield of particles in the nuclear-fragmentation region is due to a cascade of Reggeon exchanges (it cannot be reduced to a cascade of particle interactions) was formulated in [6]. According to [6], hadron–nucleus interactions may proceed not only through a succession of nucleon-knockout events in time (ordinary cascade) but also through a simultaneous nucleon knockout, which is described by so-called enhanced nonplanar diagrams. Since all nucleons knocked out simultaneously occur in the same situation, it is natural to expect that, in the regions of nuclear fragmentation, the shape of nucleon spectra is weakly dependent on the degree of collision centrality. Central and peripheral interactions differ predominantly in the number of primary intranuclear collisions. If the number of primary collisions is large, multiple rescatterings of participant nucleons must lead to their concentration in the central rapidity region. According to the Reggeon approach, the shape of nucleon spectra in nuclear-fragmentation regions that is associated with the cascading mechanism must then remain unchanged; at the same time, the yield of nucleons must first increase with decreasing impact parameter and then decrease at very small values of the impact parameter because of a decrease in the mass of the residual nucleus where the Reggeon cascade develops.

A somewhat different situation may be realized according to the cascade–evaporation model. As the impact parameter is reduced, the number of secondaries and the number of cascade interactions in residual nuclei increase. Therefore, one can expect that nucleons are predominantly produced in the regions of nuclear fragmentation. In central collisions—that is, at small values of the impact parameter—the yield of nucleons in the regions of nuclear fragmentation must be minimal because of a large number of primary interactions. It follows that, according to the cascade–evaporation model, the shape of the nucleon spectra in the regions of nuclear fragmentation must undergo changes. This argument is supported by the calculations presented in [7]. However, experiments show an inverse pattern—with increasing degree of collision centrality, a relative increase in the yield of protons is observed in the central region rather than in the region of nuclear

*e-mail: klad@sunhe.jinr.ru

[1)]The FRITIOF [3], RQMD [4], and HIJING [5] models assume a cascade of interactions of intermediate systems, quark strings or excited nucleons, but this does not lead to substantial changes in the pattern of the interactions.

fragmentation [7], the shape of the spectra of slow nucleons remaining virtually unchanged.

In principle, the experimental situation can be understood within the Reggeon approach, but there is not much hope that relevant processes will be described in detail on this basis because the computational formalism of Reggeon theory is very involved. Nonetheless, the simplified computational scheme proposed in [8] enables one to estimate the yield of fast nucleons, whereas the method for determining the momentum features of nucleons that is based on a treatment of nucleons in the Reggeon cascade on equal terms and which was expounded in [9] provides a convenient framework for an exclusive description of the reactions in question. Within this simplified approach, it proved to be possible to describe successfully experimental data on the interactions of gold nuclei with photoemulsion nuclei at an energy of 10.7 GeV per nucleon [9]. Of course, it is of interest to apply this approach, which is implemented in a modified version of the FRITIOF code [10], to an analysis of a different set of experimental data.

The present article reports on a continuation of an analysis of experimental data on the interactions of light nuclei with carbon nuclei at a momentum of 4.2 GeV/c per nucleon on the basis of the FRITIOF model [11] adapted to energies below 10 GeV [10, 12].

In comparing the inclusive features of negative pions and protons from pC, dC, αC, and CC interactions (AC interactions) at a momentum 4.2 GeV/c, it was previously found [11] that the experimental and calculated mean multiplicities of negative pions and protons are in satisfactory agreement and that so are the distributions of negative pions in kinematical variables for all AC interactions. Only in dealing with the distributions of protons in the regions of fragmentation of colliding nuclei did there arise a problem. In order to remove it, we had to take into account here elastic nucleon rescatterings in the interaction process. This made it possible to describe, to a very high precision, the inclusive distributions of protons with respect to kinematical variables in CC interactions. Investigation of nucleus–nucleus interactions characterized by various values of the impact parameter furnishes additional possibilities for assessing the applicability of the aforementioned modified version of the FRITIOF model. Here, we will consider only CC interactions, because the accumulated statistics of experimental events of such interactions are the vastest.

Events in which carbon nuclei collided at specific values of the impact parameter were selected on the basis of the number of protons that participated in such interaction events. As is well known, the number of participant protons is correlated with the impact parameter [7]. This approach to separating events in the number of participant protons was applied both to the experimental ensemble of CC interactions and to the set of simulated events. Previously, the dependence of the mean multiplicity of secondaries and of their momentum and angular distributions on the impact parameter of AC interactions at 4.2 GeV/c was explored in a number of studies (see [7, 13–16]).

Here, we compare the calculated and the measured features of product pions and protons for various degrees of centrality of CC interactions at a momentum of 4.2 GeV/c per nucleon.

1. EXPERIMENTAL DATA

In this study, use was made of data obtained by exposing the 2-m propane bubble chamber installed at the Laboratory of High Energies at the Joint Institute for Nuclear Research (JINR, Dubna) to a beam of ^{12}C nuclei accelerated to a momentum of 4.2 GeV/c per nucleon at the JINR synchrophasotron. The experiment was performed in a magnetic field of strength 1.5 T. Procedures for separating events of inelastic CC interactions from the total ensemble of interactions between carbon nuclei and propane and for introducing corrections for the number of secondaries and their momentum and angular features are described in detail elsewhere [17]. We recall that, because of a short range (less than 2 mm) of protons with momenta below 150 MeV/c and of negative pions with momenta below 40 MeV/c, they are not recorded in the bubble chamber.

In the ensemble of CC interactions that was subjected to an analysis here, charged pions, slow protons ($p < 0.3$ GeV/c) originating from the evaporation process, stripping fragments of the projectile nucleus ($\theta < 4^\circ$ and $p > 3$ GeV/c), and participant protons ($p > 0.3$ GeV/c, stripping particles being excluded) were singled out among secondaries. In the following, we also consider two groups of protons: that which includes protons of momenta in the range between 0.3 and 0.75 GeV/c (these are predominantly participant protons from the target) and that which includes protons of momenta in the region $p >$ 0.75 GeV/c. The last group comprises predominantly participant protons from the projectile nucleus.

The entire ensemble of inelastic CC interactions was broken down into three groups. Events featuring not greater than four participant protons were classified with peripheral events, the mean impact parameter $\langle b \rangle$ for them being greater than 4 fm [7]. This group is dominated by $n_p^{\text{part}} < \langle n_p^{\text{part}} \rangle_{\text{CC}}^{\text{in}} = 4.43$ events. The second and the third group comprise,

respectively, $4 < n_p^{\rm part} \le 9$ and $n_p^{\rm part} > 9$ events (as a matter of fact, $n_p^{\rm part} > 2\langle n_p^{\rm part}\rangle_{\rm CC}^{\rm in}$ in the last case). In the following, events belonging to the third group will be referred to as central events ($\langle b\rangle < 2$ fm) [7].

In addition, we singled out the group of CC events in which the total charge of the stripping fragments of the projectile nucleus is equal to zero. This criterion is frequently used to select central nucleus–nucleus interactions [18–22].

2. MODIFIED VERSION OF THE FRITIOF CODE

2.1. Fundamentals of the Model

The FRITIOF model presumes the two-body kinematics of inelastic hadron–hadron interactions, $a + b \longrightarrow a' + b'$; here, a' and b' are excited states of the primary hadrons a and b. Either excited state is characterized by its mass. In order to choose hadron masses, we use the approach described in [3] (see also [9, 11]). The parameters of the model were refined in [12].

In the case of hadron–nucleus and nucleus–nucleus interactions, it is assumed that nucleons excited in primary collisions can interact with one another and with other intranuclear nucleons, increasing their masses. Thus, the model takes into account the interaction between cascade particles from the point of view of the cascade–evaporation model. The probabilities of multiple collisions are calculated within the Glauber approach.

Excited hadrons are treated as QCD strings, whose fragmentation leads to the production of hadrons. The multiplicity of secondaries grows with increasing string masses. These are the factors that explain an increase in the particle multiplicity when we go over from hadron–hadron to hadron–nucleus and nucleus–nucleus interactions.

Following [23], we took phenomenologically into account not only inelastic collisions of nucleons but also their elastic rescatterings. Specifically, we assumed that two nucleons belonging to the different nuclei interact if the impact parameter of their collision satisfies the condition $b_{ij} \le \sqrt{\sigma_{NN}^{\rm tot}/\pi}$. In the case where there was interaction, we simulated elastic scattering with the probability $\sigma_{NN}^{\rm el}/\sigma_{NN}^{\rm tot}$ and an inelastic collision with the probability $\left(1 - \sigma_{NN}^{\rm el}/\sigma_{NN}^{\rm tot}\right)$.

2.2. Simulation of the Breakup of Nuclei at the Fast Stage of Interactions

The Glauber approximation is used to determine the time succession of nucleon–nucleon collisions in hadron–nucleus and nucleus–nucleus interactions within the FRITIOF model. Since the cascading of secondaries is disregarded here, the model is unable to reproduce the features of slow particles associated with the breakup of the nuclei involved. In order to remedy this drawback, it was proposed in [9, 10] to supplement the FRITIOF model with the Reggeon model of nuclear breakup [8].

The breakup of nuclei is taken into account into two steps. At the first step, the number of inelastically interacted (hit) nucleons is determined with the aid of the Glauber approximation [24]. Noninteracted nucleons are considered at the second step. It is assumed that a noninteracted nucleon occurring at a distance r from a hit nucleon can be involved in a Reggeon cascade with the probability

$$W = C_{nd} e^{-r^2/r_{nd}^2}.$$

The nucleon involved can involve another spectator nucleon, etc. It is assumed that all hit nucleons and all nucleons involved escape from the nucleus.

In order to describe the multiplicity of spectator protons in the interactions considered here, we choose the following parameter values:

$$C_{nd} = 1, \quad r_{nd} = 1.2 \text{ fm}.$$

The excitation energy of the residual nucleus was calculated by employing the approach proposed in [25] and by invoking the method described comprehensively in [9]. The relaxation of excited nuclei was simulated on the basis of the evaporation model [26] (see also [1]).

2.3. Determination of the Momenta of Knock-on Nucleons

In the modified FRITIOF code, it is assumed [9, 27] that the distribution of nucleons knocked out, for example, from the target nucleus with respect to kinematical variables has the form

$$P(\{x_i^-\}, \{\mathbf{p}_{i\perp}\}) \propto \prod_{i=1}^{N_T} \exp[-\mathbf{p}_{i\perp}^2/\langle p_\perp^2\rangle]$$
$$\times \exp[-(x_i^- - 1/N_T)^2/(d_x/N_T)^2],$$
$$\sum_{i=1}^{N_T} \mathbf{p}_{i\perp} = 0, \quad \sum_{i=1}^{N_T} x_i^- = 1,$$

where N_T is the multiplicity of knock-on nucleons; $\mathbf{p}_{i\perp}$ is the transverse momentum of the ith knock-on nucleon; and x_i^- is the light-cone variable given by

$$x_i^- = (E_i - p_{i\|})/W_T^-,$$

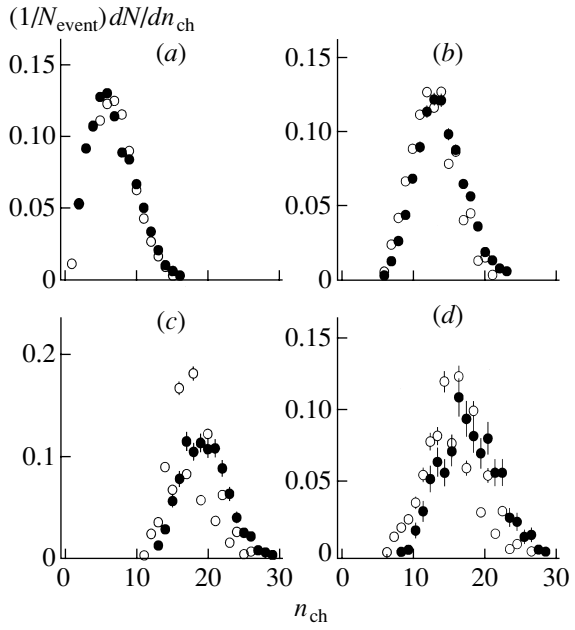

Fig. 1. Distributions of CC interactions with respect to the multiplicity of charged particles for (*a*) $n_p^{\text{part}} \leq 4$, (*b*) $4 < n_p^{\text{part}} \leq 9$, (*c*) $n_p^{\text{part}} > 9$, and (*d*) $Q_{\text{str}} = 0$ events. The closed and the open circles represent, respectively, experimental data and the results of model calculations performed on the basis of the modified FRITIOF code.

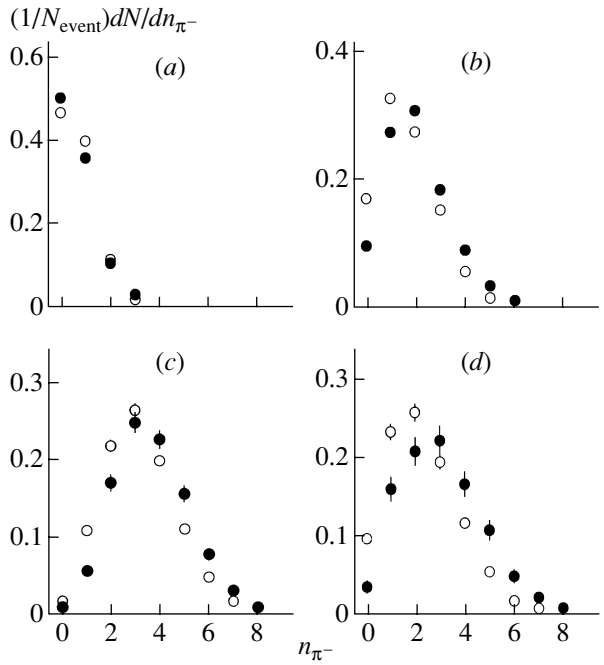

Fig. 2. Distributions of CC interactions with respect to the multiplicity of negative pions. The notation is identical to that in Fig. 1.

with E_i and $p_{i\|}$ being the nucleon energy and the longitudinal momentum, respectively.

The law of energy–momentum conservation is used to determine the quantity W_T^- and the analogous quantity W_P^+ for nucleons knocked out from the projectile nucleus [9].

For the parameters of the above distribution, the values of $\langle p_\perp^2 \rangle = 0.296\,(\text{GeV}/c)^2$ and $d_x = 0.25$ were determined here by analyzing the spectra of particles emitted in hadron–nucleus and nucleus–nucleus interactions into the backward hemisphere.

3. RESULTS

For the above groups of CC interactions, the mean multiplicities of secondaries are given in Table 1, which also displays the number of events in each group. We note that more than half of CC interactions are peripheral, the fraction of central interactions being only a few percent.

As is obvious from this table (see also Fig. 1), the multiplicity of charged particles increases with decreasing impact parameter. Concurrently, the fraction of pions among charged particles increases from 23% in peripheral to about 35% in central interactions.

In the $n_p^{\text{part}} \leq 4$ group, the mean multiplicity of positive pions is greater than the mean multiplicity of negative pions. The reason for this is that, in the $n_p^{\text{part}} \leq 4$ group, the number of events of the proton-to-neutron charge-exchange process $p \to n + \pi^+$ is greater than the number of events of the neutron-to-proton charge-exchange process $n \to p + \pi^-$. The inverse relationship $\langle n_{\pi^-} \rangle > \langle n_{\pi^+} \rangle$ is observed in the group of $n_p^{\text{part}} > 9$ events. In events where nucleon-charge-exchange processes are equiprobable, we have $\langle n_{\pi^-} \rangle = \langle n_{\pi^+} \rangle$. This relationship was obtained for the $4 < n_p^{\text{part}} \leq 9$ and the $Q_{\text{str}} = 0$ group (see Table 1).

The shape of the distribution of events with respect to the number of pions changes as one goes over from peripheral to central CC interactions (for negative pions, see Fig. 2). The number of events not involving pion production decreases sharply, while the fraction of multimeson events increases; as a consequence, the mean multiplicities of positive and negative pions grow (see Table 1). Upon rescaling the mean multiplicities of pions per participant proton, it turned out that, in events characterized by equal $\langle n_{\pi^-} \rangle$ and $\langle n_{\pi^+} \rangle$, the ratio $\langle n_{\pi^-} \rangle / \langle n_p^{\text{part}} \rangle$ is compatible with the corresponding ratio for inelastic CC interactions (0.325 ± 0.003) [11]. The different relationships between the mean multiplicities of negative and

Table 1. Mean multiplicities of secondaries from CC interactions characterized by various numbers of participant protons

		Event type			
		$n_p^{\text{part}} \le 4$	$4 < n_p^{\text{part}} \le 9$	$n_p^{\text{part}} > 9$	$Q_{\text{str}} = 0$
N_{event}	expt	12004 58.3%	7107 34.5%	1483 7.2%	665 3.2%
	model	24495 49.0%	21357 42.7%	4148 8.3%	2299 4.6%
$\langle n_{\text{ch}} \rangle$	expt	6.86 ± 0.02	13.84 ± 0.04	19.52 ± 0.09	17.33 ± 0.16
	model	6.65 ± 0.02	12.92 ± 0.02	17.70 ± 0.05	15.11 ± 0.08
$\langle n_{\pi^-} \rangle$	expt	0.719 ± 0.005	2.166 ± 0.016	4.00 ± 0.04	3.16 ± 0.07
	model	0.689 ± 0.005	1.664 ± 0.008	3.17 ± 0.02	2.32 ± 0.03
$\langle n_{\pi^+} \rangle$	expt	0.886 ± 0.006	2.134 ± 0.018	2.90 ± 0.04	3.31 ± 0.07
	model	0.894 ± 0.006	1.642 ± 0.010	1.95 ± 0.02	2.58 ± 0.03
$\langle n_p \rangle$, $p_p < 0.15$	expt	4.110 ± 0.039	1.819 ± 0.023	0.37 ± 0.10	1.00 ± 0.08
	model	4.389 ± 0.028	2.009 ± 0.014	0.63 ± 0.09	1.52 ± 0.04
$\langle n_p \rangle$, $0.15 \le p_p < 0.3$	expt	0.653 ± 0.006	0.889 ± 0.012	0.50 ± 0.02	0.80 ± 0.04
	model	0.348 ± 0.005	0.663 ± 0.006	0.48 ± 0.01	0.53 ± 0.02
$\langle n_p \rangle$, $0.3 \le p_p < 0.75$	expt	0.717 ± 0.005	1.717 ± 0.015	2.61 ± 0.04	1.91 ± 0.06
	model	0.613 ± 0.005	1.736 ± 0.009	2.48 ± 0.02	1.61 ± 0.03
$\langle n_p \rangle$, $p_p \ge 0.75$	expt	1.586 ± 0.007	4.925 ± 0.019	8.41 ± 0.05	8.15 ± 0.09
	model	1.712 ± 0.007	4.957 ± 0.012	8.44 ± 0.03	8.07 ± 0.04
$\langle n_p^{\text{part}} \rangle$	expt	2.304 ± 0.007	6.643 ± 0.016	11.02 ± 0.03	10.06 ± 0.09
	model	2.325 ± 0.008	6.693 ± 0.009	10.92 ± 0.02	9.68 ± 0.05
$\langle n \rangle_{\text{str}}^{Z=1}$	expt	1.092 ± 0.007	1.440 ± 0.014	0.98 ± 0.02	–
	model	1.577 ± 0.011	2.038 ± 0.009	1.17 ± 0.02	–
$\langle n \rangle_{\text{str}}^{Z \ge 2}$	expt	1.205 ± 0.004	0.565 ± 0.014	0.119 ± 0.024	–
	model	0.819 ± 0.003	0.218 ± 0.003	0.012 ± 0.002	–

Note: The momentum values are given here in GeV/c units; the model values were computed by using the FRITIOF code.

positive pions in peripheral and central ($n_p^{\text{part}} > 9$) CC interactions lead to different dependences of $\langle n_{\pi^-} \rangle$ and $\langle n_{\pi^+} \rangle$ on the degree of centrality (see Table 2).

From Table 2, it can be seen that, upon going over from $n_p^{\text{part}} < 4$ to $n_p^{\text{part}} > 9$ CC events, there is a modest decrease (of about 10%) in the yield of charged pions per participant proton. With decreasing impact parameter, the mean number of participant protons both from the projectile and from the target nucleus naturally increases; accordingly, the multiplicity of the stripping fragments of the projectile nucleus and the multiplicity of evaporated protons ($p_p < 0.3$ GeV/c) from the target nucleus both decrease, which is associated predominantly with protons of momenta less than 0.15 GeV/c (see Table 1 and Figs. 3, 4). The mean number of $p < 0.15$ GeV/c protons was estimated by the missing charge in an event (see Table 1). It should be noted that the

Table 2. Relative multiplicities of negative and positive pions from CC interactions characterized by various numbers of participant protons

		Event type			
		$n_p^{\text{part}} \le 4$	$4 < n_p^{\text{part}} \le 9$	$n_p^{\text{part}} > 9$	$Q_{\text{str}} = 0$
$\dfrac{\langle n_{\pi^-}\rangle}{\langle n_p^{\text{part}}\rangle}$	expt	0.312 ± 0.003	0.326 ± 0.003	0.363 ± 0.004	0.314 ± 0.007
	model	0.296 ± 0.002	0.249 ± 0.002	0.290 ± 0.003	0.239 ± 0.004
$\dfrac{\langle n_{\pi^+}\rangle}{\langle n_p^{\text{part}}\rangle}$	expt	0.385 ± 0.003	0.321 ± 0.003	0.263 ± 0.004	0.329 ± 0.008
	model	0.384 ± 0.003	0.245 ± 0.002	0.179 ± 0.003	0.267 ± 0.006
$\dfrac{\langle n_{\pi^+}\rangle + \langle n_{\pi^-}\rangle}{\langle n_p^{\text{part}}\rangle}$	expt	0.697 ± 0.004	0.647 ± 0.004	0.626 ± 0.006	0.643 ± 0.010
	model	0.680 ± 0.004	0.494 ± 0.003	0.469 ± 0.004	0.506 ± 0.007

Note: The model values were computed by using the FRITIOF code.

mean multiplicity of participant protons grows more slowly in the subgroup where the proton momentum ranges between 0.3 and 0.75 GeV/c than in the $p > 0.75$ GeV/c subgroup (see Table 1). An analysis of experimental data revealed that, in collisions with nucleons of the projectile nucleus, the momentum transfer to part (40–50%) of the participant protons of the target nucleus is high; as a result, such participant protons occur in the $p > 0.75$ GeV/c subgroup. It follows that the mean number of participant protons whose momenta are in excess of 0.75 GeV/c increases considerably in central interactions (see Table 1).

A comparison of the mean particle multiplicities in the $n_p^{\text{part}} > 9$ and $Q_{\text{str}} = 0$ groups of CC interactions reveals that $n_p^{\text{part}} > 9$ events are characterized by a higher multiplicity of charged secondaries, a significantly lower mean multiplicity of protons from the evaporation process, and the presence of stripping fragments of the projectile nucleus (see Table 1).

By definition, all six protons of the carbon nucleus interact with the target in $Q_{\text{str}} = 0$ events; on average, 4.2 protons of the target nucleus are involved in the interaction in this case. In $n_p^{\text{part}} > 9$ events, these numbers are 4.78 ± 0.03 and 5.13 ± 0.10, respectively. They were obtained by using data from Table 1 on the mean multiplicities of stripping particles and protons from the evaporation process. We can get a clear idea of the features of two types of central CC interactions (those where $n_p^{\text{part}} > 9$ and those where $Q_{\text{str}} = 0$) by inspecting Figs. 3c and 3d. In these groups of events, the mean multiplicities of participant protons are quite close (the distinction is about 10% here; see Table 1), but their distributions in n_p^{part} are quite different. By virtue of the selection criterion, $n_p^{\text{part}} > 9$ events are concentrated in a narrow interval in n_p^{part}; at the same time, the n_p^{part} distribution of $Q_{\text{str}} = 0$ events is rather broad (see Fig. 3d). In all probability, proton–neutron interactions ($pn \to pnX$) and proton-charge-exchange interactions ($pn \to nn\pi^+$) play a significant role in $Q_{\text{str}} = 0$ events. This can explain the emergence of $n_p^{\text{part}} < 9$ events in the interaction of six protons from the projectile carbon nucleus with a carbon target. From the comparison performed in the present study, we can conclude that,

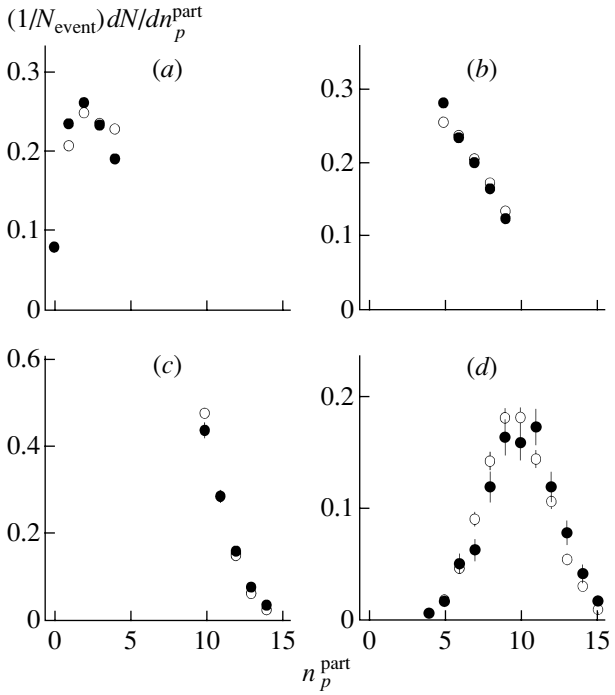

Fig. 3. Distributions of events of CC interactions with respect to the multiplicity of participant protons. The notation is identical to that in Fig. 1.

in the $n_p^{\text{part}} > 9$ and the $Q_{\text{str}} = 0$ subgroup of events, the degrees of centrality of CC interactions are approximately equal.

A comparison of experimental data on the multiplicity of secondaries with the results of the calculations based on the FRITIOF model shows that this model reproduces satisfactorily (the discrepancy is not more than 10%) the mean multiplicities of all charged particles, participant protons, and protons from the evaporation process ($p < 0.3$ GeV/c) in all CC-interaction groups analyzed here (see Table 1 and Figs. 1, 3). The greatest discrepancy between experimental data and the results of the model calculations is observed in comparing the multiplicities of pions and evaporation protons in the $p < 0.15$ GeV/c and $0.15 \le p < 0.3$ GeV/c subgroups. The momentum spectrum of evaporated protons that was computed on the basis of the FRITIOF model is softer than the corresponding experimental spectrum (see Table 1 and Figs. 2, 4).

In relation to the preceding calculations reported in [11], we have somewhat lower multiplicities of product mesons because of the inclusion of elastic rescatterings. This decrease in the multiplicity of mesons entails a decrease in the total multiplicity of charged particles. Within the phenomenological approach underlying the cascade–evaporation model, it is rather difficult to improve the description of the interactions in question. In the Glauber–Sitenko theory of multiple scattering, there is unfortunately no consistent procedure for taking into account elastic rescatterings in inelastic nuclear–nuclear interactions. At the same time, the description of the multiplicity of participant protons has been considerably improved. The discrepancy between the results of the calculations and experimental data on the multiplicity of evaporated protons with momenta of 0.15 to 0.3 GeV/c and of stripping protons and multiply charged fragments of the projectile nucleus ($\langle n \rangle^{Z=1}$ and $\langle n \rangle^{Z\ge 2}$, respectively) stems from the use of the evaporation model. As a rule, the evaporation model yields many singly charged fragments and one multiply charged fragment. In order to improve the description of experimental data, it is necessary to take into account nuclear multifragmentation. This is also suggested by the relationship between the multiplicities of stripping protons and multiply charged fragments. The model used here overestimates the multiplicity of stripping protons and the multiplicity of protons whose momenta are below 0.15 GeV/c.

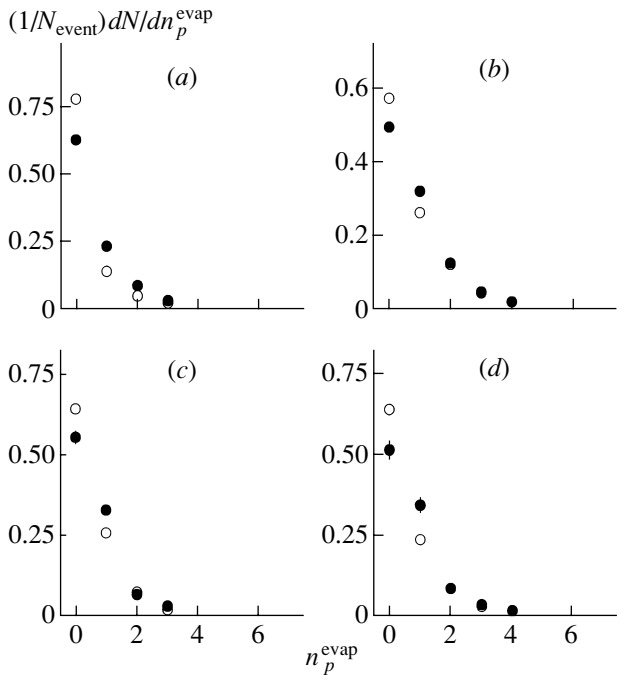

Fig. 4. Distributions of events of CC interactions with respect to the number of protons originating from the evaporation process and having momenta between 0.15 and 0.3 GeV/c. The notation is identical to that in Fig. 1.

For CC interactions studied here, a comparative analysis of the momentum and angular features of secondaries versus the collision-centrality degree as determined from the number of participant protons revealed that, for negative pions, these features are virtually independent of the impact parameter. By way of example, we indicate that, upon going over from peripheral to central interactions, the mean momenta of negative pions and their transverse momenta and emission angles change within 5% (see Table 3). The shape of the corresponding distributions does not change either (Figs. 5, 6). The above features of negative pions behave in this way only in the case of interactions of symmetric nuclei [13, 14, 20]. It is noteworthy that, in the transverse-momentum distributions of negative pions, there is a deviation from an exponential dependence in the region $p_T^{\pi^-} > 1$ GeV/c. This feature is observed in all subgroups of CC interactions (see Fig. 6).

The situation for protons is different. An increase in the degree of centrality of CC interactions leads to an increase in the mean values of the total and the transverse momentum of participant protons (see Table 3) and to significant changes in their rapidity (y) and transverse-momentum (p_T) distributions (see Figs. 7, 8). In peripheral collisions ($n_p^{\text{part}} \le 4$), the rapidity distribution of participant protons has a pronounced two-peak structure caused by the contribution of protons originating from the fragmentation of the projectile and the target nucleus (see Fig. 7*a*). The two-peak structure is less spectacular

Table 3. Mean values of the variables p, p_T, and θ (the θ values are given in degrees) for secondary particles from CC interactions characterized by various numbers of participant protons

		Event type			
		$n_p^{\text{part}} \le 4$	$4 < n_p^{\text{part}} \le 9$	$n_p^{\text{part}} > 9$	$Q_{\text{str}} = 0$
$\langle p_{\pi^-} \rangle$	expt	0.593 ± 0.005	0.588 ± 0.004	0.599 ± 0.007	0.628 ± 0.011
	model	0.617 ± 0.004	0.616 ± 0.003	0.626 ± 0.004	0.636 ± 0.007
$\langle p_T^{\pi^-} \rangle$	expt	0.238 ± 0.001	0.240 ± 0.001	0.248 ± 0.002	0.243 ± 0.004
	model	0.249 ± 0.001	0.253 ± 0.001	0.259 ± 0.001	0.256 ± 0.002
$\langle \theta_{\pi^-} \rangle$	expt	41.3 ± 0.3	40.9 ± 0.3	40.7 ± 0.4	37.7 ± 0.6
	model	39.4 ± 0.2	39.4 ± 0.2	39.0 ± 0.3	37.4 ± 0.4
$\langle p_p^{\text{part}} \rangle$	expt	1.802 ± 0.006	1.886 ± 0.006	1.866 ± 0.011	2.084 ± 0.019
	model	1.935 ± 0.006	1.961 ± 0.004	1.951 ± 0.006	2.308 ± 0.010
$\langle p_T^{\text{part}} \rangle$	expt	0.446 ± 0.001	0.484 ± 0.001	0.504 ± 0.002	0.516 ± 0.004
	model	0.498 ± 0.001	0.513 ± 0.001	0.525 ± 0.001	0.526 ± 0.002
$\langle \theta_p^{\text{part}} \rangle$	expt	28.7 ± 0.1	27.2 ± 0.1	26.5 ± 0.2	23.2 ± 0.3
	model	30.6 ± 0.1	30.85 ± 0.08	28.94 ± 0.13	24.0 ± 0.2
$\langle p_p \rangle$, $0.3 \le p_p < 0.75$	expt	0.481 ± 0.001	0.494 ± 0.001	0.509 ± 0.002	0.513 ± 0.004
	model	0.508 ± 0.001	0.503 ± 0.001	0.509 ± 0.001	0.515 ± 0.002
$\langle p_T^p \rangle$, $0.3 \le p_p < 0.75$	expt	0.326 ± 0.001	0.331 ± 0.001	0.333 ± 0.002	0.330 ± 0.004
	model	0.378 ± 0.001	0.378 ± 0.001	0.374 ± 0.002	0.376 ± 0.002
$\langle \theta_p \rangle$, $0.3 \le p_p < 0.75$	expt	55.0 ± 0.2	54.0 ± 0.2	51.6 ± 0.4	49.1 ± 0.8
	model	65.5 ± 0.3	65.8 ± 0.2	62.4 ± 0.3	61.2 ± 0.5
$\langle p_p \rangle$, $p_p \ge 0.75$	expt	2.399 ± 0.007	2.372 ± 0.008	2.287 ± 0.012	2.453 ± 0.020
	model	2.445 ± 0.006	2.471 ± 0.004	2.375 ± 0.007	2.664 ± 0.010
$\langle p_T^p \rangle$, $p_p \ge 0.75$	expt	0.500 ± 0.002	0.537 ± 0.002	0.557 ± 0.003	0.560 ± 0.005
	model	0.541 ± 0.001	0.561 ± 0.001	0.570 ± 0.002	0.556 ± 0.002
$\langle \theta_p \rangle$, $p_p \ge 0.75$	expt	16.8 ± 0.1	17.9 ± 0.1	18.7 ± 0.2	17.0 ± 0.2
	model	18.13 ± 0.8	18.62 ± 0.05	19.11 ± 0.08	16.6 ± 0.1

Note: The momentum values are given here in GeV/c units; the model values were computed by using the FRITIOF code.

in the group of $4 < n_p^{\text{part}} \le 9$ events (see Fig. 7*b*); in central events ($n_p^{\text{part}} > 9$ and $Q_{\text{str}} = 0$), it disappears completely, giving way to a broad plateau in the central rapidity region (see Figs. 7*c*, 7*d*). The latter is indicative of the increasing contribution of secondary interactions in colliding carbon nuclei. The asymmetry of the rapidity distribution in Fig. 7 is partly due to a small (10–15%) admixture of deuterons, which shift the spectrum toward the region of high rapidities if they are assigned the proton mass. The distinction between the multiplicities of interacting protons from the projectile and from the target nucleus (see

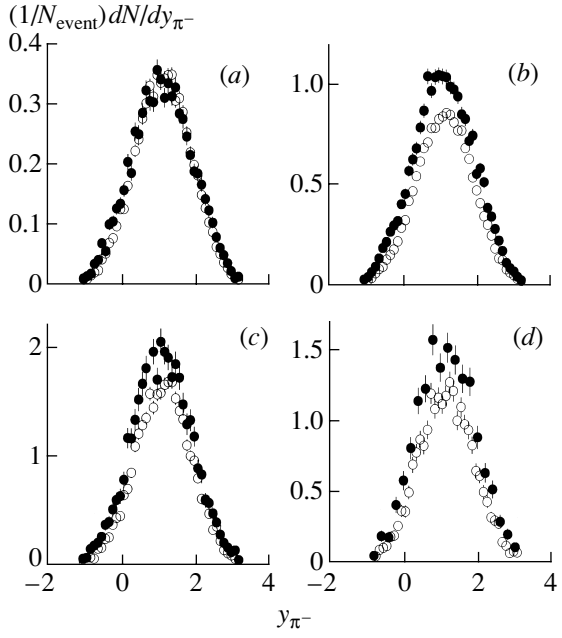

Fig. 5. Rapidity distributions of negative pions in CC interactions characterized by various degrees of centrality. The notation is identical to that in Fig. 1.

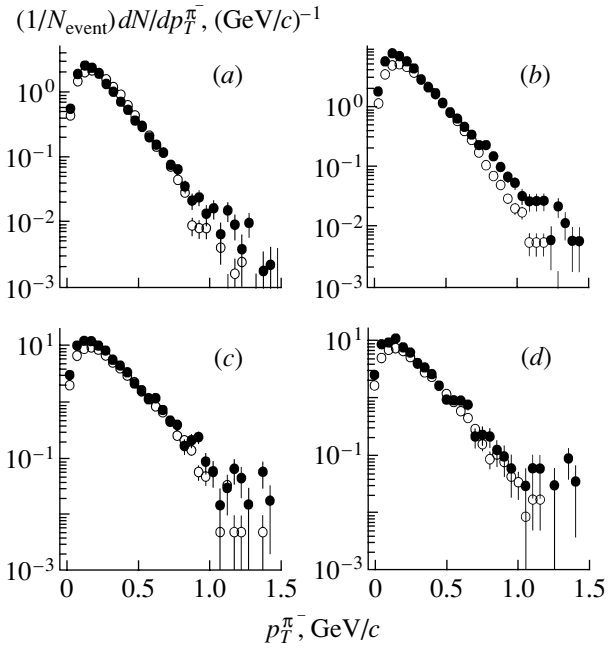

Fig. 6. Transverse-momentum distributions of negative pions. The notation is identical to that in Fig. 1.

Fig. 7*d*) is also operative. It can be seen from Fig. 8 that, in central interactions, the fraction of protons having high transverse momenta ($p_T > 1$ GeV/c) increases, which is manifested in an increase in the mean values of p_T (see Table 3).

It is of interest to trace the behavior of the angular and momentum distributions of participant protons in various momentum intervals versus the degree of collision centrality. In the case being considered, we analyze the distributions of protons having momenta in the range between 0.3 and 0.75 GeV/c (these are predominantly target fragments) and in the region $p > 0.75$ GeV/c (these are predominantly projectile fragments) (see Figs. 9–11). As the number of participant protons in an event grows, we observe a slight increase in the mean momenta and a decrease in the mean emission angles $\langle\theta\rangle$ for protons of momenta in the range $0.3 \leq p < 0.75$ GeV/c. At the same time, the mean transverse momenta of the protons remain unchanged (see Table 3). The transverse-momentum and angular distributions of protons from this group are displayed in Figs. 10 and 11, respectively. For $p > 0.75$ GeV/c protons, the transverse momentum grows with decreasing impact parameter (see Table 3 and Fig. 9). Thus, an increase in the fraction of participant protons with high transverse momenta in central interactions is due to $p > 0.75$ GeV/c protons, whose fraction amounts to 76% (80%) in $n_p^{\text{part}} > 9$ ($Q_{\text{str}} = 0$) events.

Presented in Figs. 5–11 are the results of our FRITIOF calculations for the angular and momentum features of negative pions and participant protons from carbon–carbon interactions. It can be seen that the experimental rapidity distributions of negative pi-

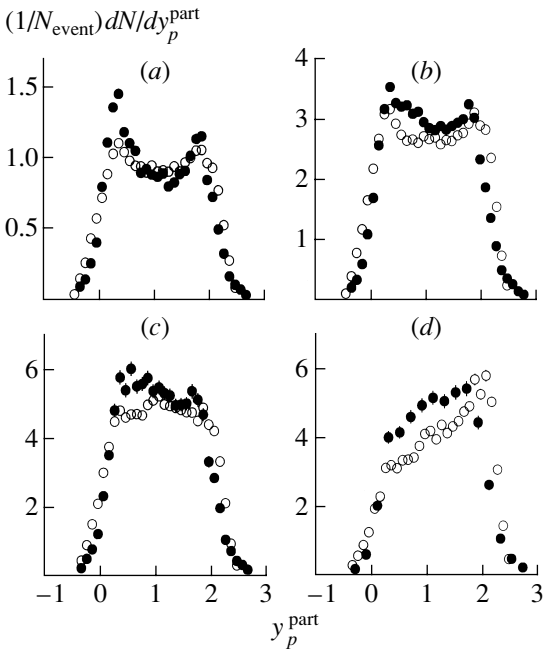

Fig. 7. Rapidity distributions of participant protons. The notation is identical to that in Fig. 1.

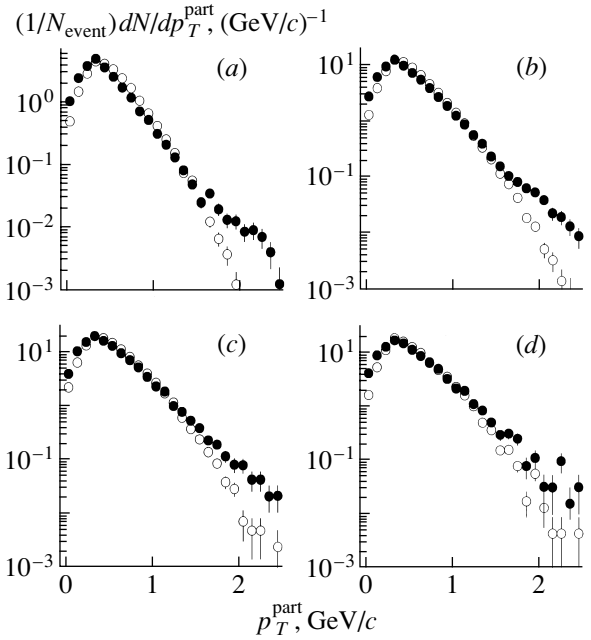

Fig. 8. Transverse-momentum distributions of participant protons. The notation is identical to that in Fig. 1.

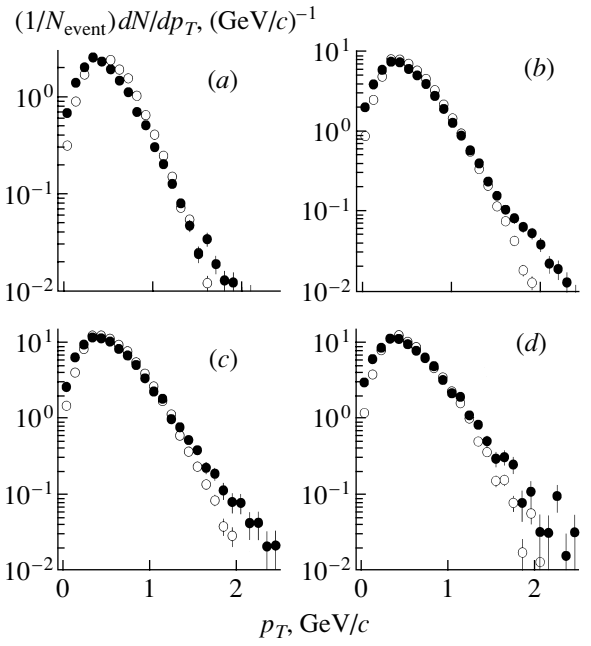

Fig. 9. Transverse-momentum distributions of protons with momenta in excess of 0.75 GeV/c. The notation is identical to that in Fig. 1.

ons from peripheral interactions are faithfully reproduced (Fig. 5*a*) and that the theoretical predictions for the rapidity distributions of negative pions from other subgroups deviate considerably from the corresponding experimental distributions (Figs. 5*b*–5*d*), because the multiplicity of negative pions is underestimated in these subgroups. The model description of the transverse-momentum distributions of negative pions is quite satisfactory (Fig. 6).

The most interesting distribution is that of participant protons with respect to the rapidity y (Fig. 7). According to the model underlying our calculations, the peaks at $y \sim 0.2$ and $y \sim 1.8$ are largely due to elastically scattered protons. The distributions of protons involved in inelastic interactions do not display such peaks. The contribution of elastically scattered protons decreases with increasing degree of collision centrality. They take virtually no part in central interactions. The peaks from elastically scattered protons or from protons involved in secondary interactions are present in the results of cascade calculations (see [7]). It should be noted that the shape of experimental and the shape of calculated distributions undergo virtually no changes in the regions around $y \sim 0$ and $y \sim 2$. In the calculations based on the cascade–evaporation model, the spectra of protons in the region around $y \sim 0$ ($y \sim 2$) undergo an ever increasing shift toward negative (positive) rapidity values as the degree of collision centrality becomes higher. Therefore, investigation of the proton yields in the regions of nuclear fragmentation for interactions that occurs at various degrees of collision centrality can furnish valuable information about the mechanism of nuclear breakup.

The model used provides a satisfactory description of the transverse-momentum distributions of partic-

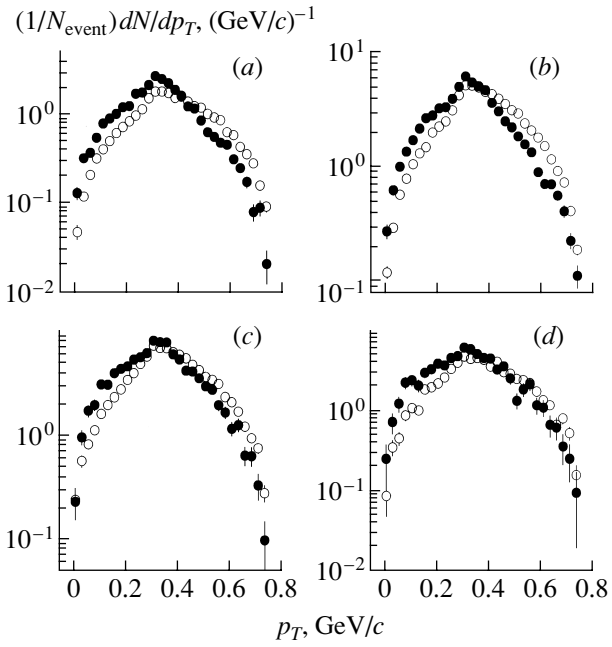

Fig. 10. Transverse-momentum distributions of protons in the range 0.3–0.75 GeV/c. The notation is identical to that in Fig. 1.

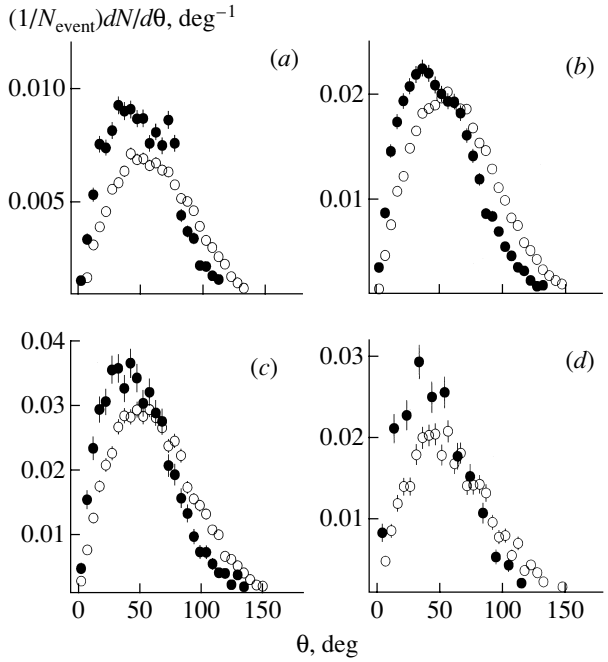

Fig. 11. Angular distributions of protons with momenta in the range 0.3–0.75 GeV/c. The notation is identical to that in Fig. 1.

ipant protons in the range 0.2–1.5 GeV/c. A glaring discrepancy between the model and the experiment is observed in the region of higher transverse-momentum values (see Fig. 8).

The model reproduces best of all the transverse-momentum distribution of participant protons with momenta in excess of 0.75 GeV/c from peripheral interactions (Fig. 9a). In other subgroups ($4 < n_p^{\text{part}} \leq 9$ and $n_p^{\text{part}} > 9$), there are discrepancies at high transverse-momentum values.

The properties of slower protons are described by the model less satisfactorily. From Table 3 and from Fig. 10, it can be seen that the model overestimates the mean transverse momenta of $0.3 \leq p < 0.75$ GeV/c protons and underestimates their longitudinal momenta, with the result that proton emission angles prove to be overly large (see Fig. 11). Since $0.3 \leq p < 0.75$ GeV/c protons constitute only one-third of participant protons, the discrepancy between the experimental and the calculated values is less spectacular in their total distributions.

4. CONCLUSIONS

(i) New experimental data on the features of pions and protons from CC interactions at a momentum of 4.2 GeV/c per nucleon that are characterized by various degrees of collision centrality have been presented.

(ii) It has been shown that the mean kinematical features of mesons are weakly dependent on the degree of collision centrality.

(iii) With increasing degree of collision centrality, the angular and momentum features of protons participating in carbon–carbon interactions undergo the following variations: the shape of their rapidity distributions changes substantially, and the fraction of protons of high transverse momenta increases.

(iv) The FRITIOF model modified by taking into account elastic rescatterings reproduces satisfactorily the experimental features of mesons and participant protons in all groups of events considered here. The multiplicities of slow protons from the evaporation process are described poorly because of the use of the evaporation model for simulating the deexcitation of residual nuclei.

(v) In order to refine the model further, it is necessary to take into account nuclear-multifragmentation processes.

ACKNOWLEDGMENTS

We are grateful to the members of a collaboration involved in investigations with the 2-m propane bubble chamber at JINR for obtaining experimental data used in our study, to technicians for scanning relevant films and for measuring events of CC interactions, and to Yu. Karachuk for assistance in processing experimental data.

REFERENCES

1. V. S. Barashenkov and V. D. Toneev, *Interactions of High-Energy Particles and Nuclei with Nuclei* (Atomizdat, Moscow, 1972).
2. N. W. Bertini *et al.*, Phys. Rev. C **9**, 522 (1974); **14**, 590 (1976); J. P. Bondorf *et al.*, Phys. Lett. B **65B**, 217 (1976); Z. Phys. A **279**, 385 (1976); V. D. Toneev and K. K. Gudima, Nucl. Phys. A **400**, 173 (1982).
3. B. Andersson *et al.*, Nucl. Phys. B **281**, 289 (1987); B. Nilsson-Almquist and E. Stenlund, Comput. Phys. Commun. **43**, 387 (1987).
4. H. Sorge, H. Stöker, and W. Greiner, Ann. Phys. (N.Y.) **192**, 260 (1989); Nucl. Phys. A **498**, 567c (1989); H. Sorge, A. von Keitz, R. Mattiello, *et al.*, Z. Phys. C **47**, 629 (1990); H. Sorge, L. A. Winckelmann, H. Stöker, and W. Greiner, Z. Phys. C **59**, 85 (1993).
5. M. Gyulassy and M. Plumer, Phys. Lett. B **243**, 432 (1990); X.-N. Wang and M. Gyulassy, Phys. Rev. D **44**, 3501 (1991).
6. K. G. Boreskov, A. B. Kaĭdalov, S. M. Kiselev, and N. Ya. Smorodinskaya, Yad. Fiz. **53**, 569 (1991) [Sov. J. Nucl. Phys. **53**, 356 (1991)].
7. Lj. Simic *et al.*, Phys. Rev. C **37**, 2064 (1988).
8. Kh. El-Waged and V. V. Uzhinsky, Yad. Fiz. **60**, 925 (1997) [Phys. At. Nucl. **60**, 828 (1997)].

9. EMU-01 Collab. (M. I. Adamovich *et al.*), Z. Phys. A **358**, 337 (1997).
10. V. V. Uzhinskii, Preprint No. E2-96-192, OIYaI (Joint Inst. for Nuclear Research, Dubna, 1996).
11. Ts. Baatar *et al.*, Preprint No. R1-99-45, OIYaI (Joint Inst. for Nuclear Research, Dubna, 1999); Yad. Fiz. **63**, 909 (2000) [Phys. At. Nucl. **63**, 839 (2000)].
12. B. Gankhuyag and V. V. Uzhinskii, Soobshch. Ob'edin. Inst. Yad. Issled., No. R1-97-315, No. R2-97-397 (Dubna, 1997); B. Gankhuyag, Soobshch. Ob'edin. Inst. Yad. Issled., No. R2-98-26 (Dubna, 1998).
13. Lj. Simic *et al.*, Phys. Rev. D **34**, 692 (1986).
14. Lj. Simic *et al.*, Z. Phys. C **48**, 577 (1990).
15. G. N. Agakishiev *et al.*, Yad. Fiz. **51**, 758 (1990) [Sov. J. Nucl. Phys. **51**, 481 (1990)].
16. Lj. Simic *et al.*, Phys. Rev. C **52**, 356 (1995).
17. A. I. Bondarenko *et al.*, Soobshch. Ob'edin. Inst. Yad. Issled., No. R1-98-292 (Dubna, 1998).
18. A. U. Abdurakhimov *et al.*, Nucl. Phys. A **362**, 376 (1981).
19. V. Boldea, A. P. Gasparyan, V. G. Grishin, *et al.*, Yad. Fiz. **44**, 149 (1986) [Sov. J. Nucl. Phys. **44**, 94 (1986)].
20. M. Anikina *et al.*, Phys. Rev. C **33**, 895 (1986).
21. SKM-200 Collab. (M. Kh. Anikina *et al.*), Yad. Fiz. **45**, 1680 (1987) [Sov. J. Nucl. Phys. **45**, 1040 (1987)].
22. A. Sandoval *et al.*, Phys. Rev. Lett. **45**, 874 (1980).
23. V. V. Uzhinskii and A. S. Pak, Yad. Fiz. **59**, 1109 (1996).
24. S. Yu. Shmakov, V. V. Uzhinskii, and A. M. Zadorojny, Comput. Phys. Commun. **54**, 125 (1989).
25. A. Y. Abul-Magd, W. A. Friedman, and J. Hufner, Phys. Rev. C **34**, 113 (1986).
26. V. Weisskopf, Phys. Rev. **52**, 295 (1937).
27. S. Yu. Shmakov, N. V. Slavin, and V. V. Uzhinskii, Preprint No. E2-88-792, OIYaI (Joint Inst. for Nuclear Research, Dubna, 1988).

Translated by A. Isaakyan